



Understanding the drivers of recent Southern Ocean sea ice and surface temperature trends

Ariaan Purich

June 2018

Supervised by Prof. Matthew H. England and Dr Wenju Cai

Climate Change Research Centre
School of Biological, Earth and Environmental Sciences
Faculty of Science
University of New South Wales

A thesis submitted in fulfillment of the requirements for the degree of
Doctor of Philosophy

THE UNIVERSITY OF NEW SOUTH WALES
Thesis/Dissertation Sheet

Surname or Family name: Purich

First name: Ariaan

Other name/s: Fiamma

Abbreviation for degree as given in the University calendar: PhD

School: Biological, Earth and Environmental Sciences

Faculty: Science

Title: Understanding the drivers of recent Southern Ocean sea ice and surface temperature trends

Abstract 350 words maximum: (PLEASE TYPE)

Antarctic sea ice plays a critical role in modulating global climate, influencing surface albedo, air-sea carbon fluxes and the global ocean overturning circulation. Despite global warming, overall Antarctic sea ice extent increased during 1979–2013, however the majority of Coupled Model Intercomparison Project phase five (CMIP5) models simulate a decline, and mechanisms causing this discrepancy remained elusive. Here I show that weaker westerly-wind jet intensification trends simulated by CMIP5 models may contribute to the disparity. During austral summer a strengthened jet increases upwelling of cooler subsurface water and strengthens equatorward transport, conducive to increased sea ice. This cooling process is underestimated in the majority of models and is insufficient to offset global warming. Through the sea ice-albedo feedback, models produce a high-latitude surface warming and sea-ice decline, contrasting observations. A realistic simulation of observed wind changes may be crucial for reproducing observed sea ice trends.

A strengthened Amundsen Sea Low has also been shown to largely explain the recent sea ice increase in the Ross Sea and decrease in the Bellingshausen Sea. While these changes are not generally seen in CMIP5 simulations, I show they can be reproduced in simulations of two independent coupled climate models constrained by observed tropical variability. I further show that the phase change in the Interdecadal Pacific Oscillation from positive to negative over 1979–2013 likely contributed to the strengthened Amundsen Sea Low and pattern of sea ice trends, highlighting the importance of accounting for teleconnections from low to high latitudes.

The Southern Ocean surface freshened in recent decades, yet CMIP5 models underestimate this. I demonstrate that imposing a broad-scale surface freshening to the Southern Ocean in global coupled climate model experiments causes a surface cooling and sea-ice increase, due to reduced ocean convection and weakened entrainment of warm subsurface waters to the surface. Additional experiments with surface salinity restoration applied to capture observed regional salinity trends accurately represent the spatial pattern of surface temperature and sea-ice trends around Antarctica. These results highlight the importance of accurately simulating changes in Southern Ocean precipitation, meltwater and salinity to capture changes in ocean circulation, surface temperature and sea ice.

Declaration relating to disposition of project thesis/dissertation

I hereby grant to the University of New South Wales or its agents the right to archive and to make available my thesis or dissertation in whole or in part in the University libraries in all forms of media, now or here after known, subject to the provisions of the Copyright Act 1968. I retain all property rights, such as patent rights. I also retain the right to use in future works (such as articles or books) all or part of this thesis or dissertation.

I also authorise University Microfilms to use the 350 word abstract of my thesis in Dissertation Abstracts International (this is applicable to doctoral theses only).

Signature

Witness Signature

18 / 06 / 2018

Date


The University recognises that there may be exceptional circumstances requiring restrictions on copying or conditions on use. Requests for restriction for a period of up to 2 years must be made in writing. Requests for a longer period of restriction may be considered in exceptional circumstances and require the approval of the Dean of Graduate Research.

FOR OFFICE USE ONLY

Date of completion of requirements for Award:

Originality Statement

I hereby declare that this submission is my own work and to the best of my knowledge it contains no materials previously published or written by another person, or substantial proportions of material which have been accepted for the award of any other degree or diploma at UNSW or any other educational institution, except where due acknowledgment is made in the thesis. Any contribution made to the research by others, with whom I have worked at UNSW or elsewhere, is explicitly acknowledged in the thesis. I also declare that the intellectual content of this thesis is the product of my own work, except to the extent that assistance from others in the project's design and conception or in style, presentation and linguistic expression is acknowledged.

Signed: 

Date: 18 / 06 / 2018

Copyright Statement


I hereby grant to the University of New South Wales or its agents the right to archive and to make available my thesis or dissertation in whole or part in the University libraries in all forms of media, now or hereafter known, subject to the provisions of the Copyright Act 1968. I retain all proprietary rights, such as patent rights. I also retain the right to use in future works (such as articles or books) all or part of this thesis or dissertation. I also authorise University Microfilms to use the abstract of my thesis in Dissertations Abstract International (this is applicable to doctoral theses only). I have either used no substantial portions of copyright material in my thesis or I have obtained permission to use copyright material; where permission has not been granted I have applied/will apply for a partial restriction of the digital copy of my thesis or dissertation.

Signed: 

Date: 18 / 06 / 2018

Authenticity Statement

I certify that the Library deposit digital copy is a direct equivalent of the final officially approved version of my thesis. No emendation of content has occurred and if there are any minor variations in formatting, they are the result of the conversion to digital format.

Signed: 

Date: 18 / 06 / 2018

Abstract

Antarctic sea ice plays a critical role in modulating global climate, influencing surface albedo, air-sea carbon fluxes and the global ocean overturning circulation. Despite global warming, overall Antarctic sea ice extent increased during 1979–2013, however the majority of Coupled Model Intercomparison Project phase five (CMIP5) models simulate a decline, and mechanisms causing this discrepancy remained elusive. Here I show that weaker westerly-wind jet intensification trends simulated by CMIP5 models may contribute to the disparity. During austral summer a strengthened jet increases upwelling of cooler subsurface water and strengthens equatorward transport, conducive to increased sea ice. This cooling process is underestimated in the majority of models and is insufficient to offset global warming. Through the sea ice-albedo feedback, models produce a high-latitude surface warming and sea-ice decline, contrasting observations. A realistic simulation of observed wind changes may be crucial for reproducing observed sea ice trends.

A strengthened Amundsen Sea Low has also been shown to largely explain the recent sea ice increase in the Ross Sea and decrease in the Bellingshausen Sea. While these changes are not generally seen in CMIP5 simulations, I show they can be reproduced in simulations of two independent coupled climate models constrained by observed tropical variability. I further show that the phase change in the Interdecadal Pacific Oscillation from positive to negative over 1979–2013 likely contributed to the strengthened Amundsen Sea Low and pattern of sea ice trends, highlighting the importance of accounting for teleconnections from low to high latitudes.

The Southern Ocean surface freshened in recent decades, yet CMIP5 models underestimate this. I demonstrate that imposing a broad-scale surface freshening to the Southern Ocean in global coupled climate model experiments causes a surface cooling and sea-ice increase, due to reduced ocean convection and weakened entrainment of warm subsurface waters to the surface. Additional experiments with surface salinity restoration applied to capture observed regional salinity trends accurately represent the spatial pattern of surface temperature and sea-ice trends around Antarctica. These results highlight the importance of accurately simulating changes in Southern Ocean precipitation, meltwater and salinity to capture changes in ocean circulation, surface temperature and sea ice.

Acknowledgments

First and foremost, I acknowledge the contributions from both of my supervisors, Matthew England and Wenju Cai. It has been such a privilege to be supervised by Matt and Cai, and I have learnt so much along the way. Matt has shown such enthusiasm for my project that whenever I ran into a problem or lull, conversations with him would reinvigorate my research. Matt also spent two years encouraging me to run climate model experiments, and despite my hesitance, learning how to run a model is one of the most important skills I have gained during my PhD, so I am very grateful for his persistence. Cai has always been very supportive and generous with his time, both when I worked with him as a support scientist at CSIRO and during my PhD candidature. It is largely thanks to Cai's supervision that I have matured so much as a researcher during the past six years, and that I have learnt the importance of story telling in science. Both Matt and Cai's guidance throughout this project has been invaluable and greatly appreciated.

I also acknowledge the contributions from a number of coauthors. Tim Cowan helped with data analysis and the development of ideas in Part 1. Yoshi Chikamoto and John Fyfe provided data from pacemaker experiments and contributed to the development of ideas in Part 2. Axel Timmermann, Leela Frankcombe, Jerry Meehl and Julie Arblaster contributed to the development of ideas in Part 2. Arnold Sullivan was hugely helpful in teaching me how to run ACCESS1.0, and the model experiments in Part 3 would not have been possible without his guidance. Paul Durack provided dataset expertise and contributed to the development of ideas in Part 3.

Additional project input came from a number of others. Thanks to Ian Eisenmann for a discussion on which sea ice concentration dataset to use, Jean-Baptiste Sallée for providing me with his CMIP5 mixed layer depth dataset, Steve Rintoul for his photos of Antarctic sea ice, Nicola Maher for providing me with her CMIP5 IPO spatial patterns, Kaitlin Naughten for providing me with her CMIP5 Southern Ocean comparison metrics, Esteban Abellán for his assistance with thesis formatting, and the whole CMS team, especially Scott Wales, for their help with computing questions and running ACCESS1.0. Thanks also to John Fyfe, Will Hobbs and seven anonymous reviewers who provided helpful comments on the three manuscripts resulting from this research.

I extend my thanks to Tim Cowan for providing encouragement and support from both near and far, Peter van Rensch for many science and non-science related discussions, and Kaitlin Naughten for squeezing many months worth of conversation into a couple of days each Sydney visit and for making me feel truly part of the CCRC.

This research was undertaken with the assistance of resources and services from the National Computational Infrastructure (NCI), which is supported by the Australian Government. Figures were produced using the NCAR Command Language. I acknowledge the

ACKNOWLEDGMENTS

World Climate Research Programme's Working Group on Coupled Modelling, which is responsible for CMIP, and thank the climate modelling groups for producing and making available their model output.

I have been supported financially by an Australian Government Research Training Program scholarship, a UNSW Research Excellence scholarship, a CCRC scholarship, and a CSIRO Office of the Chief Executive Science Leader scholarship, for which I am extremely grateful. I also acknowledge financial assistance from the ARC Centre of Excellence for Climate System Science to attend the 2015 winter school, the 2016 and 2017 annual workshops, and for frequent trips to the CCRC in Sydney; and assistance from AMOS to attend the 2017 national conference.

Finally, thank you to my family and friends. Particular mention goes to my wonderful parents, whose constant love and support in all of my pursuits is so greatly appreciated. And lastly, all my love and thanks to Vaughn for his unwavering support and encouragement along my entire PhD journey, for learning enough about Antarctic sea ice to deserve an honorary degree in climate science, and for always being happy to forget about it all and go bushwalking; and to Adelie for being the most beautiful PhD distraction in the world.

Contents

Title	i
Originality Statement	iii
Copyright Statement	iv
Authenticity Statement	v
Abstract	vii
Acknowledgments	ix
Contents	xi
List of Figures	xv
List of Tables	xix
Nomenclature	xxi
Supporting Publications	xxv
Preface	1
Motivation and objectives	1
Background	2
Atmospheric circulation	2
Southern Ocean	5
Antarctic sea ice	6
Thesis overview	9
1 Evidence for link between modelled trends in Antarctic sea ice and under-estimated westerly wind changes	11
Abstract	12
1.1 Introduction	12
1.2 Data and methods	13
1.2.1 Data	13
1.2.2 Metrics	15
1.3 Results	16
1.3.1 Sea ice and SST spatial trends	16
1.3.2 Sea ice, SST and jet relationships	16
1.3.3 Wind-induced effects on SST	19

1.3.4	Timescales of Ekman response	22
1.3.5	Ekman contribution to observed-modelled disparity	23
1.3.6	Considering other mechanisms	23
1.4	Discussion	25
1.5	Supplementary material	27
1.5.1	Scale analysis	33
2	Tropical Pacific SST drivers of recent Antarctic sea ice trends	39
	Abstract	40
2.1	Introduction	40
2.2	Data and methods	42
2.2.1	Data and model experiments	42
2.2.2	Analysis methods	44
2.3	Results	47
2.3.1	Observed trends	47
2.3.2	Pacemaker trends	47
2.3.3	Seasonality of trends	52
2.3.4	IPO-related sea ice trends	53
2.3.5	IPO modulation of ENSO teleconnection	56
2.4	Discussion	58
2.5	Supplementary material	61
3	Impacts of broad-scale surface freshening of the Southern Ocean in a coupled climate model	73
	Abstract	74
3.1	Introduction	74
3.2	Data and methods	78
3.2.1	Model description	78
3.2.2	Experimental design	79
3.2.3	Observational and CMIP5 datasets	80
3.2.4	Data analysis	81
3.3	Results	83
3.3.1	Freshwater simulations	83
3.3.2	Further assessment of subsurface trends	87
3.3.3	Inter-model trend comparison	89
3.3.4	Salinity restoring simulations	92
3.4	Discussion	94
3.5	Supplementary material	97
	Concluding Remarks	98
	Summary of findings	109
	Part 1	109
	Part 2	110

Part 3	112
Recent Antarctic sea ice behaviour	113
Future perspectives	116
Decadal to interdecadal variability	116
El Niño-Southern Oscillation and Indian Ocean Dipole	117
Southern Annular Mode	118
Surface freshening	119
Regionality of sea ice trends	119
Final remark	120
Bibliography	121
Appendix A	139
Appendix B	149
Appendix C	168
Appendix D	190
Appendix E	201
Appendix F	213
Appendix G	228

List of Figures

P.1	Observed annual surface atmosphere trends over 1979–2013.	3
P.2	Schematic atmosphere-ocean response to the positive phase of the SAM. . .	4
P.3	Observed annual surface ocean trends over recent decades.	5
P.4	Observed and CMIP5 annual SIC trends over 1979–2013.	7
1.1	Annual SIC and SST trends over 1979–2013.	17
1.2	Trends in SIE versus trends in high-latitude SST over 1979–2013.	18
1.3	Trends in jet strength versus trends in high-latitude SST over 1979–2013. .	19
1.4	Potential temperature profiles and Ekman pumping trends over 1979–2013.	21
1.5	Schematic of decadal scale wind induced surface layer changes during summer.	26
1.6	Annual SIC trends for observations and models over 1979–2013.	29
1.7	Annual SST trends for observations and models over 1979–2013.	30
1.8	Interannual correlation coefficients between jet strength, high-latitude SST and SIE over 1979–2013.	31
1.9	Zonal-mean temperature versus latitude, and Ekman transport trends over 1979–2013.	32
1.10	DJF horizontal versus vertical mean-state temperature advection over 1979– 2013.	34
1.11	DJF trends in SST and downward total heat flux over 1979–2013.	35
1.12	Trends in downward total heat flux versus SST over 1979–2013.	36
1.13	DJF trends over 1979–2013 and mean-state salinity profiles.	37
1.14	DJF correlations between SST and Ekman pumping PCs for observations and models.	38
2.1	Trends in SST and MSLP, and time series of the IPO, Niño 3.4, Amundsen Sea Low and area-averaged SIC over 1979–2013.	45
2.2	SIC and MSLP trends over 1979–2013 with historical forcings removed. . .	48
2.3	As for Fig. 2.2, but showing total trends.	49
2.4	As for Fig. 2.2, but showing trends due to historical forcings.	50
2.5	As for Fig. 2.2, but showing trends from the CESM1 Atlantic assimilation.	51
2.6	SST and MSLP trends congruent with trends in the IPO due to its transition from positive to negative.	54
2.7	As for Fig. 2.6, but for SIC and MSLP trends congruent with trends in the IPO due to its transition from positive to negative.	55
2.8	Observed SIC and MSLP cumulative anomalies during different IPO phases.	57
2.9	As for Fig. 2.8, but showing cumulative anomalies during different ENSO phases.	58
2.10	CanESM2 mean-state SST and MSLP.	63
2.11	As for Fig. 2.2, but showing DJF SIC and MSLP trends.	64

LIST OF FIGURES

2.12	As for Fig. 2.2, but showing MAM SIC and MSLP trends.	65
2.13	As for Fig. 2.2, but showing JJA SIC and MSLP trends.	66
2.14	As for Fig. 2.2, but showing SON SIC and MSLP trends.	67
2.15	As for Fig. 2.4, but showing DJF SIC and MSLP trends.	68
2.16	As for Fig. 2.7, but for additional experiment ensembles.	69
2.17	As for Fig. 2.7, but showing DJF IPO-congruent trends.	70
2.18	As for Fig. 2.7, but showing MAM IPO-congruent trends.	70
2.19	As for Fig. 2.7, but showing JJA IPO-congruent trends.	71
2.20	As for Fig. 2.7, but showing SON IPO-congruent trends.	71
2.21	As for Fig. 2.8, but for linearly detrended SIC and MSLP time series. . . .	72
2.22	As for Fig. 2.9, but for linearly detrended SIC and MSLP time series. . . .	72
3.1	Trends in SSS, precipitation and P–E over 1950–2000.	76
3.2	Area-averaged trends in SSS over 50–60°S and 1950–2000.	78
3.3	Trends in SSS, SST and SIC for observations and ACCESS1.0 freshwater simulations.	84
3.4	Zonal-mean trends in salinity for observations, ACCESS1.0 freshwater simulations and the CMIP5 multi-model mean.	85
3.5	Zonal-mean trends in potential temperature for observations, ACCESS1.0 freshwater simulations and the CMIP5 multi-model mean.	86
3.6	Trends in potential temperature and water age for ACCESS1.0 freshwater simulations.	87
3.7	Trends in surface heat fluxes and mixed layer depth for ACCESS1.0 freshwater simulations.	88
3.8	Trend inter-relationships between SSS, SST and SIE for observations, ACCESS1.0 freshwater simulations and CMIP5 models.	90
3.9	Trends in SSS, SST and SIC for observations and ACCESS1.0 SSS restoring simulations.	93
3.10	As for Fig. 3.2, but showing all available ensemble members for each CMIP5 model.	99
3.11	Observed SSS trends from Durack and Wijffels (2010) and EN4.2.0.	99
3.12	Grid point SST trends versus grid point SSS trends for observations and ACCESS1.0 freshwater simulations.	100
3.13	Grid point potential temperature trends versus grid point water age trends for ACCESS1.0 freshwater simulations.	101
3.14	As for Fig. 3.3, but for DJF.	102
3.15	As for Fig. 3.3, but for JJA.	103
3.16	As for Fig. 3.8, but for DJF.	104
3.17	As for Fig. 3.8, but for JJA.	105
3.18	As for Fig. 3.8, but for 50-year annual-mean trends in ACCESS1.0 freshwater simulations and CMIP5 models.	106
3.19	SIC trends for observations, ACCESS1.0 freshwater simulations and the ACCESS1.0 CMIP5 simulation.	107

CR.1	Observed seasonal and annual SIE anomaly time series.	114
CR.2	Observed anomalies during 2016 SON.	115
D.1	Surface trends in SSS, SST and SIC from observations and ACCESS1.0 historical simulations.	195
D.2	Zonal-mean trends in salinity and temperature from observations and AC- CESS1.0 historical simulations.	197
D.3	Sector trends in salinity and temperature from observations and ACCESS1.0 historical simulations.	198
D.4	MOC mean-state and trends from ACCESS1.0 historical simulations. . . .	200

List of Tables

1.1	Inter-model correlation coefficients between trends over 1979–2013.	27
1.2	Interannual correlation coefficients between seasonal metrics over 1979–2013.	28
1.3	Additional inter-model correlation coefficients between trends over 1979–2013.	28
2.1	CMIP5 models used in Part 2 and their expansions.	61
3.1	CMIP5 models used in Part 3 and their expansions.	97

Nomenclature

General abbreviations

AABW	Antarctic Bottom Water
ACC	Antarctic Circumpolar Current
CDW	Circumpolar Deep Water
DJF	December-January-February
ENSO	El Niño-Southern Oscillation
EOF	Empirical orthogonal function
IOD	Indian Ocean Dipole
IPO	Interdecadal Pacific Oscillation
JJA	June-July-August
MAM	March-April-May
MMM	Multi-model mean
MOC	Meridional Overturning Circulation
MSLP	Mean sea level pressure
PC	Principal component
P-E	Precipitation minus evaporation
PSA	Pacific South American
SAM	Southern Annular Mode
SAT	Surface air temperature
SIC	Sea ice concentration
SIE	Sea ice extent
SON	September-October-November
SPCZ	South Pacific Convergence Zone
SSS	Sea surface salinity
SST	Sea surface temperature
TPI	Tripole Index

Dataset abbreviations

CFSR	Climate Forecast System Reanalysis
CMAP	Climate Prediction Center Merged Analysis of Precipitation
COREv2	Coordinated Ocean Research Experiments version 2
DOE	United States Department of Energy
EN4.2.0	Hadley Centre subsurface temperature and salinity

	objective analyses version 4.2.0
ERA-Interim	European Centre for Medium-Range Weather Forecasts Interim Reanalysis
GPCPv2.2	Global Precipitation Climatology Project version 2.2
HadISST	Hadley Centre Sea Ice and Sea Surface Temperature
MERRA	Modern Era-Retrospective analysis for Research and Applications
NASA	National Aeronautics and Space Administration
NCAR	National Center for Atmospheric Research
NCEP	National Centers for Environmental Prediction
NSIDC	National Snow and Ice Data Center
ORA-S4	Ocean Reanalysis System 4
SODA	Simple Ocean Data Assimilation

Modelling abbreviations

ACCESS1.0	Australian Community Climate and Earth System Simulator version 1.0
A10 Hist	ACCESS1.0 historical simulation
A10 D&W	ACCESS1.0 Durack and Wijffels (2010) simulation
AMIP	Atmospheric Model Intercomparison Project
CAM4	Community Atmosphere Model version 4
CanESM2	Canadian Earth System Model version 2
CanESM2-CLIM	CanESM2 climatology wind-stress assimilation
CanESM2-GLOB	CanESM2 global wind-stress assimilation
CanESM2-TROP	CanESM2 tropical wind-stress assimilation
CESM1	Community Earth System Model version 1.0.3
CESM1-HIST	CESM1 historical scenario
CESM1-GLOB	CESM1 global ocean assimilation
CESM1-eqPAC	CESM1 equatorial Pacific Ocean assimilation
CESM1-ATL	CESM1 Atlantic Ocean assimilation
CICE4.1	Sea ice model version 4.1
CMIP5	Coupled Model Intercomparison Project phase 5
CMIP6	Coupled Model Intercomparison Project phase 6
HadGEM2	Hadley Centre Global Environment Model version 2
MOM4p1	Modular Ocean Model version 4p1
OASIS3.2	Ocean Atmosphere Sea Ice Soil version 3.2
RCP	Representative Concentration Pathway
RCP4.5	Representative Concentration Pathway 4.5
RCP8.5	Representative Concentration Pathway 8.5
UK	United Kingdom

UM Unified Model

CMIP5 model abbreviations listed in Table 2.1

Variables

f	Coriolis parameter
h	Depth of surface layer
N	Sample size
N_{eff}	Effective sample size
p	p-value
r	Correlation coefficient
r_1	Lag-1 autocorrelation of time series 1
r_2	Lag-1 autocorrelation of time series 2
\overline{T}_y	Horizontal temperature gradient
\overline{T}_z	Vertical temperature gradient
V_E	Meridional Ekman transport
w_E	Ekman pumping
z	Depth
α	Ratio of horizontal and vertical advection
ρ	Density
σ	Scaled pressure
τ	Wind stress
τ_x	Eastward component of wind stress

Units

$^{\circ}\text{C}$	Degree Celsius
$^{\circ}\text{C m}^{-1}$	Degree Celsius per metre
$^{\circ}\text{C (10 y)}^{-1}$	Degree Celsius per decade
$^{\circ}\text{C }^{\circ}\text{C}^{-1} \text{ GW}$	Degree Celsius per degree Celsius of global warming
$^{\circ}\text{C}^{-1} \text{ GW}$	Per degree Celsius of global warming
$^{\circ}\text{S}$	Degree South
$^{\circ}\text{N}$	Degree North
%	Percent
$\% (10 \text{ y})^{-1}$	Percent per decade
$\% ^{\circ}\text{C}^{-1} \text{ GW}$	Percent per degree Celsius of global warming
Gt	Gigatonne

NOMENCLATURE

Gt y^{-1}	Gigatonne per year
Gt y^{-2}	Gigatonne per year per year
hPa	Hectapascal
hPa (10 y)^{-1}	Hectapascal per decade
$\text{km}^2 \text{ (10 y)}^{-1}$	Square kilometre per decade
$\text{km}^2 \text{ }^{\circ}\text{C}^{-1} \text{ GW}$	Square kilometre per degree Celsius of global warming
m	Metre
m (10 y)^{-1}	Metre per decade
m s^{-1}	Metre per second
$\text{m s}^{-1} \text{ (10 y)}^{-1}$	Metre per second per decade
$\text{m s}^{-1} \text{ }^{\circ}\text{C}^{-1} \text{ GW}$	Metre per second per degree Celsius of global warming
$\text{m}^2 \text{ s}^{-1}$	Square metre per second
mm day^{-1}	Millimetre per day
$\text{mm day}^{-1} \text{ (10 y)}^{-1}$	Millimetre per day per decade
$\text{mm day}^{-1} \text{ }^{\circ}\text{C}^{-1} \text{ GW}$	Millimetre per day per degree Celsius of global warming
W m^{-2}	Watt per square metre
$\text{W m}^{-2} \text{ (10y)}^{-1}$	Watt per square metre per decade
$\text{W m}^{-2} \text{ }^{\circ}\text{C}^{-1} \text{ GW}$	Watt per square metre per degree Celsius of global warming
PSU	Practical salinity unit
PSU (10 y)^{-1}	Practical salinity unit per decade
$\text{PSU }^{\circ}\text{C}^{-1} \text{ GW}$	Practical salinity unit per degree Celsius of global warming
y	Year
y (10 y)^{-1}	Year per decade

Supporting Publications

The following three publications form the basis of this thesis:

1. **Purich, A.**, W. Cai, M. H. England, and T. Cowan, 2016: Evidence for link between modelled trends in Antarctic sea ice and underestimated westerly wind changes. *Nature Communications*, **7**, 10409, doi:10.1038/ncomms10409.
2. **Purich, A.**, M. H. England, W. Cai, Y. Chikamoto, A. Timmermann, J. C. Fyfe, L. Frankcombe, G. A. Meehl, and J. M. Arblaster, 2016: Tropical Pacific SST drivers of recent Antarctic sea ice trends. *Journal of Climate*, **29**, 8931–8948, doi:10.1175/JCLI-D-16-0440.1.
3. **Purich, A.**, M. H. England, W. Cai, A. Sullivan, and P. J. Durack, 2018: Impacts of broad-scale surface freshening of the Southern Ocean in a coupled climate model. *Journal of Climate*, **31**, 2613–2632, doi:10.1175/JCLI-D-17-0092.1.

Other Publications

I also contributed to the following publications during my PhD candidature:

4. Boschat, G., I. Simmonds, **A. Purich**, T. Cowan, and A. B. Pezza, 2016: On the use of composite analyses to form physical hypotheses: An example from heat wave – SST associations. *Scientific Reports*, **6**, 29599, doi:10.1038/srep29599.
5. Perkins-Kirkpatrick, S. E., C. J. White, L. V. Alexander, D. Argüeso, G. Boschat, T. Cowan, J. P. Evans, M. Ekström, E. C. J. Oliver, A. Phatak, and **A. Purich**, 2016: Natural hazards in Australia: heatwaves. *Climatic Change*, **139**, 101–114, doi:10.1007/s10584-016-1650-0.
6. Cowan, T., G. C. Hegerl, I. Colfescu, M. Bollasina, **A. Purich**, and G. Boschat, 2017: Factors contributing to record-breaking heat waves over the Great Plains during the 1930s Dust Bowl. *Journal of Climate*, **30**, 2437–2461, doi:10.1175/JCLI-D-16-0436.1.

Preface

Motivation and objectives

Over recent decades an overall warming of the Southern Ocean (e.g. Gille, 2008) and Antarctic Peninsula (e.g. Turner et al., 2005) has occurred, however the Antarctic continent and high-latitude sea surface temperature (SST) have largely cooled, and total sea ice coverage has expanded (e.g. Fan et al., 2014). A poleward shift and intensification of the extratropical westerly-wind jet has also been observed (e.g. Thompson et al., 2011), attributed to increasing greenhouse gases and stratospheric ozone depletion (e.g. Arblaster and Meehl, 2006; Son et al., 2009). Questions relating to the causes of these changes, their interplay, and their relationship with global ocean and atmospheric circulations remain. In particular, understanding the observed increase in Antarctic sea ice despite global warming has proven to be complicated. Antarctic sea ice impacts global climate by influencing surface albedo (e.g. Meehl, 1984; Stammerjohn et al., 2012) and the global ocean overturning circulation (e.g. Marshall and Speer, 2012). Thus to better understand global climate change it is critical to understand the ocean-ice changes occurring in the high latitudes of the Southern Hemisphere.

Climate models are essential tools for investigating climate variability and change. The latest generation of coupled global climate models, those participating in the Coupled Model Intercomparison Project phase 5 (CMIP5; Taylor et al., 2012), provide an unprecedented opportunity for inter-model comparison studies. In contrast to the observed increase in total Antarctic sea ice observed since regular satellite observations began in 1979 (Parkinson and Cavalieri, 2012; Vaughan et al., 2013), the majority of CMIP5 models simulate a decline. Antarctic sea ice trends in the CMIP5 models have been investigated previously (Mahlstein et al., 2013; Polvani and Smith, 2013; Swart and Fyfe, 2013; Turner et al., 2013a; Zunz et al., 2013), however at the time of commencing this thesis, an explanation for the physical mechanisms leading to the disparity of simulated Antarctic sea ice trends had yet to be fully established. To improve confidence in CMIP5 projections, it is important to understand why their average Antarctic sea ice trends differ so markedly from those observed.

Understanding both observed and simulated changes in Southern Hemisphere high-latitude climate has been the focus of much research over the past few years. When this project was first established, the overall objective was to better understand contemporary changes in Southern Hemisphere high-latitude climate, including changes in Antarctic sea ice, Southern Ocean surface temperature and large-scale atmospheric circulation. As the project progressed, three overarching goals were established:

1. To compare physical mechanisms affecting Antarctic sea ice in the CMIP5 models and observations, with the aim of reconciling the disparity between the recent multi-decadal observed increase and the modelled decline;
2. To examine simulations from two different partial-coupled climate model experiments forced by observed variability in certain pre-defined regions, to investigate how tropical Pacific decadal variability affects Antarctic sea ice trends; and
3. To perform experiments using a global coupled climate model with additional fresh-water applied to the Southern Ocean to assess the influence of recent surface freshening on surface temperature and Antarctic sea ice trends.

The findings from each of these topics are presented chronologically in Parts 1–3 of this thesis. Each Part includes additional discussion of relevant new studies, as they have become available. The Concluding Remarks section brings together how research since this project commenced in 2014, including the important findings of this thesis, have improved the state of our understanding of Southern Hemisphere high-latitude climate.

Background

Changes in Southern Hemisphere climate since the mid-twentieth century are outlined below in terms of atmospheric circulation, Southern Ocean, and Antarctic sea ice. Data sparsity is a considerable challenge in the poorly sampled Southern Hemisphere. In this research I mainly consider atmospheric, SST and sea ice changes since 1979, when regular satellite records are available to constrain reanalyses and surface datasets. Assessing the pre-Argo period for ocean temperature and salinity changes is particularly problematic, so I use longer term trend estimates (e.g. since ~ 1950), as over shorter time periods interannual/decadal variability dominates, whereas over longer periods, trends are more coherent and physically interpretable (Durack and Wijffels, 2010). I consider observations available at the time this project commenced in 2014; that is, those up until and including 2013. The behaviour of Antarctic sea ice extent during 2014–2017 is compared to the results presented throughout this thesis for 1979–2013 in the Concluding Remarks.

Atmospheric circulation

Surface air temperature changes in the mid-to-high latitude Southern Hemisphere since the mid-twentieth century include warming of the Antarctic Peninsula, Argentina, Tasmania and southern New Zealand (Gillett et al., 2006; Thompson et al., 2011), but surface cooling over parts of the Antarctic continent and the high-latitude Southern Ocean (Fan et al., 2014; Thompson et al., 2011), as shown in Fig. P.1a. Changes in atmospheric circulation have resulted in a shift in atmospheric mass from high to mid latitudes and an increase in westerly wind speeds over the Southern Ocean (Fig. P.1a,b; see also Thompson and

Solomon, 2002; Marshall, 2003; Thompson et al., 2011), a poleward expansion of the tropical belt and subtropical dry zone (Hu and Fu, 2007; Hu et al., 2011), and a poleward shift in storm tracks, leading to changed precipitation across much of the hemisphere (Fig. P.1b; Gillett et al., 2006; Thompson et al., 2011).

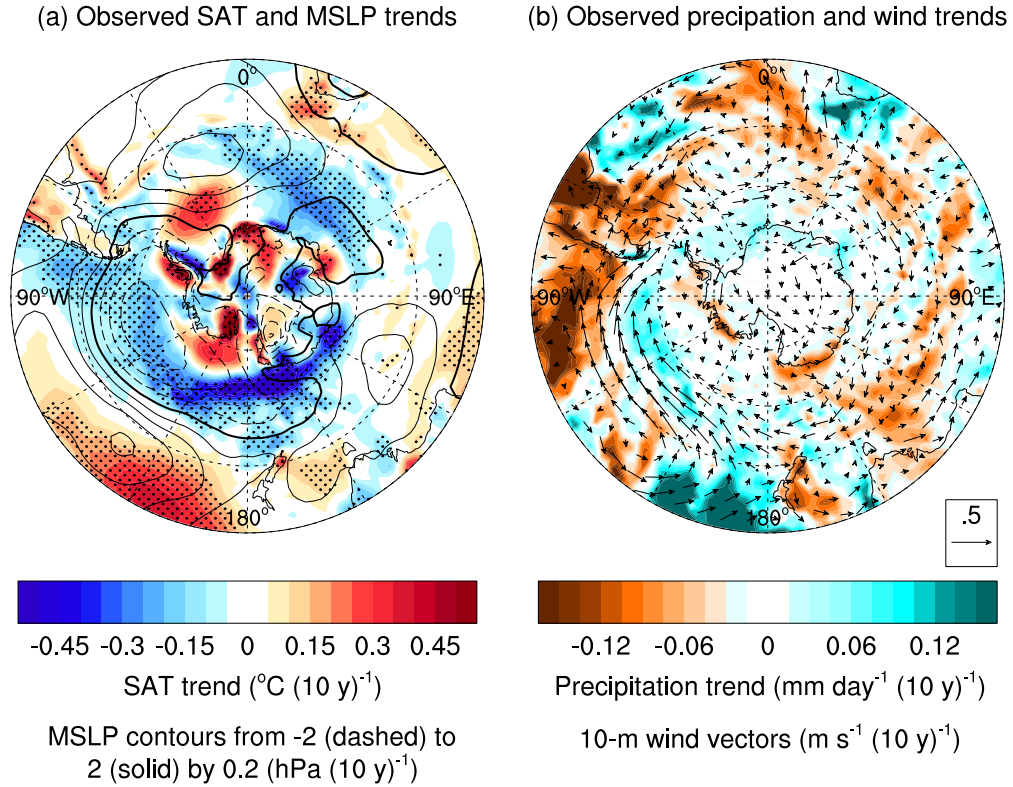


Figure P.1: Observed annual surface atmosphere trends over 1979–2013. (a) Surface air temperature (SAT) trends in colour with significance at the 95% level as determined by a two-sided Student’s t test shown in stippling, and mean sea level pressure (MSLP) trends overlain in contours with negative trends shown by dashed contours and the zero contour shown in bold; and (b) precipitation trends in colour with 10-m wind trends overlain as vectors. All fields are from ERA-Interim.

Many of these changes are consistent with the positive trend in the Southern Annular Mode (SAM), the dominant mode of variability in the extratropical Southern Hemisphere (Thompson and Wallace, 2000; Thompson et al., 2011), as depicted in Fig. P.2. In recent decades the SAM has exhibited pronounced tropospheric trends towards its positive phase during austral summer and autumn (Thompson and Solomon, 2002; Marshall, 2003). There has been an associated poleward shift in the extratropical eddy-driven westerly jet and storm tracks (e.g. Thompson and Solomon, 2002; Fyfe, 2003; Frederiksen and Frederiksen, 2007) as well as an intensification and poleward shift of the oceanic gyre circulations (Cai and Cowan, 2007). These SAM changes have previously been suggested to increase precipitation over the high-latitude Southern Ocean (whilst decreasing precipitation in mid latitudes; e.g. Son et al., 2009), with less influence on evaporation (Purich and Son, 2012), thus enhancing total precipitation minus evaporation (P–E) over a broad region of the high-latitude Southern Ocean. The SAM trend is consistent with atmospheric circu-

lation changes associated with both a decrease in stratospheric ozone and an increase in greenhouse gas concentrations (Shindell and Schmidt, 2004; Arblaster and Meehl, 2006; Son et al., 2009, 2010), although ozone depletion is thought to dominate Southern Hemisphere surface climate changes during austral summer (Perlwitz et al., 2008; Son et al., 2009; Polvani et al., 2011).

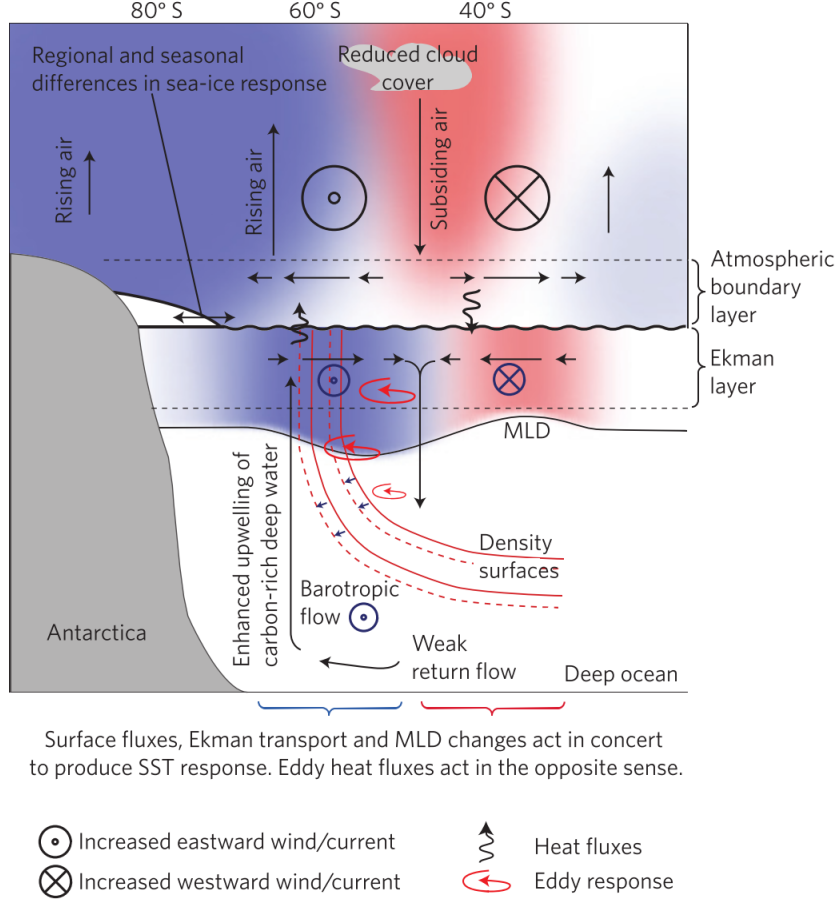


Figure P.2: Schematic atmosphere-ocean response to the positive phase of the SAM, from Thompson et al. (2011). Blue shading indicates cooling, red shading indicates warming, arrows indicate meridional and vertical motions, and arrow heads indicate eastward and westward motions.

A strengthening of the Amundsen Sea Low has also been observed (Fig. P.1a; Turner et al., 2013b). This has been linked to both the positive trend in the SAM (Turner et al., 2013b), and changes in tropical Pacific SST (Schneider et al., 2012) and tropical Atlantic SST (Li et al., 2014; Simpkins et al., 2014) via convectively generated atmospheric Rossby wavetrains.

The CMIP5 models simulate the spatial pattern of the SAM reasonably well, although these models have a tendency to overestimate the variance explained by the SAM (Zheng et al., 2013), and some models also simulate a spatial structure that is too zonal (Purich et al., 2013). An equatorward bias in the location of the mean-state westerly-wind jet is also seen for the majority of models (e.g. Bracegirdle et al., 2013). The CMIP5 models underestimate the magnitude of observed changes in the SAM, and also in the westerly-

wind jet (Swart and Fyfe, 2012; Wilcox et al., 2012; Bracegirdle et al., 2013; Mahlstein et al., 2013; Purich et al., 2013), and surface winds have been identified as one of the major components of inter-model variability in the Southern Hemisphere high latitudes (Sen Gupta et al., 2009). The CMIP5 multi-model mean does not capture the observed strengthening of the Amundsen Sea Low, even though a few individual models do capture this trend (Meehl et al., 2016a).

Southern Ocean

Over recent decades warming has occurred over much of the extent of the Southern Ocean, extending to depths of up to 1200 m in the Antarctic Circumpolar Current (ACC; Gille, 2008; Böning et al., 2008), and onto the continental shelf in the Amundsen and Bellingshausen Seas (Schmidtke et al., 2014). Despite this overall warming, a surface cooling at high latitudes has been observed for most regions (e.g. Fan et al., 2014; Marshall et al., 2014), as shown in Fig. P.3a.

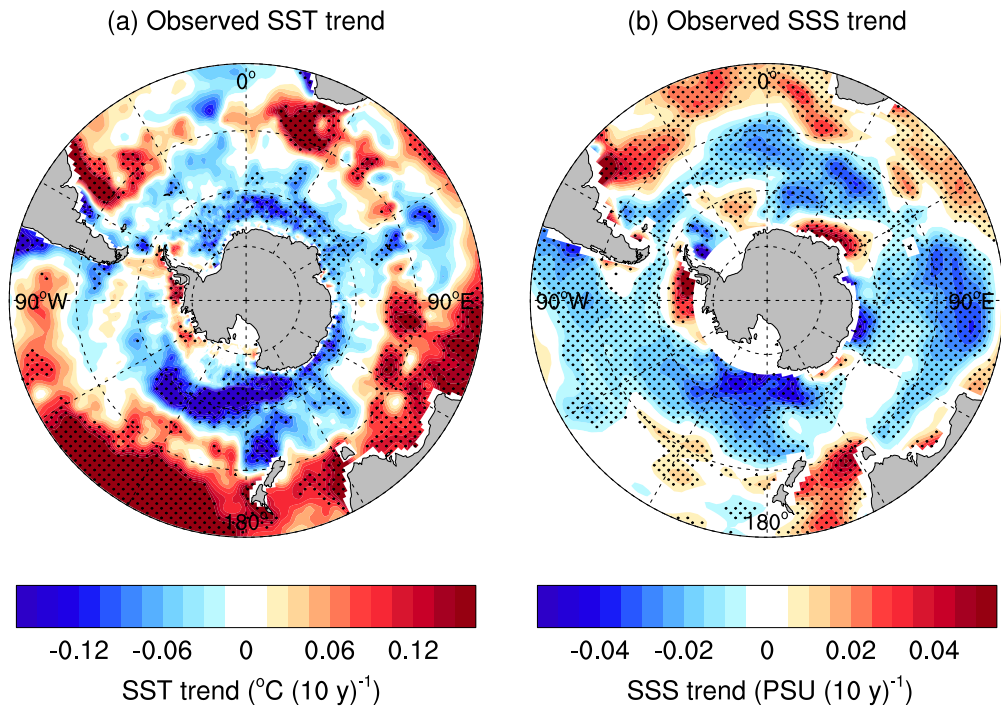


Figure P.3: Observed annual surface ocean trends. (a) SST trends from HadISST over 1979–2013, and (b) SSS trends from Durack and Wijffels (2010) over 1950–2000. Stippling indicates significance at the 95% level.

Surface freshening has also been observed across the Southern Ocean (Fig. P.3b; Böning et al., 2008; Durack and Wijffels, 2010; Durack et al., 2012; de Lavergne et al., 2014), as well as at depths further north in Subantarctic Mode Water and Antarctic Intermediate Water (Wong et al., 1999; Boyer et al., 2005). This has been linked with increased precipitation resulting from poleward-shifted storm tracks (Figs P.1b, P.2; Thompson and

Solomon, 2002; Marshall, 2003; Fyfe, 2003; Thompson et al., 2011) and increased melt-water from Antarctic ice shelves and/or ice sheets (Bintanja et al., 2013; Swart and Fyfe, 2013). Surface freshening increases surface stratification and in the Southern Ocean this reduces convective mixing of warmer subsurface waters, leading to a surface cooling (e.g. Marsland and Wolff, 2001; Aiken and England, 2008; Liu and Curry, 2010; de Lavergne et al., 2014).

The ACC has been observed to accelerate eastwards and shift poleward (Jacobs, 2006; Böning et al., 2008; Toggweiler and Russell, 2008), however little change in the tilt of outcropping isopycnals has been observed (Böning et al., 2008). Theoretical and numerical analyses suggests that in an eddy-saturated state, increased wind stress could increase the meridional overturning without changing the tilt of the isopycnals (Meredith et al., 2012; Morrison and Hogg, 2013), providing an explanation for this behaviour of the Southern Ocean density field.

Changes to the Southern Ocean are significant not just in themselves, but also because the Southern Ocean is an important heat and carbon sink and thus regulates global climate. The importance of the Southern Ocean to global climate depends on the strength of the ACC and the fluxes that mix subtropical waters into and across the ACC (Gille, 2002, 2003). Changes in the carbon uptake of the Southern Ocean as well as in deep ocean circulation have already been observed and are predicted to continue into the future (Le Quéré et al., 2007), although due to uncertainty in observations and in models, and considerable decadal variations, there is uncertainty over predicted trends (Law et al., 2008; Zickfeld et al., 2008).

Southern Ocean representation in the CMIP5 models has been well documented. The CMIP5 models have a consistent warm and buoyant bias spread over the entire water column, with the greatest bias in the Mode and Intermediate Waters (Sallée et al., 2013b; Downes and Hogg, 2013). The Mode Water is poorly represented and both the Mode and Intermediate Waters have a significant fresh bias (Sallée et al., 2013b). Further, the CMIP5 models simulate a Southern Ocean mixed layer depth that is too shallow, too light and shifted equatorward compared to observations (Sallée et al., 2013a). The shallow bias has been attributed to excess freshwater input at the surface that over-stratifies the surface layer and inhibits deep convection (Sallée et al., 2013a). Compared to observations, the CMIP5 models also show a larger rate of meridional overturning in the upper cell and a lower rate in the lower cell (Sallée et al., 2013b). The CMIP5 models accurately represent the position of the ACC, although a range of transports are simulated, accompanied by variations in the density structure amongst models (Meijers et al., 2012).

Antarctic sea ice

When averaged across all longitudes, Antarctic sea ice expanded over 1979–2013 (Cavalieri and Parkinson, 2008; Comiso and Nishio, 2008; Parkinson and Cavalieri, 2012; Vaughan

et al., 2013). Spatial analysis of sea ice trends, however, reveals opposing regional changes off Antarctica since satellite observations began in 1979; with decreasing sea ice in the Amundsen and Bellingshausen Seas outweighed by increasing sea ice in the Ross Sea and around eastern Antarctica, leading to the overall increase (Fig. P.4a; Stammerjohn et al., 2008; Holland and Kwok, 2012; Simpkins et al., 2013). While the circumpolar ice increase is statistically significant, it has been suggested that it may still be due to natural variability (Latif et al., 2013; Mahlstein et al., 2013; Polvani and Smith, 2013; Simpkins et al., 2013; Zunz et al., 2013; Fan et al., 2014). For example, observations over the satellite era coincide with a phase change in the Interdecadal Pacific Oscillation (IPO) from positive to negative, and as such the IPO influence on Antarctic sea ice could present as a trend, even though it is due to natural variability.

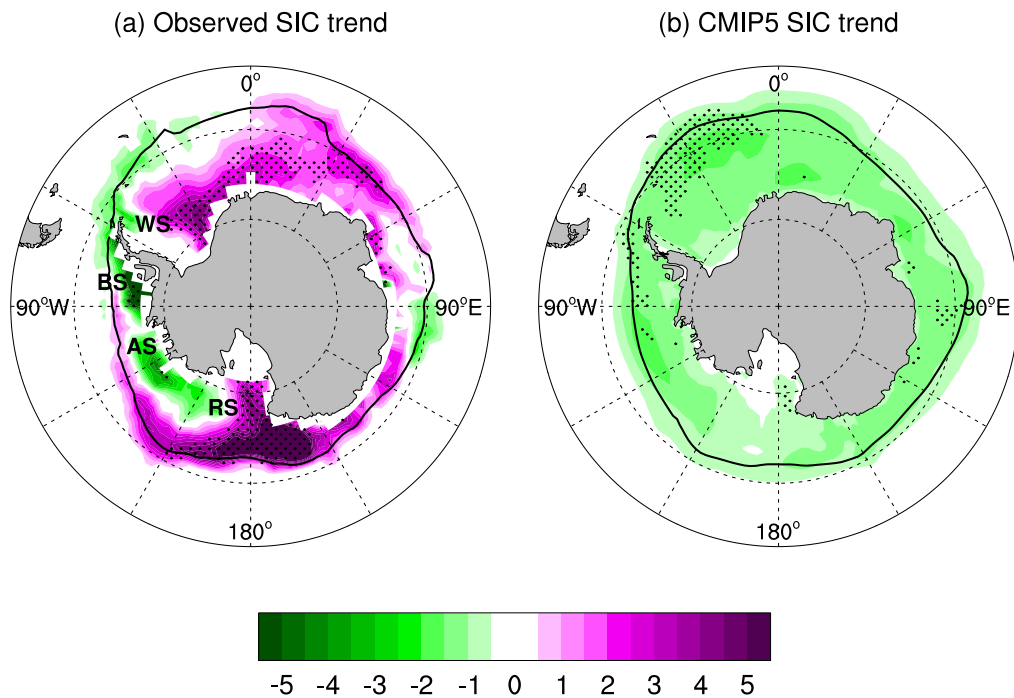


Figure P.4: Annual SIC trends over 1979–2013. (a) Observed SIC from the NSIDC Bootstrap algorithm, and (b) CMIP5 multi-model mean SIC. The CMIP5 multi-model mean is calculated using the first available ensemble member for each model as in Part 1. Stippling indicates significance: (a) at the 95% level as determined by a two-sided Student's t test, and (b) where 80% of models agree on the sign of the mean trend (Purich et al., 2013), which corresponds to 33 out of 41 models. The mean-state 15% SIC contour is shown in black. In (a), RS=Ross Sea, AS=Amundsen Sea, BS=Bellingshausen Sea, and WS=Weddell Sea.

Contrasting the observed sea ice increase, the majority of CMIP5 models and the multi-model mean simulate a decrease in Antarctic sea ice over 1979–2013 (Fig. P.4b; Mahlstein et al., 2013; Polvani and Smith, 2013; Zunz et al., 2013; Turner et al., 2013a; Swart and Fyfe, 2013). There is also considerable bias in many models' sea ice extent (SIE) and seasonal cycle, which complicates comparisons with observations (Turner et al., 2013a). The observed increase has also been suggested to lie within the range of modelled natural variability (Mahlstein et al., 2013; Polvani and Smith, 2013; Swart and Fyfe,

2013), although modelled Antarctic sea ice variability tends to be overestimated (Zunz et al., 2013; Turner et al., 2013a). At the time of commencing this thesis, few studies had proposed physical mechanisms that may be responsible for the difference between observed and simulated Antarctic sea ice trends (Bintanja et al., 2013; Swart and Fyfe, 2013; Haumann et al., 2014), and among these, there was considerable disagreement about the mechanisms at play.

Freshwater fluxes into the Southern Ocean control surface stratification and as such SIE. A freshening of the Southern Ocean due to accelerated Antarctic ice shelf and/or ice sheet melting was proposed as a possible mechanism contributing to the observed increase in Antarctic sea ice (Bintanja et al., 2013). As the CMIP5 models do not simulate dynamic ice sheet mass loss, this lack of freshwater input could affect their simulated sea ice trends and contribute to the disparity with the observed increase. Early model studies of the influence of surface freshening on Antarctic sea ice found freshening to be associated with an increase in ice coverage in ocean-ice models (Marsland and Wolff, 2001; Beckmann and Goosse, 2002; Hellmer, 2004; Aiken and England, 2008). However, recent studies using global coupled climate models with additional freshwater applied around the Antarctic margins to simulate increased ice sheet melt/runoff have found conflicting results: Bintanja et al. (2013) find that increased freshwater has likely contributed to the increase in Antarctic SIE, while Swart and Fyfe (2013) find the influence to be small and not able to explain the observed sea-ice changes.

With the role of surface freshening on Antarctic sea ice trends remaining unclear, the recent observed sea ice increase has been largely attributed to regionally changing winds (Turner et al., 2009; Holland and Kwok, 2012; Fan et al., 2014; Li et al., 2014). Using tracked sea ice motion, wind-driven changes in ice advection were identified in West Antarctica, and wind-driven thermodynamic changes elsewhere (Holland and Kwok, 2012). Global-warming modulated teleconnections to the Amundsen Sea Low (Turner et al., 2009) have been linked to the reduced sea ice in the Amundsen and Bellingshausen Seas and the increased sea ice in the Ross Sea (Li et al., 2014; Simpkins et al., 2014).

Hemispheric-scale wind changes associated with the positive trend in the SAM (Marshall, 2003) were also hypothesised to have caused observed sea ice changes (Turner et al., 2009). On interannual timescales, a positive SAM strengthens the jet and shifts it polewards, resulting in cool SST and increased SIE at most longitudes due to enhanced Ekman drift (Fig. P.2; Hall and Visbeck, 2002; Sen Gupta and England, 2006; Lefebvre and Goosse, 2008; Thompson et al., 2011). However, in association with the positive SAM trend, a number of observational (Simpkins et al., 2012) and modelling (Sigmond and Fyfe, 2010; Bitz and Polvani, 2012; Smith et al., 2012) studies found Southern Ocean warming and an overall sea ice decline on these longer time scales, contrasting the interannual relationship found between the SAM, SST and SIE. The recent identification of a two-time-scale SST response to high-latitude wind changes in model experiments explains how long-term SAM trends might induce an SST response opposite to that associated with interannual variations. Namely, under a continual positive SAM and enhanced northward Ekman

transport, an initial high-latitude SST cooling, caused by equatorward transport of cool water, is followed by an eventual warming (on the order of years to decades), due to the eventual upwelling of warm subsurface water overwhelming the initial cooling response (Marshall et al., 2014).

Thesis overview

The remainder of this thesis consists of three Parts presenting the scientific findings of this research project, followed by the Concluding Remarks. Each Part is organised as a self-contained study with its own abstract, introduction, methods, results and discussion, along with supplementary material included at the end of each Part. For brevity, the references from each Part have been consolidated and appended in the single Bibliography at the end of the thesis. Finally, Appendices A, B and C contain copies of three published journal articles that have resulted from this research. Appendix D presents additional scientific findings building upon Part 3. Appendices E, F and G contain copies of three additional published journal articles that I have coauthored during my PhD tenure.

Part 1 focusses on the discrepancy between observed and CMIP5 trends in total Antarctic sea ice coverage over 1979–2013. I show that weaker trends in the intensification of the Southern Hemisphere westerly-wind jet simulated by the models may contribute to this disparity. During austral summer a strengthened jet leads to increased upwelling of cooler subsurface water and strengthened equatorward transport, conducive to increased sea ice. Because the majority of models underestimate summer jet trends, this cooling process is underestimated compared to observations, and is insufficient to offset warming in the models. The findings of Part 1 suggest that a realistic simulation of observed wind changes, as well as of near-surface ocean temperature structure, may be crucial for reproducing the recent observed sea ice increase.

Part 2 investigates the role of interannual variability in contributing to trends in regional Antarctic sea ice coverage over 1979–2013. A strengthening of the Amundsen Sea Low (Turner et al., 2013b) has been shown to largely explain the observed increase in Antarctic sea ice in the eastern Ross Sea and decrease in the Bellingshausen Sea (Li et al., 2014; Turner et al., 2015b; Meehl et al., 2016a). I show that while these changes are not generally seen in CMIP5 model simulations, they are reproduced in simulations of two independent coupled climate models when these models are constrained by tropical Pacific variability. My analysis suggests that the phase change in the Interdecadal Pacific Oscillation from positive to negative over 1979–2013 contributed to the observed strengthening of the Amundsen Sea Low and associated pattern of Antarctic sea ice change during this period. The findings of Part 2 highlight the importance of accounting for teleconnections from low to high latitudes in both model simulations and observations of Antarctic sea ice variability and change.

Part 3 examines the impact of broad-scale surface freshening of the high-latitude Southern Ocean in a global coupled climate model, using the Australian Community Climate and Earth System Simulator version 1.0 (ACCESS1.0). I perform experiments using ACCESS1.0 with additional freshwater applied to the Southern Ocean to assess the influence of recent surface freshening. The simulations explore the impact of persistent and long-term broad-scale freshening due to processes including precipitation minus evaporation changes. Thus, unlike previous studies, the freshening is applied as far north as 55°S, beyond the Antarctic sea ice margin. I find that imposing a large-scale surface freshening trend, as estimated from observations, causes a surface cooling and sea-ice increase. This surface cooling occurs due to a reduction in ocean convection and weakened entrainment of warm subsurface waters into the surface ocean. Additional experiments are conducted with surface salinity restoration applied to capture observed regional salinity trends under pre-industrial conditions. Remarkably, without any mechanical wind trend forcing, these simulations overall accurately represent the spatial pattern of observed surface temperature and sea-ice trends around Antarctica. The findings of Part 3 demonstrate the importance of accurately simulating changes in Southern Ocean salinity, and thus changes in processes such as precipitation, ice-shelf melt and sea-ice freshwater fluxes, to capture changes in ocean circulation, SST and sea ice.

Part 1

Evidence for link between modelled trends in Antarctic sea ice and underestimated westerly wind changes

The material in this Part is based around work published as:

Purich, A., W. Cai, M. H. England, and T. Cowan, 2016: Evidence for link between modelled trends in Antarctic sea ice and underestimated westerly wind changes. *Nature Communications*, **7**, 10409, doi:10.1038/ncomms10409.

A. P., W. C. and M. H. E. conceived the study and undertook the initial analyses. A. P. assembled and analysed the observational and CMIP5 data, prepared all figures and wrote the first draft of the manuscript. T. C. assisted with data analysis. All authors contributed to the development of ideas, writing and revising the manuscript.

Accompanying supplementary material is included at the end of this Part in Section 1.5. The published version of this material is included in Appendix A.

Abstract

Despite global warming, total Antarctic sea ice coverage increased over 1979–2013. However the majority of Coupled Model Intercomparison Project phase five models simulate a decline. Mechanisms causing this discrepancy have so far remained elusive. Here we show that weaker trends in the intensification of the Southern Hemisphere westerly-wind jet simulated by the models may contribute to this disparity. During austral summer a strengthened jet leads to increased upwelling of cooler subsurface water and strengthened equatorward transport, conducive to increased sea ice. Because the majority of models underestimate summer jet trends, this cooling process is underestimated compared to observations, and is insufficient to offset warming in the models. Through the sea ice-albedo feedback, models produce a high-latitude surface ocean warming and sea ice decline, contrasting the observed net cooling and sea ice increase. A realistic simulation of observed wind changes may be crucial for reproducing the recent observed sea ice increase.

1.1 Introduction

Despite regional melting, total Antarctic sea ice has been expanding over the past 35 years (Cavalieri and Parkinson, 2008; Comiso and Nishio, 2008; Parkinson and Cavalieri, 2012). Such changes impact surface albedo and deep water formation, and thus are important to global climate. Spatial analysis of sea ice concentration (SIC) trends reveals opposing regional changes since satellite observations began in 1979; decreasing sea ice in the Amundsen and Bellingshausen Seas is outweighed by increasing sea ice in the Ross Sea and around eastern Antarctica, leading to an overall increase (Fig. 1.1a; Stammerjohn et al., 2008; Holland and Kwok, 2012; Simpkins et al., 2013). Although the circumpolar ice increase is statistically significant, it has been suggested that it may still be within the range of natural variability (Simpkins et al., 2013; Mahlstein et al., 2013; Polvani and Smith, 2013; Zunz et al., 2013; Fan et al., 2014; Gagné et al., 2015). However, as the most recent years of the sea ice record are included, the strength and the statistical significance of the trend has increased (Simmonds, 2015).

The sea ice increase has been attributed to regional-scale wind trends causing both dynamic and thermodynamic changes (Turner et al., 2009; Holland and Kwok, 2012; Fan et al., 2014; Li et al., 2014; Simpkins et al., 2014; Turner et al., 2015a). On the other hand, models have linked hemispheric-scale wind changes associated with the positive trend in the Southern Annular Mode (SAM; Marshall, 2003), induced by increasing greenhouse gases and stratospheric ozone depletion (Arblaster and Meehl, 2006; Son et al., 2010; Polvani et al., 2011), to Southern Ocean warming and a sea ice decline (Sigmond and Fyfe, 2010; Bitz and Polvani, 2012; Smith et al., 2012). This contrasts interannual variations, in which a positive SAM intensifies the westerly jet and shifts it polewards, resulting in cool sea surface temperature (SST) and increased sea ice extent (SIE) at most longitudes due

to enhanced Ekman drift (Hall and Visbeck, 2002; Sen Gupta and England, 2006; Lefebvre and Goosse, 2008). An exception is along the Antarctic Peninsula, where a positive SAM is associated with reduced sea ice, due to circulation changes associated with the Amundsen Sea Low (Stammerjohn et al., 2008; Turner et al., 2013b).

Most Coupled Model Intercomparison Project phase 5 (CMIP5) models fail to simulate the observed SIE increase in their historical experiments (Mahlstein et al., 2013; Polvani and Smith, 2013; Zunz et al., 2013; Turner et al., 2013a; Swart and Fyfe, 2013; Gagné et al., 2015). The vast majority of models produce a decrease in SIE and simulate considerable bias in mean-state SIE and its seasonal cycle (Turner et al., 2013a). The observed increase is suggested to lie within the range of modelled natural variability (Mahlstein et al., 2013; Polvani and Smith, 2013; Swart and Fyfe, 2013), although modelled Antarctic sea ice variability tends to be overestimated (Zunz et al., 2013; Turner et al., 2013a), and when the spatial pattern of sea ice trends is considered, the observed changes are distinguishable from the modelled pattern during austral summer and autumn (Hobbs et al., 2015). To date, few studies have proposed mechanisms that may be responsible for the difference between observed and simulated Antarctic sea ice trends (Bintanja et al., 2013; Swart and Fyfe, 2013; Haumann et al., 2014).

This study compares physical mechanisms affecting Antarctic sea ice in the CMIP5 models and observations, with the aim of explaining the difference between the observed increase and the modelled decline. We analyse monthly-mean observations and output from 41 CMIP5 models with 87 realisations, over 1979–2013, the period for which regular satellite observations are available. Observed and modelled trends are assessed, and inter-model relationships used to gain insight into why models overall generate too great a sea ice loss and what the important processes behind this are. Because the CMIP5 models underestimate recent changes in the SAM and the westerly-wind jet intensification (Swart and Fyfe, 2012; Bracegirdle et al., 2013; Mahlstein et al., 2013; Purich et al., 2013), we investigate the influence of jet trends on Antarctic sea ice and Southern Ocean SST. We find that underestimated changes in wind-induced ocean circulation in the models may contribute, in part, to their large Antarctic sea ice decline.

1.2 Data and methods

1.2.1 Data

CMIP5 data from the historical and Representative Concentration Pathway 8.5 (RCP8.5; high-emission scenario) experiments are concatenated to match the observational period. The choice of RCP scenario over 2006–2013 has minimal influence on results, as all forcing scenarios are very similar over this time frame. We analyse all CMIP5 models that have SIC data available for both the historical and RCP8.5 experiments. This includes 41 CMIP5 models, with a total of 87 realisations (between one and 10 runs are available per

model), listed in the legend of Fig. 1.2. We also make use of SST, potential temperature, sea surface salinity, subsurface salinity (historical experiment only), surface air temperature, zonal wind, surface wind stresses, evaporation, precipitation, total cloud cover, mean sea level pressure and surface heat fluxes from the CMIP5 archive. At the time of analysis potential temperature was not available for FGOALS-s2 and FIO-ESM, and salinity was not available for HadGEM2-AO. Various surface heat flux terms were not available for CMCC-CMS, FIO-ESM, GISS-E2-R (r1i1p2 only), HadGEM2-AO, MPI-ESM-LR (r2i1p1 and r3i1p1 only) and MRI-ESM1.

For comparison to observations, we use passive microwave SIC processed using the National Snow and Ice Data Center (NSIDC) Bootstrap algorithm (Comiso and Nishio, 2008). The possibility for spurious trends in this SIC dataset has been identified (Eisenman et al., 2014), so results are compared to those obtained with SIC processed using the National Aeronautics and Space Administration (NASA) Team algorithm, and found to be very similar. For area-averaged SIE we make use of the pre-calculated NSIDC SIE index (Fetterer et al., 2002) commonly used in other studies (Simmonds, 2015; Gagné et al., 2015). Results from the NSIDC Bootstrap SIC are very similar. We use SST data from the Hadley Centre Sea Ice and Sea Surface Temperature dataset (HadISST; Rayner et al., 2003). For ocean temperature and salinity we take an average of the Simple Ocean Data Assimilation (SODA) v2.2.4 (Carton and Giese, 2008) and Ishii (Ishii and Kimoto, 2009) reanalyses. For atmospheric variables, we use the European Centre for Medium-Range Weather Forecasts (ECMWF) ERA-Interim reanalysis (Dee et al., 2011), regarded as the most reliable reanalysis over the Amundsen and Bellingshausen Seas (Bracegirdle et al., 2013), and over Antarctica (Bromwich et al., 2011; Bracegirdle and Marshall, 2012). Uncertainty exists in ERA-Interim wind trends (Swart et al., 2015), however considering trends evident in the National Centers for Environmental Prediction (NCEP)/National Center for Atmospheric Research (NCAR) reanalysis, NCEP/Department of Energy (DOE) reanalysis and Twentieth Century reanalysis v2, ERA-Interim winds may modestly underestimate the jet intensification, as this product yields the weakest trend among these four reanalyses (Swart et al., 2015). Weaker jet intensification is seen in NASA Modern Era-Retrospective analysis for Research and Applications (MERRA) and NCEP Climate Forecast System Reanalysis (CFSR), although these products have previously been excluded when examining Southern Ocean wind strength trends, due to possible issues with reanalysis data assimilation (Swart and Fyfe, 2012). The overall balance of evidence suggests that ERA-Interim winds provide one of the best estimates of wind trends over the Southern Ocean for the full study period of 1979–2013.

All data is bilinearly interpolated to a standard $2^\circ \times 2^\circ$ grid. This resolution is chosen to avoid over extrapolating low resolution (atmospheric) data from some models to higher resolutions. Potential temperature is converted from σ to z levels where required, and vertically interpolated to 40-depth levels (matching the SODA reanalysis). Data is stratified into seasonal and annual mean fields. The year of an austral summer corresponds to the year of the January-February.

1.2.2 Metrics

A number of metrics are calculated for observations and each model. Time series of metrics are used to investigate and compare linear trends and interannual variability between models and observations. For inter-model relationships, each ensemble member is included in analysis and weighted evenly. Linear trends are calculated using the least squares regression method, and are scaled by linear trends in global-mean temperature to take into account the different climate sensitivity of the models. Statistical significance is determined using the two-sided Student's t test. When assessing the significance of interannual correlation coefficients, the lag-1 autocorrelation is accounted for by estimating the effective sample size, N_{eff} , as:

$$N_{eff} = N \left(\frac{1 - r_1 r_2}{1 + r_1 r_2} \right) \quad (1.1)$$

Where N is the sample size, and r_1 and r_2 are the lag-1 autocorrelations of the time series of interest (Ciasto and Thompson, 2008).

SIE in the models is defined as the circumpolar area where SIC exceeds 15% (Turner et al., 2013a). We focus on SIE as an area-averaged metric, as it is commonly assessed (Mahlstein et al., 2013; Polvani and Smith, 2013; Swart and Fyfe, 2013; Turner et al., 2013a; Zunz et al., 2013), although we also present SIC trends to display regional trend characteristics (Fig. 1.1). High-latitude metrics [e.g. SST, sea surface salinity, precipitation minus evaporation (P-E)] are defined as area-averaged fields south of 55°S, except where noted otherwise. Only ocean grid points are considered in area averages. We note that in HadISST, the SST in grid cells partially covered by sea ice is determined based on a statistical relationship between SST and SIC (Rayner et al., 2003), whereas in the CMIP5 models SST is defined as the temperature of the uppermost model layer. The choice of latitude is assessed and results are found to be robust over a range of high-latitudes. Jet strength is defined as the maximum 925-hPa westerly wind between 35–70°S, where a cubic spline approximation is applied to the zonal-mean zonal wind (Bracegirdle et al., 2013).

Meridional Ekman transport, V_E , is calculated from the surface zonal wind stress ($V_E = -\tau_x/\rho f$), and Ekman pumping, w_E , from the curl of surface wind stresses ($w_E = \nabla \times (\boldsymbol{\tau}/f)/\rho$), where $\boldsymbol{\tau}$ is the wind stress, ρ is the density of seawater and f is the Coriolis parameter. Trends calculated from area-averaged Ekman transport and pumping time series are sensitive to the choice of latitude band, due to variations in the wind fields amongst models and observations. To allow for spatial variations amongst models, we calculate the first empirical orthogonal function (EOF) of both Ekman transport and pumping over 55–70°S and use the standardised principal components (PCs) to represent the Ekman transport and pumping time series, respectively. During summer, the first EOFs for both Ekman transport and pumping are well separated (North et al., 1982) from subsequent patterns in all models and observations. The first EOFs are related to the SAM,

the leading mode of atmospheric variability in the extratropical Southern Hemisphere (Thompson et al., 2011), and have a more coherent influence on SST (Supplementary Fig. 9). To account for the effect that equatorward Ekman transport has on SST, we estimate horizontal temperature advection by multiplying the Ekman transport PC by the mean-state horizontal temperature difference between 55–60°S and 65–70°S, calculated for the zonal-mean surface layer (0–25 m). Likewise, to account for the effect that Ekman pumping has on SST, we estimate the vertical temperature advection by multiplying the Ekman pumping PC by the mean-state vertical temperature difference between the surface layer (0–25 m) and the layer just below the summer thermocline (70–80 m), calculated for the zonal-mean over 55–70°S.

1.3 Results

1.3.1 Sea ice and SST spatial trends

In contrast to observations (Fig. 1.1a), multi-model mean SIC trends (Fig. 1.1b) show a decrease in all sea ice regions. The majority of models show an overall decrease in sea ice, despite inter-model variations in simulated spatial patterns, with many models showing small regions of increasing SIC (Fig. 1.6 in Section 1.5). The multi-model mean regional decrease lacks broad significance, except in the Bellingshausen and northern Weddell Seas, and in isolated pockets of eastern Antarctica and the Ross Sea. Coincident with the observed increase in Antarctic sea ice, high-latitude SST has also decreased over 1979–2013 (Fig. 1.1c; see also Bintanja et al., 2013; Fan et al., 2014; Marshall et al., 2014), with cooling strongest in the Ross Sea. In contrast, the CMIP5 models show Southern Ocean surface warming over most regions (Fig. 1.1d), although there is no inter-model consensus in terms of warming at high latitudes.

1.3.2 Sea ice, SST and jet relationships

Comparing SIC and SST trend patterns exhibited by individual models (Figs 1.6, 1.7 in Section 1.5) reveals that models with stronger SST warming show a larger SIC decrease, as expected (Mahlstein et al., 2013). A strong inter-model relationship exists between trends in area-averaged high-latitude (south of 55°S) SST and in circumpolar SIE: models that simulate greater warming produce a greater reduction in ice (Fig. 1.2). This relationship is highly statistically significant ($p < 0.001$), and is evident in all seasons [shown for austral summer (December–February; DJF) and austral winter (June–August; JJA), Fig. 1.2a and b, respectively; all seasons in Table 1.1 in Section 1.5]. The observed trends fit the tail-end of the spread in model trends. When trends are scaled by global mean temperature trends to take into account differences in climate sensitivity between observations and models, the observed SIE trend lies outside the 95% confidence interval of model trends. However, in absolute terms, the observed Antarctic sea ice trend is not statistically distinguishable

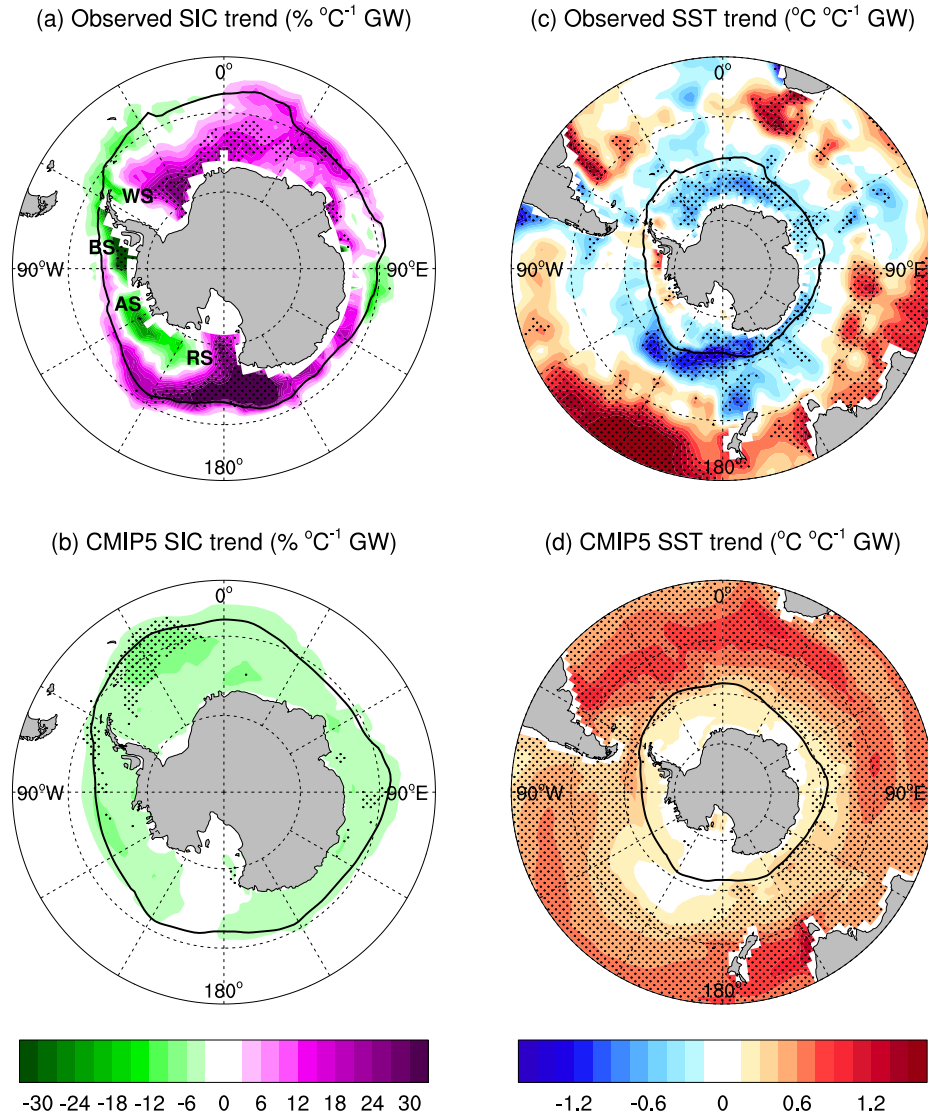


Figure 1.1: Annual SIC and SST trends over 1979–2013. (a) observed SIC from the NSIDC Bootstrap algorithm; (b) CMIP5 multi-model mean SIC; (c) observed SST from HadISST; and (d) CMIP5 multi-model mean SST. Trends are expressed as a change per degree of global warming. Multi-model means are calculated using the first available ensemble member for each model. Stippling indicates significance: (a,c) at the 95% level as determined by a two-sided Student’s t test; and (b,d) where 80% of models agree on the sign of the mean trend (Purich et al., 2013), which corresponds to 33 out of 41 models. The mean-state 15% SIC contour is shown in black. In (a), RS=Ross Sea, AS=Amundsen Sea, BS=Bellingshausen Sea, and WS=Weddell Sea.

from the modelled trends at the 95% confidence level. As such, natural internal variability remains a viable explanation for the observed trend. Despite this, it is still of interest to investigate mechanisms that lead to the range in observed and modelled SIE trends. The SIE–SST relationship (Fig. 1.2) suggests that ocean changes may influence sea ice trends. As such, to explain why the majority of CMIP5 models simulate a decrease in Antarctic sea ice in contrast to the observed increase, we must understand why modelled high-latitude SST warms too fast.

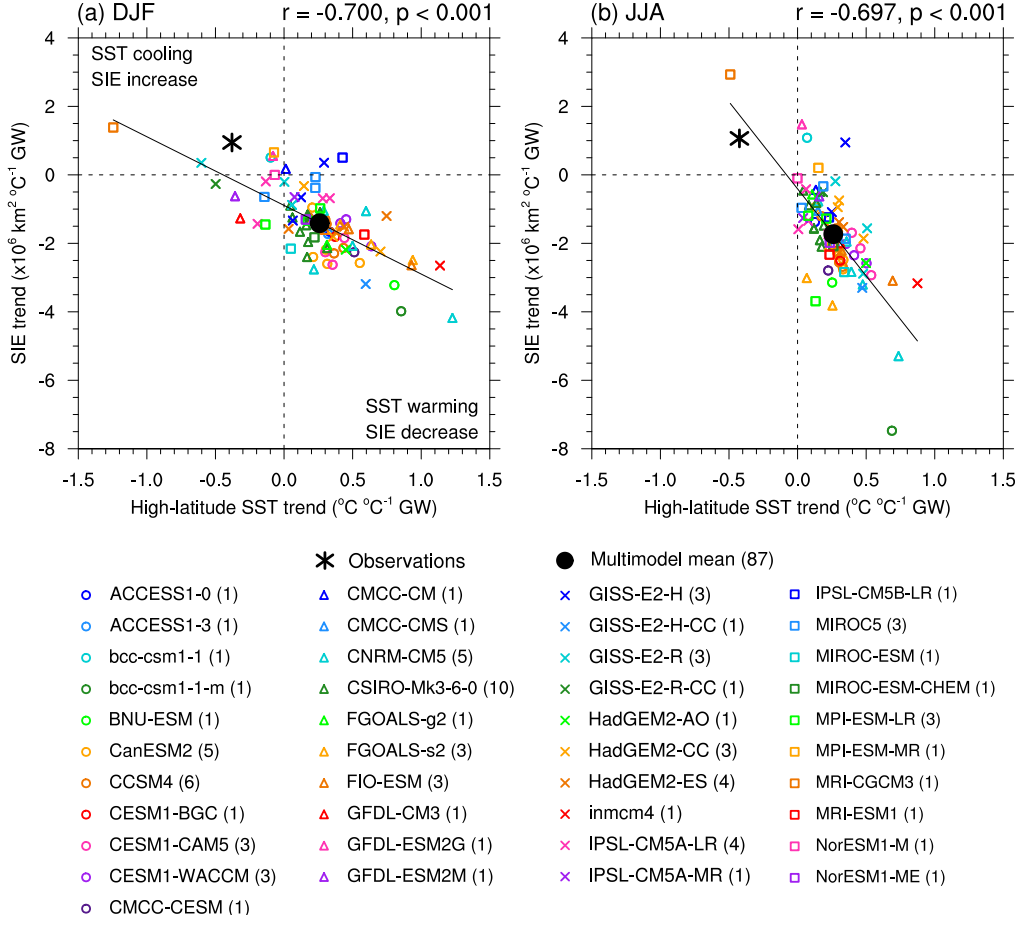


Figure 1.2: Trends in SIE versus trends in high-latitude SST over 1979–2013. (a) DJF; and (b) JJA. Trends are expressed as a change per degree of global warming. All available model ensemble members are shown (87 realisations). Observed SST from HadISST and SIE from NSIDC. Each model is shown by a marker with the number of runs per model indicated in the legend, the multi-model mean is shown by a black dot, and observations are shown by a black asterisk. The inter-model correlation coefficient and p-value are shown above each panel. For $p < 0.05$, the inter-model regression is shown by a black line.

Given the links between the westerly-wind jet, sea ice and SST (Sigmond and Fyfe, 2010; Bitz and Polvani, 2012; Smith et al., 2012; Hall and Visbeck, 2002; Sen Gupta and England, 2006; Lefebvre and Goosse, 2008), we next investigate the influence of jet intensification trends. There is a significant inter-model relationship between jet strength trends and SIE trends during austral summer and autumn ($p < 0.01$; Table 1.1 in Section 1.5). During these seasons, there is also a strong and significant relationship between high-latitude SST and jet strength ($p < 0.001$; Fig. 1.3a; Table 1.1 in Section 1.5). In contrast, during winter there is no inter-model relationship between jet strength trends and SIE trends, although the relationship between jet strength trends and SST trends persists ($p < 0.001$; Fig. 1.3b). This relationship shows that models with a more intensified jet cool, or warm less, while models with a weaker intensification, or weakened jet, warm more. In summer, significant relationships are also found between trends in jet position and high-latitude SST, with a stronger poleward shift in the jet associated with high-latitude SST cooling or weaker warming (Table 1.1 in Section 1.5).

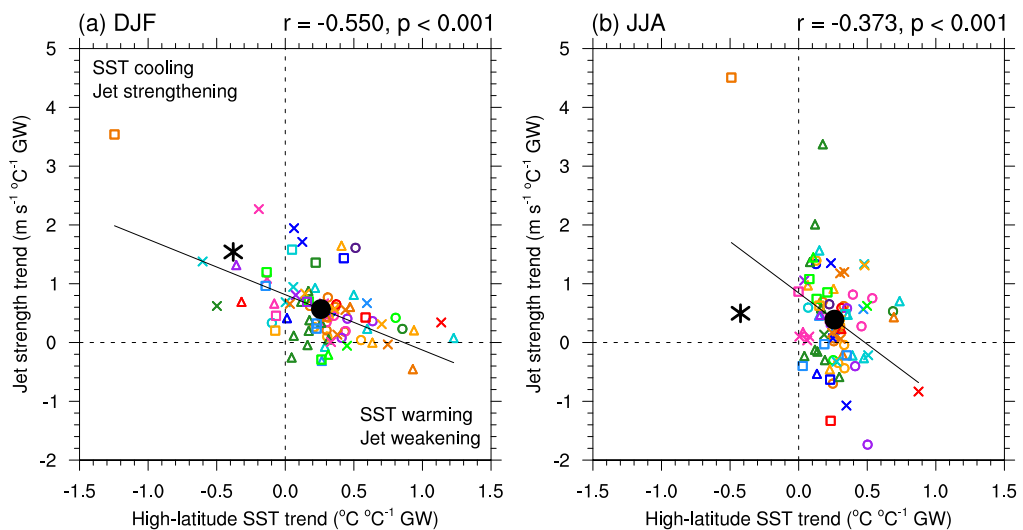


Figure 1.3: Trends in jet strength versus trends in high-latitude SST over 1979–2013. (a) DJF; and (b) JJA. Trends are expressed as a change per degree of global warming. All available model ensemble members are shown. Observed jet strength from ERA-Interim. Figure details as per Fig. 1.2.

Processes embedded in the inter-model trend relationships appear to also operate in the inter-model relationship in the mean state: models with stronger mean-state zonal-winds south of 55°S tend to have a larger ice area, particularly during autumn (Mahlstein et al., 2013). On interannual timescales, an intensified summer and autumn jet is associated with above average SIE in the observations ($p < 0.05$; Table 1.2 and Fig. 1.8 in Section 1.5). However, the majority of CMIP5 models do not capture this interannual relationship (median $p > 0.2$), indicating a failure to simulate wind-ice interactions adequately. This may explain the somewhat weak inter-model relationship between trends in jet strength and SIE (Table 1.1 in Section 1.5).

Within individual CMIP5 models, interannual jet strength is more strongly correlated with high-latitude SST (Table 1.2 and Fig. 1.8 in Section 1.5). An intensified jet is associated with cooler high-latitude SST (Hall and Visbeck, 2002; Sen Gupta and England, 2006). The observed relationship is significant over summer ($p < 0.05$), while for the majority of CMIP5 models it is statistically significant in both spring and summer (median $p < 0.05$ and $p < 0.01$, respectively). Thus relative to observations, variations in the modelled jet have a weaker influence on variations in sea ice yet more influence on SST. As such, we focus on jet-SST dynamics, noting the strong relationship between SST and SIE (Fig. 1.2) that links wind changes back to sea ice.

1.3.3 Wind-induced effects on SST

We hypothesise that the jet-SST trend relationship in the CMIP5 models is conducted through a high-latitude Ekman response to changing winds. There, the wind stress forces equatorward Ekman transport, and the wind stress curl forces upward Ekman pumping

(Section 1.2.2; Marshall and Speer, 2012; Marshall et al., 2014). As such, an intensified jet results in strengthened equatorward Ekman transport and usually increased Ekman upwelling at high latitudes.

Ekman upwelling has a strong cooling effect on SST during summer when warm water resides at the surface forming a cap over cool Winter Water at depths $\sim 20\text{--}150$ m (Fig. 1.4a). The warm surface water results from short-wave radiation being received by the summer ice-free surface waters as sea ice melts. Beneath this, the permanent pycnocline with cold, fresh water overlying warm, salty water is apparent. By contrast, during winter surface waters are colder than water below (Fig. 1.4b), consistent with the typical temperature profile described for the high-latitude Southern Ocean (Marshall and Speer, 2012), caused by seasonal sea ice melt/freeze and advection processes that freshen the surface layer. Because of the seasonal stratification, during summer enhanced Ekman upwelling brings cooler waters to the surface, and this surface cooling spreads further north due to enhanced equatorward transport.

Consistently, summer Ekman pumping trends are significantly correlated with SST trends at high latitudes ($p < 0.001$; Fig. 1.4c): models with a strong increase in Ekman upwelling show SST cooling or weak warming, whereas models with weak trends in Ekman pumping show strong warming. Ekman transport trends are also significantly correlated with high-latitude SST trends in summer ($p < 0.001$; Fig. 1.9 in Section 1.5): models with a strong increase in equatorward Ekman transport show cooling or weak warming. Scale analysis (Ferreira et al., 2015) has suggested that horizontal Ekman transport should initially dominate over vertical Ekman upwelling; in contrast, here we find that south of $\sim 60^\circ\text{S}$, both Ekman transport and Ekman pumping are important (Section 1.5.1; Fig. 1.10 in Section 1.5).

The CMIP5 models underestimate the summer intensification (Fig. 1.3a) and poleward shift in the jet (Mahlstein et al., 2013; Bracegirdle et al., 2013), and therefore also underestimate the increased upward Ekman pumping (Fig. 1.4c) and equatorward Ekman transport (Fig. 1.9c in Section 1.5) compared to observed trends. Many models underestimate the vertical temperature advection despite overestimating the surface stratification during summer (Fig. 1.4a). This contributes to their high-latitude SST warming trends in contrast to observed cooling.

We note that there is considerable uncertainty in the observed jet trend, due to sparse observations over the high-latitude Southern Hemisphere (Son et al., 2010; Swart and Fyfe, 2012). While only ERA-Interim jet trends are presented here, stronger jet intensification is also seen in three other reanalyses (Section 1.2.2; Swart et al., 2015). Increased wind speed is also evident in station-based wind observations (Yang et al., 2007; Handle et al., 2012). However, satellite-based wind observations available over the shorter 1988–2011 period may cast some doubt over reanalysis trends (Swart et al., 2015), although the satellite products themselves contain uncertainty (Foreman et al., 2011). Overall, the analyses presented here depend on an accurate wind trend estimate over

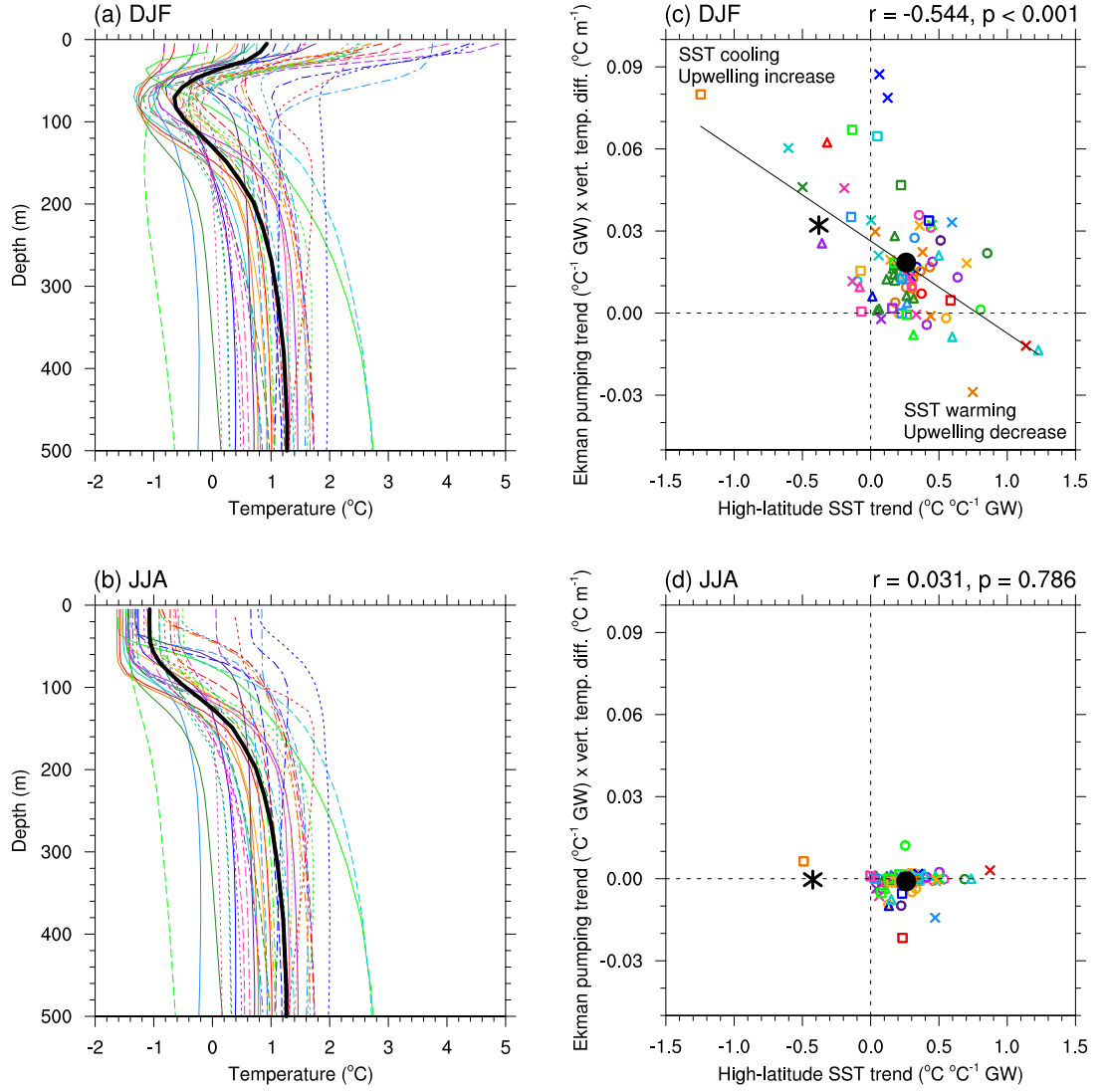


Figure 1.4: Potential temperature profiles and Ekman pumping trends over 1979–2013. Seasonal zonal-mean potential temperature profiles averaged over 60–70°S for: (a) DJF; and (b) JJA. The first available ensemble members for each model is shown. The observed profile (black) is an average of SODA and Ishii over 1979–2011. Trends in Ekman pumping versus trends in high-latitude SST for: (c) DJF; and (d) JJA. Trends are expressed as a change per degree of global warming. Ekman pumping trends are calculated as the trend in the Ekman pumping PC multiplied by the mean-state vertical temperature gradient near the surface. All available model ensemble members are shown. Details in (c,d) as per Fig. 1.2.

the Southern Ocean, although the mechanisms described remain robust. Further, while the observed (ERA-Interim) jet intensification is stronger than the multi-model mean, it does lie within the model spread (Fig. 1.3a). Nevertheless, as discussed above, the strong inter-model relationship shown here suggests that the strength of jet intensification is an important process influencing high-latitude SST in observations and coupled models, and the majority of models produce a weaker intensification.

No significant relationship between trends in Ekman pumping and SST exists during

winter (Fig. 1.4d; Table 1.1 in Section 1.5). This is to be expected, given the seasonal variation in vertical temperature stratification: during winter increased upwelling would cause warming, offsetting cooling from increased equatorward transport (Table 1.1 in Section 1.5).

1.3.4 Timescales of Ekman response

On interannual time scales a positive SAM is associated with cool high-latitude SST (Fig. P.2; Hall and Visbeck, 2002; Sen Gupta and England, 2006; Lefebvre and Goosse, 2008), whereas over longer periods a positive trend in the SAM has been linked to high-latitude SST warming (Sigmond and Fyfe, 2010; Bitz and Polvani, 2012; Smith et al., 2012). The apparent contradiction between the SAM-SST relationship over interannual versus multidecadal time scales has been explained by a two-time-scale SST response to high-latitude wind changes (Marshall et al., 2014; Ferreira et al., 2015). Initially, a positive SAM trend is associated with short-term cooling, by increasing the northward Ekman transport of cold surface waters in the prevailing westerly wind regions (Sen Gupta and England, 2006; Marshall et al., 2014; Ferreira et al., 2015), consistent with the inter-model trend relationship here (Fig. 1.9 in Section 1.5). Over time, however, the cooling is replaced with a warming, accounted for by prolonged enhanced upwelling in a region where a temperature inversion occurs (Sigmond and Fyfe, 2010; Bitz and Polvani, 2012; Smith et al., 2012). Our results are consistent with these previous studies: most CMIP5 models simulate a positive SAM trend (i.e. jet intensification; Fig. 1.3a), increased upwelling and high-latitude SST warming (upper right quadrant of Fig. 1.4c). Our results suggest, however, that over the 35-year period assessed here, Ekman upwelling is not responsible for the surface warming during summer, because due to the seasonal stratification profile, models that simulate a stronger upwelling trend show a weaker rate of surface warming. Instead, the inter-model relationship suggests that cooling due to Ekman upwelling offsets other warming factors. Importantly, most models underestimate the increase in Ekman upwelling, resulting in a weaker cooling effect that is insufficient to offset warming from other processes, most notably surface heat fluxes.

The seasonal variation in the subsurface temperature profile is not discussed in previous studies, and is key to interpreting our results: in contrast to previous studies which link initial cooling to equatorward Ekman transport only (Marshall et al., 2014; Ferreira et al., 2015), our results suggest that Ekman pumping during summer is also important. It is plausible that the cooling associated with summer upwelling may eventually be replaced by warming as water from below the mixed layer is entrained (Marshall et al., 2014; Ferreira et al., 2015), however over the time scale assessed here (1979–2013), this does not appear to be the case. In previous model experiments, the time required for this temperature-trend transition varies from an order of years to a couple of decades (Ferreira et al., 2015). If the time scale to a complete transition from initial cooling to later warming was at the longer end of this estimate, then the surface cooling seen in the observations

and in some models could be consistent with this mechanism. The seasonal variation in the temperature profile may also contribute to a longer transitional time scale.

1.3.5 Ekman contribution to observed-modelled disparity

The mechanisms identified above are present during summer. Using the difference between the observed (ERA-Interim) and multi-model mean jet strength trends, the sensitivity of SST trends to jet trends (i.e. the inverse of Fig. 1.3a), and the sensitivity of SIE to SST (Fig. 1.2a), >25% of the difference in the CMIP5 SIE trends can be attributed to their underestimated jet intensification. As such, the underestimation of wind trends in CMIP5 models likely contributes to the sea ice decreases simulated by the majority of models.

Due to the thermal inertia of the ocean, SST anomalies in summer are likely to persist and exert an influence beyond this season. Observed spring ice tendencies have been found to persist until the following winter (Stammerjohn et al., 2012; Holland, 2014), and here we find that in both observations and models, summer ice tendencies persist significantly during autumn and winter. This confirms that the summer Ekman-SST mechanism can influence trends throughout much of the year (Smith et al., 2012; Ferreira et al., 2015).

Positive feedbacks associated with the wind-induced circulation changes could also contribute to the difference between observed and modelled trends. In observations, the magnitude of Ekman pumping and transport increases such that the associated cooling more than offsets the high-latitude heat flux increase. Cooler SST leads to increased sea ice, particularly in the Ross Sea sector. Through the sea ice-albedo feedback, solar radiation decreases, conducive to further cooling and increased sea ice (Stammerjohn et al., 2012). The consequence is decreased zonal-mean downward heat flux in the sea-ice zone (Fig. 1.11c in Section 1.5). In the majority of the models, although the magnitude of Ekman pumping and transport also increases, it is to a smaller extent such that the associated cooling is not sufficient to offset the heat flux increase. The above sea ice-albedo feedback process operates in reverse, leading to an increased heat flux into the ocean in the sea-ice zone (Fig. 1.11d in Section 1.5). Based on the occurrence of opposite reinforcing feedback mechanisms occurring in observations and the majority of CMIP5 models, the difference between observed and modelled jet strength trends can lead to very different sea ice changes.

1.3.6 Considering other mechanisms

Further support for the importance of Ekman upwelling and transport comes from considering other potential mechanisms. Here we explore other possible processes and find that none of these contradict or offer an alternative explanation for the results described above.

It could be hypothesised that models with stronger jet trends show reduced high-

latitude SST warming as a result of changed cloud cover or evaporative cooling, and that the correlations presented above between Ekman pumping and SST (Fig. 1.4c) are coincidental. No inter-model relationship is found between trends in SST and trends in overlying cloud cover during summer ($p > 0.15$; Table 1.3 in Section 1.5), possibly due to differing cloud-jet relationships present in the models (Grise and Polvani, 2014). A significant inter-model relationship is found between high-latitude SST trends and evaporation trends ($p < 0.001$; Table 1.3 in Section 1.5), in which models with increasing SST show an increase in evaporation, and vice-versa. This suggests that SST anomalies are driving evaporation variations, as warmer waters evaporate more readily, whereas evaporative cooling would have the opposite effect on SST. Thus evaporative fluxes are not the cause of the excessive warming in most CMIP5 models, instead they are a response to this warming. These results support our hypothesis above; namely, that the relationship between the westerly-wind jet and SST trends occurs due to changes in ocean circulation.

Outside of the summer sea-ice zone, spatial trends in total downward heat flux oppose those in SST (Fig. 1.11 in Section 1.5), i.e. regions of SST cooling are associated with increased heat flux into the ocean, suggesting that changes in SST are driving changes in heat flux and not the other way around. During summer the inter-model relationship between trends in SST and surface heat fluxes over these predominantly ice-free areas (55–65°S) is insignificant, although the sense of the relationship suggests that models with SST cooling show increased heat flux into the ocean (Fig. 1.12 in Section 1.5), again suggesting that changes in SST are driving changes in heat flux. Thus net heat flux trends are of the wrong sign to account for model SST trends. It is also noted that area-averaged trends in observed heat fluxes, although uncertain, are comparable to those in CMIP5 models over this region.

Southern Ocean freshening due to accelerated Antarctic ice shelf and/or ice sheet melting, not simulated by CMIP5 models, was proposed as a possible mechanism contributing to the Antarctic sea ice increase (Bintanja et al., 2013). However, further model experiments found the influence of ice sheet melt on sea-ice trends to be minimal (Swart and Fyfe, 2013). As such, this deficiency alone in CMIP5 models cannot account for the disparity between observed and simulated Antarctic sea ice trends. Nevertheless, reduced Southern Ocean convection in CMIP5 models has been linked with surface freshening (de Lavergne et al., 2014), suggesting that overall changes in freshwater fluxes may be important for surface temperature trends (Morrison et al., 2015).

Inter-model trends in SIE are strongly related with trends in sea surface salinity ($p < 0.001$; Table 1.3 and Fig. 1.13a in Section 1.5): models with increasing salinity show a strong decrease in sea ice while models with surface freshening show an increase, or weaker decrease, in sea ice. The sense of this relationship suggests that ocean surface salinity is influencing sea ice, not the other way around, as sea-ice driven salinity changes would see freshening correspond to higher rates of sea-ice melt. Instead, greater sea-ice coverage is linked to fresher surface conditions and increased surface stratification, which suppresses convective overturning; and vice versa for reduced sea-ice coverage.

Sea surface salinity trends cannot be explained by trends in high-latitude P–E, as surprisingly increasing P–E is associated with increasing salinity ($p=0.05$ during summer; Table 1.3 and Fig. 1.13b in Section 1.5), opposite to what would be expected, because both P–E and surface salinity trends co-vary with the jet. Again, changes in wind-induced ocean circulation provide the likely explanation. Namely, surface salinity trends are weakly related with Ekman pumping trends ($p<0.1$ during summer; Table 1.3 and Fig. 1.13c in Section 1.5): models with a stronger increase in Ekman upwelling show an increase in surface salinity, and models with a weaker increase (or decrease) in Ekman upwelling show a decrease in surface salinity, due to the upwelling (or lack thereof) of saltier water from depth (Fig. 1.13d in Section 1.5). The temperature response associated with the Ekman upwelling of salty subsurface water (warming due to decreased stability and increased convective overturning) dampens the direct Ekman-SST response (upwelling of cool Winter Water), and may be why no significant Ekman-SIE relationship is found directly in the models over the 35-year period assessed.

1.4 Discussion

Both the observed and CMIP5 SIE trends are linked to the westerly-wind jet intensification through the influence of SST. The models underestimate the observed jet intensification during summer, although we caution that the observed jet trend is uncertain. This causes a weaker strengthening of high-latitude Ekman pumping and transport than observed. Although increased Ekman upwelling of cool Winter Water and the associated equatorward Ekman transport contribute to the observed SST cooling, because their trends are underestimated in the models, these terms are insufficient to offset warming from increased surface heat fluxes. This leads to faster surface warming and a decreasing sea-ice trend in most of the models (summarised in Fig. 1.5). Once these trends are initiated, the sea ice-albedo positive feedback ensures the trend is sustained. These findings demonstrate the importance of accurately simulating changes in the wind (Sen Gupta et al., 2009; Mahlstein et al., 2013). By contrast, in the observations, the cooling effect from the wind changes appears to be sufficient to offset the warming tendency resulting in an initial cooling. The same sea ice-albedo positive feedback operates in reverse, leading to further cooling and an increasing sea ice trend. While analyses are largely conducted over circumpolar regions, when repeated for the Ross Sea sector where observed SIE has increased most substantially, results remain robust.

Our finding, that underestimated wind trends contribute to the discrepancy between the observed and model sea-ice changes, occurs despite the fact these models do not resolve eddies, although almost all include a suitable eddy-induced advection scheme to approximate their effects. In the real world eddy-compensation would partially counteract wind-induced changes (Downes and Hogg, 2013; Ferreira et al., 2015), although Ekman changes still dominate in the surface layer (Meredith et al., 2012; Morrison and Hogg, 2013). In the presence of an eddy compensation effect, the underestimation of the impact

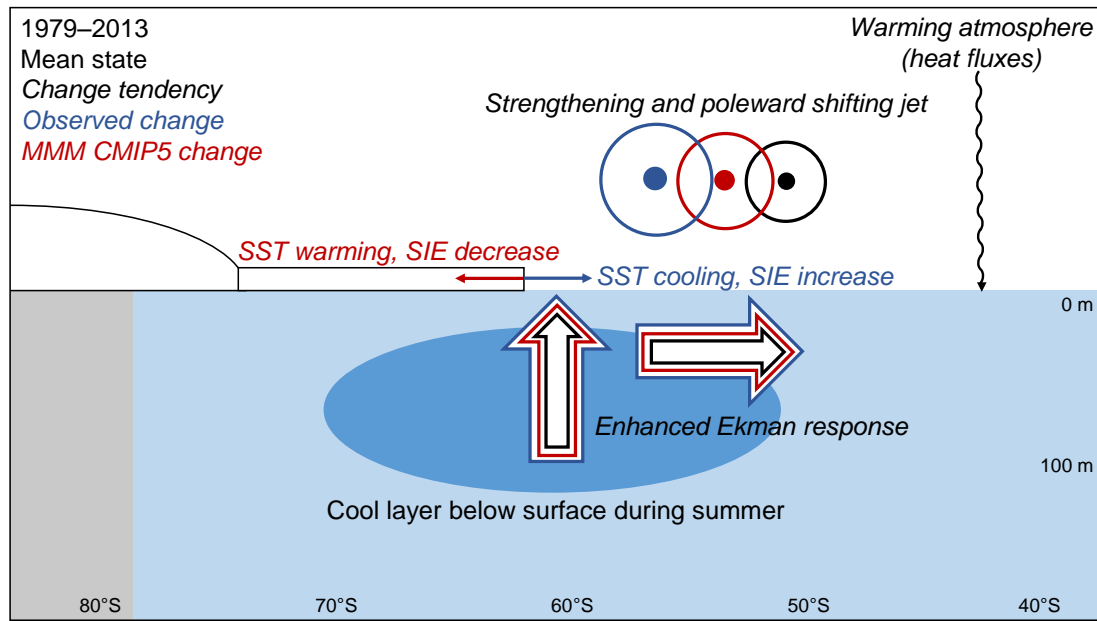


Figure 1.5: Schematic of decadal scale wind induced surface layer changes during summer. Over recent decades, the observed westerly-wind jet has strengthened and shifted poleward during austral summer (circles with dots). This has increased the upward Ekman pumping and equatorward Ekman transport (large arrows). During summer increased upwelling at high latitudes brings cooler Winter Water to the surface. Combined with equatorward transport, this leads to SST cooling in observations. Multi-model mean (MMM) CMIP5 changes (red) are weaker than observed changes (blue). Under global warming these weaker Ekman changes are insufficient to offset warming from other factors (curvy arrow). As such, multi-model mean CMIP5 high-latitude SST has warmed rather than cooled, and Antarctic sea ice has declined rather than expanded (small arrows).

in the models could be even larger. This influence and others, such as the role of deep ocean overturning or convection, will provide fertile ground for further research into the recent Southern Ocean circulation and sea ice changes.

1.5 Supplementary material

Table 1.1: Inter-model correlation coefficients between trends over 1979–2013. Correlation coefficients between modelled trends in two metrics (p values in brackets), calculated for all available model ensemble members. Correlations significant at the 95% confidence level are shown in bold. Jet position defined such that an equatorward trend is positive and a poleward trend is negative. Ekman pumping and Ekman transport trends are calculated as the trends in the Ekman PCs multiplied by the mean-state vertical and horizontal temperature gradients, respectively (as in Figs 1.4, Fig. 1.9).

	<i>DJF</i>	<i>MAM</i>	<i>JJA</i>	<i>SON</i>
SIE–SST	-0.70 (<0.001)	-0.75 (<0.001)	-0.70 (<0.001)	-0.73 (<0.001)
Jet strength–SIE	0.30 (0.004)	0.29 (0.006)	0.18 (0.10)	0.10 (0.38)
Jet strength–SST	-0.55 (<0.001)	-0.38 (<0.001)	-0.37 (<0.001)	-0.18 (0.10)
Jet position–SIE	-0.06 (0.57)	-0.17 (0.12)	-0.09 (0.41)	0.05 (0.66)
Jet position–SST	0.52 (<0.001)	0.29 (0.007)	0.28 (0.010)	0.14 (0.20)
Ekman pumping–SIE	0.17 (0.13)	0.13 (0.25)	0.05 (0.64)	0.10 (0.37)
Ekman pumping–SST	-0.54 (<0.001)	-0.12 (0.30)	-0.03 (0.79)	-0.19 (0.087)
Ekman transport–SIE	0.03 (0.42)	0.16 (0.15)	0.16 (0.16)	-0.03 (0.82)
Ekman transport–SST	-0.50 (<0.001)	-0.21 (0.065)	-0.28 (0.011)	-0.03 (0.82)

Table 1.2: Interannual correlation coefficients between seasonal metrics over 1979–2013. Observed and median CMIP5 correlation coefficients (p values in brackets). Significance takes into account the lag-1 autocorrelation. For the median CMIP5 correlation, the p value is calculated using the median lag-1 autocorrelation. Correlations significant at the 95% confidence level are shown in bold. Individual CMIP5 correlation coefficients are shown in Fig. 1.8.

	<i>DJF</i>	<i>MAM</i>	<i>JJA</i>	<i>SON</i>
<i>Jet strength–SIE</i>				
Observed	0.39 (0.025)	0.35 (0.039)	0.21 (0.23)	0.03 (0.87)
CMIP5 median	0.16 (0.37)	0.18 (0.29)	0.06 (0.75)	0.10 (0.56)
<i>Jet strength–SST</i>				
Observed	-0.40 (0.016)	-0.14 (0.43)	-0.01 (0.95)	-0.10 (0.58)
CMIP5 median	-0.47 (0.005)	-0.21 (0.22)	-0.17 (0.33)	-0.39 (0.020)

Table 1.3: Additional inter-model correlation coefficients between trends over 1979–2013. As for Table 1.1, for additional metrics assessed in Section 1.3.6. SSS refers to sea surface salinity. Ekman pumping trends in this table are calculated as the trend in the Ekman pumping PC.

	<i>DJF</i>	<i>MAM</i>	<i>JJA</i>	<i>SON</i>
Evaporation–SST	0.69 (<0.001)	0.76 (<0.001)	0.63 (<0.001)	0.51 (<0.001)
Cloud cover–SST	-0.15 (0.16)	0.08 (0.48)	0.19 (0.076)	0.23 (0.033)
SIE–SSS	-0.44 (<0.001)	-0.11 (0.35)	-0.37 (0.002)	-0.42 (<0.001)
Ekman pumping–SSS	0.20 (0.094)	0.23 (0.058)	0.12 (0.34)	-0.02 (0.89)
P–E–SSS	0.24 (0.050)	0.15 (0.21)	0.11 (0.38)	0.00 (0.99)

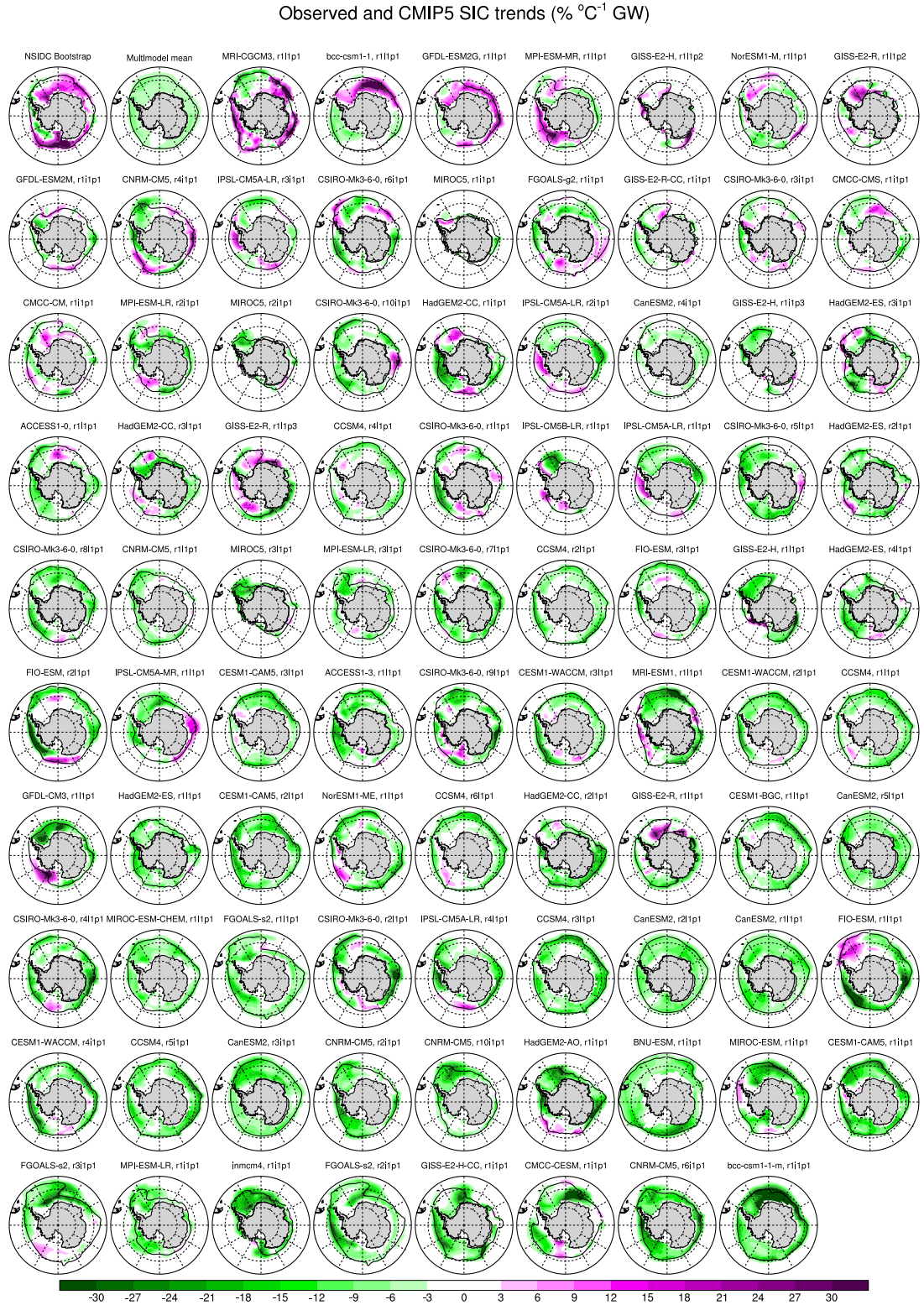


Figure 1.6: Annual SIC trends for observations and models over 1979–2013. Trends are expressed as a change per degree of global warming. (top left) Observed SIC from the NSIDC Bootstrap algorithm. (top second left) Multi-model mean. Individual models are ordered based on their annual SIE trend, with models with the largest SIE increase shown first (top rows) and models with the largest SIE decrease shown last (bottom rows).



Figure 1.7: Annual SST trends for observations and models over 1979–2013. Trends are expressed as a change per degree of global warming. (top left) Observed SST from HadISST. (top second left) Multi-model mean. Individual models are ordered as per Fig. 1.6.

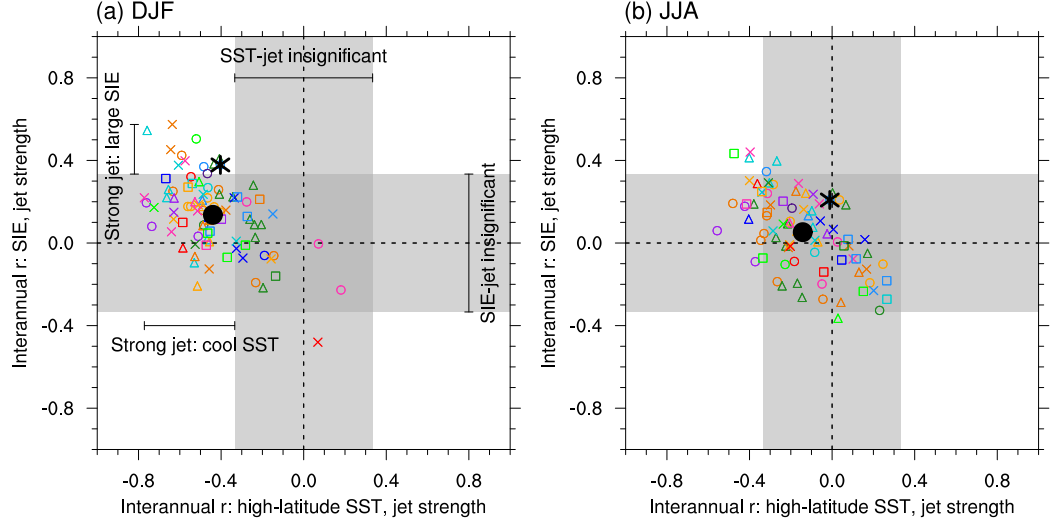


Figure 1.8: Interannual correlation coefficients between jet strength, high-latitude SST and SIE over 1979–2013. (a) DJF; and (b) JJA. Interannual correlations are calculated for observations and each model realisation separately, using linearly de-trended time series. The interannual correlations between high-latitude SST and jet strength are shown on the horizontal axes. The interannual correlations between SIE and jet strength are shown on the vertical axes. All available model ensemble members are shown. Observed SST from HadISST, SIE from NSIDC and jet strength from ERA-Interim. Figure details as per Fig. 1.2. Grey shading indicates correlations insignificant at the 95% confidence level, as determined by a two-sided Student’s t test. Autocorrelation is not accounted for in this shading, but has very little influence on the significance of individual models (p values change by <0.005). SST-jet correlations within the vertical grey band are insignificant. SIE-jet correlations within the horizontal grey band are insignificant. Both SST-jet and SIE-jet correlations within the centre darker grey square are insignificant. Most of the JJA correlations shown in (b) lie in the centre darker grey square and are insignificant. In DJF (a), more correlations lie outside the vertical band of grey shading, but not outside the horizontal band of grey shading, indicating that in most models there is a stronger interannual jet-SST relationship than there is interannual jet-SIE relationship.

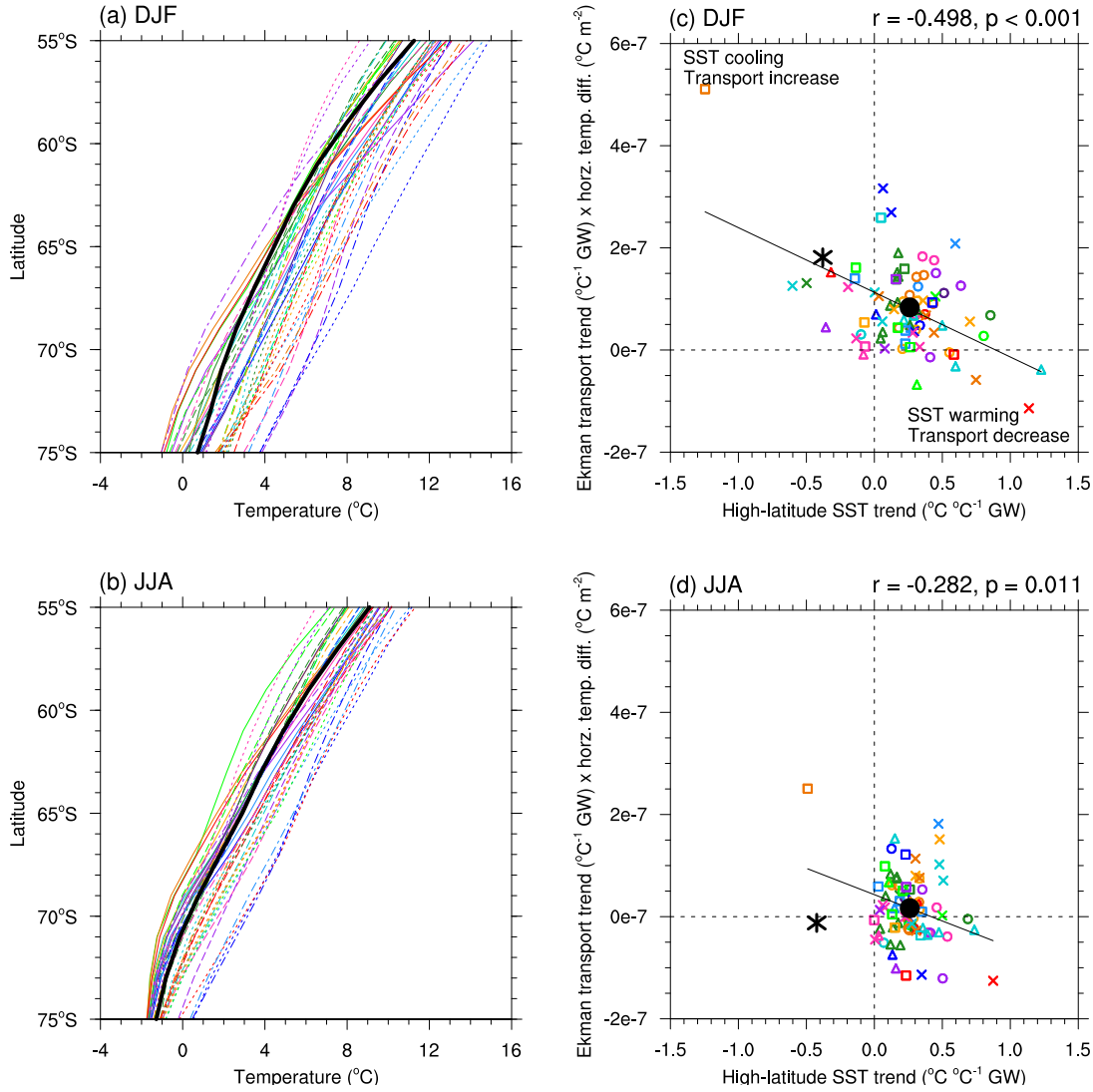


Figure 1.9: Zonal-mean temperature versus latitude, and Ekman transport trends over 1979–2013. Seasonal zonal-mean temperature averaged over 0–25 m for: (a) DJF; and (b) JJA. The first available ensemble member for each model is shown. The observed profile (black) is an average of SODA and Ishii over 1979–2011. Trends in Ekman transport versus trends in high-latitude SST for: (c) DJF; and (d) JJA. Trends are expressed as a change per degree of global warming. Ekman transport trends are calculated as the trend in the Ekman transport PC multiplied by the mean-state horizontal temperature gradient at high latitudes. All available model ensemble members are shown. Figure details as per Fig. 1.2.

1.5.1 Scale analysis

Horizontal temperature advection due to Ekman transport is compared with vertical temperature advection due to Ekman upwelling (Fig. 1.10). We use area-averaged terms for calculations so that various latitude bands can be assessed; as we are interested in mean-state orders of magnitude rather than linear trends, comparing area averages rather than PCs is reasonable.

Horizontal and vertical advection terms are compared as follows:

$$\alpha = \frac{V_E \bar{T}_y / h}{w_E \bar{T}_z} \quad (1.2)$$

Where \bar{T}_y is the horizontal temperature gradient over the latitude bands assessed, h is the depth of the surface layer (25 m), and \bar{T}_z is the vertical temperature gradient at the base of the summer mixed layer. The inclusion of h in the numerator is necessary to directly compare terms as Ekman transport is a depth-integrated flow in the upper h metres, whereas Ekman pumping is a velocity.

Over all latitude bands assessed $V_E \gg w_E$, however $\bar{T}_y / h \ll \bar{T}_z$. As a result, we find the numerator and denominator in Equation 1.2 to be of similar orders of magnitude. Further equatorward, where τ_x is relatively large and $\nabla \times \boldsymbol{\tau}$ small, northward Ekman transport is larger and $\alpha \sim 5\text{--}10$, but between $60\text{--}75^\circ\text{S}$, where the zonal wind transitions from westerly to easterly, $\alpha \sim 0.5\text{--}2$. As such, we conclude that over these latitude bands, both Ekman transport and Ekman pumping terms are important in driving variations in SST, and hence sea ice.

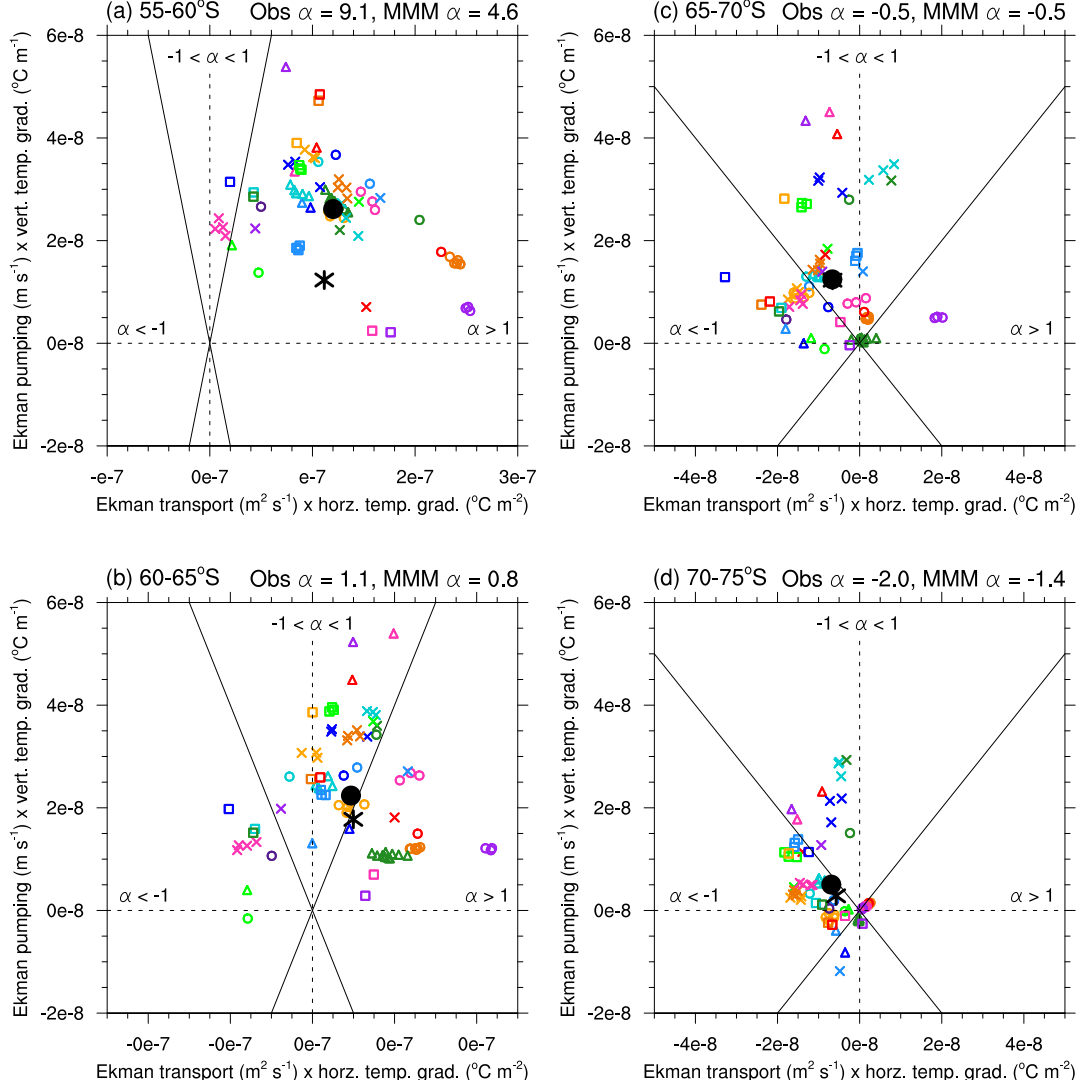


Figure 1.10: DJF horizontal versus vertical mean-state temperature advection over 1979–2013. Advection terms are averaged over: (a) 55–60°S; (b) 60–65°S; (c) 65–70°S; and (d) 70–75°S. The horizontal axes show the numerator from Equation 1.2 (horizontal temperature advection) and the vertical axes show the denominator from Equation 1.2 (vertical temperature advection). The ratio of horizontal to vertical advection (α) is shown for the observations and the multi-model mean (MMM) above each panel. The $\alpha=1$ and the $\alpha=-1$ lines are shown. Points that lie to the right of the two lines (as in a) indicate that $\alpha>1$ and horizontal temperature advection dominates over vertical temperature advection. Points that lie above the two lines (as in c) indicate that $-1<\alpha<1$ and vertical temperature advection dominates over horizontal temperature advection. All available model ensemble members are shown. Figure details as per Fig. 1.2.

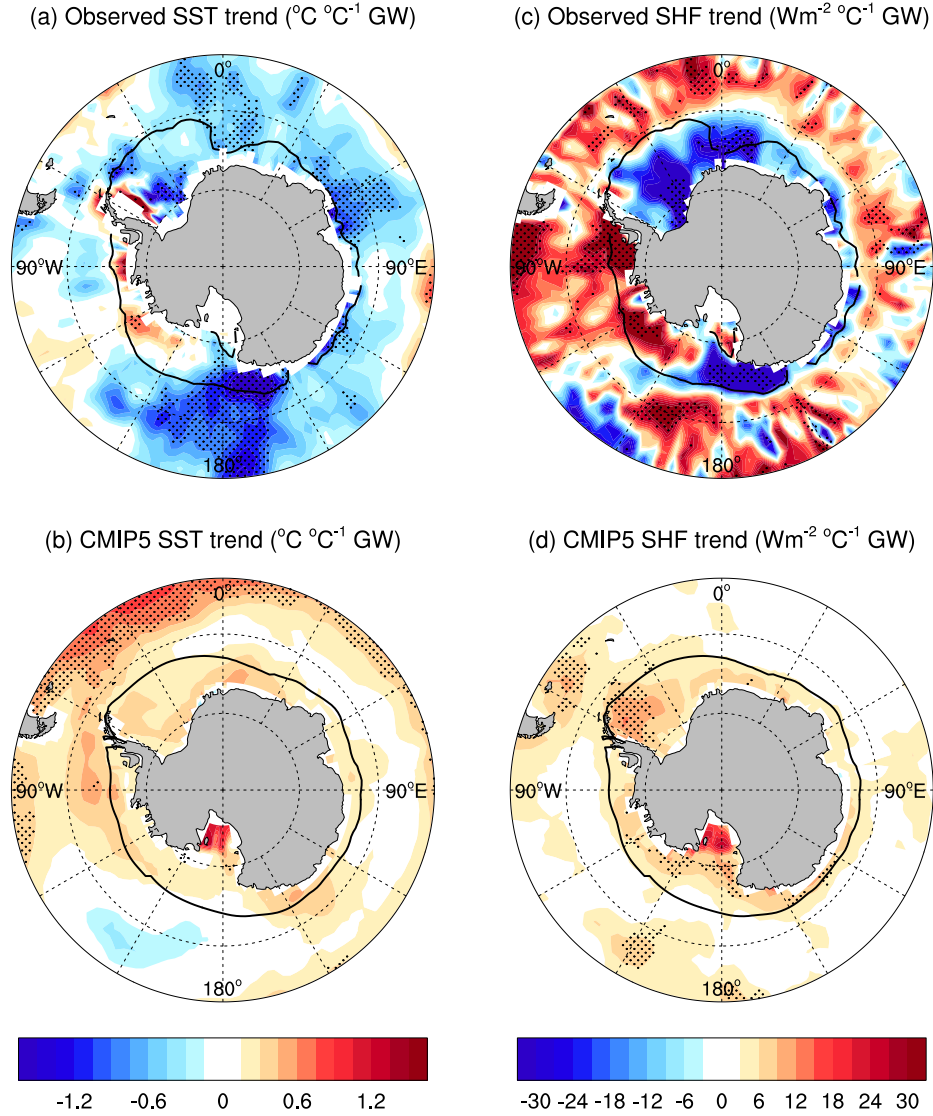


Figure 1.11: DJF trends in SST and downward total heat flux (positive heating the ocean) over 1979–2013. (a) Observed SST from HadISST; (b) CMIP5 multi-model mean SST; (c) observed heat flux from ERA-Interim; and (d) CMIP5 multi-model mean heat flux. Trends are expressed as a change per degree of global warming. Multi-model means are calculated using the first available ensemble member for each model. Stippling indicates significance: (a,c) at the 95% level as determined by a two-sided Student's t test; and (b,d) where 80% of models agree on the sign of the mean trend, which corresponds to 30 out of 37 models. The mean-state 15% SIC contour is shown in black.

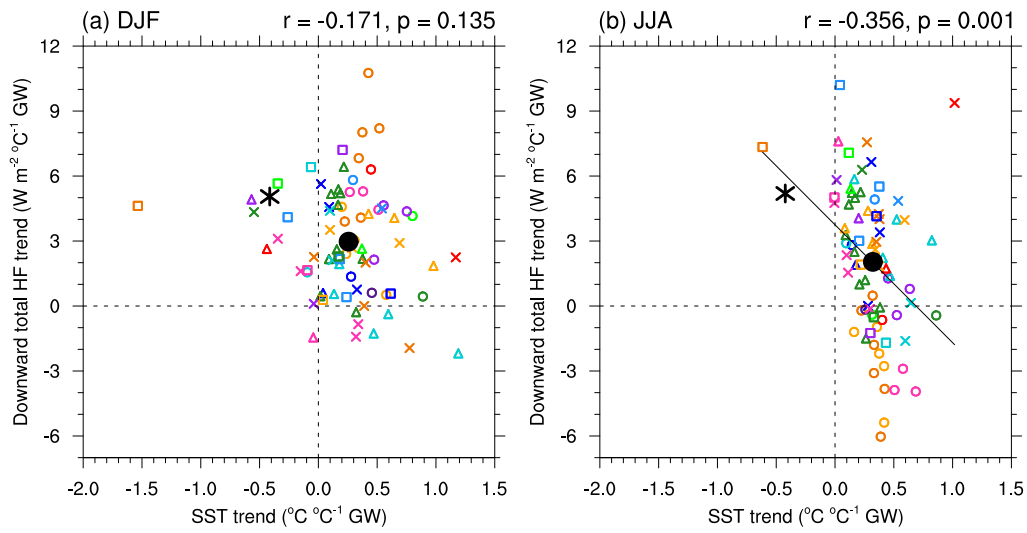


Figure 1.12: Trends in downward total heat flux (positive heating the ocean) versus SST over 1979–2013. (a) DJF; and (b) JJA. Trends are expressed as a change per degree of global warming and are calculated over 55–65°S. Observed heat flux from ERA-Interim, although considerable uncertainty exists in this estimate. Figure details as per Fig. 1.2.

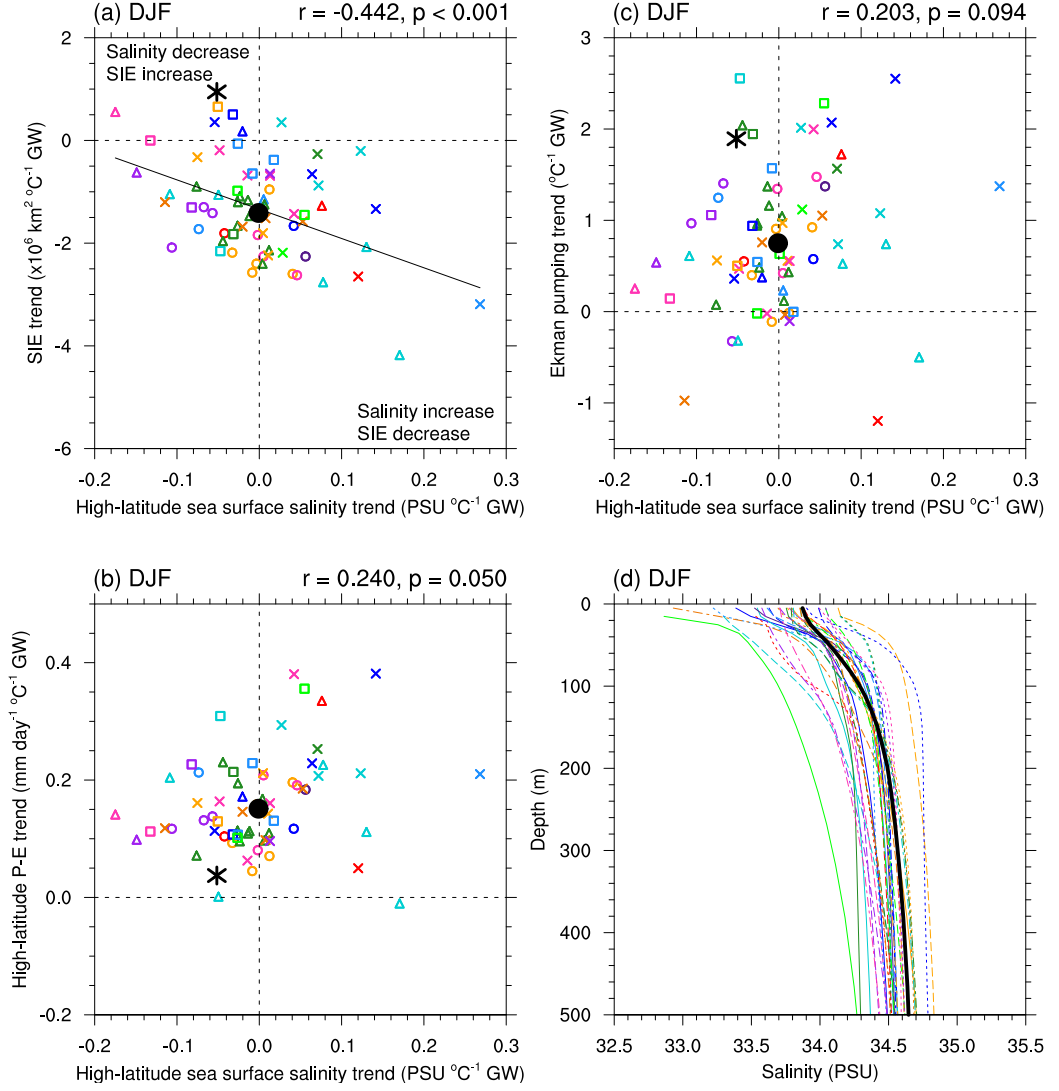


Figure 1.13: DJF trends over 1979–2013 and mean-state salinity profiles over 1979–2005. (a) trends in SIE versus trends in high-latitude sea surface salinity; (b) trends in high-latitude ocean P–E versus trends in high-latitude sea surface salinity; (c) trends in Ekman pumping versus trends in high-latitude sea surface salinity; and (d) climatological zonal-mean salinity profiles averaged over $60\text{--}70^\circ\text{S}$. Trends are expressed as a change per degree of global warming. All available model ensemble members are shown in (a–c). The first available ensemble member is shown in (d). Observed salinity (black line in d) from SODA and Ishii, and precipitation from ERA-Interim. Ekman pumping trends in (c) are calculated as the trend in the Ekman pumping PC. Figure details for (a–c) as per Fig. 1.2.

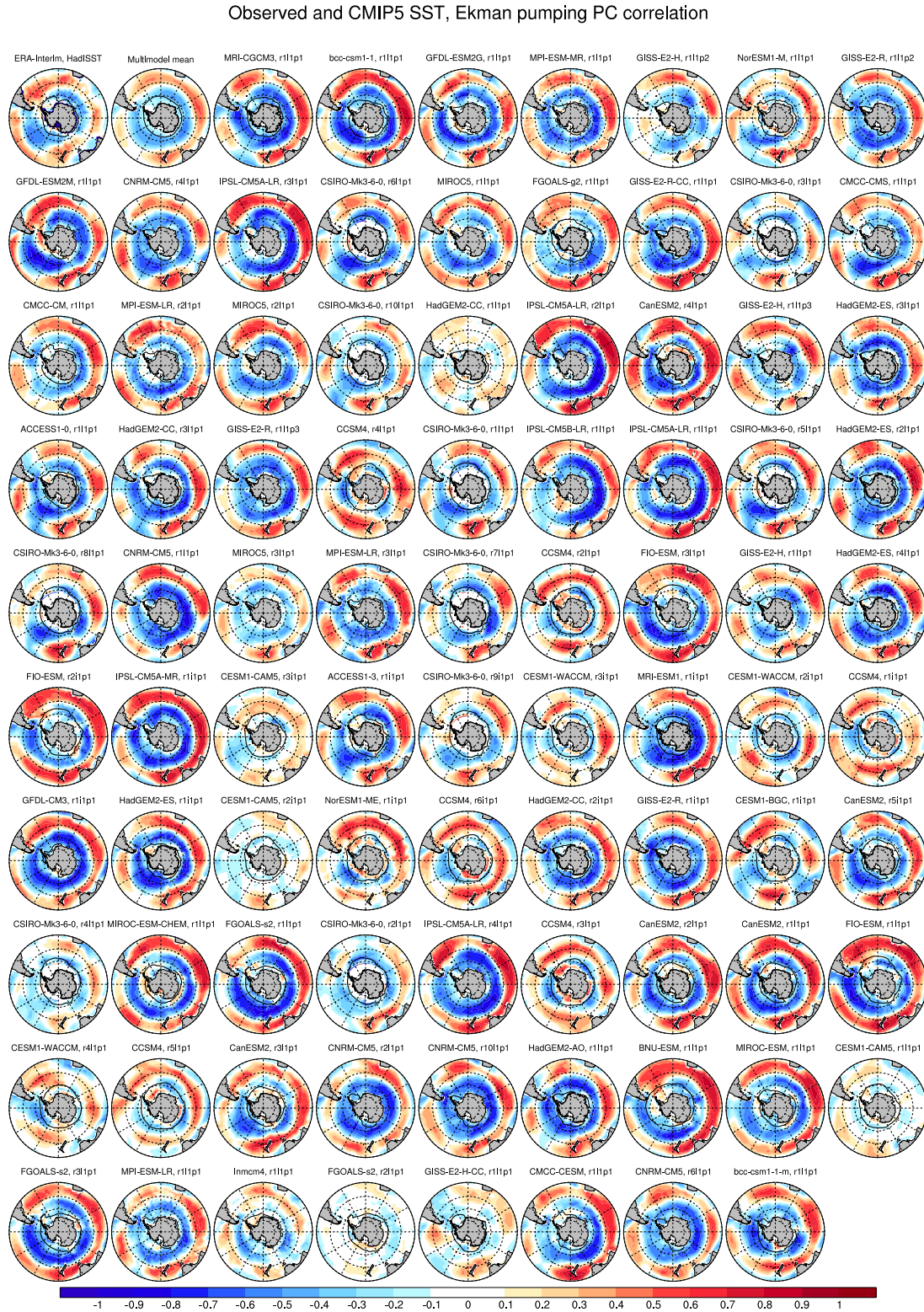


Figure 1.14: DJF correlations between SST and Ekman pumping PCs for observations and models over 1979–2013. Interannual correlations are calculated using linearly de-trended time series. (top left) Observed wind stress from ERA-Interim, SST from HadISST. (top second left) Multi-model mean. Individual models are ordered as per Fig. 1.6.

Part 2

Tropical Pacific SST drivers of recent Antarctic sea ice trends

The material in this Part is based around work published as:

Purich, A., M. H. England, W. Cai, Y. Chikamoto, A. Timmermann, J. C. Fyfe, L. Frankcombe, G. A. Meehl, and J. M. Arblaster, 2016: Tropical Pacific SST drivers of recent Antarctic sea ice trends. *Journal of Climate*, **29**, 8931–8948, doi:10.1175/JCLI-D-16-0440.1.

A. P. and M. H. E. conceived the study. Y. C. and J. C. F. undertook the model simulations. A. P. assembled the observational data, undertook all analyses, prepared all figures and wrote the first draft of the manuscript. All authors contributed to the development of ideas, writing and revising the manuscript.

Accompanying supplementary material is included at the end of this Part in Section 2.5. The published version of this material is included in Appendix B.

Abstract

A strengthening of the Amundsen Sea Low from 1979–2013 has been shown to largely explain the observed increase in Antarctic sea ice concentration in the eastern Ross Sea and decrease in the Bellingshausen Sea. Here we show that while these changes are not generally seen in freely-running coupled climate model simulations, they are reproduced in simulations of two independent coupled climate models; one constrained by observed sea surface temperature anomalies in the tropical Pacific, and the other by observed surface wind-stress in the tropics. Our analysis confirms previous results and strengthens the conclusion that the phase change in the Interdecadal Pacific Oscillation from positive to negative over 1979–2013 contributed to the observed strengthening of the Amundsen Sea Low and associated pattern of Antarctic sea ice change during this period. New support for this conclusion is provided by simulated trends in spatial patterns of sea ice concentrations that are similar to those observed. Our results highlight the importance of accounting for teleconnections from low to high latitudes in both model simulations and observations of Antarctic sea ice variability and change.

2.1 Introduction

The dipole pattern of recent Pacific sector sea ice trends, with decreasing ice in the Bellingshausen Sea and increasing ice in the Ross Sea, has been attributed to changing winds (Holland and Kwok, 2012; Fan et al., 2014), and specifically to the strengthening of the Amundsen Sea Low (Turner et al., 2009, 2015b; Clem and Fogt, 2015; Clem and Renwick, 2015; Meehl et al., 2016a; Raphael et al., 2016). There is some suggestion that recent increasing Antarctic sea ice trends since 1979 can be explained by interdecadal variability (Fan et al., 2014; Gagné et al., 2015), particularly arising from the phase change of the Interdecadal Pacific Oscillation (IPO) to negative after the late-1990s (Meehl et al., 2016a), rather than by direct anthropogenic forcing. As such, it is pertinent to scrutinise the proposed causes of these trends. Here we further examine the concept that recent trends in tropical sea surface temperature (SST) and tropical-to-extratropical teleconnections influenced the Amundsen Sea Low, thus contributing to the observed pattern of Antarctic sea ice trends. The goal of this study is to address and quantify the influence of tropical Pacific SST variability on Antarctic sea ice trends, specifically focussing on the role of the IPO.

Tropical Pacific SST variability influences the Amundsen Sea Low via convectively generated atmospheric Rossby wavetrains, including the well-known Pacific South American (PSA) pattern (Hoskins and Karoly, 1981; Mo and Higgins, 1998; Mo, 2000; Yuan and Martinson, 2000; Irving and Simmonds, 2016) as well as a meridionally oriented wavetrain during spring (Clem and Fogt, 2015). Through its influence on equatorial and off equatorial convection, El Niño-Southern Oscillation (ENSO) teleconnections to Antarctic sea

ice have been previously noted. La Niña is associated with a strengthened Amundsen Sea Low, causing increased sea ice in the eastern Ross and Amundsen Seas due to increased southerly flow at the surface, and decreased sea ice in the Bellingshausen Sea due to increased northerly flow in this region; and vice versa for El Niño (Renwick, 2002; Turner, 2004; Stammerjohn et al., 2008; Ciaso and England, 2011; L’Heureux and Thompson, 2006; Simpkins et al., 2012; Ciaso et al., 2015). There are seasonal variations in the ENSO teleconnection, with a link between El Niño and the negative Southern Annular Mode (SAM; and La Niña and the positive SAM), present during austral summer, but not during austral winter (e.g. L’Heureux and Thompson, 2006; Simpkins et al., 2012). The magnitude of atmospheric circulation anomalies associated with ENSO are roughly comparable for all seasons (relative to the seasonal cycle of ENSO), although are strongest during austral spring, and the strongest influence on sea ice occurs during austral winter and particularly spring (Jin and Kirtman, 2009; Simpkins et al., 2012). There are also differences in the teleconnections for different types of El Niño events (e.g. eastern Pacific versus central Pacific events; Ciaso et al., 2015).

Tropical Pacific SSTs have been connected to sea ice reductions in the Bellingshausen Sea via a strengthened Amundsen Sea Low during austral autumn (Ding and Steig, 2013). Atmospheric wind forcing associated with ENSO variability has been linked to seasonal sea-ice duration trends over 1990–2007 in the Atlantic and Pacific sectors (Matear et al., 2015). Clem and Fogt (2015) found that the negative trend in the Pacific Decadal Oscillation since 1979 has contributed to the deepening of the Amundsen Sea Low during austral spring. Recently, as noted above, Meehl et al. (2016a) have also linked the increase in Ross Sea ice trends to the phase shift of the IPO to negative (below normal tropical eastern Pacific SST on the decadal timescale) that occurred in the late-1990s. Warming of the tropical Atlantic Ocean has also been linked with a deepening Amundsen Sea Low, and thus to sea ice changes (Li et al., 2014, 2015a,b; Simpkins et al., 2014). However, recent evidence suggests that the tropical eastern Pacific rather than the tropical Atlantic provides the dominant forcing since the late 1990s with the shift to the negative phase of the IPO at this time (Meehl et al., 2016a).

To date, investigation of changes in the tropical Pacific and Atlantic and their teleconnections to Antarctic sea ice have been tested using atmospheric general circulation models (Li et al., 2014, 2015a,b; Simpkins et al., 2014; Meehl et al., 2016a) and an ocean-ice general circulation model (Matear et al., 2015); potentially neglecting important coupled ocean-atmosphere-ice feedbacks. We also note that Simpkins et al. (2012) found no significant relationship between trends in sea ice concentration (SIC) and trends in ENSO over 1980–2008, while Liu et al. (2004) and Yu et al. (2011) found that the trends in the SAM and ENSO produce similar spatial patterns in sea ice compared to the observed trends, but explain less than a third of the magnitude of total SIC trends over 1979–2002 and 1979–2007, respectively. With the additional years in the analysis period assessed here (1979–2013), as well as consideration of the phase change of the IPO over this period in the late-1990s (e.g. Meehl et al., 2016b), it is worth revisiting how changes in the

tropical Pacific may have influenced Antarctic sea ice trends in a coupled framework. We also attempt to separate the externally forced signal from the signal generated by internal variability in the Pacific, something not attempted in previous studies. We examine simulations from two different partially-coupled experiments that are forced by observed variability in certain pre-defined regions (termed “pacemaker” experiments) to investigate how observed tropical Pacific decadal variability affected observed Antarctic sea ice trends. The use of these pacemaker experiments enables an estimate of the role of Pacific Ocean SST variability forcing on SIC trends.

2.2 Data and methods

2.2.1 Data and model experiments

We utilise passive microwave SIC processed using the National Snow and Ice Data Center (NSIDC) Bootstrap algorithm (Comiso and Nishio, 2008), and SST from Hadley Centre Sea Ice and Sea Surface Temperature (HadISST; Rayner et al., 2003). We also assess SIC processed using the National Aeronautics and Space Administration (NASA) Team algorithm, as it is possible that spurious trends are present in the Bootstrap algorithm dataset (Eisenman et al., 2014) and results are found to be almost identical. Mean sea level pressure (MSLP) is taken from ERA-Interim (Dee et al., 2011), regarded to be the most reliable reanalysis over Antarctica (Bromwich et al., 2011; Bracegirdle and Marshall, 2012), and the Amundsen and Bellingshausen Seas (Bracegirdle et al., 2013).

To estimate the forced SIC and MSLP responses, we use the Coupled Model Inter-comparison Project phase 5 (CMIP5) multi-model mean. To match observations, CMIP5 data from the historical and Representative Concentration Pathway (RCP) 8.5 experiments are concatenated over 1979–2013. The choice of RCP scenario for the time period assessed (i.e. 2006–2013) has minimal influence, as all forcing scenarios are very similar over this period. We include all CMIP5 models that have SIC data available for both of these experiments, totalling 87 realisations from 41 CMIP5 models (listed in Table 2.1 in Section 2.5). Each realisation is weighted evenly in the multi-model mean. While the majority of CMIP5 models do not capture the observed increase in Antarctic sea ice, the observed sea ice trend lies within the spread of models (Gagné et al., 2015; Purich et al., 2016a), and the large ensemble of realisations provides the best available estimate of forced SIC and MSLP responses.

Ocean assimilation coupled pacemaker experiments are run using the low-resolution Community Earth System Model version 1.0.3 (CESM1; Shields et al., 2012; Chikamoto et al., 2015b). This version of CESM1 uses the Community Atmosphere Model version 4 (CAM4) and has atmosphere and land T31 ($\sim 3.75^\circ$) horizontal resolution, and ocean and sea ice $\sim 3.75^\circ$ horizontal resolution. CMIP5 anthropogenic and natural forcings are used, based on the CMIP5 historical and RCP4.5 (after 2005) scenarios, including greenhouse

gases, aerosols, stratospheric ozone, solar variations and volcanic eruptions.

The CESM1 pacemaker experiments assimilate observed three-dimensional temperature and salinity anomalies (ORA-S4; Balmaseda et al., 2013) into the ocean component of the coupled model. Data in sea-ice regions is not assimilated, so temperature anomalies in the sea-ice region are not constrained by observations and sea-ice variations are completely controlled by modelled internal dynamics. Because these experiments assimilate anomalies rather than absolute fields, the assimilation takes into account model biases related to the climatology, as well as having an externally forced component. Based on this, the assimilation runs have the same climatology and externally forced component as the historical runs. Therefore, the difference between assimilation runs and historical runs is the first order representation of internal climate variability.

Four CESM1 ensemble experiments with a partial assimilation approach in global or regional oceans similar to Chikamoto et al. (2015a) are conducted for the time period 1979–2013, with ten ensemble members each:

- Historical scenario (CESM1-HIST; historical forcings, no assimilation);
- Global ocean assimilation (CESM1-GLOB; historical forcings, with global ocean assimilated, excluding sea-ice regions);
- Equatorial Pacific Ocean assimilation (CESM1-eqPAC; historical forcings, with the entire equatorial Pacific Ocean between 10°S–10°N assimilated¹, remaining ocean unconstrained); and
- Atlantic Ocean assimilation (CESM1-ATL; historical forcings, with the Atlantic Ocean between 30°S–70°N assimilated, remaining ocean unconstrained).

To complement the CESM1 pacemaker experiments, wind-stress assimilation pacemaker experiments are conducted using an updated version of the Canadian Earth System Model version 2 (CanESM2; Arora et al., 2011) with an improved representation of ocean mesoscale eddy transfer coefficients (Saenko et al., 2016). CMIP5 anthropogenic forcings are applied in all CanESM2 experiments, based on the CMIP5 historical and RCP4.5 (after 2005) scenarios, including greenhouse gases, aerosols and stratospheric ozone. Half of the ensemble members also include solar variations and volcanic eruptions, while the other half do not. As the influence of these natural forcings over the latter part of the experimental period has been shown to be small (Saenko et al., 2016; Sigmond and Fyfe, 2016), the two subsets are combined.

The CanESM2 pacemaker experiments assimilate the wind-stress felt by the ocean, using the monthly surface wind stress field from ERA-Interim, which is closely constrained by observations. Three CanESM2 ensemble experiments with surface wind-stress assimilation in global or regional oceans as in Saenko et al. (2016) and Sigmond and Fyfe (2016)

¹Note that this differs from the experimental setup of (Kosaka and Xie, 2013), in which only the eastern equatorial Pacific was assimilated.

are conducted for the time period 1979–2012 (note that 2013 is not available for these CanESM2 experiments), with ten ensemble members each:

- Climatology (CanESM2-CLIM; time-varying historical forcings, with annually repeating climatological global wind-stress assimilated);
- Global wind-stress assimilation (CanESM2-GLOB; time-varying historical forcings, with monthly-evolving global wind-stress assimilated); and
- Tropical wind-stress assimilation (CanESM2-TROP; time-varying historical forcings, with monthly-evolving wind-stress between 35°S–35°N across all three ocean basins assimilated).

For CanESM2, all experiments include historical forcings, but only the time-varying assimilation experiments include internal variability in the assimilated wind stress field. The experiments have similar, although not identical climatologies (the CanESM2-CLIM annually repeating wind stress is based on 1979–1984, while the CanESM2-GLOB and CanESM2-TROP wind stress covers 1979–2012; Fig. 2.10 in Section 2.5). We again assume that the difference between the time-varying assimilation experiments (CanESM2-GLOB and CanESM2-TROP) and the climatology assimilation (CanESM2-CLIM) provides an estimate of the internal variability. This has previously been shown to be reasonable (Sigmond and Fyfe, 2016).

2.2.2 Analysis methods

For comparison between observations and models, all data are first bilinearly interpolated to a $2^\circ \times 2^\circ$ horizontal grid. All data are then annually averaged over the typical ENSO-cycle year (May through to the following April and referred to using the year of the January–April; Fig. 2.1). This averaging year is chosen to keep ENSO signals together (e.g. Fogt and Bromwich, 2006). Data from May 1979 to April 2013 are analysed (May 1979 to April 2012 for CanESM2), and we refer to this period as 1979–2013. The seasonality of teleconnections has previously been shown to be important (e.g. Jin and Kirtman, 2009; Li et al., 2014, 2015a,b; Simpkins et al., 2014). Here we focus on the annual average from May to April, but have also assessed seasonal averages, which are presented in the supplementary material (Section 2.5) and discussed briefly below.

To characterise ENSO we use SST anomalies in the Niño 3.4 region (5°S – 5°N , 170°E – 120°W ; Fig. 2.1), with anomalies referenced to the full period, 1979–2013. El Niño and La Niña events are defined here as occurrences when the Niño 3.4 index exceeds ± 0.75 standard deviations (based on the full 12-month average; Fig. 2.1c). Sensitivity to the choice of ENSO index and threshold are tested and results are found to be robust. To define the IPO we use the Tripole Index (TPI) as in Henley et al. (2015), calculated as equatorial Pacific SST anomalies (10°S – 10°N , 170°E – 90°W) minus averaged mid-latitude SST anomalies (25°N – 45°N , 140°E – 145°W and 50°S – 15°S , 150°E – 160°W ; Fig. 2.1b). Notably,

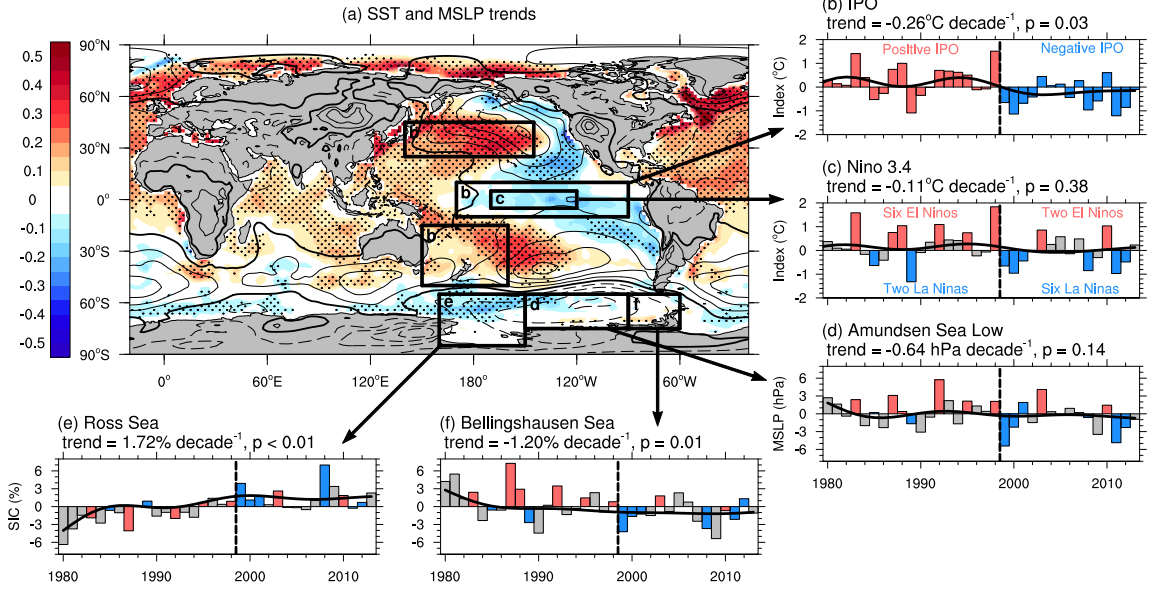


Figure 2.1: (a) SST and MSLP trends [$^{\circ}\text{C}$ and $\text{hPa} (10 \text{ y})^{-1}$] over 1979–2013. SST is shown in colour (blue=negative, red=positive) with MSLP contours overlain [-2 (dashed) to 2 (solid) by $0.2 \text{ hPa} (10 \text{ y})^{-1}$, with the zero contour in bold]. Stippling indicates statistical significance of SST trends at the 95% confidence level using a two-sided Student’s t test. Area-averaged time series for the regions indicated by black boxes: (b) unfiltered IPO (positive phase in red, negative phase in blue), with the filtered IPO (calculated from HadISST; Henley et al. 2015) shown by the black curve; (c) Niño 3.4 index; (d) Amundsen Sea Low MSLP; (e) Ross Sea SIC; and (f) Bellingshausen Sea SIC. The transition from positive IPO to negative IPO is marked with a dashed black line. In (c–f) El Niño events in red, La Niña events in blue, neutral years in grey, and 13-year low-pass filtered time series overlain in black.

we do not filter the IPO index. This is because we are interested in both the long-term trend in the IPO, which is in itself a low-pass filter analysis, as well as its interannual variations (e.g. for calculating the interannual regression with SIC). Without filtering, the TPI strongly resembles the Niño 3.4 index (e.g. Newman et al., 2016); however, the TPI also takes into account variability in mid-latitude regions (black boxes marked with ‘b’ in Fig. 2.1a), important when considering the influence of the tropical Pacific on the high latitudes. Over the period assessed here, while there has been no significant trend in the Niño 3.4 index ($p=0.38$), there has been a significant trend in the unfiltered IPO TPI ($p=0.03$; Fig. 2.1b,c) due to the transition from positive to negative that occurred in the late-1990s (e.g. Lee and McPhaden, 2008). Here we assume that the “trend” arises from subsampling multi-decadal climate variability, not from changes in external forcing. This is supported by the fact that the historical CMIP5 experiments do not capture a phase shift of the IPO during this time (refer to Section 2.3.4). As such, there are important differences between the IPO and the Niño 3.4 index emanating from the off-equatorial components of the IPO (Fig. 2.1a).

Linear trends in SIC and MSLP are calculated using least squares regression. Observed trend significance is determined using a two-sided Student’s t test at the 95%

confidence level. Autocorrelation is accounted for by defining the effective sample size, N_{eff} as:

$$N_{eff} = N \left(\frac{1 - r_1}{1 + r_1} \right) \quad (2.1)$$

where N is the sample size and r_1 is the lag-1 autocorrelation of the detrended SIC time series (Simpkins et al., 2012). The CMIP5 forced response for the period of interest is then subtracted from observed trends, to provide a rough estimate of unforced long-term trends in the observations.

For both CESM1 and CanESM2, trends are calculated for each ensemble member and then averaged (ten runs per ensemble). Ensemble average trend significance is determined when the simulated ensemble mean trend exceeds two standard deviations of individual ensemble member trends ($\sim 95\%$ confidence level). Difference trends between assimilation runs and the historical or climatology runs are also calculated for each model (for example, CESM1-GLOB minus CESM1-HIST). Difference trend significance is determined using a t test to compare two means at the 95% confidence level.

IPO-related trends in SIC and MSLP are calculated as the IPO trend (arising from internal decadal timescale variability) multiplied by the regression coefficient between the linearly-detrended IPO and linearly-detrended SIC or MSLP (e.g. Purich et al., 2013; Clem and Fogt, 2015). Significance of the observed IPO-related trends is assessed using a two-sided Student's t test at the 95% confidence level, testing both the IPO trend and the regression coefficient. Autocorrelation in the regression coefficient significance test was accounted for by defining the effective sample size, N_{eff} as:

$$N_{eff} = N \left(\frac{1 - r_1 r_2}{1 + r_1 r_2} \right) \quad (2.2)$$

where N is the sample size, r_1 is the lag-1 autocorrelation of the detrended SIC time series and r_2 is the lag-1 autocorrelation of the IPO time series (Ciasto and Thompson, 2008). Modelled significance is determined when the average modelled trend exceeds two standard deviations of individual ensemble member trends ($\sim 95\%$ confidence level).

To examine how the IPO-modulation of ENSO events has contributed to changes in the Amundsen Sea Low and the regional SIC surplus (e.g. Ross Sea) and deficit (e.g. Bellingshausen Sea), observed cumulative maps are calculated for SIC and MSLP. This procedure is similar to calculating composites but without dividing by the number of events. The benefit of using cumulative anomaly maps in this case is that the magnitude of different cumulative anomalies can be directly compared. For example, the cumulative anomalies during all years of the negative IPO phase can be directly compared to the cumulative anomalies during only ENSO years of this IPO phase, to see what contribution ENSO years make to the total cumulative anomalies. Significance is calculated using a t test to compare two means at the 95% confidence level (for example, El Niño years versus all years, La Niña years versus all years, and El Niño years versus La Niña years). The sample size is defined as the number of events in the smallest group being compared.

2.3 Results

2.3.1 Observed trends

The observed annual mean SIC trend pattern with the external CMIP5 forcing signal removed (Fig. 2.2a) looks similar to the total trend pattern (Fig. 2.3a). Significant increases in SIC are seen around much of Antarctica (Fig. 2a magenta shading; Stammerjohn et al., 2008; Holland and Kwok, 2012; Simpkins et al., 2012), with a particularly strong increase in the Ross Sea. Smaller areas of significant decreases in SIC are seen in the Amundsen and Bellingshausen Seas (Fig. 2.2a green shading). In these areas the observed sea ice decline (Fig. 2.3a) is stronger than the CMIP5 ensemble trend (Fig. 2.4a). The observed SIC trend pattern shows similarity to the SIC composite difference pattern for ENSO events (Stammerjohn et al., 2008; Simpkins et al., 2012; Ciaso et al., 2015). This motivates further investigation into the role of the tropical Pacific SST anomalies in influencing Antarctic SIC trends, particularly the dipole SIC trends between the Ross and Bellingshausen Seas.

2.3.2 Pacemaker trends

If decadal SST variability in the tropical Pacific is remotely influencing Antarctic SIC trends via changed atmospheric circulation, assuming that atmospheric teleconnections are adequately represented in the models, we would expect that coupled model experiments in which tropical Pacific SST variability matches the observations should simulate SIC trends similar to those observed. Therefore, we next consider the SIC trends from the pacemaker experiments. As described above (Section 2.2.1), the CESM1 assimilation runs have the same climatology and externally forced component as the historical runs. Therefore, we assume that subtracting CESM1-HIST from both CESM1-GLOB and CESM1-eqPAC gives a first order estimate of the internal (linearly unforced) variability. Similarly, we interpret the difference between CanESM2-GLOB and CanESM2-TROP from CanESM2-CLIM as a rough linear indicator of internal variability with the caveats discussed above. Subtracting out the CESM1-HIST or CanESM2-CLIM trends (Fig. 2.4b,c) from the assimilation trends (Fig. 2.3b–e) thus provides a first order estimate of the decadal variability without the influence of anthropogenic forcings such as increasing greenhouse gases, aerosols and stratospheric ozone depletion. That is, this method highlights the influence of tropical teleconnections, as well as the decadal component of the SAM trend due to tropical interactions and intrinsic variability.

We note that the forced trends as simulated by the CMIP5 multi-model mean (Fig. 2.4a), CESM1-HIST (Fig. 2.4b) and CanESM2-CLIM (Fig. 2.4c) are similar, although the CMIP5 multi-model mean is more zonally symmetric, as expected due to averaging across 41 different models. In all panels, the positive trend in the SAM is seen through the negative MSLP trend encompassing the Antarctic continent. In the CMIP5 multi-model mean there is a circumpolar decrease in SIC, and while there are regions in CESM1-HIST

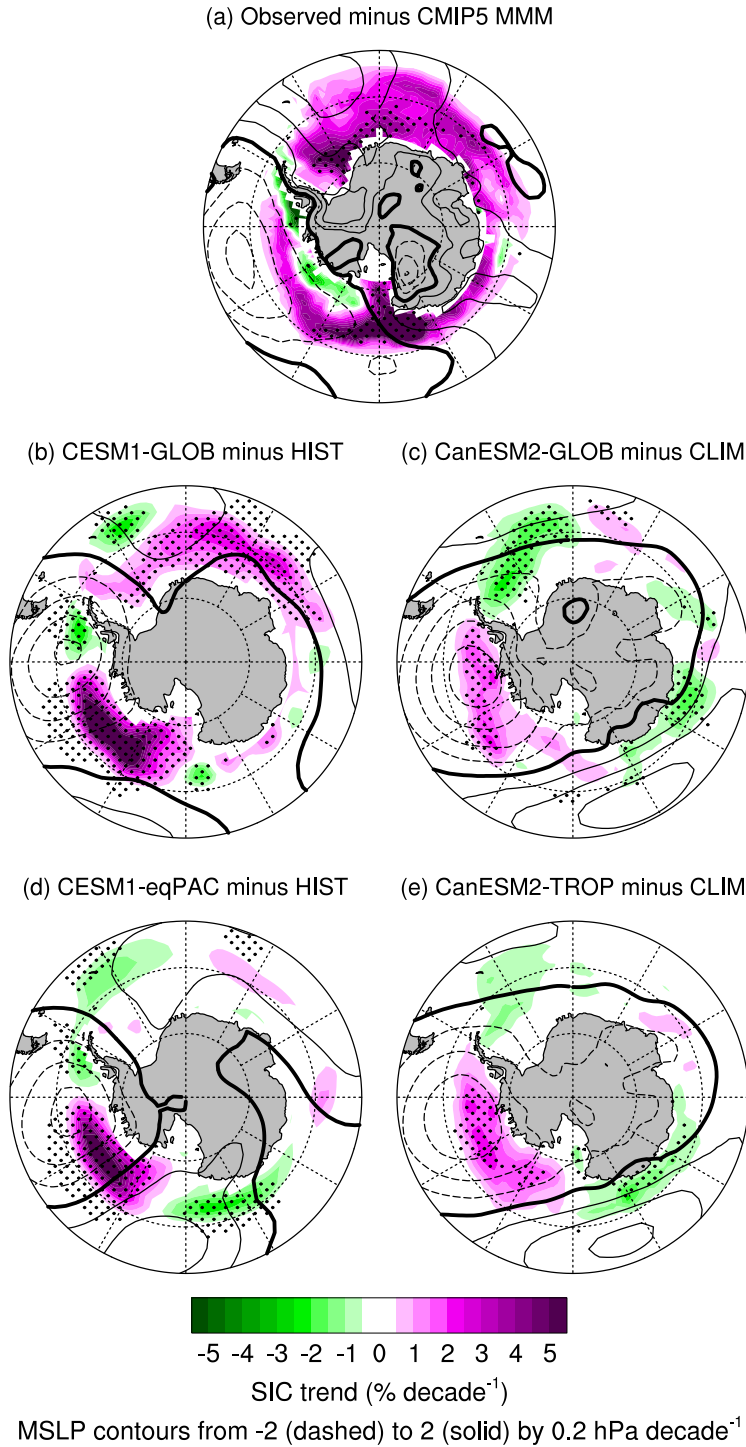


Figure 2.2: SIC and MSLP trends ($\%$ and $\text{hPa} (10 \text{ y})^{-1}$), with trends due to historical forcings removed: (a) observed minus CMIP5 multi-model ensemble; (b) CESM1-GLOB minus CESM1-HIST; (c) CanESM2-GLOB minus CanESM2-CLIM; (d) CESM1-eqPAC minus CESM1-HIST; and (e) CanESM2-TROP minus CanESM2-CLIM. In all Figs, SIC is shown in colour (green=negative, magenta=positive) with MSLP contours overlain (dashed=negative, bold=zero and solid=positive contours). Ensemble average trends are calculated over 1979–2013 using annually averaged SIC. Stippling indicates statistical significance of SIC trends at the 95% confidence level: (a) using a two-sided Student’s t test; and (b–e) using a t test to compare two means.

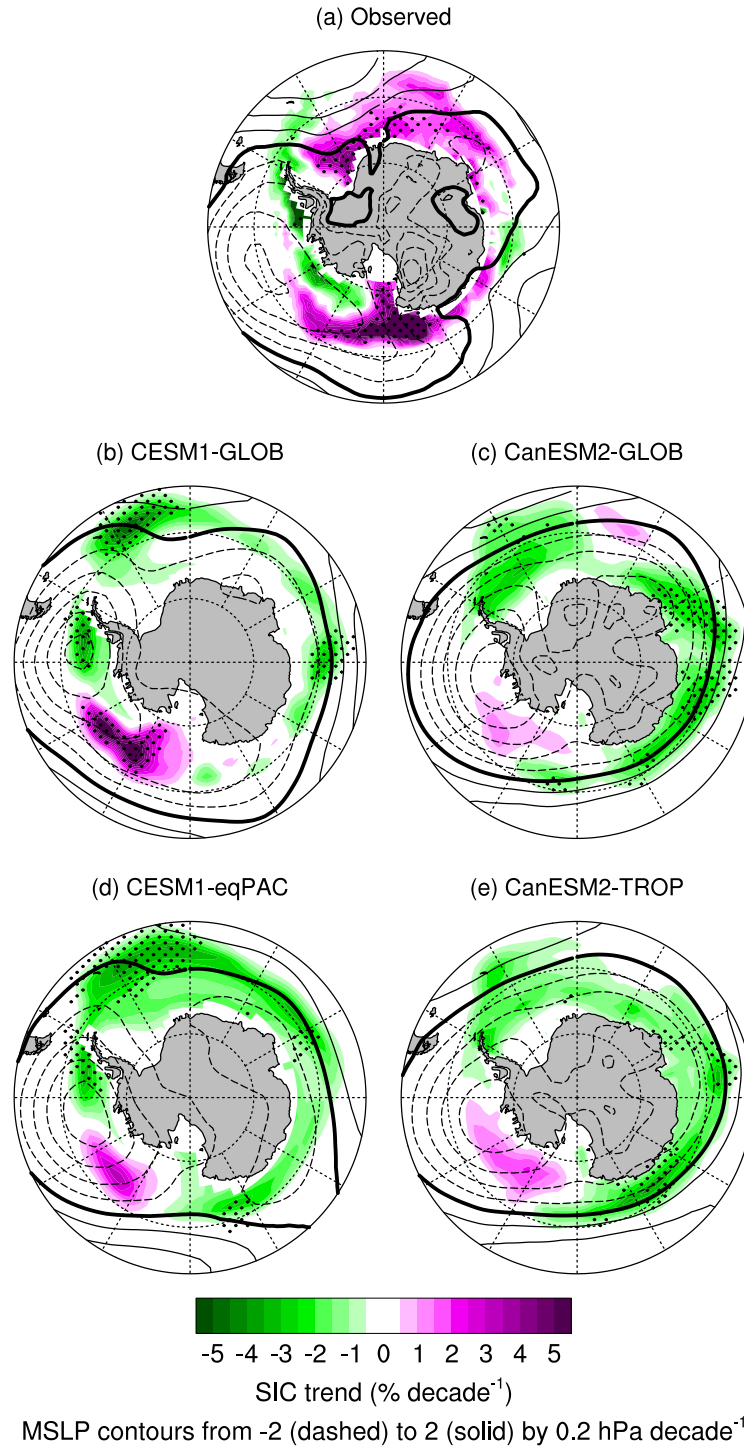


Figure 2.3: As for Fig. 2.2, but showing total SIC and MSLP trends (i.e. including trends due to natural variability and historical forcings).

and CanESM2-CLIM where there are very weak or no trends in SIC, most regions also show a decrease. As such, subtracting the forced trends (Fig. 2.4) from the total trends (Fig. 2.3) to obtain the decadal variability signal (i.e. trends due to internal variability; Fig. 2.2) has the result of weakening the negative MSLP trends over the Antarctic continent that are also seen in Fig. 2.3, and of largely reducing the vast areas of total decreasing SIC seen in both the CESM1 (Fig. 2.3b,d) and CanESM2 (Fig. 2.3c,e) simulations. Because the

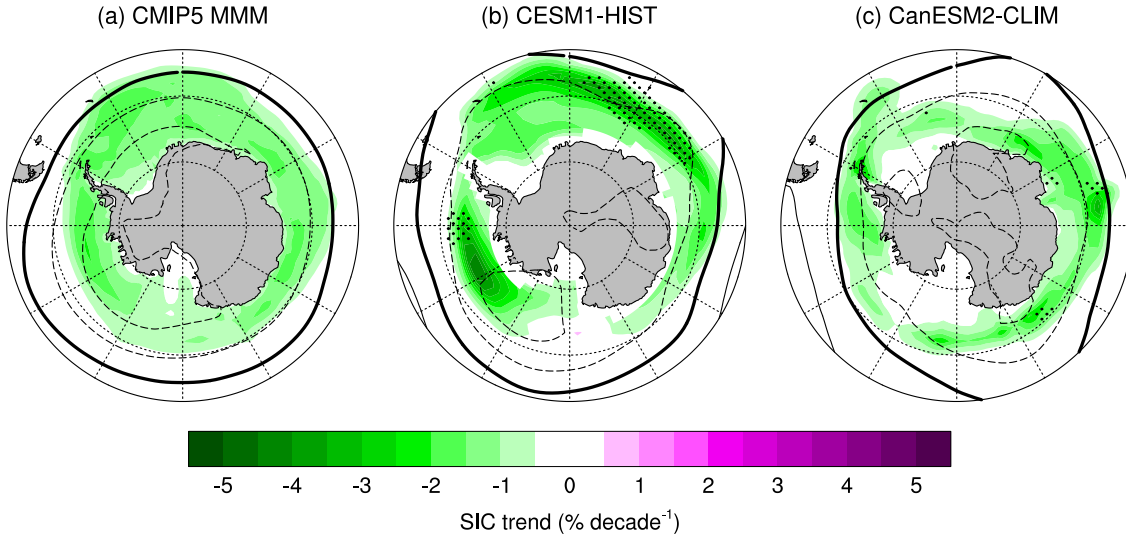


Figure 2.4: As for Fig. 2.2, but showing the SIC and MSLP trends due to historical forcings: (a) CMIP5 multi-model mean; (b) CESM1-HIST; and (c) CanESM2-CLIM.

CMIP5 multi-model mean SIC trend is largely zonally symmetric (Fig. 2.4a), subtracting this from the total observed SIC trend (Fig. 2.3a) does not substantially change the regional pattern of SIC trends in the observed decadal variability signal, although decreases are made weaker and increases are made stronger (Fig. 2.2a).

CESM1-GLOB decadal variability (minus HIST) signals (Fig. 2.2b) in SIC and MSLP look qualitatively similar to the observed trends (Fig. 2.2a): there are large regions of increasing SIC in eastern Antarctica and in the eastern Ross and Amundsen Seas (although notably the observed increasing SIC in the western Ross Sea is not captured), while a decrease in SIC is seen in the Bellingshausen Sea. A strengthening of the Amundsen Sea Low is apparent; however the strongest decrease in MSLP is located further towards the Antarctic Peninsula than observed, and does not extend as far west. As a result, the strong increase in the Ross and Amundsen Seas SIC is shifted eastward compared to the satellite data. Meehl et al. (2016a) show that the position of the convective heating anomaly in the tropical Pacific influences the location of the resulting teleconnection, so these biases may be due to differences in the position of tropical Pacific precipitation anomalies between observations and CESM1.

CESM1-eqPAC decadal variability signals (Fig. 2.2d) show very similar trends in MSLP to CESM1-GLOB (Fig. 2.2b), along with decreasing SIC in the Bellingshausen Sea and increasing SIC in the eastern Ross and Amundsen Seas, suggesting that tropical Pacific variability is driving signals in these regions in CESM1-GLOB (Fig. 2.2b). The overall MSLP pattern in these experiments is consistent with the PSA pattern. Elsewhere, CESM1-eqPAC trend signals do not resemble CESM1-GLOB signals, however increasing SIC in CESM1-ATL (Fig. 2.5) suggests that Atlantic SST anomaly forcing is driving the CESM1-GLOB signals in the Atlantic and Indian sectors. Further, while CESM1-

eqPAC variability shows a weak decrease in the eastern Ross Sea (Fig. 2.2d), CESM1-ATL variability shows an increase (Fig. 2.5a). It also appears that CESM1-eqPAC and CESM1-ATL forcings are largely additive (as in Li et al., 2015b), explaining the majority of the decadal SIC signals in CESM1-GLOB. We note that the increase in SIC in the eastern Ross and Amundsen Seas is slightly weaker in CESM1-eqPAC (Fig. 2.2d) compared to CESM1-GLOB (Fig. 2.2b), suggesting that a portion of this decadal signal must come from outside of the tropical Pacific and Atlantic Oceans, likely from the extratropics.

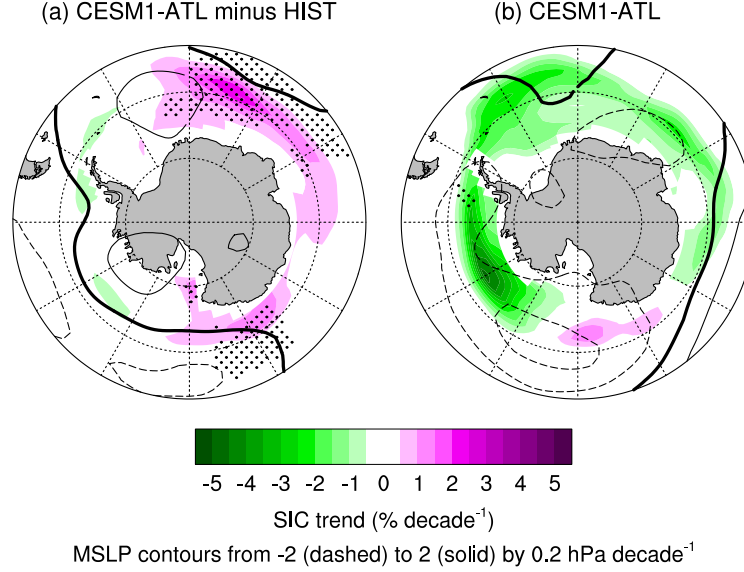


Figure 2.5: As for Fig. 2.2, but showing CESM1 trends from the Atlantic assimilation: (a) CESM1-ATL minus HIST; and (b) CESM1-ATL trends (i.e. including trends due to natural variability and historical forcings).

In Li et al. (2015b) tropical Atlantic forcing, rather than Pacific forcing, leads to the strongest deepening of the Amundsen Sea Low. Li et al. (2015b) use CAM4, the same atmospheric component of CESM used in this study, although at a higher resolution (approximately 2° horizontal resolution, compared to approximately 3.75° resolution here) and with a different dynamical core (a finite volume core, compared to a spectral core here). However, Li et al. (2015b) used Atmospheric Model Intercomparison Project (AMIP)-type specified SST forcing compared to the partially coupled experiments here. Previous studies have suggested the lack of coupling in AMIP-type runs can cause errors by the atmosphere responding too strongly in certain regions to SST perturbations (e.g. Barsugli and Battisti, 1998). In convective heating anomaly experiments designed to specify the actual dynamic heating that forces teleconnections (as opposed to SST), negative convective heating anomalies in the eastern equatorial Pacific (arising from the observed negative phase of the IPO) produced a stronger response in the Amundsen Sea Low compared to a positive convective heating anomaly in the equatorial Atlantic (arising from observed positive tropical Atlantic SSTs; Meehl et al., 2016a). Thus, there are contributions to the deepening of the Amundsen Sea Low from convective heating anomalies in both the tropical Atlantic and tropical Pacific, but evidence from Meehl et al. (2016a) shows that the equatorial eastern Pacific makes the larger contribution. Other differences

in the dominance of Atlantic or Pacific teleconnections may be due to resolution and/or dynamical differences in the atmospheric model, to differences arising from the coupled system, and/or to differences in the SST fields assimilated (total observed SST, compared to observed SST anomalies here) and the differing climatologies that follow.

We next compare results from CESM1 to CanESM2 (Fig. 2.2c,e). While both models show a strengthening of the Amundsen Sea Low, the wavetrain structure differs. In contrast to the clear PSA pattern displayed by CESM1 (Fig. 2.2b,d), CanESM2 shows a positive MSLP signal further west. Both CanESM2-GLOB (Fig. 2.2c) and CanESM2-TROP (Fig. 2.2e) show an increase in sea ice in the Amundsen and eastern Ross Seas, as also simulated by CESM1, and the decrease in the western Ross Sea seen in CESM1-eqPAC is also seen in CanESM2-TROP. Whereas CESM1 captures the observed decrease in sea ice in the Bellingshausen Sea, CanESM2 decadal variability shows an increase here, but a decrease in the Weddell Sea (CanESM2-GLOB), possibly due to the eastward elongation of the negative MSLP signal. While there are differences in the decadal variability signals of SIC and MSLP between CESM1 and CanESM2, both models capture a strengthening of the Amundsen Sea Low, and the corresponding increase in sea ice in the Amundsen and eastern Ross Seas.

2.3.3 Seasonality of trends

While our focus is on annual mean trends, patterns do vary seasonally (L’Heureux and Thompson, 2006; Simpkins et al., 2012; Ciasto et al., 2015). We briefly discuss the seasonality of the observed and simulated SIC and MSLP trends, noting that trends in CESM1-GLOB and CESM1-eqPAC are largely similar, and likewise for CanESM2-GLOB and CanESM2-TROP; as such, we group the simulations from each model together in our discussion.

Observed decadal variability signals in SIC during austral summer (Fig. 2.11a in Section 2.5) and autumn (Fig. 2.12a in Section 2.5) show decreasing SIC in the Amundsen and Bellingshausen Seas, and increases elsewhere. However, CESM1 (Figs 2.11b,d and 2.12b,d in Section 2.5) and CanESM2 (Figs 2.11c,e and 2.12c,e in Section 2.5) show an increase in SIC in the Amundsen Sea, and little trend in the western Ross Sea. In austral winter (Fig. 2.13a in Section 2.5) and spring (Fig. 2.14a in Section 2.5) the region of observed decreasing SIC shifts eastward to the Antarctic Peninsula, with increases elsewhere. Both models show an increase in SIC in the eastern Ross and Amundsen Seas, and CESM1 shows a decrease in SIC in the Bellingshausen Sea (Figs 2.13b,d and 2.14b,d in Section 2.5). The biases in seasonal SIC variability are rendered in the annual mean (Fig. 2.2).

While a strengthening of the Amundsen Sea Low is seen for observations and both CESM1 and CanESM2 in the annual-mean (Fig. 2.2), this signal is largely due to strengthening occurring during austral autumn and winter (Figs 2.12 and 2.13 in Section 2.5, respectively). During summer, there is a strong positive SAM trend in the forced trends

simulated by the CMIP5 multi-model mean, CESM1-HIST and CESM1-CLIM (Fig. 2.15 in Section 2.5). When subtracted to obtain decadal variability, only a weak negative MSLP signal is seen in observations over the eastern Ross Sea (Fig. 2.11a in Section 2.5). In CESM1 there is a weak negative signal located over the Bellingshausen Sea (Fig. 2.11b,d in Section 2.5). In CanESM2, despite removing the SAM trend there is a clear deepening of the Amundsen Sea Low (Fig. 2.11c,e in Section 2.5). During autumn, a clear PSA wavetrain pattern is evident in observations, as also reported in Ding and Steig (2013). Both models capture the PSA pattern, although it is weaker than observed, particularly in CanESM2. In winter the wavetrain pattern is more meridionally oriented in observations and for CESM1. A similar negative MSLP signal is seen in both models during spring (Fig. 2.14 in Section 2.5), however in observations the signal is centred over the eastern Ross Sea, rather than over the Amundsen and Bellingshausen Seas (Fig. 2.14a in Section 2.5). While PSA-like wavetrains are shown by CESM1 and CanESM2, a more meridionally-oriented wavetrain is seen in observations (Clem and Fogt, 2015).

2.3.4 IPO-related sea ice trends

We next examine the contribution of tropical decadal SST variability on Antarctic sea ice in these pacemaker experiments. Based on the similarity between decadal variability SIC and MSLP signals in the Pacific sector in CESM1-GLOB and CESM1-eqPAC (*cf.* Fig. 2.2b and d), we focus on tropical Pacific variability. Due to the experimental setup, for CanESM2 all tropical variability is considered (i.e. CanESM2-TROP; including Pacific, Atlantic and Indian Oceans). We calculate SIC and MSLP trends congruent with decadal variability in the IPO, which is manifested as a trend from positive to negative in subsampling multi-decadal variability, using an unfiltered TPI to represent the IPO. As described above (Section 2.2.2), without filtering the TPI strongly resembles the Niño 3.4 index (*cf.* Fig. 2.1b and c; Newman et al., 2016); however, the TPI also takes into account variability of subtropical and mid-latitude regions, which could be potentially important when considering the influence of the tropical Pacific on the high latitudes [such as the influenced of the South Pacific Convergence Zone (SPCZ), e.g. Schneider et al., 2012; Clem and Renwick, 2015; Meehl et al., 2016b]. As also mentioned above (Section 2.2.2), while there has been no significant trend in the Niño 3.4 index, there has been a significant trend in the IPO during the time period under consideration due to the transition from the positive phase of the IPO to negative in the late-1990s (Fig. 2.1b,c). There have also been changes in the frequency (more La Niña than El Niño events; e.g. Ummenhofer et al., 2009) and spatial characteristics (more central Pacific than eastern Pacific El Niño events; e.g. McPhaden et al., 2011) of ENSO. These ENSO changes coincide with the IPO transition from the positive to the negative phase (Figs 2.1 and 2.6; Lee and McPhaden, 2008; Meehl et al., 2014; Fyfe et al., 2016) and motivate our interest in the significant trend of the IPO.

The observed IPO-related SIC trends (Fig. 2.7a) show a decrease in the Belling-

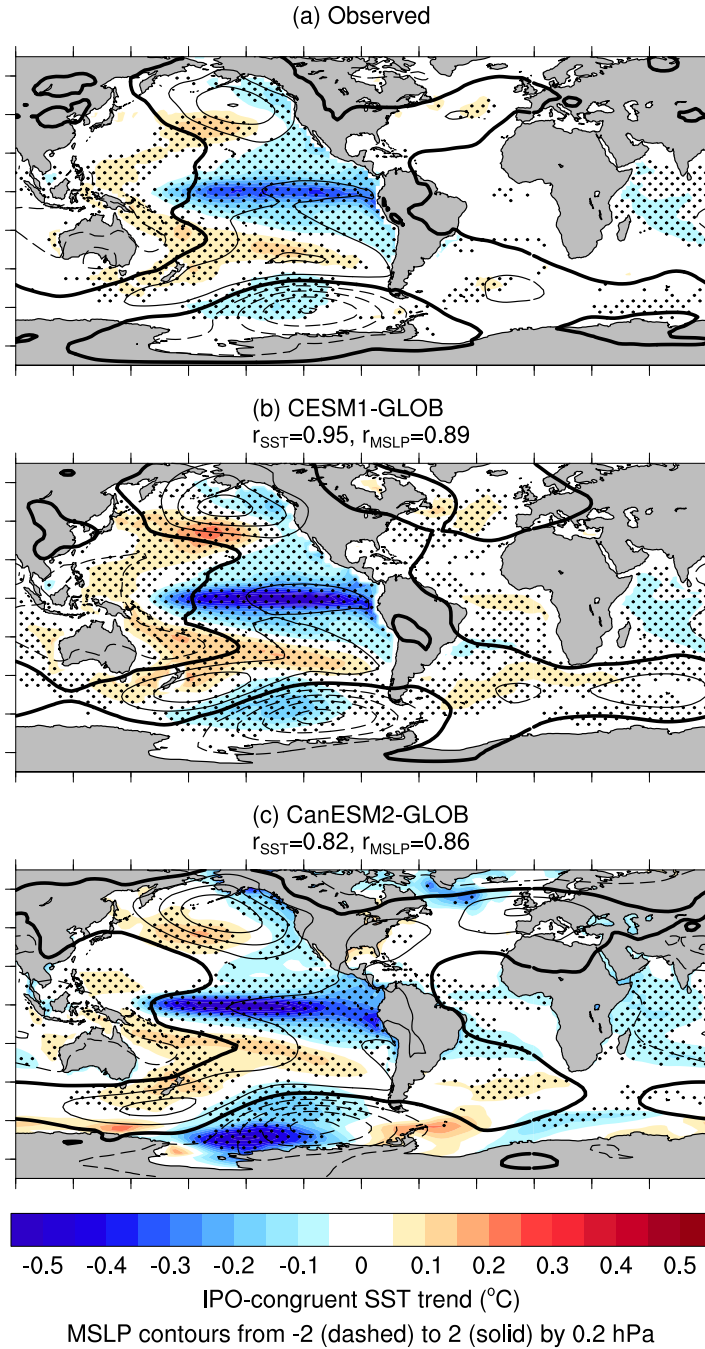


Figure 2.6: SST and MSLP trends congruent with trends in the IPO due to its transition from positive to negative [$^{\circ}\text{C}$ and $\text{hPa} (10 \text{ y})^{-1}$]: (a) observed; (b) CESM1-GLOB; and (c) CanESM2-GLOB. Congruent trends are calculated over 1979–2013 as the linear regression of detrended SST onto the detrended IPO, multiplied by the trend in the IPO. In (b–c) congruent trends are calculated for each ensemble member individually and then averaged across members. Stippling indicates statistical significance of SST trends at the 95% confidence level: (a) using a two-sided Student’s t test to test significance of both the IPO trend and the regression coefficient; and (b–c) where the ensemble average trend exceeds two standard deviations. Pattern correlations between observed and modelled trends are calculated over the global domain and indicated above panels (b–c).

shausen Sea and an increase in the eastern Ross and Amundsen Seas, in association with a strengthened Amundsen Sea Low (Fig. 2.7a). This pattern is similar to the total trend pattern in the Pacific sector (Fig. 2.1a), albeit weaker, and the region of increasing SIC is shifted eastwards. In particular, the IPO-related SIC trends (Fig. 2.7a) cannot account for the observed increase in the western Ross Sea (Figs 2.2a, 2.3a). The CMIP5 multi-model mean, CESM1-HIST and CanESM2-CLIM show essentially no congruent trends (Fig. 2.16a,b,d in Section 2.5), as expected because the unconstrained model runs or ensemble members all have different phases of the IPO, which cancel out in the multi-model mean or ensemble averages. This also indicates that the external forcing is not causing one phase of the IPO to be favoured. IPO-related SIC and MSLP trends in CESM1-GLOB (Fig. 2.7b) and CESM1-eqPAC (Fig. 2.16c in Section 2.5) both agree well with the observations, showing a deepening of the Amundsen Sea Low as part of the PSA pattern, and a corresponding positive SIC trend in the eastern Ross and Amundsen Seas and a negative SIC trend in the Bellingshausen Sea. Further, these IPO-related SIC trends are very similar to the decadal variability signals discussed above (Fig. 2.1b,c). CanESM2-GLOB (Fig. 2.7c) and CanESM2-TROP (Fig. 2.16e in Section 2.5) also show similar IPO-related SIC and MSLP trends. The pattern correlations between simulated and observed congruent trends are high for both models, particularly for MSLP (Fig. 2.7). The agreement between the IPO-related SIC trends and total SIC trends thus suggest that the IPO is contributing to the regional dipole pattern of SIC trends in the Pacific sector, with the exception of the western Ross Sea, where the observed SIC increase is not explained by the IPO, nor simulated by either model (Figs 2.2b,c and 2.3b,c).

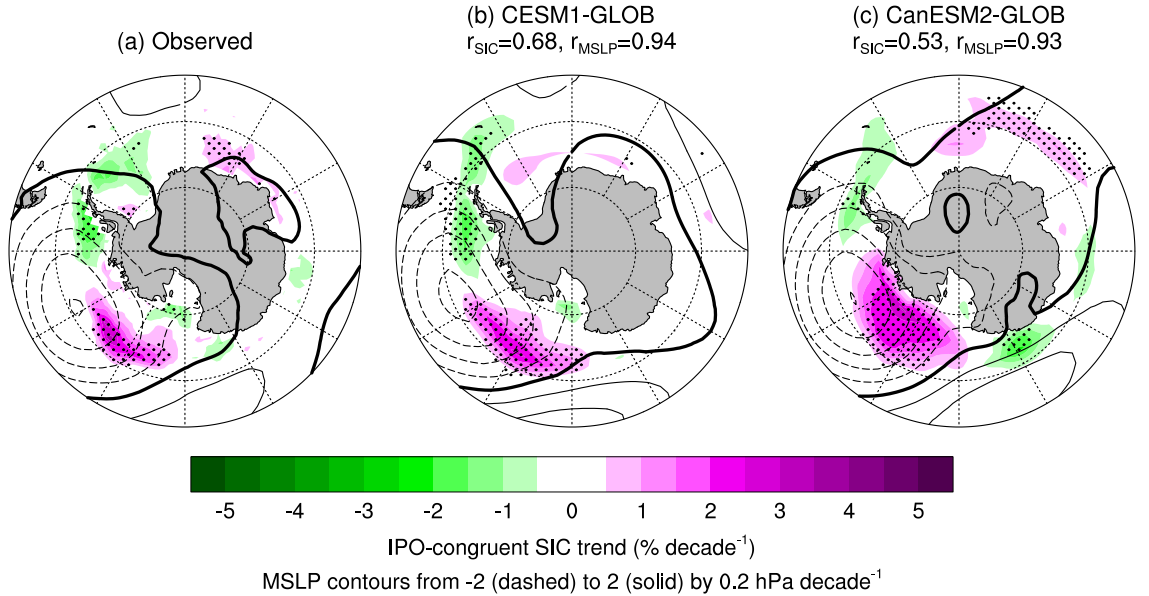


Figure 2.7: As for Fig. 2.6, but for SIC and MSLP trends congruent with trends in the IPO due to its transition from positive to negative $[\% \text{ and hPa } (10 \text{ y})^{-1}]$. Pattern correlations are calculated over the domain shown ($50\text{--}90^\circ\text{S}$).

The IPO-related SIC and MSLP trends are largely similar across all seasons (Figs 2.17 to 2.20 in Section 2.5). A strengthened Amundsen Sea Low is seen in all seasons, strongest

during austral winter and spring in observations and CESM1-GLOB, and strongest from austral autumn to spring in CanESM2-GLOB. Increased SIC in association with these circulation changes is seen in the eastern Ross and Amundsen Seas in all seasons, for observations, CESM1-GLOB and CanESM2-GLOB. Decreased SIC in the Bellingshausen Sea is also seen for most seasons and across the observations and both models, however it often lacks significance, and is not seen for CanESM2-GLOB during austral summer (Fig. 2.17c in Section 2.5). Overall, the strong agreement between the observations, CESM1 and CanESM2, and the similarity in IPO-related SIC trends across the seasons strengthens the conclusions made above regarding the annual-mean IPO-related trends.

2.3.5 IPO modulation of ENSO teleconnection

Meehl et al. (2016a) proposed that Ross Sea SIC trends have been influenced by the phase shift of the IPO (Fig. 2.1b). In their study, they find that changes in precipitation and convective heating primarily in the eastern Pacific and secondarily in the SPCZ region associated with the phase shift of the IPO in the late-1990s force anomalous Rossby waves, teleconnecting to the Amundsen Sea Low and causing a strengthening (as also described in Schneider et al., 2012; Clem and Renwick, 2015). From this, they infer that changes in the geostrophic wind result in more southerly flow over the Ross Sea, leading to increased sea ice in this region. In addition to increased Ross Sea ice, other studies relating the strengthened Amundsen Sea Low to Antarctic sea ice trends also find reduced sea ice in the Bellingshausen Sea due to increased northerly flow, (e.g. Li et al., 2014; Simpkins et al., 2014). We have confirmed here that the regional SIC trend characteristics associated with the IPO are due to a deepening of the Amundsen Sea Low (Fig. 2.7).

As described above (Section 2.1), the ENSO teleconnection to Antarctic sea ice has been widely studied (e.g. Renwick, 2002; Stammerjohn et al., 2008; Simpkins et al., 2012; Ciasto et al., 2015). Despite no significant trend in the Niño 3.4 index over 1979–2013, during the positive phase of the IPO more El Niño events occurred (between 1979–1998 there were six El Niños and two La Niñas; Fig. 2.1c), whereas during the negative phase of the IPO more La Niña events occurred (between 1999–2013 there were two El Niños and six La Niñas; Fig. 2.1c). Through Rossby wavetrain teleconnections to the Southern Hemisphere, a change in the frequency and spatial character of ENSO could impact the strength of the Amundsen Sea Low (Fig. 2.1d), which may lead to a rectification and a net surplus or deficit of SIC in different regions over 1979–2013 (Fig. 2.1e,f). Over 1990–2007, Matear et al. (2015) found that wind forcing associated with ENSO contributed to sea-ice duration trends in both the east and west Pacific sectors, further motivating examination of the ENSO contribution over the longer period here.

Comparing the cumulative anomalies of observed SIC and MSLP during the positive phase of the IPO with those during only ENSO years of the positive IPO (*cf.* Fig. 2.8a and d), it is clear that the two patterns are similar to each other, dominated by El Niño (Fig. 2.9a). Likewise, the cumulative anomalies during the negative phase of the IPO are similar

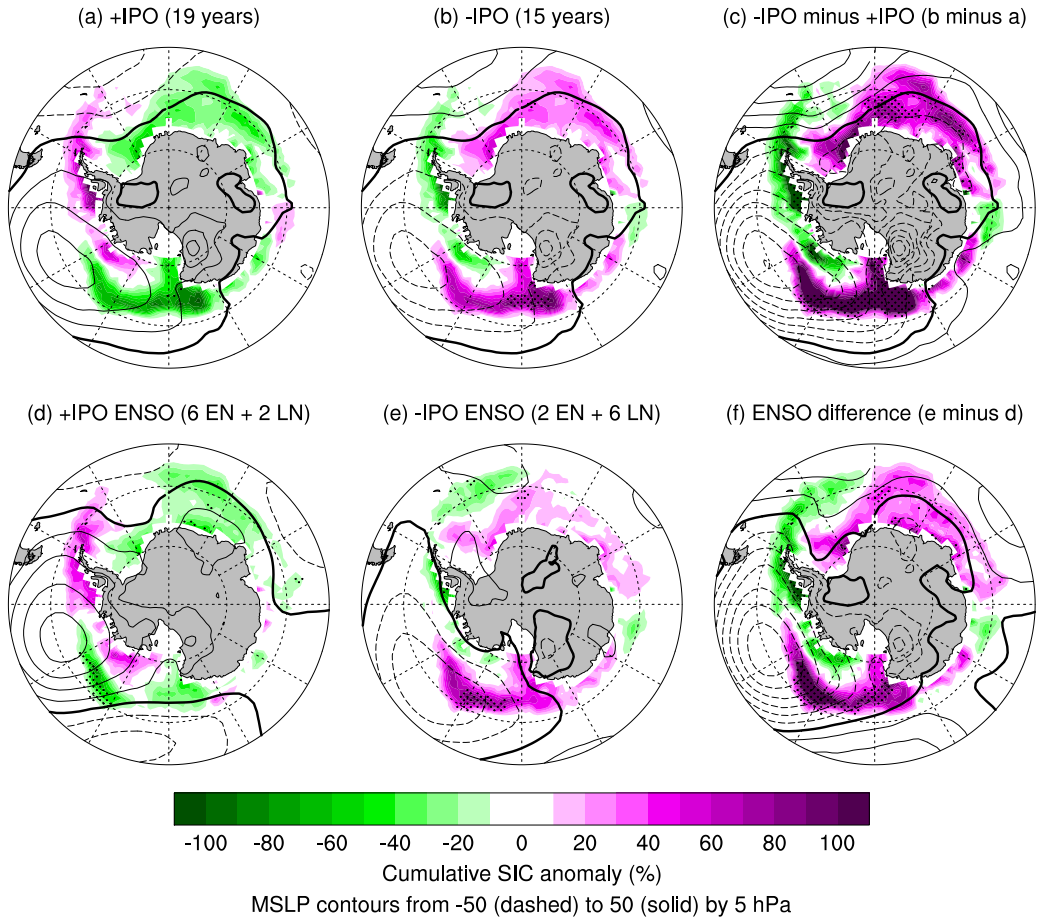


Figure 2.8: Observed SIC and MSLP cumulative anomalies (% and hPa): (a) positive IPO (1979–1999); (b) negative IPO (2000–2013); (c) IPO difference (b minus a); (d) ENSO years during positive IPO (six El Niños and two La Niñas); (e) ENSO years during negative IPO (two El Niños and six La Niñas); and (f) ENSO difference (e minus d). Cumulative anomalies are calculated as the sum of SIC and MSLP anomalies during specified events, without normalising by the number of events. Stippling indicates statistical significance of cumulative SIC anomalies at the 95% confidence level using a t test to compare two means: (a,b,d,e) comparing the select events to all years; and (c,f) comparing the two differenced groups.

to those during only ENSO years of the negative IPO (*cf.* Fig. 2.8b and e), dominated by La Niña (Fig. 2.9b). Following on, comparing their difference patterns (i.e. negative IPO minus positive IPO; negative IPO ENSO events minus positive IPO ENSO events; *cf.* Fig. 2.8c and f) shows that the ENSO cumulative anomaly pattern difference is very similar to the corresponding IPO cumulative anomaly difference, and is dominated by the difference between El Niño and La Niña (Fig. 2.9c). We note that these results should be considered with caution, as there is a trend in the IPO, as well as in the SIC and MSLP time series used in this analysis. However, repeating the analysis with linearly detrended time series (Figs 2.21, 2.22 in Section 2.5) finds that the spatial pattern of cumulative SIC anomalies in the eastern Ross, Amundsen and Bellingshausen Seas that occur during the two phases of the IPO are largely explained by the ENSO events in these phases. This supports the interpretation of Fig. 2.8.

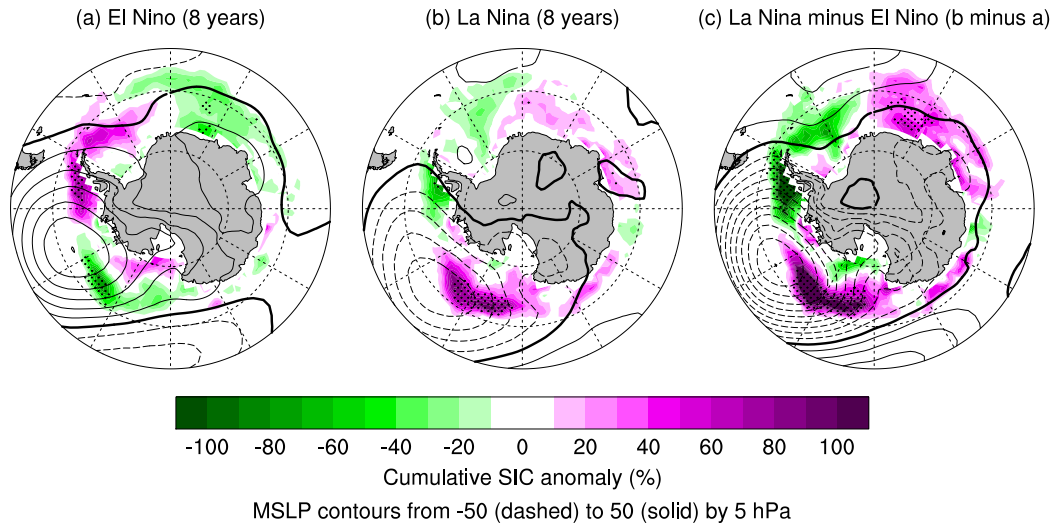


Figure 2.9: As for Fig. 2.8, but showing cumulative anomalies for: (a) El Niño; (b) La Niña; and (c) La Niña minus El Niño (b minus a).

The total SIC trends resulting from the impact of IPO can also be understood via the unequal number of El Niño and La Niña events during each IPO phase; i.e. more El Niño events during positive IPO and more La Niña events during negative IPO, as well as a change in the nature of events (Ashok et al., 2007; McPhaden et al., 2011). Furthermore, the ENSO teleconnection to high latitudes appears nonlinear and asymmetric with respect to El Niño and La Niña (Fig. 2.8d,e; also noted by Ciasco et al. 2015). As such, the cumulative impacts from El Niño and from La Niña do not completely offset, but rectify into mean changes. These mean changes are especially conspicuous when there are more El Niño events during positive IPO and more La Niña events during negative IPO (Fig. 2.8f). The difference between the cumulative impact during the negative IPO phase and during the positive IPO phase accounts for a large portion of the trend, suggesting that the influence of the IPO on the Amundsen Sea Low and SIC is overall manifest via its association with an unequal number of El Niño and La Niña events during the two phases of the IPO.

2.4 Discussion

Since regular satellite observations became available in 1979, Antarctic SIC has increased in most regions, despite greenhouse warming over the same period (Cavalieri and Parkinson, 2008; Comiso and Nishio, 2008; Parkinson and Cavalieri, 2012) and multi-model averages that show decreasing SIC. A particularly large increase in sea ice has been observed in the Ross Sea, although sea ice has been declining near the Antarctic Peninsula in the Amundsen and Bellingshausen Seas (Stammerjohn et al., 2008; Holland and Kwok, 2012; Simpkins et al., 2012). Utilising coupled pacemaker experiments we provide further evidence in support of internal decadal climate variability associated with the IPO as a driving influence on Antarctic sea ice trends in the Pacific sector, specifically in the east-

ern Ross, Amundsen and Bellingshausen Seas. We note, however, that the IPO cannot account for sea ice trends in the western Ross Sea. Our analysis suggests that tropical Pacific SST anomalies associated with the IPO and ENSO contribute to the rectification of observed trends on Antarctic sea ice.

The pacemaker experiments assessed here are based on coupled atmosphere-ocean-sea ice models, which differ from previous studies using atmospheric-only models (Li et al., 2014, 2015a,b; Simpkins et al., 2014; Meehl et al., 2016a). This is notable, because although these studies suggest that a strengthening of the Amundsen Sea Low due to tropical teleconnections can be linked to observed changes in the sea ice, the sea ice response is not directly simulated in the latter.

The majority of CMIP5 models simulate a decline in Antarctic sea ice extent (Turner et al., 2013a; Zunz et al., 2013), and while the overall observed trend has been shown to lie within modelled variability (Mahlstein et al., 2013; Polvani and Smith, 2013; Swart and Fyfe, 2013; Turner et al., 2013a; Zunz et al., 2013), when the regionality of sea ice trends is accounted for, trends during austral summer and autumn are outside the modelled range of variability (Hobbs et al., 2015). As with the majority of CMIP5 models, CESM1-HIST and CanESM2-CLIM lose too much sea ice compared to observed. However, CMIP5 ensemble members that happened to match the timing of the negative phase of the IPO also simulated an increase of Antarctic sea ice during the early 2000s (Meehl et al., 2014).

In both the CESM1 and CanESM2 assimilation experiments, the strengthened Amundsen Sea Low associated with the phase shift of the IPO results in an increase in sea ice in the eastern Ross and Amundsen Seas, however this increase is weaker than observed. Further, neither model captures the strong observed increase in sea ice in the western Ross Sea, and due to the lack of IPO-related sea ice trends in this region even in observations (Fig. 2.7a), it is unlikely that trends in this region are linked to the IPO phase change. Sea ice increases elsewhere around Antarctica are also not simulated in these models. Based on the assessment of decadal variability signals it appears that the CESM1 and CanESM2 assimilation experiments capture the observed variability well, but one interpretation is that greenhouse warming overwhelms the total trends in SIC in these experiments. Another possibility is that the locations of anomalous precipitation and convective heating anomalies may not be in the same locations or magnitudes as observed. It could be possible that either Antarctic sea ice variations in both CESM1 and CanESM2 are too sensitive to global warming, or that these models underestimate the amplitude of decadal variability of Antarctic sea ice by an overly damped response to tropical Pacific variability. A damped response may be the result of the cold SST bias in both models in the SPCZ region, suppressing convection there and damping the remote atmospheric response, because it has been shown that positive SST/precipitation/convective heating anomalies there during negative IPO can contribute to a deepening of the Amundsen Sea Low (Clem and Renwick, 2015; Meehl et al., 2016a). More realistic simulations of recent Antarctic sea ice variations could thus be achieved by improving model deficiencies involved in the climate response to external forcings and the remote impact of tropical regions. Other

caveats include issues with how sea ice is modelled in current coupled climate models, and how the simulated sea ice interacts with ocean, surface air temperature and winds.

Due to the various feedbacks between sea ice and the climate system (e.g. Goosse and Zunz, 2014), assessing coupled models is important to fully understand how tropical teleconnections influence Antarctic sea ice. For example, while changed surface wind trends may be conducive to a sea ice increase in the Ross Sea, it is likely that a net SST cooling is also required for sea ice to increase and to accurately capture positive ice-albedo and ocean thermal warming feedbacks (Stammerjohn et al., 2012). For both CESM1 and CanESM2, the assimilation experiments show less ice loss in most sectors than their corresponding CESM1-HIST or CanESM2-CLIM experiments, but not a net ice increase. Without simulating the correct sign of observed sea ice changes, positive feedbacks will reinforce the ice loss, rather than the ice growth, propagating differences (e.g. Purich et al., 2016a).

Finally, we note that a number of previous studies have found teleconnections from the tropical Atlantic to the Amundsen Sea Low to be important in driving Ross and Bellingshausen Seas sea ice changes (Li et al., 2014, 2015a,b; Simpkins et al., 2014). Therefore, it is likely that details of the decadal patterns of tropical SST, precipitation and convective heating anomalies, as well as seasonality, are important in model simulations and the observed SIC, at least until 2013. Since the IPO has apparently changed phase around 2014 (Meehl et al., 2016b) the overall trend of SIC should now become less positive and may eventually turn negative on decadal timescales. While Atlantic forcing appears to play a role in influencing sea ice trends in the Atlantic and Indian sectors, in CESM1 the equatorial Pacific forcing seems to dominate sea ice trends in the Pacific sector. The design of the CanESM2 experiments does not allow for a direct comparison. Further work using coupled models is required to isolate the influences of the tropical Atlantic and Pacific oceans on different sectors of Antarctic sea ice in a fully coupled framework.

2.5 Supplementary material

Table 2.1: CMIP5 models used in this study and their expansions.

<i>Model</i>	<i>Expansion</i>
ACCESS1.0	Australian Community Climate and Earth-System Simulator, version 1.0
ACCESS1.3	Australian Community Climate and Earth-System Simulator, version 1.3
bcc-csm1-1	Beijing Climate Center Climate System Model, version 1.1
bcc-csm1-1-m	Beijing Climate Center Climate System Model, version 1.1, moderate resolution
BNU-ESM	Beijing Normal University Earth System Model
CanESM2	Second Generation Canadian Earth System Model
CCSM4	Community Climate System Model, version 4
CESM1-BGC	Community Earth System Model, version 1, Biogeochemistry
CESM1-CAM5	Community Earth System Model, version 1, Community Atmosphere Model, version 5
CESM1-WACCM	Community Earth System Model, version 1, Whole Atmosphere Community Climate Model
CMCC-CESM	Centro Euro-Mediterraneo sui Cambiamenti Climatici Carbon Earth System Model
CMCC-CM	Centro Euro-Mediterraneo sui Cambiamenti Climatici Climate Model
CMCC-CMS	Centro Euro-Mediterraneo sui Cambiamenti Climatici Climate Model with a resolved Stratosphere
CNRM-CM5	Centre National de Recherches Météorologiques Coupled Global Climate Model, version 5
CSIRO-Mk3-6-0	Commonwealth Scientific and Industrial Research Organisation Mark 3.6.0
FGOALS-g2	Flexible Global Ocean-Atmosphere-Land System Model, grid-point version 2
FGOALS-s2	Flexible Global Ocean-Atmosphere-Land System Model, spectral version 2
FIO-ESM	First Institute of Oceanography-Earth System Model
GFDL-CM3	Geophysical Fluid Dynamics Laboratory Climate Model, version 3
GFDL-ESM2G	Geophysical Fluid Dynamics Laboratory Earth System Model with Generalized Ocean Layer Dynamics (GOLD) component

Continued on next page

Table 2.1: Continued from previous page.

<i>Model</i>	<i>Expansion</i>
GFDL-ESM2M	Geophysical Fluid Dynamics Laboratory Earth System Model with Modular Ocean Model, version 4 (MOM4) component
GISS-E2-H	Goddard Institute for Space Studies ModelE/Hycom
GISS-E2-H-CC	Goddard Institute for Space Studies ModelE/Hycom, interactive Carbon Cycle
GISS-E2-R	Goddard Institute for Space Studies ModelE/Russell
GISS-E2-R-CC	Goddard Institute for Space Studies ModelE/Russell, interactive Carbon Cycle
HadGEM2-AO	Hadley Centre Global Environment Model, version 2, Atmosphere Ocean
HadGEM2-CC	Hadley Centre Global Environment Model, version 2, Carbon Cycle
HadGEM2-ES	Hadley Centre Global Environment Model, version 2, Earth System
inmcm4	Institute of Numerical Mathematics Climate Model, version 4
IPSL-CM5A-LR	Institut Pierre Simon Laplace Coupled Model, version 5A, low resolution
IPSL-CM5A-MR	Institut Pierre Simon Laplace Coupled Model, version 5A, mid resolution
IPSL-CM5B-LR	Institut Pierre Simon Laplace Coupled Model, version 5B, low resolution
MIROC5	Model for Interdisciplinary Research on Climate, version 5
MIROC-ESM	Model for Interdisciplinary Research on Climate, Earth System Model
MIROC-ESM-CHEM	Model for Interdisciplinary Research on Climate, Earth System Model, Chemistry Coupled
MPI-ESM-LR	Max Planck Institute Earth System Model, low resolution
MPI-ESM-MR	Max Planck Institute Earth System Model, medium resolution
MRI-CGCM3	Meteorological Research Institute Coupled Atmosphere–Ocean General Circulation Model, version 3
MRI-ESM1	Meteorological Research Institute Earth System Model, version 1
NorESM1-M	Norwegian Earth System Model, version 1, medium resolution
NorESM1-ME	Norwegian Earth System Model, version 1, medium resolution with capability to be fully emission driven

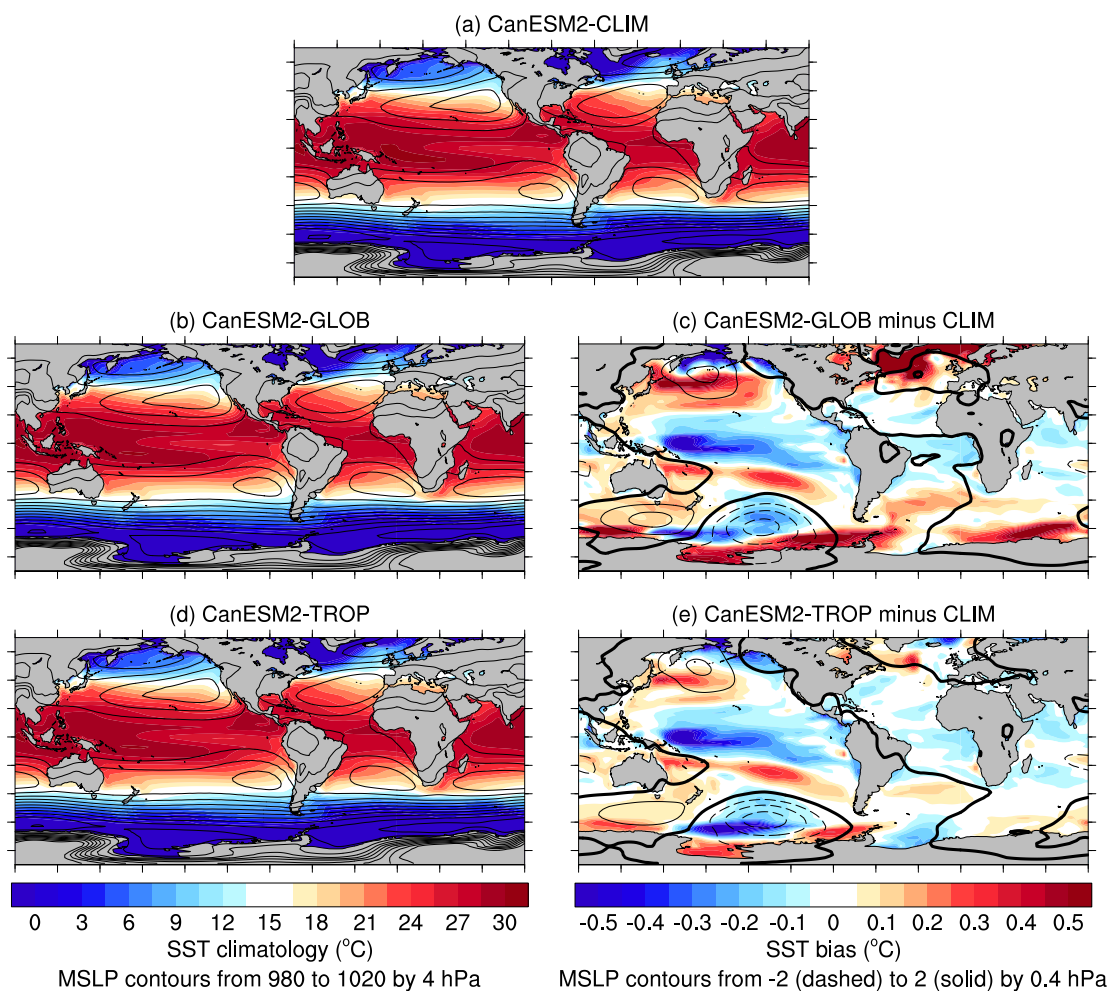


Figure 2.10: CanESM2 mean-state SST and MSLP: (a) CanESM2-CLIM; (b) CanESM2-GLOB; and (d) CanESM2-TROP. Bias compared to CanESM2-CLIM: (c) CanESM2-GLOB; and (e) CanESM2-TROP.

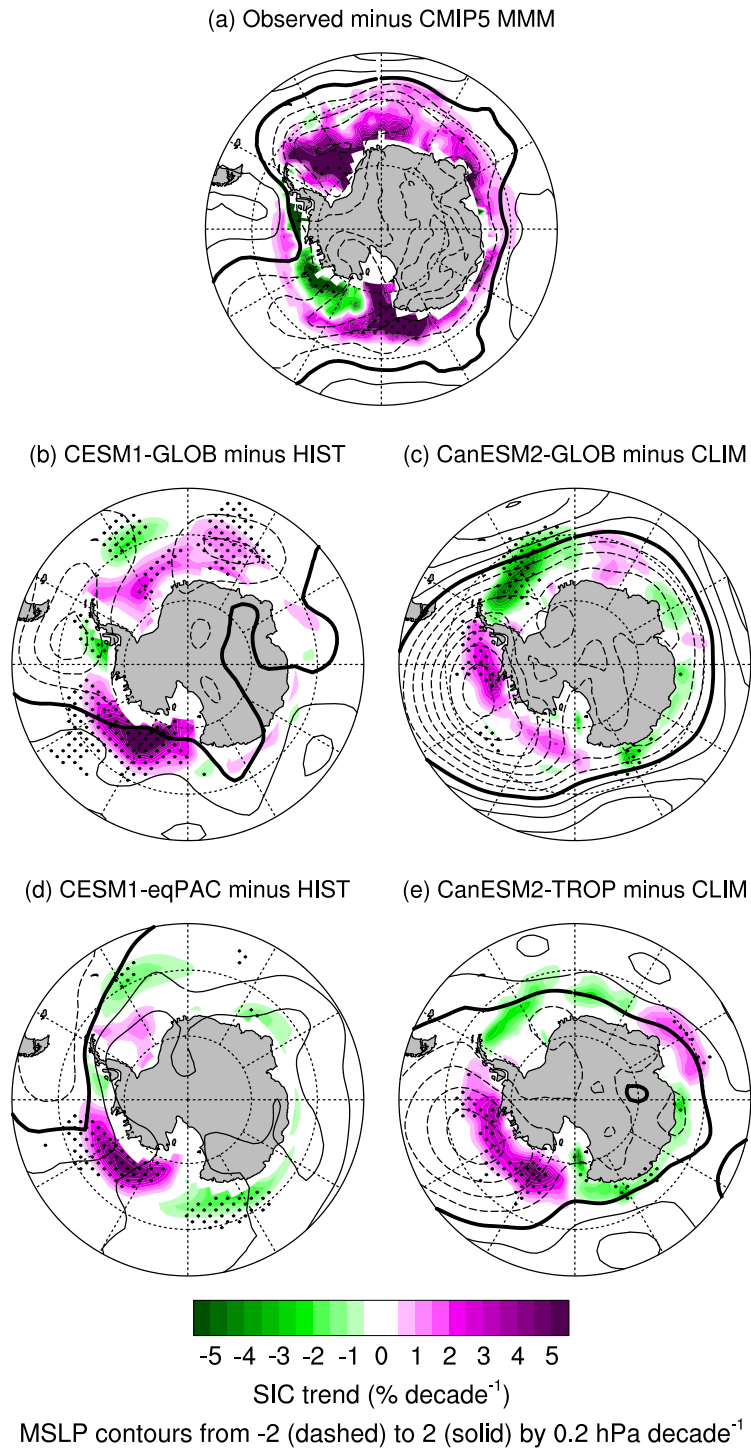


Figure 2.11: As for Fig. 2.2, but showing austral summer (December–February) SIC and MSLP trends.

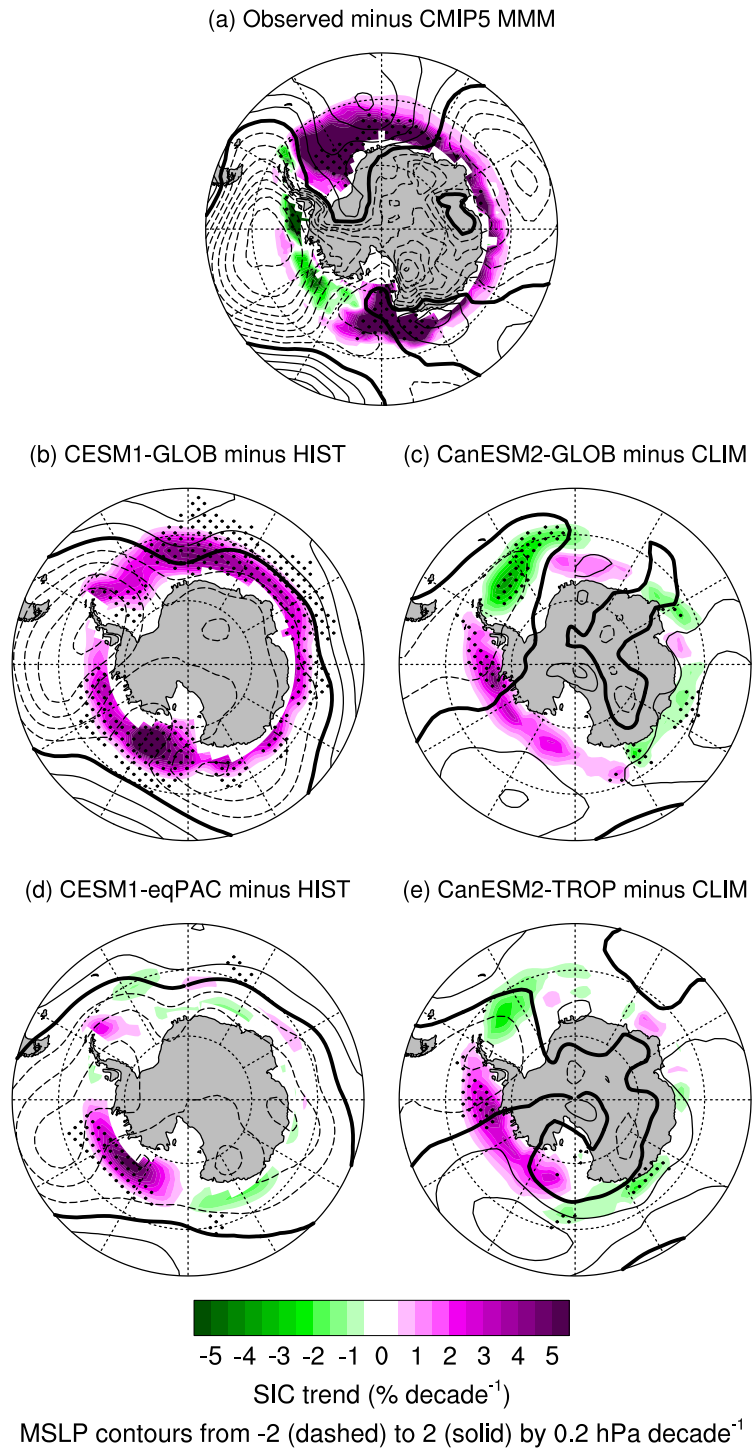


Figure 2.12: As for Fig. 2.2, but showing austral autumn (March–May) SIC and MSLP trends.

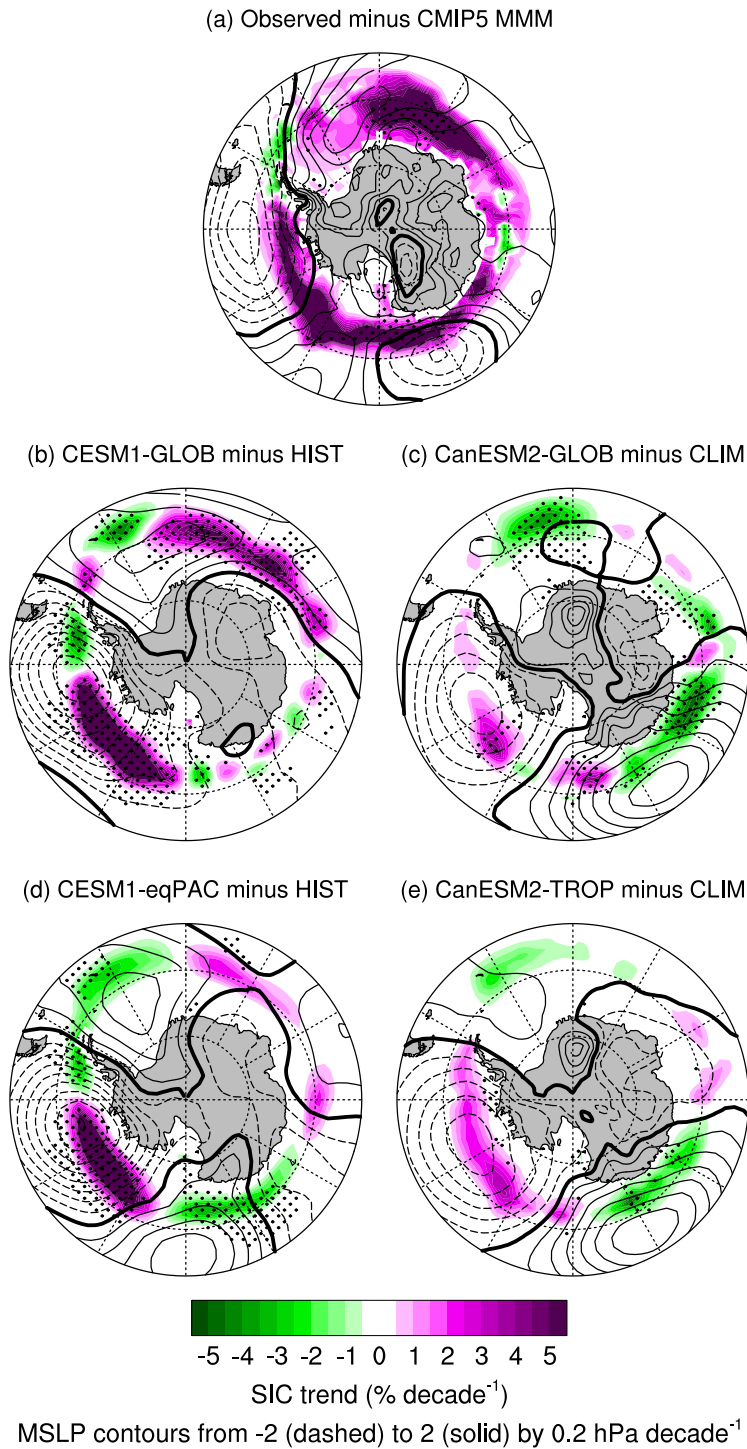


Figure 2.13: As for Fig. 2.2, but showing austral winter (June–August) SIC and MSLP trends.

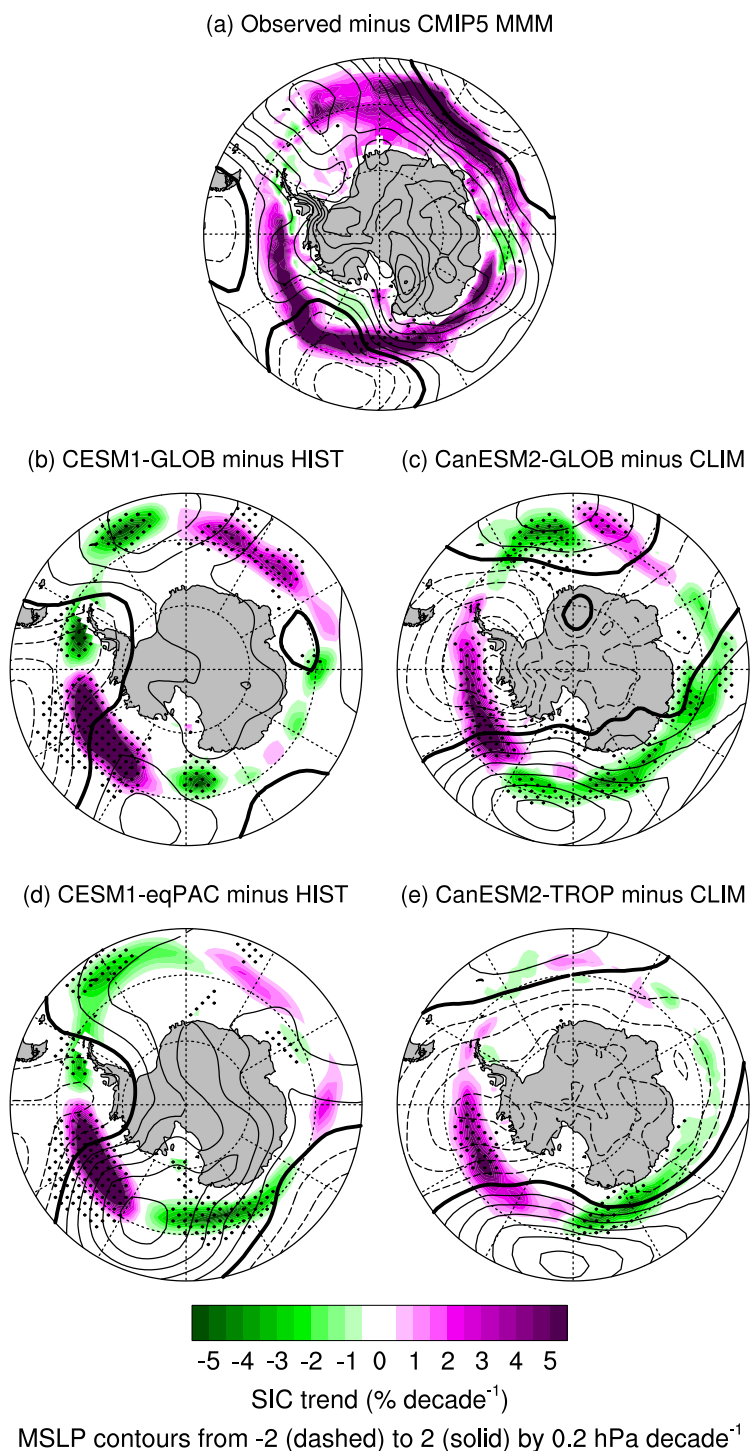


Figure 2.14: As for Fig. 2.2, but showing austral spring (September–November) SIC and MSLP trends.

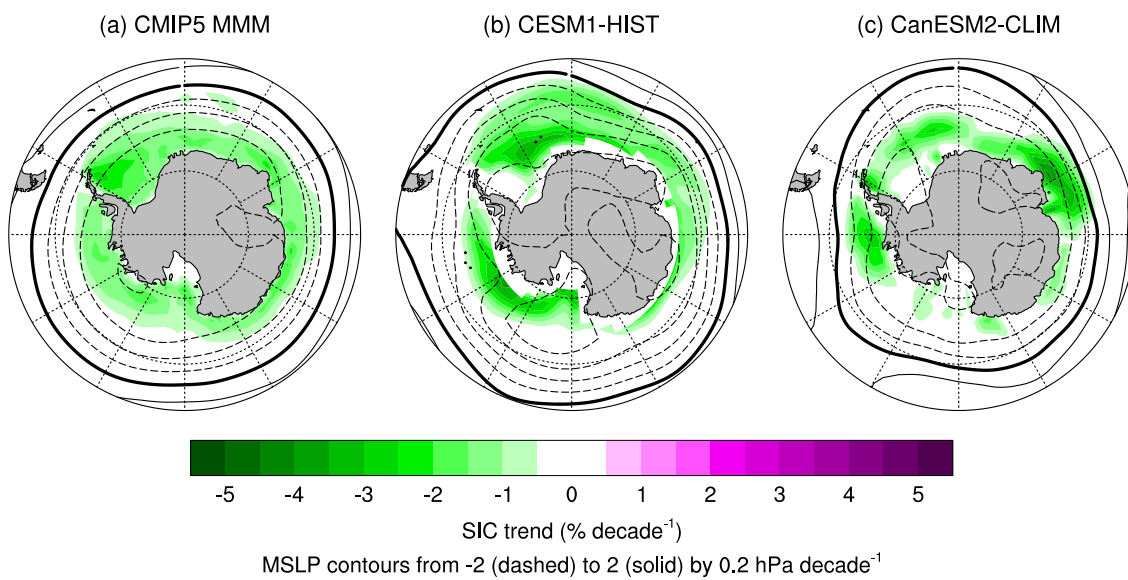


Figure 2.15: As for Fig. 2.4, but showing austral summer SIC and MSLP trends. A positive trend in the SAM is evident as the strong zonally-symmetric dipole pattern in MSLP trends, with decreasing pressure at high latitudes and increasing pressure at mid latitudes.

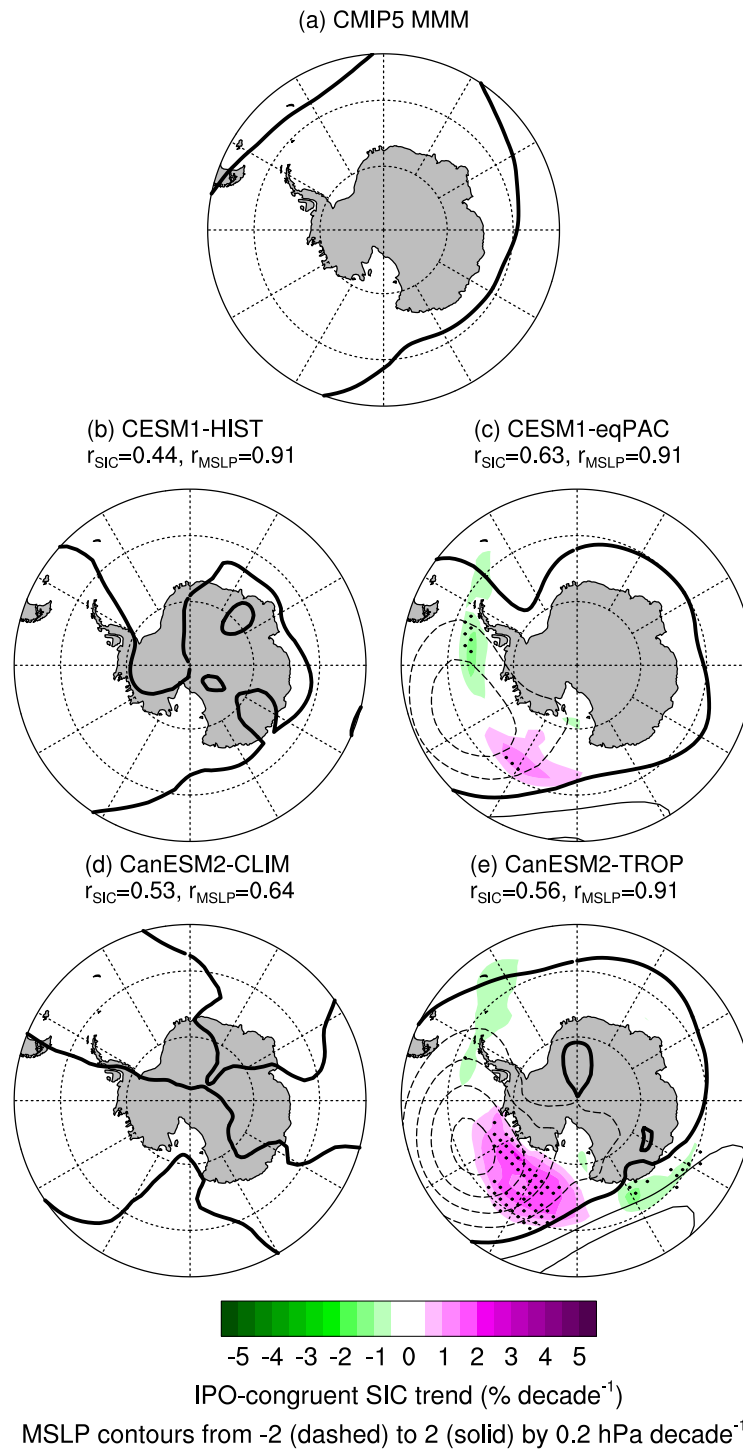


Figure 2.16: As for Fig. 2.7, but for: (a) CMIP5 multi-model mean; (b) CESM1-HIST; (c) CESM1-eqPAC; (d) CanESM2-CLIM; and (e) CanESM2-TROP. The lack of SIC and MSLP signals in (a,b,d) is due to different models or members having different phases of the IPO, and congruent trends thus cancelling out in the multi-model or ensemble means.

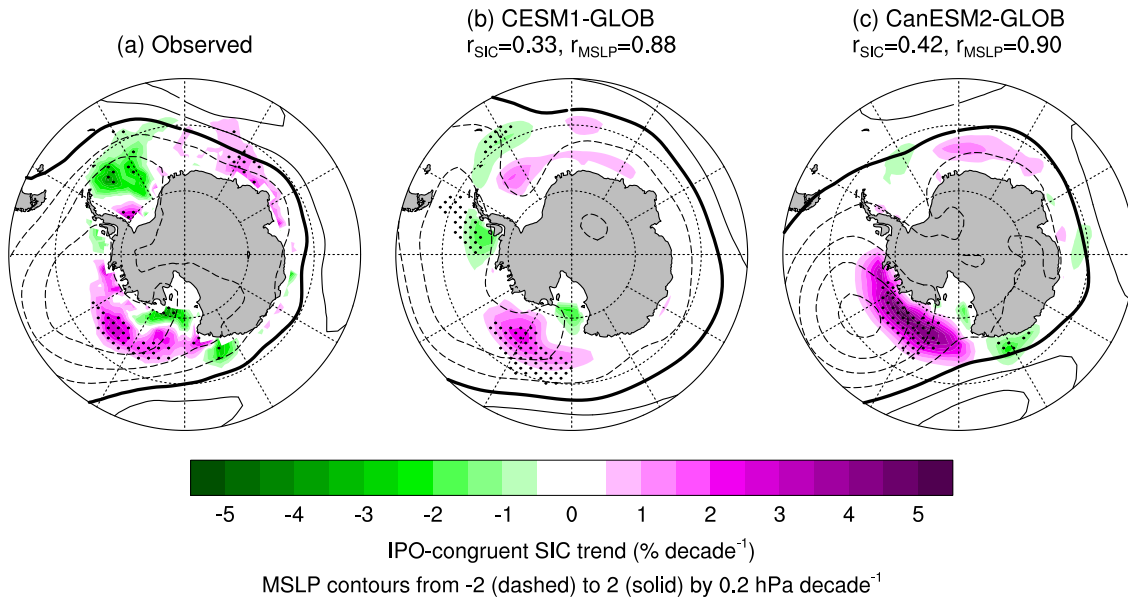


Figure 2.17: As for Fig. 2.7, but showing austral summer IPO-congruent trends.

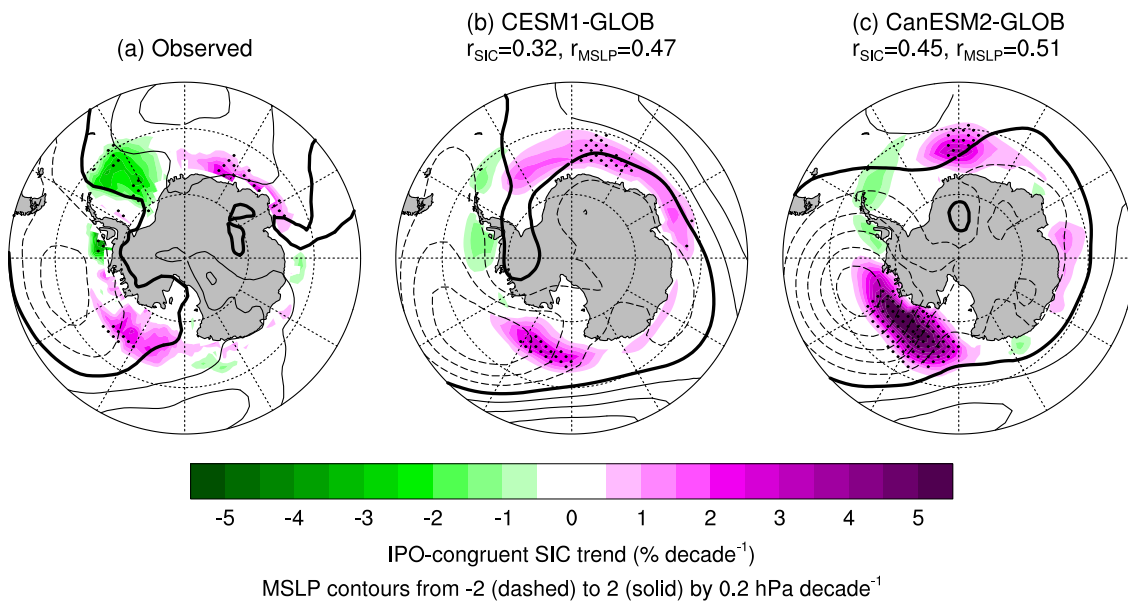


Figure 2.18: As for Fig. 2.7, but showing austral autumn IPO-congruent trends.

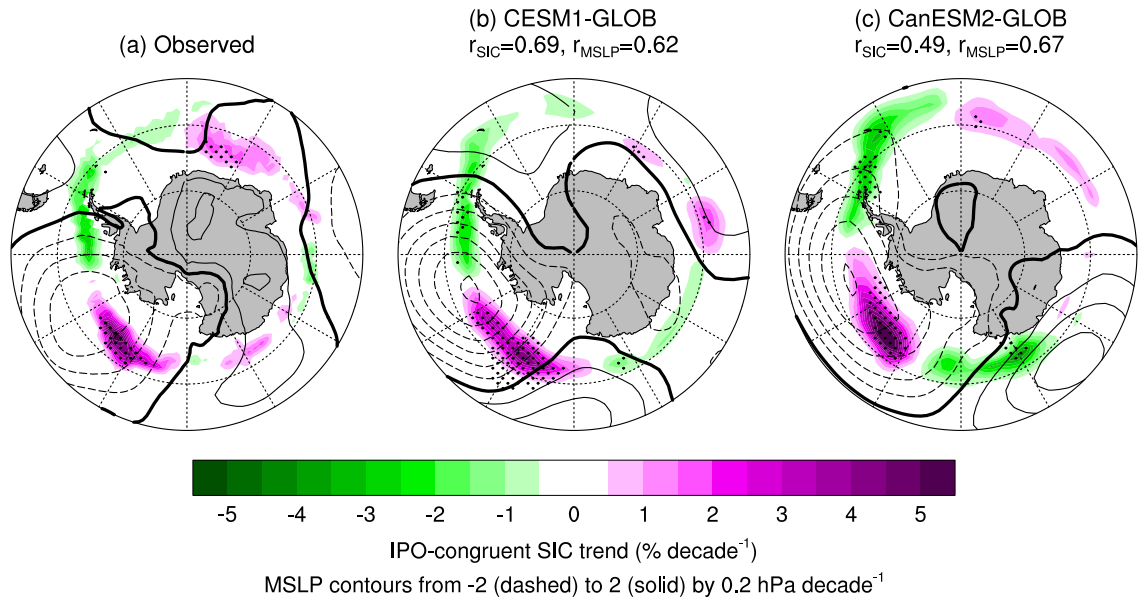


Figure 2.19: As for Fig. 2.7, but showing austral winter IPO-congruent trends.

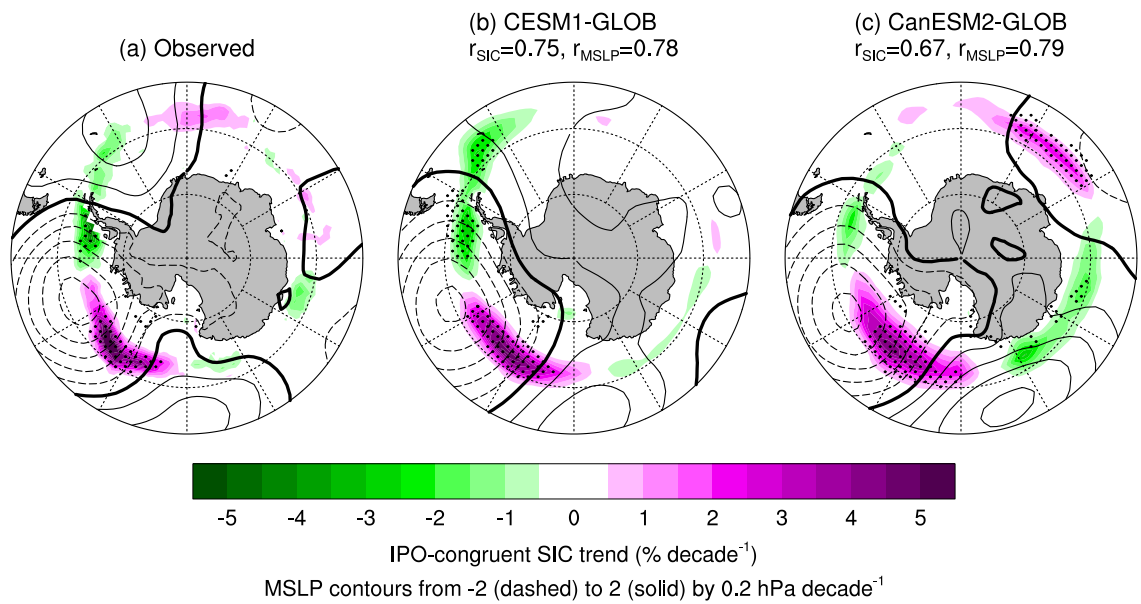


Figure 2.20: As for Fig. 2.7, but showing austral spring IPO-congruent trends.

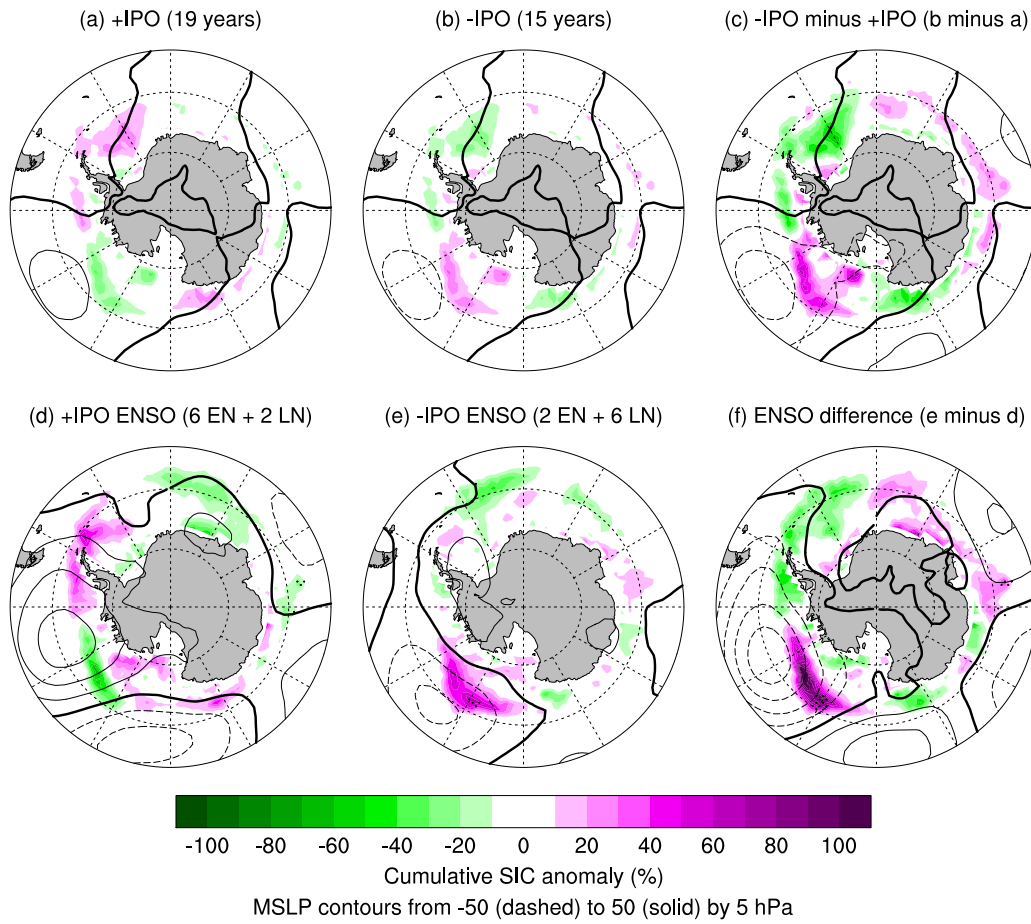


Figure 2.21: As for Fig. 2.8, but for linearly detrended SIC and MSLP time series.

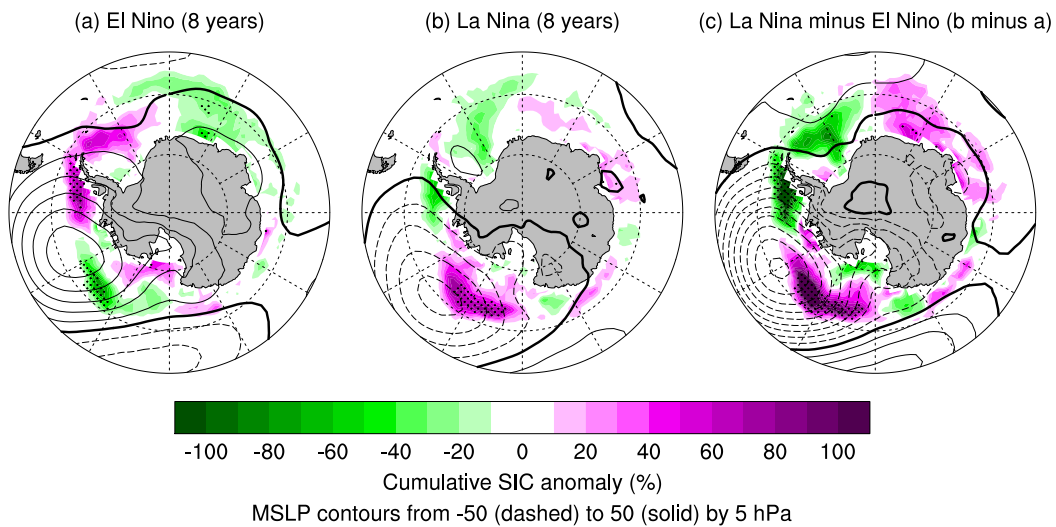


Figure 2.22: As for Fig. 2.9, but for linearly detrended SIC and MSLP time series.

Part 3

Impacts of broad-scale surface freshening of the Southern Ocean in a coupled climate model

The material in this Part is based around work published as:

Purich, A., M. H. England, W. Cai, A. Sullivan, and P. J. Durack, 2018: Impacts of broad-scale surface freshening of the Southern Ocean in a coupled climate model. *Journal of Climate*, **31**, 2613–2632, doi:10.1175/JCLI-D-17-0092.1.

A. P. and M. H. E. conceived the study. A. P. undertook the model simulations with assistance from A. S. A. P. assembled the observational and model data, undertook all analyses, prepared all figures and wrote the first draft of the manuscript. All authors contributed to the development of ideas, writing and revising the manuscript.

Accompanying supplementary material is included at the end of this Part in Section 3.5. The published version of this material is included in Appendix C. Additional material building upon the findings from this Part are included in Appendix D.

Abstract

The Southern Ocean surface has freshened in recent decades, increasing water column stability and reducing upwelling of warmer subsurface waters. The majority of Coupled Model Intercomparison Project phase five (CMIP5) models underestimate or fail to capture this historical surface freshening, yet little is known about the impact of this model bias on regional ocean circulation and hydrography. Here we perform experiments using a global coupled climate model with additional freshwater applied to the Southern Ocean to assess the influence of recent surface freshening. The simulations explore the impact of persistent and long-term broad-scale freshening due to processes including precipitation minus evaporation changes. Thus, unlike previous studies, the freshening is applied as far north as 55°S , beyond the Antarctic ice margin. We find that imposing a large-scale surface freshening causes a surface cooling and sea-ice increase under pre-industrial conditions, due to a reduction in ocean convection and weakened entrainment of warm subsurface waters into the surface ocean. This is consistent with inter-model relationships between CMIP5 models and our simulations, which suggest that models with larger surface freshening also exhibit stronger surface cooling and increased sea ice. Additional experiments are conducted with surface salinity restoration applied to capture observed regional salinity trends. Remarkably, without any mechanical wind trend forcing, these simulations accurately represent the spatial pattern of observed surface temperature and sea-ice trends around Antarctica. This study highlights the importance of accurately simulating changes in Southern Ocean salinity to capture changes in ocean circulation, sea surface temperature and sea ice.

3.1 Introduction

Observed Southern Ocean changes over recent decades include a surface freshening (Durack and Wijffels, 2010; Durack et al., 2012; de Lavergne et al., 2014), surface cooling (Fan et al., 2014; Marshall et al., 2014; Armour et al., 2016; Purich et al., 2016a) and circumpolar increase in Antarctic sea ice (Cavalieri and Parkinson, 2008; Comiso and Nishio, 2008; Parkinson and Cavalieri, 2012). Various explanations for the increase in Antarctic sea ice extent (SIE) seen since regular satellite observations began in 1979, which has occurred despite global warming over this period, have been proposed (Hobbs et al., 2016). These include natural variability (Mahlstein et al., 2013; Polvani and Smith, 2013; Zunz et al., 2013; Li et al., 2014; Simpkins et al., 2014; Gagné et al., 2015; Meehl et al., 2016a; Purich et al., 2016b), changes in surface winds (Holland and Kwok, 2012; Fan et al., 2014; Turner et al., 2009; Li et al., 2014; Simpkins et al., 2014; Purich et al., 2016a), surface freshening due to ice sheet and shelf runoff and iceberg fluxes (Bintanja et al., 2013, 2015; Swart and Fyfe, 2013; Pauling et al., 2016) and surface freshening due to sea ice transport (Haumann et al., 2016).

Surface freshening can act to increase sea ice coverage by increasing surface stratification, reducing convective mixing of warmer subsurface waters and causing a surface cooling (e.g. Marsland and Wolff, 2001; Liu and Curry, 2010; de Lavergne et al., 2014; Morrison et al., 2015). Early model studies of the influence of surface freshening on Antarctic sea ice found freshening to be associated with an increase in ice coverage in ocean-ice models (Marsland and Wolff, 2001; Beckmann and Goosse, 2002; Hellmer, 2004; Aiken and England, 2008). However, more recent studies using global coupled climate models with additional freshwater applied around the Antarctic margins to simulate increased ice sheet melt/runoff have found conflicting results: Bintanja et al. (2013, 2015) found that the increased freshwater has likely contributed to the increase in Antarctic SIE, while Swart and Fyfe (2013) found the influence to be small and not able to explain the observed sea-ice changes. Pauling et al. (2016) also found that applying an extra freshwater flux around the continental margins was insufficient to offset anthropogenic forcing. Zunz and Goosse (2015) find that the inclusion of an additional freshwater flux in simulations with data assimilation improves the reconstruction of sea ice trends, however it does not seem to be required to obtain an increase in sea ice extent in hindcast simulations. Meanwhile, Kirkman and Bitz (2011) find that under global warming conditions, increased melting of sea ice leads to surface freshening, which in turn leads to surface cooling of the Southern Ocean.

These previous studies (Bintanja et al., 2013, 2015; Swart and Fyfe, 2013; Pauling et al., 2016) focussed on runoff from Antarctic ice-sheet/shelf melt as the source of freshwater to the Southern Ocean, in part motivated by the fact that models participating in the Coupled Model Intercomparison Project phase 5 (CMIP5) explicitly exclude such melt contributions. However, Pauling et al. (2016) find that the CMIP5 models happen to simulate runoff changes due to precipitation changes over Antarctica that are approximately the same as estimated land-ice and ice-shelf melt rates. Further, the largest source of freshwater to the Southern Ocean is the precipitation minus evaporation (P–E) falling directly onto the ocean (Pauling et al., 2016). Increased P–E leads to stronger stratification and a reduction in oceanic vertical heat transfer, and thus to increased sea ice (Martinson, 1990; Marsland and Wolff, 2001; Goosse and Zunz, 2014). Observational estimates of P–E over the Southern Ocean are highly uncertain: there are no direct measurements of precipitation over the ocean and satellite estimates provide only a snapshot in time based on the time of the scan (e.g. Trenberth et al., 2017), while evaporation is estimated from bulk formula with many uncertain inputs, leading to considerable imbalances in global surface flux estimates (e.g. Josey et al., 2013). As such there is a large spread in observational products and reanalyses (Fig. 3.1). A detailed assessment of P–E trends in various reanalyses since 1989 found no robust widespread precipitation trends over the sea ice region, and a large disagreement between reanalyses (Bromwich et al., 2011). However, most estimates suggest there has been an increase in precipitation and P–E over the Southern Ocean south of 50°S since 1979 (Fig. 3.1) and this is consistent with the multidecadal broad-scale freshening that has been reported in numerous independent studies (Durack and Wijffels, 2010; Helm et al., 2010; de Lavergne et al., 2014; Haumann et al., 2016).

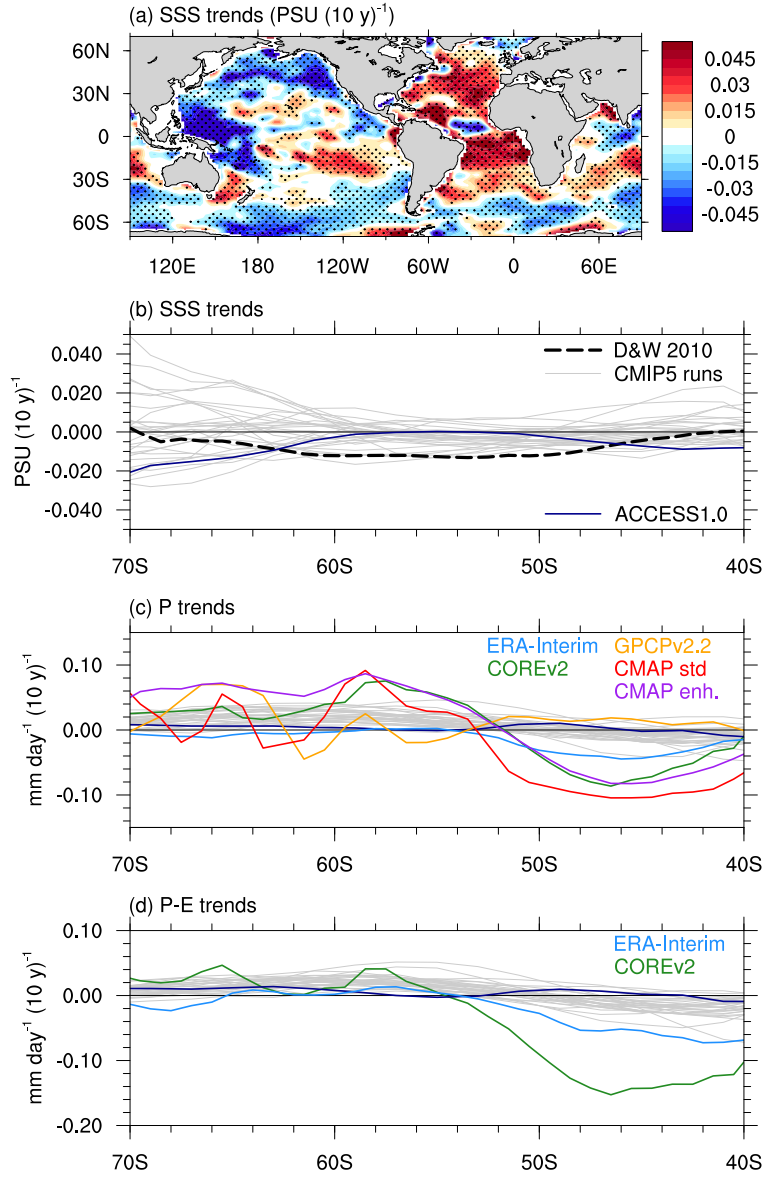


Figure 3.1: Salinity and precipitation trends over 1950–2000. (a) Observed sea surface salinity (SSS) trends from Durack and Wijffels (2010); (b) zonal-mean SSS trends for observations (Durack and Wijffels, 2010) and CMIP5 models; (c) zonal-mean precipitation trends for observations (ERA-Interim, COREv2, GPCPv2.2, CMAP standard, CMAP enhanced) and CMIP5 models; and (d) zonal-mean P–E trends for observations (ERA-Interim, COREv2) and CMIP5 models. In (a), stippling indicates significance at the 95% level. In (b) observations are shown in dashed black. In (c–d) observations are shown in colours, and vary in the time periods they cover (refer to Section 3.2.3). In (b–d) CMIP5 models are shown in grey, and the ACCESS1.0 CMIP5 run is shown in dark blue.

Measurements of surface salinity provide an integrated view of freshwater input changes, and the surface freshening seen since 1950 (Fig. 3.1a; Durack and Wijffels, 2010; de Lavergne et al., 2014), along with interior freshening (e.g. Wong et al., 1999), further suggest that there has been an increase in broad-scale freshwater input, likely including an increase in P–E over the Southern Ocean (e.g. Durack et al., 2012; de Lavergne et al., 2014). This increase is also in agreement with the positive trend in the Southern Annular

Mode (SAM) observed over the latter half of the twentieth century (Marshall, 2003), associated with a poleward shift and intensification in the extratropical westerly wind jet and storm tracks (e.g. Thompson and Solomon, 2002; Fyfe, 2003; Frederiksen and Frederiksen, 2007). These SAM changes have previously been suggested to increase precipitation over the high-latitude Southern Ocean (whilst decreasing precipitation in mid latitudes; e.g. Son et al., 2009), with less influence on evaporation (Purich and Son, 2012), thus enhancing total P–E over a broad region of the high-latitude Southern Ocean (including well north of the sea-ice margin). The goal of this study is to better understand the role of this broad-scale freshening of the surface Southern Ocean on both surface cooling and Antarctic sea ice trends.

Further, while CMIP5 models capture the observed sign of the recent SAM trend, they tend to underestimate its strength, and equivalently the trend in the westerly-wind jet (Swart and Fyfe, 2012; Wilcox et al., 2012; Bracegirdle et al., 2013; Mahlstein et al., 2013; Purich et al., 2013). The CMIP5 models also either underestimate or fail to capture the surface freshening seen in observations over 1950–2000 between 50–60°S; of the models that exhibit surface freshening, all underestimate the strength of the observed freshening, and only five models are within the observational uncertainty range (Figs 3.1b, 3.2; Durack, 2015). That is, 26 out of 31 CMIP5 models assessed in this study show sea surface salinity (SSS) trends over 50–60°S that are inconsistent with the observed freshening (Fig. 3.2). When multiple realisations per model are considered, 60 out of 68 CMIP5 realisations show SSS trends that are inconsistent with the observed freshening (Fig. 3.10 in Section 3.5). This is likely due to model precipitation and cloud biases, however uncertainty in observed P–E makes it difficult to assess the extent to which models underestimate changes in precipitation (Fig. 3.1c) and P–E (Fig. 3.1d). Internal variability may also play a role in contributing to the observed trend. In any case, Figs 3.1b, 3.2 indicates that for almost all cases, the models’ simulation of the recent multi-decadal surface freshening is weaker than observed. In addition to precipitation biases, a component of the SSS freshening could be due to increased ice shelf melt, land-ice melt, or an increase in northward sea-ice advection and melt. It is thus difficult to fully separate the processes that might be biased in CMIP5 models. Either way, as high-latitude surface freshening is associated with surface cooling and a sea ice increase, this may be another factor contributing to the CMIP5 models excessive Southern Ocean surface warming contrasting the observed surface cooling (Marshall et al., 2014; Purich et al., 2016a), and sea ice decline contrasting the observed increases (Mahlstein et al., 2013; Polvani and Smith, 2013; Swart and Fyfe, 2013; Turner et al., 2013a; Zunz et al., 2013; Gagné et al., 2015) over recent decades. Understanding whether an underestimated broad-scale freshening may have contributed to the differences between observed and CMIP5 trends provides further motivation for investigating the role of broad-scale freshening in driving Southern Ocean surface changes.

In this study we perform experiments using the Australian Community Climate and Earth System Simulator version 1.0 (ACCESS1.0), a global coupled climate model participating in CMIP5. In a recent CMIP5 assessment this model was found to be one of

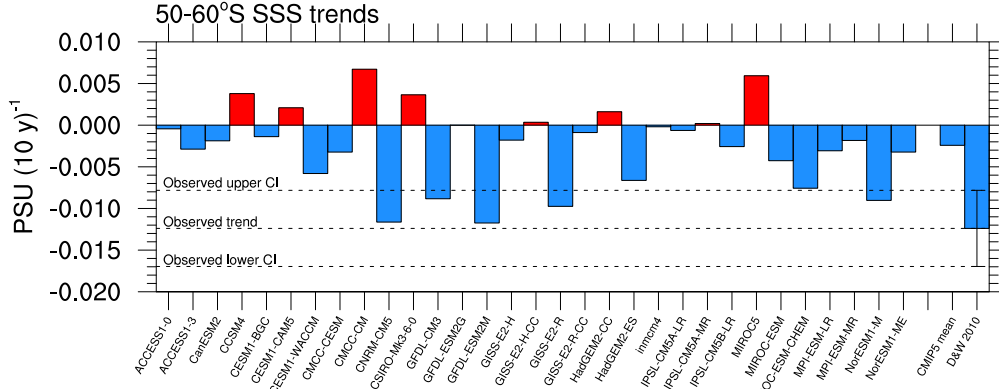


Figure 3.2: Trends in SSS over 1950–2000, area averaged over 50–60°S. The first available realisation for each CMIP5 model is shown, along with the CMIP5 multi-model mean and the Durack and Wijffels (2010) observational estimate. Error bars show the approximate 95% confidence estimates of the observed trend, and horizontal dashed lines are included for comparison between the CMIP5 trends and observations.

the best in the suite for simulating regional distribution and extent of Antarctic sea-ice (Ivanova et al., 2016). We apply an idealised freshwater flux over the high-latitude Southern Ocean between 55–70°S, with the aim of achieving a SSS trend similar in magnitude to the Durack and Wijffels (2010) trend. The sea surface temperature (SST) and sea ice responses to the broad-scale freshwater input are examined and the regional pattern of changes and sea ice feedbacks are discussed. We also make a comparison with CMIP5 output. Our results suggest that recent multi-decadal trends in large-scale surface salinity over the Southern Ocean have played a role in the observed surface cooling seen in this region. In addition, our simulations suggest that the underestimation of observed surface freshening by CMIP5 models is an important factor contributing to the SST warming and Antarctic sea ice decline seen in almost all CMIP5 models, at odds with observed trends. While diagnosed as an important factor here, we find that a uniform freshening alone cannot fully account for the model-observed differences. Other factors, such as decadal variability (Li et al., 2014; Simpkins et al., 2014; Meehl et al., 2016a; Purich et al., 2016b), responses to greenhouse gas forcing (Armour et al., 2016) and stratospheric ozone forcing (Turner et al., 2009), and wind forcing effects (Holland and Kwok, 2012; Fan et al., 2014; Purich et al., 2016a) are likely also important.

3.2 Data and methods

3.2.1 Model description

The ACCESS model is a fully-coupled global climate model, developed by the Commonwealth Scientific and Industrial Research Organisation and the Australian Bureau of Meteorology (Bi et al., 2013b). It is built by coupling the United Kingdom (UK) Met Office atmospheric Unified Model (UM; Davies et al., 2005; Martin et al., 2010, 2011) to the

Geophysical Fluid Dynamics Laboratory Modular Ocean Model version 4p1 (MOM4p1; Griffies et al., 2010) and the Los Alamos National Laboratory sea ice model version 4.1 (CICE4.1; Hunke and Lipscomb, 2010), as described in Bi et al. (2013a). These model components are coupled using the Centre Européen de Recherche et de Formation Avancée en Calcul Scientifique Ocean Atmosphere Sea Ice Soil version 3.2 (OASIS3.2; Valcke, 2006) coupling framework. ACCESS1.0 is configured with the UK Met Office Hadley Centre Global Environment Model, version 2 (HadGEM2, r1.1) atmospheric physics and the UK Met Office Surface Exchange Scheme land surface model version 2. The atmospheric component of the model used here has an N96 horizontal resolution of approximately 1.25° latitude by 1.875° longitude, and 38 vertical levels. The ACCESS configuration of MOM4p1 and CICE4.1 has 360 longitude by 300 latitude points on a logically rectangular grid with enhanced resolution at the equator, and 50 vertical levels with 10 m resolution in the upper 200 m (Bi et al., 2013b).

3.2.2 Experimental design

Using ACCESS1.0 in fully coupled configuration, simulations with an additional freshwater flux into the ocean component are branched from a pre-industrial control (piControl) run. We refer to these as the freshwater simulations. Freshwater simulations have the same forcings as for the ACCESS1.0 CMIP5 piControl run, including pre-industrial atmospheric concentrations of CO_2 , CH_4 , N_2O and O_3 , the solar constant, and aerosol emissions, seasonally-varying biogenic aerosol concentrations and a background SO_2 outgassing flux but with the stratosphere clear of volcanic aerosols (Bi et al., 2013b; Dix et al., 2013). This experimental design was chosen rather than including historical and future scenario forcings to isolate the influence of Southern Ocean surface freshening on the climate system from other confounding factors. Five ensemble members are branched from different years of the piControl run, each five years apart, and run for 50 years. We consider the five member ensemble to investigate the role of unforced variability on these relatively short simulations.

Our aim is to simulate a clear freshening signal of similar magnitude to the broad-scale freshening of the Durack and Wijffels (2010) SSS trend that will allow an investigation into the influence of this observed surface freshening on regional hydrography and circulation. We are not initially trying to replicate the observed SSS trend exactly (although later on we consider SSS restoring experiments that match the observed geographic distribution), but rather use an idealised freshwater forcing to obtain freshening trends of approximately comparable magnitude. To achieve this, an identical freshwater flux is added to each ensemble member as an additional P–E flux into the ocean model component over $55\text{--}70^\circ\text{S}$, while the atmosphere is able to freely evolve to this additional flux. The additional P–E flux is applied as a P–E flux correction, to augment the P–E flux received due to atmospheric processes, rather than by prescribing the total P–E. This yields a surface freshening trend under otherwise piControl conditions. The added freshwater flux is constant over

55–70°S, and zero elsewhere, and increases by a constant amount each year, representing an annually increasing linear trend in P–E. Due to model sensitivity assessed in short tests, a freshwater flux trend of $0.1 \text{ mm day}^{-1} (10 \text{ y})^{-1}$ is applied, which yields a clear freshening signal as desired (Fig. 3.3b). This is considerably larger than the P–E trend simulated by the CMIP5 models as shown in Fig. 3.1d.

3.2.3 Observational and CMIP5 datasets

We compare output from the ACCESS1.0 freshwater simulations to various observationally based datasets. For surface and subsurface salinity, we utilise trends from Durack and Wijffels (2010), calculated for 1950–2000. We also utilise potential temperature trends from Durack and Wijffels (2010). For surface trends over 1979–2013 we use SST from the Hadley Centre Sea Ice and Sea Surface Temperature dataset (HadISST; Rayner et al., 2003) and passive microwave sea ice concentration (SIC) processed using the National Snow and Ice Data Center (NSIDC) Bootstrap algorithm (Comiso and Nishio, 2008; Meier et al., 2013, updated 2016). For area-averaged SIE we make use of the NSIDC SIE index (Fetterer et al., 2002). We note that there is an inconsistency in the time periods of the different observational datasets assessed here. Continuous observations of Antarctic sea ice are limited to the satellite period, 1979–2013, and one of the motivations of this research is to better understand the drivers of Antarctic sea ice trends over this time. While the HadISST SST dataset extends back far earlier than 1979, analysing the same period as for sea ice is useful in understanding how SST and sea ice trends are related. This also has the added benefit of using the temporal period where satellite data coverage provides the dominant measurement inputs for HadISST. Unfortunately, observations of SSS and subsurface fields are severely limited, and while shorter period trend estimates do exist (e.g. over 1970–2004; Durack et al., 2014), error estimates increase markedly, as the primary limitation in Southern Hemisphere trends are a lack of data. Over shorter time periods interannual/decadal variability also dominates, whereas over longer periods such as 1950–2000, trends are more coherent and physically interpretable. Based on this limitation, despite not aligning with the satellite-measured sea ice and SST period, we choose to assess the 1950–2000 SSS and subsurface trends. Changes over the various periods are all scaled to show the trend per decade, to allow for an easier comparison across the differing time scales of the products analysed.

Data sparsity is a considerable challenge when assessing the pre-Argo period for global ocean temperature and salinity changes, and is a particular problem in the sparsely sampled Southern Hemisphere. Durack and Wijffels (2010) discuss the issue of data sparsity, and provide uncertainty estimates for the presented trend results. Their Table 1 also includes error estimates for regional comparisons to other published literature. We note that other studies that have assessed trends in salinity have also attempted to provide uncertainty estimates: the Durack and Wijffels (2010) analysis is one of at least five studies (see also Boyer et al., 2005; Hosoda et al., 2009; Helm et al., 2010; Skliris et al., 2014) that

have assessed salinity changes for the global ocean. Each of these studies reports a considerable broad-scale freshening for the Southern Ocean. A recent Southern Ocean regionally focused study by de Lavergne et al. (2014) has reproduced the freshening patterns using very different methodologies to previous studies (see their Fig. 2), strongly suggesting that the Southern Ocean surface freshening is a real observed feature, with the obvious caveat that all observed estimates are limited by measurements.

To support our findings based on the Durack and Wijffels (2010) dataset, we undertook a parallel analysis using the EN4.2.0 dataset (Good et al. 2013; Fig. 3.11 in Section 3.5). The EN4.2.0 dataset is not optimised for trend calculation (rather the dataset is focused on “reconstructing” each month of the ocean state from 1900–2017), and therefore is highly sensitive to data sparsity and “zero anomalies”. However, when we contrast the same period analysed in Durack and Wijffels (2010), we get similar spatial patterns for the key features we are assessing (e.g. broad-scale freshening south of 50°S but with increased salinity in the Bellingshausen and eastern Amundsen Seas, part of the Weddell Sea, the Cosmonauts Sea and around 140°E), however with smaller magnitudes.

As mentioned above, observational estimates of P–E over the Southern Ocean are highly uncertain (e.g. Josey et al., 2013; Bromwich et al., 2011). We compare various precipitation and evaporation datasets, including Global Precipitation Climatology Project version 2.2 (GPCPv2.2) precipitation over 1979–2013 (Adler et al., 2003), CPC Merged Analysis of Precipitation (CMAP) standard and enhanced precipitation over 1979–2013 (Xie and Arkin, 1997), ERA-Interim precipitation and evaporation over 1979–2013 (Dee et al., 2011), and Coordinated Ocean Research Experiments version 2 (COREv2) precipitation and evaporation over 1979–2006 (Large and Yeager, 2009). We do not include the National Centers for Environmental Prediction/National Center for Atmospheric Research precipitation and evaporation, as this reanalysis is already incorporated in the CMAP enhanced precipitation product, and in the COREv2 fields. We emphasise the limitations with observational precipitation and evaporation products over the Southern Ocean, as discussed in Section 3.1, and as such rely on surface salinity to provide an integrated view of freshwater input changes.

CMIP5 data from 31 models with a total of 68 runs are also analysed (refer to Table 3.1 in Section 3.5 for a list of models). All models with required variables available (SSS, SST, SIC, potential temperature, precipitation and evaporation) for the historical experiment over 1950–2005 and the Representation Concentration Pathway 8.5 (RCP8.5; high emission scenario) experiment over 2006–2013 are included in the analysis. As all scenarios have similar forcings over 2006–2013, the choice of RCP8.5 is arbitrary.

3.2.4 Data analysis

Prior to analysis all ACCESS1.0 and observational data is bilinearly regridded to a $1^\circ \times 1^\circ$ grid. Due to the large amount of data dealing with the CMIP5 ensemble, CMIP5 data is

bilinearly regridded to a $2^\circ \times 2^\circ$ grid. Annual and seasonal averages are then calculated.

Grid point linear trends of surface fields are calculated. Significance of observed trends is determined using a two-sided Student's t test at the 95% confidence level. Autocorrelation is accounted for by defining the effective sample size N_{eff} as follows:

$$N_{\text{eff}} = N \left(\frac{1 - r_1}{1 + r_1} \right) \quad (3.1)$$

where N is the sample size, and r_1 is the lag-1 autocorrelation of the detrended time series of interest (Simpkins et al., 2012). Note that grid-point SSS trends and an estimate of error are provided directly from Durack and Wijffels (2010) and are simply area averaged here, and that the different observational products vary in the time periods for which they are available. Ensemble mean trends for the freshwater simulations are calculated by taking the linear trend in each 50-year simulation, de-drifting by removing the linear trend in the piControl for the corresponding 50-year period (e.g. Sen Gupta et al., 2013), and then averaging across the five simulations. Significance of ensemble mean trends is determined when the absolute value of the ensemble mean trend is greater than two standard deviations of the inter-member spread ($\sim 95\%$ confidence level).

Zonal mean linear trends of subsurface fields are calculated by first taking the three-dimensional trends and then averaging zonally. Salinity and potential temperature trends provided by Durack and Wijffels (2010) are simply averaged zonally. Note that significance of these observed trends is also averaged zonally, so should be considered as a guide only. As for the surface fields, 50-year trends for individual ensemble members are first calculated, and then de-drifted by removing the zonal-mean trend in the piControl for the corresponding 50-year period. De-drifted trends are then averaged to determine the ensemble mean trend. Significance is determined when the absolute value of the ensemble mean trend is greater than two standard deviations of the inter-member spread ($\sim 95\%$ confidence level).

Zonal mean trends are calculated for the CMIP5 models over 1950–2000. However, for area-averaged metrics we consider trends over 1979–2013, for comparison with satellite-based observational estimates of SST (HadISST) and SIC (NSIDC Bootstrap). Area-averaged SSS and SST are calculated over $55\text{--}70^\circ\text{S}$ and SIE is calculated as the total area where SIC exceeds 15%. Comparable metrics are calculated for the observational products and for the freshwater simulations.

3.3 Results

3.3.1 Freshwater simulations

Observed and ensemble mean trend maps are shown in Fig. 3.3, displaying the regional patterns of trends. The Durack and Wijffels (2010) SSS trends (Fig. 3.3a) show substantial freshening over the Southern Ocean, although there is a notable increase in surface salinity in the Bellingshausen Sea. HadISST cooling (Fig. 3.3c) is seen in all regions, except near the coast in the Amundsen and Bellingshausen Seas, where a significant warming is seen. Except for a region of increased salinity off east Antarctica and a weak increase in the Weddell Sea, the regions of cooling tend to align well with the regions of freshening, and vice versa, despite comparing the Durack and Wijffels (2010) and HadISST datasets over different periods for the reasons outlined in Section 3.2.3. These two trend maps (Fig. 3.3a,c) have an uncentred pattern correlation coefficient of $r=0.50$ (see also Fig. 3.12 in Section 3.5). Sea ice changes largely mirror SST changes (Fig. 3.3e), with increased SIC in most regions around Antarctica, but decreased SIC in the Amundsen and Bellingshausen Seas, and in the outer Weddell Sea.

The broad scale trends seen in the observations are also captured in the freshwater simulations: applying an idealised increased freshwater flux into the ocean causes an SSS freshening (Fig. 3.3b), increasing the surface stability. All ensemble members simulate a freshening trend in SSS over 50–70°S in response to the applied freshwater flux, although it is worth noting that the simulated zonal-mean freshening in response to the applied P–E flux is stronger than the observed freshening. The increased stability reduces convective overturning, resulting in less entrainment of heat into the mixed layer, and can also result in reduced upward vertical isopycnal heat transport (Gregory, 2000; Kirkman and Bitz, 2011). In response to the surface freshening, all ensemble members also show a broad-scale surface cooling, accompanied by increased sea ice coverage occurs in most regions (Fig. 3.3d,f). As for the observations, there is a strong relationship between regions of freshening (Fig. 3.3b) and cooling (Fig. 3.3d) in the freshwater simulations, with these two trend maps having an uncentred pattern correlation of $r=0.86$ (see also Fig. 3.12 in Section 3.5).

Zonal-mean trend patterns in simulated salinity (Fig. 3.4b) and potential temperature (Fig. 3.5b) reveal a high-latitude freshening and cooling of the surface layer, with warming below (discussed further in Section 3.3.2). These patterns indicate a reduction in cool-season convective overturning between ~60–70°S (Fig. 3.5b) due to increased surface stability, with less entrainment of warmer subsurface waters to the surface ocean when convection is reduced. Similar to Kirkman and Bitz (2011), we also assess trends in “water age”, which acts as a tracer in ACCESS1.0 and indicates the length of time since a parcel of water has been at the surface. Regional agreement between areas of subsurface warming

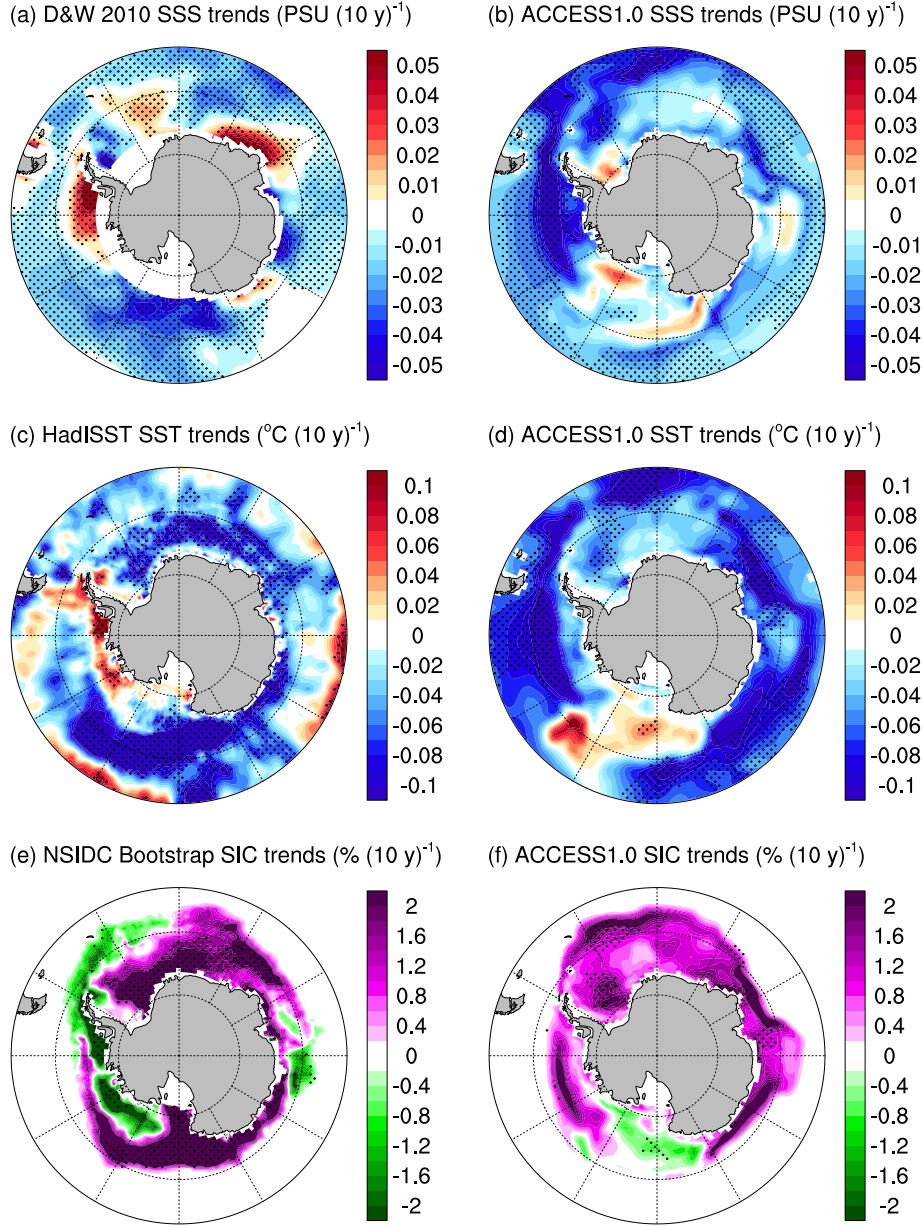


Figure 3.3: (left) Observed; and (right) ensemble-mean 50-year trends from the ACCESS1.0 freshwater simulations. (a,b) SSS trends; (c,d) SST trends; and (e,f) SIC trends. In all panels, stippling indicates trend significance at the 95% level. Observations are from (a) Durack and Wijffels (2010; 1950–2000); (c) HadISST (1979–2013); and (e) NSIDC Bootstrap (1979–2013).

and increased water age (Fig. 3.6)¹ provides further indication that reduced ocean convection is causing the subsurface warming (and surface cooling), as this corresponds to a decreased input of young water, as also identified in the simulations by Kirkman and Bitz (2011). Along-isopycnal mixing changes may also contribute to the similarities between potential temperature and water age trends (Gregory, 2000; Kirkman and Bitz, 2011).

¹The uncentred pattern correlation coefficients between potential temperature and water age increase with depth from $r = 0.01$ at 55 m, to $r = 0.46$ at 537 m, and $r = 0.92$ at 2183 m (see also Fig. 3.13 in Section 3.5).

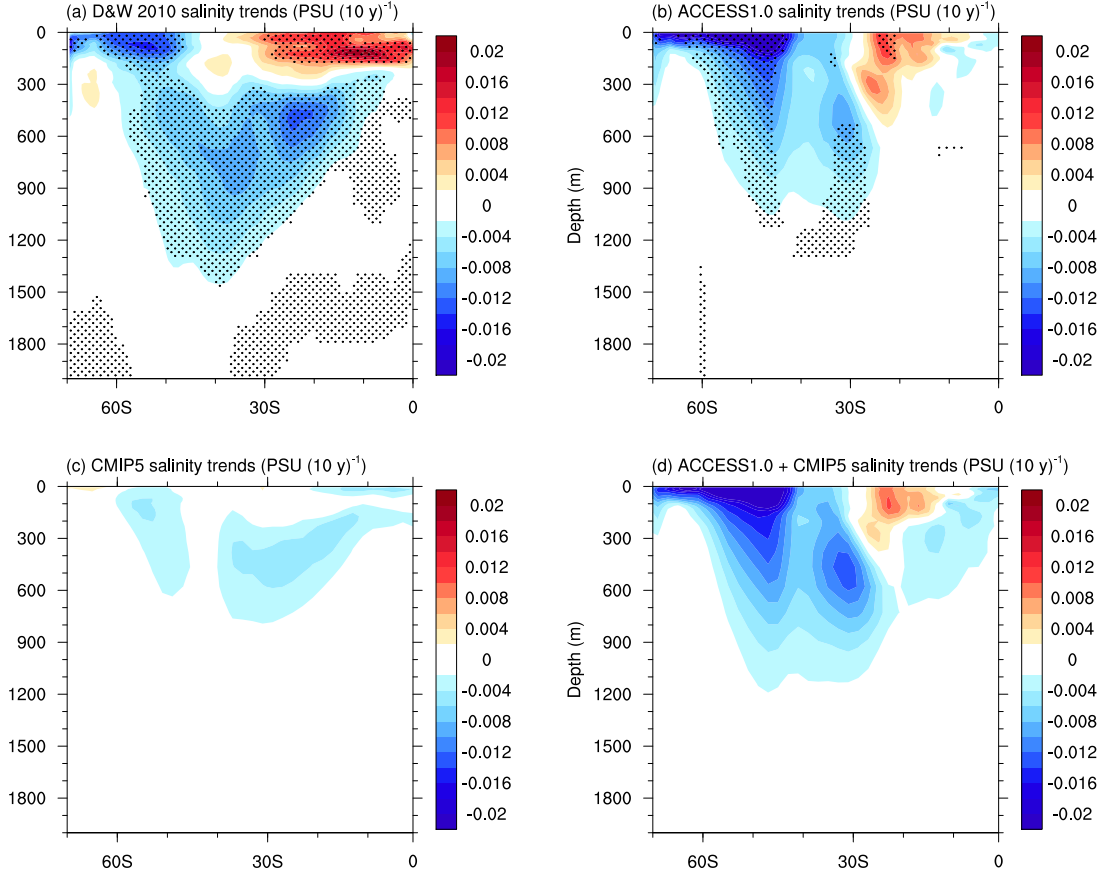


Figure 3.4: Zonal-mean 50-year salinity trends. (a) Observed salinity trends from Durack and Wijffels (2010); (b) ensemble-mean trends from the ACCESS1.0 freshwater simulations; (c) CMIP5 multi-model mean trends over 1950–2000; and (d) sum of ACCESS1.0 freshwater ensemble mean trends and CMIP5 multi-model mean trends, i.e. (b)+(c). In (a–c), stippling indicates trend significance at the 95% level.

Increased total surface heat fluxes into the ocean between 60–70°S (Fig. 3.7a) suggest that the surface heat fluxes largely respond to the SST and sea-ice changes, not the other way around. In particular, the heat flux trends are an indicator of increased sea ice and surface cooling in response to the changes in ocean circulation (i.e. less heat is lost to the atmosphere when ice cover is increased, and in ice-free areas more sensible heat is transferred from the atmosphere to the cooler ocean surface; and there is also reduced heat loss via outgoing longwave radiation changes). However, between 50–60°S there is a weak decrease in the total surface heat flux into the ocean (Fig. 3.7a). This is likely due to a secondary mechanism related to the reduced ocean convection, whereby a broad-scale shoaling of the mixed layer (Fig. 3.7b), particularly during austral winter (Fig. 3.7d), allows more sensible heat loss from the surface during wintertime (Fig. 3.7c). This leads to a weak decrease in the annual-mean total heat flux into the ocean over 50–60°S, contributing to the surface cooling in this region.

Despite a zonal-mean freshwater flux being applied in the simulations, regional patterns also emerge. Of particular note, broad significant SSS trends are not seen in the Ross Sea, which may be a result of spurious deep convection simulated by ACCESS1.0 in this

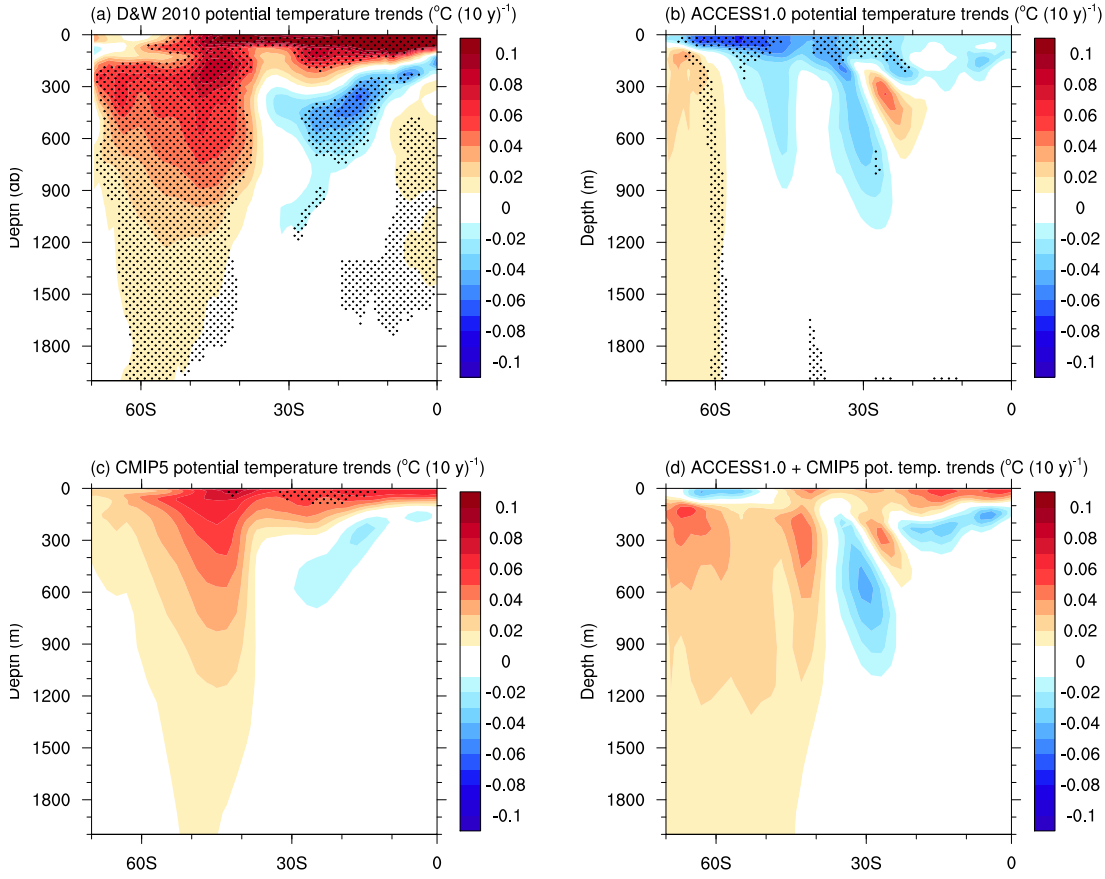


Figure 3.5: Zonal-mean 50-year potential temperature trends. (a) Observed potential temperature trends from Durack and Wijffels (2010); (b) ensemble-mean trends from the ACCESS1.0 freshwater simulations; (c) CMIP5 multi-model mean trends over 1950–2000; and (d) sum of ACCESS1.0 freshwater ensemble mean trends and CMIP5 multi-model mean trends, i.e. (b)+(c). In (a–c), stippling indicates trend significance at the 95% level.

region (e.g. Fig. 3.7b; de Lavergne et al., 2014), and as a result there is weak (and largely insignificant) warming in this region (Fig. 3.3d), and a decreasing sea ice trend (a portion of which is significant, Fig. 3.3f). This contrasts the strong cooling and sea ice growth in the Ross Sea seen in observations (Fig. 3.3c,e), which have been linked to atmospheric circulation patterns associated with decadal variability (e.g. Meehl et al., 2016a; Purich et al., 2016b). A zonal-mean surface freshening and cooling can be seen in all seasons (shown for austral summer in Fig. 3.14 and for austral winter in Fig. 3.15 in Section 3.5). Sea ice trends respond to the seasonal cycle of growth and retreat, being largest closer to the coast in summer (Fig. 3.14), and in the outer ice pack in winter (Fig. 3.15). While a constant freshwater flux is applied into the ocean model component of ACCESS1.0 over 55–70°S, the model is free to redistribute this freshwater elsewhere. Over the annual cycle, the additional freshwater input at high latitudes in the model increases SIC, and exports sea ice equatorward where it melts, highlighting the importance of the freshwater redistribution by sea ice, as also discussed in Kirkman and Bitz (2011) and Haumann et al. (2016).

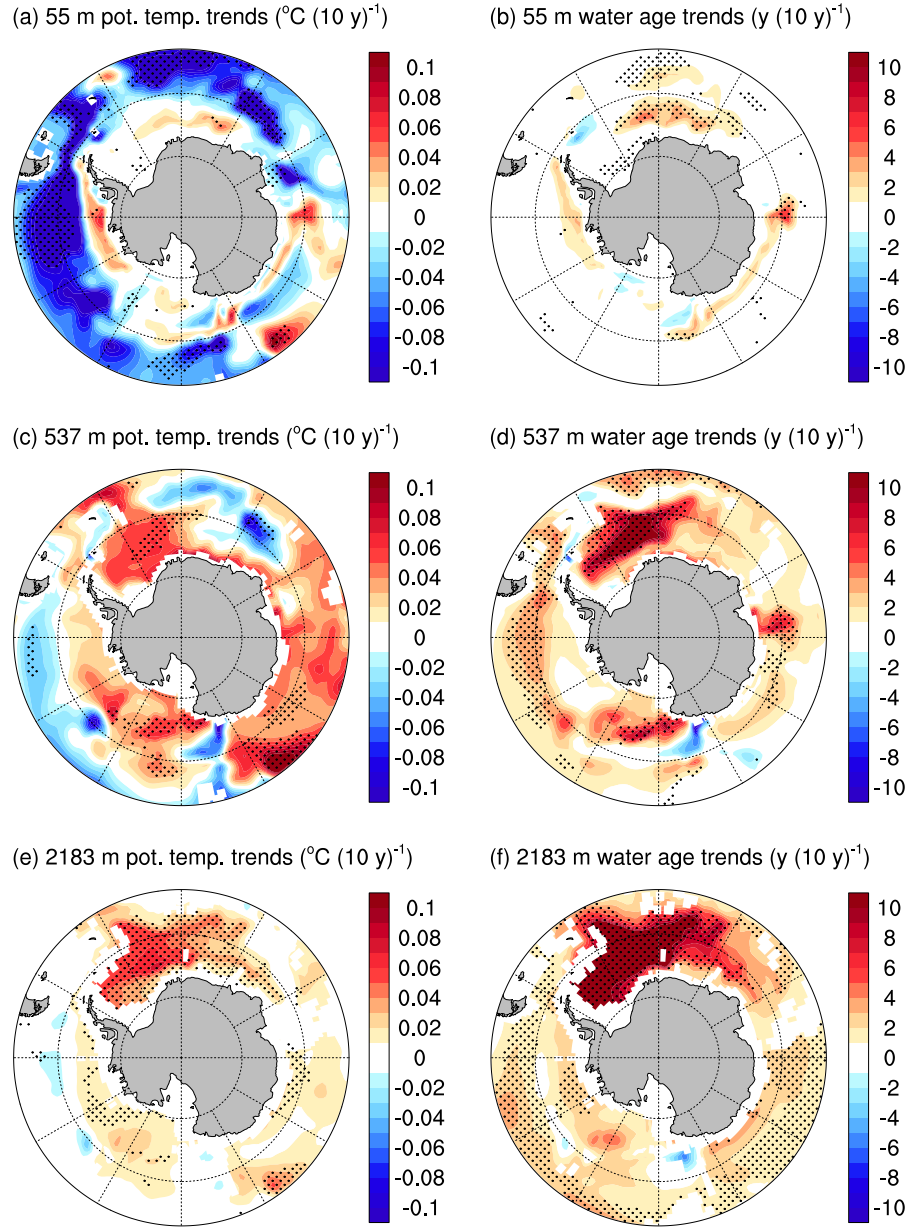


Figure 3.6: Ensemble-mean 50-year trends. (left) Potential temperature; and (right) water age from the ACCESS1.0 freshwater simulations. Water age acts as a tracer in ACCESS1.0 and indicates the length of time since a parcel of water has been at the surface. Trends are shown for depths of: (a,b) 55 m; (c,d) 537 m; and (e,f) 2183 m. In all panels, stippling indicates trend significance at the 95% level.

3.3.2 Further assessment of subsurface trends

Given the idealised nature of the applied freshwater forcing simulations, it is far from surprising to see differences between the zonal-mean latitude versus depth salinity trends in observations and the freshwater simulations. The observed freshening (Fig. 3.4a) is strongest at the surface to 150 m between 45–70°S, and extends to 1500 m depth between 30–40°S, whereas the simulated freshening (Fig. 3.4b) is strongest at the surface to 150 m between 40–70°S. The simulated subsurface freshening does not extend as deep as

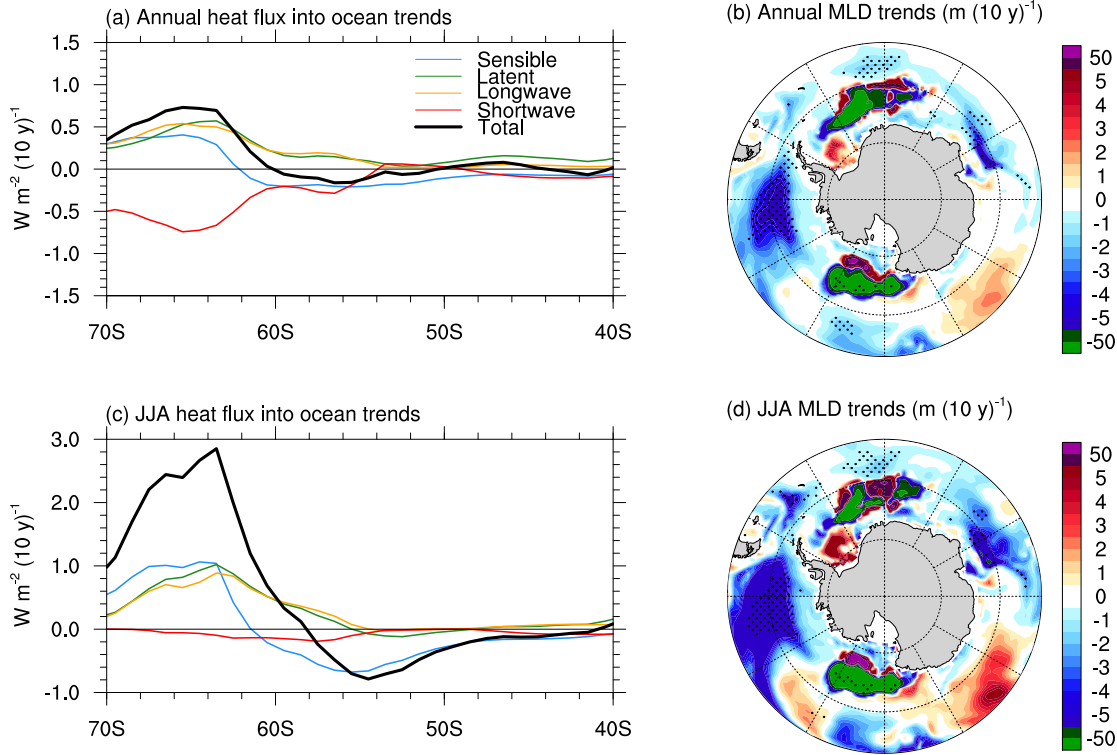


Figure 3.7: Ensemble-mean 50-year trends. (left) Zonal-mean surface heat fluxes; and (right) mixed layer depth. Trends are shown for: (a,b) the annual-mean; and (c,d) austral winter (JJA). In (b,d) the colour bar is non-linear, with green and magenta shading indicating trends in the regions of deep ocean convection, and stippling indicates trend significance at the 95% level.

observed, extending to 1100 m between 30–40°S, nor does it extend as far equatorward. This could be due to overly strong diffusive mixing of the anomalous low-salinity waters, a chronic problem in non eddy-resolving ocean models (England, 1993), or because the freshwater simulations don’t include surface temperature changes, which have been shown to be important to replicate observed subsurface salinity changes (Lago et al., 2016). Both observations and the freshwater forcing simulations also exhibit a surface salinification north of 30°S. Salinity increases are stronger and more pervasive in observations than in the freshwater forcing simulations, because the primary drivers of the observed SSS increase relate to a poleward migration of the mid-latitude westerly-wind jet and storm tracks, which in turn sees precipitation and the northward transport of cool fresh water diminish at this latitude band (e.g. Sen Gupta and England, 2006). In contrast, in the freshwater forcing simulations no wind shift is imposed, leaving only the local stratification changes (and any other associated feedbacks) as the major mechanism for surface water-mass change.

The observed trend in potential temperature (Fig. 3.5a) shows strong warming at the surface for all latitudes (likely driven by greenhouse warming) except between 55–70°S, where there is an absence of warming. Warming of the Southern Ocean below 150 m occurs between 40–70°S. The freshwater simulations (Fig. 3.5b) show a surface cooling over

the Southern Ocean, strongest between 40–70°S to 100 m. Between 60–70°S a significant warming signal is seen extending to 3000 m. As discussed above, the simulated salinity and potential temperature signals indicate an increase in surface stability, reducing convective overturning in the Southern Ocean, and thus also the upwelling of warmer subsurface waters, causing a cooling at the surface and warming below (as in e.g. Martinson, 1990; Marsland and Wolff, 2001). This surface cooling is then conducive to increased sea ice, as seen in the surface trend map (Fig. 3.3e).

Despite the differences discussed above, the freshwater simulations capture the observed subsurface salinity pattern much more accurately than the CMIP5 multi-model mean does (Fig. 3.4c). However, without increased radiative forcing in the freshwater simulations, it is not expected that the simulated potential temperature trends (Fig. 3.5b) will capture all characteristics of the observed trends (Fig. 3.5a). For comparison, the potential temperature trends from the CMIP5 multi-model mean are shown in Fig. 3.5c. This panel represents the modelled estimate of the long-term mean climate system response to increased radiative forcing with variability averaged out. As with observations, a surface warming is seen in the CMIP5 multi-model mean, extending to 2000 m around 50°S. However, as discussed in Section 3.1, the CMIP5 multi-model mean does not exhibit Southern Ocean surface cooling, or freshening, in contrast to observations. Further, the CMIP5 multi-model mean warming is weaker than observed between 150–900 m at 70°S. Linear addition of the freshwater simulation trend pattern (Fig. 3.5b) and the CMIP5 multi-model mean trend pattern (Fig. 3.5c) yields the pattern shown in Fig. 3.5d. We add these two trend patterns as while many of the CMIP5 models do show some freshening associated with historical forcings (Figs 3.1b, 3.2), it is generally underestimated compared to observations over the high latitudes. Adding the CMIP5 multi-model mean with underestimated surface freshening (Figs 3.4c, 3.5c) to the freshwater simulations without historical forcings (Figs 3.4b, 3.5b) thus provides a useful qualitative comparison to the observations (Figs 3.4d, 3.5d). Qualitatively, this pattern better captures the 55–70°S surface cooling and subsurface warming than the CMIP5 multi-model mean alone. This suggests that Southern Ocean surface freshening along with increased radiative forcing are both important components in influencing the high-latitude trends in temperature.

3.3.3 Inter-model trend comparison

We next consider the inter-model relationships between the CMIP5 models and the freshwater simulations, to better understand the role freshwater forcing has in influencing Southern Ocean trends. Figure 3.8 shows area-averaged trends in Southern Ocean SSS, SST and SIE for observations, the freshwater simulations and the CMIP5 models. For comparison, the trend from the ACCESS1.0 realisation submitted to CMIP5 is also highlighted (hereafter referred to as ACCESS1.0 CMIP5).

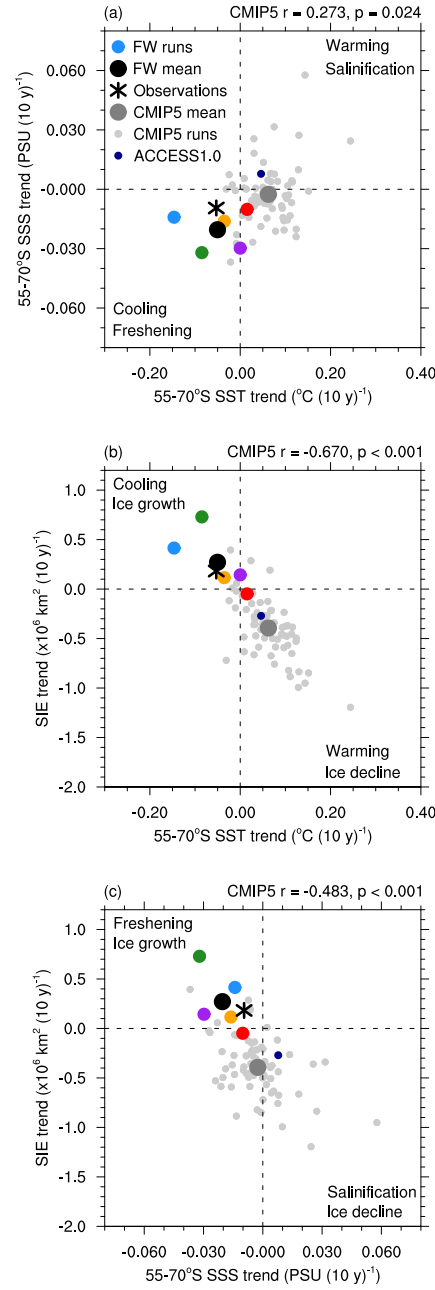


Figure 3.8: 35-year trends in SSS, SST and SIE for the ACCESS1.0 freshwater simulations, observations and CMIP5 models. (a) SSS versus SST; (b) SIE versus SST; and (c) SIE versus SSS. SSS and SST are area-averaged over $55-70^{\circ}\text{S}$. Coloured markers show individual freshwater simulations, the freshwater ensemble mean is shown by a black dot, observations are shown by a black asterisk, the CMIP5 multi-model mean is shown by a dark grey dot, the CMIP5 models are shown by light grey markers, and the ACCESS1.0 CMIP5 run is shown by a small dark blue marker. Observed SST and SIE trends, and CMIP5 trends are calculated over 1979–2013. Freshwater simulation trends are calculated for the last 35 years of the experiments, to cover a comparable length period to the CMIP5 models, and SIE and SST observations. Due to observational limitations as discussed in Section 3.2.3, observed SSS trends are calculated over 1950–2000, i.e. the observed SSS trends cover a different period of different length than all other points shown.

We are particularly interested in the role freshwater forcing plays in influencing the observed sea ice trends, so here we focus on 35-year trends in all metrics to match the observational sea ice record (as opposed to the 50-year trends considered previously). Observed SIE and SST trends and CMIP5 SIE, SST and SSS trends are all calculated over 1979–2013, and all freshwater simulation trends are calculated over the last 35 years of each run to compare periods of equal length. However, due to observational limitations as discussed in Section 3.2.3, observed SSS trends are still calculated over 1950–2000.

A moderate inter-model relationship is seen between trends in SSS and SST (Fig. 3.8a), and strong inter-model relationships are seen between trends in SIE and SST (Fig. 3.8b), and trends in SIE and SSS (Fig. 3.8c). In all cases the inter-model relationship between CMIP5 models is statistically significant ($p < 0.05$), although we note that the SST-SSS significance (Fig. 3.8a) is dependent on inclusion of models at the tail end of the distribution (strong warming and increased salinity), and the observed and ACCESS1.0 freshwater simulation trends fit the relationship shown by the CMIP5 models. Models/runs that show a stronger surface freshening also tend to show a stronger surface cooling and an increase in sea ice (or at least a weaker decrease in sea ice). Models/runs that show a stronger surface salinification tend to warm more, and show a larger decline in sea ice.

The majority of CMIP5 models do not simulate a surface cooling and increase in sea ice (Fig. 3.8b), as seen in observations, which has previously been linked in part to a summertime mechanism related to underestimation of the westerly-wind intensification, leading to an underestimation of increased Ekman upwelling, which in summer is associated with surface cooling (Purich et al., 2016a). This inter-model relationship occurs because during summer the surface water that receives shortwave radiation resides in a thin layer at the surface (0–20 m), forming a cap over cool Winter Water (20–150 m). Thus, enhanced Ekman upwelling during summer brings cooler Winter Water to the surface, and this surface cooling spreads north due to equatorward Ekman transport. Wind-driven Ekman upwelling seems to dominate over salinity-driven stratification during summer, and as a result the inter-model trend relationship between SSS and SST is not statistically significant during this season (Fig. 3.16 in Section 3.5).

During winter there is no warm layer at the surface, and the ocean is stratified between cold fresh water at the surface and warm salty water at depth. Given these water column characteristics, salinity-driven stratification becomes more strongly linked to surface temperature, and the inter-model trend relationship between SSS and SST is strengthened during the winter season (Fig. 3.17; $p < 0.01$; although again the significance of this relationship is dependent on including models at the tail ends of the distribution). When considering the annual-mean temperature profile, on average warmer waters reside below cooler surface waters, and as such, increased stability and reduced upwelling causes surface cooling, as seen in the relationship between SSS and SST trends in Fig. 3.8a. While the vast majority of CMIP5 models do not lie in the same quadrant as the observed trends (with SSS trends over 1950–2000), the majority of the freshwater simulations and the

freshwater ensemble mean trends do, demonstrating a similarity between the freshwater simulations and observations not shared by the majority of CMIP5 models. However we note that while the observed SSS trend over 1950–2000 provides a general indication of the long-term trend, due to observational limitations, we cannot actually know what quadrant the observed trends with SSS calculated over 1979–2013 lie in (Fig. 3.8a,c). We also note that our freshwater simulations do not include anthropogenic forcings, so while they do indeed simulate a freshening and cooling, this may not be the case with the same freshening imposed under global warming conditions.

It is also worth noting the spread across the five freshwater simulations (Fig. 3.8), which have identical forcings and differ only in their initial conditions. While the freshwater simulations fit the CMIP5 inter-model trend relationship in each case (Fig. 3.8a,b,c), the spread amongst the five ensemble members highlights that the Southern Ocean hydrography exhibits notable multi-decadal variability, presumably driven by multi-decadal secular variability in atmospheric forcing (e.g. via decadal variability in the SAM). This also emphasises the limitations of assessing Southern Ocean trends over 35 years, a period which may not accurately represent longer-term trends due to aliased multi-decadal variability (Goosse et al., 2009; Jones et al., 2016; Hobbs et al., 2016). When 50-year trends are considered for all metrics for both the freshwater simulations and the CMIP5 realisations (Fig. 3.18 in Section 3.5), the variability across ensemble member trends greatly reduces, diminishing the spread across both the freshwater and CMIP5 simulations.

3.3.4 Salinity restoring simulations

While this study focuses on the output from the ACCESS1.0 idealised freshwater simulations, regional differences between observations and modelled trends in SSS can be seen (Fig. 3.3a,b). In particular, the model redistribution of the applied idealised freshwater flux results in little surface freshening of the Ross Sea, but considerable pooling of freshwater in the Bellingshausen Sea (Fig. 3.3b), resulting in SSS trends that exhibit an opposite dipole pattern to what is observed in these regions (Fig. 3.3a). To complement the idealised freshwater simulations and apply more realistic geographic distributions of trends, we also conduct a pair of SSS restoring simulations: one is an unperturbed control run and the second is identical to the control, but with an applied freshening of surface salinity that spatially matches the Durack and Wijffels (2010) trends. In the first simulation, SSS between 40–70°S (with tapering either side) is restored to the annually and monthly varying SSS of the piControl over a 50-year reanalysed segment of the run. In the second simulation, an annually increasing trend is superimposed onto the piControl SSS in the 40–70°S restoring region. This applied SSS trend is set to exactly match the observed Durack and Wijffels (2010) trends. Due to the different experimental set-up, compared to the idealised freshwater simulations, these SSS restoring simulations enable better resolution of the geographic distribution of observed SSS trends. Both restoring simulations are branched from the same year of the piControl and run for 50 years each.

The SSS restoring timescale is 15 days over the upper ocean model layer.

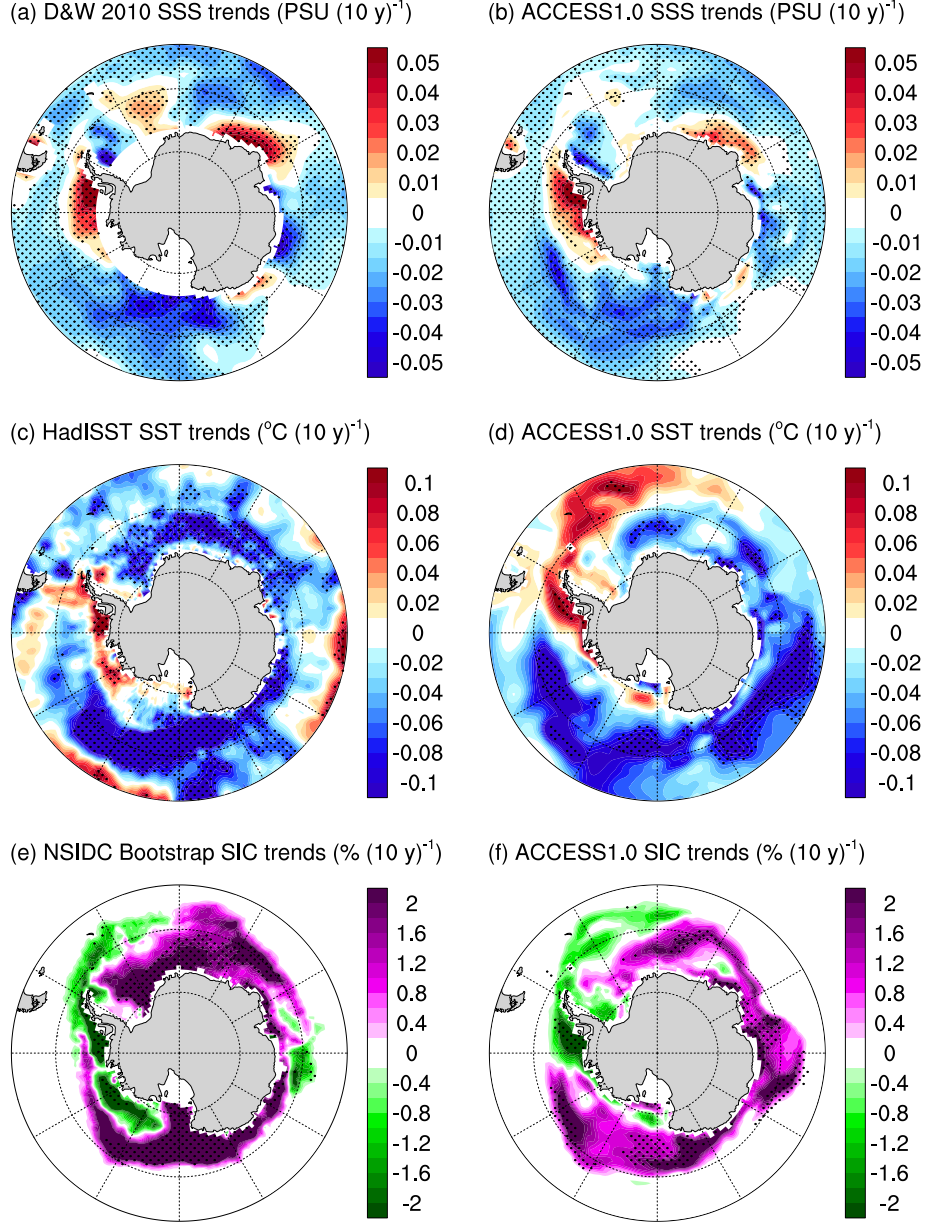


Figure 3.9: (left) Observed; and (right) 50-year trends from differencing the ACCESS1.0 SSS restoring simulations. (a,b) SSS trends; (c,d) SST trends; and (e,f) SIC trends. (a,c,e) are identical to Fig. 3.3a,c,e and are included here for direct comparison. In all panels, stippling indicates trend significance at the 95% level. Observations are as in Fig. 3.3.

We difference the two SSS restoring simulations to obtain the signal due to the Durack and Wijffels (2010) SSS trend, shown in Fig. 3.9. The SSS restoring difference pattern (Fig. 3.9b) accurately captures the observed SSS trend pattern (Fig. 9a), as expected given the restoring technique, with only minor differences evident. The SST (Fig. 3.9d) and SIC (Fig. 3.9f) trend patterns that result from this SSS restoring approach also resemble the observed (Fig. 3.9c,e) trends remarkably well. The observed SSS changes drive cooling around most regions of Antarctica and an accompanying increase in sea ice in the restoring simulations, as well as the characteristic warming and decrease in SIC in the Bellingshausen Sea and

along the Antarctic Peninsula. There are also some differences between the observed and simulated trends. In particular, in contrast to the observed cooling, a strong warming is simulated in the South Atlantic (Fig. 3.9c,d). Overall however, the SST trend patterns south of 60°S show remarkable agreement. Minor regional differences in the SIC trend patterns (Fig. 3.9e,f) include in the inner Amundsen Sea and at 90°E, but overall the SIC trend patterns show strong similarities. These SSS restoring simulations demonstrate that without any mechanical forcing associated with changing winds, SSS can drive changes in SST, and remarkably that the regional pattern of SSS trends can drive the dipole trends in SST and sea ice in the Pacific sector. This reinforces the findings presented above based on the freshwater simulations, that demonstrate how reduced upwelling of warmer subsurface waters induced by large-scale surface freshening trends has played an important role in the recent multi-decadal cooling of the surface Southern Ocean.

3.4 Discussion

The Southern Ocean surface has freshened in recent decades (Durack and Wijffels, 2010; de Lavergne et al., 2014), increasing water column stability and reducing the upwelling of warm subsurface waters. While previous studies have investigated the influence of increased freshwater from Antarctic ice sheet/shelf runoff and iceberg fluxes around the continental margins (Bintanja et al., 2013, 2015; Swart and Fyfe, 2013; Pauling et al., 2016), the impact of broad-scale freshening due to a combination of factors, including freshwater redistribution by sea ice and icebergs, increased ice sheet and ice shelf runoff, and P–E changes likely associated with the positive SAM trend, have received little attention. The possible role that this broad-scale freshening has had on Antarctic sea-ice trends and surface Southern Ocean cooling provided the overall motivation for this study. To this end, we examined targeted coupled climate model simulations run using ACCESS1.0 with increased freshwater applied to the ocean model component over the Southern Ocean.

In terms of the total mass of freshwater applied in our simulations, the freshwater trend of $0.1 \text{ mm day}^{-1} (10 \text{ y})^{-1}$ applied in our simulations over 55–70°S corresponds to a freshwater mass acceleration of $\sim 112 \text{ Gt y}^{-2}$ ($\sim 5600 \text{ Gt y}^{-1}$ in the last year of the simulations), chosen to simulate a clear surface freshening, as observed. To put this into context, Pauling et al. (2016) found the increase in P–E over the Southern Ocean (south of 50°S and not including Antarctica) from the pre-industrial period to the present day to be $\sim 2000 \text{ Gt y}^{-1}$ in the CMIP5 models, although with considerable spread across models (see their Fig. 5c). The additional freshwater applied in our idealised simulations is considerably higher than this, as the majority of CMIP5 models underestimate the surface freshening trends over the Southern Ocean (Fig. 3.1b). Our idealised freshwater simulations show that a surface freshening causes a decrease in SST and an increase in sea ice, attributed primarily to a reduction in ocean convection. However, to achieve a cooling and SIE increase similar to observations, a stronger than observed zonal-mean freshening was applied (Fig. 3.8). This suggests that a uniform broad-scale surface freshening from

processes including increased P–E is only one component contributing to observed sea ice changes and surface cooling; other factors such as decadal variability (Meehl et al., 2016a; Purich et al., 2016b), direct wind effects (Holland and Kwok, 2012; Purich et al., 2016a) and zonal variations in SSS (as per our SSS restoring simulations; Fig. 3.9) also play a critical role.

Comparisons with results from Bintanja et al. (2013), Bintanja et al. (2015) and Pauling et al. (2016) are difficult, as their experiments added constant, rather than increasing, amounts of freshwater, and in addition their focus is on the impacts of Antarctic meltwater discharge, not the broad-scale freshening due to precipitation trends examined here. While Bintanja et al. (2013) added a relatively modest 250 Gt y^{-1} over 31 years with radiative forcing held fixed, when differenced from their control experiment, sea ice was found to increase. In similar simulations with increased radiative forcing Bintanja et al. (2015) added only $10\text{--}120 \text{ Gt y}^{-1}$ of freshwater, and found that 120 Gt y^{-1} was enough to offset radiative forcing and result in a weak increase in sea ice. On the other hand, the surface freshwater experiments by Pauling et al. (2016) added $1000\text{--}3000 \text{ Gt y}^{-1}$, and while they found an increase in mean-state sea ice area, they did not find a positive trend in sea ice under increased radiative forcing conditions. While these studies are very useful in better understanding how a constant additional freshwater flux governs changes in sea ice, motivated by the lack of constant Antarctic ice shelf/sheet and iceberg fluxes in the CMIP5 models, without time-varying freshwater fluxes, it is difficult to compare these studies to the real-world surface freshening trend that has been observed (Durack and Wijffels, 2010).

The study by Swart and Fyfe (2013) is more comparable to this study, as they also applied increasing amounts of freshwater, although their freshwater flux was only applied around the Antarctic margin, compared to the broad-scale additional flux in our simulations. Their additions ranged from $3.15\text{--}15.77 \text{ Gt y}^{-2}$ over 47 years ($\sim 740 \text{ Gt y}^{-1}$ in the last year of the simulation for the highest acceleration rate), and from $3.15\text{--}31.54 \text{ Gt y}^{-2}$ over 29 years ($\sim 910 \text{ Gt y}^{-1}$ in the last year of the simulation for the highest acceleration rate). These freshwater additions are considerably less than those applied in our experiments, as we are interested in broad-scale freshening from processes including P–E changes, whereas Swart and Fyfe (2013) were interested in the Antarctic ice sheet meltwater. The simulations by Swart and Fyfe (2013) also included increased radiative forcing, and they found that the additional freshwater in their simulations reduced the amount of sea ice lost, but could not reverse the negative sea ice trend. Despite this, relative to their control experiment, their strongest freshwater mass accelerations gave regional SIC trends of the order $0.5\text{--}2.5\% (10 \text{ y})^{-1}$ (their Fig. 4d), which are comparable to our SIC trends (Fig. 3.3f).

We show that the majority of CMIP5 models underestimate the observed surface freshening over the Southern Ocean over the latter half of the twentieth century. Based on the inter-model CMIP5 trend relationships assessed here, alongside our freshwater anomaly experiments conducted using ACCESS1.0, this reduced or absent freshening highly likely

contributes to the poor simulation of observed Southern Ocean surface cooling and Antarctic sea ice trends in CMIP5 models. However, compared to the CMIP5 models and the real world, we note that our freshwater simulations are idealised and do not include anthropogenic greenhouse warming. The historical and RCP8.5 ACCESS1.0 simulation participating in CMIP5 shows a Southern Ocean SST warming of $\sim +0.05^{\circ}\text{C} (10 \text{ y})^{-1}$ over 1979–2013, between 55–70°S, as well as a weak increase in surface salinity over this latitude band. In contrast, the ensemble mean of our idealised freshwater simulations shows a cooling over this same latitude band of $\sim -0.05^{\circ}\text{C} (10 \text{ y})^{-1}$. Similarly, the CMIP5 historical and RCP8.5 ACCESS1.0 simulation exhibits a significant sea-ice retreat over this period [$\sim -0.27 \times 10^6 \text{ km}^2 (10 \text{ y})^{-1}$], while adding a surface freshening trend in our idealised freshwater simulations leads to the opposite sea-ice tendencies; namely, an ensemble-mean expansion in Antarctic sea-ice that happens to be of similar magnitude [$\sim +0.27 \times 10^6 \text{ km}^2 (10 \text{ y})^{-1}$]. The freshening induced cooling we obtain could thus clearly be one of the important factors accounting for the regional model-observed mismatch in recent SST and SIC trends, alongside decadal variability and direct wind effects. Furthermore, the strong relationships obtained between Southern Ocean surface salinity and temperature trends demonstrate the importance of surface freshening in this region for upper ocean thermal properties.

Had the historical greenhouse warming been added alongside the surface freshening in our idealised freshwater simulations, the influence of these two factors may have more-or-less cancelled to yield a minimal trend in Southern Ocean SST and SIE (Fig. 3.19 in Section 3.5). Additional ACCESS1.0 simulations conducted under historical greenhouse warming are presented and discussed in Appendix D. Indeed, the combined influence of surface freshening and greenhouse warming in ACCESS1.0 results in a minimal trend in Antarctic SIE.

Many of the features of both SST and sea-ice trends in the region, including warming and reduced sea ice in the Amundsen and Bellingshausen Seas, and cooling and increased sea ice in the Ross Sea, can be accurately simulated when simply imposing the observed SSS trends over the Southern Ocean in SSS restoring simulations. This demonstrates that upper ocean SSS trends have been an important component in driving regional hydrography and circulation changes around Antarctica over the last half century. This study also highlights the importance of accurately simulating changes in clouds, storm tracks, P–E and surface salinity over the Southern Ocean to capture changes in ocean circulation and sea ice.

3.5 Supplementary material

Table 3.1: CMIP5 models used in this study and their expansions. The first available run per model is shown in Figs 3.1, 3.2, 3.4 and 3.5. All available runs are shown in Figs 3.8, 3.10, 3.16, 3.17 and 3.18 as indicated in the runs column.

<i>Model</i>	<i>Runs</i>	<i>Expansion</i>
ACCESS1.0	1	Australian Community Climate and Earth-System Simulator, version 1.0
ACCESS1.3	1	Australian Community Climate and Earth-System Simulator, version 1.3
CanESM2	5	Second Generation Canadian Earth System Model
CCSM4	1	Community Climate System Model, version 4
CESM1-BGC	1	Community Earth System Model, version 1, Biogeochemistry
CESM1-CAM5	3	Community Earth System Model, version 1, Community Atmosphere Model, version 5
CESM1-WACCM	3	Community Earth System Model, version 1, Whole Atmosphere Community Climate Model
CMCC-CESM	1	Centro Euro-Mediterraneo sui Cambiamenti Climatici Carbon Earth System Model
CMCC-CM	1	Centro Euro-Mediterraneo sui Cambiamenti Climatici Climate Model
CNRM-CM5	5	Centre National de Recherches Météorologiques Coupled Global Climate Model, version 5
CSIRO-Mk3-6-0	10	Commonwealth Scientific and Industrial Research Organisation Mark 3.6.0
GFDL-CM3	1	Geophysical Fluid Dynamics Laboratory Climate Model, version 3
GFDL-ESM2G	1	Geophysical Fluid Dynamics Laboratory Earth System Model with Generalized Ocean Layer Dynamics (GOLD) component
GFDL-ESM2M	1	Geophysical Fluid Dynamics Laboratory Earth System Model with Modular Ocean Model, version 4 (MOM4) component
GISS-E2-H	3	Goddard Institute for Space Studies ModelE/Hycom
GISS-E2-H-CC	1	Goddard Institute for Space Studies ModelE/Hycom, interactive Carbon Cycle
GISS-E2-R	3	Goddard Institute for Space Studies ModelE/Russell
GISS-E2-R-CC	1	Goddard Institute for Space Studies ModelE/Russell, interactive Carbon Cycle
HadGEM2-CC	3	Hadley Centre Global Environment Model, version 2, Carbon Cycle

Continued on next page

Table 3.1: Continued from previous page.

<i>Model</i>	<i>Runs</i>	<i>Expansion</i>
HadGEM2-ES	4	Hadley Centre Global Environment Model, version 2, Earth System
inmcm4	1	Institute of Numerical Mathematics Climate Model, version 4
IPSL-CM5A-LR	4	Institut Pierre Simon Laplace Coupled Model, version 5A, low resolution
IPSL-CM5A-MR	1	Institut Pierre Simon Laplace Coupled Model, version 5A, mid resolution
IPSL-CM5B-LR	1	Institut Pierre Simon Laplace Coupled Model, version 5B, low resolution
MIROC5	3	Model for Interdisciplinary Research on Climate, version 5
MIROC-ESM	1	Model for Interdisciplinary Research on Climate, Earth System Model
MIROC-ESM-CHEM	1	Model for Interdisciplinary Research on Climate, Earth System Model, Chemistry Coupled
MPI-ESM-LR	3	Max Planck Institute Earth System Model, low resolution
MPI-ESM-MR	1	Max Planck Institute Earth System Model, medium resolution
NorESM1-M	1	Norwegian Earth System Model, version 1, medium resolution
NorESM1-ME	1	Norwegian Earth System Model, version 1, medium resolution with capability to be fully emission driven

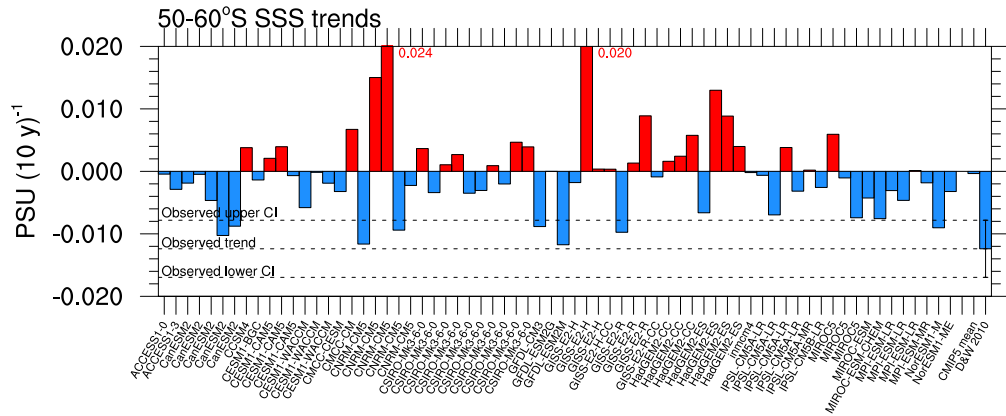


Figure 3.10: As for Fig. 3.2 but showing all available ensemble members for each CMIP5 model.

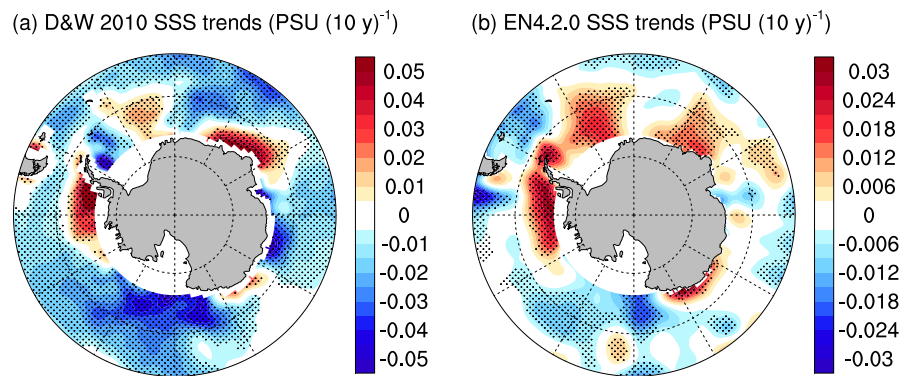


Figure 3.11: Observed SSS trends. (a) Durack and Wijffels (2010) changes; and (b) EN4.2.0 changes over 1950–2008. Stippling indicates trend significance.

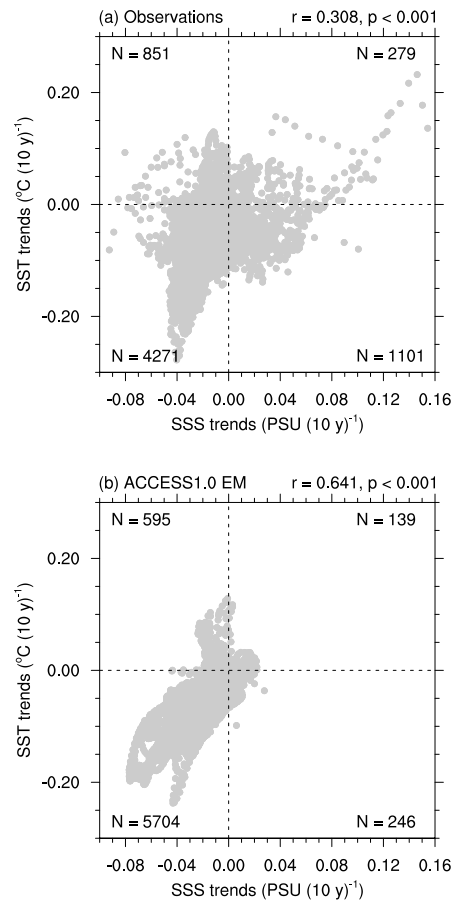


Figure 3.12: Grid point SST trends versus grid point SSS trends for: (a) observations (Durack and Wijffels 2010 and HadISST); and (b) the ACCESS1.0 freshwater simulations ensemble mean. A grey marker shows each grid point with the number of points in each quadrant indicated, and the correlation coefficient and p value are indicated above each panel.

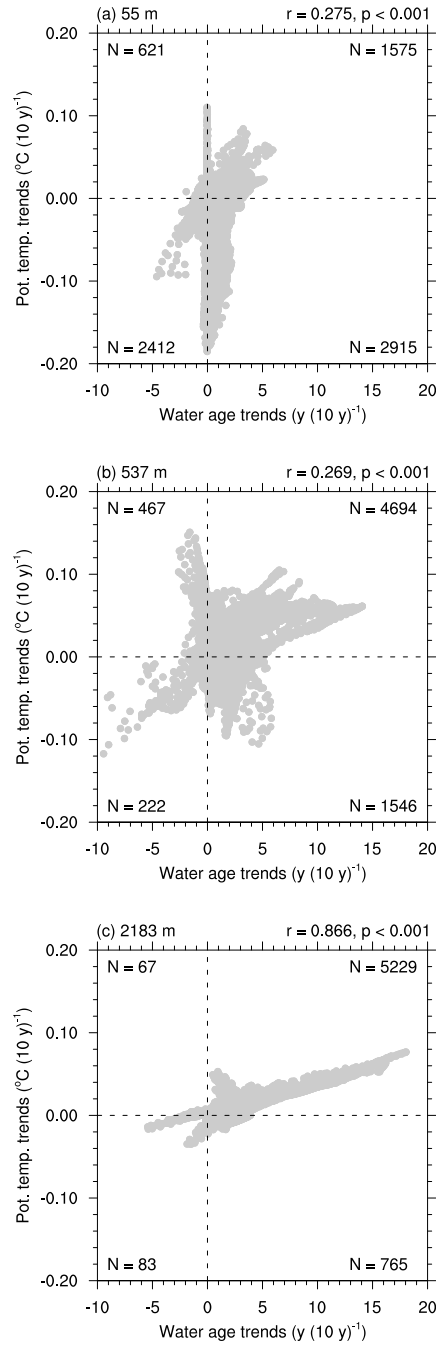


Figure 3.13: ACCESS1.0 freshwater simulations ensemble mean grid point potential temperature trends versus grid point water age trends at depths of: (a) 55 m; (b) the 537 m; and (c) 2183 m. A grey marker shows each grid point with the number of points in each quadrant indicated, and the correlation coefficient and p value are indicated above each panel.

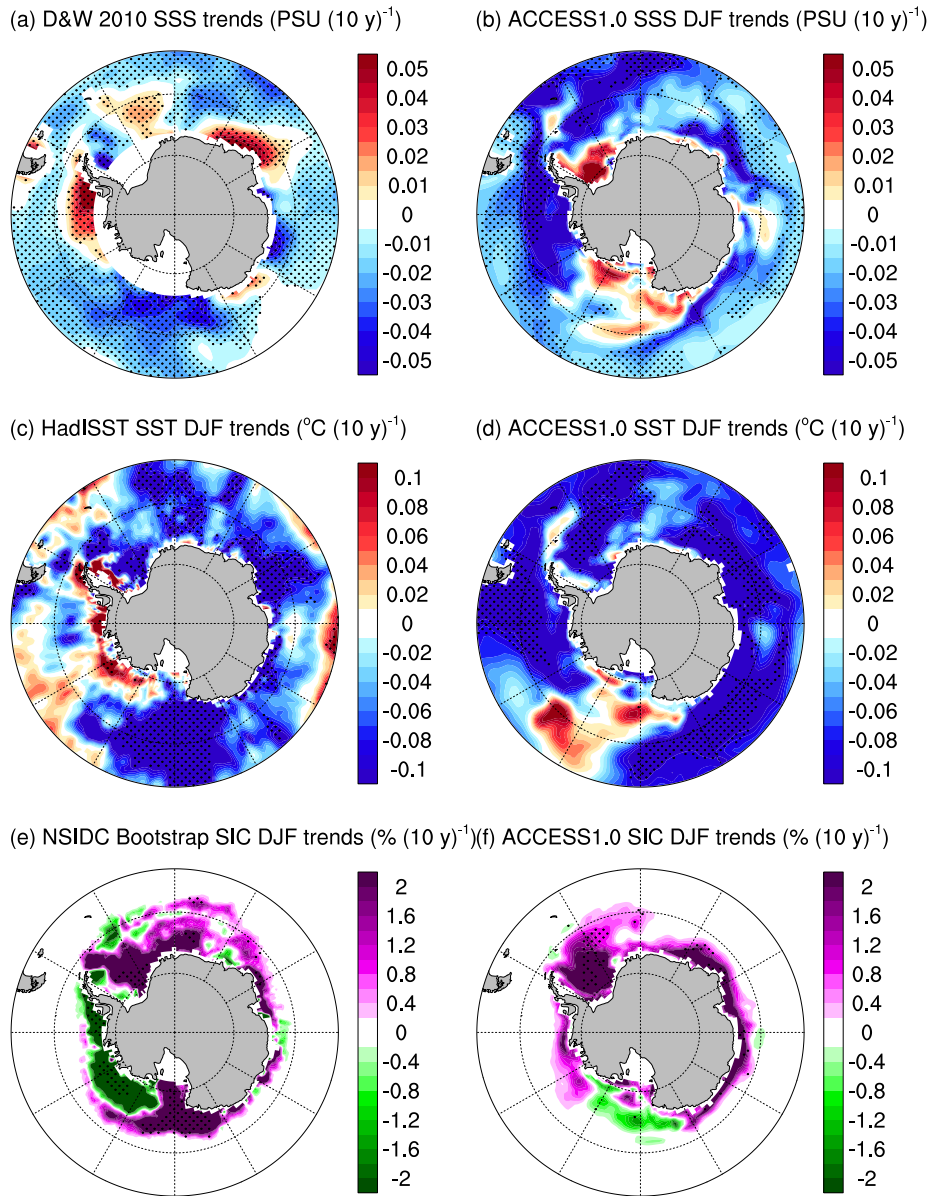


Figure 3.14: As for Fig. 3.3 but for austral summer (DJF). Note that the annual observed SSS trend is shown.

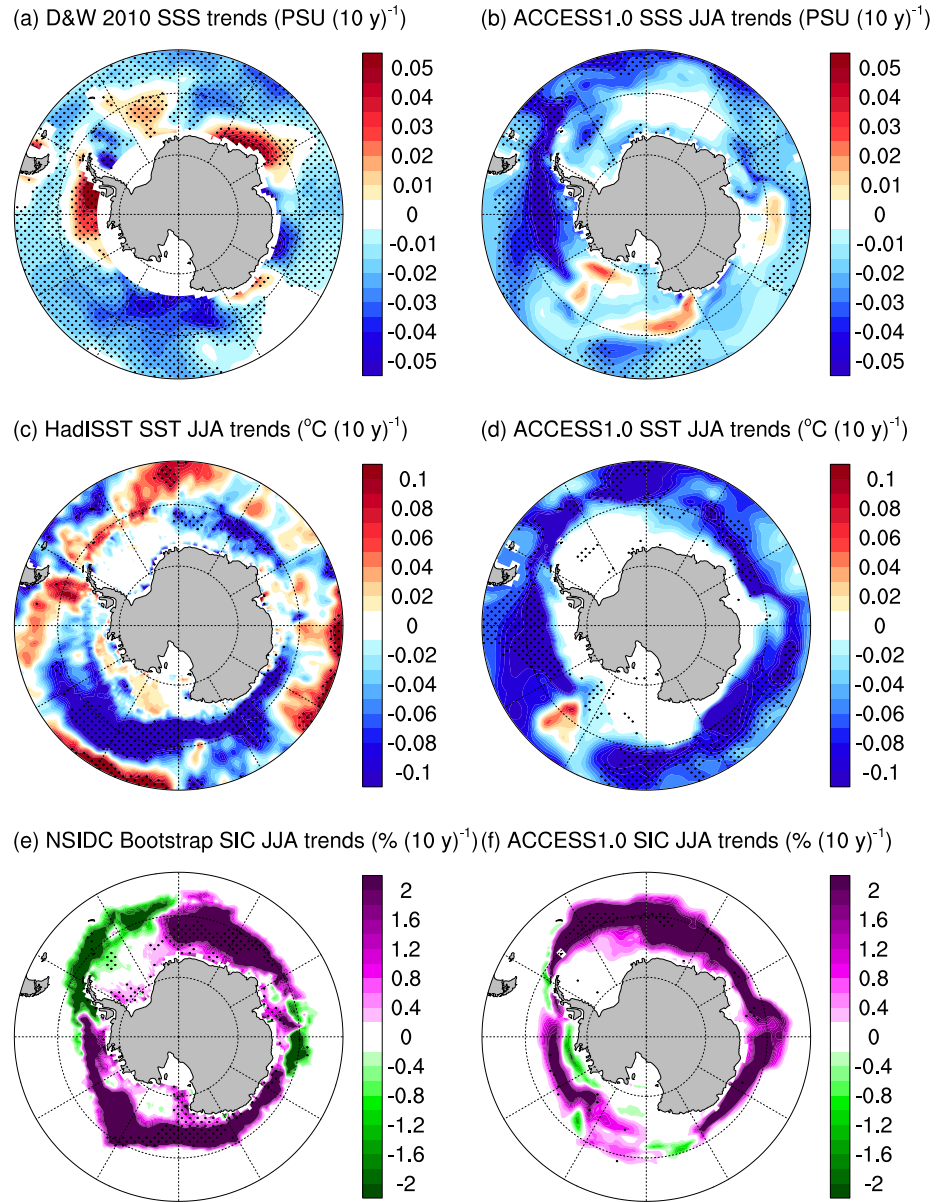


Figure 3.15: As for Fig. 3.3 but for austral winter (JJA). Note that the annual observed SSS trend is shown.

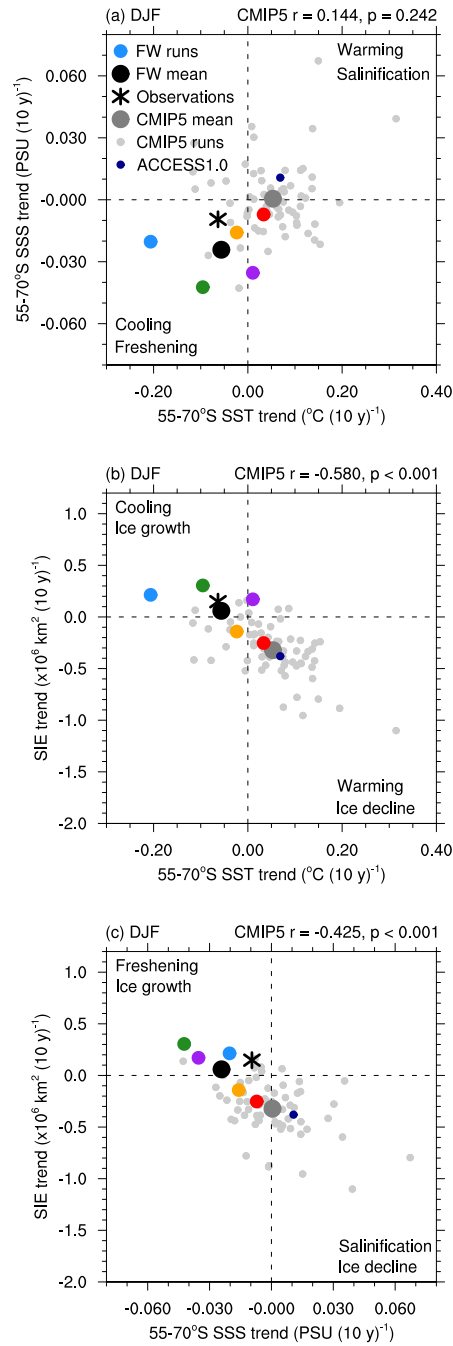


Figure 3.16: As for Fig. 3.8 but for austral summer (DJF). Note that the annual observed SSS trend is shown.

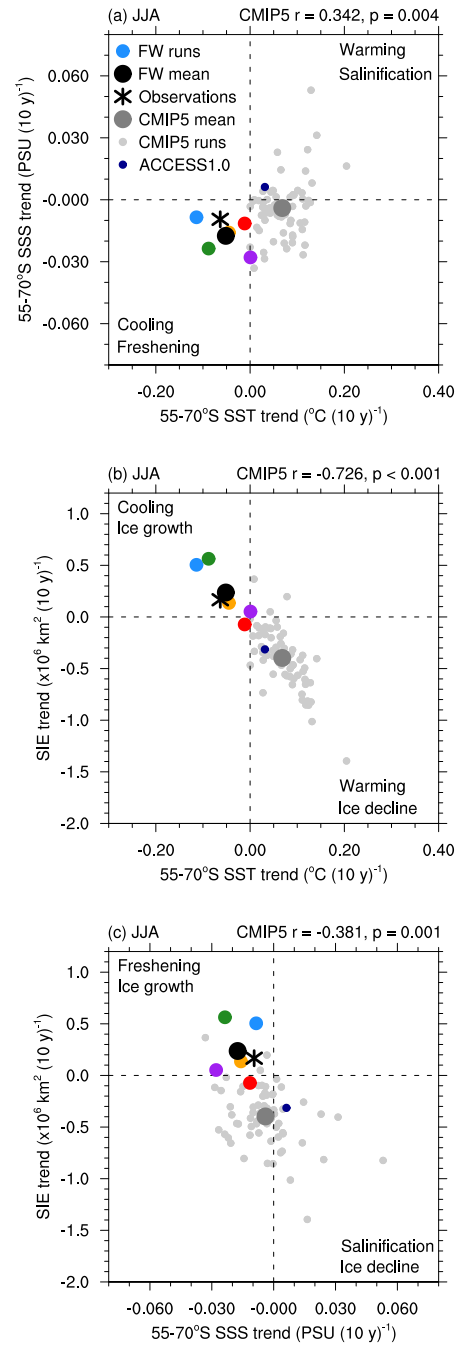


Figure 3.17: As for Fig. 3.8 but for austral winter (JJA). Note that the annual observed SSS trend is shown.

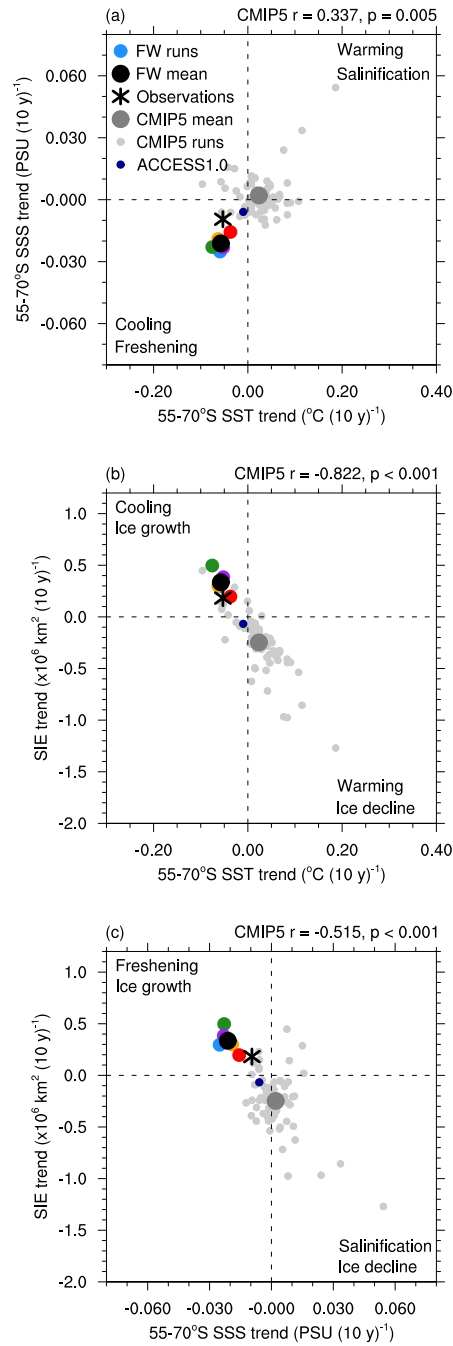


Figure 3.18: As for Fig. 3.8 but for 50-year annual-mean trends in the ACCESS1.0 fresh-water simulations and the CMIP5 models. Observed SST and SIE trends are calculated over 1979–2013. Observed SSS and CMIP5 trends are calculated over 1950–2000.

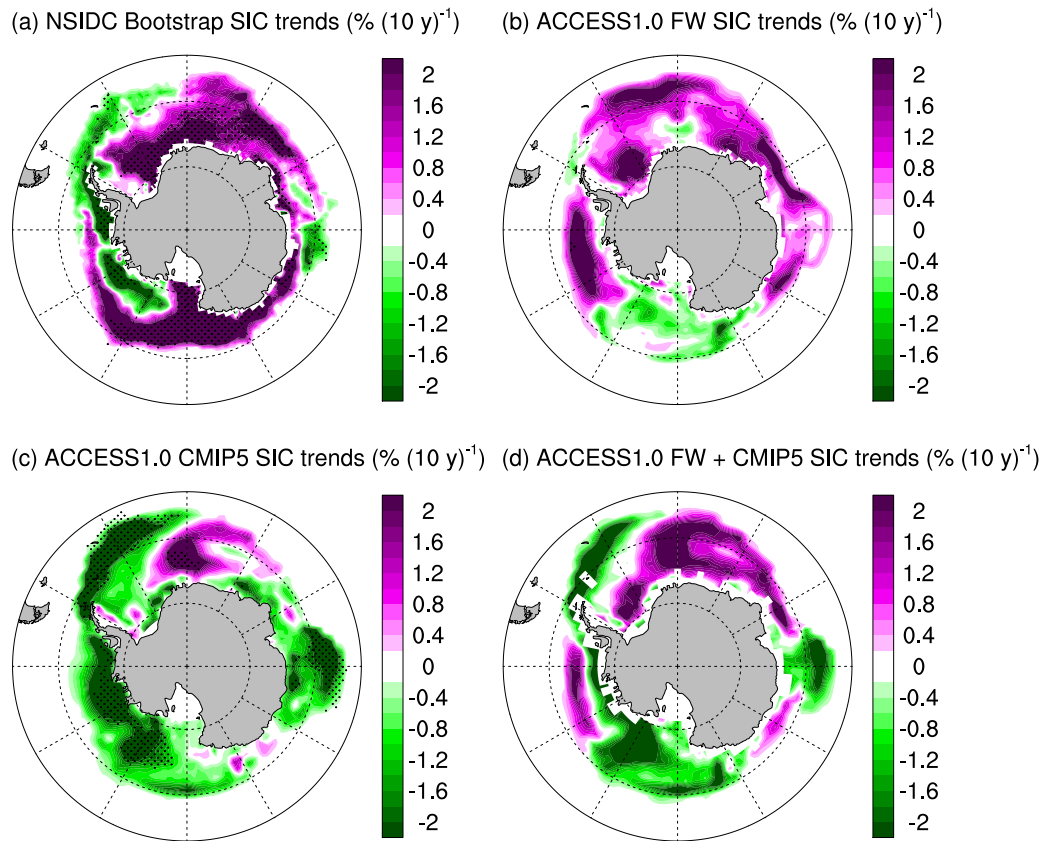


Figure 3.19: 35-year SIC trends. (a) Observed SIC trends from NSIDC Bootstrap over 1979–2013; (b) ensemble-mean trends from the ACCESS1.0 freshwater simulations over the last 35 years of each simulation; (c) ACCESS1.0 CMIP5 trends over 1979–2013; and (d) sum of ACCESS1.0 freshwater ensemble mean trends and ACCESS1.0 CMIP5 trends, i.e. (b)+(c). In (a–c), stippling indicates trend significance at the 95% level.

Concluding Remarks

Summary of findings

A major challenge confronting the climate research community is that despite global warming, total Antarctic sea ice coverage increased over 1979–2013 (Cavalieri and Parkinson, 2008; Comiso and Nishio, 2008; Parkinson and Cavalieri, 2012; Vaughan et al., 2013; Comiso et al., 2017). In striking contrast, the great majority of Coupled Model Intercomparison Project phase five (CMIP5) global coupled climate models simulated a declined in Antarctic sea ice over this period (Mahlstein et al., 2013; Polvani and Smith, 2013; Swart and Fyfe, 2013; Turner et al., 2013a; Zunz et al., 2013; Gagné et al., 2015; Shu et al., 2015). This represents a fundamental challenge in understanding high-latitude climate processes in a warming world. Explanations of mechanisms causing this discrepancy – important to better understand observed trends and for model improvement – had, when this thesis began, remained elusive. Understanding these changes is critical for global climate, as Antarctic sea ice plays an important role in influencing surface albedo (e.g. England et al., 2017) and both the upper and lower branches of the global ocean overturning circulation, influencing the ocean uptake of heat and carbon (e.g. Marshall and Speer, 2012; Abernathey et al., 2016). Thus, this research sought to improve our understanding of the physical mechanisms driving Southern Ocean surface trends, and in particular the observed increase in Antarctic sea ice.

Since this research project began in 2014, the findings of this thesis, along with considerable work from many others (e.g. Bintanja et al., 2015; Clem and Fogt, 2015; Clem and Renwick, 2015; Ferreira et al., 2015; Gagné et al., 2015; Li et al., 2015a,b; Morrison et al., 2015; Shu et al., 2015; Turner et al., 2015b; Armour et al., 2016; Jones et al., 2016; Kostov et al., 2016; Kwok et al., 2016; Meehl et al., 2016a; Pauling et al., 2016; Raphael et al., 2016; Turner et al., 2016; Comiso et al., 2017; Holland et al., 2017; Lecomte et al., 2017; Pauling et al., 2017; Stuecker et al., 2017; Su, 2017; Turner et al., 2017; Schlosser et al., 2018; Meehl et al., 2018; Wang et al., 2018) has led to a considerable advance in our understanding of high-latitude climate processes in a warming world, as outlined below.

Part 1

To improve both our understanding of observed trends and confidence in future climate projections, the first overarching goal of this research was to reconcile the disparity between the recent multi-decadal observed increase in Antarctic sea ice extent and the CMIP5

multi-model mean decline. While Antarctic sea ice trends in the CMIP5 models had been extensively investigated (Mahlstein et al., 2013; Polvani and Smith, 2013; Swart and Fyfe, 2013; Turner et al., 2013a; Zunz et al., 2013; Gagné et al., 2015; Shu et al., 2015), at the time of commencing this thesis, few studies had proposed physical mechanisms responsible for the disparity with observations (Bintanja et al., 2013; Swart and Fyfe, 2013; Haumann et al., 2014).

Part 1 of this thesis shows that the weaker trends in the intensification and poleward shift of the austral summer Southern Hemisphere westerly-wind jet simulated by the CMIP5 models has contributed to the disparity between model and observed sea ice trends. In particular, during summer an intensified jet leads to increased upwelling of cooler subsurface water and strengthened equatorward transport, conducive to sea-ice expansion. Because CMIP5 models underestimate observed trends in the summer jet, the Ekman response to climate change is also underestimated. As such, the models produce a high-latitude surface warming, contrasting with the observed cooling, and contributing to the modelled sea-ice decline. Persistence in sea ice and the surface ocean means that mechanisms acting during summer can impact trends beyond this season. Ultimately this Ekman effect brings up warmer deep water to the surface, from below the permanent pycnocline. This two time-scale response to poleward intensifying winds (cooling then warming) had been previously noted (Marshall et al., 2014; Ferreira et al., 2015), but Part 1 of this thesis was the first study to resolve seasonality.

While changes in the CMIP5 models' wind-driven circulation contribute to surface cooling, these trends are underestimated, and are in fact too weak to offset the simulated warming from increased radiative heat fluxes. The findings from Part 1 are important because they highlight the balance between the processes controlling surface climate trends around Antarctica. These results suggest that a realistic simulation of observed wind changes is crucial for reproducing the recent sea ice increase around Antarctica. The two-time scale response to poleward intensifying winds (Marshall et al., 2014; Ferreira et al., 2015) also emphasises how anthropogenic climate change results counter-intuitively in an initial surface cooling of the Southern Ocean that will eventually get overwhelmed by a surface warming (Armour et al., 2016; Kostov et al., 2016; Holland et al., 2017). The findings from Part 1 have important implications for interpreting recent Antarctic trends and also provide an explanation as to why Antarctic sea ice has increased despite global warming.

Part 2

With the identification of the hemispheric-scale mechanism influencing Antarctic sea ice in Part 1 of this thesis, Part 2 then turned to focus on the regionality of Antarctic sea ice trends. While overall Antarctic sea ice coverage increased over 1979–2013, the strong regional trends, in particular the strong decrease in sea ice in the Amundsen and Bellingshausen Seas and the strong increase in the Ross Sea (which contributes largely to the

circumpolar increase) deserve additional consideration. As such, Part 2 of this thesis investigated the role of interannual variability in contributing to trends in regional Antarctic sea ice coverage over 1979–2013.

Prior to this Part, the sea ice and atmospheric circulation trends in the Pacific sector had already received considerable attention. A strengthening of the Amundsen Sea Low has been observed (Turner et al., 2013b), due to both the positive trend in the Southern Annular Mode (SAM; Turner et al., 2013b), and teleconnections from the tropical Pacific (Schneider et al., 2012; Clem and Renwick, 2015; Meehl et al., 2016a) and tropical Atlantic (Li et al., 2014, 2015a,b; Simpkins et al., 2014). The strengthened Amundsen Sea Low has been linked to the reduced sea ice in the Amundsen and Bellingshausen Seas and the increased sea ice in the Ross Sea (Li et al., 2014; Simpkins et al., 2014; Kwok et al., 2016). However, the CMIP5 multi-model mean does not simulate a strengthening of the Amundsen Sea Low (or the dipole pattern of sea ice trends in Pacific sector), suggesting that decadal variability might be playing a role in the observed strengthening of the Amundsen Sea Low (Li et al., 2014, 2015a,b; Simpkins et al., 2014; Meehl et al., 2016a).

To better understand the contribution of decadal variability to the strengthened Amundsen Sea Low and corresponding regional sea ice trends, Part 2 utilised coupled pacemaker experiments constrained by tropical Pacific variability. In doing so, I provide further evidence in support of internal decadal climate variability associated with the phase change in the Interdecadal Pacific Oscillation (IPO) from positive to negative over 1979–2013, via a strengthened Amundsen Sea Low, as a driving influence on Antarctic sea ice trends in the eastern Ross, Amundsen, and Bellingshausen Seas.

Identifying the teleconnection from the tropical Pacific to the Amundsen Sea Low as one of the mechanisms driving the regional sea ice trends and contributing to the overall increase in sea ice (by contributing to the increase in the Ross Sea) also helps explain the discrepancy between the observed and CMIP5 multi-model mean sea ice trends. While IPO-related sea ice trends for observations and the pacemaker experiments are presented in Part 2 (Fig. 2.7), essentially no IPO-congruent trends are seen for the CMIP5 multi-model mean (Fig. 2.16), because the unconstrained model simulations all have different phases of the IPO that cancel out in the multi-model mean. This also indicates that the historical forcings in the CMIP5 experiments are not causing one phase of the IPO to be favoured.

Importantly, the pacemaker experiments assessed in Part 2 are based on coupled atmosphere-ocean-sea ice models, which differ from previous studies using atmospheric-only models (Li et al., 2014, 2015a,b; Simpkins et al., 2014; Meehl et al., 2016a). While these previous studies suggest that a strengthening of the Amundsen Sea Low due to tropical teleconnections can be linked to observed changes in the sea ice, the sea ice response is not directly simulated. This study was the first such study to utilise coupled climate models and thus to directly simulate sea ice. These findings highlight the importance of accounting for teleconnections from low to high latitudes in both model simulations and

observations of Antarctic sea ice variability and change. Building upon the findings from Part 1 that highlight the balance between the processes controlling surface climate around Antarctica, the findings of Part 2 suggest that because of the various feedbacks between sea ice and the climate system (e.g. Goosse and Zunz, 2014; England et al., 2017), assessing coupled models is important to fully understand how tropical teleconnections influence Antarctic sea ice.

Part 3

Part 3 of this thesis examined the impact of broad-scale surface freshening of the high-latitude Southern Ocean using the Australian Community Climate and Earth System Simulator version 1.0 (ACCESS1.0), a global coupled climate model, with additional freshwater applied to the Southern Ocean to assess the influence of recent observed surface freshening (Durack and Wijffels, 2010; de Lavergne et al., 2014). While recent studies have focussed on additional freshwater applied around the Antarctic margins to simulate increased ice sheet melt/runoff (Bintanja et al., 2013, 2015; Swart and Fyfe, 2013; Pauling et al., 2016, 2017), the impact of broad-scale freshening resulting from a combination of factors, including freshwater redistribution by sea ice and icebergs, increased ice sheet and ice shelf runoff, and precipitation minus evaporation (P–E) changes likely associated with the positive SAM trend had received little attention. As such, the simulations conducted in Part 3 explore the impact of persistent and long-term broad-scale freshening due to processes including P–E changes. Using ACCESS1.0, I find that imposing a large-scale surface freshening trend, as estimated from observations, causes a surface cooling and sea-ice increase under pre-industrial conditions due to a reduction in ocean convection and weakened entrainment of warm sub-surface waters into the surface ocean.

To complement the idealised freshwater experiments, Part 3 also presents results from additional sea surface salinity restoration experiments that capture the observed regional salinity trends. These simulations accurately represent the spatial pattern of observed surface temperature and sea-ice trends around Antarctica via the mechanisms described above. Recently, Lecomte et al. (2017) also identified a positive ice-ocean feedback mechanism, whereby surface trends in the Ross Sea may be sustained via a vertical redistribution of near-surface salt and energy over the seasonal cycle, and an analysis presented by Su (2017) emphasises the importance of upper-ocean stratification, dominated by salinity in the high-latitude Southern Ocean, in controlling sea ice extent. These findings from Part 3 and these recent studies collectively demonstrate that upper-ocean sea surface salinity trends have been an important component in driving regional hydrography and circulation changes around Antarctica over the last half century.

In Part 3 I also showed that the majority of CMIP5 models underestimate the observed surface freshening over the Southern Ocean over the latter half of the twentieth century. Based on the inter-model CMIP5 trend relationships, alongside our freshwater anomaly experiments conducted using ACCESS1.0, this reduced or absent freshening

is likely another contributor to the poor simulation of observed Southern Ocean surface cooling and Antarctic sea ice trends in CMIP5 models, in addition to the mechanisms identified in Parts 1 and 2. The findings from Part 3 highlight the importance of accurately simulating changes in clouds, storm tracks, P–E, ice-sheet and ice-shelf melt, and surface salinity over the Southern Ocean to capture changes in ocean circulation, SST and sea ice.

Recent Antarctic sea ice behaviour

This thesis considers Antarctic sea ice trends over 1979–2013; chosen from when regular satellite observations began in 1979, up until the time this project commenced. Increased Antarctic sea ice extent continued in 2014 and 2015 (e.g. Massonnet et al., 2015; Schlosser et al., 2018). However, in 2016 there was a drastic decline in Antarctic sea ice during austral spring (Figs CR.1, CR.2a), with anomalously low sea ice continuing through into the austral autumn of 2017 (Fig. CR.1; see also Turner et al., 2017; Stuecker et al., 2017). Warm SSTs accompanied the low sea ice extent (Fig. CR.2b; Turner et al., 2017; Stuecker et al., 2017). The recent behaviour of Antarctic sea ice, opposing the increasing trends seen over 1979–2015, has received considerable attention: what caused such an exceptional decline during the spring of 2016? And do these anomalies signal an end to the multi-decadal increasing trend, or are they simply part of the large interannual variations in Antarctic sea ice?

While sea ice retreat can only occur when temperatures are slightly above freezing (Schlosser et al., 2018), certain events may have pre-conditioned the exceptional sea ice retreat of austral spring 2016. Via the teleconnections discussed in Part 2, the extreme El Niño event of 2015/2016 contributed to high-latitude SST and sea ice anomalies in the austral summer of 2015/2016 (similar to the pattern shown in Fig. 2.9a; Stuecker et al., 2017). Usually, a strong La Niña event follows an extreme El Niño event (e.g. Cai et al., 2015), however only a weak La Niña developed in the austral winter-spring of 2016 (Fig. CR.2b), which may have contributed to the persistence of the preceding El Niño-induced high-latitude SST anomalies (Stuecker et al., 2017). A positive zonal-wave three pattern during the austral winter of 2016 also pre-conditioned ice retreat due to considerable heat transport associated with strong meridional flow (Schlosser et al., 2018).

During the austral spring of 2016 a combination of factors coincided to give the record retreat (Fig. CR.1). The melt season started unusually early, with total sea ice area beginning retreat in July and sea ice extent beginning retreat in August (Schlosser et al., 2018). During September a record deep Amundsen Sea Low reduced ice in the Bellingshausen Sea, and led to a rapid retreat in the outer Weddell Sea (while leading to positive sea ice anomalies in the eastern Ross Sea; Turner et al., 2017). During October, anomalous meridional flow continued sea ice retreat (Turner et al., 2017). These springtime circulation anomalies have been linked to convective heating anomalies in the equatorial

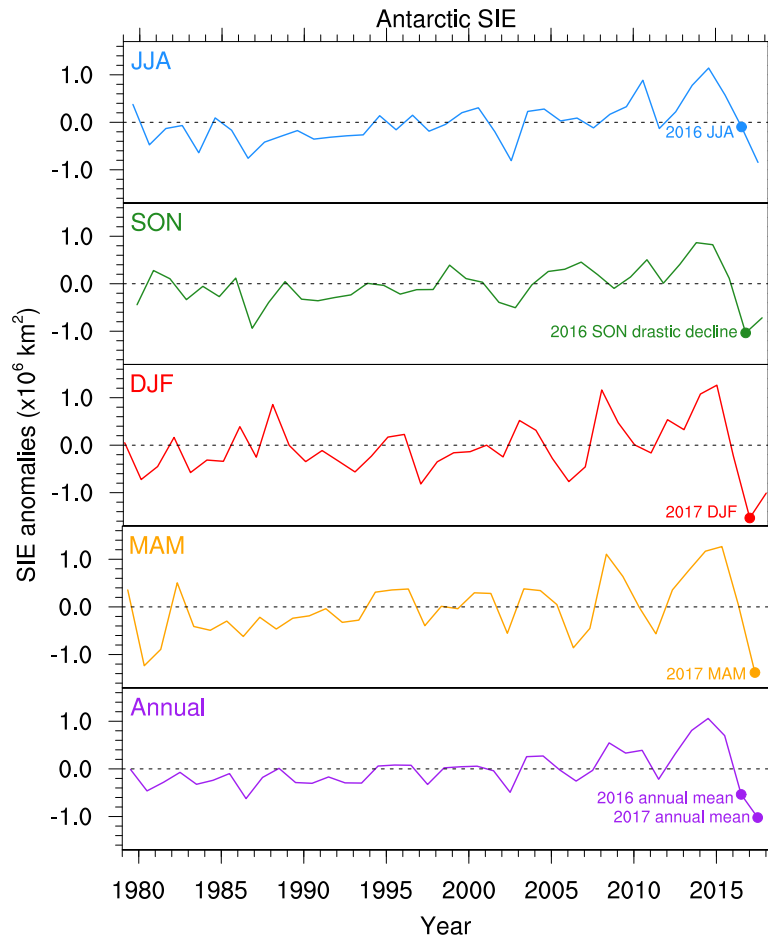


Figure CR.1: Observed seasonal and annual SIE anomaly time series from December 1978 to February 2018. From top to bottom: austral winter (JJA); spring (SON); summer (DJF); autumn (MAM); and annual mean. Markers indicate the drastic decline in 2016 SON, as well as the lead up and follow on from this event. Seasonal and annual SIE anomalies are calculated from the NSIDC SIE index. The year of each DJF corresponds to the year of the January-February.

Indian Ocean and western Pacific (Meehl et al., 2018), with suggestion that the Indian Ocean Dipole (IOD) may have made a strong contribution to the Pacific South American (PSA) teleconnection pattern in this season (Wang et al., 2018). During November there was a record negative SAM, further leading to rapid melt-back, especially in the Ross Sea (Turner et al., 2017; Stuecker et al., 2017). La Niña events are typically associated with the positive phase of the SAM, so the negative SAM (and associated warm SST and reduced sea ice, e.g. Fig. P.2; Hall and Visbeck, 2002) that occurred was unusual (Stuecker et al., 2017). Wang et al. (2018) also identified contributions from the Madden-Julian Oscillation and stratospheric wind anomalies to the negative SAM during this time.

Once the anomalous retreat of sea ice was initiated by the atmospheric circulation anomalies described above, it was reinforced by the strong positive ice-ocean albedo feedback (Turner et al., 2017; Stuecker et al., 2017). The timing of the atmospheric circulation anomalies allowed this positive feedback to be especially effective, as the anomalously ice-

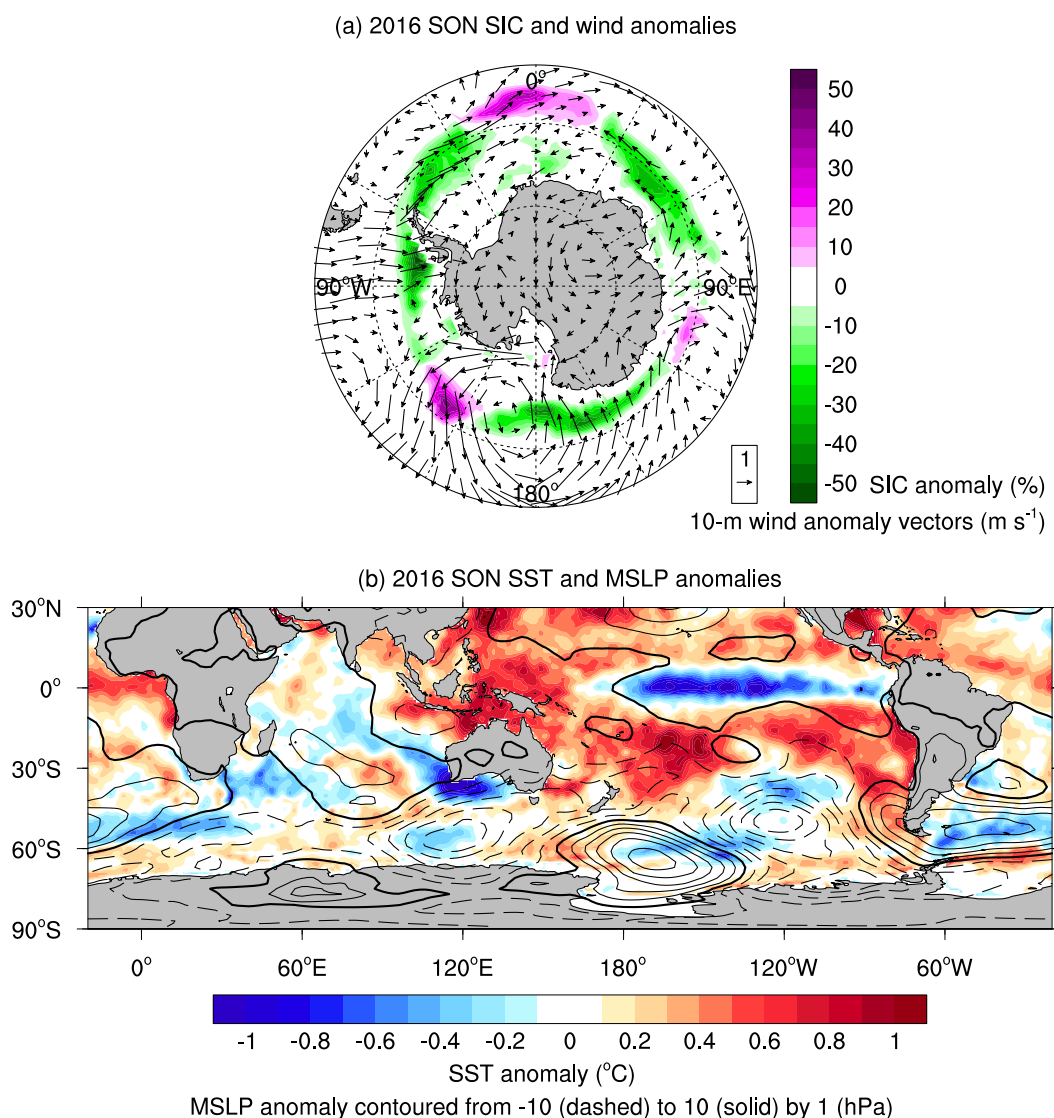


Figure CR.2: Observed anomalies during the austral spring of 2016. (a) SIC anomalies shown in colour with 10-m wind anomalies overlain as vectors; and (b) SST anomalies shown in colour with MSLP anomalies overlain in contours with negative trends shown by dashed contours and the zero contour shown in bold. Fields are seasonally averaged over SON and anomalies are calculated relative to the 1979–2015 climatology. SIC from NSIDC Bootstrap, SST from HadISST, 10-m wind and MSLP from ERA-Interim.

free ocean coincided with maximum incoming shortwave radiation during late spring and summer, allowing the ocean to warm quickly and leading to persistently low sea ice until austral autumn 2017 (Fig. CR.1; Turner et al., 2017; Schlosser et al., 2018).

The rapid departure in 2016 from the behaviour of Antarctic sea ice in the preceding years serves as a reminder that natural variability of Antarctic sea ice is high (Turner et al., 2015a), and suggests that trends calculated over ~ 35 years (e.g. 1979–2013) may not be long enough to represent long-term high-latitude climate change, as discussed in the comparison of trends over 35- and 50-year periods in Part 3 of this thesis (Section 3.3.3). Indeed, it is likely that the trends over 1979–2013 contain a strong inter-decadal

signal due to the phase change of the IPO over this period, as presented in Part 2 of this thesis. This reinforces the findings from a number of studies that have suggested that the observed sea ice increase lies within the range of CMIP5 modelled natural variability (Mahlstein et al., 2013; Polvani and Smith, 2013; Swart and Fyfe, 2013).

While two years of anomalously low sea ice extent (2016 and 2017; Fig. CR.1) do not signal an end to the increasing trend in Antarctic sea ice seen over 1979–2015 (Stuecker et al., 2017), there may still be a contribution from decadal and longer-term changes. The IPO may be transitioning to the positive phase (Meehl et al., 2016b), and if this is the case a reduction in overall Antarctic sea ice extent may be expected in the coming decade, opposite to what was seen over 2000–2013 (e.g. Part 2 of this thesis; Meehl et al., 2016a). Further, the rapid decline in sea ice during spring in 2016 has been linked with the record negative IOD during that time (Wang et al., 2018). Lim and Hendon (2017) implicated long-term warming in contributing to this record IOD event, suggesting an anthropogenic influence on the drastic sea ice changes in 2016 (Wang et al., 2018). On longer timescales, increasing global temperature due to continued anthropogenic greenhouse gas emissions is expected to cause a decrease in Antarctic sea ice (Armour and Bitz, 2015), however, the sea ice decrease and accompanying surface cooling of the Southern Ocean are projected to occur more slowly than global mean warming, due to characteristics of the mean-state ocean circulation (Armour et al., 2016).

Future perspectives

While this thesis identifies and describes physical processes that contributed to the overall increase in Antarctic sea ice coverage over 1979–2013, the considerable departure from the multi-decadal trend that occurred during the spring of 2016 highlights that there is still much to learn about the behaviour of this high-latitude climate system. Opportunities for future research on the drivers of change and variability of Antarctic sea ice, both building upon the topics covered in this thesis and more broadly, are presented below.

Decadal to interdecadal variability

Given the relatively short observational period, continued investigation into the role decadal-to-interdecadal variability plays in influencing Antarctic sea ice is required. Part 2 of this thesis highlights that having only one positive and one negative phase of the IPO over the satellite era makes differentiating between interdecadal variability and long-term trends difficult. Fan et al. (2014) examined a wide range of datasets, including pre-satellite data from uninterpolated gridded marine archives, and found that while decreasing broad-scale SST and strengthening westerly winds were observed over 1979–2011, there was evidence of increasing SST and weakening westerly winds over the earlier period 1950–1978. Their findings suggest that the Southern Ocean is subject to multi-decadal climate variability

(Fan et al., 2014). Future work aimed at disentangling decadal-to-interdecadal variability and long-term trends in this high-latitude region should include both observational and modelling approaches.

Looking at the past, it would be pertinent to utilise longer-term historical observational datasets such as those assessed by Fan et al. (2014) to examine whether there is a relationship with the IPO prior to 1979. The feasibility of using paleo records could also be investigated. Looking into the future, as the observational record is extended in coming years, regional and total sea ice behaviour should be considered in the context of longer-term variability, especially if/when the IPO transitions to positive (Meehl et al., 2016b).

Additional research utilising existing model output from the CMIP5 archive could examine the role of the IPO and other modes of decadal-to-interdecadal variability on Antarctic sea ice in these models. This work could be extended to include the upcoming Coupled Model Intercomparison Project phase 6 (CMIP6) output when it becomes available. While overall natural variability of total Antarctic sea ice in the CMIP5 models has been assessed (Mahlstein et al., 2013; Polvani and Smith, 2013), there has been less focus on specific modes of variability. Meehl et al. (2016a) found that the CMIP5 models that happen, coincidentally, to align with the real world and simulate a negative phase of the IPO during the 2000s also simulate an increase in Antarctic sea ice during this period. Future work could examine the influence of the IPO over longer timescales in the CMIP5 and CMIP6 models, under both pre-industrial and global warming conditions. The regionality of IPO related sea ice anomalies in the CMIP5 and CMIP6 models could also be examined to better understand how well these models simulate the tropical-to-high-latitude relationship. Analysis could also be extended to other modes of longer term variability, such as the Atlantic Multidecadal Oscillation (Li et al., 2014; Simpkins et al., 2014). Such research will help to further our understanding of the longer-term decadal variability of Antarctic sea ice and the Southern Ocean, and to put future changes into context. It will also allow future projections of Antarctic sea ice to be better understood.

El Niño-Southern Oscillation and Indian Ocean Dipole

Compared to the IPO, the scientific community has a better understanding of how interannual to decadal modes of variability, such as El Niño-Southern Oscillation (ENSO), influence Antarctic sea ice – in part due to the higher frequency of these shorter timescale events in the observational record; and thus the greater number of replications of events that can be analysed. Nevertheless, there is still more to learn, as highlighted by the recent anomalous Antarctic sea ice behaviour since 2016. For example, the IOD was linked with the drastic decline in sea ice during the austral spring of 2016 (Wang et al., 2018), yet there has been little focus on the influence of the IOD on Antarctic sea ice prior to this event. The interplay between large-scale modes of variability has received some attention (e.g. ENSO and SAM as presented in Ciasco et al., 2015), yet the austral spring of 2016

again tested our understanding (Stuecker et al., 2017). Further, understanding how the teleconnections from ENSO and the IOD to the high southern latitudes will change under future global warming needs to be considered. Future work focussing on these areas will improve our understanding of remote drivers of Antarctic sea ice, and again, will allow us to place future changes into context.

Southern Annular Mode

The SAM is the dominant mode of variability in the Southern Hemisphere extratropics, and its influence on surface climate has been examined extensively (e.g. Thompson and Solomon, 2002; Hall and Visbeck, 2002; Sen Gupta and England, 2006; Thompson et al., 2011; Jones et al., 2016). Yet, unanswered questions still remain: firstly, in relation to tropical drivers of decadal variability and links with the SAM over the historical period; and secondly, in relation to the influence the SAM will exert on Southern Ocean surface temperatures and Antarctic sea ice in the twenty-first century.

Part 2 of this thesis demonstrated the importance of accounting for tropical teleconnections when considering changes in Antarctic sea ice – but the links between longer term variability such as the IPO with the SAM, which further influences Antarctic sea ice, has received little attention. During austral summer, El Niño events are typically associated with the negative SAM phase, and La Niña events with the positive SAM phase. There has been extensive research attributing the positive trend in the SAM during austral summer to stratospheric ozone depletion and increasing greenhouse gases (Shindell and Schmidt, 2004; Arblaster and Meehl, 2006; Perlwitz et al., 2008; Son et al., 2009, 2010; Polvani et al., 2011). Could the phase change of the IPO, with more El Niño events occurring over 1979–1999 and more La Niña events occurring between 2000–2013 also have contributed to the positive SAM trend during austral summer? Future research aimed at answering this question would be beneficial in understanding drivers of SAM changes and Antarctic sea ice, and may also provide an explanation as to why the majority of CMIP5 models underestimate the westerly-wind changes during summer, as presented in Part 1 of this thesis.

Better understanding of the seasonality of westerly-wind changes over the Southern Ocean is critical for understanding surface changes, due to the seasonally changing stratification of the surface ocean, as also presented in Part 1 of this thesis. Increasing greenhouse gases contribute to a positive SAM trend all year around, and over 1979–2013, stratospheric ozone depletion also contributed to a positive SAM trend during austral summer – leading to the strongest westerly-wind trends occurring in this season. In the twenty-first century, stratospheric ozone recovery will likely contribute to a negative SAM trend during austral summer, so the projected surface wind changes are weakest during austral summer (when ozone and greenhouse gas changes oppose each other) and strongest during austral winter (when only increasing greenhouse gases are acting; Barnes et al., 2014; Wang et al., 2014). The projected SAM changes are also highly dependent on future

emissions scenarios, with stronger positive SAM trends associated with higher greenhouse gas concentrations, and the exact pace of ozone recovery. Future research should aim to understand how the shift in seasonality of the strongest wind trends will affect ocean circulation and sea ice.

The identification of the two-time-scale SST response to high-latitude wind changes in model experiments explains how long-term SAM trends induce an SST response opposite to that associated with interannual variations, as discussed in Part 1. Under a continual positive SAM and enhanced northward Ekman transport, an initial high-latitude SST cooling, caused by equatorward transport of cool water, is followed by an eventual warming (on the order of years to decades), due to the upwelling of warm subsurface water (Marshall et al., 2014; Ferreira et al., 2015). However, there is a large spread in the two-timescale response to SAM anomalies in the CMIP5 models, and not all models transition from a surface cooling to a surface warming (Kostov et al., 2016; Holland et al., 2017). Future research investigating how representative the model experiments that display the two-timescale SST response are of reality will enable a better estimation of when the real-world high-latitude Southern Ocean will transition from surface cooling to surface warming.

Surface freshening

Part 3 of this thesis demonstrated that surface salinity plays a critical role in the Southern Ocean, influencing surface stability, and thus surface temperature and sea ice coverage. More realistic simulations with additional freshwater may also be needed to understand the real world, for example including realistic iceberg and basal melt distributions, and employing higher resolution ocean models that have more realistic bottom water formation. The latter is crucial to better understand the implications Southern Ocean surface freshening and sea ice changes have on global climate through its uptake of heat and carbon and changes to the Meridional Overturning Circulation.

It would also be useful to estimate the contributions of different physical processes including precipitation, evaporation, ice sheet and ice shelf melt, and sea ice changes to the observed salinity changes. While doing so using climate models is a relatively straightforward task, observations of these processes across the high-latitudes are extremely challenging. Under sea-ice measurements, such as those with autonomous vehicles, could provide a better estimate of sea-ice thickness, which when paired with satellite observations, would allow an estimate of the contribution of sea ice processes to surface salinity changes. Future efforts such as Polar Argo floats and elephant seal tracking will also increase oceanographic observations, allowing better understanding of the observed surface and subsurface salinity changes. This would lead to a greater understanding of the overarching drivers of the observed Southern Ocean surface cooling and sea ice increase.

Regionality of sea ice trends

To date, the majority of studies investigating the regionality of Antarctic sea ice trends, in particular the observed sea ice decline in the Amundsen and Bellingshausen Seas and the strong increase in the Ross Sea, have largely attributed these changes to changed atmospheric conditions associated with a strengthened Amundsen Sea Low (see Part 2 and references therein). The role of the ocean in contributing to the regionality of observed trends has received considerably less attention. As discussed in Part 2, while the sea ice increase in the eastern Ross Sea can be linked with the strengthened Amundsen Sea Low, the sea ice increase in the western Ross Sea cannot. Meanwhile, Lecomte et al. (2017) recently identified an important ice-ocean feedback involving the vertical redistribution of salt and heat that may account for the sea ice trends in the Ross Sea sector, suggesting that indeed the ocean is contributing to the regionality of observed trends. Future work aimed at better understanding the role of the ocean in contributing to the sea ice loss in the Amundsen and Bellingshausen Seas is needed. Questions that may guide such work include: is the sea ice decline in this region partially a consequence of deep ocean warming and shoaling of Circumpolar Deep Water? What are the interactions between the deep ocean warming, ice sheet and ice shelf melting and sea ice decrease in this region? And are there remote or downstream effects, for example is the increase in sea ice in the Ross Sea linked to changes occurring over the Amundsen Sea?

Final remark

Understanding Antarctic sea ice and Southern Ocean changes is crucial to understanding global climate. Over recent decades warming has occurred over much of the extent of the Southern Ocean (Roemmich et al., 2015), however high-latitude SST has cooled (Fan et al., 2014; Armour et al., 2016; Jones et al., 2016) and total sea ice coverage has expanded (Comiso et al., 2017). While there is clearly much work still to be done, this thesis has demonstrated that surface westerly-wind trends during austral summer, a strengthened Amundsen Sea Low associated with the phase change of the IPO, and broad-scale surface freshening all made important contributions to Antarctic sea ice and Southern Ocean surface temperature trends over 1979–2013. These findings enable us to better understand Southern Hemisphere high-latitude climate and its far reaching influence.

Bibliography

- Abernathey, R. P., I. Cerovecki, P. R. Holland, E. R. Newsom, M. Mazloff, and L. D. Talley, 2016: Water-mass transformation by sea ice in the upper branch of the Southern Ocean overturning. *Nature Geoscience*, **9**, 596–601, doi:10.1038/ngeo2749.
- Adler, R. F., and Coauthors, 2003: The version-2 Global Precipitation Climatology Project (GPCP) monthly precipitation analysis (1979–present). *Journal of Hydrometeorology*, **4**, 1147–1167, doi:10.1175/1525-7541(2003)004<1147:TVGPCP>2.0.CO;2.
- Aiken, C. M., and M. H. England, 2008: Sensitivity of the present-day climate to freshwater forcing associated with Antarctic sea ice loss. *Journal of Climate*, **21**, 3936–3946, doi:10.1175/2007JCLI1901.1.
- Arblaster, J. M., and G. A. Meehl, 2006: Contributions of external forcings to Southern Annular Mode trends. *Journal of Climate*, **19**, 2896–2905, doi:10.1175/JCLI3774.1.
- Armour, K. C., and C. M. Bitz, 2015: Observed and projected trends in Antarctic sea ice. *U.S. Clivar Variations*, **13**, 12–19.
- Armour, K. C., J. Marshall, J. R. Scott, A. Donohoe, and E. R. Newsom, 2016: Southern Ocean warming delayed by circumpolar upwelling and equatorward transport. *Nature Geoscience*, **9**, 549–554, doi:10.1038/ngeo2731.
- Arora, V., and Coauthors, 2011: Carbon emission limits required to satisfy future representative concentration pathways of greenhouse gases. *Geophysical Research Letters*, **38**, L05 805, doi:10.1029/2010GL046270.
- Ashok, K., S. K. Behera, S. A. Rao, H. Weng, and T. Yamagata, 2007: El Niño Modoki and its possible teleconnection. *Journal of Geophysical Research: Oceans*, **112**, C11 007, doi:10.1029/2006JC003798.
- Balmaseda, M. A., K. Mogensen, and A. T. Weaver, 2013: Evaluation of the ECMWF ocean reanalysis system ORAS4. *Quarterly Journal of the Royal Meteorological Society*, **139**, 1132–1161, doi:10.1002/qj.2063.
- Barnes, E. A., N. W. Barnes, and L. M. Polvani, 2014: Delayed Southern Hemisphere climate change induced by stratospheric ozone recovery, as projected by the CMIP5 models. *Journal of Climate*, **27**, 852–867, doi:10.1175/JCLI-D-13-00246.1.
- Barsugli, J. J., and D. S. Battisti, 1998: The basic effects of atmosphere-ocean thermal coupling on midlatitude variability. *Journal of the Atmospheric Sciences*, **55**, 477–493, doi:10.1175/1520-0469(1998)055<0477:TBEAO>2.0.CO;2.

- Beckmann, A., and H. Goosse, 2002: A parameterization of ice shelf-ocean interaction for climate models. *Ocean Modelling*, **5**, 157–170, doi:10.1016/S1463-5003(02)00019-7.
- Bi, D., and Coauthors, 2013a: ACCESS-OM: the ocean and sea-ice core of the ACCESS coupled model. *Australian Meteorological and Oceanographic Journal*, **63**, 213–232.
- Bi, D., and Coauthors, 2013b: The ACCESS coupled model: description, control climate and evaluation. *Australian Meteorological and Oceanographic Journal*, **63**, 41–64.
- Bintanja, R., G. van Oldenborgh, S. Drijfhout, B. Wouters, and C. Katsman, 2013: Important role for ocean warming and increased ice-shelf melt in Antarctic sea-ice expansion. *Nature Geoscience*, **6**, 376–379, doi:10.1038/ngeo1767.
- Bintanja, R., G. van Oldenborgh, and C. Katsman, 2015: The effect of increased fresh water from Antarctic ice shelves on future trends in Antarctic sea ice. *Annals of Glaciology*, **56**, 120–126, doi:10.3189/2015AoG69A001.
- Bitz, C. M., and L. M. Polvani, 2012: Antarctic climate response to stratospheric ozone depletion in a fine resolution ocean climate model. *Geophysical Research Letters*, **39**, L20 705, doi:10.1029/2012GL053393.
- Böning, C. W., A. Dispert, M. Visbeck, S. R. Rintoul, and F. Schwarzkopf, 2008: The response of the Antarctic Circumpolar Current to recent climate change. *Nature Geoscience*, **1**, 864–869, doi:10.1038/ngeo362.
- Boyer, T. P., S. Levitus, J. Antonov, R. Locarnini, and H. Garcia, 2005: Linear trends in salinity for the World Ocean, 1955–1998. *Geophysical Research Letters*, **32**, L01 604, doi:10.1029/2004GL021791.
- Bracegirdle, T. J., and G. J. Marshall, 2012: The reliability of Antarctic tropospheric pressure and temperature in the latest global reanalyses. *Journal of Climate*, **25**, 7138–7146, doi:10.1175/JCLI-D-11-00685.1.
- Bracegirdle, T. J., E. F. Shuckburgh, J.-B. Sallée, Z. Wang, A. J. Meijers, N. Bruneau, T. Phillips, and L. J. Wilcox, 2013: Assessment of surface winds over the Atlantic, Indian, and Pacific ocean sectors of the Southern Ocean in CMIP5 models: historical bias, forcing response, and state dependence. *Journal of Geophysical Research: Atmospheres*, **118**, 547–562, doi:10.1002/jgrd.50153.
- Bromwich, D., J. Nicolas, and A. Monaghan, 2011: An assessment of precipitation changes over Antarctica and the Southern Ocean since 1989 in contemporary global reanalyses. *Journal of Climate*, **24**, 4189–4209, doi:10.1175/2011JCLI4074.1.
- Cai, W., and T. Cowan, 2007: Trends in Southern Hemisphere circulation in IPCC AR4 models over 1950–99: ozone depletion versus greenhouse forcing. *Journal of Climate*, **20**, 681–693, doi:10.1175/JCLI4028.1.
- Cai, W., and Coauthors, 2015: Increased frequency of extreme La Niña events under greenhouse warming. *Nature Climate Change*, **5**, 132–137, doi:10.1038/nclimate2492.

- Carton, J. A., and B. S. Giese, 2008: A reanalysis of ocean climate using Simple Ocean Data Assimilation (SODA). *Monthly Weather Review*, **136**, 2999–3017, doi:10.1175/2007MWR1978.1.
- Cavalieri, D., and C. Parkinson, 2008: Antarctic sea ice variability and trends, 1979–2006. *Journal of Geophysical Research*, **113**, C07004, doi:10.1029/2007JC004564.
- Chikamoto, Y., A. Timmermann, S. Stevenson, P. DiNezio, and S. Langford, 2015a: Decadal predictability of soil water, vegetation, and wildfire frequency over North America. *Climate Dynamics*, **45**, 2213–2235, doi:10.1007/s00382-015-2469-5.
- Chikamoto, Y., and Coauthors, 2015b: Skilful multi-year predictions of tropical trans-basin climate variability. *Nature Communications*, **6**, 6869, doi:10.1038/ncomms7869.
- Ciasto, L. M., and M. H. England, 2011: Observed ENSO teleconnections to Southern Ocean SST anomalies diagnosed from a surface mixed layer heat budget. *Geophysical Research Letters*, **38**, L09701, doi:10.1029/2011GL046895.
- Ciasto, L. M., G. R. Simpkins, and M. H. England, 2015: Teleconnections between tropical Pacific SST anomalies and extratropical Southern Hemisphere climate. *Journal of Climate*, **28**, 56–65, doi:10.1175/JCLI-D-14-00438.1.
- Ciasto, L. M., and D. W. Thompson, 2008: Observations of large-scale ocean–atmosphere interaction in the Southern Hemisphere. *Journal of Climate*, **21**, 1244–1259, doi:10.1175/2007JCLI1809.1.
- Clem, K. R., and R. L. Fogt, 2015: South Pacific circulation changes and their connection to the tropics and regional Antarctic warming in austral spring, 1979–2012. *Journal of Geophysical Research: Atmospheres*, **120**, 2773–2792, doi:10.1002/2014JD022940.
- Clem, K. R., and J. A. Renwick, 2015: Austral spring Southern Hemisphere circulation and temperature changes and links to the SPCZ. *Journal of Climate*, **28**, 7371–7384, doi:10.1175/JCLI-D-15-0125.1.
- Comiso, J. C., R. A. Gersten, L. V. Stock, J. Turner, G. J. Perez, and K. Cho, 2017: Positive trend in the Antarctic sea ice cover and associated changes in surface temperature. *Journal of Climate*, **30**, 2251–2267, doi:10.1175/JCLI-D-16-0408.1.
- Comiso, J. C., and F. Nishio, 2008: Trends in the sea ice cover using enhanced and compatible AMSR-E, SSM/I, and SMMR data. *Journal of Geophysical Research: Oceans*, **113**, C02S07, doi:10.1029/2007JC004257.
- Davies, T., M. J. P. Cullen, A. J. Malcolm, M. H. Mawson, A. Staniforth, A. A. White, and N. Wood, 2005: A new dynamical core for the Met Office’s global and regional modelling of the atmosphere. *Quarterly Journal of the Royal Meteorological Society*, **131**, 1759–1782, doi:10.1256/qj.04.101.

- de Lavergne, C., J. B. Palter, E. D. Galbraith, R. Bernardello, and I. Marinov, 2014: Cessation of deep convection in the open Southern Ocean under anthropogenic climate change. *Nature Climate Change*, **4**, 278–282, doi:10.1038/nclimate2132.
- Dee, D. P., and Coauthors, 2011: The ERA-Interim reanalysis: configuration and performance of the data assimilation system. *Quarterly Journal of the Royal Meteorological Society*, **137**, 553–597, doi:10.1002/qj.828.
- Ding, Q., and E. J. Steig, 2013: Temperature change on the Antarctic Peninsula linked to the tropical Pacific. *Journal of Climate*, **26**, 7570–7585, doi:10.1175/JCLI-D-12-00729.1.
- Dix, M., and Coauthors, 2013: The ACCESS coupled model: documentation of core CMIP5 simulations and initial results. *Australian Meteorological and Oceanographic Journal*, **63**, 83–99.
- Downes, S. M., and A. M. Hogg, 2013: Southern Ocean circulation and eddy compensation in CMIP5 models. *Journal of Climate*, **26**, 7198–7220, doi:10.1175/JCLI-D-12-00504.1.
- Durack, P., 2015: Ocean salinity and the global water cycle. *Oceanography*, **28**, 20–31, doi:10.5670/oceanog.2015.03.
- Durack, P. J., P. J. Gleckler, F. W. Landerer, and K. E. Taylor, 2014: Quantifying underestimates of long-term upper-ocean warming. *Nature Climate Change*, **4**, 999–1005, doi:10.1038/nclimate2389.
- Durack, P. J., and S. E. Wijffels, 2010: Fifty-year trends in global ocean salinities and their relationship to broad-scale warming. *Journal of Climate*, **23**, 4342–4362, doi:10.1175/2010JCLI3377.1.
- Durack, P. J., S. E. Wijffels, and R. J. Matear, 2012: Ocean salinities reveal strong global water cycle intensification during 1950 to 2000. *Science*, **336**, 455–458, doi:10.1126/science.1212222.
- Eisenman, I., W. Meier, and J. Norris, 2014: A spurious jump in the satellite record: has Antarctic sea ice expansion been overestimated? *The Cryosphere*, **8**, 1289–1296, doi:10.5194/tc-8-1289-2014.
- England, M. H., 1993: Representing the global-scale water masses in ocean general circulation models. *Journal of Physical Oceanography*, **23**, 1523–1552, doi:10.1175/1520-0485(1993)023<1523:RTGSWM>2.0.CO;2.
- England, M. H., D. K. Hutchinson, A. Santoso, and W. P. Sijp, 2017: Ice-atmosphere feedbacks dominate the response of the climate system to Drake Passage closure. *Journal of Climate*, **30**, 5775–5790, doi:10.1175/JCLI-D-15-0554.1.
- Fan, T., C. Deser, and D. P. Schneider, 2014: Recent Antarctic sea ice trends in the context of Southern Ocean surface climate variations since 1950. *Geophysical Research Letters*, **41**, 2419–2426, doi:10.1002/2014GL059239.

- Ferreira, D., J. Marshall, C. M. Bitz, S. Solomon, and A. Plumb, 2015: Antarctic ocean and sea ice response to ozone depletion: a two-time-scale problem. *Journal of Climate*, **28**, 1206–1226, doi:10.1175/JCLI-D-14-00313.1.
- Fetterer, F., K. Knowles, W. Meier, and M. Savoie, 2002: Sea Ice Index. Tech. rep., Boulder, Colorado USA: National Snow and Ice Data Center. Digital media. doi:10.7265/N5QJ7F7W.
- Fogt, R. L., and D. H. Bromwich, 2006: Decadal variability of the ENSO teleconnection to the high-latitude South Pacific governed by coupling with the Southern Annular Mode. *Journal of Climate*, **19**, 979–997, doi:10.1175/JCLI3671.1.
- Foreman, M., B. Pal, and W. Merryfield, 2011: Trends in upwelling and downwelling winds along the British Columbia shelf. *Journal of Geophysical Research*, **116**, C10 023, doi:10.1029/2011JC006995.
- Frederiksen, J. S., and C. S. Frederiksen, 2007: Interdecadal changes in Southern Hemisphere winter storm track modes. *Tellus A*, **59**, 599–617, doi:10.1111/j.1600-0870.2007.00264.x.
- Fyfe, J. C., 2003: Extratropical Southern Hemisphere cyclones: Harbingers of climate change? *Journal of Climate*, **16**, 2802–2805, doi:10.1175/1520-0442(2003)016<2802:ESHCHO>2.0.CO;2.
- Fyfe, J. C., and Coauthors, 2016: Making sense of the early-2000s warming slowdown. *Nature Climate Change*, **6**, 224–228, doi:10.1038/nclimate2938.
- Gagné, M.-E., N. P. Gillett, and J. C. Fyfe, 2015: Observed and simulated changes in Antarctic sea ice extent over the past 50 years. *Geophysical Research Letters*, **42**, 90–95, doi:10.1002/2014GL062231.
- Gille, S., 2002: Warming of the Southern Ocean since the 1950s. *Science*, **295**, 1275–1277, doi:10.1126/science.1065863.
- Gille, S., 2003: Float observations of the Southern Ocean. Part I: estimating mean fields, bottom velocities, and topographic steering. *Journal of Physical Oceanography*, **33**, 1167–1181, doi:10.1175/1520-0485(2003)033<1167:FOOTSO>2.0.CO;2.
- Gille, S. T., 2008: Decadal-scale temperature trends in the Southern Hemisphere ocean. *Journal of Climate*, **21**, 4749–4765, doi:10.1175/2008JCLI2131.1.
- Gillett, N. P., T. Kell, and P. D. Jones, 2006: Regional climate impacts of the Southern Annular Mode. *Geophysical Research Letters*, **33**, L23 704, doi:10.1029/2006GL027721.
- Goosse, H., W. Lefebvre, A. de Montety, E. Cresspin, and A. Orsi, 2009: Consistent past half-century trends in the atmosphere, the sea ice and the ocean at high southern latitudes. *Climate Dynamics*, **33**, 999–1016, doi:10.1007/s00382-008-0500-9.

BIBLIOGRAPHY

- Goosse, H., and V. Zunz, 2014: Decadal trends in the Antarctic sea ice extent ultimately controlled by ice-ocean feedback. *The Cryosphere*, **8**, 453–470, doi:10.5194/tc-8-453-2014.
- Gregory, J. M., 2000: Vertical heat transports in the ocean and their effect on time-dependent climate change. *Climate Dynamics*, **16**, 501–515, doi:10.1007/s003820000059.
- Griffies, S., M. Schmidt, and M. Herzfeld, 2010: Elements of mom4p1. *GFDL Ocean Group Technical Report*, **6**, doi:10.1002/047174882X.
- Grise, K. M., and L. M. Polvani, 2014: Southern Hemisphere cloud-dynamics biases in CMIP5 models and their implications for climate projections. *Journal of Climate*, **27**, 6074–6092, doi:10.1175/JCLI-D-14-00113.1.
- Hall, A., and M. Visbeck, 2002: Synchronous variability in the Southern Hemisphere atmosphere, sea ice, and ocean resulting from the annular mode. *Journal of Climate*, **15**, 3043–3057, doi:10.1175/1520-0442(2002)015<3043:SVITSH>2.0.CO;2.
- Handle, L., S. Siems, and M. Manton, 2012: Observed trends in wind speed over the Southern Ocean. *Geophysical Research Letters*, **39**, L11 802, doi:10.1029/2012GL051734.
- Haumann, F. A., N. Gruber, M. Münnich, I. Frenger, and S. Kern, 2016: Sea-ice transport driving Southern Ocean salinity and its recent trends. *Nature*, **537**, 89–92, doi:10.1038/nature19101.
- Haumann, F. A., D. Notz, and H. Schmidt, 2014: Anthropogenic influence on recent circulation-driven Antarctic sea ice changes. *Geophysical Research Letters*, **41**, 8429–8437, doi:10.1002/2014GL061659.
- Hellmer, H. H., 2004: Impact of Antarctic ice shelf basal melting on sea ice and deep ocean properties. *Geophysical Research Letters*, **31**, L10 307, doi:10.1029/2004GL019506.
- Helm, K. P., N. L. Bindoff, and J. A. Church, 2010: Changes in the global hydrological-cycle inferred from ocean salinity. *Geophysical Research Letters*, **37**, L1870, doi:10.1029/2010GL044222.
- Henley, B. J., J. Gergis, D. J. Karoly, S. B. Power, J. Kennedy, and C. K. Folland, 2015: A tripole index for the Interdecadal Pacific Oscillation. *Climate Dynamics*, **45**, 3077–3090, doi:10.1007/s00382-015-2525-1.
- Heuzé, C., K. J. Heywood, D. P. Stevens, and J. K. Ridley, 2013: Southern Ocean bottom water characteristics in CMIP5 models. *Geophysical Research Letters*, **40**, 1409–1414, doi:10.1002/grl.50287.
- Heuzé, C., K. J. Heywood, D. P. Stevens, and J. K. Ridley, 2015: Changes in Global Ocean bottom properties and volume transports in CMIP5 models under climate change scenarios. *Journal of Climate*, **28**, 2917–2944, doi:10.1175/JCLI-D-14-00381.1.

- Hobbs, W. R., N. L. Bindoff, and M. N. Raphael, 2015: New perspectives on observed and simulated Antarctic sea ice extent trends using optimal fingerprinting techniques. *Journal of Climate*, **28**, 1543–1560, doi:10.1175/JCLI-D-14-00367.1.
- Hobbs, W. R., R. Massom, S. Stammerjohn, P. Reid, G. Williams, and W. Meier, 2016: A review of recent changes in Southern Ocean sea ice, their drivers and forcings. *Global and Planetary Change*, **143**, 228–250, doi:10.1016/j.gloplacha.2016.06.008.
- Holland, M. M., L. Landrum, Y. Kostov, and J. Marshall, 2017: Sensitivity of Antarctic sea ice to the Southern Annular Mode in coupled climate models. *Climate Dynamics*, **49**, 1813–1831, doi:10.1007/s00382-016-3424-9.
- Holland, P. R., 2014: The seasonality of Antarctic sea ice trends. *Geophysical Research Letters*, **41**, 4230–4237, doi:10.1002/2014GL060172.
- Holland, P. R., and R. Kwok, 2012: Wind-driven trends in Antarctic sea-ice drift. *Nature Geoscience*, **5**, 872–875, doi:10.1038/ngeo1627.
- Hoskins, B. J., and D. J. Karoly, 1981: The steady linear response of a spherical atmosphere to thermal and orographic forcing. *Journal of the Atmospheric Sciences*, **38**, 1179–1196, doi:10.1175/1520-0469(1981)038<1179:TSLROA>2.0.CO;2.
- Hosoda, S., T. Suga, N. Shikama, and K. Mizuno, 2009: Global surface layer salinity change detected by Argo and its implication for hydrological cycle intensification. *Journal of Oceanography*, **65**, 579–586, doi:10.1007/s10872-009-0049-1.
- Hu, Y., and Q. Fu, 2007: Observed poleward expansion of the Hadley circulation since 1979. *Atmospheric Chemistry and Physics*, **7**, 5229–5236, doi:10.5194/acp-7-5229-2007.
- Hu, Y., C. Zhou, and J. Liu, 2011: Observational evidence for poleward expansion of the Hadley circulation. *Advances in Atmospheric Sciences*, **28**, 33–44, doi:10.1007/s00376-010-0032-1.
- Hunke, E. C., and W. H. Lipscomb, 2010: CICE: the Los Alamos Sea Ice Model Documentation and Software User’s Manual Version 4.1 LA-CC-06-012. Tech. rep., Los Alamos National Laboratory.
- Irving, D., and I. Simmonds, 2016: A new method for identifying the Pacific-South American pattern and its influence on regional climate variability. *Journal of Climate*, **29**, 6109–6125, doi:10.1175/JCLI-D-15-0843.1.
- Ishii, M., and M. Kimoto, 2009: Reevaluation of historical ocean heat content variations with time-varying XBT and MBT depth bias corrections. *Journal of Oceanography*, **65**, 287–299, doi:10.1007/s10872-009-0027-7.
- Ivanova, D. P., P. J. Gleckler, K. E. Taylor, P. J. Durack, and K. D. Marvel, 2016: Moving beyond the total sea ice extent in gauging model biases. *Journal of Climate*, **29**, 8965–8987, doi:10.1175/JCLI-D-16-0026.1.

BIBLIOGRAPHY

- Jacobs, S., 2006: Observations of change in the Southern Ocean. *Philosophical Transactions of The Royal Society A*, **364**, 1657–1681, doi:10.1098/rsta.2006.1794.
- Jin, D., and B. P. Kirtman, 2009: Why the Southern Hemisphere ENSO responses lead ENSO. *Journal of Geophysical Research Atmospheres*, **114**, D23 101, doi:10.1029/2009JD012657.
- Johnson, G. C., 2008: Quantifying Antarctic Bottom Water and North Atlantic Deep Water volumes. *Journal of Geophysical Research: Oceans*, **113**, C05 027, doi:10.1029/2007JC004477.
- Jones, J. M., and Coauthors, 2016: Assessing recent trends in high-latitude Southern Hemisphere surface climate. *Nature Climate Change*, **6**, 917–926, doi:10.1038/nclimate3103.
- Josey, S. A., S. Gulev, and L. Yu, 2013: *Exchanges through the ocean surface*, **103**, International Geophysics, 115–140, doi:10.1016/B978-0-12-391851-2.00005-2.
- Jourdain, N. C., P. Mathiot, N. Merino, G. Durand, J. Le Sommer, P. Spence, P. Dutrieux, and G. Madec, 2017: Ocean circulation and sea-ice thinning induced by melting ice shelves in the Amundsen Sea. *Journal of Geophysical Research: Oceans*, **122**, 2550–2573, doi:10.1002/2016JC012509.
- Kirkman, C. H., and C. M. Bitz, 2011: The effect of the sea ice freshwater flux on Southern Ocean temperatures in CCSM3: deep-ocean warming and delayed surface warming. *Journal of Climate*, **24**, 2224–2237, doi:10.1175/2010JCLI3625.1.
- Kosaka, Y., and S.-P. Xie, 2013: Recent global-warming hiatus tied to equatorial Pacific surface cooling. *Nature*, **501**, 403–407, doi:10.1038/nature12534.
- Kostov, Y., J. Marshall, U. Hausmann, K. C. Armour, D. Ferreira, and M. M. Holland, 2016: Fast and slow responses of Southern Ocean sea surface temperature to SAM in coupled climate models. *Climate Dynamics*, **48**, 1595–1609, doi:10.1007/s00382-016-3162-z.
- Kwok, R., J. C. Comiso, T. Lee, and P. R. Holland, 2016: Linked trends in the South Pacific sea ice edge and Southern Oscillation Index. *Geophysical Research Letters*, **43**, 10 295–10 302, doi:10.1002/2016GL070655.
- Lago, V., S. E. Wijffels, P. J. Durack, J. A. Church, N. L. Bindoff, and S. J. Marsland, 2016: Simulating the role of surface forcing on observed multidecadal upper-ocean salinity changes. *Journal of Climate*, **29**, 5575–5588, doi:10.1175/JCLI-D-15-0519.1.
- Large, W. G., and S. G. Yeager, 2009: The global climatology of an interannually varying air-sea flux data set. *Climate Dynamics*, **33**, 341–364, doi:10.1007/s00382-008-0441-3.
- Latif, M., T. Martin, and W. Park, 2013: Southern Ocean sector centennial climate variability and recent decadal trends. *Journal of Climate*, **26**, 7767–7782, doi:10.1175/JCLI-D-12-00281.1.

- Law, R., R. Matear, and R. Francey, 2008: Comment on “Saturation of the Southern Ocean CO₂ sink due to recent climate change”. *Science*, **319**, 570a, doi:10.1126/science.1149077.
- Le Quéré, C., and Coauthors, 2007: Saturation of the Southern Ocean CO₂ sink due to recent climate change. *Science*, **316**, 1735–1738, doi:10.1126/science.1136188.
- Lecomte, O., H. Goosse, T. Fichefet, C. de Lavergne, A. Barthélemy, and V. Zunz, 2017: Vertical ocean heat redistribution sustaining sea-ice concentration trends in the Ross Sea. *Nature Communications*, **8**, 258, doi:10.1038/s41467-017-00347-4.
- Lee, T., and M. J. McPhaden, 2008: Decadal phase change in large-scale sea level and winds in the Indo-Pacific region at the end of the 20th century. *Geophysical Research Letters*, **35**, L01 605, doi:10.1029/2007GL032419.
- Lefebvre, W., and H. Goosse, 2008: An analysis of the atmospheric processes driving the large-scale winter sea ice variability in the Southern Ocean. *Journal of Geophysical Research: Oceans*, **113**, C02 004, doi:10.1029/2006JC004032.
- L’Heureux, M. L., and D. W. Thompson, 2006: Observed relationships between the El-Niño-Southern Oscillation and the extratropical zonal-mean circulation. *Journal of Climate*, **19**, 276–287, doi:10.1175/JCLI3617.1.
- Li, X., E. P. Gerber, D. M. Holland, and C. Yoo, 2015a: A Rossby wave bridge from the tropical Atlantic to West Antarctica. *Journal of Climate*, **28**, 2256–2273, doi:10.1175/JCLI-D-14-00450.1.
- Li, X., D. M. Holland, E. P. Gerber, and C. Yoo, 2014: Impacts of the north and tropical Atlantic Ocean on the Antarctic Peninsula and sea ice. *Nature*, **505**, 538–42, doi:10.1038/nature12945.
- Li, X., D. M. Holland, E. P. Gerber, and C. Yoo, 2015b: Rossby waves mediate impacts of tropical oceans on West Antarctic atmospheric circulation in austral winter. *Journal of Climate*, **28**, 8151–8164, doi:10.1175/JCLI-D-15-0113.1.
- Lim, E.-P., and H. H. Hendon, 2017: Causes and predictability of the negative Indian Ocean Dipole and its impact on La Niña during 2016. *Scientific Reports*, **7**, 12 619, doi:10.1038/s41598-017-12674-z.
- Liu, J., and J. A. Curry, 2010: Accelerated warming of the Southern Ocean and its impacts on the hydrological cycle and sea ice. *Proceedings of the National Academy of Sciences*, **107**, 14 987–14 992, doi:10.1073/pnas.1003336107.
- Liu, J., J. A. Curry, and D. G. Martinson, 2004: Interpretation of recent Antarctic sea ice variability. *Geophysical Research Letters*, **31**, L02 205, doi:10.1029/2003GL018732.
- Mahlstein, I., P. R. Gent, and S. Solomon, 2013: Historical Antarctic mean sea ice area, sea ice trends, and winds in CMIP5 simulations. *Journal of Geophysical Research: Atmospheres*, **118**, 5105–5110, doi:10.1002/jgrd.50443.

BIBLIOGRAPHY

- Marshall, G. J., 2003: Trends in the Southern Annular Mode from observations and reanalyses. *Journal of Climate*, **16**, 4134–4143, doi:10.1175/1520-0442(2003)016<4134:TITSAM>2.0.CO;2.
- Marshall, J., K. C. Armour, J. R. Scott, Y. Kostov, U. Hausmann, D. Ferreira, T. G. Shepherd, and C. M. Bitz, 2014: The ocean’s role in polar climate change: asymmetric Arctic and Antarctic responses to greenhouse gas and ozone forcing. *Philosophical Transactions of The Royal Society A*, **372**, 20130 040, doi:10.1098/rsta.2013.0040.
- Marshall, J., and K. Speer, 2012: Closure of the meridional overturning circulation through Southern Ocean upwelling. *Nature Geoscience*, **5**, 171–180, doi:10.1038/ngeo1391.
- Marsland, S. J., and J.-O. Wolff, 2001: On the sensitivity of Southern Ocean sea ice to the surface freshwater flux: a model study. *Journal of Geophysical Research*, **106**, 2723–2741, doi:10.1029/2000JC900086.
- Martin, G. M., S. F. Milton, C. A. Senior, M. E. Brooks, S. Ineson, T. Reichler, and J. Kim, 2010: Analysis and reduction of systematic errors through a seamless approach to modeling weather and climate. *Journal of Climate*, **23**, 5933–5957, doi:10.1175/2010JCLI3541.1.
- Martin, G. M., and Coauthors, 2011: The HadGEM2 family of Met Office Unified Model climate configurations. *Geoscientific Model Development*, **4**, 723–757, doi:10.5194/gmd-4-723-2011.
- Martinson, D. G., 1990: Evolution of the Southern Ocean winter mixed layer and sea ice: open ocean deepwater formation and ventilation. *Journal of Geophysical Research Oceans*, **95**, 11 641–11 654, doi:10.1029/JC095iC07p11641.
- Massonnet, F., V. Guemas, N. S. Fućkar, and F. J. Doblas-Reyes, 2015: The 2014 high record of Antarctic sea ice extent [in “Explaining extremes of 2014 from a climate perspective”]. *Bulletin of the American Meteorological Society*, **96**, S163–S167, doi:10.1175/BAMS-D-15-00093.1.
- Matear, R. J., T. J. O’Kane, J. S. Risbey, and M. Chamberlain, 2015: Sources of heterogeneous variability and trends in Antarctic sea-ice. *Nature Communications*, **6**, 8656, doi:10.1038/ncomms9656.
- McPhaden, M. J., T. Lee, and D. McClurg, 2011: El Niño and its relationship to changing background conditions in the tropical Pacific Ocean. *Geophysical Research Letters*, **38**, L15 709, doi:10.1029/2011GL048275.
- Meehl, G., 1984: Modeling the Earth’s Climate. *Climatic Change*, **6**, 259–286, doi:10.1007/BF00142476.
- Meehl, G. A., J. M. Arblaster, C. Bitz, C. C. Chung, and H. Teng, 2018: Antarctic sea-ice expansion between 2000 and 2014 driven by tropical Pacific decadal climate variability. Presented at AMOS-ICSHMO, Sydney, 7 February 2018.

- Meehl, G. A., J. M. Arblaster, C. M. Bitz, C. T. Chung, and H. Teng, 2016a: Antarctic sea-ice expansion between 2000 and 2014 driven by tropical Pacific decadal climate variability. *Nature Geoscience*, **9**, 590–595, doi:10.1038/ngeo2751.
- Meehl, G. A., A. Hu, and H. Teng, 2016b: Initialized decadal prediction for transition to positive phase of the Interdecadal Pacific Oscillation. *Nature Communications*, **7**, 11 718, doi:10.1038/ncomms11718.
- Meehl, G. A., H. Teng, and J. M. Arblaster, 2014: Climate model simulations of the observed early-2000s hiatus of global warming. *Nature Climate Change*, **4**, 898–902, doi:10.1038/nclimate2357.
- Meier, W., F. Fetterer, M. Savoie, S. Mallory, R. Duerr, and J. Stroeve, 2013, updated 2016: NOAA/NSIDC climate data record of passive microwave sea ice concentration, version 2. Boulder, CO, digital media. doi:10.7265/N55M63M1.
- Meijers, A. J., E. F. Shuckburgh, N. Bruneau, J.-B. Sallée, T. J. Bracegirdle, and Z. Wang, 2012: Representation of the Antarctic Circumpolar Current in the CMIP5 climate models and future changes under warming scenarios. *Journal of Geophysical Research*, **117**, C12 008, doi:10.1029/2012JC008412.
- Meredith, M. P., A. C. Naveira Garabato, A. M. Hogg, and R. Farneti, 2012: Sensitivity of the overturning circulation in the Southern Ocean to decadal changes in wind forcing. *Journal of Climate*, **25**, 99–110, doi:10.1175/2011JCLI4204.1.
- Mo, K. C., 2000: Relationships between low-frequency variability in the Southern Hemisphere and sea surface temperature anomalies. *Journal of Climate*, **13**, 3599–3610, doi:10.1175/1520-0442(2000)013<3599:RBLFVI>2.0.CO;2.
- Mo, K. C., and R. W. Higgins, 1998: The Pacific–South American modes and tropical convection during the Southern Hemisphere winter. *Monthly Weather Review*, **126**, 1581–1596, doi:10.1175/1520-0493(1998)126<1581:TPSAMA>2.0.CO;2.
- Morrison, A. K., M. H. England, and A. M. Hogg, 2015: Response of Southern Ocean convection and abyssal overturning to surface buoyancy perturbations. *Journal of Climate*, **28**, 4263–4278, doi:10.1175/JCLI-D-14-00110.1.
- Morrison, A. K., and A. M. Hogg, 2013: On the relationship between Southern Ocean overturning and ACC transport. *Journal of Physical Oceanography*, **43**, 140–148, doi:10.1175/JPO-D-12-057.1.
- Naughten, K. A., K. J. Meissner, B. K. Galton-Fenzi, M. H. England, R. Timmermann, and H. H. Hellmer, 2018: Future projections of Antarctic ice shelf melting based on CMIP5 scenarios. *Journal of Climate*, **31**, 5243–5261, doi:10.1175/JCLI-D-17-0854.1.
- Newman, M., and Coauthors, 2016: The Pacific Decadal Oscillation, revisited. *Journal of Climate*, **29**, 4399–4427, doi:10.1175/JCLI-D-15-0508.1.

BIBLIOGRAPHY

- Newsom, E. R., C. M. Bitz, F. O. Bryan, R. Abernathey, and P. R. Gent, 2016: Southern Ocean deep circulation and heat uptake in a high-resolution climate model. *Journal of Climate*, **29**, 2597–2619, doi:10.1175/JCLI-D-15-0513.1.
- North, G. R., T. L. Bell, and R. F. Cahalan, 1982: Sampling errors in the estimation of Empirical Orthogonal Functions. *Monthly Weather Review*, **110**, 699–706, doi:10.1175/1520-0493(1982)110<0699:SEITEO>2.0.CO;2.
- Parkinson, C., and D. Cavalieri, 2012: Antarctic sea ice variability and trends, 1979–2010. *The Cryosphere*, **6**, 871–880, doi:10.5194/tc-6-871-2012.
- Pauling, A. G., C. M. Bitz, I. J. Smith, and P. J. Langhorne, 2016: The response of the Southern Ocean and Antarctic sea ice to fresh water from ice shelves in an earth system model. *Journal of Climate*, **29**, 1655–1672, doi:10.1175/JCLI-D-15-0501.1.
- Pauling, A. G., I. J. Smith, P. J. Langhorne, and C. M. Bitz, 2017: Time-dependent freshwater input from ice shelves: impacts on Antarctic sea ice and the Southern Ocean in an earth system model. *Geophysical Research Letters*, **44**, 10 454–10 461, doi:10.1002/2017GL075017.
- Perlwitz, J., S. Pawson, R. Fogt, J. Nielson, and W. Neff, 2008: Impact of stratospheric ozone hole recovery on Antarctic climate. *Geophysical Research Letters*, **35**, L08 714, doi:10.1029/2008GL033317.
- Polvani, L. M., and K. L. Smith, 2013: Can natural variability explain observed Antarctic sea ice trends? New modeling evidence from CMIP5. *Geophysical Research Letters*, **40**, 3195–3199, doi:10.1002/grl.50578.
- Polvani, L. M., D. W. Waugh, G. J. Correa, and S.-W. Son, 2011: Stratospheric ozone depletion: the main driver of twentieth-century atmospheric circulation changes in the Southern Hemisphere. *Journal of Climate*, **24**, 795–812, doi:10.1175/2010JCLI3772.1.
- Purich, A., W. Cai, M. H. England, and T. Cowan, 2016a: Evidence for link between modelled trends in Antarctic sea ice and underestimated westerly wind changes. *Nature Communications*, **7**, 10 409, doi:10.1038/ncomms10409.
- Purich, A., T. Cowan, S.-K. Min, and W. Cai, 2013: Autumn precipitation trends over Southern Hemisphere midlatitudes as simulated by CMIP5 models. *Journal of Climate*, **26**, 8341–8356, doi:10.1175/JCLI-D-13-00007.1.
- Purich, A., M. H. England, W. Cai, and Y. Chikamoto, 2016b: Tropical Pacific SST drivers of recent Antarctic sea ice trends. *Journal of Climate*, **29**, 8931–8948, doi:10.1175/JCLI-D-16-0440.1.
- Purich, A., and S.-W. Son, 2012: Impact of Antarctic ozone depletion and recovery on Southern Hemisphere precipitation, evaporation, and extreme changes. *Journal of Climate*, **25**, 3145–3154, doi:10.1175/JCLI-D-11-00383.1.

- Raphael, M. N., and Coauthors, 2016: The Amundsen Sea Low: variability, change, and impact on Antarctic climate. *Bulletin of the American Meteorological Society*, **97**, 111–121, doi:10.1175/BAMS-D-14-00018.1.
- Rayner, N., D. Parker, E. Horton, C. Folland, L. Alexander, D. Rowell, E. Kent, and A. Kaplan, 2003: Global analyses of sea surface temperature, sea ice, and night marine air temperature since the late nineteenth century. *Journal of Geophysical Research*, **108**, 4407, doi:10.1029/2002JD002670.
- Renwick, J. A., 2002: Southern Hemisphere circulation and relations with sea ice and sea surface temperature. *Journal of Climate*, **15**, 3058–3068, doi:10.1175/1520-0442(2002)015<3058:SHCARW>2.0.CO;2.
- Roemmich, D., J. Church, J. Gilson, D. Monselesan, P. Sutton, and S. Wijffels, 2015: Unabated planetary warming and its ocean structure since 2006. *Nature Climate Change*, **5**, 240–245, doi:10.1038/nclimate2513.
- Saenko, O. A., J. C. Fyfe, N. C. Swart, W. G. Lee, and M. H. England, 2016: Influence of tropical wind on global temperature from months to decades. *Climate Dynamics*, **47**, 2193–2203, doi:10.1007/s00382-015-2958-6.
- Sallée, J.-B., E. F. Shuckburgh, N. Bruneau, A. J. Meijers, T. J. Bracegirdle, and Z. Wang, 2013a: Assessment of Southern Ocean mixed-layer depths in CMIP5 models: historical bias and forcing response. *Journal of Geophysical Research: Oceans*, **118**, 1845–1862, doi:10.1002/jgrc.20157.
- Sallée, J.-B., E. F. Shuckburgh, N. Bruneau, A. J. Meijers, T. J. Bracegirdle, Z. Wang, and T. Roy, 2013b: Assessment of Southern Ocean water mass circulation and characteristics in CMIP5 models: historical bias and forcing response. *Journal of Geophysical Research: Oceans*, **118**, 1830–1844, doi:10.1002/jgrc.20135.
- Schlosser, E., F. A. Haumann, and M. N. Raphael, 2018: Atmospheric influences on the anomalous 2016 Antarctic sea ice decay. *The Cryosphere*, **12**, 1103–1119, doi:10.5194/tc-12-1103-2018.
- Schmidtko, S., K. J. Heywood, A. F. Thompson, and S. Aoki, 2014: Multidecadal warming of Antarctic waters. *Science*, **346**, 1227–1231, doi:10.1126/science.1256117.
- Schneider, D. P., C. Deser, and Y. M. Okumura, 2012: An assessment and interpretation of the observed warming of West Antarctica in the austral spring. *Climate Dynamics*, **38**, 323–347, doi:10.1007/s00382-010-0985-x.
- Sen Gupta, A., and M. H. England, 2006: Coupled ocean-atmosphere-ice response to variations in the Southern Annular Mode. *Journal of Climate*, **19**, 4457–4486, doi:10.1175/JCLI3843.1.
- Sen Gupta, A., N. C. Jourdain, J. N. Brown, and D. P. Monselesan, 2013: Climate drift in the CMIP5 models. *Journal of Climate*, **26**, 8597–8615, doi:10.1175/JCLI-D-12-00521.1.

BIBLIOGRAPHY

- Sen Gupta, A., A. Santoso, A. S. Taschetto, C. C. Ummenhofer, J. Trevena, and M. H. England, 2009: Projected changes to the Southern Hemisphere ocean and sea ice in the IPCC AR4 climate models. *Journal of Climate*, **22**, 3047–3078, doi:10.1175/2008JCLI2827.1.
- Shields, C. A., D. A. Bailey, G. Danabasoglu, M. Jochum, J. T. Kiehl, S. Levis, and S. Park, 2012: The low-resolution CCSM4. *Journal of Climate*, **25**, 3993–4014, doi:10.1175/JCLI-D-11-00260.1.
- Shindell, D., and G. Schmidt, 2004: Southern Hemisphere climate responses to ozone changes and greenhouse gas increases. *Geophysical Research Letters*, **31**, L18 209, doi:10.1029/2004GL020724.
- Shu, Q., Z. Song, and F. Qiao, 2015: Assessment of sea ice simulations in the CMIP5 models. *The Cryosphere*, **9**, 399–409, doi:10.5194/tc-9-399-2015.
- Sigmond, M., and J. C. Fyfe, 2010: Has the ozone hole contributed to increased Antarctic sea ice extent? *Geophysical Research Letters*, **37**, L18 502, doi:10.1029/2010GL044301.
- Sigmond, M., and J. C. Fyfe, 2016: Tropical Pacific impacts on cooling North American winters. *Nature Climate Change*, **6**, 970–974, doi:10.1038/NCLIMATE3069.
- Simmonds, I., 2015: Comparing and contrasting the behaviour of Arctic and Antarctic sea ice over the 35 year period 1979–2013. *Annals of Glaciology*, **56**, 18–28, doi:10.3189/2015AoG69A909.
- Simpkins, G. R., L. M. Ciasto, and M. H. England, 2013: Observed variations in multi-decadal Antarctic sea ice trends during 1979–2012. *Geophysical Research Letters*, **40**, 3643–3648, doi:10.1002/grl.50715.
- Simpkins, G. R., L. M. Ciasto, D. W. Thompson, and M. H. England, 2012: Seasonal relationships between large-scale climate variability and Antarctic sea ice concentration. *Journal of Climate*, **25**, 5451–5469, doi:10.1175/JCLI-D-11-00367.1.
- Simpkins, G. R., S. McGregor, A. S. Taschetto, L. M. Ciasto, and M. H. England, 2014: Tropical connections to climatic change in the extratropical Southern Hemisphere: the role of Atlantic SST trends. *Journal of Climate*, **27**, 4923–4936, doi:10.1175/JCLI-D-13-00615.1.
- Skliris, N., R. Marsh, S. A. Josey, S. A. Good, C. Liu, and R. P. Allan, 2014: Salinity changes in the world ocean since 1950 in relation to changing surface freshwater fluxes. *Climate Dynamics*, **43**, 709–736, doi:10.1007/s00382-014-2131-7.
- Smith, K. L., L. M. Polvani, and D. R. Marsh, 2012: Mitigation of 21st century Antarctic sea ice loss by stratospheric ozone recovery. *Geophysical Research Letters*, **39**, L20 701, doi:10.1029/2012GL053325.

- Son, S.-W., N. F. Tandon, L. M. Polvani, and D. W. Waugh, 2009: Ozone hole and Southern Hemisphere climate change. *Geophysical Research Letters*, **36**, L15 705, doi:10.1029/2009GL038671.
- Son, S.-W., and Coauthors, 2010: Impact of stratospheric ozone on Southern Hemisphere circulation change: a multimodel assessment. *Journal of Geophysical Research: Atmospheres*, **115**, D00M07, doi:10.1029/2010JD014271.
- Stammerjohn, S., D. G. Martinson, R. Smith, X. Yuan, and D. Rind, 2008: Trends in Antarctic annual sea ice retreat and advance and their relation to El Niño-Southern Oscillation and Southern Annular Mode variability. *Journal of Geophysical Research*, **113**, C03S90, doi:10.1029/2007JC004269.
- Stammerjohn, S., R. A. Massom, D. Rind, and D. G. Martinson, 2012: Regions of rapid sea ice change: An inter-hemispheric seasonal comparison. *Geophysical Research Letters*, **39**, L06 501, doi:10.1029/2012GL050874.
- Stuecker, M. F., C. M. Bitz, and K. C. Armour, 2017: Conditions leading to the unprecedented low Antarctic sea ice extent during the 2016 austral spring season. *Geophysical Research Letters*, **44**, 9008–9019, doi:10.1002/2017GL074691.
- Su, Z., 2017: Preconditioning of Antarctic maximum sea ice extent by upper ocean stratification on a seasonal timescale. *Geophysical Research Letters*, **44**, 6307–6315, doi:10.1002/2017GL073236.
- Swart, N., and J. Fyfe, 2012: Observed and simulated changes in the Southern Hemisphere surface westerly wind-stress. *Geophysical Research Letters*, **39**, L16 711, doi:10.1029/2012GL052810.
- Swart, N., J. Fyfe, N. Gillett, and G. Marshall, 2015: Comparing trends in the Southern Annular Mode and surface westerly jet. *Journal of Climate*, **28**, 8840–8859, doi:10.1175/JCLI-D-15-0334.1.
- Swart, N., and J. C. Fyfe, 2013: The influence of recent Antarctic ice sheet retreat on simulated sea ice area trends. *Geophysical Research Letters*, **40**, 4328–4332, doi:10.1002/grl.50820.
- Taylor, K., R. Stouffer, and G. Meehl, 2012: An overview of CMIP5 and the experiment design. *Bulletin of the American Meteorological Society*, **93**, 485–498, doi:10.1175/BAMS-D-11-00094.1.
- Thompson, D. W., and S. Solomon, 2002: Interpretation of recent Southern Hemisphere climate change. *Science*, **296**, 895–899, doi:10.1126/science.1069270.
- Thompson, D. W., S. Solomon, P. J. Kushner, M. H. England, K. M. Grise, and D. J. Karoly, 2011: Signatures of the Antarctic ozone hole in Southern Hemisphere surface climate change. *Nature Geoscience*, **4**, 741–749, doi:10.1038/ngeo1296.

BIBLIOGRAPHY

- Thompson, D. W., and J. M. Wallace, 2000: Annular modes in the extratropical circulation. Part I: month-to-month variability. *Journal of Climate*, **13**, 1000–1016, doi:10.1175/1520-0442(2000)013<1000:AMITEC>2.0.CO;2.
- Toggweiler, J., and J. Russell, 2008: Ocean circulation in a warming climate. *Nature*, **451**, 286–288, doi:doi:10.1038/nature06590.
- Trenberth, K. E., Y. Zhang, and M. Gehne, 2017: Intermittency in precipitation: duration, frequency, intensity and amounts using hourly data. *Journal of Hydrometeorology*, **18**, 1393–1412, doi:10.1175/JHM-D-16-0263.1.
- Turner, J., 2004: The El Niño-Southern Oscillation and Antarctica. *International Journal of Climatology*, **24**, 1–31, doi:10.1002/joc.965.
- Turner, J., T. J. Bracegirdle, T. Phillips, G. J. Marshall, and J. S. Hosking, 2013a: An initial assessment of Antarctic sea ice extent in the CMIP5 models. *Journal of Climate*, **26**, 1473–1484, doi:10.1175/JCLI-D-12-00068.1.
- Turner, J., J. S. Hosking, T. J. Bracegirdle, G. J. Marshall, and T. Phillips, 2015a: Recent changes in Antarctic Sea Ice. *Philosophical Transactions of The Royal Society A*, **373**, 20140163, doi:10.1098/rsta.2014.0163.
- Turner, J., J. S. Hosking, G. J. Marshall, T. Phillips, and T. J. Bracegirdle, 2015b: Antarctic sea ice increase consistent with intrinsic variability of the Amundsen Sea Low. *Climate Dynamics*, **46**, 2391–2402, doi:10.1007/s00382-015-2708-9.
- Turner, J., T. Phillips, J. S. Hosking, G. J. Marshall, and A. Orr, 2013b: The Amundsen Sea low. *International Journal of Climatology*, **33**, 1818–1829, doi:10.1002/joc.3558.
- Turner, J., T. Phillips, G. J. Marshall, J. S. Hosking, J. O. Pope, T. J. Bracegirdle, and P. Deb, 2017: Unprecedented springtime retreat of Antarctic sea ice in 2016. *Geophysical Research Letters*, **44**, 6868–6875, doi:10.1002/2017GL073656.
- Turner, J., and Coauthors, 2005: Antarctic climate change during the last 50 years. *International Journal of Climatology*, **25**, 279–294, doi:10.1002/joc.1130.
- Turner, J., and Coauthors, 2009: Non-annular atmospheric circulation change induced by stratospheric ozone depletion and its role in the recent increase of Antarctic sea ice extent. *Geophysical Research Letters*, **36**, L08502, doi:10.1029/2009GL037524.
- Turner, J., and Coauthors, 2016: Absence of 21st century warming on Antarctic Peninsula consistent with natural variability. *Nature*, **535**, 411–415, doi:10.1038/nature18645.
- Ummenhofer, C. C., A. Sen Gupta, and M. H. England, 2009: Causes of late twentieth-century trends in New Zealand precipitation. *Journal of Climate*, **22**, 3–19, doi:10.1175/2008JCLI2323.1.
- Valcke, S., 2006: OASIS3 User Guide. *PRISM-Support Initiative Report No 3, CERFACS TR/CMGC/06/73*.

- Vaughan, D., and Coauthors, 2013: Observations: Cryosphere. *IPCC AR5: The Physical Science Basis*, 317–382, doi:10.1017/CBO9781107415324.012.
- Wang, G., W. Cai, and A. Purich, 2014: Trends in Southern Hemisphere wind-driven circulation in CMIP5 models over the 21st century: ozone recovery versus greenhouse forcing. *Journal of Geophysical Research: Oceans*, **119**, 2974–2986, doi:10.1002/2013JC009589.
- Wang, G., H. Hendon, and J. M. Arblaster, 2018: On the role of the tropical Indian Ocean for the sharp decline of Antarctic Sea-Ice in austral spring 2016. Presented at AMOS-ICSHMO, Sydney, 7 February 2018.
- Wilcox, L. J., A. Charlton-Perez, and L. Gray, 2012: Trends in austral jet position in ensembles of high- and low-top CMIP5 models. *Journal of Geophysical Research*, **117**, D13 115, doi:10.1029/2012JD017597.
- Wong, A. P. S., N. L. Bindoff, and J. a. Church, 1999: Large-scale freshening of intermediate waters in the Pacific and Indian oceans. *Nature*, **400**, 440–443, doi:doi:10.1038/22733.
- Xie, P., and P. A. Arkin, 1997: Global precipitation: a 17-year monthly analysis based on gauge observations, satellite estimates, and numerical model outputs. *Bulletin of the American Meteorological Society*, **78**, 2539–2558, doi:10.1175/1520-0477(1997)078<2539:GPAYMA>2.0.CO;2.
- Yang, X.-Y., R. Huang, and D. Wang, 2007: Decadal changes of wind stress over the Southern Ocean associated with Antarctic ozone depletion. *Journal of Climate*, **20**, 3395–3410, doi:10.1175/JCLI4195.1.
- Yu, L., and Coauthors, 2011: Interpretation of recent trends in Antarctic sea ice concentration. *Journal of Applied Remote Sensing*, **5**, 053 557, doi:10.1117/1.3643691.
- Yuan, X., and D. G. Martinson, 2000: Antarctic sea ice extent variability and its global connectivity. *Journal of Climate*, **13**, 1697–1717, doi:10.1175/1520-0442(2000)013<1697:ASIEVA>2.0.CO;2.
- Zheng, F., J. Li, R. T. Clark, and H. C. Nnamchi, 2013: Simulation and projection of the Southern Hemisphere annular mode in CMIP5 models. *Journal of Climate*, **26**, 9860–9879, doi:10.1175/JCLI-D-13-00204.1.
- Zickfeld, K., J. Fyfe, M. Eby, and A. Weaver, 2008: Comment on “Saturation of the Southern Ocean CO₂ sink due to recent climate change”. *Science*, **319**, 570b, doi:10.1126/science.1146886.
- Zunz, V., and H. Goosse, 2015: Influence of freshwater input on the skill of decadal forecast of sea ice in the Southern Ocean. *Cryosphere*, **9**, 541–556, doi:10.5194/tc-9-541-2015.
- Zunz, V., H. Goosse, and F. Massonnet, 2013: How does internal variability influence the ability of CMIP5 models to reproduce the recent trend in Southern Ocean sea ice extent? *The Cryosphere*, **7**, 451–468, doi:10.5194/tc-7-451-2013.

Appendix A

Published article

A copy of the published article that constitutes the material in Part 1 is included hereafter:

Purich, A., W. Cai, M. H. England, and T. Cowan, 2016: Evidence for link between modelled trends in Antarctic sea ice and underestimated westerly wind changes. *Nature Communications*, **7**, 10409, doi:10.1038/ncomms10409.

ARTICLE

Received 21 May 2015 | Accepted 8 Dec 2015 | Published 4 Feb 2016

DOI: 10.1038/ncomms10409

OPEN

Evidence for link between modelled trends in Antarctic sea ice and underestimated westerly wind changes

Ariaan Purich^{1,2,3}, Wenju Cai¹, Matthew H. England^{2,3} & Tim Cowan^{1,4}

Despite global warming, total Antarctic sea ice coverage increased over 1979–2013. However, the majority of Coupled Model Intercomparison Project phase 5 models simulate a decline. Mechanisms causing this discrepancy have so far remained elusive. Here we show that weaker trends in the intensification of the Southern Hemisphere westerly wind jet simulated by the models may contribute to this disparity. During austral summer, a strengthened jet leads to increased upwelling of cooler subsurface water and strengthened equatorward transport, conducive to increased sea ice. As the majority of models underestimate summer jet trends, this cooling process is underestimated compared with observations and is insufficient to offset warming in the models. Through the sea ice-albedo feedback, models produce a high-latitude surface ocean warming and sea ice decline, contrasting the observed net cooling and sea ice increase. A realistic simulation of observed wind changes may be crucial for reproducing the recent observed sea ice increase.

¹CSIRO Oceans and Atmosphere, Aspendale, Victoria 3195, Australia. ²Climate Change Research Centre, University of New South Wales, Sydney, New South Wales 2052, Australia. ³ARC Centre of Excellence for Climate System Science, University of New South Wales, Sydney, New South Wales 2052, Australia. ⁴School of GeoSciences, University of Edinburgh, Edinburgh EH9 3FE, UK. Correspondence and requests for materials should be addressed to A.P. (email: ariaan.purich@csiro.au).

Despite regional melting, total Antarctic sea ice has been expanding over the past 35 years^{1–3}. Such changes have an impact on surface albedo and deep water formation, and thus are important to global climate. Spatial analysis of sea ice concentration (SIC) trends reveals opposing regional changes since satellite observations began in 1979; decreasing sea ice in the Amundsen and Bellingshausen Seas is outweighed by increasing sea ice in the Ross Sea and around eastern Antarctica, leading to an overall increase^{4–6} (Fig. 1a). Although the circumpolar ice increase is statistically significant, it may still be within the range of natural variability^{6–11}. However, as the most recent years of the sea ice record are included, the strength and statistical significance of the trend has increased¹².

The sea ice increase has been attributed to regional-scale wind trends causing both dynamic and thermodynamic changes^{5,10,13–16}. On the other hand, models have linked hemispheric-scale wind changes associated with the positive trend in the Southern Annular Mode¹⁷ (SAM), attributed to increasing greenhouse gases and stratospheric ozone depletion^{18–20}, to Southern Ocean warming and a sea ice decline^{21–23}. This contrasts interannual variations, in

which a positive SAM intensifies the westerly jet and shifts it polewards, resulting in cool sea surface temperature (SST) and increased sea ice extent (SIE) at most longitudes due to enhanced Ekman drift^{24–26}. An exception is along the Antarctic Peninsula, where a positive SAM is associated with reduced sea ice, due to circulation changes associated with the Amundsen Sea low^{4,27}.

Most Coupled Model Intercomparison Project phase 5 (CMIP5) models fail to simulate the observed SIE increase in their historical experiments^{7–9,11,28,29}. The vast majority of models produce a decrease in SIE and simulate considerable bias in mean-state SIE and its seasonal cycle²⁸. The observed increase is suggested to lie within the range of modelled natural variability^{7,8,29}, although modelled Antarctic sea ice variability tends to be overestimated^{9,28}; in addition, when the spatial pattern of sea ice trends are considered, the observed changes are distinguishable from the modelled pattern during austral summer and autumn³⁰. To date, few studies have proposed physical mechanisms that may be responsible for the difference between observed and simulated Antarctic sea ice trends^{29,31,32}.

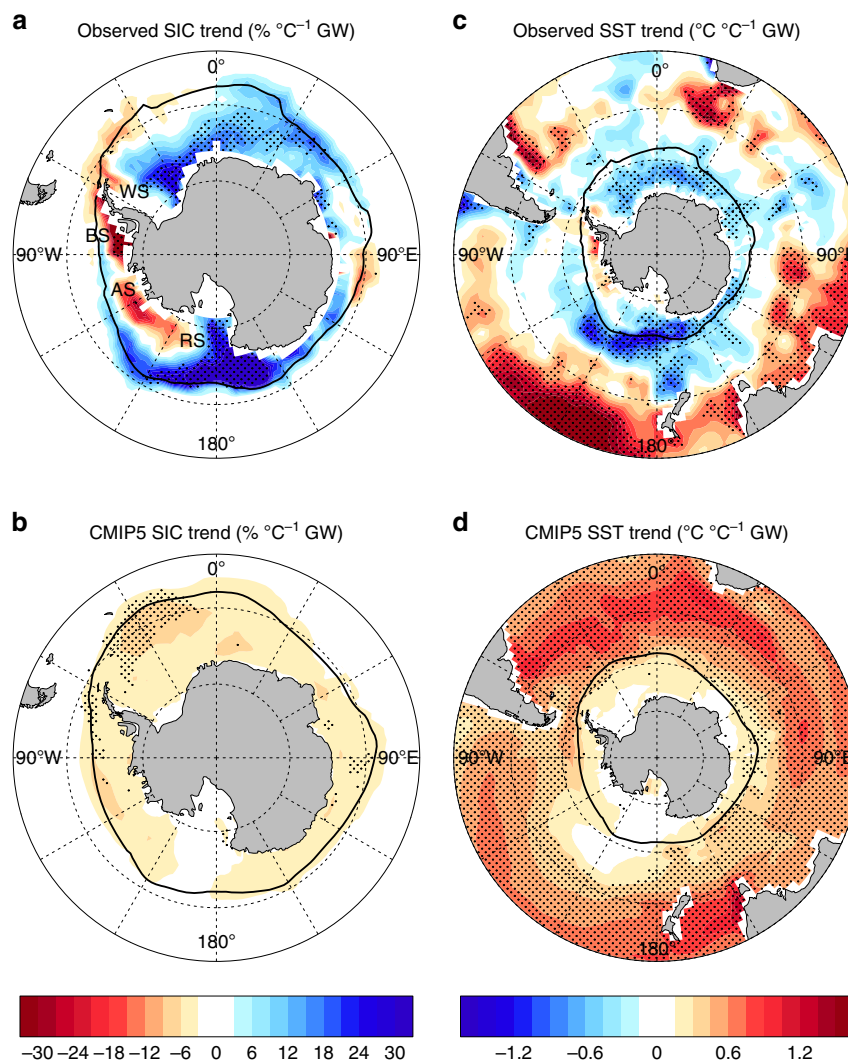


Figure 1 | Annual SIC and SST trends over 1979–2013. (a) Observed SIC from the National Snow and Ice Data Center (NSIDC) Bootstrap algorithm, (b) CMIP5 multi-model mean SIC, (c) observed SST from Hadley Centre Sea Ice and Sea Surface Temperature (HadISST) and (d) CMIP5 multi-model mean SST. Trends are expressed as a change per degree of global warming (°C⁻¹ GW). Multi-model means are calculated using the first available ensemble member for each model. Stippling indicates significance: (a,c) above the 95% level as determined by a two-sided Student's *t*-test and (b,d) where 80% of models agree on the sign of the mean trend³³, which corresponds to 33 out of 41 models. The mean-state 15% SIC contour is shown in black. In (a) AS, Amundsen Sea; BS, Bellingshausen Sea; RS, Ross Sea; WS, Weddell Sea.

This study compares physical mechanisms affecting Antarctic sea ice in the CMIP5 models and observations, with the aim of explaining the difference between the observed increase and the modelled decline. We analyse monthly mean observations and output from 41 CMIP5 models with 87 realizations, over 1979–2013, the period for which regular satellite observations are available. Observed and modelled trends are assessed, and inter-model relationships used to gain insight into why models overall generate too great a sea ice loss and what the important processes behind this are. As the CMIP5 models underestimate recent changes in the SAM and the westerly wind jet intensification^{7,33–35}, we investigate the influence of jet trends on Antarctic sea ice and Southern Ocean SST. We find that underestimated changes in wind-induced ocean circulation in the models may contribute, in part, to their large Antarctic sea ice decline.

Results

Sea ice and SST trends. In contrast to the observed (Fig. 1a), multi-model mean SIC trends (Fig. 1b) show a decrease in all sea ice regions. The majority of models show an overall decrease in sea ice, despite inter-model variations in simulated spatial patterns, with many models showing small regions of increasing SIC (Supplementary Fig. 1). The multi-model mean regional decrease lacks broad coherence, except in the Bellingshausen and northern Weddell Seas, and in isolated pockets of eastern Antarctica and the Ross Sea. Coincident with the observed increase in

Antarctic sea ice, high-latitude SST has also decreased over 1979–2013 (Fig. 1c)^{10,31,36}, with cooling strongest in the Ross Sea. In contrast, the CMIP5 models show Southern Ocean surface warming over most regions (Fig. 1d), although there is no inter-model consensus in terms of warming at high latitudes.

Comparing SIC and SST trend patterns in individual models (Supplementary Figs 1 and 2) reveals that models with stronger SST warming show a larger SIC decrease, as expected⁷. A strong inter-model relationship exists between trends in area-averaged high-latitude (south of 55°S) SST and in circumpolar SIE: models that simulate greater warming produce a greater reduction in ice (Fig. 2). This relationship is highly statistically significant ($P < 0.001$) and is evident in all seasons (shown for summer (December–February (DJF)) and winter (June–August (JJA)); Fig. 2a,b, respectively; all seasons in Supplementary Table 1). The observed trends fit the tail-end of the spread in model trends. When trends are scaled by global mean temperature trends to take into account differences in climate sensitivity between observations and models and between models (Fig. 2), the observed SIE trend lies outside the 95% confidence interval of model trends. This is despite that in absolute terms the observed Antarctic sea ice trend is not statistically distinguishable from the modelled trends at the 95% confidence level. As such, natural internal variability remains a possible contributing factor for the observed trend. However, it is still of interest to investigate mechanisms that lead to the range in observed and modelled SIE trends. The SIE–SST relationship (Fig. 2) suggests that ocean

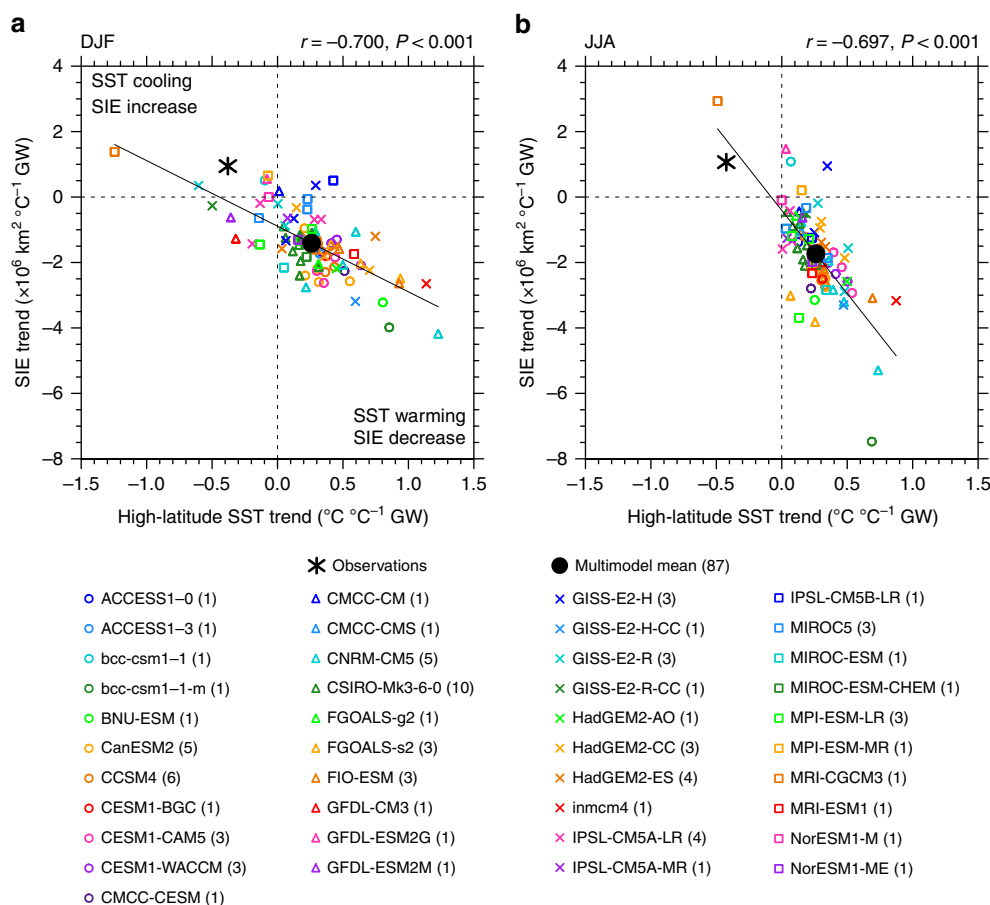


Figure 2 | Trends in SIE versus trends in high-latitude SST over 1979–2013. (a) DJF and (b) JJA. Trends are expressed as a change per degree of global warming. All available model ensemble members are shown (87 realizations). Observed SST from HadISST and SIE from NSIDC. Each model is shown by a marker with the number of runs per model indicated in the legend, the multi-model mean is shown by a black dot and observations are shown by a black asterisk. The inter-model correlation coefficient and P -value are shown above each panel. For $P < 0.05$, the inter-model regression is shown by a black line.

changes may influence sea ice trends. As such, to explain why the majority of CMIP5 models simulate a decrease in Antarctic sea ice in contrast to the observed increase, we must understand why modelled high-latitude SST warms too fast.

Sea ice and SST relationships with the westerly jet. Given the links between the westerly wind jet, sea ice and SST^{21–26}, we next investigate the influence of jet intensification trends. There is a significant inter-model relationship between jet strength trends and SIE trends during summer and autumn ($P < 0.01$; Supplementary Table 1). During these seasons, there is also a strong and significant relationship between high-latitude SST and jet strength ($P < 0.001$; Fig. 3a and Supplementary Table 1). In contrast, during winter there is no inter-model relationship between jet strength trends and SIE trends, although the relationship between jet strength trends and SST trends persists ($P < 0.001$; Fig. 3b). This relationship shows that models with a more intensified jet cool, or warm less, whereas models with a weaker intensification, or weakened jet, warm more. In summer, significant relationships are also found between trends in jet position and high-latitude SST, with a stronger poleward shift in the jet associated with high-latitude SST cooling or weaker warming (Supplementary Table 1).

Processes embedded in the inter-model trend relationships appear to also operate in the inter-model relationship in the mean state: models with stronger mean-state zonal winds south of 55°S tend to have a larger ice area, in particular during autumn⁷. On interannual timescales, an intensified summer and autumn jet is associated with above-average SIE in the observations ($P < 0.05$; Supplementary Table 2 and Supplementary Fig. 3). However, the majority of CMIP5 models do not capture this interannual relationship (median $P > 0.2$), indicating a failure to simulate wind–ice interactions adequately. This may explain the somewhat weak inter-model relationship between trends in jet strength and SIE (Supplementary Table 1).

Within individual CMIP5 models, interannual jet strength is more strongly correlated with high-latitude SST (Supplementary Table 2 and Supplementary Fig. 3). An intensified jet is associated with cooler high-latitude SST^{24,25}. The observed relationship is significant in summer ($P < 0.05$), whereas for the majority of CMIP5 models it is statistically significant in both spring and summer (median $P < 0.05$ and $P < 0.01$, respectively). Thus, relative to observations, variations in the modelled jet have a

weaker influence on variations in sea ice, yet more influence on SST. As such, we focus on jet–SST dynamics, noting the strong relationship between SST and SIE (Fig. 2) that links wind changes back to sea ice.

Mechanism for wind-induced effects on SST. We hypothesize that the jet–SST trend relationship in the CMIP5 models is conducted through a high-latitude Ekman response to changing winds. There, the wind stress forces equatorward Ekman transport and the wind stress curl forces upward Ekman pumping^{36,37} (see Methods). As such, an intensified jet results in strengthened equatorward Ekman transport and usually increased Ekman upwelling at high latitudes.

Ekman upwelling has a strong cooling effect on SST during summer when warm water resides at the surface forming a cap over cool Winter Water at depths ~ 20 – 150 m (Fig. 4a). The warm surface water results from short-wave radiation being received by the summer ice-free surface waters as sea ice melts. Beneath this, the permanent pycnocline with cold, fresh water overlying warm, salty water is apparent. By contrast, during winter surface waters are colder than water below (Fig. 4b), consistent with the typical temperature profile described for the high-latitude Southern Ocean³⁷, caused by seasonal sea ice melt/freeze and advection processes that freshen the surface layer. Because of the seasonal stratification, during summer enhanced Ekman upwelling brings cooler waters to the surface and this surface cooling spreads further north due to enhanced equatorward transport.

Consistently, summer Ekman pumping trends are significantly correlated with SST trends at high latitudes ($P < 0.001$; Fig. 4c): models with a strong increase in Ekman upwelling show SST cooling or weak warming, whereas models with weak trends in Ekman pumping show strong SST warming. Ekman transport trends are also significantly correlated with high-latitude SST trends in summer ($P < 0.001$; Supplementary Fig. 4): models with a strong increase in equatorward Ekman transport show cooling or weak warming. Scale analysis³⁸ has suggested that horizontal Ekman transport should initially dominate over vertical Ekman upwelling, although here we find that south of $\sim 60^\circ\text{S}$, both Ekman transport and Ekman pumping are important (see Methods and Supplementary Fig. 5).

The CMIP5 models underestimate the summer intensification (Fig. 3a) and poleward shift in the jet^{7,34}, and therefore also

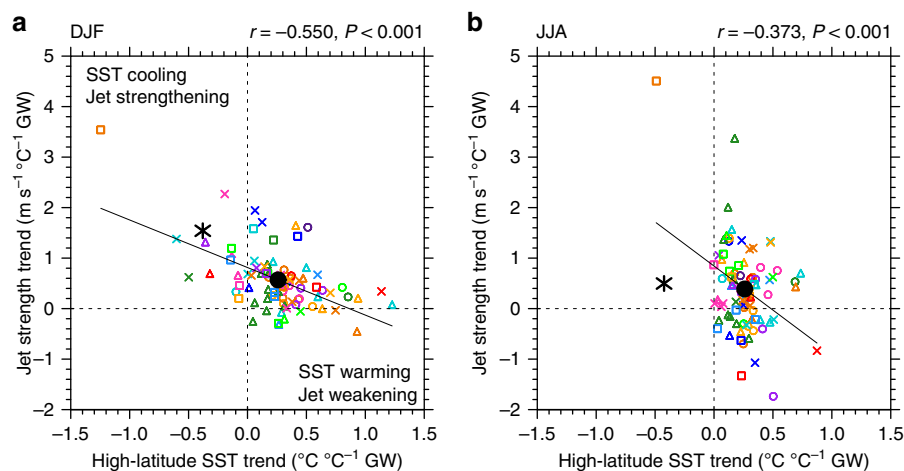


Figure 3 | Trends in jet strength versus trends in high-latitude SST over 1979–2013. (a) DJF and (b) JJA. Trends are expressed as a change per degree of global warming. All available model ensemble members are shown. Observed jet strength from European Centre for Medium-Range Weather Forecasts Interim Reanalysis (ERA-Interim). Figure details as per Fig. 2.

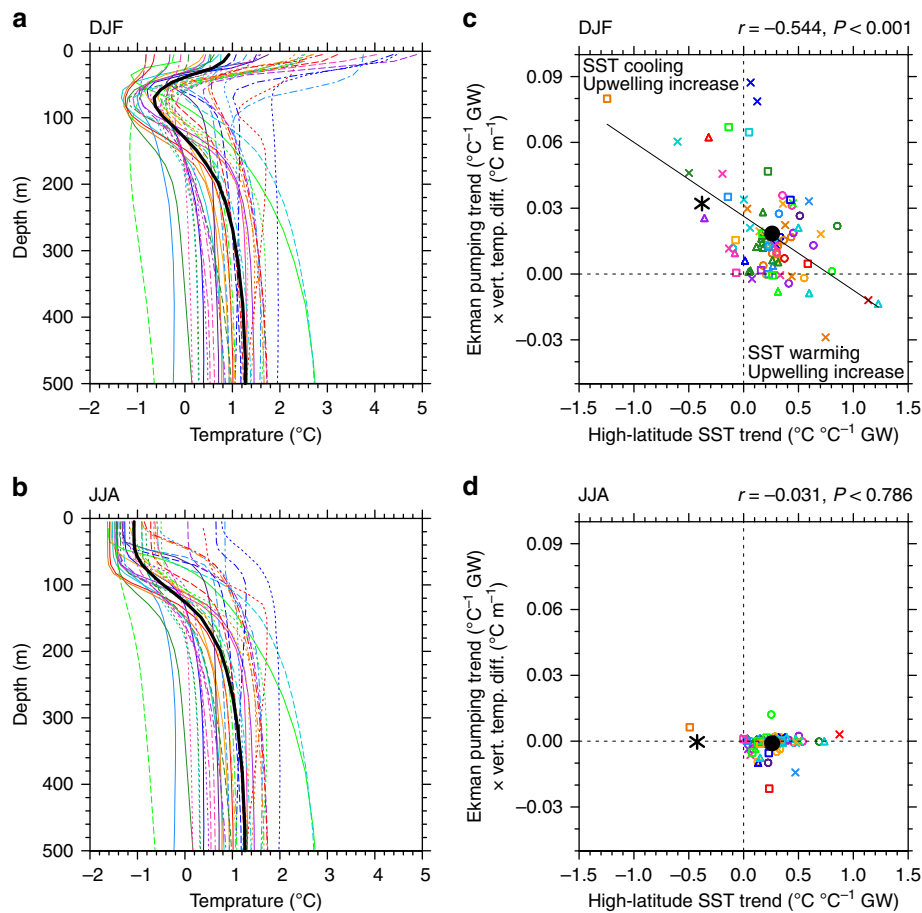


Figure 4 | Potential temperature profiles and Ekman pumping trends over 1979–2013. Seasonal zonal-mean potential temperature profiles averaged over 60–70°S for (a) DJF and (b) JJA. The first available ensemble member for each model is shown. The observed profile (black) is an average of Simple Ocean Data Assimilation (SODA) and Ishii reanalyses over 1979–2011. Trends in Ekman pumping versus trends in high-latitude SST for (c) DJF and (d) JJA. Trends are expressed as a change per degree of global warming. Ekman pumping trends are calculated as the trend in the Ekman pumping velocity principal component (PC) multiplied by the mean-state vertical temperature gradient near the surface. All available model ensemble members are shown. Details in (c,d) as per Fig. 2.

underestimate the increased upward Ekman pumping (Fig. 4c) and equatorward Ekman transport (Supplementary Fig. 4c) compared with observed trends. Many models underestimate the vertical temperature advection despite overestimating the surface stratification during summer (Fig. 4a). This contributes to their high-latitude SST warming trends in contrast to observed cooling.

There is considerable uncertainty in the observed jet trend, owing to sparse observations over the high-latitude Southern Hemisphere^{19,35}. Although only ERA-Interim jet trends are presented here, stronger jet intensification is also seen in three other reanalyses (see Methods³⁹). Increased wind speed is also evident in station-based wind observations^{40,41}. However, satellite-based wind observations available over the shorter 1988–2011 period may cast some doubt over reanalysis trends³⁹, although the satellite products themselves contain uncertainty⁴². Overall, the analyses presented here depend on an accurate wind trend estimate over the Southern Ocean, however the mechanisms described remain robust. Further, although the observed (ERA-Interim) jet intensification is stronger than the multi-model mean, it does lie within the model spread (Fig. 3a). Nevertheless, as discussed above, the strong inter-model relationship shown here suggests that the strength of jet intensification is an important process influencing high-latitude SST in observations and coupled models, and the

majority of models produce a weaker than observed intensification.

No significant relationship between trends in Ekman pumping and SST exists during winter (Fig. 4d and Supplementary Table 1). This is to be expected, given the seasonal variation in vertical temperature stratification: during winter, increased upwelling would cause warming, offsetting cooling from increased equatorward transport (Supplementary Table 1).

Timescales of Ekman response. On interannual timescales, a positive SAM is associated with cool high-latitude SST^{24–26}, whereas over longer periods a positive trend in the SAM has been linked to high-latitude SST warming^{21–23}. The apparent contradiction between the SAM–SST relationship over inter-annual versus multidecadal timescales has been explained by a two-timescale SST response to high-latitude wind changes^{36,38}. Initially, a positive SAM trend is associated with short-term cooling, by increasing the northward Ekman transport of cold surface waters in the prevailing westerly wind regions^{25,36,38}, consistent with the inter-model trend relationship here (Supplementary Fig. 4). Over time, however, the cooling is replaced with a warming, accounted for by prolonged enhanced upwelling in a region where a temperature inversion occurs^{21–23}. Our results are consistent with these previous studies in that most

CMIP5 models simulate a positive SAM trend (that is, jet intensification; Fig. 3a), increased upwelling and high-latitude SST warming (upper right quadrant of Fig. 4c). Our results suggest, however, that over the 35-year period assessed, Ekman upwelling is not responsible for the surface warming during summer, because due to the seasonal stratification profile models that simulate a stronger upwelling trend show a weaker rate of surface warming. Instead, the inter-model relationship suggests that cooling due to Ekman upwelling offsets other warming factors. Importantly, most models underestimate the increase in Ekman upwelling, resulting in a weaker cooling effect that is insufficient to offset warming from other processes, most notably surface heat fluxes.

The seasonal variation in the subsurface temperature profile is not discussed in previous studies and is key to interpreting our results: in contrast to previous studies that link initial cooling to equatorward Ekman transport only^{36,38}, our results suggest that Ekman pumping during summer is also important. It is plausible that the cooling associated with summer upwelling may eventually be replaced by warming, as water from below the mixed layer is entrained^{36,38}; however, over the timescale assessed here (1979–2013), this does not appear to be the case. In previous model experiments, the time required for this temperature-trend transition varies from an order of years to a couple of decades³⁸. If the timescale to a complete transition from initial cooling to later warming was at the longer end of this estimate, then the surface cooling seen in the observations and in some models could be consistent with this mechanism. The seasonal variation in the temperature profile may also contribute to a longer transitional timescale.

Ekman contribution to observed modelled disparity.

The mechanism identified above is present during summer. We estimate that >25% of the difference in the CMIP5 SIE trends can be attributed to their underestimated jet intensification (see Methods). As such, the underestimation of westerly wind trends in CMIP5 models probably contributes to the sea ice decrease simulated by the majority of models.

Owing to the thermal inertia of the ocean, SST anomalies in summer are likely to persist and exert an influence beyond this season. Observed spring ice tendencies have been found to persist until the following winter^{43,44}, and here we find that in both observations and models summer ice tendencies persist significantly during autumn and winter. This confirms that the summer Ekman–SST mechanism can influence trends throughout much of the year^{23,38}.

Positive feedbacks associated with the wind-induced circulation changes could also contribute to the difference between observed and modelled trends. In observations, the magnitude of Ekman pumping and transport increases such that the associated cooling more than offsets the high-latitude heat flux increase. Cooler SST leads to increased sea ice, in particular in the Ross Sea sector. Through the sea ice–albedo feedback, solar radiation decreases, conducive to further cooling and increased sea ice⁴³. The consequence is decreased zonal-mean downward heat flux in the sea-ice zone (Supplementary Fig. 6c). In the majority of the models, although the magnitude of Ekman pumping and transport also increases, it is to a smaller extent such that the associated cooling is not sufficient to offset the heat flux increase. The above sea ice–albedo feedback process operates in reverse, leading to an increased heat flux into the ocean in the sea-ice zone (Supplementary Fig. 6d). Based on the occurrence of opposite reinforcing feedback mechanisms occurring in observations and the majority of CMIP5 models, the difference between observed and modelled jet strength trends can lead to very different sea ice changes.

Considering other mechanisms. Further support for the importance of Ekman upwelling and transport comes from considering other potential mechanisms. Here we explore other possible processes and find that none of these contradict or offer an alternative explanation for the results described above.

It could be hypothesized that models with stronger jet trends show reduced high-latitude SST warming as a result of changed cloud cover or evaporative cooling, and that the correlations presented above between Ekman pumping and SST (Fig. 4c) are coincidental. No inter-model relationship is found between trends in SST and trends in overlying cloud cover during summer ($P > 0.15$; Supplementary Table 3), possibly due to differing cloud–jet relationships present in the models⁴⁵. A significant inter-model relationship is found between high-latitude SST trends and evaporation trends ($P < 0.001$; Supplementary Table 3), in which models with increasing SST show an increase in evaporation and vice-versa. This suggests that SST anomalies are driving evaporation variations, as warmer waters evaporate more readily, whereas evaporative cooling would have the opposite effect on SST. Thus, evaporative fluxes are not the cause of the excessive warming in most CMIP5 models, instead they are a response to this warming. These results support our hypothesis above; namely, that the relationship between the westerly wind jet and SST trends occurs due to changes in ocean circulation.

Outside of the summer sea-ice zone, spatial trends in total downward heat flux oppose those in SST (Supplementary Fig. 6), that is, regions of SST cooling are associated with increased heat flux into the ocean, suggesting that changes in SST are driving changes in heat flux and not the other way around. During summer, the inter-model relationship between trends in SST and surface heat fluxes over these predominantly ice-free areas (55–65°S) is insignificant, although the sense of the relationship suggests that models with SST cooling show increased heat flux into the ocean (Supplementary Fig. 7), again suggesting that changes in SST are driving changes in heat flux. Thus, net heat flux trends are of the wrong sign to account for model SST trends. It is also noted that area-averaged trends in observed heat fluxes, although uncertain, are comparable to those in CMIP5 models over this region.

Southern Ocean freshening due to accelerated Antarctic ice shelf and/or ice sheet melting, not simulated by CMIP5 models, was proposed as a possible mechanism contributing to the Antarctic sea ice increase³¹. However, further model experiments found the influence of ice sheet melt on sea-ice trends to be minimal²⁹. As such, this deficiency alone in CMIP5 models cannot account for the disparity between observed and simulated Antarctic sea ice trends. Nevertheless, reduced Southern Ocean convection in CMIP5 models has been linked with surface freshening⁴⁶, suggesting that overall changes in freshwater fluxes may be important for surface temperature trends⁴⁷.

Inter-model trends in SIE are strongly related with trends in sea surface salinity ($P < 0.001$; Supplementary Table 3 and Supplementary Fig. 8a): models with increasing salinity show a strong decrease in sea ice, whereas models with surface freshening show an increase, or weaker decrease, in sea ice. The sense of this relationship suggests that ocean surface salinity is influencing sea ice, not the other way around, as sea-ice-driven surface salinity changes would see freshening correspond to higher rates of sea-ice melt. Instead, greater sea-ice coverage is linked to fresher surface conditions and increased surface stratification, which suppresses convective overturning and vice versa for reduced sea-ice coverage.

Sea-surface salinity trends cannot be explained by trends in high-latitude precipitation minus evaporation ($P - E$), as surprisingly increasing $P - E$ is associated with increasing

salinity ($P=0.05$ during summer; Supplementary Table 3 and Supplementary Fig. 8b), opposite to what would be expected, because both $P-E$ and surface salinity trends co-vary with the jet. Again, changes in wind-induced ocean circulation provide the probable explanation. Namely, surface salinity trends are weakly related with Ekman pumping trends ($P<0.1$ during summer; Supplementary Table 3 and Supplementary Fig. 8c): models with a stronger increase in Ekman upwelling show an increase in surface salinity, whereas models with a weaker increase (or decrease) in Ekman upwelling show a decrease in surface salinity, due to the upwelling (or lack thereof) of saltier water from depth (Supplementary Fig. 8d). The temperature response associated with the Ekman upwelling of salty subsurface water (warming due to decreased stability and increased convective overturning) dampens the direct Ekman–SST response (upwelling of cool Winter Water) and this may be the reason why no significant Ekman–SIE relationship is found directly in the models over the 35-year period assessed.

Discussion

Both the observed and CMIP5 SIE trends are linked to the westerly wind jet intensification through the influence of SST. The models underestimate the observed jet intensification during summer, although we caution that the observed jet trend is uncertain. This causes a weaker strengthening of high-latitude Ekman pumping and transport than observed. Although increased Ekman upwelling of cool Winter Water and the associated equatorward Ekman transport contribute to the observed SST cooling, because their trends are underestimated in the models, these terms are insufficient to offset warming from increased surface heat fluxes. This leads to faster surface warming and a decreasing sea-ice trend in most of the models (summarized in Fig. 5). Once these trends are initiated, the sea ice–albedo positive feedback ensures the trend is sustained. These findings demonstrate the importance of accurately simulating changes in the wind^{7,48}. By contrast, in the observations, the cooling effect from the wind changes appears to be sufficient to offset the warming tendency resulting in an initial cooling. The same sea ice–albedo positive feedback operates in reverse, leading to further cooling and an increasing sea ice trend. Although

analyses are largely conducted over circumpolar regions, when repeated for the Ross Sea sector, where observed SIE has increased most substantially, results remain robust.

Our finding that underestimated wind trends contribute to the discrepancy between the observed and model sea-ice changes occurs despite the fact these models do not resolve eddies, although almost all include a suitable eddy-induced advection scheme to approximate their effects. In the real world eddy compensation would partially counteract wind-induced changes^{38,49}, although Ekman changes still dominate in the surface layer^{50,51}. In the presence of an eddy compensation effect, the underestimation of the impact in the models could be even larger. This influence and others such as the role of deep ocean overturning or convection will provide fertile ground for further research into the recent Southern Ocean circulation and sea ice changes.

Methods

Data. CMIP5 data from the historical and Representative Concentration Pathway 8.5 (RCP8.5; high-emission scenario) experiments are concatenated to match the observational period. The choice of RCP scenario over 2006–2013 has minimal influence on results, as all forcing scenarios are very similar over this time frame. We analyse all CMIP5 models that have SIC data available for both the historical and RCP8.5 experiments. This includes 41 CMIP5 models, with a total of 87 realizations (between one and ten runs are available per model), listed in the legend of Fig. 2. We also make use of SST, potential temperature, sea surface salinity, subsurface salinity (historical experiment only), surface air temperature, zonal wind, surface wind stresses, evaporation, precipitation, total cloud cover, mean sea level pressure and surface heat fluxes from the CMIP5 archive. At the time of analysis, potential temperature was not available for Flexible Global Ocean–Atmosphere–Land System model spectral version 2 and First Institute of Oceanography Earth System Model, and salinity was not available for Hadley Centre Global Environment Model version 2 Atmosphere–Ocean. Various surface heat flux terms were not available for Centro Euro-Mediterraneo sui Cambiamenti Climatici Climate Model with a resolved Stratosphere, First Institute of Oceanography Earth System Model, Goddard Institute for Space Studies ModelE/Russell (r11p2 only), Hadley Centre Global Environment Model version 2 Atmosphere–Ocean, Max Planck Institute Earth System Model Low Resolution (r211p1 and r311p1 only) and Meteorological Research Institute Earth System Model version 1.

For comparison with observations, we use passive microwave SIC processed using the NSIDC Bootstrap algorithm². The possibility for spurious trends in this SIC data set has been identified⁵²; thus, the results are compared with those obtained with SIC processed using the National Aeronautics and Space Administration Team algorithm and are found to be very similar. For area-averaged SIE, we make use of the pre-calculated NSIDC SIE index⁵³, as this index is commonly used in other studies^{11,12}. Results calculated using the NSIDC Bootstrap

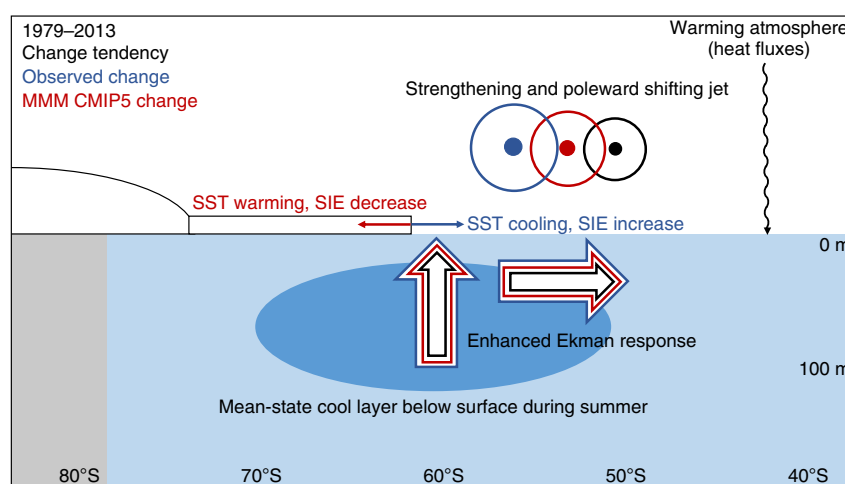


Figure 5 | Schematic of decadal scale wind induced surface layer changes during summer. Over recent decades, the observed westerly wind jet has strengthened and shifted poleward during austral summer (circles with dots). This has increased the upward Ekman pumping and equatorward Ekman transport (large arrows). During summer, increased upwelling at high latitudes brings cooler Winter Water to the surface. Combined with equatorward transport, this leads to SST cooling in observations. Multi-model mean (MMM) CMIP5 changes (red) are weaker than observed changes (blue). Under global warming, these weaker Ekman changes are insufficient to offset warming from other factors (curvy arrow). As such, multi-model mean CMIP5 high-latitude SST has warmed rather than cooled and Antarctic sea ice has declined rather than expanded (small arrows).

SIC are very similar. We use SST data from the HadISST data set⁵⁴. For ocean temperature and salinity, we take an average of the SODA v2.2.4 (ref. 55) and Ishii⁵⁶ reanalyses. For atmospheric variables, we use the ERA-Interim reanalysis⁵⁷, regarded as the most reliable reanalysis over the Amundsen and Bellingshausen Seas³⁴, and over Antarctica^{58,59}. Uncertainty exists in ERA-Interim wind trends³⁹; however, considering the trends evident in the National Centers for Environmental Prediction (NCEP)/National Center for Atmospheric Research reanalysis, NCEP/Department of Energy reanalysis and Twentieth Century reanalysis v2, ERA-Interim winds may modestly underestimate the jet intensification, as this product yields the weakest trend among these four reanalysis products³⁹. Weaker jet intensification is seen in National Aeronautics and Space Administration Modern Era-Retrospective analysis for Research and Applications and NCEP Climate Forecast System Reanalysis, although these products have previously been excluded when examining Southern Ocean wind strength trends, due to possible issues with reanalysis data assimilation³⁵. The overall balance of evidence suggests that ERA-Interim winds provide one of the best estimates of wind trends over the Southern Ocean for the full study period of 1979–2013.

All data are bilinearly interpolated to a standard $2^\circ \times 2^\circ$ grid. This resolution is chosen to avoid overextrapolating low-resolution data from some models to higher resolutions. Potential temperature is converted from σ to z -levels where required and vertically interpolated to 40-depth levels (matching the SODA reanalysis). Data are stratified into seasonal and annual mean fields. The year of an austral summer corresponds to the year of the January–February.

Metrics. A number of metrics are calculated for observations and each model. Time series of metrics are used to investigate and compare linear trends and interannual variability between models and observations. For inter-model relationships, each ensemble member is included in the analysis and weighted evenly. Linear trends are calculated using the least squares regression method and are scaled by linear trends in global-mean temperature to take into account the different climate sensitivity of the models. Statistical significance is determined using the two-sided Student's t -test. When assessing the significance of interannual correlation coefficients, the lag-1 autocorrelation is accounted for by estimating the effective sample size, N_{eff} , as:

$$N_{\text{eff}} = N \left(\frac{1 - r_1 r_2}{1 + r_1 r_2} \right) \quad (1)$$

where N is the sample size, and r_1 and r_2 are the lag-1 autocorrelations of the time series of interest⁶⁰.

SIE in the models is defined as the circumpolar area where SIC exceeds 15% (ref. 28). We focus on SIE as an area-averaged metric, as it is commonly assessed^{7–9,28,29}, although we also present SIC trends to display regional trend characteristics (Fig. 1). High-latitude metrics (for example, SST, sea surface salinity and $P-E$) are defined as the area-averaged field south of 55°S (except where noted otherwise). The choice of latitude is assessed and results are found to be robust over a range of high latitudes. Only ocean grid points are considered in area averages. In HadISST, SST in grid cells partially covered by sea ice is determined based on a statistical relationship between SST and SIC⁵⁴. In the CMIP5 models, SST is defined as the temperature of the uppermost model layer. Jet strength is defined as the maximum 925-hPa westerly wind between $35^\circ\text{--}70^\circ\text{S}$, where a cubic spline approximation is applied to the zonal-mean zonal wind³⁴.

Meridional Ekman transport, V_E , is calculated from the surface zonal wind stress ($V_E = -\tau_x/\rho f$) and Ekman pumping, w_E , from the curl of surface wind stresses ($w_E = \nabla \times (\tau/f)/\rho$), where τ is the wind stress, ρ is the density of seawater and f is the Coriolis parameter. Trends calculated from area-averaged Ekman transport and pumping time series are sensitive to the choice of latitude band, owing to variations in the wind fields among models and observations. To allow for spatial variations among models, we calculate the first empirical orthogonal function (EOF) of both Ekman transport and pumping over $55^\circ\text{--}70^\circ\text{S}$ and use the standardized PCs to represent the Ekman transport and pumping time series, respectively. During summer, the first EOFs for both Ekman transport and pumping are well separated⁶¹ from subsequent patterns in all models and observations. The first EOFs are related to the SAM, the leading mode of atmospheric variability in the extratropical Southern Hemisphere⁶², and have a more coherent influence on SST (Supplementary Fig. 9). To account for the effect that equatorward Ekman transport has on SST, we estimate horizontal temperature advection by multiplying the Ekman transport PC by the mean-state horizontal temperature difference between $55^\circ\text{--}60^\circ\text{S}$, and $65^\circ\text{--}70^\circ\text{S}$, calculated for the zonal-mean surface layer (0–25 m). Likewise, to account for the effect that Ekman pumping has on SST, we estimate the vertical temperature advection by multiplying the Ekman pumping PC by the mean-state vertical temperature difference between the surface layer (0–25 m) and the layer just below the summer thermocline (70–80 m), calculated for the zonal-mean over $55^\circ\text{--}70^\circ\text{S}$.

Scale analysis. Horizontal temperature advection due to Ekman transport is compared with vertical temperature advection due to Ekman upwelling (Supplementary Fig. 5). We use area-averaged terms for calculations so that various latitude bands can be assessed; as we are interested in mean-state orders of magnitude rather than linear trends, comparing area averages rather than PCs is reasonable.

Horizontal and vertical advection terms are compared as follows:

$$\alpha = \frac{V_E \bar{T}_y / h}{w_E \bar{T}_z} \quad (2)$$

where \bar{T}_y is the horizontal temperature gradient over the latitude bands assessed, h is the depth of the surface layer (25 m) and \bar{T}_z is the vertical temperature gradient at the base of the summer mixed layer. The inclusion of h in the numerator is necessary to directly compare terms as Ekman transport is a depth-integrated flow in the upper h metres, whereas Ekman pumping is a velocity.

Over all latitude bands assessed $V_E > w_E$; however, $\bar{T}_y/h < \bar{T}_z$. As a result, we find the numerator and denominator in equation (2) to be of similar orders of magnitude. Further equatorward, where τ_x is relatively large and $\nabla \times \tau$ small, northward Ekman transport is larger and $\alpha \sim 5\text{--}10$, but between $60^\circ\text{--}75^\circ\text{S}$, where the zonal wind transitions from westerly to easterly, $\alpha \sim 0.5\text{--}2$. As such, we conclude that over these latitude bands, both Ekman transport and Ekman pumping terms are important in driving variations in SST, and hence sea ice.

Estimating the Ekman contribution to modelled disparity. We use the difference between the observed (ERA-Interim) and multi-model mean jet strength trends and the sensitivity of SST trends to jet trends (that is, the inverse of Fig. 3a), to estimate the Ekman contribution to SST trends. From this, we use the sensitivity of SIE to SST (Fig. 2a), to further estimate the Ekman contribution to SIE trends.

References

- Cavalieri, D. & Parkinson, C. Antarctic sea ice variability and trends, 1979–2006. *J. Geophys. Res.* **113**, C07004 (2008).
- Comiso, J. C. & Nishio, F. Trends in the sea ice cover using enhanced and compatible AMSR-E, SSM/I, and SMMR data. *J. Geophys. Res. Oceans* **113**, C02S07 (2008).
- Parkinson, C. & Cavalieri, D. Antarctic sea ice variability and trends, 1979–2010. *Cryosphere* **6**, 871–880 (2012).
- Stammerjohn, S., Martinson, D. G., Smith, R., Yuan, X. & Rind, D. Trends in Antarctic annual sea ice retreat and advance and their relation to El Niño–Southern Oscillation and Southern Annular Mode variability. *J. Geophys. Res.* **113**, C03S90 (2008).
- Holland, P. R. & Kwok, R. Wind-driven trends in Antarctic sea-ice drift. *Nat. Geosci.* **5**, 872–875 (2012).
- Simpkins, G. R., Ciasio, L. M. & England, M. H. Observed variations in multidecadal Antarctic sea ice trends during 1979–2012. *Geophys. Res. Lett.* **40**, 3643–3648 (2013).
- Mahlstein, I., Gent, P. R. & Solomon, S. Historical Antarctic mean sea ice area, sea ice trends, and winds in CMIP5 simulations. *J. Geophys. Res. Atmos.* **118**, 5105–5110 (2013).
- Polvani, L. M. & Smith, K. L. Can natural variability explain observed Antarctic sea ice trends? New modeling evidence from CMIP5. *Geophys. Res. Lett.* **40**, 3195–3199 (2013).
- Zunz, V., Goosse, H. & Massonnet, F. How does internal variability influence the ability of CMIP5 models to reproduce the recent trend in Southern Ocean sea ice extent? *Cryosphere* **7**, 451–468 (2013).
- Fan, T., Deser, C. & Schneider, D. P. Recent Antarctic sea ice trends in the context of Southern Ocean surface climate variations since 1950. *Geophys. Res. Lett.* **41**, 2419–2426 (2014).
- Gagné, M.-E., Gillett, N. P. & Fyfe, J. C. Observed and simulated changes in Antarctic sea ice extent over the past 50 years. *Geophys. Res. Lett.* **42**, 90–95 (2015).
- Simmonds, I. Comparing and contrasting the behaviour of Arctic and Antarctic sea ice over the 35 year period 1979–2013. *Ann. Glaciol.* **56**, 18–28 (2015).
- Turner, J. *et al.* Non-annular atmospheric circulation change induced by stratospheric ozone depletion and its role in the recent increase of Antarctic sea ice extent. *Geophys. Res. Lett.* **36**, L08502 (2009).
- Li, X., Holland, D. M., Gerber, E. P. & Yoo, C. Impacts of the north and tropical Atlantic Ocean on the Antarctic Peninsula and sea ice. *Nature* **505**, 538–542 (2014).
- Simpkins, G. R., McGregor, S., Taschetto, A. S., Ciasio, L. M. & England, M. H. Tropical connections to climatic change in the extratropical Southern Hemisphere: the role of Atlantic SST trends. *J. Clim.* **27**, 4923–4936 (2014).
- Turner, J. *et al.* Recent changes in Antarctic Sea ice. *Phil. Trans. R. Soc. A* **373**, 1–13 (2015).
- Marshall, G. J. Trends in the Southern Annular mode from observations and reanalyses. *J. Clim.* **16**, 4134–4143 (2003).
- Arblaster, J. M. & Meehl, G. A. Contributions of external forcings to southern annular mode trends. *J. Clim.* **19**, 2896–2905 (2006).
- Son, S.-W. *et al.* Impact of stratospheric ozone on Southern Hemisphere circulation change: a multimodel assessment. *J. Geophys. Res. Atmos.* **115**, D00M07 (2010).
- Polvani, L. M., Waugh, D. W., Correa, G. J. & Son, S.-W. Stratospheric ozone depletion: the main driver of twentieth-century atmospheric circulation changes in the Southern Hemisphere. *J. Clim.* **24**, 795–812 (2011).

21. Sigmond, M. & Fyfe, J. C. Has the ozone hole contributed to increased Antarctic sea ice extent? *Geophys. Res. Lett.* **37**, L18502 (2010).
22. Bitz, C. M. & Polvani, L. M. Antarctic climate response to stratospheric ozone depletion in a fine resolution ocean climate model. *Geophys. Res. Lett.* **39**, L20705 (2012).
23. Smith, K. L., Polvani, L. M. & Marsh, D. R. Mitigation of 21st century Antarctic sea ice loss by stratospheric ozone recovery. *Geophys. Res. Lett.* **39**, L20701 (2012).
24. Hall, A. & Visbeck, M. Synchronous variability in the Southern Hemisphere atmosphere, sea ice, and ocean resulting from the annular mode. *J. Clim.* **15**, 3043–3057 (2002).
25. Sen Gupta, A. & England, M. H. Coupled ocean-atmosphere-ice response to variations in the Southern Annular Mode. *J. Clim.* **19**, 4457–4486 (2006).
26. Lefebvre, W. & Goosse, H. An analysis of the atmospheric processes driving the large-scale winter sea ice variability in the Southern Ocean. *J. Geophys. Res. Oceans* **113**, C02004 (2008).
27. Turner, J., Phillips, T., Hosking, J. S., Marshall, G. J. & Orr, A. The Amundsen Sea low. *Int. J. Climatol.* **33**, 1818–1829 (2013).
28. Turner, J., Bracegirdle, T. J., Phillips, T., Marshall, G. J. & Hosking, J. S. An initial assessment of Antarctic Sea ice extent in the CMIP5 models. *J. Clim.* **26**, 1473–1484 (2013).
29. Swart, N. & Fyfe, J. C. The influence of recent Antarctic ice sheet retreat on simulated sea ice area trends. *Geophys. Res. Lett.* **40**, 4328–4332 (2013).
30. Hobbs, W. R., Bindoff, N. L. & Raphael, M. N. New perspectives on observed and simulated Antarctic Sea ice extent trends using optimal fingerprinting techniques. *J. Clim.* **28**, 1543–1560 (2015).
31. Bintanja, R., van Oldenborgh, G., Drijfhout, S., Wouters, B. & Katsman, C. Important role for ocean warming and increased ice-shelf melt in Antarctic sea-ice expansion. *Nat. Geosci.* **6**, 376–379 (2013).
32. Haumann, F. A., Notz, D. & Schmidt, H. Anthropogenic influence on recent circulation-driven Antarctic sea ice changes. *Geophys. Res. Lett.* **41**, 8429–8437 (2014).
33. Purich, A., Cowan, T., Min, S.-K. & Cai, W. Autumn precipitation trends over Southern Hemisphere midlatitudes as simulated by CMIP5 models. *J. Clim.* **26**, 8341–8356 (2013).
34. Bracegirdle, T. J. *et al.* Assessment of surface winds over the Atlantic, Indian, and Pacific ocean sectors of the Southern Ocean in CMIP5 models: historical bias, forcing response, and state dependence. *J. Geophys. Res. Atmos.* **118**, 547–562 (2013).
35. Swart, N. & Fyfe, J. Observed and simulated changes in the Southern Hemisphere surface westerly wind-stress. *Geophys. Res. Lett.* **39**, L16711 (2012).
36. Marshall, J. *et al.* The ocean's role in polar climate change: asymmetric Arctic and Antarctic responses to greenhouse gas and ozone forcing. *Phil. Trans. R. Soc. A* **372**, 20130040 (2014).
37. Marshall, J. & Speer, K. Closure of the meridional overturning circulation through Southern Ocean upwelling. *Nat. Geosci.* **5**, 171–180 (2012).
38. Ferreira, D., Marshall, J., Bitz, C. M., Solomon, S. & Plumb, A. Antarctic Ocean and sea ice response to ozone depletion: a two-time-scale problem. *J. Clim.* **28**, 1206–1226 (2015).
39. Swart, N. C., Fyfe, J. C., Gillett, N. & Marshall, G. J. Comparing trends in the Southern Annular Mode and surface westerly jet. *J. Clim.* **28**, 8840–8859 (2015).
40. Yang, X.-Y., Huang, R. X. & Wang, D. X. Decadal changes of wind stress over the Southern Ocean associated with antarctic ozone depletion. *J. Clim.* **20**, 3395–3410 (2007).
41. Handle, L. B., Siems, S. T. & Manton, M. J. Observed trends in wind speed over the Southern Ocean. *Geophys. Res. Lett.* **39**, L11802 (2012).
42. Foreman, M. G. G., Pal, B. & Merryfield, W. J. Trends in upwelling and downwelling winds along the British Columbia shelf. *J. Geophys. Res.* **116**, C10023 (2011).
43. Stammerjohn, S., Massom, R. A., Rind, D. & Martinson, D. G. Regions of rapid sea ice change: an inter-hemispheric seasonal comparison. *Geophys. Res. Lett.* **39**, 1–8 (2012).
44. Holland, P. R. The seasonality of Antarctic sea ice trends. *Geophys. Res. Lett.* **41**, 1–8 (2014).
45. Grise, K. M. & Polvani, L. M. Southern Hemisphere cloud-dynamics biases in CMIP5 models and their implications for climate projections. *J. Clim.* **27**, 6074–6092 (2014).
46. deLavergne, C., Palter, J. B., Galbraith, E. D., Bernardello, R. & Marinov, I. Cessation of deep convection in the open Southern Ocean under anthropogenic climate change. *Nat. Climate Change* **4**, 278–282 (2014).
47. Morrison, A. K., England, M. H. & Hogg, A. M. Response of Southern Ocean convection and abyssal overturning to surface buoyancy perturbations. *J. Clim.* **28**, 4263–4278 (2015).
48. Sen Gupta, A. *et al.* Projected changes to the Southern Hemisphere ocean and sea ice in the IPCC AR4 climate models. *J. Clim.* **22**, 3047–3078 (2009).
49. Downes, S. M. & Hogg, A. M. Southern Ocean circulation and eddy compensation in CMIP5 models. *J. Clim.* **26**, 7198–7220 (2013).
50. Meredith, M. P., Naveira Garabato, A. C., Hogg, A. M. & Farneti, R. Sensitivity of the overturning circulation in the Southern Ocean to decadal changes in wind forcing. *J. Clim.* **25**, 99–110 (2012).
51. Morrison, A. K. & Hogg, A. M. On the relationship between Southern Ocean overturning and ACC transport. *J. Phys. Oceanogr.* **43**, 140–148 (2013).
52. Eisenman, I., Meier, W. & Norris, J. A spurious jump in the satellite record: has Antarctic sea ice expansion been overestimated? *Cryosphere* **8**, 1289–1296 (2014).
53. Fetterer, F., Knowles, K., Meier, W. & Savoie, M. *Sea Ice Index* (National Snow and Ice Data Center, Digital media: Boulder, Colorado USA, 2002). Available at <http://dx.doi.org/10.7265/N5QJ7F7W>.
54. Rayner, N. *et al.* Global analyses of sea surface temperature, sea ice, and night marine air temperature since the late nineteenth century. *J. Geophys. Res.* **108**, 4407 (2003).
55. Carton, J. A. & Giese, B. S. A reanalysis of ocean climate using Simple Ocean Data Assimilation (SODA). *Mon. Weather Rev.* **136**, 2999–3017 (2008).
56. Ishii, M. & Kimoto, M. Reevaluation of historical ocean heat content variations with time-varying XBT and MBT depth bias corrections. *J. Oceanogr.* **65**, 287–299 (2009).
57. Dee, D. P. *et al.* The ERA-Interim reanalysis: configuration and performance of the data assimilation system. *Q. J. R. Meteorol. Soc.* **137**, 553–597 (2011).
58. Bromwich, D. H., Nicolas, J. P. & Monaghan, A. J. An assessment of precipitation changes over Antarctica and the Southern Ocean since 1989 in contemporary global reanalyses. *J. Clim.* **24**, 4189–4209 (2011).
59. Bracegirdle, T. J. & Marshall, G. J. The reliability of Antarctic tropospheric pressure and temperature in the latest global reanalyses. *J. Clim.* **25**, 7138–7146 (2012).
60. Ciasto, L. M. & Thompson, D. W. Observations of large-scale ocean-atmosphere interaction in the Southern Hemisphere. *J. Clim.* **21**, 1244–1259 (2008).
61. North, G. R., Bell, T. L. & Cahalan, R. F. Sampling errors in the estimation of empirical orthogonal functions. *Mon. Weather Rev.* **110**, 699–706 (1982).
62. Thompson, D. W. *et al.* Signatures of the Antarctic ozone hole in Southern Hemisphere surface climate change. *Nat. Geosci.* **4**, 741–749 (2011).

Acknowledgements

This work was supported by CSIRO Oceans and Atmosphere, and the Australian Research Council (ARC) including the ARC Centre of Excellence in Climate System Science. A.P. was supported by an Australian Postgraduate Award and a CSIRO Office of the Chief Executive Science Leader scholarship. W.C. was supported by the Australian Climate Change Science Programme and a CSIRO Office of the Chief Executive Science Leader award. M.H.E. was supported by an ARC Laureate Fellowship. We thank Steve Rintoul for the thumbnail image. We acknowledge the World Climate Research Programme's Working Group on Coupled Modelling, which is responsible for CMIP, and thank the climate modelling groups (listed in Fig. 2 of this paper) for producing and making available their model output.

Author contributions

A.P., W.C. and M.H.E. conceived the study and undertook the initial analyses. A.P. assembled and analysed the observational and CMIP5 data, and wrote the first draft of the manuscript. T.C. assisted with data analysis. All authors contributed to the development of ideas, writing and revising the manuscript.

Additional information

Supplementary Information accompanies this paper at <http://www.nature.com/naturecommunications>

Competing financial interests: The authors declare no competing financial interests.

Reprints and permission information is available online at <http://npg.nature.com/reprintsandpermissions/>

How to cite this article: Purich, A. *et al.* Evidence for link between modelled trends in Antarctic sea ice and underestimated westerly wind changes. *Nat. Commun.* **7**:10409 doi: 10.1038/ncomms10409 (2016).



This work is licensed under a Creative Commons Attribution 4.0 International License. The images or other third party material in this article are included in the article's Creative Commons license, unless indicated otherwise in the credit line; if the material is not included under the Creative Commons license, users will need to obtain permission from the license holder to reproduce the material. To view a copy of this license, visit <http://creativecommons.org/licenses/by/4.0/>

Appendix B

Published article

A copy of the published article that constitutes the material in Part 2 is included hereafter:

Purich, A., M. H. England, W. Cai, Y. Chikamoto, A. Timmermann, J. C. Fyfe, L. Frankcombe, G. A. Meehl, and J. M. Arblaster, 2016: Tropical Pacific SST drivers of recent Antarctic sea ice trends. *Journal of Climate*, **29**, 8931–8948, doi:10.1175/JCLI-D-16-0440.1. ©American Meteorological Society. Used with permission.

Tropical Pacific SST Drivers of Recent Antarctic Sea Ice Trends

ARIAAN PURICH,^{a,b,c} MATTHEW H. ENGLAND,^{b,c} WENJU CAI,^a YOSHIMITSU CHIKAMOTO,^d
 AXEL TIMMERMANN,^{d,e} JOHN C. FYFE,^f LEELA FRANKCOMBE,^{b,c} GERALD A. MEEHL,^g
 AND JULIE M. ARBLASTER^{g,h}

^a CSIRO Oceans and Atmosphere, Aspendale, Victoria, Australia

^b Climate Change Research Centre, University of New South Wales, Sydney, New South Wales, Australia

^c ARC Centre of Excellence for Climate System Science, University of New South Wales, Sydney, New South Wales, Australia

^d International Pacific Research Center, University of Hawai'i at Mānoa, Honolulu, Hawaii

^e Department of Oceanography, University of Hawai'i at Mānoa, Honolulu, Hawaii

^f Canadian Centre for Climate Modelling and Analysis, Environment and Climate Change Canada, Victoria, British Columbia, Canada

^g National Center for Atmospheric Research, Boulder, Colorado

^h School of Earth, Atmosphere and Environment, Monash University, Clayton, Victoria, Australia

(Manuscript received 8 June 2016, in final form 1 September 2016)

ABSTRACT

A strengthening of the Amundsen Sea low from 1979 to 2013 has been shown to largely explain the observed increase in Antarctic sea ice concentration in the eastern Ross Sea and decrease in the Bellingshausen Sea. Here it is shown that while these changes are not generally seen in freely running coupled climate model simulations, they are reproduced in simulations of two independent coupled climate models: one constrained by observed sea surface temperature anomalies in the tropical Pacific and the other by observed surface wind stress in the tropics. This analysis confirms previous results and strengthens the conclusion that the phase change in the interdecadal Pacific oscillation from positive to negative over 1979–2013 contributed to the observed strengthening of the Amundsen Sea low and the associated pattern of Antarctic sea ice change during this period. New support for this conclusion is provided by simulated trends in spatial patterns of sea ice concentrations that are similar to those observed. These results highlight the importance of accounting for teleconnections from low to high latitudes in both model simulations and observations of Antarctic sea ice variability and change.

1. Introduction

The dipole pattern of recent Pacific sector sea ice trends, with decreasing ice in the Bellingshausen Sea and increasing ice in the Ross Sea, has been attributed to changing winds (Holland and Kwok 2012; Fan et al. 2014) and specifically to the strengthening of the Amundsen Sea low (Turner et al. 2009, 2016; Clem and Fogt 2015; Clem and Renwick 2015; Meehl et al. 2016a; Raphael et al. 2016). There is some suggestion that recent increasing Antarctic sea ice trends since 1979 can be explained by

interdecadal variability (Fan et al. 2014; Gagné et al. 2015), particularly arising from the phase change of the interdecadal Pacific oscillation (IPO) to negative after the late 1990s (Meehl et al. 2016a), rather than by direct anthropogenic forcing. As such, it is pertinent to scrutinize the proposed causes of these trends. Here we further examine the concept that recent trends in tropical SST and tropical-to-extratropical teleconnections influenced the Amundsen Sea low, thus contributing to the observed pattern of Antarctic sea ice trends. The goal of this study is to address and quantify the influence of tropical Pacific sea surface temperature (SST) variability on Antarctic sea ice trends, specifically focusing on the role of the IPO.

Tropical Pacific SST variability influences the Amundsen Sea low via convectively generated atmospheric Rossby wave trains, including the well-known Pacific–South American (PSA) pattern (Hoskins and Karoly 1981;

Supplemental information related to this paper is available at the Journals Online website: <http://dx.doi.org/10.1175/JCLI-D-16-0440.s1>.

Corresponding author address: Ariaan Purich, CSIRO Oceans and Atmosphere, PMB 1, Aspendale VIC 3195, Australia.
 E-mail: ariaan.purich@csiro.au

Mo and Higgins 1998; Mo 2000; Yuan and Martinson 2000; Irving and Simmonds 2016) as well as a meridionally oriented wave train during spring (Clem and Fogt 2015). Through its influence on equatorial and off-equatorial convection, El Niño–Southern Oscillation (ENSO) teleconnections to Antarctic sea ice have been previously noted. La Niña is associated with a strengthened Amundsen Sea low, causing increased sea ice in the eastern Ross and Amundsen Seas as a result of increased southerly flow at the surface, and decreased sea ice in the Bellingshausen Sea as a result of increased northerly flow in this region, and vice versa for El Niño (Renwick 2002; Turner 2004; Stammerjohn et al. 2008; Ciasto and England 2011; L'Heureux and Thompson 2006; Simpkins et al. 2012; Ciasto et al. 2015). There are seasonal variations in the ENSO teleconnection, with a link between El Niño and the negative southern annular mode (SAM; and La Niña and the positive SAM) present during austral summer but not during austral winter (e.g., L'Heureux and Thompson 2006; Simpkins et al. 2012). The magnitude of atmospheric circulation anomalies associated with ENSO are roughly comparable for all seasons (relative to the seasonal cycle of ENSO) although are strongest during austral spring, and the strongest influence on sea ice occurs during austral winter and particularly spring (Jin and Kirtman 2009; Simpkins et al. 2012). There are also differences in the teleconnections for different types of El Niño events (e.g., eastern Pacific vs central Pacific events; Ciasto et al. 2015).

Tropical Pacific SSTs have been connected to sea ice reductions in the Bellingshausen Sea via a strengthened Amundsen Sea low during austral autumn (Ding and Steig 2013). Atmospheric wind forcing associated with ENSO variability has been linked to seasonal sea ice duration trends over 1990–2007 in the Atlantic and Pacific sectors (Matear et al. 2015). Clem and Fogt (2015) found that the negative trend in the Pacific decadal oscillation since 1979 has contributed to the deepening of the Amundsen Sea low during austral spring. Recently, as noted above, Meehl et al. (2016a) have also linked the increase in Ross Sea ice trends to the phase shift of the IPO to negative (below normal tropical eastern Pacific SST on the decadal time scale) that occurred in the late 1990s. Warming of the tropical Atlantic Ocean has also been linked with a deepening Amundsen Sea low and thus to sea ice changes (Li et al. 2014, 2015a,b; Simpkins et al. 2014). However, recent evidence has been presented that the dominant forcing since the late 1990s has come from the tropical eastern Pacific with the shift to the negative phase of the IPO at this time (Meehl et al. 2016a).

To date, investigation of changes in the tropical Pacific and Atlantic and their teleconnections to Antarctic sea

ice have been tested using atmospheric general circulation models (Li et al. 2014, 2015a,b; Simpkins et al. 2014; Meehl et al. 2016a) and an ocean–ice general circulation model (Matear et al. 2015), potentially neglecting important coupled ocean–atmosphere–ice feedbacks. We note that Simpkins et al. (2012) found no significant relationship between trends in SIC and trends in ENSO over 1980–2008, while Liu et al. (2004) and Yu et al. (2011) found that the trends in the SAM and ENSO produce similar spatial patterns in sea ice compared to the observed trends but explain less than one-third of the magnitude of total SIC trends over 1979–2002 and 1979–2007, respectively. With the additional years in the analysis period assessed here (1979–2013), as well as consideration of the phase change of the IPO over this period in the late 1990s (e.g., Meehl et al. 2016a), it is worth revisiting how changes in the tropical Pacific may have influenced Antarctic sea ice trends. We also attempt to separate the externally forced signal from the signal generated by internal variability in the Pacific, something that was not attempted in previous studies. We examine simulations from two different partially coupled experiments that are forced by observed variability in certain predefined regions (termed “pacemaker” experiments) to investigate how observed tropical Pacific decadal variability affected observed Antarctic sea ice trends. The use of these pacemaker experiments enables an estimate of the role of Pacific Ocean SST variability forcing on SIC trends.

2. Data and methods

a. Data and model experiments

We utilize passive microwave sea ice concentration (SIC) processed using the National Snow and Ice Data Center (NSIDC) bootstrap algorithm (Comiso and Nishio 2008; Meier et al. 2015) and SST from the Hadley Centre Sea Ice and Sea Surface Temperature dataset (HadISST; Rayner et al. 2003). We also assess SIC processed using the NASA team algorithm, as it is possible that spurious trends are present in the bootstrap algorithm dataset (Eisenman et al. 2014) and results are found to be almost identical (not shown). Mean sea level pressure (MSLP) is taken from ERA-Interim (Dee et al. 2011), regarded to be the most reliable reanalysis over Antarctica (Bromwich et al. 2011; Bracegirdle and Marshall 2012) and the Amundsen and Bellingshausen Seas (Bracegirdle et al. 2013).

To estimate the forced SIC and MSLP responses, we use the multimodel mean from phase 5 of the Coupled Model Intercomparison Project (CMIP5). To match observations, CMIP5 data from the historical and representative

concentration pathway 8.5 (RCP8.5) experiments are concatenated over 1979–2013. The choice of RCP scenario for the time period assessed (i.e., 2006–13) has minimal influence, as all forcing scenarios are very similar over this period. We include all CMIP5 models that have SIC data available for both of these experiments, totaling 87 realizations from 41 CMIP5 models (listed in Table S1 of the supplementary material). Each realization is weighted evenly in the multimodel mean. While the majority of CMIP5 models do not capture the observed increase in Antarctic sea ice, the observed sea ice trend lies within the spread of models (Gagné et al. 2015; Purich et al. 2016), and the large ensemble of realizations provides the best available estimate of forced SIC and MSLP responses.

Ocean assimilation coupled pacemaker experiments are run using the low-resolution Community Earth System Model, version 1.0.3 (CESM1; Shields et al. 2012; Chikamoto et al. 2015a). This version of CESM1 uses the Community Atmosphere Model, version 4 (CAM4), and has atmosphere and land spectral T31 (~3.75°) horizontal resolution and ocean and sea ice of approximately 3.75° horizontal resolution. CMIP5 anthropogenic and natural forcings are used, based on the CMIP5 historical and RCP4.5 (after 2005) scenarios, including greenhouse gases, aerosols, stratospheric ozone, solar variations, and volcanic eruptions.

The CESM1 pacemaker experiments assimilate observed three-dimensional temperature and salinity anomalies (ORAS4; Balmaseda et al. 2013) into the ocean component of the coupled model. Data in sea ice regions are not assimilated, so temperature anomalies in the sea ice region are not constrained by observations and sea ice variations are completely controlled by the internal dynamics. Because these experiments assimilate anomalies rather than absolute fields, the assimilation takes into account model biases related to the climatology, as well as having an externally forced component. Based on this, the assimilation runs have the same climatology and externally forced component as the historical runs. Therefore, the difference between assimilation runs and historical runs is the first order representation of internal climate variability.

Four CESM1 ensemble experiments with a partial assimilation approach in global or regional oceans similar to Chikamoto et al. (2015b) are conducted for the time period 1979–2013, with 10 ensemble members each:

- historical scenario (CESM1-HIST; historical forcings, no assimilation),
- global ocean assimilation (CESM1-GLOB; historical forcings, with global ocean assimilated, excluding sea ice regions),
- equatorial Pacific Ocean assimilation (CESM1-eqPAC; historical forcings, with the entire equatorial Pacific

Ocean between 10°S and 10°N assimilated,¹ remaining ocean unconstrained), and

- Atlantic Ocean assimilation (CESM1-ATL; historical forcings, with Atlantic Ocean between 30°S and 70°N assimilated, remaining ocean unconstrained).

To complement the CESM1 pacemaker experiments, wind stress assimilation pacemaker experiments are conducted using an updated version of the Second Generation Canadian Earth System Model (CanESM2; Arora et al. 2011) with an improved representation of ocean mesoscale eddy transfer coefficients (Saenko et al. 2016). CMIP5 anthropogenic forcings are applied in all experiments, based on the CMIP5 historical and RCP4.5 (after 2005) scenarios, including greenhouse gases, aerosols, and stratospheric ozone. Half of the ensemble members also include solar variations and volcanic eruptions, while the other half do not. As the influence of these natural forcings over the latter part of the experimental period has been shown to be small (Saenko et al. 2016; Sigmond and Fyfe 2016), the two subsets are combined. As in Sigmond and Fyfe (2016), results are very similar between the two subsets (not shown).

The CanESM2 pacemaker experiments assimilate the wind stress felt by the ocean, using the monthly surface wind stress field from ERA-Interim, which is closely constrained by observations. Three CanESM2 ensemble experiments with surface wind stress assimilation in global or regional oceans as in Saenko et al. (2016) and Sigmond and Fyfe (2016) are conducted for the time period 1979–2012 (note that 2013 is not available for these CanESM2 experiments), with 10 ensemble members each:

- climatology (CanESM2-CLIM; time-varying historical forcings, with annually repeating climatological global wind stress assimilated),
- global wind stress assimilation (CanESM2-GLOB; time-varying historical forcings, with monthly evolving global wind stress assimilated), and
- tropical wind stress assimilation (CanESM2-TROP; time-varying historical forcings, with monthly evolving wind stress between 35°S and 35°N across all three ocean basins assimilated).

For CanESM2, all experiments include historical forcings, but only the time-varying assimilation experiments include internal variability in the assimilated wind stress field. The experiments have similar although not identical climatologies (CanESM2-CLIM annually repeating wind

¹ Note that this differs from the experimental setup of Kosaka and Xie (2013), in which only the eastern equatorial Pacific was assimilated.

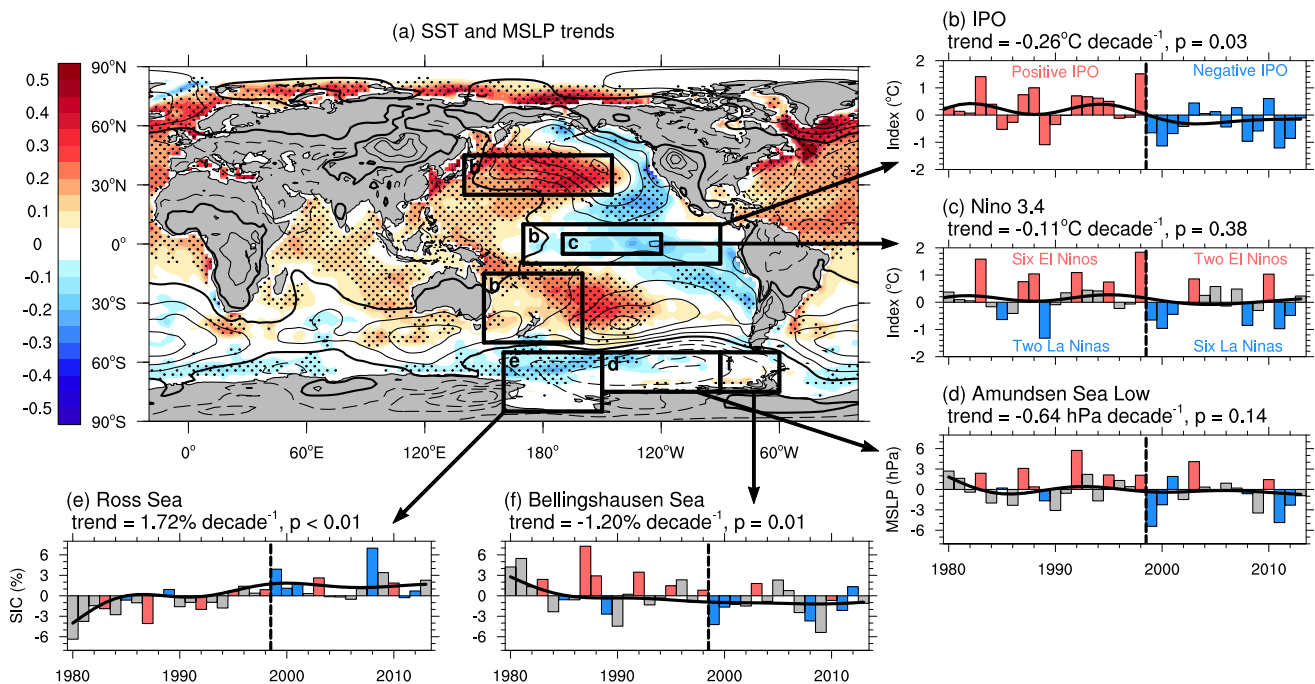


FIG. 1. (a) SST and MSLP trends ($^{\circ}\text{C}$ and hPa decade^{-1}) over 1979–2013. SST is shown in color (blue for negative and red for positive) with MSLP contours overlain [from -2 (dashed) to 2 (solid) by $0.2 \text{ hPa decade}^{-1}$, with the zero contour thickened]. Stippling indicates statistical significance of SST trends at the 95% confidence level using a two-sided Student's t test. Area-averaged time series for the regions indicated by black boxes: (b) unfiltered IPO (positive phase in red and negative phase in blue), with the filtered IPO (calculated from HadISST; Henley et al. 2015) shown by the black curve, (c) Niño-3.4 index, (d) Amundsen Sea low MSLP, (e) Ross Sea SIC, and (f) Bellingshausen Sea SIC. The transition from positive IPO to negative IPO is marked with a dashed black line. In (c)–(f) El Niño events in red, La Niña events in blue, neutral years in gray, and 13-yr low-pass-filtered time series overlain in black.

stress is based on 1979–84, while CanESM2-GLOB and CanESM2-TROP wind stress covers 1979–2012; Fig. S1 in supplementary material). We again assume that the difference between the time-varying assimilation experiments (CanESM2-GLOB and CanESM2-TROP) and the climatology assimilation (CanESM2-CLIM) provides an estimate of the internal variability. This has previously been shown to be reasonable (Sigmond and Fyfe 2016).

b. Analysis methods

For comparison between observations and models, all data are first bilinearly interpolated to a $2^{\circ} \times 2^{\circ}$ horizontal grid. All data are then annually averaged over the typical ENSO-cycle year (May through to the following April and referred to using the year of the January–April; Fig. 1). This averaging year is chosen to keep ENSO signals together (e.g., Fogt and Bromwich 2006). Data from May 1979 to April 2013 are analyzed (May 1979–April 2012 for CanESM2), and we refer to this period as 1979–2013. The seasonality of teleconnections has previously been shown to be important (e.g., Jin and Kirtman 2009; Li et al. 2014, 2015a,b; Simpkins et al. 2014). Here we focus on the annual average from May to April but have also assessed seasonal averages, which are

presented in the supplementary material (see Figs. S2–S9 in supplementary material) and discussed briefly below.

To characterize ENSO we use SST anomalies in the Niño-3.4 region (5°S – 5°N , 170°E – 120°W ; Fig. 1), with anomalies referenced to the full period, 1979–2013. El Niño and La Niña events are defined here as situations when the Niño-3.4 index exceeds ± 0.75 standard deviations (based on the full 12-month average; Fig. 1c). Sensitivity to the choice of ENSO index and threshold are tested, and results are found to be robust. To define the IPO we use the tripole index (TPI) as in Henley et al. (2015), calculated as equatorial Pacific SST anomalies (10°S – 10°N , 170°E – 90°W) minus averaged midlatitude SST anomalies (25° – 45°N , 140°E – 145°W and 50° – 15°S , 150°E – 160°W ; Fig. 1b). Notably, we do not filter the IPO index. This is because we are interested in both the long-term trend in the IPO, which is in itself a low-pass filter analysis, as well as its interannual variations (e.g., for calculating the interannual regression with SIC). Without filtering, the TPI strongly resembles the Niño-3.4 index (e.g., Newman et al. 2016); however, the TPI also takes into account variability in midlatitude regions (black boxes marked with the letter b in Fig. 1a), important when considering the influence of the tropical Pacific on the high latitudes. Over the period assessed here, while there

has been no significant trend in the Niño-3.4 index ($p = 0.38$), there has been a significant trend in the unfiltered IPO TPI ($p = 0.03$; Figs. 1b,c) due to the transition from positive to negative that occurred in the late 1990s (e.g., Lee and McPhaden 2008). Here we assume that the “trend” arises from subsampling multidecadal climate variability, not from changes in external forcing. This is supported by the fact that the historical CMIP5 experiments do not capture a phase shift of the IPO during this time (not shown). As such, there are important differences between the IPO and the Niño-3.4 index emanating from the off-equatorial components of the IPO (Fig. 1a).

Linear trends in SIC and MSLP are calculated using least squares regression. Observed trend significance is determined using a two-sided Student’s t test at the 95% confidence level. Autocorrelation was accounted for by defining the effective sample size N_{eff} as follows:

$$N_{\text{eff}} = N(1 - r_1)/(1 + r_1), \quad (1)$$

where N is the sample size and r_1 is the lag-1 autocorrelation of the detrended SIC time series (Simpkins et al. 2012). The CMIP5 forced response for the period of interest is then subtracted from the observed trends to provide a rough estimate of unforced long-term trends in the observations.

For both CESM1 and CanESM2, trends are calculated for each ensemble member and then averaged (10 runs per ensemble). Ensemble average trend significance is determined when the simulated ensemble mean trend exceeds two standard deviations of individual ensemble member trends ($\sim 95\%$ confidence level). Difference trends between assimilation runs and the historical or climatology runs are also calculated for each model (e.g., CESM1-GLOB minus CESM1-HIST). Difference trend significance is determined using the Student’s t test to compare two means at the 95% confidence level.

IPO-related trends in SIC and MSLP are calculated as the IPO trend (arising from internal decadal time-scale variability) multiplied by the regression coefficient between the linearly detrended IPO and linearly detrended SIC or MSLP (e.g., Purich et al. 2013; Clem and Fogt 2015). Significance of the observed IPO-related trends is assessed using a two-sided Student’s t test at the 95% confidence level, testing both the IPO trend and the regression coefficient. Autocorrelation in the regression coefficient significance test was accounted for by defining the effective sample size N_{eff} as follows:

$$N_{\text{eff}} = N(1 - r_1 r_2)/(1 + r_1 r_2), \quad (2)$$

where N is the sample size, r_1 is the lag-1 autocorrelation of the detrended SIC time series, and r_2 is the lag-1

autocorrelation of the IPO time series (Ciastra and Thompson 2008). Modeled significance is determined when the average modeled trend exceeds two standard deviations of modeled trends ($\sim 95\%$ confidence level).

To examine how the modulation of ENSO events via the IPO has contributed to changes in the Amundsen Sea low and to the regional SIC surplus (e.g., Ross Sea) and deficit (e.g., Bellingshausen Sea), observed cumulative maps are calculated for SIC and MSLP. This procedure is similar to calculating composites but without dividing by the number of events. The benefit of using cumulative anomaly maps in this case is that the magnitude of different cumulative anomalies can be directly compared. For example, the cumulative anomalies during all years of the negative phase of the IPO can be directly compared to the cumulative anomalies during only the ENSO years of this IPO phase to see what contribution the ENSO years make to the total cumulative anomalies. Significance is calculated using the Student’s t test to compare two means at the 95% confidence level (e.g., El Niño years vs all years, La Niña years vs all years, and El Niño years vs La Niña years). The sample size is defined as the number of events in the smallest group being compared.

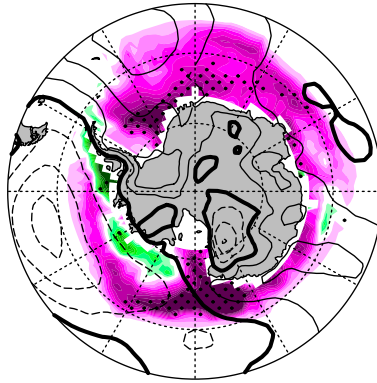
3. Results

a. Observed trends

The observed annual mean SIC trend pattern with the external CMIP5 forcing signal removed² (Fig. 2a) looks similar to the total trend pattern (Fig. 3a). Significant increases in SIC are seen around much of Antarctica (Fig. 2a; magenta shading; Stammerjohn et al. 2008; Holland and Kwok 2012; Simpkins et al. 2012), with a particularly strong increase in the Ross Sea. Smaller areas of significant decreases in SIC are seen in the Amundsen and Bellingshausen Seas (Fig. 2a; green shading). In these areas the observed sea ice decline (Fig. 3a) is stronger than the CMIP5 ensemble trend (Fig. 4a). The observed SIC trend pattern shows similarity to the SIC composite difference pattern for ENSO events (Stammerjohn et al. 2008; Simpkins et al. 2012; Ciastra et al. 2015). This motivates further investigation into the role of the tropical Pacific SST anomalies in influencing Antarctic

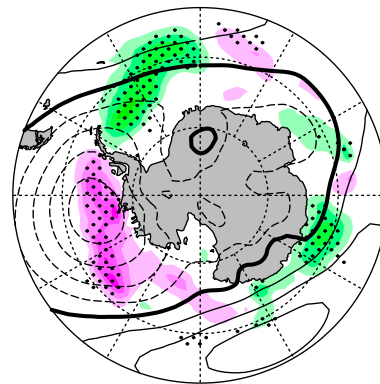
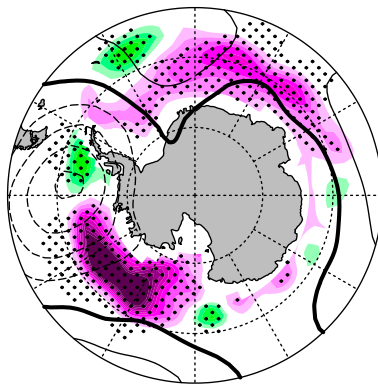
² When removing the external CMIP5 forcing signal, the CMIP5 multimodel mean trend is simply subtracted from the observed trend. As such, Fig. 2a also incorporates the differences in sea ice distributions between the models and observations, although this contributes little to the overall trends displayed.

(a) Observed minus CMIP5 MMM



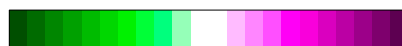
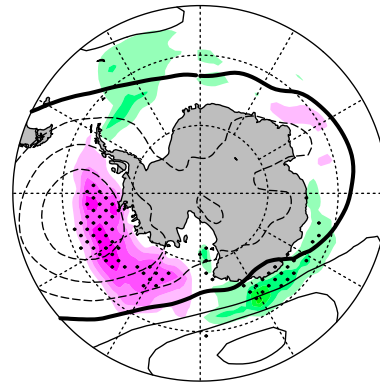
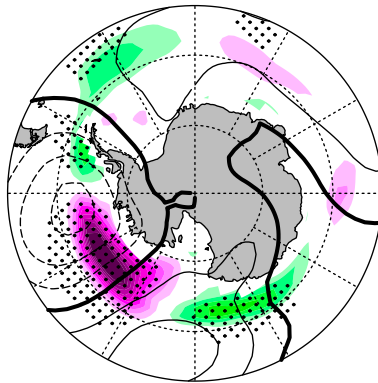
(b) CESM1-GLOB minus HIST

(c) CanESM2-GLOB minus CLIM



(d) CESM1-eqPAC minus HIST

(e) CanESM2-TROP minus CLIM



-5 -4 -3 -2 -1 0 1 2 3 4 5

SIC trend (% decade⁻¹)MSLP contours from -2 (dashed) to 2 (solid) by 0.2 hPa decade⁻¹

FIG. 2. SIC and MSLP trends (% and hPa decade⁻¹), with trends due to historical forcings removed: (a) observed minus CMIP5 multimodel ensemble, (b) CESM1-GLOB minus CESM1-HIST, (c) CanESM2-GLOB minus CanESM2-CLIM, (d) CESM1-eqPAC minus CESM1-HIST, and (e) CanESM2-TROP minus CanESM2-CLIM. In all panels, SIC is shown in color (green for negative and magenta for positive) with MSLP contours overlain (dashed for negative, thick for zero, and solid for positive contours). Ensemble average trends are calculated over 1979–2013 using annually averaged SIC. Stippling indicates statistical significance of SIC trends at the 95% confidence level using a two-sided Student's *t* test in (a) and using the Student's *t* test to compare two means in (b)–(e).

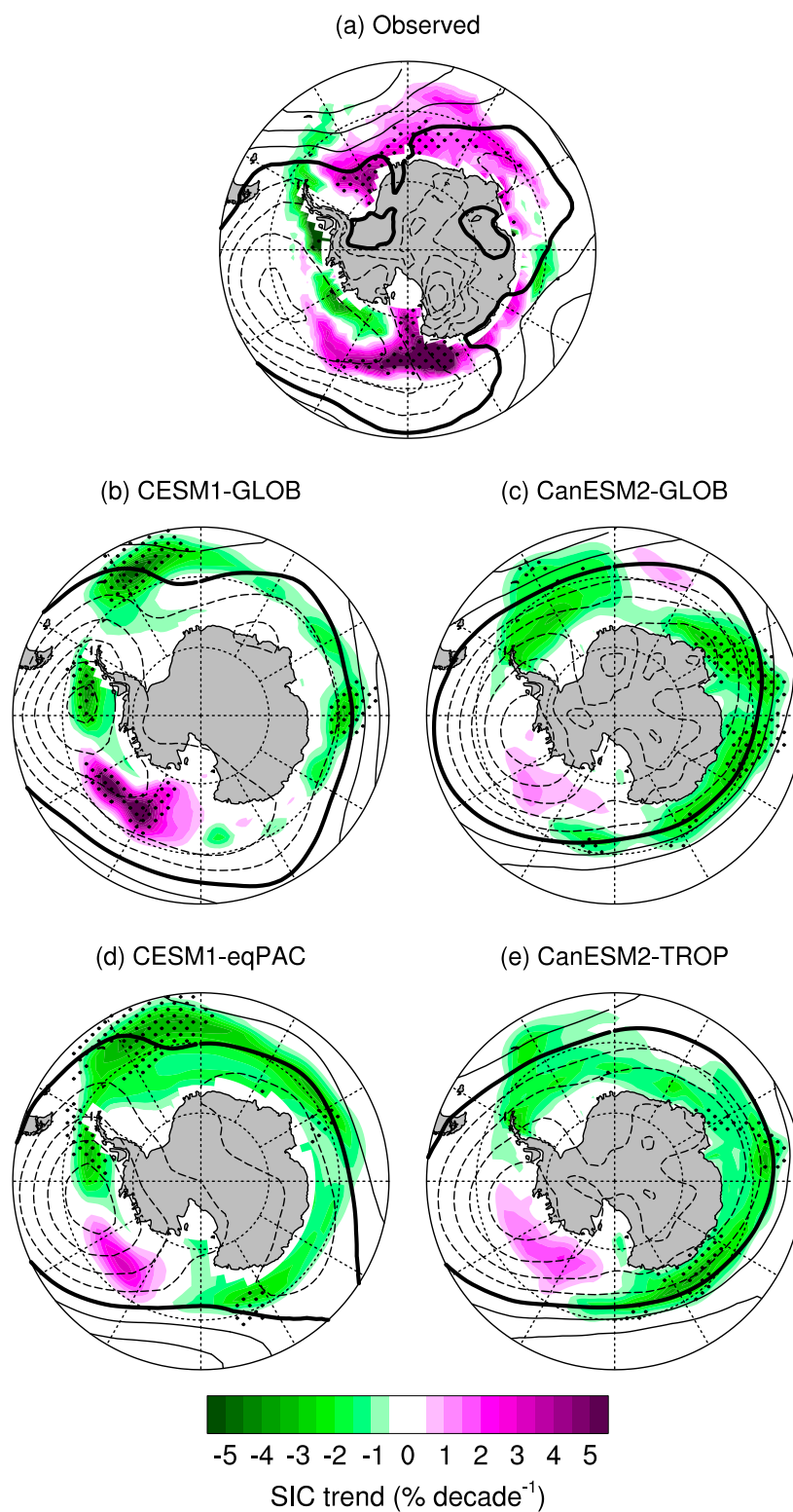


FIG. 3. As in Fig. 2, but showing total SIC and MSLP trends (i.e., including trends due to natural variability and historical forcings).

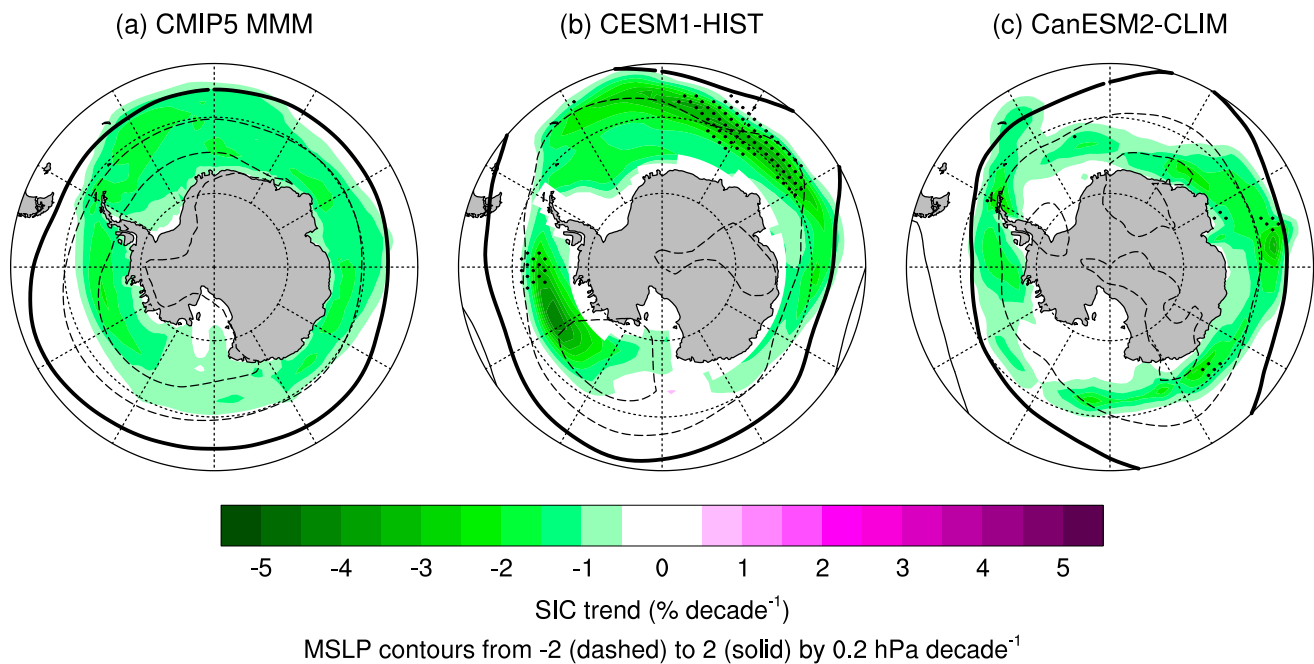


FIG. 4. As in Fig. 2, but showing the SIC and MSLP trends due to historical forcings: (a) CMIP5 multimodel mean, (b) CESM1-HIST, and (c) CanESM2-CLIM.

SIC trends, particularly the dipole SIC trends between the Ross and Bellingshausen Seas.

b. Pacemaker trends

If decadal SST variability in the tropical Pacific is remotely influencing Antarctic SIC trends via changes to the atmospheric circulation, assuming that atmospheric teleconnections are adequately represented in the models, we would expect that coupled model experiments in which tropical Pacific SST variability matches the observations should simulate SIC trends similar to those observed. Therefore, we next consider the SIC trends from the pacemaker experiments. As described above (section 2a), the ocean assimilation runs have the same climatology and externally forced component as the historical runs. Therefore, we assume that subtracting CESM1-HIST from both CESM1-GLOB and CESM1-eqPAC gives a first-order estimate of the internal (linearly unforced) variability. Similarly, we interpret the difference between CanESM2-GLOB and CanESM2-TROP from CanESM2-CLIM as a rough linear indicator of internal variability with the caveats discussed above. Subtracting out the CESM1-HIST or CanESM2-CLIM trends (Figs. 4b,c) from the assimilation trends (Figs. 3b–e) thus provides a first-order estimate of the decadal variability without the influence of anthropogenic forcings such as increasing greenhouse gases, aerosols, and stratospheric ozone depletion; that is, this method highlights the influence of tropical teleconnections, as well as the decadal component

of the SAM trend due to tropical interactions and intrinsic variability.

We note that the forced trends as simulated by the CMIP5 multimodel mean (Fig. 4a), CESM1-HIST (Fig. 4b) and CanESM2-CLIM (Fig. 4c) are similar, although the CMIP5 multimodel mean is more zonally symmetric, as expected because of averaging across 41 different models. In all panels of Fig. 4, the positive trend in the SAM is seen through the negative MSLP trend encompassing the Antarctic continent. In the CMIP5 multimodel mean there is a circumpolar decrease in SIC, and while there are regions in CESM1-HIST and CanESM2-CLIM where there are very weak or no trends in SIC, most regions also show a decrease. As such, subtracting the forced trends (Fig. 4) from the total trends (Fig. 3) to obtain the decadal variability signal (i.e., trends due to internal variability; Fig. 2) has the result of weakening the negative MSLP trends over the Antarctic continent that are also seen in Fig. 3 and of largely reducing the vast areas of total decreasing SIC seen in both the CESM1 (Figs. 3b,d) and CanESM2 (Figs. 3c,e) simulations. Because the CMIP5 multimodel mean SIC trend is largely zonally symmetric (Fig. 4a), subtracting this from the total observed SIC trend (Fig. 3a) does not substantially change the regional pattern of SIC trends in the observed decadal variability signal, although decreases are made weaker and increases are made stronger (Fig. 2a).

CESM1-GLOB decadal variability (minus HIST) signals (Fig. 2b) in SIC and MSLP look qualitatively

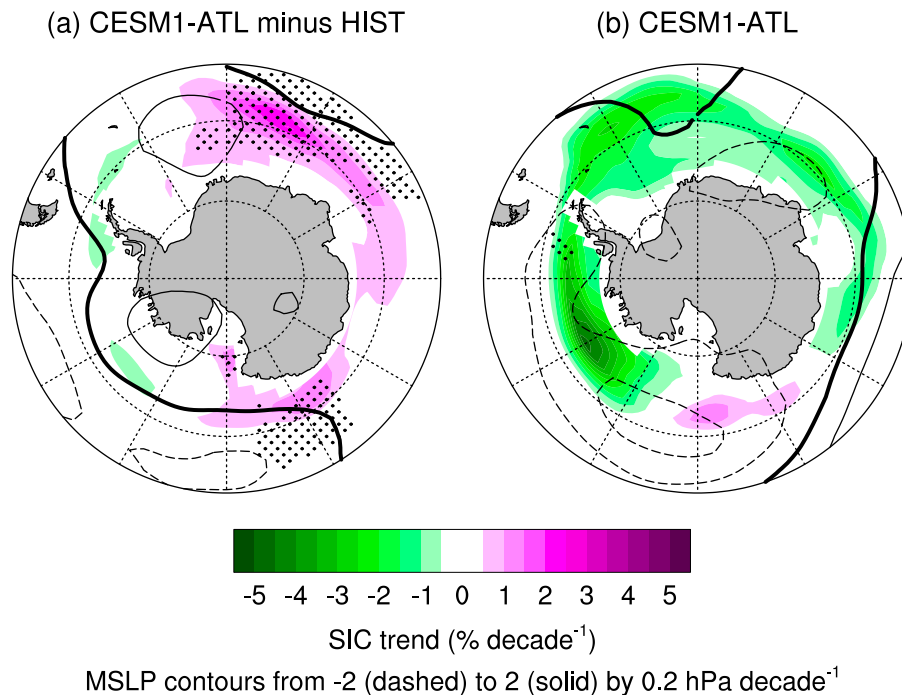


FIG. 5. As in Fig. 2, but showing CESM1 trends from the Atlantic assimilation: (a) CESM1-ATL minus HIST and (b) CESM1-ATL trends (i.e., including trends due to natural variability and historical forcings).

similar to the observed trends (Fig. 2a); there are large regions of increasing SIC in eastern Antarctica and in the eastern Ross and Amundsen Seas (although notably the observed increasing SIC in the western Ross Sea is not captured), while a decrease in SIC is seen in the Bellingshausen Sea. A strengthening of the Amundsen Sea low is apparent; however, the strongest decrease in MSLP is located farther toward the Antarctic Peninsula than observed and does not extend as far west. As a result, the strong increase in the Ross and Amundsen Sea SIC is shifted eastward compared to the satellite data. Meehl et al. (2016a) show that the position of the convective heating anomaly in the tropical Pacific influences the location of the resulting teleconnection, so these biases may be due to differences in the position of tropical Pacific precipitation anomalies between observations and CESM1.

CESM1-eqPAC decadal variability signals (Fig. 2d) show very similar trends in MSLP to CESM-GLOB (Fig. 2b), along with decreasing SIC in the Bellingshausen Sea and increasing SIC in the eastern Ross and Amundsen Seas, suggesting that tropical Pacific variability is driving signals in these regions in CESM1-GLOB (Fig. 2b). The overall MSLP pattern in these experiments is consistent with the PSA pattern. Elsewhere, CESM1-eqPAC trend signals do not resemble CESM1-GLOB signals; however, increasing SIC in CESM1-ATL (Fig. 5) suggests that Atlantic SST anomaly forcing is driving the

CESM1-GLOB signals in the Atlantic and Indian Ocean sectors. Further, while CESM1-eqPAC variability shows a weak decrease in the eastern Ross Sea (Fig. 2d), CESM1-ATL variability shows an increase (Fig. 5a). It also appears that CESM1-eqPAC and CESM1-ATL forcings are largely additive (as in Li et al. 2015b), explaining the majority of the decadal SIC signals in CESM1-GLOB. We note that the increase in SIC in the eastern Ross and Amundsen Seas is slightly weaker in CESM1-eqPAC (Fig. 2d) compared to CESM1-GLOB (Fig. 2b), suggesting that a portion of this decadal signal must come from outside of the tropical Pacific and Atlantic Oceans, likely from the extratropics.

In Li et al. (2015b) tropical Atlantic forcing, rather than Pacific forcing, leads to the strongest deepening of the Amundsen Sea low. Li et al. (2015b) use CAM4, the same atmospheric component of CESM used in this study, although at a higher resolution (approximately 2° horizontal resolution, compared to approximately 3.75° resolution here) and with a different dynamical core (a finite-volume core, compared to a spectral core here). However, Li et al. (2015b) used Atmospheric Model Intercomparison Project (AMIP)-type specified SST forcing compared to the partially coupled experiments here. Previous studies have suggested the lack of coupling in AMIP-type runs can cause errors in the atmospheric response by responding too strongly in certain regions to SST perturbations (e.g., Barsugli and Battisti 1998).

In convective heating anomaly experiments designed to specify the actual dynamic heating that forces teleconnections (as opposed to SST), negative convective heating anomalies in the eastern equatorial Pacific (arising from the observed negative phase of the IPO) produced a stronger response in the Amundsen Sea low compared to a positive convective heating anomaly (arising from observed positive tropical Atlantic SSTs; Meehl et al. 2016a). Thus, there are contributions to the deepening of the Amundsen Sea low from convective heating anomalies in both the tropical Atlantic and tropical Pacific, but evidence from Meehl et al. (2016a) shows that the equatorial eastern Pacific makes the larger contribution. Other differences in the dominance of Atlantic or Pacific teleconnections may be due to resolution and/or dynamical differences in the atmospheric model, to differences arising from the coupled system, and/or to differences in the SST fields assimilated (total observed SST, compared to observed SST anomalies here) as well as the differing climatologies that follow.

We next compare results from CESM1 to CanESM2 (Figs. 2c,e). While both models show a strengthening of the Amundsen Sea low, the wave train structure differs. In contrast to the clear PSA pattern displayed by CESM1 (Figs. 2b,d), CanESM2 shows a positive MSLP signal farther west. Both CanESM2-GLOB (Fig. 2c) and CanESM2-TROP (Fig. 2e) show an increase in sea ice in the Amundsen and eastern Ross Seas, as also simulated by CESM1, and the decrease in the western Ross Sea seen in CESM1-eqPAC is also seen in CanESM2-TROP. Whereas CESM1 captures the observed decrease in sea ice in the Bellingshausen Sea, CanESM2 decadal variability shows an increase here but a decrease in the Weddell Sea (CanESM2-GLOB), possibly due to the eastward elongation of the negative MSLP signal. While there are differences in the decadal variability signals of SIC and MSLP between CESM1 and CanESM2, both models capture a strengthening of the Amundsen Sea low and the corresponding increase in sea ice in the Amundsen and eastern Ross Seas.

c. Seasonality of trends

While our focus is on annual mean trends, patterns do vary seasonally (L'Heureux and Thompson 2006; Simpkins et al. 2012; Ciasto et al. 2015). We briefly discuss the seasonality of the observed and simulated SIC and MSLP trends, noting that trends in CESM1-GLOB and CESM1-eqPAC are largely similar, and likewise for CanESM2-GLOB and CanESM2-TROP; as such, we group the simulations from each model together in our discussion.

Observed decadal variability signals in SIC during austral summer (Fig. S2a) and autumn (Fig. S3a) show

decreasing SIC in the Amundsen and Bellingshausen Seas and increases elsewhere. However, CESM1 (Figs. S2b,d and S3b,d) and CanESM2 (Figs. S2c,e and S3c,e) show an increase in SIC in the Amundsen Sea and little trend in the western Ross Sea. In austral winter (Fig. S4a) and spring (Fig. S5a) the region of observed decreasing SIC shifts eastward to the Antarctic Peninsula, with increases elsewhere. Both models show an increase in SIC in the eastern Ross and Amundsen Seas, and CESM1 shows a decrease in SIC in the Bellingshausen Sea (Figs. S4b,d and S5b,d). The biases in seasonal SIC variability are rendered in the annual mean (Fig. 2).

While a strengthening of the Amundsen Sea low is seen for observations and both CESM1 and CanESM2 in the annual mean (Fig. 2), this signal is largely due to strengthening occurring during austral autumn and winter (Figs. S3 and S4, respectively). During summer, there is a strong positive SAM trend in the forced trends simulated by the CMIP5 multimodel mean, CESM1-HIST, and CESM1-CLIM (not shown). When subtracted to obtain decadal variability, only a weak negative MSLP signal is seen in observations over the eastern Ross Sea (Fig. S2a). In CESM1 there is a weak negative signal located over the Bellingshausen Sea (Fig. S2b,d). In CanESM2, despite removing the SAM trend there is a clear deepening of the Amundsen Sea low (Fig. S2c,e). During autumn, a clear PSA wave train pattern is evident in observations, as also reported in Ding and Steig (2013). Both models capture the PSA pattern, although it is weaker than observed, particularly in CanESM2. In winter the wave train pattern is more meridionally oriented in observations and for CESM1. A similar negative MSLP signal is seen in both models during spring (Fig. S5); however, in observations the signal is centered over the eastern Ross Sea rather than over the Amundsen and Bellingshausen Seas (Fig. S5a). While PSA-like wave trains are shown by CESM1 and CanESM2, a more meridionally oriented wave train is seen in observations (Clem and Fogt 2015).

d. IPO-related sea ice trends

We next examine the contribution of tropical decadal SST variability on Antarctic sea ice in these pacemaker experiments. Based on the similarity between decadal variability SIC and MSLP signals in the Pacific sector in CESM1-GLOB and CESM1-eqPAC (cf. Figs. 2b and 2d), we focus on tropical Pacific variability. Because of the experimental setup, all tropical variability for CanESM2 is considered (i.e., CanESM2-TROP; including Pacific, Atlantic, and Indian Oceans). We calculate SIC and MSLP trends congruent with decadal variability in the IPO, which is manifested as a trend from positive to negative in subsampling multidecadal variability, using

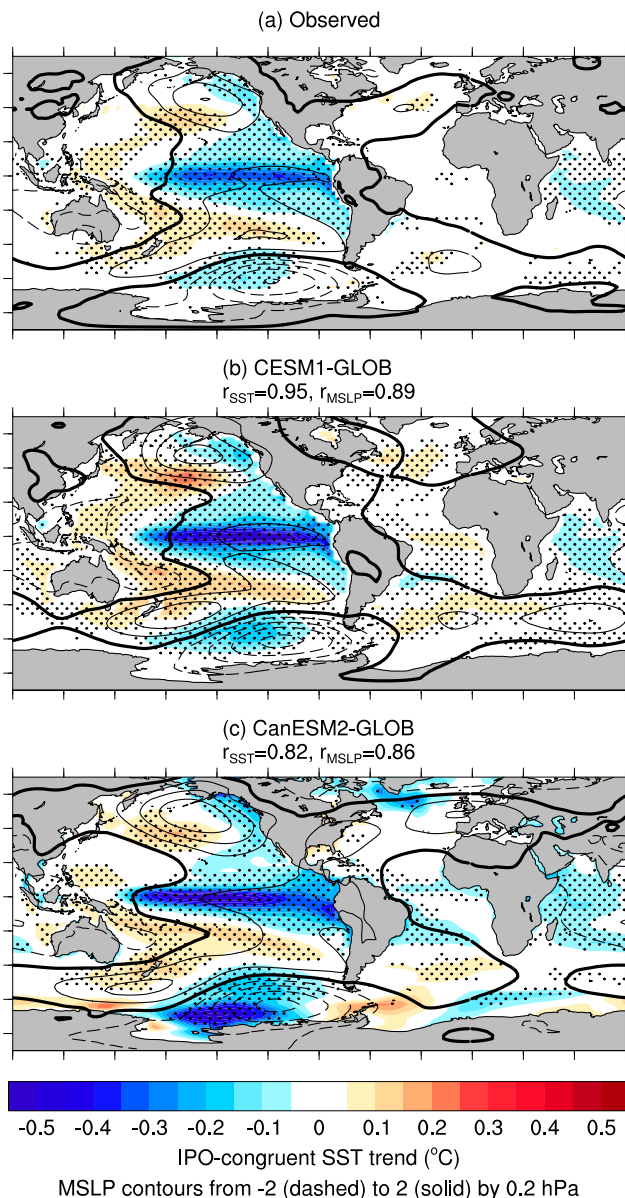


FIG. 6. SST and MSLP trends congruent with trends in the IPO because of its transition from positive to negative ($^{\circ}\text{C}$ and hPa decade^{-1}): (a) observed, (b) CESM1-GLOB, and (c) CanESM2-GLOB. Congruent trends are calculated over 1979–2013 as the linear regression of detrended SST onto the detrended IPO, multiplied by the trend in the IPO. In (b),(c), congruent trends are calculated for each ensemble member individually and then averaged across members. Stippling indicates statistical significance of SST trends at the 95% confidence level, using a two-sided Student's t test in (a) to test significance of both the IPO trend and the regression coefficient and where the ensemble average trend exceeds two standard deviations in (b),(c). Pattern correlations between observed in (a) and modeled trends are calculated over the global domain and indicated above (b),(c).

an unfiltered TPI to represent the IPO. As described above (section 2b), without filtering the TPI strongly resembles the Niño-3.4 index (cf. Figs. 1b and 1c; Newman et al. 2016); however, the TPI also takes into

account variability of subtropical and midlatitude regions, which could be potentially important when considering the influence of the tropical Pacific on the high latitudes [such as the influence of the South Pacific convergence zone (SPCZ); e.g., Schneider et al. 2012; Clem and Renwick 2015; Meehl et al. 2016a]. As also mentioned above (section 2b), while there has been no significant trend in the Niño-3.4 index, there has been a significant trend in the IPO during the time period under consideration as a result of the transition from the positive phase of the IPO to negative in the late 1990s (Figs. 1b,c). There have also been changes in the frequency (more La Niña than El Niño events; e.g., Ummenhofer et al. 2009) and spatial characteristics (more central Pacific than eastern Pacific El Niño events; e.g., McPhaden et al. 2011) of ENSO. These ENSO changes coincide with the IPO transitioning from the positive to the negative phase (Figs. 1 and 6; Lee and McPhaden 2008; Meehl et al. 2014; Fyfe et al. 2016) and motivate our interest in the significant trend of the IPO.

The observed IPO-related SIC trends (Fig. 7a) show a decrease in the Bellingshausen Sea and an increase in the eastern Ross and Amundsen Seas, in association with a strengthened Amundsen Sea low (Fig. 7a). This pattern is similar to the trend pattern in the Pacific sector (Fig. 1a), albeit weaker, and the region of increasing SIC is shifted eastward. In particular, the IPO-related SIC trends (Fig. 7a) cannot account for the observed increase in the western Ross Sea (Figs. 2a and 3a). CESM1-HIST shows essentially no congruent trends (not shown), as expected because the unconstrained ensemble members all have different phases of the IPO, which cancel out in the ensemble average. This also indicates that the external forcing is not causing one phase of the IPO to be favored. IPO-related SIC and MSLP trends in CESM1-GLOB (Fig. 7b) and CESM1-eqPAC (not shown but similar to Fig. 7b) both agree well with the observations, showing a deepening of the Amundsen Sea low as part of the PSA pattern as well as a corresponding positive SIC trend in the eastern Ross and Amundsen Seas and a negative SIC trend in the Bellingshausen Sea. Further, these IPO-related SIC trends are very similar to the decadal variability signals discussed above (Figs. 1b,c). CanESM2-GLOB (Fig. 7c) and CanESM2-TROP (not shown but similar to Fig. 7c) also show similar IPO-related SIC and MSLP trends. The pattern correlations between simulated and observed congruent trends are high for both models, particularly for MSLP (Fig. 7). The agreement between the IPO-related SIC trends and total SIC trends thus suggest that the IPO is contributing to the regional dipole pattern of SIC trends in the Pacific sector, with the exception of the

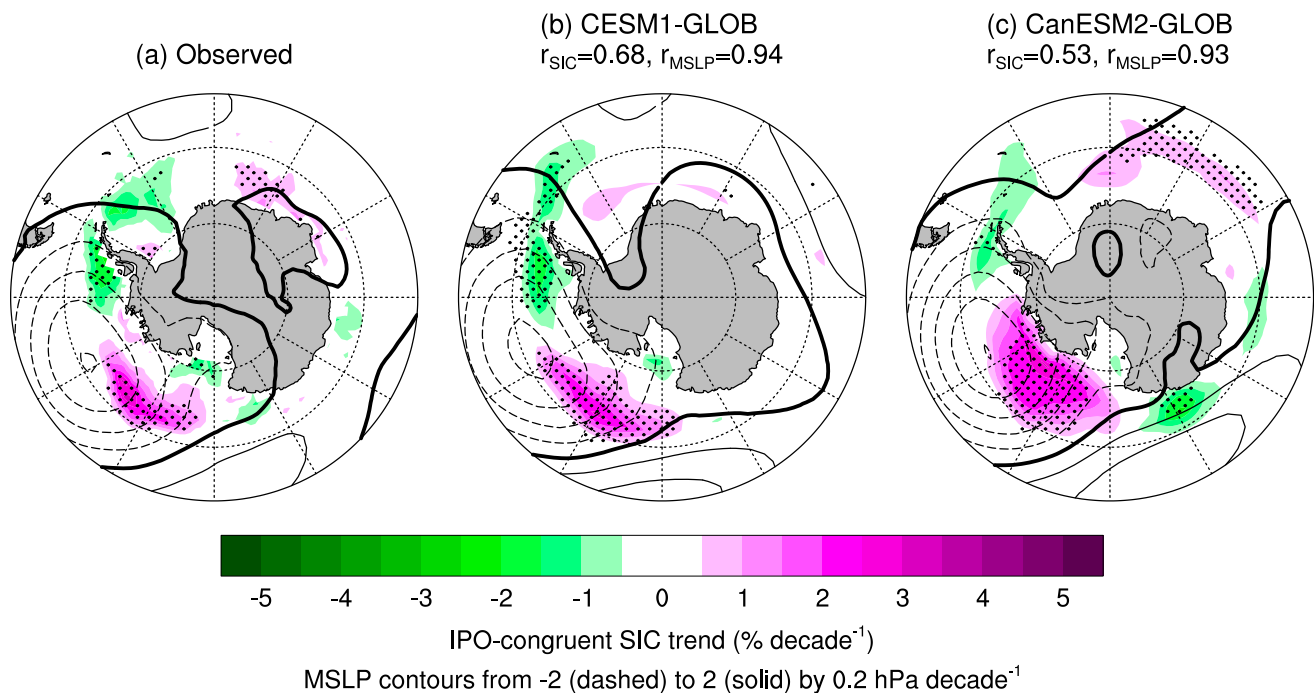


FIG. 7. As in Fig. 6, but for SIC and MSLP trends congruent with trends in the IPO because of its transition from positive to negative (% and hPa decade⁻¹). Pattern correlations are calculated over the domain shown (50°–90°S).

western Ross Sea, where the observed SIC increase is not explained by the IPO or simulated by either model (Figs. 2b,c and 3b,c).

The IPO-related SIC and MSLP trends are largely similar across all seasons (see Figs. S6–S9 in the supplementary material). A strengthened Amundsen Sea low is seen in all seasons, strongest during austral winter and spring in observations and CESM1-GLOB and strongest from austral autumn to spring in CanESM2-GLOB. Increased SIC in association with these circulation changes is seen in the eastern Ross and Amundsen Seas in all seasons for observations, CESM1-GLOB, and CanESM2-GLOB. Decreased SIC in the Bellingshausen Sea is also seen for most seasons and across the observations and both models; however, it often lacks significance and is not seen for CanESM2-GLOB during austral summer (Fig. S6c). Overall, the strong agreement between the observations, CESM1, and CanESM2 and the similarity in IPO-related SIC trends across the seasons strengthens the conclusions made above regarding the annual-mean IPO-related trends.

e. IPO modulation of ENSO teleconnection

Meehl et al. (2016a) proposed that Ross Sea SIC trends have been influenced by the phase shift of the IPO (Fig. 1b). In their study, they find that changes in precipitation and convective heating primarily in the eastern Pacific and secondarily in the SPCZ region associated with the phase shift of the IPO in the late 1990s

force anomalous Rossby waves, teleconnecting to the Amundsen Sea low and causing a strengthening (as also described in Schneider et al. 2012; Clem and Renwick 2015). From this, they infer that changes in the geostrophic wind result in more southerly flow over the Ross Sea, leading to increased sea ice in this region. In addition to increased Ross Sea ice, other studies relating the strengthened Amundsen Sea low to Antarctic sea ice trends also find reduced sea ice in the Bellingshausen Sea because of increased northerly flow, (e.g., Li et al. 2014; Simpkins et al. 2014). We have confirmed here that the regional SIC trend characteristics associated with the IPO are a result of a deepening of the Amundsen Sea low (Fig. 7).

As described above (section 1), the ENSO teleconnection to Antarctic sea ice has been widely studied (e.g., Renwick 2002; Stammerjohn et al. 2008; Simpkins et al. 2012; Ciasto et al. 2015). Despite no significant trend in the Niño-3.4 index over 1979–2013, during the positive phase of the IPO more El Niño events occurred (between 1979 and 1998 there were six El Niño and two La Niña events; Fig. 1c), whereas during the negative phase of the IPO more La Niña events occurred (between 1999 and 2013 there were two El Niño and six La Niña events; Fig. 1c). Through Rossby wave train teleconnections to the Southern Hemisphere, a change in the frequency and spatial character of ENSO could impact the strength of the Amundsen Sea low (Fig. 1d), which may lead to a rectification and a net

surplus or deficit of SIC in different regions over 1979–2013 (Figs. 1e,f). Over 1990–2007, Matear et al. (2015) found that wind forcing associated with ENSO contributed to sea ice duration trends in both the eastern and western Pacific sectors, further motivating examination of the ENSO contribution over the longer period here.

Comparing the cumulative anomalies of observed SIC and MSLP during the positive phase of the IPO with those during only ENSO years of the positive IPO (cf. Figs. 8a and 8d), it is clear that the two patterns are similar to each other, dominated by El Niño (Fig. 9a). Likewise, the cumulative anomalies during the negative phase of the IPO are similar to those during only ENSO years of the negative IPO (cf. Figs. 8b and 8e), dominated by La Niña (Fig. 9b). Following on, comparing their difference patterns (i.e., negative IPO minus positive IPO; negative IPO ENSO events minus positive IPO ENSO events; cf. Fig. 8c and 8f) shows that the ENSO cumulative anomaly pattern difference is very similar to the corresponding IPO cumulative anomaly difference and is dominated by the difference between El Niño and La Niña (Fig. 9c). We note that these results should be considered with caution, as there is a trend in the IPO as well as the SIC and MSLP time series used in this analysis. However, repeating the analysis with linearly detrended time series (not shown) finds that the spatial pattern of cumulative SIC anomalies in the eastern Ross, Amundsen, and Bellingshausen Seas that occur during the two phases of the IPO are largely explained by the ENSO events in these phases. This supports the interpretation of Fig. 8.

The total SIC trends resulting from the impact of IPO can also be understood via the unequal number of El Niño and La Niña events during each IPO phase; that is, more El Niño events during positive IPO and more La Niña events during negative IPO, as well as a change in the nature of events (Ashok et al. 2007; McPhaden et al. 2011). Furthermore, the ENSO teleconnection to high latitudes appears nonlinear and asymmetric with respect to El Niño and La Niña (Figs. 8d,e; also noted by Ciasto et al. 2015). As such, the cumulative impacts from El Niño and from La Niña do not completely offset but rectify into mean changes. These mean changes are especially conspicuous when there are more El Niño events during positive IPO and more La Niña events during negative IPO (Fig. 8f). The difference between the cumulative impact during the negative IPO phase and during the positive IPO phase accounts for a large portion of the trend, suggesting that the influence of the IPO on the Amundsen Sea low and SIC is overall manifest via its association with an unequal number of

El Niño and La Niña events during the two phases of the IPO.

4. Discussion

Since regular satellite observations became available in 1979, Antarctic SIC has increased in most regions, despite greenhouse warming over the same period (Cavalieri and Parkinson 2008; Comiso and Nishio 2008; Parkinson and Cavalieri 2012) and multimodel averages that show decreasing SIC. A particularly large increase in sea ice has been observed in the Ross Sea, although sea ice has been declining near the Antarctic Peninsula in the Amundsen and Bellingshausen Seas (Stammerjohn et al. 2008; Holland and Kwok 2012; Simpkins et al. 2012). Utilizing coupled pacemaker experiments we provide further evidence in support of internal decadal climate variability associated with the IPO as a driving influence on Antarctic sea ice trends in the Pacific sector, specifically in the eastern Ross, Amundsen, and Bellingshausen Seas. We note, however, that the IPO cannot account for sea ice trends in the western Ross Sea. Our analysis suggests that tropical Pacific SST anomalies associated with the IPO and ENSO contribute to the rectification of observed trends on Antarctic sea ice.

The pacemaker experiments assessed here are based on coupled atmosphere–ocean–sea ice models, which differ from previous studies using atmospheric-only models (Li et al. 2014, 2015a,b; Simpkins et al. 2014; Meehl et al. 2016a). This is notable because, although these studies suggest that a strengthening of the Amundsen Sea low due to tropical teleconnections can be linked to observed changes in the sea ice, the sea ice response is not directly simulated in the latter.

The majority of CMIP5 models simulate a decline in Antarctic sea ice extent (Turner et al. 2013; Zunz et al. 2013), and while the overall observed trend has been shown to lie within modeled variability (Mahlstein et al. 2013; Polvani and Smith 2013; Swart and Fyfe 2013; Turner et al. 2013; Zunz et al. 2013), when the regionality of sea ice trends is accounted for, trends during austral summer and autumn are outside the modeled range of variability (Hobbs et al. 2015). As with the majority of CMIP5 models, CESM1-HIST and CanESM2-CLIM lose too much sea ice compared to observations. However, CMIP5 ensemble members that happened to match the timing of the negative phase of the IPO also simulated an increase of Antarctic sea ice during the early 2000s (Meehl et al. 2014).

In both the CESM1 and CanESM2 assimilation experiments, the strengthened Amundsen Sea low associated with the phase shift of the IPO results in an increase in sea ice in the eastern Ross and Amundsen Seas; however, this

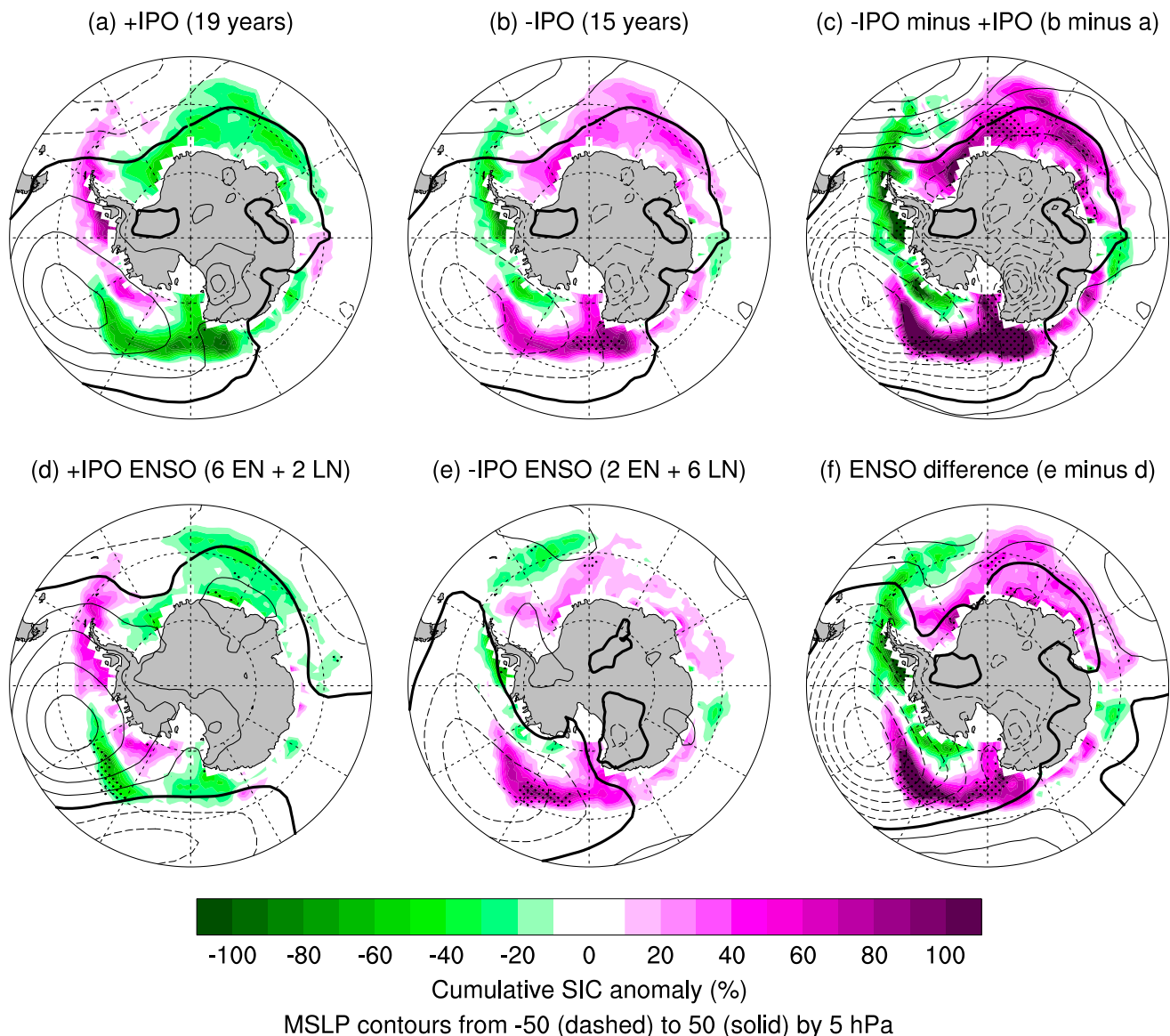


FIG. 8. Observed SIC and MSLP cumulative anomalies (% and hPa): (a) positive IPO (1979–99), (b) negative IPO (2000–13), (c) IPO difference [(b) minus (a)], (d) ENSO years during positive IPO (six El Niño and two La Niña events), (e) ENSO years during negative IPO (two El Niño and six La Niña events), and (f) ENSO difference [(e) minus (d)]. Cumulative anomalies are calculated as the sum of SIC and MSLP anomalies during specified events, without normalizing by the number of events. Stippling indicates statistical significance of cumulative SIC anomalies at the 95% confidence level using the Student's *t* test to compare two means: comparing the select events to all years in (a), (b), (d), (e) and comparing the two differenced groups in (c), (f).

increase is weaker than observed. Further, neither model captures the strong observed increase in sea ice in the western Ross Sea, and, because of the lack of IPO-related sea ice trends in this region even in observations (Fig. 7a), it is unlikely that trends in this region are linked to the IPO phase change. Sea ice increases elsewhere around Antarctica are also not simulated in these models. Based on the assessment of decadal variability signals it appears that the CESM1 and CanESM2 assimilation experiments capture the observed variability well, but one interpretation is that greenhouse warming overwhelms

the total trends in SIC in these experiments. Another possibility is that the locations of anomalous precipitation and convective heating anomalies may not be in the same locations or magnitudes as observed. It could be possible that either Antarctic sea ice variations in both CESM1 and CanESM2 are too sensitive to global warming or that these models underestimate the amplitude of decadal variability of Antarctic sea ice by an overly damped response to tropical Pacific variability. A damped response may be the result of the cold SST bias in both models in the SPCZ region, suppressing

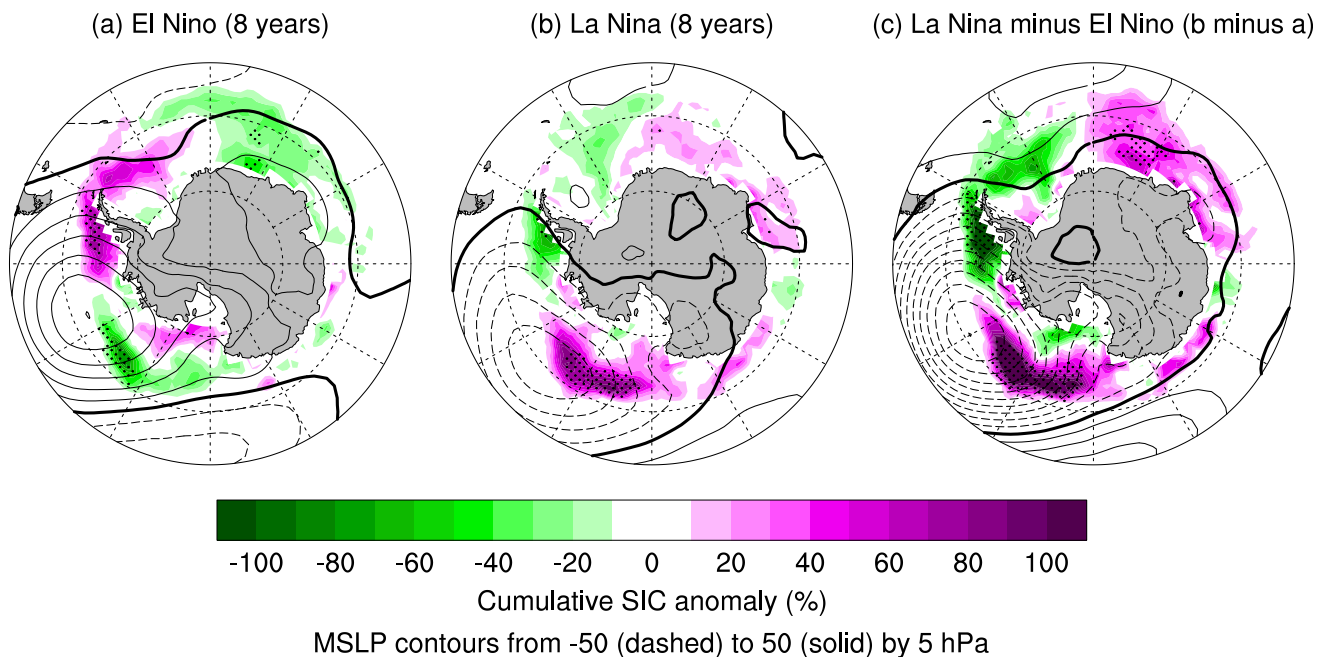


FIG. 9. As in Fig. 8, but showing cumulative anomalies for (a) El Niño, (b) La Niña, and (c) La Niña minus El Niño [(b) minus (a)].

convection there and damping the remote atmospheric response because it has been shown that positive SST, precipitation, and convective heating anomalies there during negative IPO can contribute to a deepening of the Amundsen Sea low (Clem and Renwick 2015; Meehl et al. 2016a). More realistic simulations of recent Antarctic sea ice variations could thus be achieved by improving model deficiencies involved in the climate response to external forcings and the remote impact of tropical regions. Other caveats include issues with how sea ice is modeled in current coupled climate models and how the simulated sea ice interacts with ocean and surface air temperatures and winds.

Because of the various feedbacks between sea ice and the climate system (e.g., Gooose and Zunz 2014), assessing coupled models is important to fully understand how tropical teleconnections influence Antarctic sea ice. For example, while changed surface wind trends may be conducive to a sea ice increase in the Ross Sea, it is likely that a net SST cooling is also required for sea ice to increase and to accurately capture positive ice–albedo and ocean thermal warming feedbacks (Stammerjohn et al. 2012). For both CESM1 and CanESM2, the assimilation experiments show less ice loss in most sectors than their corresponding CESM1-HIST or CanESM2-CLIM experiments but not a net ice increase. Without simulating the correct sign of observed sea ice changes, positive feedbacks will reinforce the ice loss, rather than the ice growth, propagating differences (e.g., Purich et al. 2016).

Finally, we note that a number of previous studies have found teleconnections from the tropical Atlantic to

the Amundsen Sea low to be important in driving Ross and Bellingshausen Seas sea ice changes (Li et al. 2014, 2015a,b; Simpkins et al. 2014). Therefore, it is likely that details of the decadal patterns of tropical SST, precipitation, and convective heating anomalies, as well as seasonality, are important in model simulations and the observed SIC, at least until 2013. Since the IPO has apparently changed phase around 2014 (Meehl et al. 2016b) the overall trend of SIC should now become less positive and may eventually turn negative on decadal time scales. While Atlantic forcing appears to play a role in influencing sea ice trends in the Atlantic and Indian Ocean sectors, in CESM1 the equatorial Pacific forcing seems to dominate sea ice trends in the Pacific sector. The design of the CanESM2 experiments does not allow for a direct comparison. Further work using coupled models is required to isolate the influences of the tropical Atlantic and Pacific Oceans on different sectors of Antarctic sea ice in a fully coupled framework.

Acknowledgments. This work was supported by CSIRO Oceans and Atmosphere, the Australian Research Council (ARC), including the ARC Centre of Excellence for Climate System Science, and the U.S. National Science Foundation. A. P. was supported by an Australian Postgraduate Award and a CSIRO Office of the Chief Executive Science Leader scholarship. M. H. E. was supported by an ARC Laureate Fellowship. W. C. was supported by the Australian Climate Change Science Programme and a CSIRO Office of the Chief Executive

Science Leader award. A. T. and Y. C. were supported through a National Science Foundation Award 1049219. G. A. M. and J. M. A. were partially supported by the Regional and Global Climate Modeling Program (RGCM) of the U.S. Department of Energy's Office of Biological and Environmental Research (BER) Cooperative Agreement DE-FC02-97ER62402 and the National Science Foundation. The CESM1 experiments were supported by the University of Southern California Center for High-Performance Computing and Communications (<http://hpcc.usc.edu/>) and the high-performance computing from Yellowstone (<http://n2t.net/ark:/85065/d7wd3xhc>) provided by NCAR's Computational Information Systems Laboratory sponsored by the National Science Foundation. We thank Rob DeConto for useful discussions on the 2015 tropical to high-latitude teleconnections while M. H. E. attended the SCAR Cross-Program Workshop held in Barcelona in 2015. We also thank Will Hobbs and two anonymous reviewers for their helpful comments, which improved this manuscript. We acknowledge the World Climate Research Programme's Working Group on Coupled Modelling, which is responsible for CMIP, and thank the climate modeling groups for producing and making available their model output.

REFERENCES

- Arora, V. K., and Coauthors, 2011: Carbon emission limits required to satisfy future representative concentration pathways of greenhouse gases. *Geophys. Res. Lett.*, **38**, L05805, doi:10.1029/2010GL046270.
- Ashok, K., S. K. Behera, S. A. Rao, H. Weng, and T. Yamagata, 2007: El Niño Modoki and its possible teleconnection. *J. Geophys. Res.*, **112**, C11007, doi:10.1029/2006JC003798.
- Balmaseda, M. A., K. Mogensen, and A. T. Weaver, 2013: Evaluation of the ECMWF ocean reanalysis system ORAS4. *Quart. J. Roy. Meteor. Soc.*, **139**, 1132–1161, doi:10.1002/qj.2063.
- Barsugli, J. J., and D. S. Battisti, 1998: The basic effects of atmosphere–ocean thermal coupling on midlatitude variability. *J. Atmos. Sci.*, **55**, 477–493, doi:10.1175/1520-0469(1998)055<0477:TBEAOA>2.0.CO;2.
- Bracegirdle, T. J., and G. J. Marshall, 2012: The reliability of Antarctic tropospheric pressure and temperature in the latest global reanalyses. *J. Climate*, **25**, 7138–7146, doi:10.1175/JCLI-D-11-00685.1.
- , E. Shuckburgh, J.-B. Sallee, Z. Wang, A. J. S. Meijers, N. Bruneau, T. Phillips, and L. J. Wilcox, 2013: Assessment of surface winds over the Atlantic, Indian, and Pacific Ocean sectors of the Southern Ocean in CMIP5 models: Historical bias, forcing response, and state dependence. *J. Geophys. Res. Atmos.*, **118**, 547–562, doi:10.1002/jgrd.50153.
- Bromwich, D. H., J. P. Nicolas, and A. J. Monaghan, 2011: An assessment of precipitation changes over Antarctica and the Southern Ocean since 1989 in contemporary global reanalyses. *J. Climate*, **24**, 4189–4209, doi:10.1175/2011JCLI4074.1.
- Cavalieri, D. J., and C. L. Parkinson, 2008: Antarctic sea ice variability and trends, 1979–2006. *J. Geophys. Res.*, **113**, C07004, doi:10.1029/2007JC004564.
- Chikamoto, Y., and Coauthors, 2015a: Skilful multi-year predictions of tropical trans-basin climate variability. *Nat. Commun.*, **6**, 6869, doi:10.1038/ncomms7869.
- , A. Timmermann, S. Stevenson, P. DiNezio, and S. Langford, 2015b: Decadal predictability of soil water, vegetation, and wildfire frequency over North America. *Climate Dyn.*, **45**, 2213–2235, doi:10.1007/s00382-015-2469-5.
- Ciasto, L. M., and D. W. J. Thompson, 2008: Observations of large-scale ocean–atmosphere interaction in the Southern Hemisphere. *J. Climate*, **21**, 1244–1259, doi:10.1175/2007JCLI1809.1.
- , and M. H. England, 2011: Observed ENSO teleconnections to Southern Ocean SST anomalies diagnosed from a surface mixed layer heat budget. *Geophys. Res. Lett.*, **38**, L09701, doi:10.1029/2011GL046895.
- , G. R. Simpkins, and M. H. England, 2015: Teleconnections between tropical Pacific SST anomalies and extratropical Southern Hemisphere climate. *J. Climate*, **28**, 56–65, doi:10.1175/JCLI-D-14-00438.1.
- Clem, K. R., and R. L. Fogt, 2015: South Pacific circulation changes and their connection to the tropics and regional Antarctic warming in austral spring, 1979–2012. *J. Geophys. Res. Atmos.*, **120**, 2773–2792, doi:10.1002/2014JD022940.
- , and J. A. Renwick, 2015: Austral spring Southern Hemisphere circulation and temperature changes and links to the SPCZ. *J. Climate*, **28**, 7371–7384, doi:10.1175/JCLI-D-15-0125.1.
- Comiso, J. C., and F. Nishio, 2008: Trends in the sea ice cover using enhanced and compatible AMSR-E, SSM/I, and SMMR data. *J. Geophys. Res.*, **113**, C02S07, doi:10.1029/2007JC004257.
- Dee, D. P., and Coauthors, 2011: The ERA-Interim reanalysis: Configuration and performance of the data assimilation system. *Quart. J. Roy. Meteor. Soc.*, **137**, 553–597, doi:10.1002/qj.828.
- Ding, Q., and E. J. Steig, 2013: Temperature change on the Antarctic Peninsula linked to the tropical Pacific. *J. Climate*, **26**, 7570–7585, doi:10.1175/JCLI-D-12-00729.1.
- Eisenman, I., W. N. Meier, and J. R. Norris, 2014: A spurious jump in the satellite record: Has Antarctic sea ice expansion been overestimated? *Cryosphere*, **8**, 1289–1296, doi:10.5194/tc-8-1289-2014.
- Fan, T., C. Deser, and D. P. Schneider, 2014: Recent Antarctic sea ice trends in the context of Southern Ocean surface climate variations since 1950. *Geophys. Res. Lett.*, **41**, 2419–2426, doi:10.1002/2014GL059239.
- Fogt, R. L., and D. H. Bromwich, 2006: Decadal variability of the ENSO teleconnection to the high-latitude South Pacific governed by coupling with the southern annular mode. *J. Climate*, **19**, 979–997, doi:10.1175/JCLI3671.1.
- Fyfe, J. C., and Coauthors, 2016: Making sense of the early-2000s warming slowdown. *Nat. Climate Change*, **6**, 224–228, doi:10.1038/nclimate2938.
- Gagné, M.-È., N. P. Gillett, and J. C. Fyfe, 2015: Observed and simulated changes in Antarctic sea ice extent over the past 50 years. *Geophys. Res. Lett.*, **42**, 90–95, doi:10.1002/2014GL062231.
- Goosse, H., and V. Zunz, 2014: Decadal trends in the Antarctic sea ice extent ultimately controlled by ice–ocean feedback. *Cryosphere*, **8**, 453–470, doi:10.5194/tc-8-453-2014.
- Henley, B. J., J. Gergis, D. J. Karoly, S. Power, J. Kennedy, and C. K. Folland, 2015: A tripole index for the interdecadal Pacific oscillation. *Climate Dyn.*, **45**, 3077–3090, doi:10.1007/s00382-015-2525-1.
- Hobbs, W. R., N. L. Bindoff, and M. N. Raphael, 2015: New perspectives on observed and simulated Antarctic sea ice extent trends using optimal fingerprinting techniques. *J. Climate*, **28**, 1543–1560, doi:10.1175/JCLI-D-14-00367.1.

- Holland, P. R., and R. Kwok, 2012: Wind-driven trends in Antarctic sea-ice drift. *Nat. Geosci.*, **5**, 872–875, doi:[10.1038/ngeo1627](https://doi.org/10.1038/ngeo1627).
- Hoskins, B. J., and D. J. Karoly, 1981: The steady linear response of a spherical atmosphere to thermal and orographic forcing. *J. Atmos. Sci.*, **38**, 1179–1196, doi:[10.1175/1520-0469\(1981\)038<1179:TSLROA>2.0.CO;2](https://doi.org/10.1175/1520-0469(1981)038<1179:TSLROA>2.0.CO;2).
- Irving, D., and I. Simmonds, 2016: A new method for identifying the Pacific–South American pattern and its influence on regional climate variability. *J. Climate*, **29**, 6109–6125, doi:[10.1175/JCLI-D-15-0843.1](https://doi.org/10.1175/JCLI-D-15-0843.1).
- Jin, D., and B. P. Kirtman, 2009: Why the Southern Hemisphere ENSO responses lead ENSO. *J. Geophys. Res.*, **114**, D23101, doi:[10.1029/2009JD012657](https://doi.org/10.1029/2009JD012657).
- Kosaka, Y., and S.-P. Xie, 2013: Recent global-warming hiatus tied to equatorial Pacific surface cooling. *Nature*, **501**, 403–407, doi:[10.1038/nature12534](https://doi.org/10.1038/nature12534).
- Lee, T., and M. J. McPhaden, 2008: Decadal phase change in large-scale sea level and winds in the Indo-Pacific region at the end of the 20th century. *Geophys. Res. Lett.*, **35**, L01605, doi:[10.1029/2007GL032419](https://doi.org/10.1029/2007GL032419).
- L'Heureux, M. L., and D. W. J. Thompson, 2006: Observed relationships between the El-Niño–Southern Oscillation and the extratropical zonal-mean circulation. *J. Climate*, **19**, 276–287, doi:[10.1175/JCLI3617.1](https://doi.org/10.1175/JCLI3617.1).
- Li, X., D. M. Holland, E. P. Gerber, and C. Yoo, 2014: Impacts of the north and tropical Atlantic Ocean on the Antarctic Peninsula and sea ice. *Nature*, **505**, 538–542, doi:[10.1038/nature12945](https://doi.org/10.1038/nature12945).
- , E. P. Gerber, D. M. Holland, and C. Yoo, 2015a: A Rossby wave bridge from the tropical Atlantic to West Antarctica. *J. Climate*, **28**, 2256–2273, doi:[10.1175/JCLI-D-14-00450.1](https://doi.org/10.1175/JCLI-D-14-00450.1).
- , D. M. Holland, E. P. Gerber, and C. Yoo, 2015b: Rossby waves mediate impacts of tropical oceans on West Antarctic atmospheric circulation in austral winter. *J. Climate*, **28**, 8151–8164, doi:[10.1175/JCLI-D-15-0113.1](https://doi.org/10.1175/JCLI-D-15-0113.1).
- Liu, J., J. A. Curry, and D. G. Martinson, 2004: Interpretation of recent Antarctic sea ice variability. *Geophys. Res. Lett.*, **31**, L02205, doi:[10.1029/2003GL018732](https://doi.org/10.1029/2003GL018732).
- Mahlstein, I., P. R. Gent, and S. Solomon, 2013: Historical Antarctic mean sea ice area, sea ice trends, and winds in CMIP5 simulations. *J. Geophys. Res. Atmos.*, **118**, 5105–5110, doi:[10.1002/jgrd.50443](https://doi.org/10.1002/jgrd.50443).
- Matear, R. J., T. J. O'Kane, J. S. Risbey, and M. Chamberlain, 2015: Sources of heterogeneous variability and trends in Antarctic sea-ice. *Nat. Commun.*, **6**, 8656, doi:[10.1038/ncomms9656](https://doi.org/10.1038/ncomms9656).
- McPhaden, M. J., T. Lee, and D. McClurg, 2011: El Niño and its relationship to changing background conditions in the tropical Pacific Ocean. *Geophys. Res. Lett.*, **38**, L15709, doi:[10.1029/2011GL048275](https://doi.org/10.1029/2011GL048275).
- Meehl, G. A., H. Teng, and J. M. Arblaster, 2014: Climate model simulations of the observed early-2000s hiatus of global warming. *Nat. Climate Change*, **4**, 898–902, doi:[10.1038/nclimate2357](https://doi.org/10.1038/nclimate2357).
- , J. M. Arblaster, C. M. Bitz, C. T. Y. Chung, and H. Teng, 2016a: Antarctic sea-ice expansion between 2000 and 2014 driven by tropical Pacific decadal climate variability. *Nat. Geosci.*, **9**, 590–595, doi:[10.1038/ngeo2751](https://doi.org/10.1038/ngeo2751).
- , A. Hu, and H. Teng, 2016b: Initialized decadal prediction for transition to positive phase of the interdecadal Pacific oscillation. *Nat. Commun.*, **7**, 11718, doi:[10.1038/ncomms11718](https://doi.org/10.1038/ncomms11718).
- Meier, W., F. Fetterer, M. Savoie, S. Mallory, R. Duerr, and J. Stroeve, 2015: NOAA/NSIDC climate data record of passive microwave sea ice concentration, version 2. National Snow and Ice Data Center, Boulder, CO, digital media. [Available online at <http://nsidc.org/data/G02202/versions/2/>].
- Mo, K. C., 2000: Relationships between low-frequency variability in the Southern Hemisphere and sea surface temperature anomalies. *J. Climate*, **13**, 3599–3610, doi:[10.1175/1520-0442\(2000\)013<3599:RBLFVI>2.0.CO;2](https://doi.org/10.1175/1520-0442(2000)013<3599:RBLFVI>2.0.CO;2).
- , and R. W. Higgins, 1998: The Pacific–South American modes and tropical convection during the Southern Hemisphere winter. *Mon. Wea. Rev.*, **126**, 1581–1596, doi:[10.1175/1520-0493\(1998\)126<1581:TPSAMA>2.0.CO;2](https://doi.org/10.1175/1520-0493(1998)126<1581:TPSAMA>2.0.CO;2).
- Newman, M., and Coauthors, 2016: The Pacific decadal oscillation, revisited. *J. Climate*, **29**, 4399–4427, doi:[10.1175/JCLI-D-15-0508.1](https://doi.org/10.1175/JCLI-D-15-0508.1).
- Parkinson, C. L., and D. J. Cavalieri, 2012: Antarctic sea ice variability and trends, 1979–2010. *Cryosphere*, **6**, 871–880, doi:[10.5194/tc-6-871-2012](https://doi.org/10.5194/tc-6-871-2012).
- Polvani, L. M., and K. L. Smith, 2013: Can natural variability explain observed Antarctic sea ice trends? New modeling evidence from CMIP5. *Geophys. Res. Lett.*, **40**, 3195–3199, doi:[10.1002/grl.50578](https://doi.org/10.1002/grl.50578).
- Purich, A., T. Cowan, S.-K. Min, and W. Cai, 2013: Autumn precipitation trends over Southern Hemisphere midlatitudes as simulated by CMIP5 models. *J. Climate*, **26**, 8341–8356, doi:[10.1175/JCLI-D-13-00007.1](https://doi.org/10.1175/JCLI-D-13-00007.1).
- , W. Cai, M. H. England, and T. Cowan, 2016: Evidence for link between modelled trends in Antarctic sea ice and underestimated westerly wind changes. *Nat. Commun.*, **7**, 10409, doi:[10.1038/ncomms10409](https://doi.org/10.1038/ncomms10409).
- Raphael, M. N., and Coauthors, 2016: The Amundsen Sea low: Variability, change, and impact on Antarctic climate. *Bull. Amer. Meteor. Soc.*, **97**, 111–121, doi:[10.1175/BAMS-D-14-00018.1](https://doi.org/10.1175/BAMS-D-14-00018.1).
- Rayner, N. A., D. E. Parker, E. B. Horton, C. K. Folland, L. V. Alexander, D. P. Rowell, E. C. Kent, and A. Kaplan, 2003: Global analyses of sea surface temperature, sea ice, and night marine air temperature since the late nineteenth century. *J. Geophys. Res.*, **108**, 4407, doi:[10.1029/2002JD002670](https://doi.org/10.1029/2002JD002670).
- Renwick, J. A., 2002: Southern Hemisphere circulation and relations with sea ice and sea surface temperature. *J. Climate*, **15**, 3058–3068, doi:[10.1175/1520-0442\(2002\)015<3058:SHCARW>2.0.CO;2](https://doi.org/10.1175/1520-0442(2002)015<3058:SHCARW>2.0.CO;2).
- Saenko, O. A., J. C. Fyfe, N. C. Swart, W. G. Lee, and M. H. England, 2016: Influence of tropical wind on global temperature from months to decades. *Climate Dyn.*, **47**, 2193–2203, doi:[10.1007/s00382-015-2958-6](https://doi.org/10.1007/s00382-015-2958-6).
- Schneider, D. P., C. Deser, and Y. Okumura, 2012: An assessment and interpretation of the observed warming of West Antarctica in the austral spring. *Climate Dyn.*, **38**, 323–347, doi:[10.1007/s00382-010-0985-x](https://doi.org/10.1007/s00382-010-0985-x).
- Shields, C. A., D. A. Bailey, G. Danabasoglu, M. Jochum, J. T. Kiehl, S. Levis, and S. Park, 2012: The low-resolution CCSM4. *J. Climate*, **25**, 3993–4014, doi:[10.1175/JCLI-D-11-00260.1](https://doi.org/10.1175/JCLI-D-11-00260.1).
- Sigmond, M., and J. C. Fyfe, 2016: Tropical Pacific impacts on cooling North American winters. *Nat. Climate Change*, **6**, 970–974, doi:[10.1038/nclimate3069](https://doi.org/10.1038/nclimate3069).
- Simpkins, G. R., L. M. Ciasto, D. W. J. Thompson, and M. H. England, 2012: Seasonal relationships between large-scale climate variability and Antarctic sea ice concentration. *J. Climate*, **25**, 5451–5469, doi:[10.1175/JCLI-D-11-00367.1](https://doi.org/10.1175/JCLI-D-11-00367.1).
- , S. McGregor, A. S. Taschetto, L. M. Ciasto, and M. H. England, 2014: Tropical connections to climatic change in the extra-tropical Southern Hemisphere: The role of Atlantic SST trends. *J. Climate*, **27**, 4923–4936, doi:[10.1175/JCLI-D-13-00615.1](https://doi.org/10.1175/JCLI-D-13-00615.1).
- Stammerjohn, S. E., D. G. Martinson, R. C. Smith, X. Yuan, and D. Rind, 2008: Trends in Antarctic annual sea ice retreat and advance and their relation to El Niño–Southern Oscillation and southern annular mode variability. *J. Geophys. Res.*, **113**, C03S90, doi:[10.1029/2007JC004269](https://doi.org/10.1029/2007JC004269).

- , R. Massom, D. Rind, and D. Martinson, 2012: Regions of rapid sea ice change: An inter-hemispheric seasonal comparison. *Geophys. Res. Lett.*, **39**, L06501, doi:[10.1029/2012GL050874](https://doi.org/10.1029/2012GL050874).
- Swart, N. C., and J. C. Fyfe, 2013: The influence of recent Antarctic ice sheet retreat on simulated sea ice area trends. *Geophys. Res. Lett.*, **40**, 4328–4332, doi:[10.1002/grl.50820](https://doi.org/10.1002/grl.50820).
- Turner, J., 2004: The El Niño–Southern Oscillation and Antarctica. *Int. J. Climatol.*, **24**, 1–31, doi:[10.1002/joc.965](https://doi.org/10.1002/joc.965).
- , and Coauthors, 2009: Non-annular atmospheric circulation change induced by stratospheric ozone depletion and its role in the recent increase of Antarctic sea ice extent. *Geophys. Res. Lett.*, **36**, L08502, doi:[10.1029/2009GL037524](https://doi.org/10.1029/2009GL037524).
- , T. J. Bracegirdle, T. Phillips, G. J. Marshall, and J. S. Hosking, 2013: An initial assessment of Antarctic sea ice extent in the CMIP5 models. *J. Climate*, **26**, 1473–1484, doi:[10.1175/JCLI-D-12-00068.1](https://doi.org/10.1175/JCLI-D-12-00068.1).
- , J. S. Hosking, G. J. Marshall, T. Phillips, and T. J. Bracegirdle, 2016: Antarctic sea ice increase consistent with intrinsic variability of the Amundsen Sea low. *Climate Dyn.*, **46**, 2391–2402, doi:[10.1007/s00382-015-2708-9](https://doi.org/10.1007/s00382-015-2708-9).
- Ummenhofer, C. C., A. Sen Gupta, and M. H. England, 2009: Causes of late twentieth-century trends in New Zealand precipitation. *J. Climate*, **22**, 3–19, doi:[10.1175/2008JCLI2323.1](https://doi.org/10.1175/2008JCLI2323.1).
- Yu, L., and Coauthors, 2011: Interpretation of recent trends in Antarctic sea ice concentration. *J. Appl. Remote Sens.*, **5**, 053557, doi:[10.1117/1.3643691](https://doi.org/10.1117/1.3643691).
- Yuan, X., and D. G. Martinson, 2000: Antarctic sea ice extent variability and its global connectivity. *J. Climate*, **13**, 1697–1717, doi:[10.1175/1520-0442\(2000\)013<1697:ASIEVA>2.0.CO;2](https://doi.org/10.1175/1520-0442(2000)013<1697:ASIEVA>2.0.CO;2).
- Zunz, V., H. Goosse, and F. Massonnet, 2013: How does internal variability influence the ability of CMIP5 models to reproduce the recent trend in Southern Ocean sea ice extent? *Cryosphere*, **7**, 451–468, doi:[10.5194/tc-7-451-2013](https://doi.org/10.5194/tc-7-451-2013).

Appendix C

Published article

A copy of the published article that constitutes the material in Part 3 is included hereafter:

Purich, A., M. H. England, W. Cai, A. Sullivan, and P. J. Durack, 2018: Impacts of broad-scale surface freshening of the Southern Ocean in a coupled climate model. *Journal of Climate*, **31**, 2613–2632, doi:10.1175/JCLI-D-17-0092.1. ©American Meteorological Society. Used with permission.

Impacts of Broad-Scale Surface Freshening of the Southern Ocean in a Coupled Climate Model[✉]

ARIAAN PURICH

Commonwealth Scientific and Industrial Research Organisation, Oceans and Atmosphere, Aspendale, Victoria, and Climate Change Research Centre and ARC Centre of Excellence for Climate System Science, University of New South Wales, Sydney, New South Wales, Australia

MATTHEW H. ENGLAND

Climate Change Research Centre and ARC Centre of Excellence for Climate System Science, University of New South Wales, Sydney, New South Wales, Australia

WENJU CAI^a AND ARNOLD SULLIVAN

Commonwealth Scientific and Industrial Research Organisation, Oceans and Atmosphere, Aspendale, Victoria, Australia

PAUL J. DURACK

Program for Climate Model Diagnosis and Intercomparison, Lawrence Livermore National Laboratory, Livermore, California

(Manuscript received 13 February 2017, in final form 26 December 2017)

ABSTRACT

The Southern Ocean surface has freshened in recent decades, increasing water column stability and reducing upwelling of warmer subsurface waters. The majority of CMIP5 models underestimate or fail to capture this historical surface freshening, yet little is known about the impact of this model bias on regional ocean circulation and hydrography. Here experiments are performed using a global coupled climate model with additional freshwater applied to the Southern Ocean to assess the influence of recent surface freshening. The simulations explore the impact of persistent and long-term broad-scale freshening as a result of processes including precipitation minus evaporation changes. Thus, unlike previous studies, the freshening is applied as far north as 55°S, beyond the Antarctic ice margin. It is found that imposing a large-scale surface freshening causes a surface cooling and sea ice increase under preindustrial conditions, because of a reduction in ocean convection and weakened entrainment of warm subsurface waters into the surface ocean. This is consistent with intermodel relationships between CMIP5 models and the simulations, suggesting that models with larger surface freshening also exhibit stronger surface cooling and increased sea ice. Additional experiments are conducted with surface salinity restoration applied to capture observed regional salinity trends. Remarkably, without any mechanical wind trend forcing, these simulations accurately represent the spatial pattern of observed surface temperature and sea ice trends around Antarctica. This study highlights the importance of accurately simulating changes in Southern Ocean salinity to capture changes in ocean circulation, sea surface temperature, and sea ice.

[✉] Supplemental information related to this paper is available at the Journals Online website: <https://doi.org/10.1175/JCLI-D-17-0092.s1>.

^a Current affiliations: Centre for Southern Hemisphere Oceans Research, Commonwealth Scientific and Industrial Research Organisation Oceans and Atmosphere, Aspendale, Victoria, Australia, and Physical Oceanography Laboratory, Ocean University of China, and Qingdao National Laboratory for Marine Science and Technology, Qingdao, China.

Corresponding author: Ariaan Purich, ariaan.purich@csiro.au

DOI: 10.1175/JCLI-D-17-0092.1

© 2018 American Meteorological Society. For information regarding reuse of this content and general copyright information, consult the [AMS Copyright Policy](#) (www.ametsoc.org/PUBSReuseLicenses).

1. Introduction

Observed Southern Ocean changes over recent decades include a surface freshening (Durack and Wijffels 2010; Durack et al. 2012; de Lavergne et al. 2014), surface cooling (Fan et al. 2014; Marshall et al. 2014; Armour et al. 2016; Purich et al. 2016a), and circumpolar increase in Antarctic sea ice (Cavalieri and Parkinson 2008; Comiso and Nishio 2008; Parkinson and Cavalieri 2012). Various explanations for the increase in Antarctic sea ice extent (SIE) seen since regular satellite observations began in 1979, which has occurred despite global warming over this period, have been proposed (Hobbs et al. 2016). These include natural variability (Mahlstein et al. 2013; Polvani and Smith 2013; Zunz et al. 2013; Li et al. 2014; Simpkins et al. 2014; Gagné et al. 2015; Meehl et al. 2016; Purich et al. 2016b), changes in surface winds (Holland and Kwok 2012; Fan et al. 2014; Turner et al. 2009; Li et al. 2014; Simpkins et al. 2014; Purich et al. 2016a), surface freshening as a result of ice sheet and shelf runoff and iceberg fluxes (Bintanja et al. 2013, 2015; Swart and Fyfe 2013; Pauling et al. 2016), and surface freshening as a result of sea ice transport (Haumann et al. 2016).

Surface freshening can act to increase sea ice coverage by increasing surface stratification, reducing convective mixing of warmer subsurface waters, and causing a surface cooling (e.g., Marsland and Wolff 2001; Liu and Curry 2010; de Lavergne et al. 2014; Morrison et al. 2015). Early model studies of the influence of surface freshening on Antarctic sea ice found freshening to be associated with an increase in ice coverage in ocean–ice models (Marsland and Wolff 2001; Beckmann and Goosse 2003; Hellmer 2004; Aiken and England 2008). However, more recent studies using global coupled climate models with additional freshwater applied around the Antarctic margins to simulate increased ice sheet melt and runoff have found conflicting results: Bintanja et al. (2013, 2015) found that the increased freshwater has likely contributed to the increase in Antarctic SIE, whereas Swart and Fyfe (2013) found the influence to be small and not able to explain the observed sea ice changes. Pauling et al. (2016) also found that applying an extra freshwater flux around the continental margins was insufficient to offset anthropogenic forcing. Zunz and Goosse (2015) found that the inclusion of an additional freshwater flux in simulations with data assimilation improves the reconstruction of sea ice trends; however, it does not seem to be required to obtain an increase in sea ice extent in hindcast simulations. Additionally, Kirkman and Bitz (2011) found that under global warming conditions, increased melting of sea ice leads to surface freshening, which in turn leads to surface cooling of the Southern Ocean.

Previous studies (Bintanja et al. 2013, 2015; Swart and Fyfe 2013; Pauling et al. 2016) focused on runoff from the Antarctic ice sheet and shelf melt as the source of freshwater to the Southern Ocean, in part motivated by the fact that models participating in phase 5 of the Coupled Model Intercomparison Project (CMIP5) explicitly exclude such melt contributions. However, Pauling et al. (2016) found that the CMIP5 models happen to simulate runoff changes resulting from precipitation changes over Antarctica that are approximately the same as estimated land-ice melt and ice-shelf melt rates. Further, the largest source of freshwater to the Southern Ocean is the precipitation minus evaporation ($P - E$) falling directly onto the ocean (Pauling et al. 2016). Increased $P - E$ leads to stronger stratification and a reduction in oceanic vertical heat transfer, and thus to increased sea ice (Martinson 1990; Marsland and Wolff 2001; Goosse and Zunz 2014). Observational estimates of $P - E$ over the Southern Ocean are highly uncertain: there are no direct measurements of precipitation over the ocean and satellite estimates provide only a snapshot in time based on the time of the scan (e.g., Trenberth et al. 2017), while evaporation is estimated from bulk formula with many uncertain inputs, leading to considerable imbalances in global surface flux estimates (e.g., Josey et al. 2013). As such, there is a large spread in observational products and reanalysis (Fig. 1). A detailed assessment of $P - E$ trends in various reanalyses since 1989 found no robust widespread precipitation trends over the sea ice region, and a large disagreement between different reanalyses (Bromwich et al. 2011). However, most estimates suggest that there has been an increase in precipitation and $P - E$ over the Southern Ocean south of 50°S since 1979 (Fig. 1), and this is consistent with the multidecadal broad-scale freshening that has been reported in numerous independent studies (Durack and Wijffels 2010; Helm et al. 2010; de Lavergne et al. 2014; Haumann et al. 2016).

Measurements of surface salinity provide an integrated view of freshwater input changes, and the surface freshening seen since 1950 (Fig. 1a; Durack and Wijffels 2010; de Lavergne et al. 2014), along with interior freshening (e.g., Wong et al. 1999), further suggest that there has been an increase in broad-scale freshwater input, likely including an increase in $P - E$ over the Southern Ocean (e.g., Durack et al. 2012; de Lavergne et al. 2014). This increase is also in agreement with the positive trend in the southern annular mode (SAM) observed over the latter half of the twentieth century (Marshall 2003), associated with a poleward shift and intensification in the extratropical westerly wind jet and storm tracks (e.g., Thompson and Solomon 2002; Fyfe 2003; Frederiksen and Frederiksen 2007). These SAM changes have previously

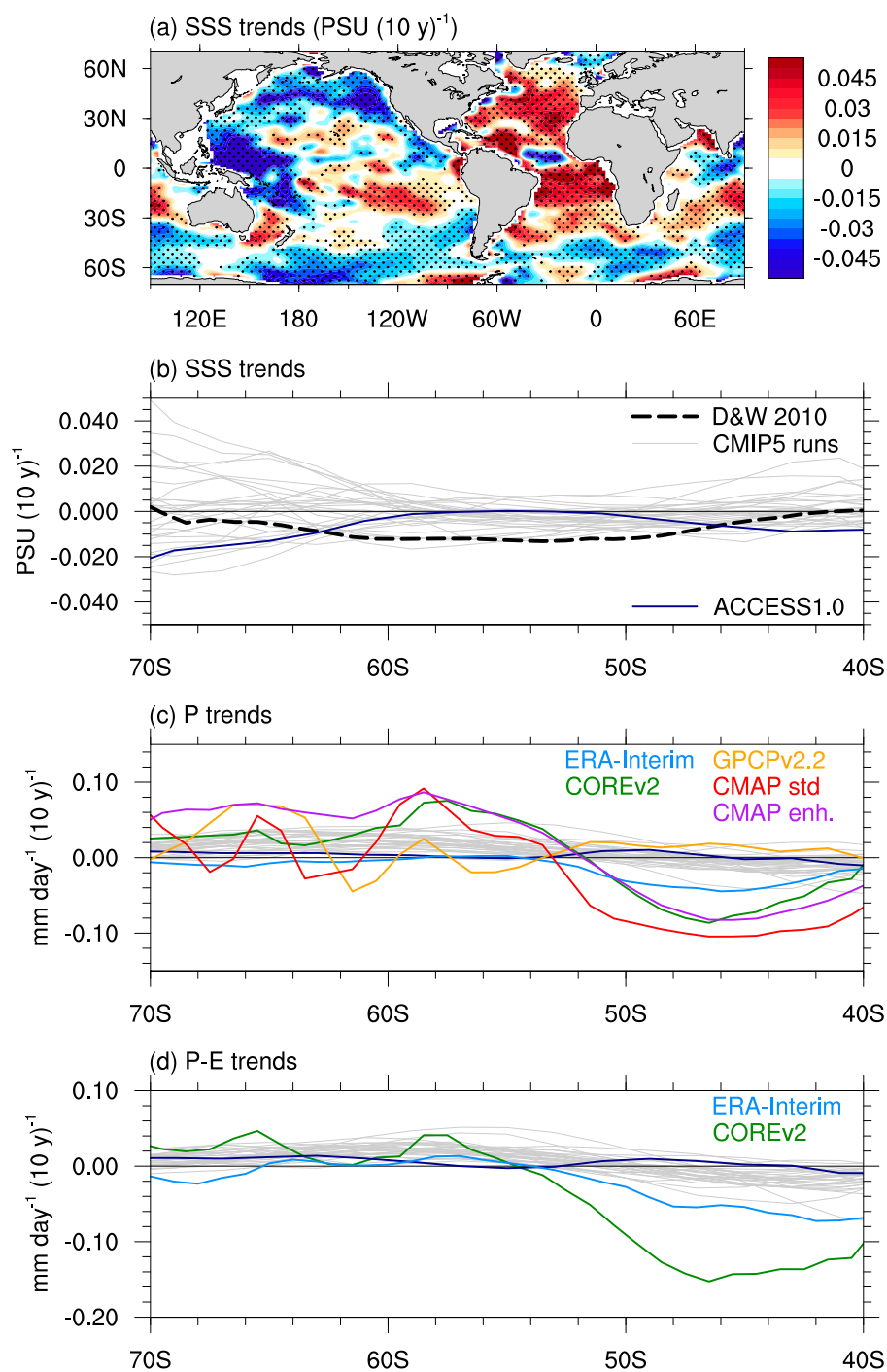


FIG. 1. Trends over 1950–2000: (a) observed SSS trends from Durack and Wijffels (2010); (b) zonal-mean SSS trends for observations (Durack and Wijffels 2010) and CMIP5 models; (c) zonal-mean precipitation trends for observations (ERA-Interim, COREv2, GPCPv2.2, CMAP standard, and CMAP enhanced) and CMIP5 models; and (d) zonal-mean $P - E$ trends for observations (ERA-Interim and COREv2) and CMIP5 models. In (a), stippling indicates significance at the 95% level. In (b), observations are shown with a dashed black line. In (c), (d), observations are shown with colored lines and vary in the time periods they cover (refer to section 2). In (b)–(d), CMIP5 models are shown with gray lines, and the ACCESS1.0 CMIP5 run is shown with a dark blue line.

been suggested to increase precipitation over the high-latitude Southern Ocean (while decreasing precipitation in midlatitudes; e.g., [Son et al. 2009](#)), with less influence on evaporation ([Purich and Son 2012](#)), thus enhancing total $P - E$ over a broad region of the high-latitude Southern Ocean (including well north of the sea ice margin). The goal of this study is to better understand the role of this broad-scale freshening of the surface Southern Ocean on both surface cooling and Antarctic sea ice trends.

Further, while CMIP5 models capture the observed sign of the recent SAM trend, they tend to underestimate its strength, and the trend in the westerly wind jet ([Swart and Fyfe 2012](#); [Wilcox et al. 2012](#); [Bracegirdle et al. 2013](#); [Mahlstein et al. 2013](#); [Purich et al. 2013](#)). The CMIP5 models also either underestimate or fail to capture the surface freshening seen in observations over 1950–2000 between 50° and 60°S: of the models that exhibit surface freshening, all underestimate the strength of the observed freshening, and only five models are within the observational uncertainty range ([Figs. 1b and 2](#); [Durack 2015](#)). That is, 26 out of 31 CMIP5 models assessed in this study show sea surface salinity (SSS) trends over 50°–60°S that are inconsistent with the observed freshening ([Fig. 2](#)). When multiple realizations per model are considered, 60 out of 68 CMIP5 realizations show SSS trends that are inconsistent with the observed freshening ([Fig. S1 in the supplemental material](#)). This is likely due to model precipitation and cloud biases; however, uncertainty in observed $P - E$ makes it difficult to assess the extent to which models underestimate changes in precipitation ([Fig. 1c](#)) and $P - E$ ([Fig. 1d](#)). Internal variability may also play a role in contributing to the observed trend. In any case, [Fig. 1b](#) indicates that for almost all cases, the model's simulation of the recent multidecadal surface freshening is weaker than observed. In addition to precipitation biases, a component of the SSS freshening could be due to increased ice shelf melt, land-ice melt, or an increase in northward sea ice advection and melt. It is thus difficult to fully separate the processes that might be biased in CMIP5 models. Either way, as high-latitude surface freshening is associated with surface cooling and a sea ice increase, this may be another factor contributing to the CMIP5 models' excessive Southern Ocean surface warming contrasting with the observed surface cooling ([Marshall et al. 2014](#); [Purich et al. 2016a](#)) and sea ice decline contrasting with the observed increases ([Mahlstein et al. 2013](#); [Polvani and Smith 2013](#); [Swart and Fyfe 2013](#); [Turner et al. 2013](#); [Zunz et al. 2013](#); [Gagné et al. 2015](#)) over recent decades. Understanding whether an underestimated broad-scale freshening may have contributed to the differences between observed and CMIP5 trends provides further motivation for investigating the role of broad-scale freshening in driving Southern Ocean surface changes.

In this study we perform experiments using the Australian Community Climate and Earth-System Simulator, version 1.0 (ACCESS1.0), a global coupled climate model participating in CMIP5. In a recent CMIP5 assessment this model was found to be one of the best in the suite for simulating regional distribution and extent of Antarctic sea ice ([Ivanova et al. 2016](#)). We apply an idealized freshwater flux over the high-latitude Southern Ocean between 55° and 70°S, with the aim of achieving a SSS trend similar in magnitude to the [Durack and Wijffels \(2010\)](#) trend. The sea surface temperature (SST) and sea ice responses to the broad-scale freshwater input are examined and the regional pattern of changes and sea ice feedbacks are discussed. We also make a comparison with CMIP5 output. Our results suggest that recent multidecadal trends in large-scale surface salinity over the Southern Ocean have played a role in the observed surface cooling seen in this region. In addition, our simulations suggest that the underestimation of observed surface freshening by CMIP5 models is an important factor contributing to the SST warming and Antarctic sea ice decline seen in almost all CMIP5 models, at odds with observed trends. While diagnosed as an important factor here, we find that a uniform freshening alone cannot fully account for the model–observation differences. Other factors, such as decadal variability ([Li et al. 2014](#); [Simpkins et al. 2014](#); [Meehl et al. 2016](#); [Purich et al. 2016b](#)), responses to greenhouse gas forcing ([Armour et al. 2016](#)) and stratospheric ozone forcing ([Turner et al. 2009](#)), and wind forcing effects ([Holland and Kwok 2012](#); [Fan et al. 2014](#); [Purich et al. 2016a](#)) are likely also important.

2. Data and methods

a. Model description

The ACCESS1.0 model is a fully coupled global climate model, developed by the Commonwealth Scientific and Industrial Research Organisation and the Australian Bureau of Meteorology ([Bi et al. 2013b](#)). It is built by coupling the United Kingdom Met Office atmospheric Unified Model (UM; [Davies et al. 2005](#); [Martin et al. 2010, 2011](#)) to the Geophysical Fluid Dynamics Laboratory Modular Ocean Model, version 4.1 (MOM4.1; [Griffies et al. 2010](#)), and the Los Alamos National Laboratory sea ice model, version 4.1 (CICE4.1; [Hunke and Lipscomb 2010](#)), as described in [Bi et al. \(2013a\)](#). These model components are coupled using the Centre Européen de Recherche et de Formation Avancée en Calcul Scientifique Ocean Atmosphere Sea Ice Soil, version 3.2 (OASIS3.2; [Valcke 2006](#)), coupling framework. ACCESS1.0 is configured

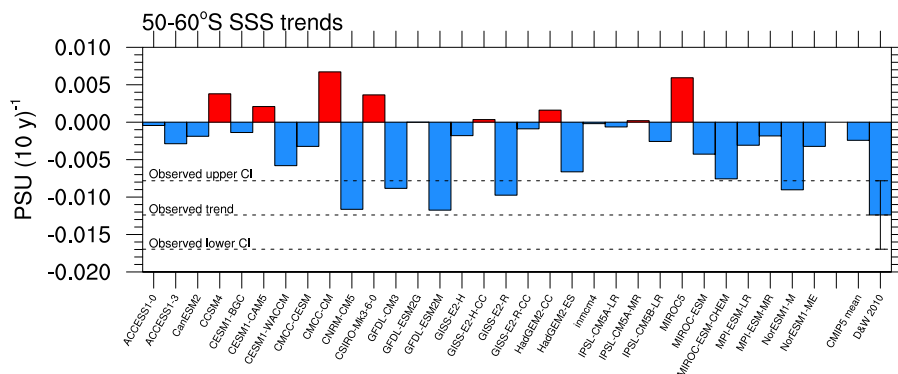


FIG. 2. Trends in SSS over 1950–2000, area averaged over 50°–60°S. The first available reanalysis for each CMIP5 model is shown, along with the CMIP5 multimodel mean and the Durack and Wijffels (2010) observational estimate. Error bars show the approximate 95% confidence estimates of the observed trend, and horizontal dashed lines are included for comparison between the CMIP5 trends and observations.

with the Met Office Hadley Centre Global Environment Model, version 2 (HadGEM2, r1.1) atmospheric physics and the Met Office Surface Exchange Scheme land surface model, version 2. The atmospheric component of the model used here has a Gaussian N96 horizontal resolution of approximately 1.25° latitude \times 1.875° longitude and 38 vertical levels. The ACCESS1.0 configuration of MOM4.1 and CICE4.1 has 360 longitude \times 300 latitude grid points on a logically rectangular grid with enhanced resolution at the equator and 50 vertical levels with 10-m resolution in the upper 200 m (Bi et al. 2013b).

b. Experimental design

Using ACCESS1.0 in fully coupled configuration, simulations with an additional freshwater flux into the ocean component are branched from a preindustrial control (piControl) run. We refer to these as the freshwater simulations. Freshwater simulations have the same forcings as for the ACCESS1.0 CMIP5 piControl run, including preindustrial atmospheric concentrations of CO_2 , CH_4 , N_2O , and O_3 , the solar constant, aerosol emissions, seasonally varying biogenic aerosol concentrations, and a background SO_2 outgassing flux, but with the stratosphere clear of volcanic aerosols (Bi et al. 2013b; Dix et al. 2013). This experimental design was chosen rather than including historical and future scenario forcings to isolate the influence of Southern Ocean surface freshening on the climate system from other confounding factors. Five ensemble members are branched from different years of the piControl run, each five years apart, and run for 50 years. We consider the five-member ensemble to investigate the role of unforced variability on these relatively short simulations.

Our aim is to simulate a clear freshening signal of similar magnitude to the broad-scale freshening of the Durack and Wijffels (2010) SSS trend that will allow an

investigation into the influence of this observed surface freshening on regional hydrography and circulation. We are not initially trying to replicate the observed SSS trend exactly (although later on we consider SSS restoring experiments that match the observed geographic distribution), but rather use an idealized freshwater forcing to obtain freshening trends of approximately comparable magnitude. To achieve this, an identical freshwater flux is added to each ensemble member as an additional $P - E$ flux into the ocean model component over 55° – 70° S, while the atmosphere, sea ice, and ocean are able to freely evolve to this additional flux. The additional $P - E$ flux is applied as a $P - E$ flux correction, to augment the $P - E$ flux received due to atmospheric processes, rather than by prescribing the total $P - E$. This yields a surface freshening trend under otherwise piControl conditions. The added freshwater flux is constant over 55° – 70° S, and zero elsewhere, and increases by a constant amount each year, representing an annually increasing linear trend in $P - E$. Because of model sensitivity assessed in short tests, a freshwater flux trend of 0.1 mm day^{-1} (10 yr^{-1}) is applied, which yields a clear freshening signal as desired (Fig. 3b). This is considerably larger than the $P - E$ trend simulated by the CMIP5 models as shown in Fig. 1d.

c. Observational and CMIP5 datasets

We compare output from the ACCESS1.0 freshwater simulations to various observationally based datasets. For surface and subsurface salinity, we utilize trends from Durack and Wijffels (2010), calculated for 1950–2000. We also utilize potential temperature trends from Durack and Wijffels (2010). For surface trends over 1979–2013 we use SST from the Hadley Centre Sea Ice and Sea Surface Temperature dataset (HadISST; Rayner et al. 2003; <http://www.metoffice.gov.uk/hadobs/hadisst/>)

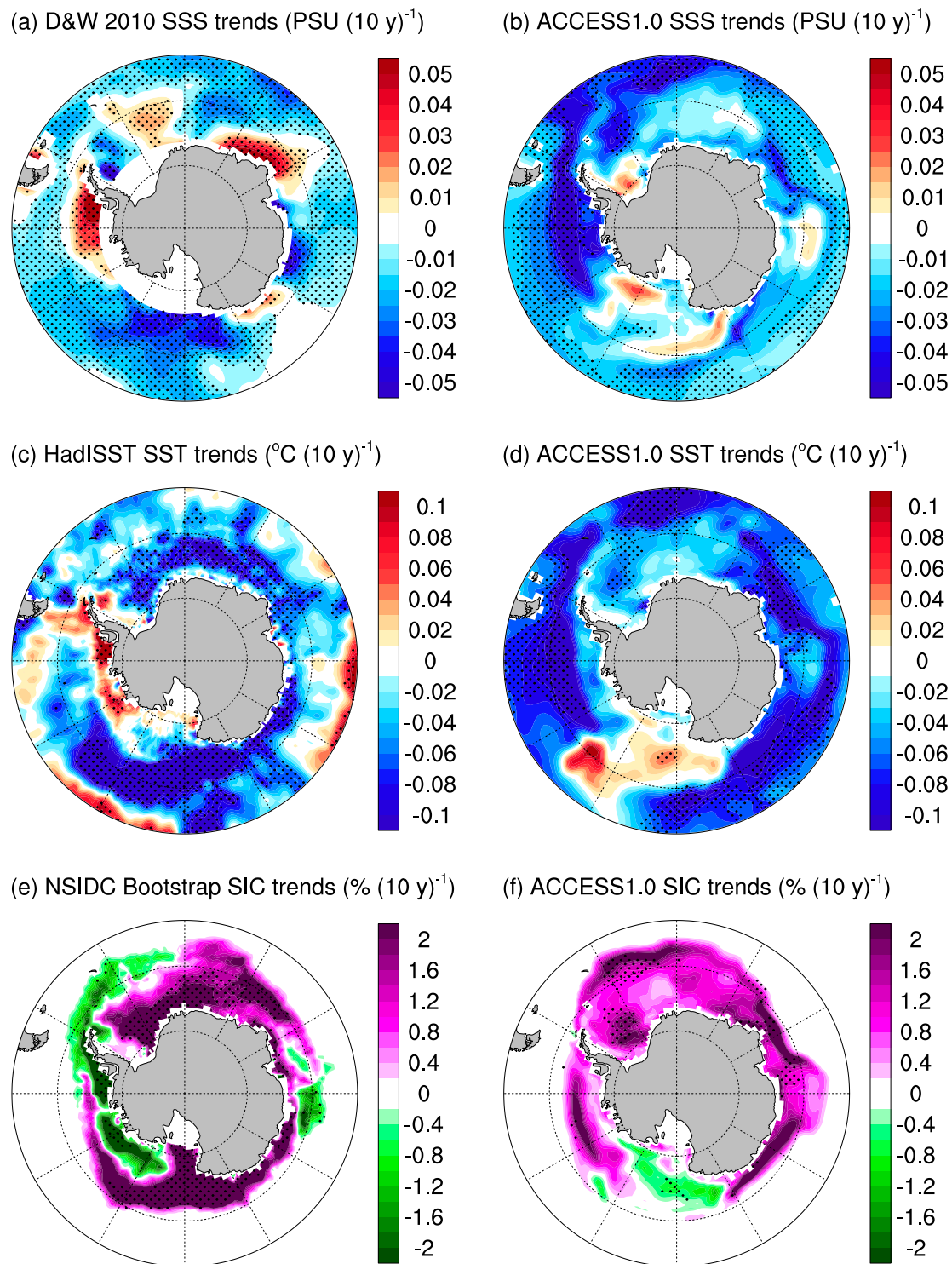


FIG. 3. (left) Observed and (right) ensemble-mean 50-yr trends from the ACCESS1.0 freshwater simulations: (a),(b) SSS trends, (c),(d) SST trends, and (e),(f) SIC trends. In all panels, stippling indicates trend significance at the 95% level. Observations are from [Durack and Wijffels \(2010\)](#) (1950–2000) in (a), HadISST (1979–2013) in (c), and NSIDC bootstrap (1979–2013) in (e).

and passive microwave sea ice concentration (SIC) processed using the National Snow and Ice Data Center (NSIDC) bootstrap algorithm ([Comiso and Nishio 2008](#); [Meier et al. 2015](#)). For area-averaged SIE we make use of

the NSIDC SIE index ([Fetterer et al. 2002](#)). We note that there is an inconsistency in the time periods of the different observational datasets assessed here. Continuous observations of Antarctic sea ice are limited to the

satellite period 1979–2013 and one of the motivations of this research is to better understand the drivers of Antarctic sea ice trends over this time. While HadISST extends back far earlier than 1979, analyzing the same period as for sea ice is useful in understanding how SST and sea ice trends are related. This also has the added benefit of using the temporal period where satellite data coverage provides the dominant measurement inputs for HadISST. Unfortunately, observations of SSS and subsurface fields are severely limited, and although shorter period trend estimates do exist (e.g., over 1970–2004 Durack et al. 2014), error estimates increase markedly, as the primary limitation in Southern Hemisphere trends is a lack of data. Over shorter time periods interannual–decadal variability also dominates, whereas over longer periods such as 1950–2000, trends are more coherent and physically interpretable. Based on this limitation, despite not aligning with the satellite-measured sea ice and SST period, we choose to assess the 1950–2000 SSS and subsurface trends. Changes over the various periods are all scaled to show the trend per decade, to allow for an easier comparison across the differing time scales of the products analyzed.

Data sparsity is a considerable challenge when assessing the pre-Argo period for global ocean temperature and salinity changes, and is a particular problem in the sparsely sampled Southern Hemisphere. Durack and Wijffels (2010) discuss the issue of data sparsity and provide uncertainty estimates for the presented trend results. Table 1 in Durack and Wijffels (2010) also includes error estimates for regional comparisons to other published literature. We note that other studies that have assessed trends in salinity have also attempted to provide uncertainty estimates: the Durack and Wijffels (2010) analysis is one of at least five studies (see also Boyer et al. 2005; Hosoda et al. 2009; Helm et al. 2010; Skliris et al. 2014) that have assessed salinity changes for the global ocean. Each of these studies reports a considerable broad-scale freshening for the Southern Ocean. A recent Southern Ocean regionally focused study by de Lavergne et al. (2014) has reproduced the freshening patterns using very different methodologies to previous studies (see their Fig. 2), strongly suggesting that the Southern Ocean surface freshening is a real observed feature, with the obvious caveat that all observed estimates are limited by measurements.

To support our findings based on the Durack and Wijffels (2010) dataset, we undertook a parallel analysis using the EN4.2.0 dataset (Good et al. 2013; see also Fig. S2 in the supplemental material). The EN4.2.0 dataset is not optimized for trend calculation (rather the dataset is focused on “reconstructing” each month of the ocean state from 1900 to 2017), and therefore is highly sensitive to data sparsity and “zero anomalies.”

However, when we contrast the same period analyzed in Durack and Wijffels (2010), we get similar spatial patterns for the key features we are assessing (e.g., broad-scale freshening south of 50°S but with increased salinity in the Bellingshausen and eastern Amundsen Seas, part of the Weddell Sea, the Cosmonauts Sea, and around 140°E), although with smaller magnitudes.

As mentioned above, observational estimates of $P - E$ over the Southern Ocean are highly uncertain (e.g., Josey et al. 2013; Bromwich et al. 2011). We compare various precipitation and evaporation datasets, including Global Precipitation Climatology Project, version 2.2 (GPCPv2.2), precipitation over 1979–2013 (Adler et al. 2003), CPC Merged Analysis of Precipitation (CMAP) standard and enhanced precipitation over 1979–2013 (Xie and Arkin 1997), ERA-Interim precipitation and evaporation over 1979–2013 (Dee et al. 2011), and Co-ordinated Ocean–Ice Reference Experiments, version 2 (COREv2), precipitation and evaporation over 1979–2006 (Large and Yeager 2009). We do not include the National Centers for Environmental Prediction (NCEP)–National Center for Atmospheric Research (NCAR) reanalysis precipitation and evaporation, as this reanalysis is already incorporated in the CMAP enhanced precipitation product, and in the COREv2 fields. We emphasize the limitations with observational precipitation and evaporation products over the Southern Ocean, as discussed in the introduction, and as such rely on surface salinity to provide an integrated view of freshwater input changes.

CMIP5 data from 31 models with a total of 68 runs are also analyzed (see Table S1 in the supplemental material for a list of models). All models with required variables available (SSS, SST, SIC, potential temperature, precipitation, and evaporation) for the historical experiment over 1950–2005 and the representative concentration pathway 8.5 (RCP8.5; high emission scenario) experiment over 2006–13 are included in the analysis. As all scenarios have similar forcings over 2006–13, the choice of RCP8.5 is arbitrary.

d. Data analysis

Prior to analysis all ACCESS1.0 and observational data are bilinearly regridded to a $1^\circ \times 1^\circ$ grid. Because of the large amount of data dealing with the CMIP5 ensemble, CMIP5 data are bilinearly regridded to a $2^\circ \times 2^\circ$ grid. Annual and seasonal averages are then calculated.

Gridpoint linear trends of surface fields are calculated. The significance of observed trends is determined using the two-sided Student's t test at the 95% confidence level. Autocorrelation was accounted for by defining the effective sample size N_{eff} as follows:

$$N_{\text{eff}} = N \left(\frac{1 - r_1}{1 + r_1} \right), \quad (1)$$

where N is the sample size, and r_1 is the lag-1 autocorrelation of the detrended time series of interest (Simpkins et al. 2012). Note that gridpoint SSS trends and an estimate of error are provided directly from Durack and Wijffels (2010) and are simply area averaged here, and that the different observational products vary in the time periods for which they are available. Ensemble mean trends for the freshwater simulations are calculated by taking the linear trend in each 50-yr simulation, dedrifted by removing the linear trend in the piControl for the corresponding 50-yr period (e.g., Sen Gupta et al. 2013), and then averaging across the five simulations. Significance of ensemble mean trends is determined when the absolute value of the ensemble mean trend is greater than two standard deviations of the intermember spread ($\sim 95\%$ confidence level).

Zonal mean linear trends of subsurface fields are calculated by first taking the three-dimensional trends and then averaging zonally. Salinity and potential temperature trends provided by Durack and Wijffels (2010) are simply averaged zonally. Note that the significance of these observed trends is also averaged zonally, and so should be considered as a guide only. As for the surface fields, 50-yr trends for individual ensemble members are first calculated, and then dedrifted by removing the zonal-mean trend in the piControl for the corresponding 50-yr period. Dedrifted trends are then averaged to determine the ensemble mean trend. Significance is determined when the absolute value of the ensemble mean trend is greater than two standard deviations of the intermember spread ($\sim 95\%$ confidence level).

Zonal mean trends are calculated for the CMIP5 models over 1950–2000. However, for area-averaged metrics we consider trends over 1979–2013, for comparison with satellite-based observational estimates of SST (HadISST) and SIC (NSIDC bootstrap). Area-averaged SSS and SST are calculated over 55° – 70° S and SIE is calculated as the total area where SIC exceeds 15%. Comparable metrics are calculated for the observational products, and for the freshwater simulations.

3. Results

a. Freshwater simulations

Observed and ensemble mean trend maps are shown in Fig. 3, displaying the regional patterns of trends. The Durack and Wijffels (2010) SSS trends (Fig. 3a) show substantial freshening over the Southern Ocean, although there is a notable increase in surface salinity in the Bellingshausen Sea. HadISST cooling (Fig. 3c) is seen in all regions, except near the coast in the Amundsen and Bellingshausen Seas, where a significant

warming is seen. Except for a region of increased salinity off east Antarctica and a weak increase in the Weddell Sea, the regions of cooling tend to align well with the regions of freshening, and vice versa, despite comparing the Durack and Wijffels (2010) and HadISST datasets over different periods for the reasons outlined in the data and methods section. These two trend maps (Figs. 3a,c) have an uncentered pattern correlation coefficient of $r = 0.50$ (see also Fig. S3 in the supplemental material). Sea ice changes largely mirror SST changes (Fig. 3e), with increased SIC in most regions around Antarctica, but decreased SIC in the Amundsen and Bellingshausen Seas, and in the outer Weddell Sea.

The broad-scale trends seen in the observations are also captured in the freshwater simulations: applying an idealized increased freshwater flux into the ocean causes an SSS freshening (Fig. 3b), increasing the surface stability. All ensemble members simulate a freshening trend in SSS over 50° – 70° S in response to the applied freshwater flux, although it is worth noting that the simulated zonal-mean freshening in response to the applied $P - E$ flux is stronger than the observed freshening. The increased stability reduces convective overturning, resulting in less entrainment of heat into the mixed layer, and can also result in reduced upward vertical isopycnal heat transport (Gregory 2000; Kirkman and Bitz 2011). In response to the surface freshening, all ensemble members also show a broad-scale surface cooling, accompanied by increased sea ice coverage occurs in most regions (Figs. 3d,f). As for the observations, there is a strong relationship between regions of freshening (Fig. 3b) and cooling (Fig. 3d) in the freshwater simulations, with these two trend maps having an uncentered pattern correlation of $r = 0.86$ (see also Fig. S3).

Zonal-mean trend patterns in simulated salinity (Fig. 4b) and potential temperature (Fig. 5b) reveal a high-latitude freshening and cooling of the surface layer, with warming below (discussed further below). These patterns indicate a reduction in cool season convective overturning between approximately 60° and 70° S (Fig. 5b) as a result of increased surface stability, with less entrainment of warmer subsurface waters to the surface ocean when convection is reduced. Similar to Kirkman and Bitz (2011), we also assess trends in water age, which acts as a tracer in ACCESS1.0 and indicates the length of time since a parcel of water has been at the surface. Regional agreement between areas of subsurface warming and increased water age¹ (Fig. 6) provides further indication that

¹ The uncentered pattern correlation coefficients between potential temperature and water age increase with depth from $r = 0.01$ at 55 m to $r = 0.46$ at 537 m and $r = 0.92$ at 2183 m (see also Fig. S4 in the supplemental material).

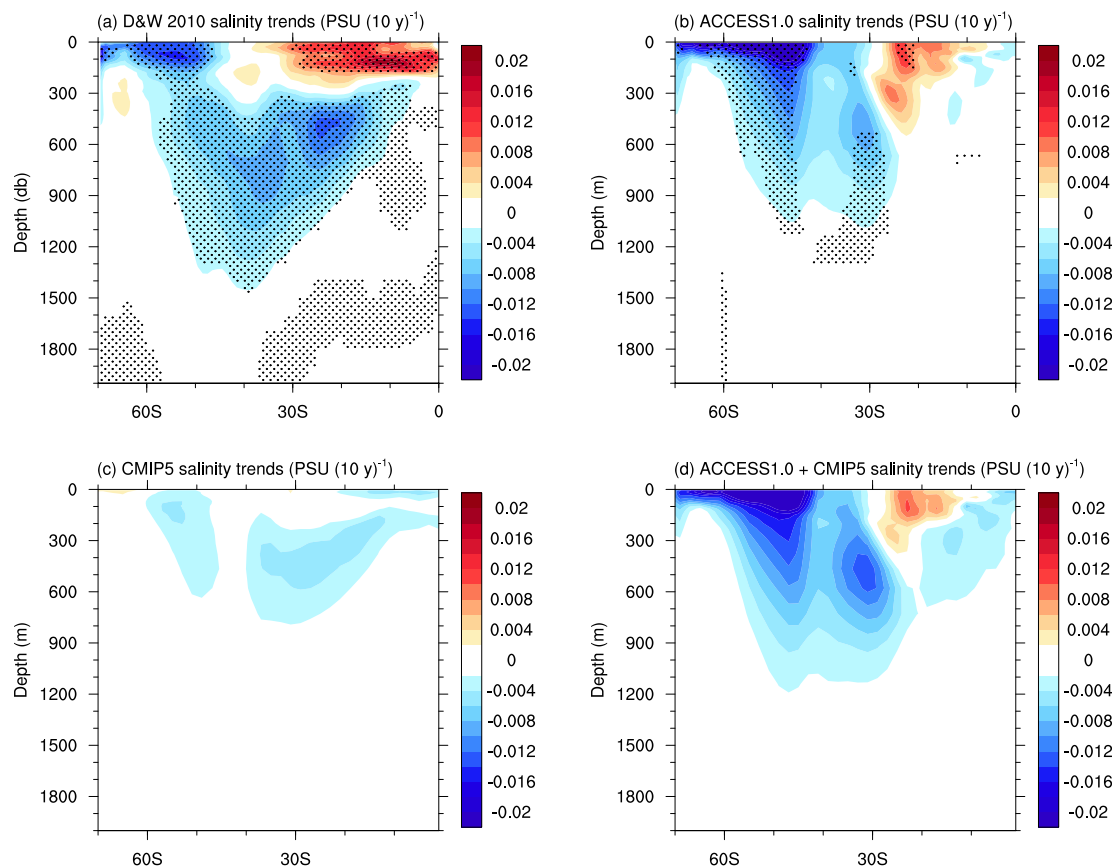


FIG. 4. Zonal-mean 50-yr salinity trends: (a) observed salinity trends from Durack and Wijffels (2010); (b) ensemble-mean trends from the ACCESS1.0 freshwater simulations; (c) CMIP5 multimodel mean trends over 1950–2000; and (d) sum of ACCESS1.0 freshwater ensemble mean trends and CMIP5 multimodel mean trends [i.e., (b) + (c)]. In (a)–(c), stippling indicates trend significance at the 95% level.

reduced ocean convection is causing the subsurface warming (and accompanying surface cooling), as this would correspond to a decreased input of young water, as also identified in the simulations by Kirkman and Bitz (2011). Along-isopycnal mixing changes may also contribute to the similarities between potential temperature and water age trends in this region (Gregory 2000; Kirkman and Bitz 2011).

Increased total surface heat fluxes into the ocean between 60° and 70°S (Fig. 7a) suggest that the surface heat fluxes largely respond to the SST and sea ice changes, not the other way around. In particular, the heat flux trends are an indicator of increased sea ice and surface cooling in response to the changes in ocean circulation (i.e., less heat is lost to the atmosphere when ice cover is increased, and in ice-free areas more sensible heat is transferred from the atmosphere to the cooler ocean surface; there is also reduced heat loss via outgoing longwave radiation changes). However, between 50° and 60°S there is a weak decrease in the total surface heat flux into the ocean (Fig. 7a). This is likely due to a secondary mechanism related to the reduced ocean

convection, whereby a broad-scale shoaling of the mixed layer (Fig. 7b), particularly during austral winter (Fig. 7d), allows more sensible heat loss from the surface during wintertime (Fig. 7c). This leads to a weak decrease in the annual-mean total heat flux into the ocean over 50°–60°S, contributing to the surface cooling in this region.

Despite a zonal-mean freshwater flux being applied in the simulations, regional patterns also emerge. Of particular note, broad significant SSS trends are not seen in the Ross Sea, which may be a result of spurious deep convection simulated by ACCESS1.0 in this region (Fig. 7b; see also de Lavergne et al. 2014), and as a result there is weak (and largely insignificant) warming in this region (Fig. 3d), and a decreasing sea ice trend (a portion of which is significant; Fig. 3f). This contrasts the strong cooling and sea ice growth in the Ross Sea seen in observations (Figs. 3c,e), which have been linked to atmospheric circulation patterns associated with decadal variability (e.g., Meehl et al. 2016; Purich et al. 2016b). A zonal-mean surface freshening and cooling can be seen in all seasons (shown for austral

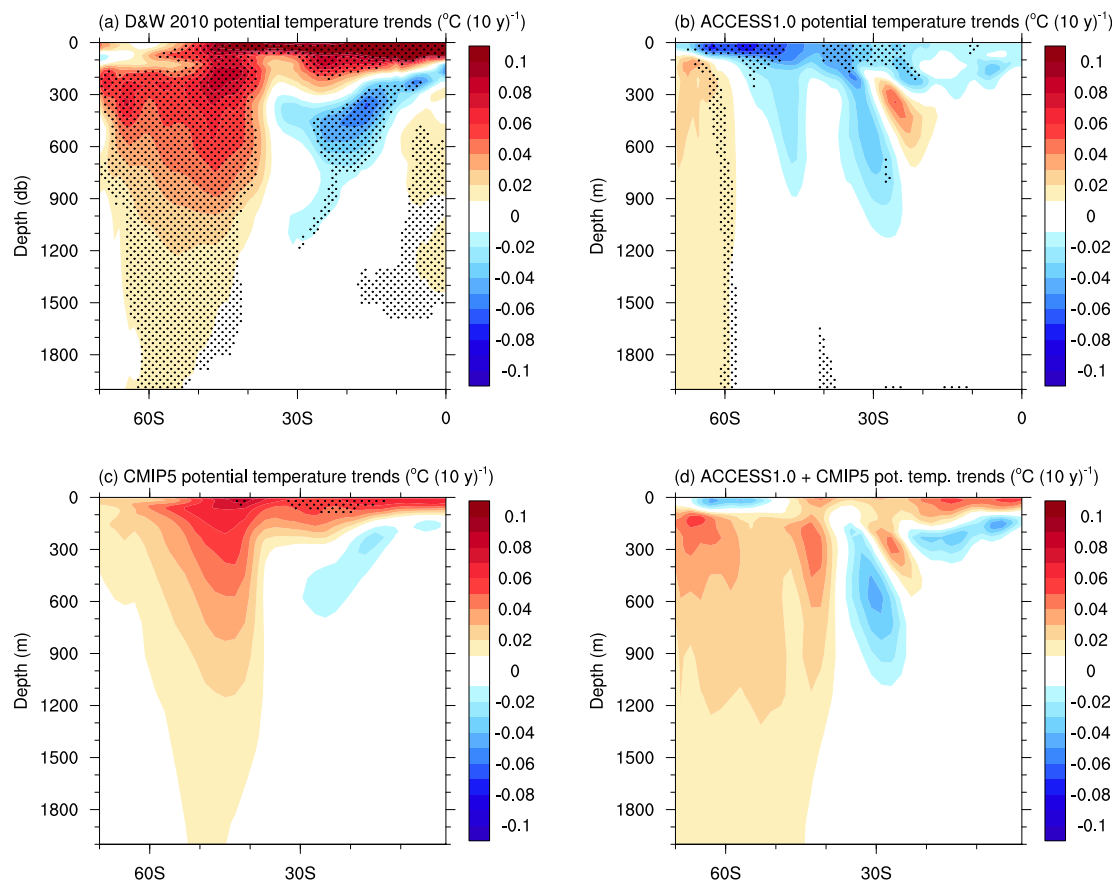


FIG. 5. As in Fig. 4, but for zonal-mean 50-yr potential temperature trends.

summer and winter in Figs. S5 and S6, respectively, in the supplemental material). Sea ice trends respond to the seasonal cycle of growth and retreat, being largest closer to the coast in summer (Fig. S5) and in the outer ice pack in winter (Fig. S6). While a constant freshwater flux is applied into the ocean model component of ACCESS1.0 over 55° – 70°S , the model is free to redistribute this freshwater elsewhere. Over the annual cycle, the additional freshwater input at high latitudes in the model increases SIC, and exports sea ice equatorward where it melts, highlighting the importance of the freshwater redistribution by sea ice, as also discussed in Kirkman and Bitz (2011) and Haumann et al. (2016).

b. Further assessment of subsurface trends

Given the idealized nature of the applied freshwater forcing simulations, it is far from surprising to see differences between the zonal-mean latitude versus depth salinity trends in observations and the freshwater simulations. The observed freshening (Fig. 4a) is strongest at the surface to 150 m between 45° and 70°S , and extends to 1500-m depth between 30° and 40°S , whereas the simulated freshening (Fig. 4b) is strongest at the

surface to 150 m between 40° and 70°S . The simulated subsurface freshening does not extend as deep as observed, extending to 1100 m between 30° and 40°S , and does not extend as far equatorward. This could be due to overly strong diffusive mixing of the anomalous low-salinity waters, a chronic problem in non-eddy-resolving ocean models (England 1993), or because the freshwater simulations do not include surface temperature changes, which have been shown to be important to replicate observed subsurface salinity changes (Lago et al. 2016). Both observations and the freshwater forcing simulations also exhibit a surface salinification north of 30°S . Salinity increases are stronger and more pervasive in observations than in the freshwater forcing simulations, because the primary drivers of the observed SSS increase relate to a poleward migration of the midlatitude westerly wind jet and storm tracks, which in turn sees precipitation and the northward transport of cool freshwater diminish at this latitude band (e.g., Sen Gupta and England 2006). In contrast, in the freshwater forcing simulations no wind shift is imposed, leaving only the local stratification changes (and any other associated feedbacks) as the major mechanism for surface water mass change.

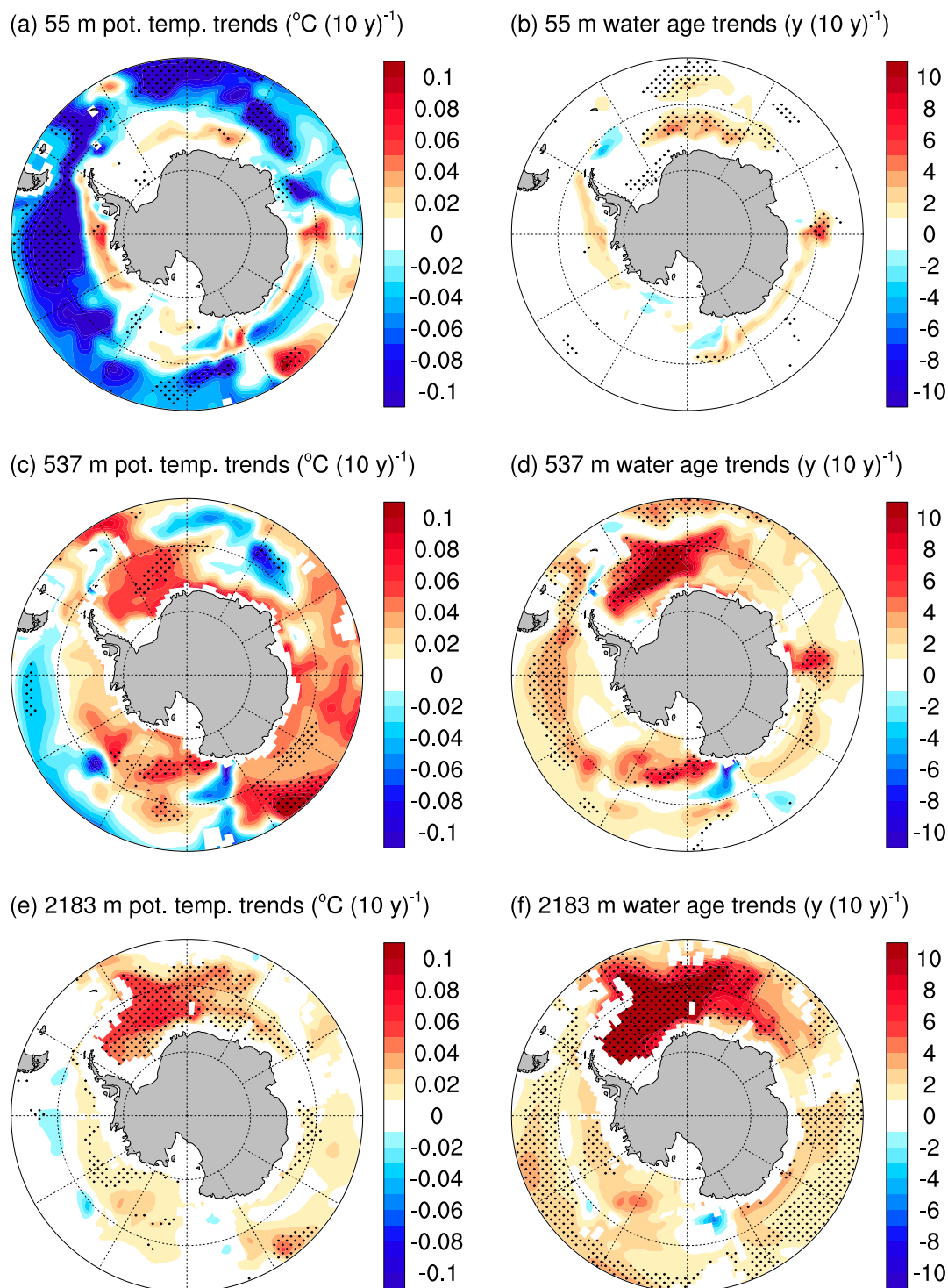


FIG. 6. Ensemble-mean 50-yr trends for (left) potential temperature and (right) water age from the ACCESS1.0 freshwater simulations. Water age acts as a tracer in ACCESS1.0 and indicates the length of time since a parcel of water has been at the surface. Trends are shown for depths of (a),(b) 55, (c),(d) 537, and (e), (f) 2183 m. In all panels, stippling indicates trend significance at the 95% level.

The observed trend in potential temperature (Fig. 5a) shows strong warming at the surface for all latitudes (likely driven by greenhouse warming) except between 55° and 70°S , where there is an absence of warming.

Warming of the Southern Ocean below 150 m occurs between 40° and 70°S . The freshwater simulations (Fig. 5b) show a surface cooling over the Southern Ocean, strongest between 40° and 70°S to 100 m.

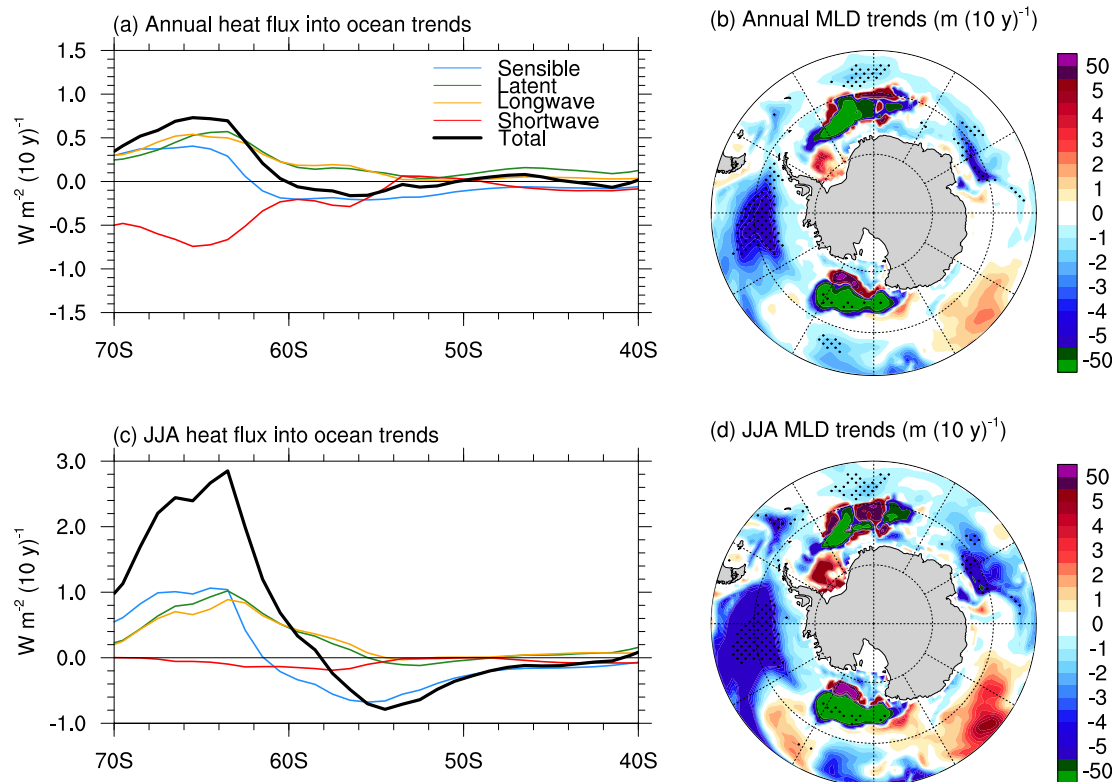


FIG. 7. Ensemble-mean 50-yr trends for (left) zonal-mean surface heat fluxes and (right) mixed layer depth. Trends are shown for (a),(b) the annual mean and (c),(d) austral winter (JJA). In (b),(d), the color bar is nonlinear, with green and purple shading indicating trends in the regions of deep ocean convection, and stippling indicates trend significance at the 95% level.

Between 60° and 70°S a significant warming signal is seen extending to 3000 m. As discussed above, the simulated salinity and potential temperature signals indicate an increase in surface stability, reducing convective overturning in the Southern Ocean, and thus also the upwelling of warmer subsurface waters, causing a cooling at the surface and warming below (as in, e.g., [Martinson 1990](#); [Marsland and Wolff 2001](#)). This surface cooling is then conducive to increased sea ice, as seen in the surface trend map ([Fig. 3e](#)).

Despite the differences discussed above, the freshwater simulations capture the observed subsurface salinity pattern much more accurately than the CMIP5 multimodel mean does ([Fig. 4c](#)). However, without increased radiative forcing in the freshwater simulations, it is not expected that the simulated potential temperature trends ([Fig. 5b](#)) will capture all characteristics of the observed trends ([Fig. 5a](#)). For comparison, the potential temperature trends from the CMIP5 multimodel mean are shown in [Fig. 5c](#). This panel represents the modeled estimate of the long-term mean climate system response to increased radiative forcing with variability averaged out. As with observations, a surface warming is seen in the CMIP5 multimodel

mean, extending to 2000 m around 50°S. However, as discussed in the introduction, the CMIP5 multimodel mean does not exhibit Southern Ocean surface cooling, or freshening, in contrast to observations. Further, the CMIP5 multimodel mean warming is weaker than observed between 150 and 900 m at 70°S. Linear addition of the freshwater simulation trend pattern ([Fig. 5b](#)) and the CMIP5 multimodel mean trend pattern ([Fig. 5c](#)) yields the pattern shown in [Fig. 5d](#). We add these two trend patterns as while many of the CMIP5 models do show some freshening associated with historical forcings ([Figs. 1b](#) and [2](#)), it is generally underestimated compared to observations over the high latitudes. Adding the CMIP5 multimodel mean with underestimated surface freshening ([Figs. 4c](#) and [5c](#)) to the freshwater simulations without historical forcings ([Figs. 4b](#) and [5b](#)) thus provides a useful qualitative comparison to the observations ([Figs. 4d](#) and [5d](#)). Qualitatively, this pattern better captures the 55°–70°S surface cooling and subsurface warming than the CMIP5 multimodel mean alone. This suggests that both Southern Ocean surface freshening and increased radiative forcing are important components in influencing the high-latitude trends in temperature.

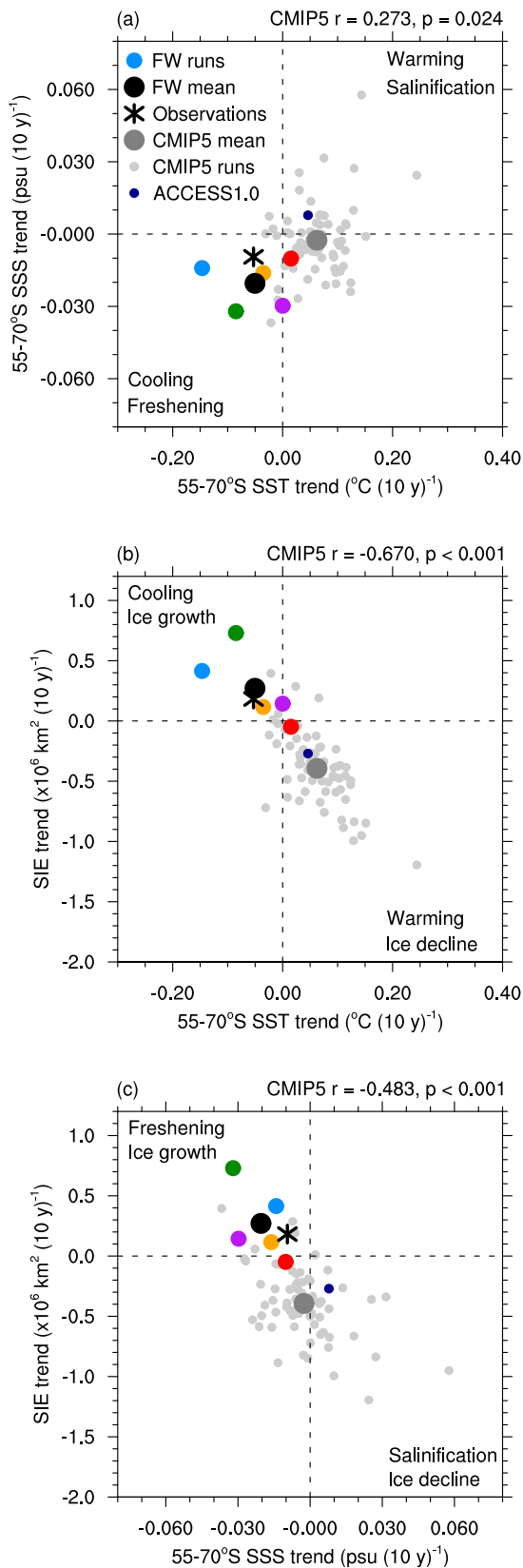


FIG. 8. The 35-yr trends in SSS, SST, and SIE for the ACCESS1.0 freshwater simulations, observations, and CMIP5 models: (a) SSS vs SST, (b) SIE vs SST, and (c) SIE vs SSS. SSS and SST are area-averaged over 55°–70°S. Colored markers show individual freshwater simulations,

c. Intermodel trend comparison

We next consider the intermodel relationships between the CMIP5 models and the freshwater simulations, to better understand the role freshwater forcing has in influencing Southern Ocean trends. Figure 8 shows area-averaged trends in Southern Ocean SSS, SST, and SIE for observations (black asterisk), freshwater simulations (colored dots), and CMIP5 models (gray dots). For comparison, the trend from the ACCESS1.0 realization submitted to CMIP5 is also highlighted (small dark blue dot and hereafter referred to as ACCESS1.0 CMIP5). We are particularly interested in the role freshwater forcing plays in influencing the observed sea ice trends, so here we focus on 35-yr trends in all metrics to match the observational sea ice record (as opposed to the 50-yr trends considered previously). Observed SIE and SST trends and CMIP5 SIE, SST, and SSS trends are all calculated over 1979–2013, and all freshwater simulation trends are calculated over the last 35 years of each run to compare periods of equal length. However, because of observational limitations as discussed in section 2c, observed SSS trends are still calculated over 1950–2000.

A moderate intermodel relationships is seen between trends in SSS and SST (Fig. 8a), and strong intermodel relationships are seen between trends in SIE and SST (Fig. 8b), and trends in SIE and SSS (Fig. 8c). In all cases the intermodel relationship between CMIP5 models is statistically significant ($p < 0.05$), although we note that the SST–SSS significance (Fig. 8a) is dependent on inclusion of models at the tail end of the distribution (strong warming and increased salinity), and the observed and ACCESS1.0 freshwater simulation trends fit the relationship shown by the CMIP5 models. Models or runs that show a stronger surface freshening also tend to show a stronger surface cooling and an increase in sea ice (or at least a weaker decrease in sea ice). Models or runs that show a stronger surface salinification tend to warm more and show a larger decline in sea ice.

←

the freshwater ensemble mean is shown by a black dot, observations are shown by a black asterisk, the CMIP5 multimodel mean is shown by a dark gray dot, the CMIP5 models are shown by light gray markers, and the ACCESS1.0 CMIP5 run is shown by a small dark blue marker. Observed SST and SIE trends and CMIP5 trends are calculated over 1979–2013. Freshwater simulation trends are calculated for the last 35 years of the experiments, to cover a comparable length period to the CMIP5 models and SIE and SST observations. Because of observational limitations as discussed in section 2c, observed SSS trends are calculated over 1950–2000 (i.e., the observed SSS trends cover a different period of different length than all other points shown).

The majority of CMIP5 models do not simulate a surface cooling and increase in sea ice (Fig. 8b), as seen in observations, which has previously been linked in part to a summertime mechanism related to underestimation of the westerly wind intensification, leading to an underestimation of increased Ekman upwelling, which in summer is associated with surface cooling (Purich et al. 2016a). This intermodel relationship occurs because during summer the surface water that receives shortwave radiation resides in a thin layer at the surface (0–20 m), forming a cap over cool winter water (20–150 m). Thus, enhanced Ekman upwelling during summer brings cooler winter water to the surface, and this surface cooling spreads north as a result of equatorward Ekman transport. Wind-driven Ekman upwelling seems to dominate over salinity-driven stratification during summer, and thus the intermodel trend relationship between SSS and SST is not statistically significant (Fig. S7 in the supplemental material).

During winter there is no warm layer at the surface, and the ocean is stratified between cold freshwater at the surface and warm salty water at depth. Given these water column characteristics, salinity-driven stratification becomes more strongly linked to surface temperature, and the intermodel trend relationship between SSS and SST is strengthened during the winter season (Fig. S8 in the supplemental material; $p < 0.01$, although again the significance of this relationship is dependent on including models at the tail ends of the distribution). When considering the annual-mean temperature profile, on average warmer waters reside below cooler surface waters; as such, increased stability and reduced upwelling cause surface cooling, as seen in the relationship between SSS and SST trends in Fig. 8a. Whereas the vast majority of CMIP5 models do not lie in the same quadrant as the observed trends (with SSS trends over 1950–2000), the majority of the freshwater simulations and the freshwater ensemble mean trends do, demonstrating a similarity between the freshwater simulations and observations not shared by the majority of CMIP5 models. However, we note that while the observed SSS trend over 1950–2000 provides a general indication of the long-term trend, because of observational limitations we cannot actually know what quadrant the observed trends with SSS calculated over 1979–2013 lie in (Figs. 8a,c). We also note that our freshwater simulations do not include anthropogenic forcings, so while they do indeed simulate a freshening and cooling, this may not be the case with the same freshening imposed under global warming conditions.

It is also worth noting the spread across the five freshwater simulations (Fig. 8), which have identical forcings and differ only in their initial conditions. While the freshwater simulations fit the CMIP5 intermodel

trend relationship in each case (Figs. 8a–c), the spread among the five ensemble members highlights that the Southern Ocean hydrography exhibits notable multidecadal variability, presumably driven by multidecadal secular variability in atmospheric forcing (e.g., via decadal variability in the SAM). This also emphasizes the limitations of assessing Southern Ocean trends over 35 years, a period that may not accurately represent longer-term trends because of aliased multidecadal variability (Goosse et al. 2009; Jones et al. 2016; Hobbs et al. 2016). When 50-yr trends are considered for all metrics for both the freshwater simulations and the CMIP5 realizations (Fig. S9 in the supplemental material), the variability across ensemble member trends greatly reduces, diminishing the spread across both the freshwater and CMIP5 simulations.

d. Salinity restoring simulations

While this study focuses on the output from the ACCESS1.0 idealized freshwater simulations, regional differences between observations and modeled trends in SSS can be seen (Figs. 3a,b). In particular, the model redistribution of the applied idealized freshwater flux results in little surface freshening of the Ross Sea, but considerable pooling of freshwater in the Bellingshausen Sea (Fig. 3b), resulting in SSS trends that exhibit an opposite dipole pattern to what is observed in these regions (Fig. 3a). To complement the idealized freshwater simulations and apply more realistic geographic distributions of trends, we also conduct a pair of SSS restoring simulations: one is an unperturbed control run and the second is identical to the control, but with an applied freshening of surface salinity that spatially matches the Durack and Wijffels (2010) trends. In the first simulation, SSS between 40° and 70°S (with tapering either side) is restored to the annually and monthly varying SSS of the piControl over a 50-yr reanalyzed segment of the run. In the second simulation, an annually increasing trend is superimposed onto the piControl SSS in the 40°–70°S restoring region. This applied SSS trend is set to exactly match the observed Durack and Wijffels (2010) trends. Because of the different experimental setup, compared to the idealized freshwater simulations, these SSS restoring simulations enable better resolution of the geographic distribution of observed SSS trends. Both restoring simulations are branched from the same year of the piControl and run for 50 years each. The SSS restoring time scale is 15 days over the upper-ocean model layer.

We difference the two SSS restoring simulations to obtain the signal due to the Durack and Wijffels (2010) SSS trend, shown in Fig. 9. The SSS restoring difference pattern (Fig. 9b) accurately captures the observed SSS

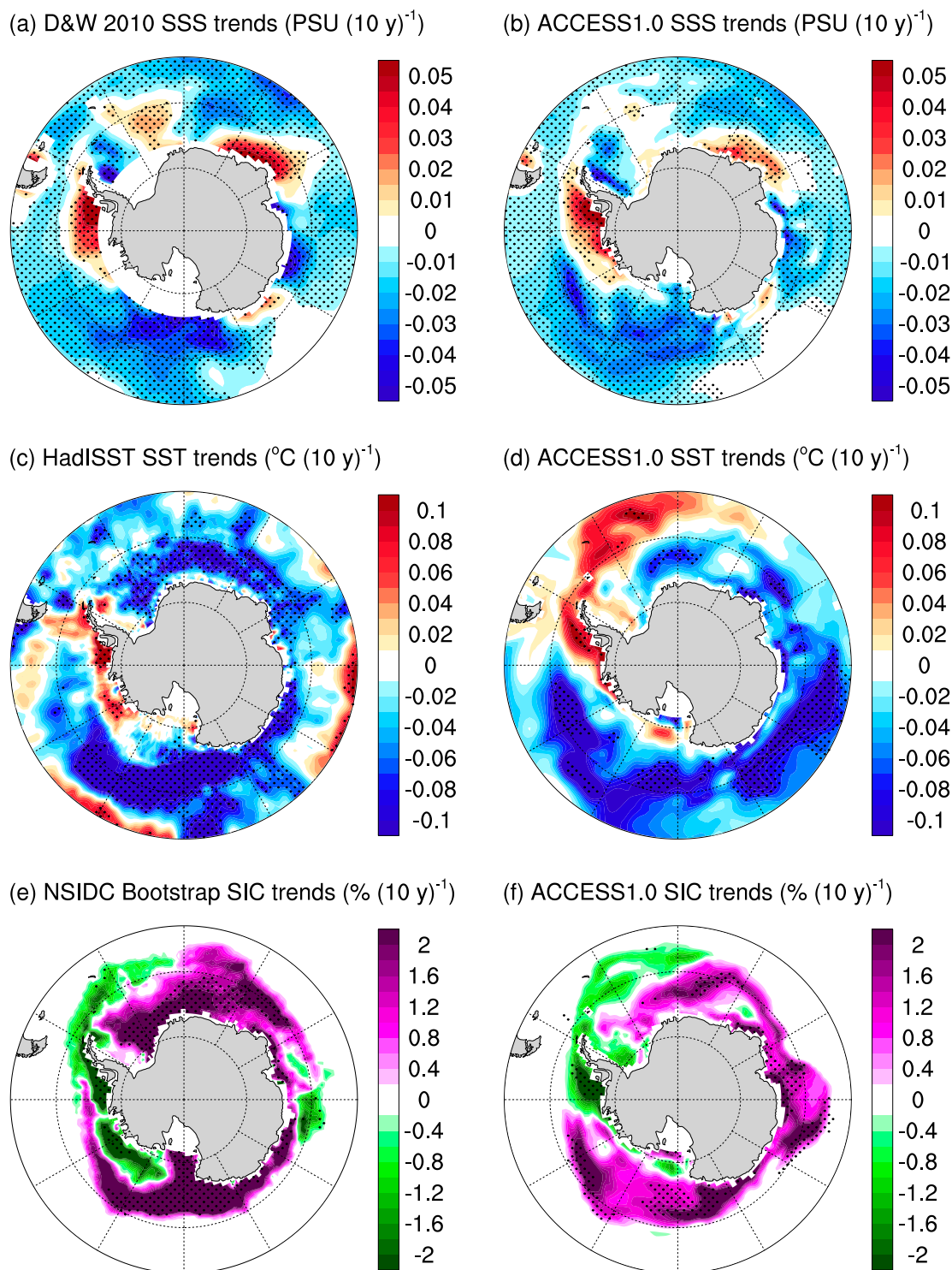


FIG. 9. (left) Observed and (right) 50-yr trends from differencing the ACCESS1.0 SSS restoring simulations: (a),(b) SSS trends, (c),(d) SST trends, and (e),(f) SIC trends. Note that (a),(c),(e) are identical to Figs. 3a,c,e and are included here for direct comparison. In all panels, stippling indicates trend significance at the 95% level. Observations are as in Fig. 3.

trend pattern (Fig. 9a), as expected given the restoring technique, with only minor differences evident. The SST (Fig. 9d) and SIC (Fig. 9f) trend patterns that result from this SSS restoring approach also resemble the observed

(Figs. 9c,e) trends remarkably well. The observed SSS changes drive cooling around most regions of Antarctica, and an accompanying increase in sea ice in the restoring simulations, as well as the characteristic

warming and decrease in SIC in the Bellingshausen Sea and along the Antarctic Peninsula. There are also some differences between the observed and simulated trends. In particular, in contrast to the observed cooling, a strong warming is simulated in the South Atlantic (Figs. 9c,d). Overall however, the SST trend patterns south of 60°S show remarkable agreement. Minor regional differences in the SIC trend patterns (Figs. 9e,f) appear in the inner Amundsen Sea and at 90°E, but overall the SIC trend patterns show strong similarities. These SSS restoring simulations demonstrate that without any mechanical forcing associated with changing winds, SSS can drive changes in SST, and remarkably that the regional pattern of SSS trends can drive the dipole trends in SST and sea ice in the Pacific sector. This reinforces the findings presented above, based on the freshwater simulations that demonstrate how reduced upwelling of warmer subsurface waters induced by large-scale freshening trends has played an important role in the recent multidecadal cooling of the surface Southern Ocean.

4. Discussion

The Southern Ocean surface has freshened in recent decades (Durack and Wijffels 2010; de Lavergne et al. 2014), increasing water column stability and reducing the upwelling of warm subsurface waters. While previous studies have investigated the influence of increased freshwater from Antarctic ice sheet and shelf runoff and iceberg fluxes around the continental margins (Bintanja et al. 2013, 2015; Swart and Fyfe 2013; Pauling et al. 2016), the impact of broad-scale freshening resulting from a combination of factors, including freshwater redistribution by sea ice and icebergs, increased ice sheet and ice shelf runoff, and $P - E$ changes likely associated with the positive SAM trend, has received little attention. The possible role that this broad-scale freshening has had on Antarctic sea ice trends and surface Southern Ocean cooling provided the overall motivation for this study. To this end, we examined targeted coupled climate model simulations run using ACCESS1.0 with increased freshwater applied to the ocean model component over the Southern Ocean.

In terms of the total mass of freshwater applied in our simulations, the freshwater trend of 0.1 mm day^{-1} (10 yr^{-1}) applied in our simulations over 55°–70°S corresponds to a freshwater mass acceleration of approximately 112 Gt yr^{-2} ($\sim 5600 \text{ Gt yr}^{-1}$ in the last year of the simulations), chosen to simulate a clear surface freshening as observed. To put this into context, Pauling et al. (2016) found the increase in $P - E$ over the Southern Ocean (south of 50°S, not including Antarctica) from the preindustrial period to the present day to be approximately

2000 Gt yr^{-1} in the CMIP5 models, although with considerable spread across models (see their Fig. 5c). The additional freshwater applied in our idealized simulations is considerably higher than this, as the majority of CMIP5 models underestimate the surface freshening trends over the Southern Ocean (Fig. 1b). Our idealized freshwater simulations show that a surface freshening causes a decrease in SST and an increase in sea ice, attributed primarily to a reduction in ocean convection. However, to achieve a cooling and SIE increase similar to observations, a stronger than observed zonal-mean freshening was applied (Fig. 8). This suggests that a uniform broad-scale surface freshening from processes including increased $P - E$ is only one component contributing to observed sea ice changes and surface cooling; other factors such as decadal variability (Meehl et al. 2016; Purich et al. 2016b), direct wind effects (Holland and Kwok 2012; Purich et al. 2016a), and zonal variations in SSS (as per our SSS restoring simulations; Fig. 9) also play a critical role.

Comparisons with results from Bintanja et al. (2013), Bintanja et al. (2015), and Pauling et al. (2016) are difficult, as their experiments added constant, rather than increasing, amounts of freshwater, and in addition their focus is on the impacts of Antarctic meltwater discharge, not the broad-scale freshening due to precipitation trends examined here. While Bintanja et al. (2013) added a relatively modest 250 Gt yr^{-1} over 31 years with radiative forcing held fixed, when differenced from their control experiment, sea ice was found to increase. In similar simulations with increased radiative forcing, Bintanja et al. (2015) added only $10\text{--}120 \text{ Gt yr}^{-1}$ of freshwater and found that 120 Gt yr^{-1} was enough to offset radiative forcing and result in a weak increase in sea ice. On the other hand, the surface freshwater experiments by Pauling et al. (2016) added $1000\text{--}3000 \text{ Gt yr}^{-1}$, and while they found an increase in mean-state sea ice area, they did not find a positive trend in sea ice under increased radiative forcing conditions. While these studies are very useful in better understanding how a constant additional freshwater flux governs changes in sea ice, motivated by the lack of constant Antarctic ice shelf and sheet runoff and iceberg fluxes in the CMIP5 models, without time-varying freshwater fluxes, it is difficult to compare these studies to the real-world surface freshening trend that has been observed (Durack and Wijffels 2010).

The study by Swart and Fyfe (2013) is more comparable to this study, as they also applied increasing amounts of freshwater, although their freshwater flux was only applied around the Antarctic margin, compared to the broad-scale additional flux in our simulations. Their additions ranged from 3.15 to 15.77 Gt yr^{-2} over 47 years ($\sim 740 \text{ Gt yr}^{-1}$ in the last year of the simulation for the highest acceleration rate) and

from 3.15 to 31.54 Gt yr⁻² over 29 years (~ 910 Gt yr⁻¹ in the last year of the simulation for the highest acceleration rate). These freshwater additions are considerably less than those applied in our experiments, as we are interested in broad-scale freshening from processes including $P - E$ changes, whereas Swart and Fyfe (2013) were interested in the Antarctic ice sheet meltwater. The simulations by Swart and Fyfe (2013) also included increased radiative forcing, and they found that the additional freshwater in their simulations reduced the amount of sea ice lost, but could not reverse the negative sea ice trend. Despite this, relative to their control experiment, their strongest freshwater mass accelerations gave regional SIC trends on the order of 0.5–2.5% (10 yr)⁻¹ [Fig. 4d in Swart and Fyfe (2013)], which are comparable to our SIC trends (Fig. 3f).

We show that the majority of CMIP5 models underestimate the observed surface freshening over the Southern Ocean over the latter half of the twentieth century. Based on the intermodel CMIP5 trend relationships assessed here, alongside our freshwater anomaly experiments conducted using ACCESS1.0, this reduced or absent freshening highly likely contributes to the poor simulation of observed Southern Ocean surface cooling and Antarctic sea ice trends in CMIP5 models. However, compared to the CMIP5 models and the real world, we note that our freshwater simulations are idealized and do not include anthropogenic greenhouse warming. The historical and RCP8.5 ACCESS1.0 simulation participating in CMIP5 shows a Southern Ocean SST warming of approximately 0.05°C (10 yr)⁻¹ over 1979–2013, between 55° and 70°S, as well as a weak increase in surface salinity over this latitude band. In contrast, the ensemble mean of our idealized freshwater simulations shows a cooling over this same latitude band of approximately -0.05°C (10 yr)⁻¹. Similarly, the historical and RCP8.5 ACCESS1.0 simulation exhibits a significant sea ice retreat over this period [$\sim -0.27 \times 10^6 \text{ km}^2$ (10 yr)⁻¹], while adding a surface freshening trend in our idealized freshwater simulations leads to the opposite sea ice tendencies; namely, an ensemble-mean expansion in Antarctic sea ice that happens to be of similar magnitude [$\sim 0.27 \times 10^6 \text{ km}^2$ (10 yr)⁻¹]. The freshening-induced cooling we obtain could thus clearly be one of the important factors accounting for the regional model–observation mismatch in recent SST and SIC trends, alongside decadal variability and direct wind effects. Furthermore, the strong relationships obtained between Southern Ocean surface salinity and temperature trends demonstrate the importance of surface freshening in this region for upper-ocean thermal properties. Had the historical greenhouse warming been added alongside the surface freshening in our idealized freshwater

simulations, the influence of these two factors might have more or less canceled to yield a minimal trend in Southern Ocean SST and SIE; this will be the focus of future work (see also Fig. S10 in the supplemental material).

Many of the features of both SST and sea ice trends in the region, including warming and reduced sea ice in the Amundsen and Bellingshausen Seas and cooling and increased sea ice in the Ross Sea, can be accurately simulated when simply imposing the observed SSS trends over the Southern Ocean in SSS restoring simulations. This demonstrates that upper-ocean SSS trends have been an important component in driving regional hydrography and circulation changes around Antarctica over the last half century. This study also highlights the importance of accurately simulating changes in clouds, storm tracks, $P - E$, and surface salinity over the Southern Ocean to capture changes in ocean circulation and sea ice.

Acknowledgments. This work was supported by the Australian Research Council (ARC) including the ARC Centre of Excellence for Climate System Science (CE110001028), and CSIRO Oceans and Atmosphere. A.P. was supported by an Australian Postgraduate Award, a UNSW Research Excellence scholarship, and a CSIRO Office of the Chief Executive Science Leader scholarship. M.H.E. was supported by an ARC Laureate Fellowship (FL100100214). W.C. was supported by the Centre for Southern Hemisphere Oceans Research, a joint research centre between QNLM and CSIRO. The work of P.J.D. from Lawrence Livermore National Laboratory was performed under the auspices of the U.S. Department of Energy, Office of Science, Climate and Environmental Sciences Division, Regional and Global Model Analysis Program under Contract DE-AC52-07NA27344. This research was undertaken with the assistance of resources and services from the National Computational Infrastructure (NCI), which is supported by the Australian Government. Figures were produced using the NCAR Command Language (<https://doi.org/10.5065/D6WD3XH5>). We acknowledge the World Climate Research Programme's Working Group on Coupled Modelling, which is responsible for CMIP, and thank the climate modelling groups for producing and making available their model output. We also thank the three anonymous reviewers for their helpful comments.

REFERENCES

- Adler, R. F., and Coauthors, 2003: The version-2 Global Precipitation Climatology Project (GPCP) monthly precipitation analysis (1979–present). *J. Hydrometeorol.*, **4**, 1147–1167, [https://doi.org/10.1175/1525-7541\(2003\)004<1147:TVGPCP>2.0.CO;2](https://doi.org/10.1175/1525-7541(2003)004<1147:TVGPCP>2.0.CO;2).
- Aiken, C. M., and M. H. England, 2008: Sensitivity of the present-day climate to freshwater forcing associated with Antarctic sea

- ice loss. *J. Climate*, **21**, 3936–3946, <https://doi.org/10.1175/2007JCLI1901.1>.
- Armour, K. C., J. Marshall, J. R. Scott, A. Donohoe, and E. R. Newsom, 2016: Southern Ocean warming delayed by circumpolar upwelling and equatorward transport. *Nat. Geosci.*, **9**, 549–554, <https://doi.org/10.1038/ngeo2731>.
- Beckmann, A., and H. Goosse, 2003: A parameterization of ice shelf–ocean interaction for climate models. *Ocean Modell.*, **5**, 157–170, [https://doi.org/10.1016/S1463-5003\(02\)00019-7](https://doi.org/10.1016/S1463-5003(02)00019-7).
- Bi, D., and Coauthors, 2013a: ACCESS-OM: The ocean and sea-ice core of the ACCESS coupled model. *Aust. Meteor. Oceanogr. J.*, **63**, 213–232, <https://doi.org/10.22499/2.6301.014>.
- , and Coauthors, 2013b: The ACCESS coupled model: Description, control climate and evaluation. *Aust. Meteor. Oceanogr. J.*, **63**, 41–64, <https://doi.org/10.22499/2.6301.004>.
- Bintanja, R., G. van Oldenborgh, S. Drijfhout, B. Wouters, and C. Katsman, 2013: Important role for ocean warming and increased ice-shelf melt in Antarctic sea-ice expansion. *Nat. Geosci.*, **6**, 376–379, <https://doi.org/10.1038/ngeo1767>.
- , —, and C. Katsman, 2015: The effect of increased fresh water from Antarctic ice shelves on future trends in Antarctic sea ice. *Ann. Glaciol.*, **56**, 120–126, <https://doi.org/10.3189/2015AoG69A001>.
- Boyer, T. P., S. Levitus, J. Antonov, R. Locarnini, and H. Garcia, 2005: Linear trends in salinity for the World Ocean, 1955–1998. *Geophys. Res. Lett.*, **32**, L01604, <https://doi.org/10.1029/2004GL021791>.
- Bracegirdle, T. J., E. F. Shuckburgh, J.-B. Sallée, Z. Wang, A. J. Meijers, N. Bruneau, T. Phillips, and L. J. Wilcox, 2013: Assessment of surface winds over the Atlantic, Indian, and Pacific ocean sectors of the Southern Ocean in CMIP5 models: Historical bias, forcing response, and state dependence. *J. Geophys. Res. Atmos.*, **118**, 547–562, <https://doi.org/10.1002/jgrd.50153>.
- Bromwich, D. H., J. P. Nicolas, and A. J. Monaghan, 2011: An assessment of precipitation changes over Antarctica and the Southern Ocean since 1989 in contemporary global reanalyses. *J. Climate*, **24**, 4189–4209, <https://doi.org/10.1175/2011JCLI4074.1>.
- Cavalieri, D., and C. L. Parkinson, 2008: Antarctic sea ice variability and trends, 1979–2006. *J. Geophys. Res.*, **113**, C07004, <https://doi.org/10.1029/2007JC004564>.
- Comiso, J. C., and F. Nishio, 2008: Trends in the sea ice cover using enhanced and compatible AMSR-E, SSM/I, and SMMR data. *J. Geophys. Res.*, **113**, C02S07, <https://doi.org/10.1029/2007JC004257>.
- Davies, T., M. J. P. Cullen, A. J. Malcolm, M. H. Mawson, A. Staniforth, A. A. White, and N. Wood, 2005: A new dynamical core for the Met Office's global and regional modelling of the atmosphere. *Quart. J. Roy. Meteor. Soc.*, **131**, 1759–1782, <https://doi.org/10.1256/qj.04.101>.
- Dee, D., and Coauthors, 2011: The ERA-Interim reanalysis: Configuration and performance of the data assimilation system. *Quart. J. Roy. Meteor. Soc.*, **137**, 553–597, <https://doi.org/10.1002/qj.828>.
- de Lavergne, C., J. B. Palter, E. D. Galbraith, R. Bernardello, and I. Marinov, 2014: Cessation of deep convection in the open Southern Ocean under anthropogenic climate change. *Nat. Climate Change*, **4**, 278–282, <https://doi.org/10.1038/nclimate2132>.
- Dix, M., and Coauthors, 2013: The ACCESS coupled model: Documentation of core CMIP5 simulations and initial results. *Aust. Meteor. Oceanogr. J.*, **63**, 83–99, <https://doi.org/10.22499/2.6301.006>.
- Durack, P. J., 2015: Ocean salinity and the global water cycle. *Oceanography*, **28**, 20–31, <https://doi.org/10.5670/oceanog.2015.03>.
- , and S. E. Wijffels, 2010: Fifty-year trends in global ocean salinities and their relationship to broad-scale warming. *J. Climate*, **23**, 4342–4362, <https://doi.org/10.1175/2010JCLI3377.1>.
- , —, and R. J. Matear, 2012: Ocean salinities reveal strong global water cycle intensification during 1950 to 2000. *Science*, **336**, 455–458, <https://doi.org/10.1126/science.1212222>.
- , P. J. Gleckler, F. W. Landerer, and K. E. Taylor, 2014: Quantifying underestimates of long-term upper-ocean warming. *Nat. Climate Change*, **4**, 999–1005, <https://doi.org/10.1038/nclimate2389>.
- England, M. H., 1993: Representing the global-scale water masses in ocean general circulation models. *J. Phys. Oceanogr.*, **23**, 1523–1552, [https://doi.org/10.1175/1520-0485\(1993\)023<1523:RTGSWM>2.0.CO;2](https://doi.org/10.1175/1520-0485(1993)023<1523:RTGSWM>2.0.CO;2).
- Fan, T., C. Deser, and D. P. Schneider, 2014: Recent Antarctic sea ice trends in the context of Southern Ocean surface climate variations since 1950. *Geophys. Res. Lett.*, **41**, 2419–2426, <https://doi.org/10.1002/2014GL059239>.
- Fetterer, F., K. Knowles, W. Meier, and M. Savoie, 2002: Sea Ice Index (subset: Antarctic). National Snow and Ice Data Center, accessed February 2015, <https://doi.org/10.7265/N5K072F8>.
- Frederiksen, J. S., and C. S. Frederiksen, 2007: Interdecadal changes in Southern Hemisphere winter storm track modes. *Tellus*, **59A**, 599–617, <https://doi.org/10.1111/j.1600-0870.2007.00264.x>.
- Fyfe, J. C., 2003: Extratropical Southern Hemisphere cyclones: Harbingers of climate change? *J. Climate*, **16**, 2802–2805, [https://doi.org/10.1175/1520-0442\(2003\)016<2802:ESHCHO>2.0.CO;2](https://doi.org/10.1175/1520-0442(2003)016<2802:ESHCHO>2.0.CO;2).
- Gagné, M.-E., N. P. Gillett, and J. C. Fyfe, 2015: Observed and simulated changes in Antarctic sea ice extent over the past 50 years. *Geophys. Res. Lett.*, **42**, 90–95, <https://doi.org/10.1002/2014GL062231>.
- Good, S. A., M. J. Martin, and N. A. Rayner, 2013: EN4: Quality controlled ocean temperature and salinity profiles and monthly objective analyses with uncertainty estimates. *J. Geophys. Res. Oceans*, **118**, 6704–6716, <https://doi.org/10.1002/2013JC009067>.
- Goosse, H., and V. Zunz, 2014: Decadal trends in the Antarctic sea ice extent ultimately controlled by ice–ocean feedback. *Cryosphere*, **8**, 453–470, <https://doi.org/10.5194/tc-8-453-2014>.
- , W. Lefebvre, A. de Montety, E. Cressin, and A. Orsi, 2009: Consistent past half-century trends in the atmosphere, the sea ice and the ocean at high southern latitudes. *Climate Dyn.*, **33**, 999–1016, <https://doi.org/10.1007/s00382-008-0500-9>.
- Gregory, J. M., 2000: Vertical heat transports in the ocean and their effect on time-dependent climate change. *Climate Dyn.*, **16**, 501–515, <https://doi.org/10.1007/s003820000059>.
- Griffies, S., M. Schmidt, and M. Herzfeld, 2010: Elements of MOM4p1. GFDL Ocean Group Tech. Rep. 6, 444 pp.
- Haumann, F. A., N. Gruber, M. Münnich, I. Frenger, and S. Kern, 2016: Sea-ice transport driving Southern Ocean salinity and its recent trends. *Nature*, **537**, 89–92, <https://doi.org/10.1038/nature19101>.
- Hellmer, H. H., 2004: Impact of Antarctic ice shelf basal melting on sea ice and deep ocean properties. *Geophys. Res. Lett.*, **31**, L10307, <https://doi.org/10.1029/2004GL019506>.
- Helm, K. P., N. L. Bindoff, and J. A. Church, 2010: Changes in the global hydrological cycle inferred from ocean salinity. *Geophys. Res. Lett.*, **37**, L18701, <https://doi.org/10.1029/2010GL044222>.
- Hobbs, W. R., R. Massom, S. Stammerjohn, P. Reid, G. Williams, and W. Meier, 2016: A review of recent changes in Southern

- Ocean sea ice, their drivers and forcings. *Global Planet. Change*, **143**, 228–250, <https://doi.org/10.1016/j.gloplacha.2016.06.008>.
- Holland, P. R., and R. Kwok, 2012: Wind-driven trends in Antarctic sea-ice drift. *Nat. Geosci.*, **5**, 872–875, <https://doi.org/10.1038/ngeo1627>.
- Hosoda, S., T. Suga, N. Shikama, and K. Mizuno, 2009: Global surface layer salinity change detected by Argo and its implication for hydrological cycle intensification. *J. Oceanogr.*, **65**, 579, <https://doi.org/10.1007/s10872-009-0049-1>.
- Hunke, E. C., and W. H. Lipscomb, 2010: CICE: The Los Alamos Sea Ice Model documentation and software user's manual version 4.1. Los Alamos National Laboratory Tech Rep. LA-CC-06-012, 76 pp.
- Ivanova, D. P., P. J. Gleckler, K. E. Taylor, P. J. Durack, and K. D. Marvel, 2016: Moving beyond the total sea ice extent in gauging model biases. *J. Climate*, **29**, 8965–8987, <https://doi.org/10.1175/JCLI-D-16-0026.1>.
- Jones, J. M., and Coauthors, 2016: Assessing recent trends in high-latitude Southern Hemisphere surface climate. *Nat. Climate Change*, **6**, 917–926, <https://doi.org/10.1038/nclimate3103>.
- Josey, S. A., S. Gulev, and L. Yu, 2013: Exchanges through the ocean surface. *Ocean Circulation and Climate: A 21 Century Perspective*, G. Siedler et al., Eds., Vol. 103, International Geophysics Series, Elsevier, 115–140, <https://doi.org/10.1016/B978-0-12-391851-2.00005-2>.
- Kirkman, C. H., and C. M. Bitz, 2011: The effect of the sea ice freshwater flux on Southern Ocean temperatures in CCSM3: Deep-ocean warming and delayed surface warming. *J. Climate*, **24**, 2224–2237, <https://doi.org/10.1175/2010JCLI3625.1>.
- Lago, V., S. E. Wijffels, P. J. Durack, J. A. Church, N. L. Bindoff, and S. J. Marsland, 2016: Simulating the role of surface forcing on observed multidecadal upper-ocean salinity changes. *J. Climate*, **29**, 5575–5588, <https://doi.org/10.1175/JCLI-D-15-0519.1>.
- Large, W. G., and S. G. Yeager, 2009: The global climatology of an interannually varying air–sea flux data set. *Climate Dyn.*, **33**, 341–364, <https://doi.org/10.1007/s00382-008-0441-3>.
- Li, X., D. M. Holland, E. P. Gerber, and C. Yoo, 2014: Impacts of the north and tropical Atlantic Ocean on the Antarctic Peninsula and sea ice. *Nature*, **505**, 538–542, <https://doi.org/10.1038/nature12945>.
- Liu, J., and J. A. Curry, 2010: Accelerated warming of the Southern Ocean and its impacts on the hydrological cycle and sea ice. *Proc. Natl. Acad. Sci. USA*, **107**, 14 987–14 992, <https://doi.org/10.1073/pnas.1003336107>.
- Mahlstein, I., P. R. Gent, and S. Solomon, 2013: Historical Antarctic mean sea ice area, sea ice trends, and winds in CMIP5 simulations. *J. Geophys. Res. Atmos.*, **118**, 5105–5110, <https://doi.org/10.1002/jgrd.50443>.
- Marshall, G. J., 2003: Trends in the southern annular mode from observations and reanalyses. *J. Climate*, **16**, 4134–4143, [https://doi.org/10.1175/1520-0442\(2003\)016<4134:TITSAM>2.0.CO;2](https://doi.org/10.1175/1520-0442(2003)016<4134:TITSAM>2.0.CO;2).
- Marshall, J., K. C. Armour, J. R. Scott, Y. Kostov, U. Hausmann, D. Ferreira, T. G. Shepherd, and C. M. Bitz, 2014: The ocean's role in polar climate change: Asymmetric Arctic and Antarctic responses to greenhouse gas and ozone forcing. *Philos. Trans. Roy. Soc.*, **372A**, 20130040, <https://doi.org/10.1098/rsta.2013.0040>.
- Marsland, S. J., and J.-O. Wolff, 2001: On the sensitivity of Southern Ocean sea ice to the surface freshwater flux: A model study. *J. Geophys. Res.*, **106**, 2723–2741, <https://doi.org/10.1029/2000JC900086>.
- Martin, G. M., and Coauthors, 2011: The HadGEM2 family of Met Office Unified Model climate configurations. *Geosci. Model Dev.*, **4**, 723–757, <https://doi.org/10.5194/gmd-4-723-2011>.
- , S. F. Milton, C. A. Senior, M. E. Brooks, S. Ineson, T. Reichler, and J. Kim, 2010: Analysis and reduction of systematic errors through a seamless approach to modeling weather and climate. *J. Climate*, **23**, 5933–5957, <https://doi.org/10.1175/2010JCLI3541.1>.
- Martinson, D. G., 1990: Evolution of the Southern Ocean winter mixed layer and sea ice: Open ocean deepwater formation and ventilation. *J. Geophys. Res. Oceans*, **95**, 11 641–11 654, <https://doi.org/10.1029/JC095iC07p11641>.
- Meehl, G. A., J. M. Arblaster, C. M. Bitz, C. T. Chung, and H. Teng, 2016: Antarctic sea-ice expansion between 2000 and 2014 driven by tropical Pacific decadal climate variability. *Nat. Geosci.*, **9**, 590–595, <https://doi.org/10.1038/ngeo2751>.
- Meier, W., F. Fetterer, M. Savoie, S. Mallory, R. Duerr, and J. Stroeve, 2015: NOAA/NSIDC climate data record of passive microwave sea ice concentration, version 2 (subset: Southern Hemisphere). NSIDC, accessed August 2014, <http://nsidc.org/data/G02202/versions/2>.
- Morrison, A. K., M. H. England, and A. M. Hogg, 2015: Response of Southern Ocean convection and abyssal overturning to surface buoyancy perturbations. *J. Climate*, **28**, 4263–4278, <https://doi.org/10.1175/JCLI-D-14-00110.1>.
- Parkinson, C. L., and D. Cavalieri, 2012: Antarctic sea ice variability and trends, 1979–2010. *Cryosphere*, **6**, 871–880, <https://doi.org/10.5194/tc-6-871-2012>.
- Pauling, A. G., C. M. Bitz, I. J. Smith, and P. J. Langhorne, 2016: The response of the Southern Ocean and Antarctic sea ice to fresh water from ice shelves in an Earth system model. *J. Climate*, **29**, 1655–1672, <https://doi.org/10.1175/JCLI-D-15-0501.1>.
- Polvani, L. M., and K. L. Smith, 2013: Can natural variability explain observed Antarctic sea ice trends? New modeling evidence from CMIP5. *Geophys. Res. Lett.*, **40**, 3195–3199, <https://doi.org/10.1002/grl.50578>.
- Purich, A., and S.-W. Son, 2012: Impact of Antarctic ozone depletion and recovery on Southern Hemisphere precipitation, evaporation, and extreme changes. *J. Climate*, **25**, 3145–3154, <https://doi.org/10.1175/JCLI-D-11-00383.1>.
- , T. Cowan, S.-K. Min, and W. Cai, 2013: Autumn precipitation trends over Southern Hemisphere midlatitudes as simulated by CMIP5 models. *J. Climate*, **26**, 8341–8356, <https://doi.org/10.1175/JCLI-D-13-00007.1>.
- , W. Cai, M. H. England, and T. Cowan, 2016a: Evidence for link between modelled trends in Antarctic sea ice and underestimated westerly wind changes. *Nat. Commun.*, **7**, 10409, <https://doi.org/10.1038/ncomms10409>.
- , and Coauthors, 2016b: Tropical Pacific SST drivers of recent Antarctic sea ice trends. *J. Climate*, **29**, 8931–8948, <https://doi.org/10.1175/JCLI-D-16-0440.1>.
- Rayner, N., D. E. Parker, E. Horton, C. K. Folland, L. Alexander, D. Rowell, E. Kent, and A. Kaplan, 2003: Global analyses of sea surface temperature, sea ice, and night marine air temperature since the late nineteenth century. *J. Geophys. Res.*, **108**, 4407, <https://doi.org/10.1029/2002JD002670>.
- Sen Gupta, A., and M. H. England, 2006: Coupled ocean-atmosphere-ice response to variations in the southern annular mode. *J. Climate*, **19**, 4457–4486, <https://doi.org/10.1175/JCLI3843.1>.
- , N. C. Jourdain, J. N. Brown, and D. P. Monselesan, 2013: Climate drift in the CMIP5 models. *J. Climate*, **26**, 8597–8615, <https://doi.org/10.1175/JCLI-D-12-00521.1>.

- Simpkins, G. R., L. M. Ciasto, D. W. Thompson, and M. H. England, 2012: Seasonal relationships between large-scale climate variability and Antarctic sea ice concentration. *J. Climate*, **25**, 5451–5469, <https://doi.org/10.1175/JCLI-D-11-00367.1>.
- , S. McGregor, A. S. Taschetto, L. M. Ciasto, and M. H. England, 2014: Tropical connections to climatic change in the extratropical Southern Hemisphere: The role of Atlantic SST trends. *J. Climate*, **27**, 4923–4936, <https://doi.org/10.1175/JCLI-D-13-00615.1>.
- Skirris, N., R. Marsh, S. A. Josey, S. A. Good, C. Liu, and R. P. Allan, 2014: Salinity changes in the World Ocean since 1950 in relation to changing surface freshwater fluxes. *Climate Dyn.*, **43**, 709–736, <https://doi.org/10.1007/s00382-014-2131-7>.
- Son, S.-W., N. F. Tandon, L. M. Polvani, and D. W. Waugh, 2009: Ozone hole and Southern Hemisphere climate change. *Geophys. Res. Lett.*, **36**, L15705, <https://doi.org/10.1029/2009GL038671>.
- Swart, N. C., and J. C. Fyfe, 2012: Observed and simulated changes in the Southern Hemisphere surface westerly wind-stress. *Geophys. Res. Lett.*, **39**, L16711, <https://doi.org/10.1029/2012GL052810>.
- , and —, 2013: The influence of recent Antarctic ice sheet retreat on simulated sea ice area trends. *Geophys. Res. Lett.*, **40**, 4328–4332, <https://doi.org/10.1002/grl.50820>.
- Thompson, D. W., and S. Solomon, 2002: Interpretation of recent Southern Hemisphere climate change. *Science*, **296**, 895–899, <https://doi.org/10.1126/science.1069270>.
- Trenberth, K. E., Y. Zhang, and M. Gehne, 2017: Intermittency in precipitation: Duration, frequency, intensity, and amounts using hourly data. *J. Hydrometeor.*, **18**, 1393–1412, <https://doi.org/10.1175/JHM-D-16-0263.1>.
- Turner, J., and Coauthors, 2009: Non-annular atmospheric circulation change induced by stratospheric ozone depletion and its role in the recent increase of Antarctic sea ice extent. *Geophys. Res. Lett.*, **36**, L08502, <https://doi.org/10.1029/2009GL037524>.
- , T. J. Bracegirdle, T. Phillips, G. J. Marshall, and J. S. Hosking, 2013: An initial assessment of Antarctic sea ice extent in the CMIP5 models. *J. Climate*, **26**, 1473–1484, <https://doi.org/10.1175/JCLI-D-12-00068.1>.
- Valcke, S., 2006: OASIS3 User Guide. PRISM-Support Initiative Rep. 3, CERFACS TR/CMGC/06/73, 68 pp.
- Wilcox, L. J., A. Charlton-Perez, and L. Gray, 2012: Trends in austral jet position in ensembles of high- and low-top CMIP5 models. *J. Geophys. Res.*, **117**, D13115, <https://doi.org/10.1029/2012JD017597>.
- Wong, A. P. S., N. L. Bindoff, and J. A. Church, 1999: Large-scale freshening of intermediate waters in the Pacific and Indian Oceans. *Nature*, **400**, 440–443, <https://doi.org/10.1038/22733>.
- Xie, P., and P. A. Arkin, 1997: Global precipitation: A 17-year monthly analysis based on gauge observations, satellite estimates, and numerical model outputs. *Bull. Amer. Meteor. Soc.*, **78**, 2539–2558, [https://doi.org/10.1175/1520-0477\(1997\)078<2539:GPAYMA>2.0.CO;2](https://doi.org/10.1175/1520-0477(1997)078<2539:GPAYMA>2.0.CO;2).
- Zunz, V., and H. Goosse, 2015: Influence of freshwater input on the skill of decadal forecast of sea ice in the Southern Ocean. *Cryosphere*, **9**, 541–556, <https://doi.org/10.5194/tc-9-541-2015>.
- , —, and F. Massonnet, 2013: How does internal variability influence the ability of CMIP5 models to reproduce the recent trend in Southern Ocean sea ice extent? *Cryosphere*, **7**, 451–468, <https://doi.org/10.5194/tc-7-451-2013>.

Appendix D

Historical Southern Ocean surface freshening in a coupled climate model

The material in this Appendix builds upon the findings presented in Part 3.

A. P. conceived the study, undertook the model simulations and analyses, and wrote the manuscript.

Abstract

Appendix D builds upon the findings from Part 3 to further our understanding of the role of the observed Southern Ocean surface salinity trends under global warming conditions. I perform further experiments using a global coupled climate model with sea surface salinity restoring applied over the Southern Ocean under increasing greenhouse conditions for 1951–2000. When Southern Ocean surface salinity is restored to obtain the observed trends, sea surface temperature and sea ice trends in the Pacific sector align well with observations, showing a broad-scale cooling and sea ice increase, except in the Amundsen and Bellingshausen Seas where there is a warming and sea ice decline. However, in the Atlantic sector global warming or model bias dominates and a strong warming is seen. These findings further demonstrate the importance of surface salinity in driving trends in sea surface temperature and sea ice in the Pacific sector.

Introduction

Observed historical surface freshening of the Southern Ocean (Durack and Wijffels, 2010; de Lavergne et al., 2014) has increased water column stability, reducing the upwelling of warm subsurface waters and contributing to a surface cooling (Marsland and Wolff, 2001; Liu and Curry, 2010; de Lavergne et al., 2014; Morrison et al., 2015). The influence that coastal freshening around Antarctica due to ice sheet and ice shelf runoff and iceberg fluxes has on sea ice has been investigated in various model studies (Bintanja et al., 2013, 2015; Swart and Fyfe, 2013; Pauling et al., 2016, 2017). However, the impact of broad-scale freshening from these processes as well as due to the sea ice re-distribution of freshwater (Haumann et al., 2016) and large-scale precipitation minus evaporation (P–E) changes due to a poleward displacement of the westerly-wind jet and storm tracks (Thompson and Solomon, 2002; Marshall, 2003; Fyfe, 2003) has received less attention.

In Part 3 I conducted idealised broad-scale Southern Ocean freshwater simulations under pre-industrial conditions and identified the surface-freshening induced cooling to be one of the important factors contributing to the observed-model difference in Southern Ocean sea surface temperature (SST) and Antarctic sea ice trends over recent decades. Comparing our freshwater simulations run using the Australian Community Climate and Earth System Simulator version 1.0 (ACCESS1.0) to trends in ACCESS1.0 under Coupled Model Intercomparison phase five (CMIP5) scenarios, similar magnitude but opposite sign trends in SST and sea ice extent (SIE) were found. I postulated that had historical greenhouse warming been added alongside surface freshening, there might have been a minimal trend in Southern Ocean SST and SIE.

Lecomte et al. (2017) also found salinity in the Ross Sea to be important for an ice-ocean feedback that sustains sea ice perturbations, further demonstrating the importance of surface salinity to regional hydrography around Antarctica. In Part 3 I found that many

of the regional SST and sea ice trend features can be accurately simulated by ACCESS1.0 when the observed sea surface salinity (SSS) trends over the Southern Ocean are imposed under pre-industrial conditions, highlighting the importance of upper ocean SSS trends in driving Southern Ocean circulation changes. To better understand the role of the observed surface salinity trends on Southern Ocean surface cooling and Antarctic sea ice trends, here I conduct targeted coupled climate model simulations using ACCESS1.0 with sea surface salinity restoring applied over the Southern Ocean under increasing greenhouse conditions over 1951–2000. This study builds on the findings of Part 3 by examining the combined influence of observed SSS trends and historical greenhouse warming.

Data and methods

Experimental design

As in Part 3, I use ACCESS1.0 in fully coupled configuration (Bi et al., 2013a). My aim is to simulate a clear freshening signal of the same magnitude and with the same regional variations as observed under global warming conditions. I conduct SSS restoring simulations (as in Section 3.3.4), with the same forcings as the ACCESS1.0 CMIP5 historical runs, including historically evolving atmospheric concentrations of greenhouse gases, aerosol emissions, and ozone (described in more detail for the pre-industrial runs in Part 3; see also Bi et al., 2013a; Dix et al., 2013).

I conduct two sets of simulations, with three ensemble members in each set. In the first set of simulations I restore SSS to the annually and monthly varying SSS of the archived ACCESS1.0 historical runs r1i1p1, r2i1p1 and r3i1p1 (as submitted to CMIP5). These re-analysed runs thus capture the SSS trends from freely running simulations whilst under an SSS restoring regime. Hereafter I refer to these runs as the “A10 Hist” runs. In the second set of simulations I restore SSS as above, but with an annually increasing trend superimposed onto each historical SSS field (r1i1p1, r2i1p1 and r3i1p1), to yield the observed Durack and Wijffels (2010) SSS trend. Hereafter I refer to these runs as the “A10 D&W” runs. All restoring simulations are branched from year 1951 of the archived historical runs and run for 50 years.

Utilising SSS restoring allows examination of the SST and sea ice response to a realistic geographic distribution of SSS trends. As I am interested in the Southern Ocean surface freshening, SSS between 40–70°S (with tapering either side) is restored. The SSS restoring timescale is 15 days over the upper ocean model layer.

Observational datasets

I use the same observational datasets as in Part 3: surface and subsurface salinity and potential temperature trends over 1950–2000 from Durack and Wijffels (2010); SST from the Hadley Centre Sea Ice and Sea Surface Temperature dataset (HadISST; Rayner et al., 2003); passive microwave sea ice concentration (SIC) processed using the National Snow and Ice Data Center (NSIDC) Bootstrap algorithm (Comiso and Nishio, 2008; Meier et al., 2013, updated 2016); and the NSIDC SIE index (Fetterer et al., 2002). As in Part 3, observed SST and sea ice trends are calculated over 1979–2013. A comprehensive discussion of the limitations of these datasets and the periods chosen for analysis is included in Part 3 (Section 3.2.3). The same data analysis techniques as in Part 3 are utilised here.

Results

Surface trends

Ensemble mean surface trends are shown alongside observed trends in Fig. D.1. As described in detail in Part 3, the observations show a broad-scale surface freshening, cooling and sea ice increase; however, in the Amundsen and Bellingshausen Seas there is a surface salinification, warming and sea ice decrease (Fig. D.1a,b,c). The A10 Hist ensemble mean shows a broad-scale surface freshening, but it is substantially weaker than observed and lacks significance (Fig. D.1d), motivating the A10 D&W simulations. In A10 Hist surface warming is seen across the Southern Ocean and is particularly strong in the Atlantic and Indian sectors (Fig. D.1e). Coincident with this warming, sea ice concentration (SIC) decreases almost everywhere in A10 Hist (Fig. D.1f). By design the A10 D&W ensemble mean shows a clear broad-scale surface freshening as observed (Fig. D.1g), and a strong surface cooling and SIC increase in the Pacific sector are also seen (Fig. D.1h,i). A10 D&W shows good regional agreement with observed SST and SIC trends in the Australian sector and in the Ross, Amundsen and Bellingshausen Seas. In both the Indian sector and the Weddell Sea there are regions of increased SSS, which is associated with surface warming and decreased sea ice in A10 D&W. In the observations there is a surface cooling and sea ice increase in these regions of increased salinity, possibly due to the differing time periods of the observational datasets. A strong warming trend in the South Atlantic is seen in A10 D&W (Fig. D.1h), contrasting the observed cooling (Fig. D.1b). This is unexpected based on the surface freshening trend in this region and may be due to a model bias or drift. In the pre-industrial control SSS restoring runs (Part 3) a spurious warming is also seen in this region, although under historical conditions the warming is more extensive and the portion of the Weddell Sea with a SIC decrease is larger. In addition to possible model bias in this region, the stronger warming under historical conditions suggests the South Atlantic may be quite sensitive to global warming in ACCESS1.0.

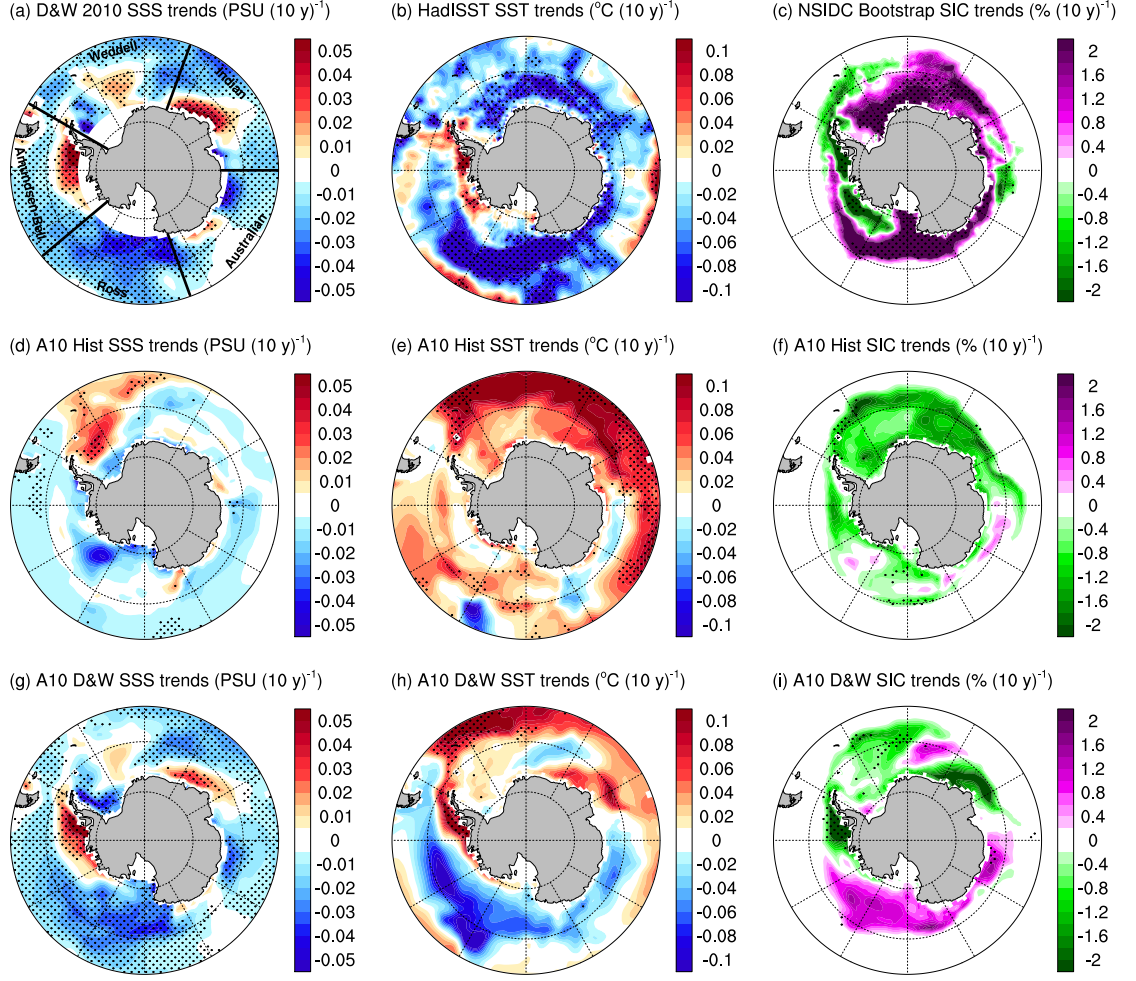


Figure D.1: Historical fifty-year surface trends: (first column) SSS; (second column) SST; and (third column) SIC. (first row) Observations from Durack and Wijffels (2010), HadISST and NSIDC Bootstrap, respectively; (second row) ensemble mean from ACCESS1.0 historical SSS restoring simulations (A10 Hist); and (third row) ensemble mean from ACCESS1.0 observed SSS restoring simulations (A10 D&W). Stippling indicates trend significance at the 95% level. HadISST and NSIDC trends are over 1979–2013. Sectors are shown in (a).

Comparing the surface trends between the two ensembles, A10 Hist and A10 D&W, it is apparent that a stronger surface freshening (A10 D&W) is associated with a surface cooling and an increase in sea ice in the Pacific sector. When considering area-averaged trends, global warming overwhelms the relatively weak surface freshening in A10 Hist, leading to an overall surface warming of the high-latitude Southern Ocean [$+0.04^{\circ}\text{C} (10 \text{ yr})^{-1}$ over the last 35 years of the simulations², between $55\text{--}70^{\circ}\text{S}$] and a corresponding decline in SIE [$-0.20 \times 10^6 \text{ km}^2 (10 \text{ yr})^{-1}$]. The stronger surface freshening in A10 D&W leads to an overall surface cooling of the high-latitude Southern Ocean [$-0.04^{\circ}\text{C} (10 \text{ yr})^{-1}$ over the same period and region as above] and a weak increase in SIE [$+0.06 \times 10^6 \text{ km}^2$

²For direct comparison with the area-averaged trends presented in Part 3, Section 3.3.3, here I consider trends over the last 35 years of the historical simulations (1966–2000), rather than over the full 50 years (1951–2000) considered in the rest of this Appendix.

(10 yr)⁻¹]. In Part 3, I postulated that had historical greenhouse warming been added alongside surface freshening, there might have been a minimal trend in Southern Ocean SST and SIE. While A10 D&W still shows a clear cooling trend (two thirds as strong as observed), the combined greenhouse warming and surface freshening in ACCESS1.0 does indeed lead to a fairly minimal SIE trend (one third as large as observed), as anticipated³.

Comparing the surface trends between the same prescribed SSS trends but different forcing scenarios, A10 D&W here (with historical forcings) and the SSS restoring simulations in Part 3 (Fig. 3.9; with pre-industrial forcings), a weaker SST cooling and sea ice increase is seen under global warming conditions [-0.04°C (10 yr)⁻¹ compared to -0.05°C (10 yr)⁻¹ over the last 35 years of the simulations between 55°–70°S; and $+0.06 \times 10^6 \text{ km}^2$ (10 yr)⁻¹ compared to $+0.13 \times 10^6 \text{ km}^2$ (10 yr)⁻¹ over the last 35 years of the simulations], again as expected.

Subsurface trends

Zonal-mean salinity and potential temperature trends are shown in Fig. D.2. Compared to the zonal-mean potential temperature trends for the idealised freshwater simulations carried out under pre-industrial conditions (Fig. 3.5), the global warming signal and strong similarity with the observations is evident for both A10 Hist and A10 D&W (Fig. D.2).

Comparing A10 Hist and A10 D&W ensemble mean trends, the stronger surface freshening in A10 D&W (Fig. D.2e) is associated with a zonal-mean surface cooling (Fig. D.2f), whereas there is a surface warming in A10 Hist (Fig. D.2d). Indicative of reduced convective overturning, there is stronger high-latitude subsurface warming in A10 D&W (Fig. D.2f) compared to A10 Hist (Fig. D.2d). A10 D&W subsurface temperature trends are more similar to observed trends (Fig. D.2b) than A10 Hist, demonstrating the importance of accurately simulating surface salinity trends to capture subsurface temperature trends. Overall, interpretation of Fig. D.2 supports the findings of Part 3, namely that stronger surface freshening results in surface cooling and stronger subsurface warming due to increased surface stability, reduced convective overturning and reduced entrainment of subsurface waters into the surface waters. These results further highlight the importance of accurately simulating historical surface trends in salinity to capture subsurface trends in temperature.

³While A10 D&W is constrained by the observed SSS trends, I don't expect it to simulate as strong a cooling and particularly as strong a SIE increase as observed because other mechanisms have also likely contributed to the observed trends. For example, responses to wind forcing (Holland and Kwok, 2012; Fan et al., 2014; Purich et al., 2016a) and decadal variability (Li et al., 2014; Simpkins et al., 2014; Meehl et al., 2016a; Purich et al., 2016b) have also been shown to be important.

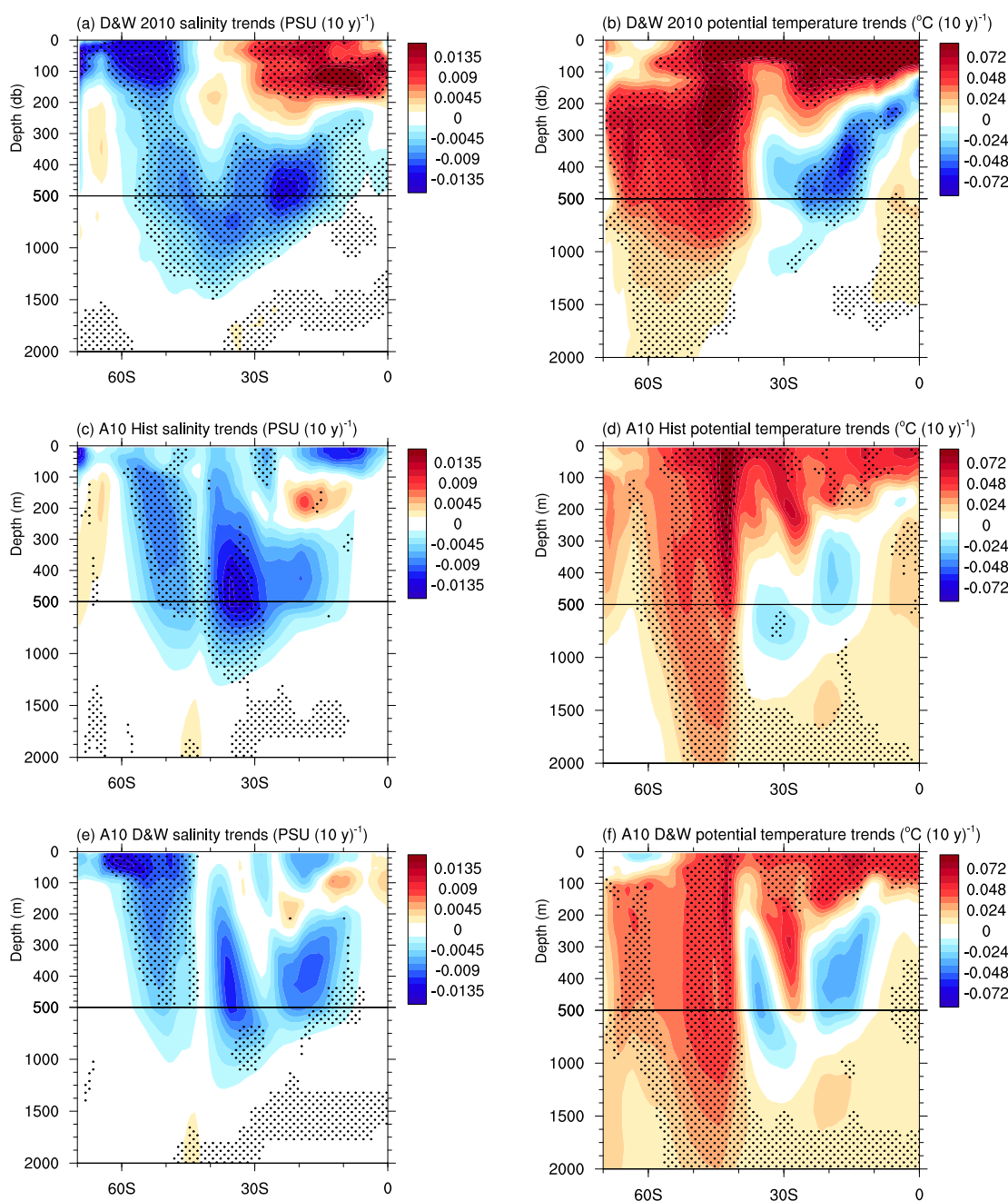


Figure D.2: Historical fifty-year zonal-mean trends: (first column) salinity; and (second column) potential temperature. (first row) Observations from Durack and Wijffels (2010); (second row) A10 Hist; and (third row) A10 D&W. Stippling indicates trend significance at the 95% level. The vertical scale is expanded over the top 500 m.

Sector trends

I next consider the contribution of different sectors to the zonal-mean changes in observations and A10 D&W in more detail. Figure D.3 shows observed and A10 D&W trends in salinity and potential temperature separated by sector as defined in Fig. D.1a. When the zonal-mean trends are separated by sector, the characteristic surface freshening and cool-

ing and subsurface warming, indicating increased surface stability and reduced convective overturning, are most clear in the Ross Sea (Fig. D.3 first column) and Weddell Sea (Fig. D.3 third column). These trend features are seen for both observations and A10 D&W. The Ross Sea trends agree with the ice-ocean feedback presented in Lecomte et al. (2017) and emphasise the importance of surface salinity in driving trends in this sector.

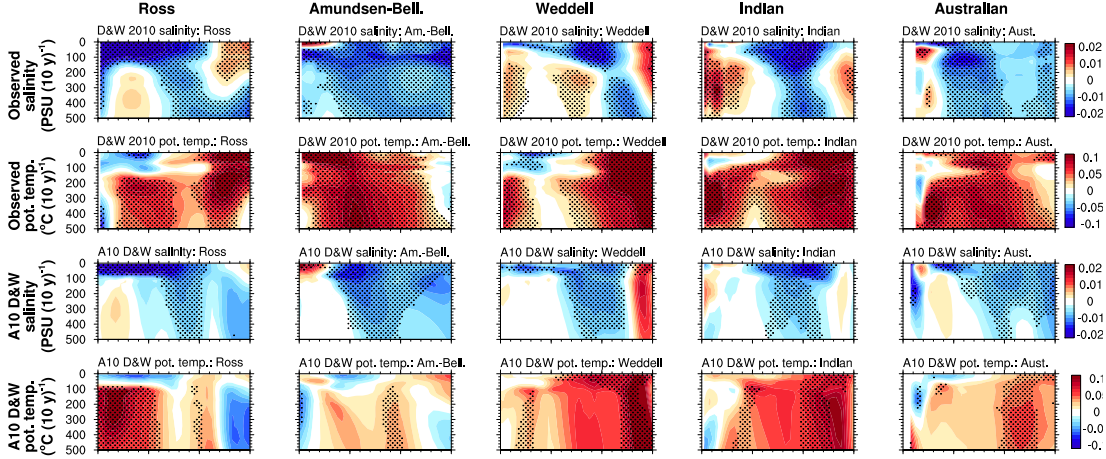


Figure D.3: Historical fifty-year sector trends: (first column) Ross Sea (160°E – 130°W); (second column) Amundsen and Bellingshausen Seas (60 – 130°W); (third column) Weddell Sea (60°W – 20°E); (fourth column) Indian sector (20 – 90°E); and (fifth column) Australian sector (90 – 160°E). (first row) Observed salinity trends from Durack and Wijffels (2010); (second row) observed potential temperature trends from Durack and Wijffels (2010)); (third row) A10 D&W salinity trends; and (fourth row) A10 D&W potential temperature trends. Sectors are defined in Fig. D.1a. Stippling indicates trend significance at the 95% level.

Trends in the other sectors are not as easily interpreted. In the Amundsen and Bellingshausen Seas (Fig. D.3 second column), surface salinification and warming are seen in both observations and A10 D&W. However, subsurface freshening and warming are seen in the observations, whereas in A10 D&W a subsurface cooling with little change in salinity are seen below the surface layer. In A10 D&W it appears that the reduced surface stability associated with the increased salinity is increasing mixing with depth, leading to the subsurface cooling; that is, by experimental design, the changes in surface salinity are driving the surface and subsurface changes in temperature. In the real world this may not be the case, but the driver of the observed patterns of change is not clear. The warming and shoaling of Circumpolar Deep Water (CDW; Schmidtko et al., 2014) may account for the observed warming throughout much of the water column shown in Fig. D.3, however this alone may cause increased salinity throughout the water column. As the observations show subsurface freshening, this points to an alternative or additional process occurring in the real world. One possibility is that the shoaling of CDW increases basal ice shelf melt, which could freshen the subsurface waters⁴, however the observed surface salinification still needs to be accounted for if this is the case. It is also possible

⁴Jourdain et al. (2017) find the inflow of warm CDW into ice-shelf cavities in the Amundsen Sea provides more heat than required for melting ice, so the outflow from cavities is both warm and fresh.

that in this sparsely sampled region, the trends presented in Durack and Wijffels (2010) are uncertain: for example, Schmidt et al. (2014) report little trends in CDW salinity around Antarctica. As ACCESS1.0 does not include ice sheets or ice shelves, examining such processes is beyond the scope of this study; however, this has been the focus of others (e.g. Jourdain et al., 2017; Naughten et al., 2018). Also, CMIP5 models such as ACCESS1.0 have limitations in representing mixed layer processes in the Southern Ocean, so may not capture the CDW shoaling (Heuzé et al., 2013; Schmidt et al., 2014).

Near-surface salinity and temperature trends in the Indian (Fig. D.3 fourth column) and Australian (Fig. D.3 fifth column) sectors are spatially inhomogeneous. In the Indian sector there is strong subsurface warming around 70°S in observations that is not seen in A10 D&W. As for the Amundsen and Bellinghausen Seas, this suggests that additional processes may also be at play in determining the subsurface temperature trends.

Meridional Overturning Circulation

Finally, I also consider the Meridional Overturning Circulation (MOC) in the A10 Hist and A10 D&W simulations. Antarctic Bottom Water (AABW) formed around Antarctica comprises a substantial portion of the abyssal ocean waters (Johnson, 2008), and thus the rate of AABW formation critically controls the global uptake of heat and carbon into the abyssal ocean (Newsom et al., 2016). Buoyancy loss sustains the descending branch of the lower MOC cell (e.g. Orsi et al. 1999) and as such, understanding the role of Southern Ocean surface freshening on the global MOC is important. I hypothesise that the stronger surface freshening in A10 D&W may lead to a stronger reduction in AABW formation than in A10 Hist, and as such I investigate the role of Southern Ocean surface freshening on global ocean circulation.

Figure D.4 shows the mean state MOC for both A10 Hist (Fig. D.4a) and A10 D&W (Fig. D.4d) along with their trends (Fig. D.4b,e respectively). In both A10 Hist and A10 D&W the positive trends (shown in red in Fig. D.4b,e) seen from the surface to depth across the Southern Hemisphere and below 3000 m in the Northern Hemisphere indicate a slowdown of the AABW circulation (anticlockwise/negative in the mean state; shown in blue in Fig. D.4a,d), as expected due to the increased Southern Ocean surface stratification caused by surface freshening in both sets of experiments. However, the spatial MOC trends largely lack significance – only isolated regions of significant trends are seen for both A10 Hist and A10 D&W above 1000 m in the Southern Ocean, and below 4000 m between 0–30°N. In addition, A10 D&W shows significant trends in the Southern Ocean extending to 2500 m, suggesting that a stronger slowdown of AABW formation may be occurring in this ensemble in association with the stronger surface freshening.

Considering MOC timeseries (Fig. D.4c,f), a slowdown is seen for both A10 Hist and A10 D&W in three different indices chosen to represent AABW circulation: the Southern MOC [SMOC; as in Heuzé et al. (2015); shown in orange in Fig. D.4c,f]; the lower cell [as

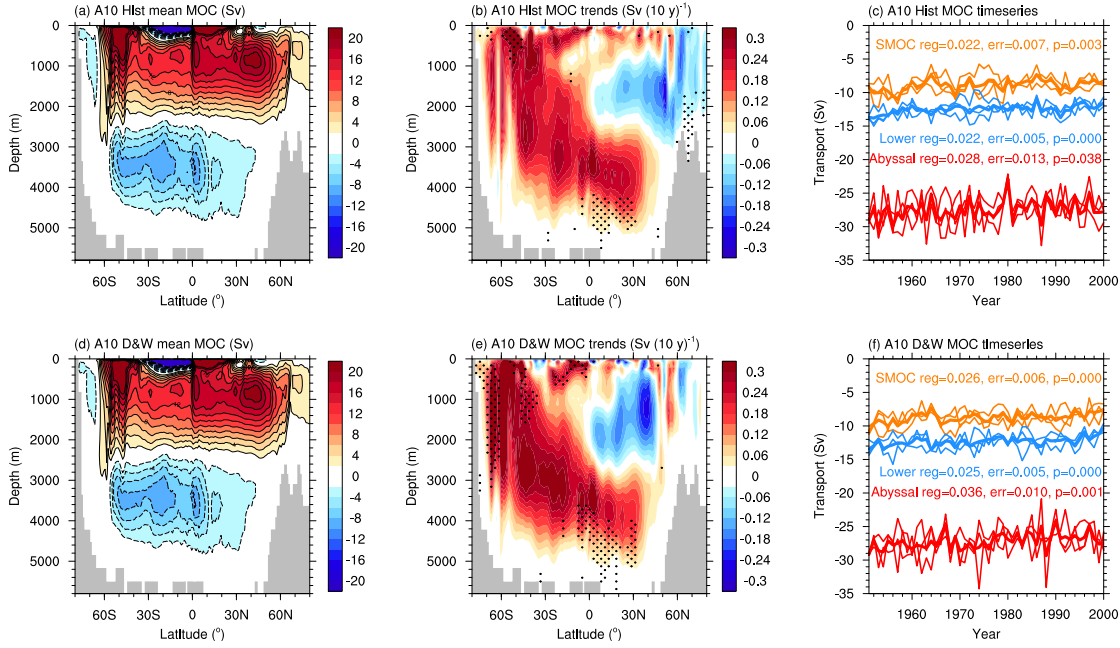


Figure D.4: Global MOC: (first column) mean-state; (second column) fifty-year trends; and (third column) overturning time series. (first row) A10 Hist; and (second row) A10 D&W. In (b,e) stippling indicates trend significance at the 95% level. In (c,f) three indices of MOC are shown: SMOc (minimum at 30°S, 2500–6000 m) is shown in orange, lower (minimum 50–30°S, 2500–5000 m) is shown in blue, and abyssal (minimum 50°S–20°N, 2500–6000 m) is shown in red; linear trends and significance are indicated for the ensemble mean time series.

in Downes and Hogg (2013); shown in blue in Fig. D.4c,f]; and the more broad abyssal cell (shown in red in Fig. D.4c,f). Comparing the trends in these indices between A10 Hist and A10 D&W, a stronger slowdown is seen in A10 D&W for all three indices (trends are displayed in Fig. D.4c,f), however the ensemble mean trends between these two sets of simulations are not statistically distinguishable when considering the linear regression \pm one standard error. Over the fifty-year runs, the percentage reduction in the MOC for each time series is also relatively modest – the strongest percentage reductions are seen in the SMOc (weakest mean state index), with A10 Hist showing a 12.6% reduction and A10 D&W showing a 14.9% reduction. These relatively modest circulation slowdowns and low sensitivity to degree of surface freshening are likely, at least in part, due to the low resolution of ACCESS1.0. A previous assessment of CMIP5 models found that these models do a poor job of AABW formation, forming deep water via open ocean deep convection, rather than via cold dense water shelf spills as predominantly occurs in the real world (Heuzé et al., 2013). Further, a comparison of bottom water formation between a low- and high-resolution version (1° and 0.1° respectively) of a coupled climate model found a more substantial slowdown of lower cell circulation under global warming in the high-resolution version (Newsom et al., 2016). It seems plausible that a higher resolution model may also show a stronger AABW-formation sensitivity to surface freshening.

Discussion

The simulations presented in Part 3 were carried out under pre-industrial conditions specifically to isolate the role of Southern Ocean surface freshening on SST and sea ice trends. However, given that the observed twentieth-century surface freshening occurred under anthropogenic conditions including increasing greenhouse gas concentrations, aerosol emissions and stratospheric ozone depletion, investigating the role of surface freshening under these historical conditions was an obvious extension of this work. As such, this Appendix builds upon the findings from Part 3. I performed additional SSS restoring experiments using ACCESS1.0. When Southern Ocean surface salinity is restored to obtain the observed trends under 1951–2000 conditions, the spatial pattern of SST and sea ice trends in the Pacific sector show a broad-scale cooling and sea ice increase, except in the Amundsen and Bellingshausen Seas where there is a warming and sea ice decline, in strong agreement with the observed trends. However, in the Atlantic sector a strong spurious surface warming is seen. A surface warming is also seen in this region in the SSS restoring simulations under pre-industrial conditions (Part 3) suggesting there may be a bias in ACCESS1.0 in this region.

As in Part 3, the mechanism for freshening-induced surface cooling is an increase in surface stability, reducing convective overturning and reducing the entrainment of warmer subsurface waters into the surface ocean. As well as contributing to a surface cooling, these circulation changes contribute to a subsurface warming. These zonal-mean temperature and salinity trends, indicative of reduced convective overturning, are dominated by trends in the Ross and Weddell Seas. While both A10 Hist and A10 D&W display zonal-mean surface freshening trends, a stronger freshening (A10 D&W) is needed to overcome global warming and simulate an overall surface cooling and increase in sea ice. The stronger surface freshening of A10 D&W also leads to a stronger slowdown of the MOC, although the differences in overturning trends between the two sets of simulations are not large.

Overall, the findings of this Appendix further demonstrate the importance of surface salinity in driving trends in sea surface temperature and sea ice. Despite global warming, when constrained by observed SSS trends, an overall surface cooling and sea ice increase is simulated by ACCESS1.0, and there is strong spatial agreement between observed and simulated trends in the Pacific sector.

Appendix E

Coauthored article

A copy of a published article coauthored during my PhD tenure and my contribution is included hereafter:

Boschat, G., I. Simmonds, **A. Purich**, T. Cowan, and A. B. Pezza, 2016: On the use of composite analyses to form physical hypotheses: An example from heat wave – SST associations. *Scientific Reports*, 6, 29599, doi:10.1038/srep29599.

A. P. processed the CMIP5 data and helped to perform the sensitivity tests, and prepare the corresponding figures. A. P. contributed to the development of ideas, writing and revising the manuscript.

SCIENTIFIC REPORTS

OPEN

On the use of composite analyses to form physical hypotheses: An example from heat wave – SST associations

Received: 26 January 2016

Accepted: 22 June 2016

Published: 14 July 2016

Ghyslaine Boschat^{1,2}, Ian Simmonds¹, Ariaan Purich³, Tim Cowan⁴ & Alexandre Bernardes Pezza⁵

This paper highlights some caveats in using composite analyses to form physical hypotheses on the associations between environmental variables. This is illustrated using a specific example, namely the apparent links between heat waves (HWs) and sea surface temperatures (SSTs). In this case study, a composite analysis is performed to show the large-scale and regional SST conditions observed during summer HWs in Perth, southwest Australia. Composite results initially point to the importance of the subtropical South Indian Ocean, where physically coherent SST dipole anomalies appear to form a *necessary* condition for HWs to develop across southwest Australia. However, sensitivity tests based on pattern correlation analyses indicate that the vast majority of days when the identified SST pattern appears are overwhelmingly *not* associated with observed HWs, which suggests that this is definitely *not a sufficient* condition for HW development. Very similar findings are obtained from the analyses of 15 coupled climate model simulations. The results presented here have pertinent implications and applications for other climate case studies, and highlight the importance of applying comprehensive statistical approaches before making physical inferences on apparent climate associations.

Statistical analyses are commonly used in climate science as they provide deep insights into the variability of climate occurrences at various spatial and time scales. Composite analyses, in particular, are recognized as being a simple and effective tool to identify conditions observed during specific states of the climate. They can point to connections between a phenomenon and key surrounding regions^{1,2} and provide valuable information for hypotheses to be formed as to the physical mechanisms that may be involved in these connections. However, testing the actual significance of these hypothesized connections or unravelling the causality in these relationships³ often requires a combination of various statistical methods, and above all needs to be supported by an appropriate physical understanding of the climate system itself.

This study highlights the caveats of using composite analyses to form physical hypotheses on the associations between environmental variables. These caveats are illustrated using the example of the apparent links between heat waves (HWs) and regional sea surface temperatures (SSTs). This is an important and timely example given that in recent decades HWs have become more prevalent in many regions, e.g. across Europe^{4–6}, North America⁷, China⁸ and Australia^{9,10}. These events have increased in frequency, duration and intensity during the 20th century^{11–13} and climate models project these trends to continue under the influence of climate change^{14–17}. Across Australia, HWs are responsible for more deaths than any other natural hazard¹⁸, the inherent susceptibility to drought conditions making the country particularly vulnerable to the impacts of extreme heat. It is therefore of great interest to the community and other affected sectors to understand the factors contributing to HWs, and as such is an area of much research attention.

SSTs have been identified as key players in HW development in many regions across the globe. For example, SSTs in the Mediterranean and Black Seas have been shown to be closely correlated with eastern European HWs,

¹School of Earth Sciences, The University of Melbourne, Victoria, Australia. ²Australian Research Council's Centre of Excellence for Climate System Science, Australia. ³CSIRO Oceans and Atmosphere, Aspendale, Victoria, Australia.

⁴School of Geosciences, University of Edinburgh, Edinburgh, United Kingdom. ⁵Greater Wellington Regional Council and Victoria University of Wellington, Wellington, New Zealand. Correspondence and requests for materials should be addressed to G.B. (email: ghyslaine.boschat@unimelb.edu.au)

as they can maintain or reinforce upper level anticyclonic flow^{19,20}. Tropical SSTs and convection in the Atlantic Ocean have also been associated with Rossby wave train formation and atmospheric blocking conditions that can lead to summer HW formation across Europe and Russia^{5,21,22}. Warm SST anomalies in the north Atlantic and northeast Pacific during boreal spring are also thought to have contributed to record heat extremes during the severe Dust Bowl drought over central United States in the 1930s²³. A recent study has also found that HWs in eastern United States are associated with characteristic SST patterns in the extratropical Pacific and that these anomalies may provide skill in predicting HWs at lead times up to 50 days²⁴. For Australia there are suggestions that SSTs in the Indian Ocean or over the Tasman and Coral Seas may contribute to the onset of HWs across the southwest and southeast regions by interacting with local atmospheric circulations^{25–27}. However, the limited evidence provided so far by observations and the lack of agreement in models simulating these observed SST patterns²⁸ suggest that further work is needed to understand the role of SSTs for Australian HWs, especially as the global ocean continues to warm²⁹.

In light of these considerations, we explore the association between summer HWs in Perth, southwest Australia, and large-scale and regional SSTs, as an *illustrative* case study of the use of composite analyses. The data and methods are described in the first section and results from composite and correlation analyses are then presented. The final section discusses some caveats when interpreting the composite results, and more generally highlights the importance of combining different statistical approaches before forming physical hypotheses regarding climate connections.

Methods

Classifying heat waves. We take as our example of composite analysis the case of HW occurrences in southwest Australia and their relationship with SSTs in observations and in coupled climate models. For illustrative purposes, we have chosen the populated city of Perth²⁸ for our case study and consider HW events during austral summer (December to February, DJF), the season when they have the greatest impact on human health, and can interact with other natural disasters such as bushfires^{30,31}.

HWs can be defined as a period of consecutive days when conditions are excessively hotter than normal, with little relief at night³². The specific definition we adopt here is a period of three or more consecutive days, during which daily maximum temperature (T_{\max}) exceeds its monthly 90th percentile, and daily minimum temperature (T_{\min}) also exceeds its monthly 90th percentile on the second and third days. All days in a HW are referenced to the monthly threshold on the first HW day²⁵. HW dates in Perth are determined using the daily T_{\max} and T_{\min} time series provided by the Australian Bureau of Meteorology station at Perth Airport (31.9°S, 116.0°E, WMO Number 94610) during 1948–2014. The use of daily station data helps preserve the small-scale spatial and temporal variability that is important for representing extremes, and the temperature threshold we chose is dependent on both the time and location of the station. HW dates were compared across (four) neighbouring stations in the southwest Australian region and despite the potential for the urban heat island effect to influence HWs in Perth, the list of HW events and composite patterns are robust across the stations (not shown).

To explore the potential association between these HW events and SST anomalies, we perform composite and correlation analyses using daily SST fields from the ERA-Interim reanalysis³³, available from 1979 onwards at 1.5° spatial resolution. We calculate composites of daily anomalies (as a deviation from the 1979–2014 daily climatology for that specific calendar day), and the statistical significance of these composite anomalies is determined by a Monte-Carlo procedure³⁴. This method describes the areas in the composite that depart significantly from the background variability in the available data, and for our purpose is considered more robust than the commonly-applied (parametric) Student's *t* test³⁵.

SST composites and model experiments. Based on the significant SST anomalies from the composite maps, five key spatial regions are identified: the Southern Hemisphere (extending into the northern tropics, SH; [70°S–20°N]), the South Indian Ocean (SIO; [30°E–120°E; 55°S–15°S]), the West ([35°E–80°E; 38°S–52°S]), East ([80°E–120°E; 15°S–40°S]) and both West and East poles in the South Indian Ocean. To assess the relative importance of these large-scale and regional SSTs, pattern correlation coefficients are then calculated between daily summer SST anomalies and the observed SST composite over each domain. Results are fundamentally unchanged when we use SST anomalies in the week or month leading up to the HW, or other SST observational datasets (not shown).

Sensitivity tests are designed to test the physical implications from our composite analyses, using outputs from 15 coupled climate model simulations (Supplementary Fig. S1) from phase 5 of the Coupled Model Intercomparison Project (CMIP5)^{16,28}. Daily T_{\max} and T_{\min} data from each model are interpolated to the Perth station location, and used to determine the dates of simulated HW events over the historical 1950–2005 period. SST composites for the first day of HWs are constructed for individual models, for the multi-model mean (shown in Supplementary Fig. S1), and compared to observations. Pattern correlations are then computed between daily SST anomalies from each model and the observed (ERA-Interim) SST composite over the previously selected domains to quantify the likelihood of a HW to be simulated during specific SST conditions.

Results

Selection of HW events. Using the above HW definition for observations, we detect 38 HW events for Perth during 1948–2014. Figure 1 lists the first day of each of these events, and shows the average T_{\max} and T_{\min} conditions recorded for the first three days of each event. The colour of each bar also indicates the concurrent phase of El Niño Southern Oscillation (ENSO) in the tropical Pacific during DJF, based on a threshold of $\pm 0.5^\circ\text{C}$ for the Oceanic Niño Index [three-month running mean of SST anomalies over the Niño 3.4 region (5°N–5°S, 120°–170°W)]. Overall, this figure illustrates the diversity that is observed in Perth HW characteristics, as T_{\min} and T_{\max} values vary quite substantially (especially T_{\min} with $\sim 2^\circ\text{C}$ standard deviation, possibly linked to the

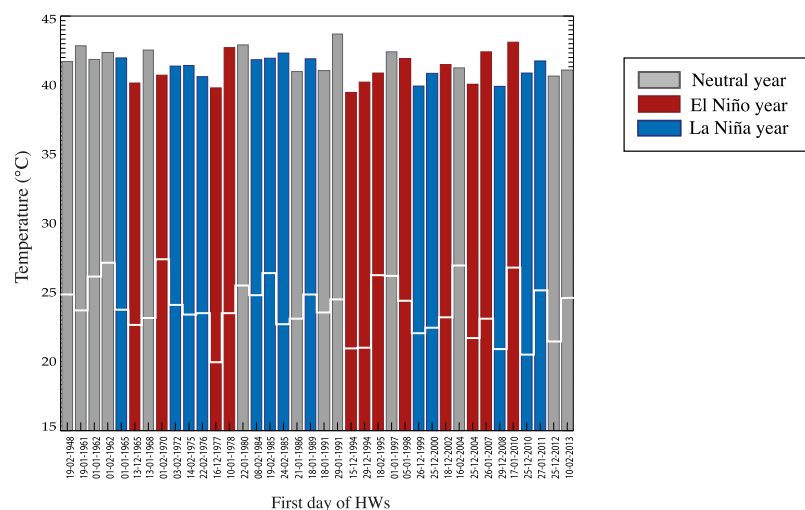


Figure 1. Bar plot of observed temperature extremes for each Perth HW event. Average T_{\max} conditions over the first three HW days (*bar*) and average T_{\min} conditions during the second and third of those days (*white line*). The colour of each bar shows the concurrent phase of El Niño Southern Oscillation during austral summer, based on a threshold of $\pm 0.5^\circ\text{C}$ for the Oceanic Niño Index [3-month running mean of SST anomalies in the Niño 3.4 region (5°N – 5°S , 120° – 170°W)].

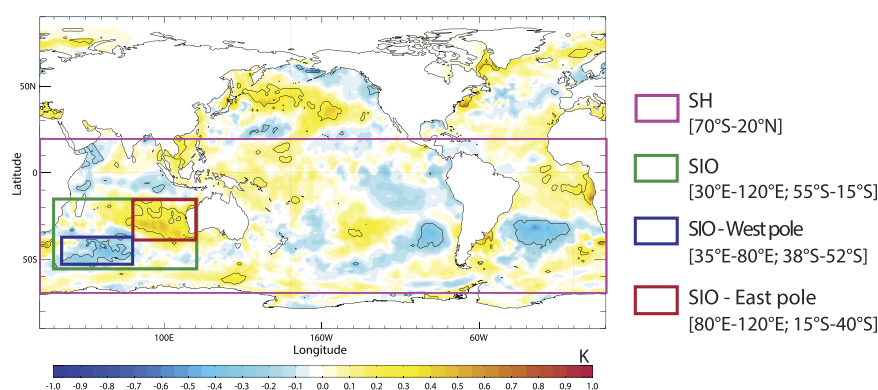


Figure 2. Composite SST anomalies for the first day of Perth HWs observed over 1979–2014. (The 25 HW events are listed across the x -axis in Fig. 1.) Composite anomalies that are significant at the 90% confidence level using a Monte-Carlo procedure³⁴ are shown in black contours. Boxes indicate key areas where SST indices (mean SST anomalies) are computed: over the Southern Hemisphere (SH, pink box), South Indian Ocean (SIO, green box) and SIO West (blue box) and East pole (red box) domains. This figure was produced with IDL version 8.1 software (2011, Exelis Visual Information Solutions, Boulder, Colorado, https://www.exelisvis.com/docs/whatsnew_in_8_1.html).

occurrence and timing of sea breezes in the area). The amplitudes of the bars suggest no obvious trend in the severity of HWs since 1948. However there is some indication of an increase in frequency of events, and indeed the mean of the observed HW years (*i.e.* 1987.5) differs significantly from the mean of all years of the study period (*i.e.* 1980) at the 95% confidence level [using a t test to reject the null hypothesis of no statistical significance difference between the means³⁶]. Figure 1 also suggests no obvious relationship between the occurrence of HWs in Perth and ENSO during 1948–2014 (with 12 occurring during El Niño, 13 in La Niña and 13 in neutral years), consistent with recent findings from Perkins *et al.*³⁷ (their Fig. 2a).

Formation of composites. To explore the climate signature associated with observed HWs in Perth, SST composites are computed for the first day of each HW event during the 1979–2014 (satellite) period for which ERA-Interim data are available (*i.e.* the 25 most recent events listed in Fig. 1). The average anomalous SST conditions for these events are shown in Fig. 2, where statistically significant anomalies (at the 90% confidence level) are identified within black contours.

This composite suggests that HWs in Perth are associated with little or no significant SST signal over the tropics, consistent with the absence of a relationship with ENSO revealed in Fig. 1. A number of studies have shown that HWs occurring in midlatitude regions are more generally associated with extratropical wave-activity. In the case of southwest Australia, it has been suggested that HWs develop through Rossby wave amplification

over the South Indian Ocean. A persistent high-pressure system then forms over the Great Australian Bight and is responsible for advecting warm continental air towards Perth and the surrounding coastline^{25,28}. [Note that in summer there is a very high frequency of anticyclones in the Bight³⁸.] In line with these previous studies, our composite results point to the importance of mid-to-high southern latitudes, and in particular of the subtropical South Indian Ocean where physically coherent SST dipole anomalies are observed (Fig. 2). This dipole has a southwest-northeast tilt and is characterized by cold SST anomalies in the southwest (southeast of southern Africa) and warm anomalies in the northeast (off the western coast of Australia).

The CMIP5 models are generally quite successful in capturing this SST dipole pattern in the South Indian Ocean, despite the different number of HWs considered for each model composite (Supplementary Fig. S1). The position and intensity of the dipole is remarkably well simulated by the multi-model mean (a pattern correlation of 0.78 with the observed composite over the SIO domain, see Supplementary Fig. S1), despite model-to-model variations in the spatial extent of the warm pole and amplitude of the cold pole. Interestingly, this SST pattern is also the most dominant signal in the multi-model mean composite, reflecting a consistent occurrence of this pattern across models despite the diverse and contrasting ENSO signals simulated in the tropical Pacific Ocean.

Overall, the location and structure of this SST dipole is consistent with the synoptic signature of a wave train propagating over the subtropical Indian Ocean. However, as such, the composite does not allow us to infer any causal relationship between HWs and SSTs. On one hand, the SST pattern could be viewed as a result of the anomalously low-pressure component of the wave train associated with Perth HWs over the subtropical Indian Ocean²⁵. On the other, this dipole pattern could also be playing a key role in the onset of HWs, by contributing to the synoptic set up that is required for a HW to occur in Perth. Interestingly, this SST anomaly is similar to the negative phase of the Indian Ocean subtropical dipole (IODS)^{39–43}. [It should be noted that the structure of the SST composite between 80°–120°E, 0°–40°S in Fig. 2 is also the inverse of that which is strongly associated with ‘northwest cloudbands’ and cooler conditions across central Australia⁴⁴. This is consistent with enhanced continental temperatures along the trajectory of air parcels that ultimately reach Perth as HWs]. The IODS events have been shown to develop through local air-sea interactions from austral spring to summer, linked with the strengthening/weakening of the Mascarene High over the South Indian Ocean. During a negative dipole event (as observed in Fig. 2), a low-pressure anomaly is induced over the central South Indian Ocean due to a southward shift and strengthening of the subtropical high. The resulting anomalous southeasterly winds cause increased evaporation and upper ocean mixing, and thus SST cooling over the western pole, while reduced evaporation and latent heat loss associated with the northwesterly wind anomalies generate a warming over the eastern pole^{45,46}. Our composite analysis (in Fig. 2) suggests that this subtropical SST dipole may form a *necessary* (seasonal) condition for HWs to occur in Perth.

In this specific case of HW-SST associations, we can ask whether this ‘statistically significant’ signal observed in the South Indian Ocean (and also present in the CMIP5 models) is sufficient to actually establish a link with HW occurrence. In other words, if HWs tend to occur during specific SST dipole conditions, does this necessarily (and reversibly) imply that SST plays a significant role in the occurrence and/or variability of HWs in Perth? The following analyses address these questions to determine the potential role and predictive power of SST for HWs in Perth.

Correlation analyses. One way to explore this notion of reversibility and SST ‘predictive power’ is to evaluate whether the composite SST pattern shown in Fig. 2 is *specifically* linked to the occurrence of HWs in Perth or if it can also appear on ‘normal’ (non-HW) days. The approach we take is to assess how often summer SST conditions ‘resemble’ the composite SST pattern, and determine whether when this occurs it leads systematically to a HW in Perth.

To quantify the degree of resemblance, we calculate the pattern correlation between each daily SST field in DJF and the composite SST pattern shown in Fig. 2, separately for each of the key domains. This test is performed using daily summer SST anomalies from observations during 1979–2014 (a total of 3150 days) and using the longer time series provided by the 15 CMIP5 model simulations during 1950–2005 (a net total of 75698 days). Results for observations are shown in Table 1, in terms of the number of days when the pattern correlation falls within bins of 0.1 width, for all days in DJF (black values) and for HW days only (green values). (Results for the model simulations are shown in a similar form in Supplementary Table S1.) The number of days obtained when the pattern correlation approaches 1.0 reflect how often during summer the daily SST anomalies would resemble the typical HW conditions over each domain.

As could be expected, this correlation analysis shows that SST conditions over the large SH domain are very rarely in the same configuration as the typical HW state shown in Fig. 2. Indeed, the pattern correlation between daily SST and the composite SST for this domain ranges from -0.4 to 0.5 but remains close to 0 for most days in DJF including HW days (with 45–50% of summer days between -0.1 and 0.1 , see Table 1). Although this distribution is shifted towards slightly higher correlation values for the HW days, the SST for most of the HW events is still poorly correlated with the composite signal in Fig. 2 (between 0–0.3 pattern correlation).

Compared to the large SH domain, SST in the regional SIO domains exhibit higher correlation scores, with generally more (HW) days when pattern correlations exceed 0.5 (see last columns in Table 1). However, if SST anomalies have a stronger tendency to resemble the ‘typical HW’ pattern in the SIO domain, does this necessarily lead to the occurrence of a HW?

Figure 3 illustrates the likelihood of a HW occurring in summer, given a specific resemblance or pattern correlation between daily SST and the composite HW state in Fig. 2. This likelihood is calculated as the ratio of HW days to all summer days for each correlation bin (the values presented in the two rows, for each domain, in Table 1), and plotted as a percentage for each domain and separately for observed and simulated SSTs. These plots indicate that even when daily SST anomalies over the SH domain strongly resemble the composite pattern in Fig. 2 (e.g. for correlations >0.5), HWs are very unlikely to occur (ratio close to 0 for both observations and

		CORRELATION VALUES																					
		-1	-0.9	-0.8	-0.7	-0.6	-0.5	-0.4	-0.3	-0.2	-0.1	0	0.1	0.2	0.3	0.4	0.5	0.6	0.7	0.8	0.9	1	
SH	3150 DJF days							15	225	669	763	732	463	212	44	27							
	25 HW days									1	1	4	7	8	1	3							
SIO	3150 DJF days			10	92	167	139	151	305	412	328	345	274	268	233	208	107	80	31				
	25 HW days								3	0	2	3	2	2	3	0	4	5	1				
SIO - West pole	3150 DJF days			2	24	44	99	217	331	365	498	473	418	280	202	94	54	49					
	25 HW days									1	4	3	3	5	3	3	2	1					
SIO - East pole	3150 DJF days			6	43	77	191	199	285	402	368	397	352	267	233	168	98	46	17	1			
	25 HW days						1	1	2	1	1	1	4	3	3	3	3	1		1			
SIO - two poles	3150 DJF days		31	100	161	120	161	222	318	230	258	237	225	232	243	176	179	127	90	40			
	25 HW days							1	2		3	1	1	4		3	2	4	2	2			

Table 1. Frequency of the number of days when the pattern correlation between the Perth HW SST composite (Fig. 2) and daily SST anomalies falls within each 0.1 correlation bin, using ERA-Interim data. Results are computed for the entire 3150 days in DJF (black values) and for the 25 HW days selected in DJF (bold italic) during 1979–2014, and are shown separately for the SH, SIO, SIO - West pole, SIO - East pole, and the SIO - two poles domains (shown in Fig. 2).

model simulations, see Fig. 3a). In contrast, for the SIO domains, peak ratio values are obtained for higher correlation bins (between 0.6–0.7 correlation for the SIO domain and between 0.8–0.9 correlation for the domain centered on the two SIO poles, Fig. 3b,e), consistently for both observations and all model simulations. This suggests that HWs are *more likely* to occur when daily SST anomalies strongly resemble the SIO dipole configuration shown in Fig. 2, which is consistent with the initial inferences from our composite analysis. However, it should be noted that these peak values are quite small, and remain below 7% for observations and most models in the SIO domains (Fig. 3b,e) - with the exception of one model (MIROC-ESM-CHEM) simulating a maximum ratio of 16.7% in Fig. 3e. Therefore, although it may be more likely for a HW to occur when a SIO dipole-like SST pattern appears, this is still very rarely the case during summer. There are even a larger number of days in the season when this SST dipole appears (*i.e.* the correlation is high) but a HW does not occur (see Table 1).

Discussion

This work highlights some caveats in using composite analyses to form physical hypotheses on climate connections, and we have presented a concrete example of this for the case of the relationship between HWs in Perth, southwest Australia and surface ocean temperatures. Results from our composite analysis initially suggest that SST dipole conditions in the South Indian Ocean may form a *necessary* condition for summer HWs to develop across southwest Australia. However, sensitivity tests based on pattern correlation analyses indicate that the vast majority of days when the SST pattern appears are *not* associated with HWs, which suggests that this is definitely *not a sufficient* condition. This example illustrates the non-reversibility of the HW-SST relationship observed in Fig. 2, as well as some of the limitations of forming physical hypotheses based solely on the use of composites.

Composites have been used in the literature as ‘indicators’ of the typical atmospheric and oceanic conditions accompanying specific climate states^{25,27}. Composite patterns also carry useful climatic information, as they generally provide some interesting insight into forcing or connection pathways⁴⁷. No assumption is made about the structure of the connection, since a composite analysis is by definition ‘non-parametric’⁴⁸. Compared to other statistical methods (*e.g.* correlations), it has the advantage of taking into account the non-linearity of the climate system and therefore highlighting the asymmetry in certain relationships⁴⁹. Many studies use these composite patterns as speculative basis to develop first hypotheses on potential climate connections and their underlying physical processes⁵⁰. Carefully designed numerical experiments can then be conducted to test such hypotheses⁵¹.

However, while the composite approach appears straightforward, inconsistencies in the design, creation, interpretation and/or evaluation of composites can strongly affect the conclusions of some of these studies^{52,53}. For instance, individual cases from the composite might occur under a different synoptic pattern, thereby raising the question whether these associations are statistically and physically robust. Various methods have been proposed to determine the statistical significance of composite patterns and account for this event-to-event variability. However, there is still much debate on the relevance and limitations of such statistical approaches, while fixating on statistical significance can also misdirect us from physically important processes³⁵. More importantly, we need to bear in mind that the potential forcing or connection highlighted in composites has been ‘conditioned’ on a chosen subset of climate states, and this conditioned perspective is probably not reversible. The correlation analysis in our example is a clear illustration of this non-reversibility associated with composites. It shows that a

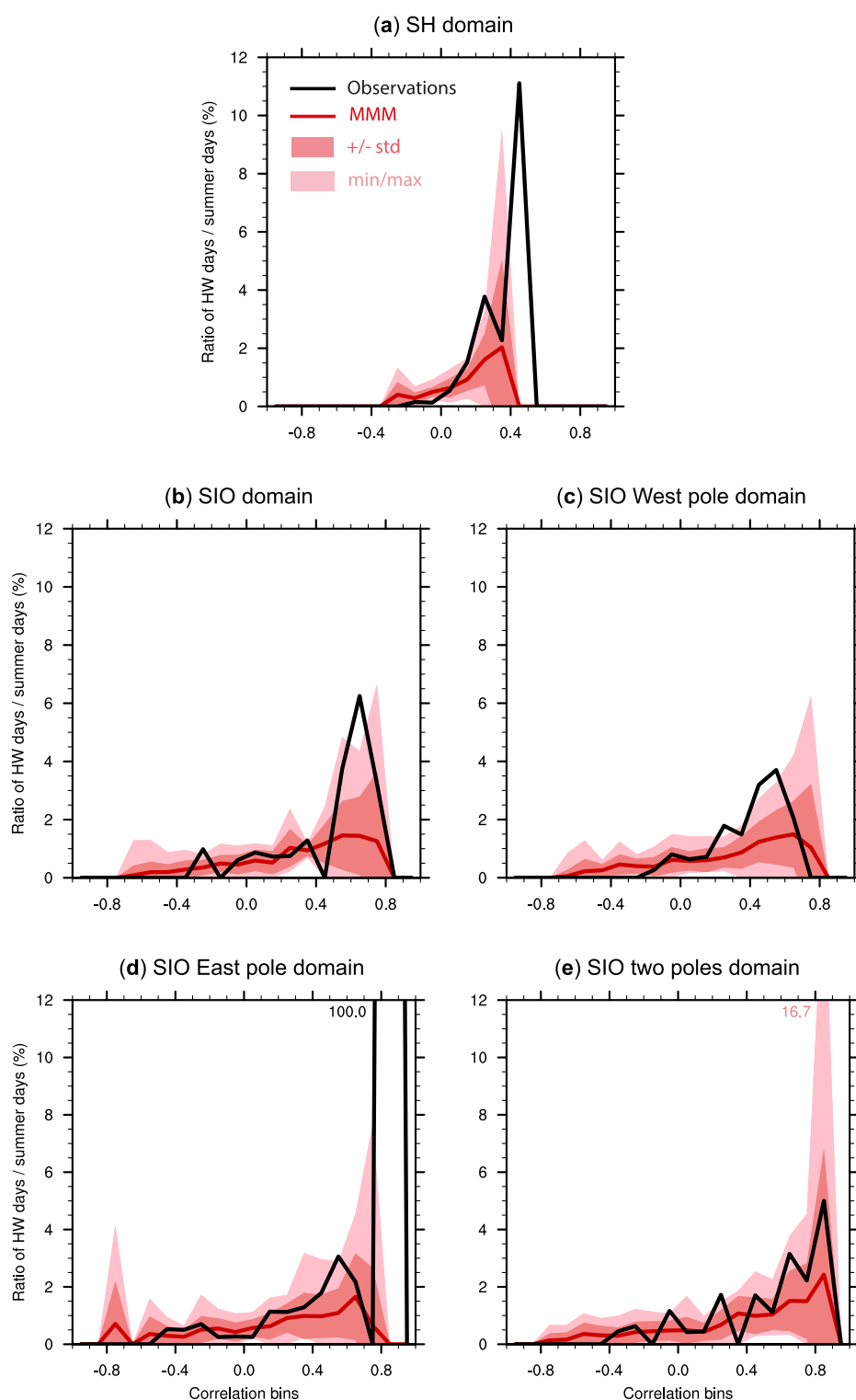


Figure 3. HW likelihood. Percentage ratio of HW days compared to total DJF days during which the pattern correlation between the Perth HW SST composite (Fig. 2) and daily SST anomalies falls within each 0.1 correlation bin, for the (a) SH, (b) SIO, (c) SIO-West pole, (d) SIO-East pole, and (e) SIO-two poles domains. The black curve shows the ratio calculated with daily SST anomalies from ERA-Interim (see values in Table 1). The pattern correlation is also calculated with daily SST anomalies from each CMIP5 model, and the red curve shows the multi-model mean (MMM) ratio. The dark (light) pink shading illustrates the ± 1 standard deviation (minimum and maximum) for all model ratios, with maximum values printed when exceeding 12%. Note that the values of some ratios for small domains can be misleading, e.g. the 100% ratio for observations over the SIO-East pole domain (d), is due to only one day with a high pattern correlation (>0.8) being a HW day (see Table 1).

statistically significant signal appearing during a specific state of the climate might appear as frequently, or even more frequently, during completely different states of the climate. In this case, correlations provide a simple and complementary angle to exploit the HW-SST association, along with valuable information to consider before making any physical interpretation of the initial composite patterns.

A number of studies have already pointed to the misinterpretation dangers inherent in many commonly used statistical techniques^{3,53,54}. For example, Dommenget & Latif⁵⁵ have shown from a synthetic example that patterns derived from Empirical Orthogonal Function analyses can be misleading at times and associated with very little climate physics. In the case of the HW-SST association, it is salutary to keep in mind that the response of the atmosphere to oceanic forcing assumes rather different forms in the tropics and extratropics: the response to surface heating in the tropics occurs toward the ‘diabatic limit’, while in the higher latitudes advective terms become more important⁵⁶. The atmospheric response to extratropical SSTs therefore tends to be much less vertically organised and more spatially dispersed, and very dependent on the larger scale circulation obtaining at the time. Our analyses seem to suggest that the atmospheric circulation patterns in the days and weeks preceding a HW can impact on the SST, and separately also culminate in a downstream midlatitude HW event. With this perspective there would be no direct connection between the mid-to-high latitude SST and HW occurrences, and model sensitivity experiments conducted with the identified Indian Ocean SST dipole would be expected to have limited success in simulating HWs. Indeed, we find the likelihood of a Perth HW when the dipole appears to be very small, in both the observations and model simulations.

In closing, we suggest that the message contained in the structure of composites may be quite misleading unless interpreted carefully, and that physical hypotheses framed from these should be rigorously tested with appropriate tools. By design, composites point to the possible importance of one parameter for a specific type of event, and SSTs have been the causal focus of this study. However extreme events are rarely attributed to a single physical “root cause”, and HWs have been shown to be influenced by other factors, including feedbacks between the atmosphere and surface related to antecedent soil moisture^{57,58}, which are not discussed here. This HW-SST example serves as a simple case study and illustration of how much relevant climatic information can be extracted from composites and the limitations associated with our physical interpretation of these results.

References

- Myers, D. S. & Waliser D. E. Three-dimensional water vapor and cloud variations associated with the Madden–Julian Oscillation during northern hemisphere winter. *J. Clim.* **16**, 929–950 (2003).
- Tian, B. *et al.* Intraseasonal variations of the tropical total ozone and their connection to the Madden-Julian Oscillation. *Geophys. Res. Lett.* **34**, L08704 (2007).
- Hannart, A., Pearl, J., Otto, F. E. L., Naveau, P. & Ghil, M. Causal counterfactual theory for the attribution of weather and climate-related events. *Bull. Amer. Meteor. Soc.* **97**, 99–110 (2016).
- Fischer, E. M. & Schär C. Consistent geographical patterns of changes in high-impact European heatwaves. *Nat. Geosci.* **3**, 398–403 (2010).
- Trenberth, K. & Fasullo, J. Climate extremes and climate change: The Russian heat wave and other climate extremes of 2010. *J. Geophys. Res.* **117**, D17103 (2012).
- Screen, J. A. & Simmonds I. Amplified mid-latitude planetary waves favour particular regional weather extremes. *Nat. Clim. Chang.* **4**, 704–709 (2014).
- Bumbaco, K. A., Dello, K. D. & Bond, N. A. History of Pacific Northwest heat waves: synoptic pattern and trends. *J. Appl. Meteor. Climatol.* **52**, 1618–1631 (2013).
- Ding, Y. H. *et al.* Detection, causes and projection of climate change over China: An overview of recent progresses. *Adv. Atmos. Sci.* **24**, 954–971 (2007).
- Nairn, J. & Fawcett, R. Defining heatwaves: Heatwave defined as a heat-impact event servicing all community and business sectors in Australia. Centre for Australian Weather and Climate Research Technical Report. Available at: http://www.cawcr.gov.au/publications/technicalreports/CTR_060.pdf. (2013).
- Perkins, S. E. A review on the scientific understanding of heatwaves—their measurement, driving mechanisms, and changes at the global scale. *J. Atm. Res.* **164**, 242–267 (2015).
- Collins, D. A., Della-Marta, P. M., Plummer, N. & Trewin, B. C. Trends in annual frequencies of extreme temperature events in Australia. *Aust. Met. Mag.* **49**, 277–292 (2000).
- Alexander, L. V. *et al.* Trends in Australia’s climate means and extremes: a global context. *Aust. Met. Mag.* **56**, 1–18 (2007).
- Perkins, S. E., Alexander, L. V. & Nairn, J. R. Increasing frequency, intensity and duration of observed global heatwaves and warm spells. *Geophys. Res. Lett.* **39**, L20714 (2012).
- IPCC. [Summary for Policymakers]. In: *Climate Change 2013: The Physical Science Basis. Contribution of Working Group I to the Fifth Assessment Report of the Intergovernmental Panel on Climate Change* (eds Stocker, T. F. *et al.*) 3–29 (Cambridge Univ. Press, Cambridge, UK, and New York, USA, 2013). Available at: http://www.climatechange2013.org/images/report/WG1AR5_SPM_FINAL.pdf.
- Coumou, D. & Robinson, A. Historic and future increase in the global land area affected by monthly heat extremes. *Environ. Res. Lett.* **8**, 034018 (2013).
- Cowan, T. *et al.* More frequent, longer, and hotter heat waves for Australia in the twenty-first century. *J. Clim.* **27**, 5851–5871 (2014).
- Christidis, N., Jones, G. S. & Stott, P. A. Dramatically increasing chance of extremely hot summers since the 2003 European heatwave. *Nat. Clim. Chang.* **5**, 46–50 (2015).
- Coates, L., Haynes, K., O’Brien, J., McAneney, J. & de Oliveira, F. D. Exploring 167 years of vulnerability: An examination of extreme heat events in Australia. 1844–2010, *Environmental Science and Policy* **42**, 33–44 (2014).
- Feudale, L. & Shukla J. Role of Mediterranean SST in enhancing the European heat wave of summer 2003. *Geophys. Res. Lett.* **34**, L03811 (2007).
- Unal, Y., Tan, E. & Montes, S. Summer heat waves over western Turkey between 1965 and 2006. *Theor. Appl. Climatol.* **112**, 339–350 (2013).
- Cassou, C., Terray, L. & Phillips, A. S. Tropical Atlantic influence on European heat waves. *J. Clim.* **18**, 2805–2811 (2005).
- Della-Marta, P. *et al.* Summer heat waves over western Europe 1880–2003, their relationship to large-scale forcings and predictability. *Clim. Dyn.* **29**, 251–275 (2007).
- Donat, M. G. *et al.* Extraordinary heat during the 1930s US Dust Bowl and associated large-scale conditions. *Clim. Dyn.* **46**, 413–426 (2016).

24. McKinnon, K. A., Rhines, A., Tingley, M. P. & Huybers P. Long-lead predictions of Eastern US hot days from Pacific sea surface temperatures. *Nat. Geosci.* **9**, 389–394 (2016).
25. Pezza, A. B., van Rensch, P. & Cai, W. Severe heat waves in southern Australia: synoptic climatology and large-scale connections. *Clim. Dyn.* **38**, 209–224 (2012).
26. Sadler, K. J., Pezza, A. B. & Cai, W. Cool Sea Surface Temperatures in the Tasman Sea Associated with Blocking and Heat Waves in Melbourne. *Bull. Aust. Meteorol. and Ocean. Soc.* **29**, 81–83 (2012).
27. Boschat, G. *et al.* Large scale and sub-regional connections in the lead up to summer heat wave and extreme rainfall events in eastern Australia. *Clim. Dyn.* **44**, 1823–1840 (2015).
28. Purich, A. *et al.* Atmospheric and oceanic conditions associated with southern Australian heat waves: a CMIP5 analysis. *J. Clim.* **27**, 7807–7829 (2014).
29. Rhein, M. *et al.* Observations: [Ocean. Climate Change 2013]: The Physical Science Basis. Contribution of Working Group I to the Fifth Assessment Report of the Intergovernmental Panel on Climate Change. (eds Stocker, T. F. *et al.*) 255–315 Available at: <https://www.ipcc.ch/report/ar5/wg1/>. (Cambridge Univ. Press, 2013).
30. Karoly, D. The recent bushfires and extreme heat wave in south-east Australia. *Bull. Austr. Meteor. Oceanogr. Soc.* **22**, 10–13 (2009).
31. Williams, S. *et al.* The impact of summer temperatures and heatwaves on mortality and morbidity in Perth, Australia 1994–2008. *Environ. Int.* **40**, 33–38 (2012).
32. Perkins, S. E. & Alexander, L. V. On the measurement of heatwaves. *J. Clim.* **26**, 4500–4517 (2013).
33. Dee, D. *et al.* The ERA-Interim Reanalysis: Configuration and Performance of the Data Assimilation System. *Q. J. R. Meteorol. Soc.* **137**, 553–597 (2011).
34. Terray, P., Delecluse, P., Labattu, S. & Terray, L. Sea surface temperature associations with the late Indian summer monsoon. *Clim. Dyn.* **21**, 593–618 (2003).
35. Nicholls, N. The insignificance of significance testing. *Bull. Am. Meteorol. Soc.* **81**, 981–986 (2001).
36. Simmonds, I. & Rudeva, I. A comparison of tracking methods for extreme cyclones in the Arctic basin. *Tellus* **66A**, 25252 (2014).
37. Perkins, S. E., Argüeso, D. & White, C. J. Relationships between climate variability, soil moisture, and Australian heatwaves. *J. Geophys. Res.* **120**, 8144–8164 (2015).
38. Jones, D. A. & Simmonds, I. A climatology of Southern Hemisphere anticyclones. *Clim. Dyn.* **10**, 333–348 (1994).
39. Behera, S. & Yamagata, T. Subtropical SST dipole events in the southern Indian Ocean. *Geophys. Res. Lett.* **28**, 327–330 (2001).
40. Reason, C. J. C. Subtropical Indian Ocean SST dipole events and southern African rainfall. *Geophys. Res. Lett.* **28**, 2225–2227 (2001).
41. Reason, C. J. C. Sensitivity of the southern African circulation to dipole sea-surface temperature patterns in the South Indian Ocean. *Int. J. Climatol.* **22**, 377–393 (2002).
42. Fischer, A. S., Terray, P., Guilyardi, E., Gualdi, S. & Delecluse, P. Two independent triggers for the Indian Ocean dipole/zonal mode in a coupled GCM. *J. Clim.* **18**, 3428–3449 (2005).
43. Terray, P. Southern Hemisphere extra-tropical forcing: A new paradigm for El Niño–Southern Oscillation. *Clim. Dyn.* **36**, 2171–2199 (2011).
44. Simmonds, I. & Rocha, A. The association of Australian winter climate with ocean temperatures to the west. *J. Clim.* **4**, 1147–1161 (1991).
45. Morioka, Y. *et al.* Subtropical dipole modes simulated in a coupled general circulation model. *J. Clim.* **25**, 4029–4047 (2012).
46. Suzuki, R., Behera, S., Iizuka, S. & Yamagata, T. Indian Ocean subtropical dipole simulated using a coupled general circulation model. *J. Geophys. Res.* **109**, C09001 (2004).
47. Vautard, R. *et al.* Summertime European heat and drought waves induced by wintertime Mediterranean rainfall deficit. *Geophys. Res. Lett.* **34**, L07711 (2007).
48. von Storch, H. & Zwiers, F. W. *Statistical Analysis in Climate*. Research Cambridge University Press (484 pp) (1999).
49. Risbey, J., Pook, M., McIntosh, P., Wheeler, M. & Hendon, H. On the remote drivers of rainfall variability in Australia. *Mon. Wea. Rev.* **137**, 3233–3253 (2009).
50. Ummenhofer, C. *et al.* What causes southeast Australia's worst droughts? *Geophys. Res. Lett.* **36**, L04706 (2009).
51. Ummenhofer, C., Sen Gupta, A., Taschetto A. & England, M. Modulation of Australian precipitation by meridional gradients in East Indian Ocean sea surface temperature. *J. Clim.* **22**, 5597–5610 (2009).
52. Laken, B. A. & Calogovic, J. Composite analysis with Monte Carlo methods: an example with cosmic rays and clouds. *J. Space Weather Space Clim.* **3**, A29 (2013).
53. Simmonds, I. & Govekar, P. D. What are the physical links between Arctic sea ice loss and Eurasian winter climate? *Environ. Res. Lett.* **9**, 101003 (2014).
54. van Oldenborgh, G. J. *et al.* A commentary on lack of robust relationships identified in statistical analyses when verifying proposed mechanistic explanations for the 2013/2014 winter floods in the UK. *Nature Clim. Change* **5**, 490–491 (2015).
55. Dommenget, D. & Latif, M. A cautionary note on the interpretation of EOFs. *J. Clim.* **15**, 216–225 (2002).
56. Webster, P. J. Mechanisms Determining the Atmospheric Response to Sea Surface Temperature Anomalies. *J. Atmos. Sci.* **38**, 554–571 (1981).
57. Mueller, B. & Seneviratne, S. I. Hot days induced by precipitation deficits at the global scale. *Proc. Natl. Acad. Sci.* **109**, 31, 12398–12403 (2012).
58. Miralles, D. G., Teuling, A. J., van Heerwaarden, C. C. & de Arellano, J. V.-G. Mega-heatwave temperatures due to combined soil desiccation and atmospheric heat accumulation. *Nat. Geosci.* **7**, 345–349 (2014).

Acknowledgements

This work has been financially supported by the Australian Research Council grants numbers DP140102855 and DP120103950. T.C. and A.P. are supported by the Goyder Institute for Water Research, and the Australian Climate Change Science Program. The T_{\max} and T_{\min} data at Perth station can be downloaded at <http://www.bom.gov.au/climate/data/> and the ERA-Interim data is available at <http://apps.ecmwf.int/datasets/data/interim-full-daily>. We acknowledge the World Climate Research Programme's Working Group on Coupled Modelling, which is responsible for CMIP, and thank the various climate groups for producing and making their model output available. Finally, we thank Dr P. Terray for the use of his STATPACK statistical set of tools.

Author Contributions

G.B. and I.S. conceived the study and G.B. performed the analyses. A.P. processed the CMIP5 data and helped to perform the sensitivity tests, and prepare the corresponding figures. G.B. wrote the main text and I.S., A.P., T.C. and A.B.P. contributed to the reviewing of the manuscript.

Additional Information

Supplementary information accompanies this paper at <http://www.nature.com/srep>

Competing financial interests: The authors declare no competing financial interests.

How to cite this article: Bosch, G. *et al.* On the use of composite analyses to form physical hypotheses: An example from heat wave – SST associations. *Sci. Rep.* **6**, 29599; doi: 10.1038/srep29599 (2016).



This work is licensed under a Creative Commons Attribution 4.0 International License. The images or other third party material in this article are included in the article's Creative Commons license, unless indicated otherwise in the credit line; if the material is not included under the Creative Commons license, users will need to obtain permission from the license holder to reproduce the material. To view a copy of this license, visit <http://creativecommons.org/licenses/by/4.0/>

Appendix F


Coauthored article

A copy of a published article coauthored during my PhD tenure and my contribution is included hereafter:

Perkins-Kirkpatrick, S. E., C. J. White, L. V. Alexander, D. Argüeso, G. Boschat, T. Cowan, J. P. Evans, M. Ekström, E. C. J. Oliver, A. Phatak, and **A. Purich**, 2016: Natural hazards in Australia: heatwaves. *Climatic Change*, 139, 101–114, doi:10.1007/s10584-016-1650-0. Reprinted by permission from Springer Nature ©2016.

A. P. prepared Fig. 3 and wrote part of the draft of Section 4. A. P. contributed to the development of ideas, writing and revising the manuscript.

Natural hazards in Australia: heatwaves

S. E. Perkins-Kirkpatrick¹  · C. J. White^{2,3} ·
L. V. Alexander¹ · D. Argüeso¹ · G. Boschat⁴ ·
T. Cowan^{5,6} · J. P. Evans¹ · M. Ekström⁷ ·
E. C. J. Oliver^{8,9} · A. Phatak¹⁰ · A. Purich^{1,5}

Received: 20 September 2015 / Accepted: 4 March 2016 / Published online: 11 April 2016
© Springer Science+Business Media Dordrecht 2016

Abstract As part of a special issue on natural hazards, this paper reviews the current state of scientific knowledge of Australian heatwaves. Over recent years, progress has been made in understanding both the causes of and changes to heatwaves. Relationships between atmospheric heatwaves and large-scale and synoptic variability have been identified, with increasing trends in heatwave intensity, frequency and duration projected to continue throughout the 21st century. However, more research is required to further our understanding of the dynamical interactions of atmospheric

This article is part of a Special Issue on “The effect of historical and future climate changes on natural hazards in Australia” edited by Seth Westra, Chris White and Anthony Kiem.

✉ S. E. Perkins-Kirkpatrick
Sarah.Kirkpatrick@unsw.edu.au

- ¹ Climate Change Research Centre & ARC Centre of Excellence for Climate System Science, UNSW, Sydney, Australia
- ² School of Engineering and ICT, University of Tasmania, Hobart, Australia
- ³ Antarctic Climate and Ecosystems Cooperative Research Centre, University of Tasmania, Hobart, Australia
- ⁴ School of Earth Sciences and ARC Centre of Excellence for Climate System Science, Melbourne University, Melbourne, Australia
- ⁵ CSIRO Oceans and Atmosphere, Aspendale, Australia
- ⁶ School of GeoSciences, The University of Edinburgh, Edinburgh, UK
- ⁷ CSIRO Land and Water, Canberra, Australia
- ⁸ Institute for Marine and Antarctic Studies, University of Tasmania, Hobart, Australia
- ⁹ ARC Centre of Excellence for Climate System Science, University of Tasmania, Hobart, Australia
- ¹⁰ Department of Mathematics and Statistics, Curtin University, Bentley, Australia

heatwaves, particularly with the land surface. Research into marine heatwaves is still in its infancy, with little known about driving mechanisms, and observed and future changes. In order to address these knowledge gaps, recommendations include: focusing on a comprehensive assessment of atmospheric heatwave dynamics; understanding links with droughts; working towards a unified measurement framework; and investigating observed and future trends in marine heatwaves. Such work requires comprehensive and long-term collaboration activities. However, benefits will extend to the international community, thus addressing global grand challenges surrounding these extreme events.

1 Introduction

Heatwaves are natural hazards that have substantial impacts on human health, the economy and environment, occurring in the atmosphere and the ocean. They are Australia's most deadly natural hazard, causing 55 % of all natural disaster related deaths (Coates et al. 2014) and burden the Australian workforce by ~US\$6.2 billion every year (Zander et al. 2015). The January 2009 Victorian heatwave killed over 370 people (Alexander and Tebaldi 2012) with an insured loss of US\$1.3 billion (Munich Re 2009). Heatwaves are also a key contributor to bushfires.

Heatwaves also occur in the marine environment; for example, the 2011 Western Australia marine heatwave (Pearce and Feng 2013) had substantial impacts on marine biodiversity (Wernberg et al. 2013). Extreme heat events also impact agriculture and aquaculture industries, respectively harming grain harvest yields (Barlow et al. 2013) and reducing livestock in salmon farming.

Despite their importance, research into atmospheric heatwaves in Australia is generally lagging behind the global effort. Recent studies over Europe have demonstrated how the land interacts with synoptic systems (e.g. Fischer et al. 2012; Quesada et al. 2012) to influencing heatwave variability. Moreover, several studies have indicated that anthropogenic forcing has contributed to specific European events (e.g. Stott et al. 2004), while others indicate increases in the frequency of future heatwaves under greenhouse conditions (Orlowsky and Seneviratne 2012). However, a unified approach in understanding and characterizing atmospheric heatwaves in Australia is currently missing. This is lacking despite improved understanding of relationships between heatwaves and large-scale modes of climate variability (Parker et al. 2014a; Perkins et al. 2015) dominant synoptic patterns (Pezza et al. 2012) and increases in heatwave frequency since the 1950s (Indian Ocean Climate Initiative 2012; Perkins and Alexander 2013). In the case of marine heatwaves, only a handful of studies focus on the dynamics and impacts of specific events (Oliver et al. 2014a; Benthuisen et al. 2014), with a measurement framework only recently proposed (Hobday et al. 2016).

This paper reviews the scientific literature on the measurement, causes, observed trends and future projections of both atmospheric and marine heatwaves across Australia. We conclude with principal findings and provide key recommendations on future research priorities. While atmospheric heatwaves also occur during cooler seasons. The focus here is limited to austral summer heatwaves when the scale of impacts are generally larger.

2 Understanding heatwaves

2.1 Measuring atmospheric heatwaves

Atmospheric heatwaves are often classified as prolonged periods of excessive heat (Perkins and Alexander 2013), although no universal definition exists. They can be measured using different characteristics – such as intensity, frequency, duration, timing and spatial extent – and calculated using daily maximum, minimum, or average temperatures (e.g. Furrer et al. 2010; Fischer and Schär 2010; Russo et al. 2014). In most Australian studies, a relative threshold (or percentile) is used to determine excessive heat, where prolonged periods of heat last for at least 3 days (Tryhorn and Risbey 2006; Alexander and Arblaster 2009; Pezza et al. 2012). A relative threshold is useful since what is considered extreme in one location and/or time of year may not be extreme under other circumstances (Perkins and Alexander 2013).

The Australian Bureau of Meteorology has devised the Excess Heat Factor (EHF; Nairn and Fawcett 2013) index that takes account how hot a three-day period is compared to the previous month, as well as the climatological 95th percentile. Furthermore, a multi-characteristic framework has been developed (Perkins and Alexander 2013), employing five metrics of heatwave intensity, frequency and duration (see Fischer and Schär 2010) for three different definitions. This approach allows for a more consistent analysis, whilst providing useful information to a range of impacts communities, and is similar to the “hot-spell” (periods of extreme heat similar to heatwaves) approach of Furrer et al. (2010), where heatwave characteristics are modelled as a function of covariates, for example, time.

2.2 Large-scale mechanisms of atmospheric heatwaves

Recently, there have been Australian and international advances in understanding drivers and mechanisms of atmospheric heatwaves (e.g. Loikith and Broccoli 2012; Horton et al. 2015; Krueger et al. 2015; Grotjahn et al. 2015). Figure 1 explains how physical mechanisms underpinning atmospheric heatwaves over various timescales may interact in the lead-up to a heatwave. Several studies have examined the relationship between modes of large-scale climate variability and land surface temperatures across Australia (Nicholls et al. 1996; Jones and Trewin 2000; Arblaster and Alexander 2012). While the El Niño-Southern Oscillation (ENSO) is regarded as the primary large-scale driver of inter-annual variations of Australian rainfall (Risbey et al. 2009), its role on temperature extremes is more varied (e.g. Arblaster and Alexander 2012; Min et al. 2013). Significantly more heatwave days, and longer and more intense events are observed over northern and eastern Australia during El Niño compared to La Niña (Perkins et al. 2015), yet different relationships occur in the southeast (Trewin 2009; Parker et al. 2014a; Boschat et al. 2015). White et al. (2013a) found that the Indian Ocean Dipole has a positive relationship over southern Australia for austral winter and spring.

Southeastern Australia heatwaves are associated with the Madden Julian Oscillation (MJO) phases 3–6 during austral summer (Parker et al. 2014a), yet during spring, MJO phases 2–3 are more influential (Marshall et al. 2013). Over most of Australia, the likelihood of extreme temperature increases during negative phases of the Southern Annular Mode (Marshall et al. 2013), but relationships with summertime heatwaves are less clear (Perkins et al. 2015). Large-scale teleconnections to sea surface temperature (SST) and atmospheric conditions are also suggested (e.g. Pezza et al. 2012).

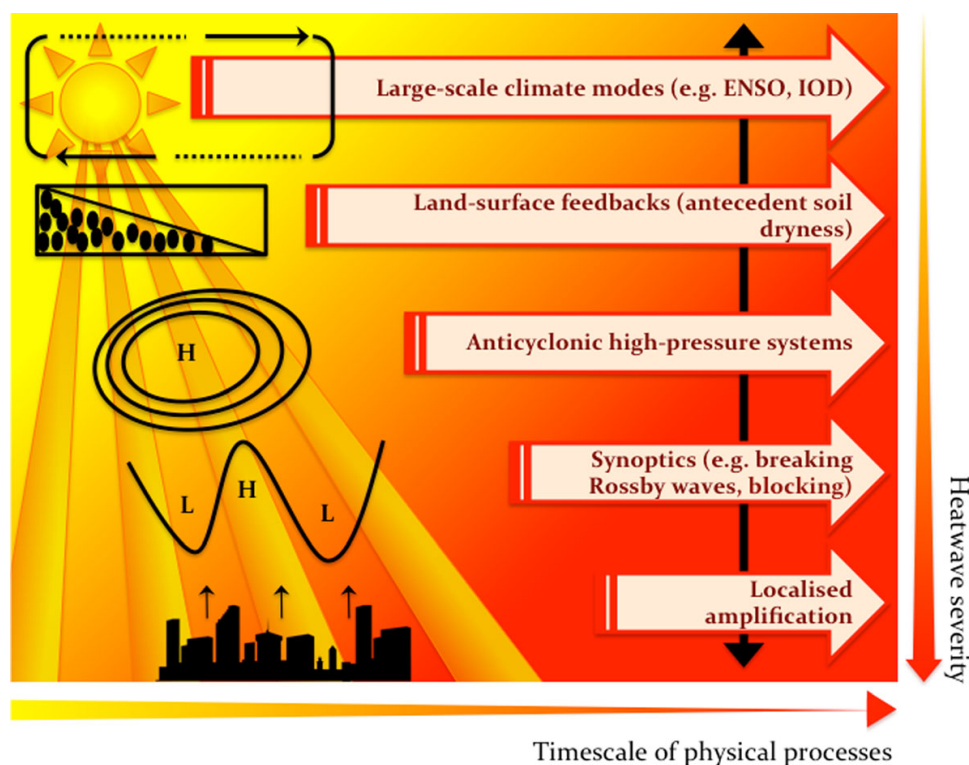


Fig. 1 Heatwave schematic illustrating the various physical processes contributing to heatwaves, the interactions and feedbacks existing between them, and timescales on which they operate. Note that not all processes need to be present for a heatwave to occur (Fischer et al. 2007; Miralles et al. 2014). *Coloured shading* indicates the severity of a heatwave (*red* being more severe), the *arrow thickness* on the x-axis indicates the temporal length of key mechanisms, and the *arrow* on the y-axis indicates how the mechanisms on their various timescales may amplify heatwave severity. For example, A particular phase of climate modes may increase the likelihood of heatwaves, which then become more severe once other, shorter time-scale mechanisms (e.g. dry soil and high-pressure systems) also occur

2.3 Atmospheric heatwave meteorology and land surface influences

The most important weather system for Australian heatwaves is the persistent anticyclone, positioned adjacent to the affected area (Marshall et al. 2013) and largely associated with planetary-scale Rossby waves (Pezza et al. 2012; Parker et al. 2014b). Anticyclonic high-pressure systems bring warm air from the interior of the continent to the heatwave affected area, sustaining conditions for a number of days (Steffen et al. 2014). For southeastern Australia, anticyclone systems are generally centred over the Tasman Sea in line with the subtropical ridge (Hudson et al. 2011; Marshall et al. 2013). Parker et al. (2014b) found an association with propagating and overturning Rossby waves, dynamically influencing the development of southeast heatwaves. Across the southwest, anticyclone systems are typically centred over the Great Australian Bight (Pezza et al. 2012). Other influential features include intra-seasonal drivers of variability (Marshall et al. 2013; White et al. 2013a), rainfall deficits (Nicholls 2004), the Australian monsoon and tropical cyclones (Parker et al. 2013). Mechanisms of extreme-heat build-up include advection from lower latitudes, large-scale subsidence transporting higher potential temperature air from upper levels, or development and replacement of the diurnal mixed layer (McBride et al. 2009).

International studies have shown that the land surface provides important feedbacks (including the albedo, surface roughness and soil moisture; e.g. Miralles et al. 2012, 2014) that can exacerbate or dampen heatwave intensity (Seneviratne et al. 2006). Kala et al. (2015)

demonstrated the impact of soil moisture on the meteorology of the 2009 Black Saturday heatwave, highlighting the significant contribution desiccated soil can have on extreme heat events. Such studies are important, as a better understanding of the strength of these feedback mechanisms may allow for improved land cover management, potentially reducing heatwave severity (Davin et al. 2014). This may be particularly important in urban environments where the urban heat island effect can compound extreme temperature (Argüeso et al. 2014, 2015).

2.4 Measuring marine heatwaves

Marine heatwaves are often measured by the magnitude of ocean temperature anomalies above the monthly seasonal climatology (e.g. Pearce and Feng 2013). Temperature anomalies for specific events have been reported on weekly, daily and finer time scales, using satellite measurements and data loggers (e.g. Olita et al. 2007; Mills et al. 2013). Other studies use more sophisticated metrics including a period (~ 3 to 5 days) where ocean temperatures were at least 3–5 °C above average (Sorte et al. 2010), thermal stress anomalies (Selig et al. 2010) or degree-heating weeks (Gleeson and Strong 1995). Extreme ocean temperatures have been examined using the frequency of days above the 95th percentile (Lima and Wetthey 2012) and extreme value theory (Oliver et al. 2014a, b). A standardized definition has been recently constructed, based on consecutive exceedances of the calendar day 90th percentile of temperature for at least five consecutive days (Hobday et al. 2016). From this definition, a set of metrics are computed that measure marine heatwave intensity, duration, cumulative intensity and rate of onset/decline.

2.5 Large-scale mechanisms of marine heatwaves

Large-scale mechanisms of marine heatwaves are less well understood. ENSO is known to play a role in driving temperature events such as the unprecedented 2011 “Ningaloo Niño” (Pearce and Feng 2013), whereby La Niña conditions drove a stronger than average Leeuwin Current southward along the coast of Western Australia (Kataoka et al. 2014). Off the southeast coast, mesoscale eddies from instabilities in the East Australian Current drive marine heatwaves along the continental shelf (Oliver et al. 2014a). In regions such as coastal South Australia (e.g. Kämpf et al. 2004) and New South Wales (NSW) (e.g. Roughan and Middleton 2004), local winds drive temperature variations due to upwelling and downwelling processes. Globally, high atmospheric temperatures and low winds commonly drive marine heatwaves and this relationship can be expected to hold around Australia (e.g. Olita et al. 2007; Pearce and Feng 2013).

3 Observed changes

3.1 Observed changes and attribution of atmospheric heatwaves

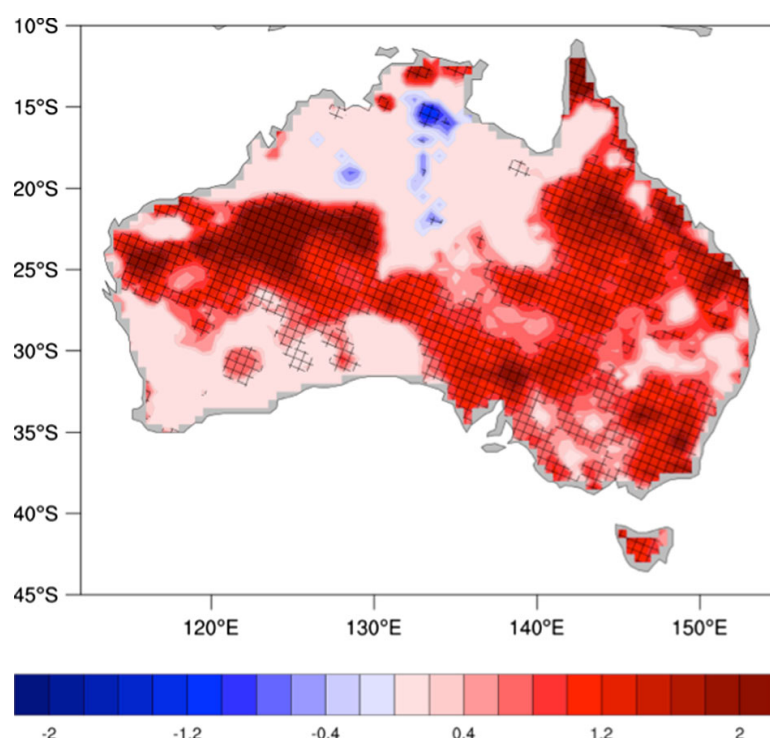
The continentally averaged Australian mean temperature has increased by 0.9 °C since 1950, which is slightly higher than the combined ocean-land global average of 0.85 °C (Bureau of Meteorology 2012), though it is worth noting that globally averaged land-only temperatures have warmed twice as fast as the combined average. There have been various assessments of Australian extreme temperature trends (e.g. Tryhorn and Risbey 2006; Alexander and

Arblaster 2009; Trewin and Vermont 2010; Pezza et al. 2012; Donat et al. 2013), however heatwave characteristics – and the metrics used to define them – can vary markedly, limiting consistent comparisons.

Heatwave characteristics have increased across many Australian regions since the mid 20th century (Alexander and Arblaster 2009; Donat et al. 2013; Perkins and Alexander 2013). Over 1971–2008, the hottest day in a heatwave increased faster than average heatwave intensity, with a measurable increase in the duration and frequency of heatwaves (Perkins and Alexander 2013). Similar patterns are found when extending the analysis to 1950–2013 (Steffen et al. 2014; see Fig. 2). Throughout southwest Western Australia the frequency and intensity of hot spells (periods of relative extreme heat that can occur throughout the year) increased over 1958–2010, but their duration decreased slightly (Indian Ocean Climate Initiative 2012). Over the same period, inland areas of northwest Western Australia experienced increases in intensity, frequency, and duration, but along coastal areas, intensity decreased. While emerging studies are explaining the dynamic/thermodynamic components of changes in Northern Hemisphere extreme temperatures (e.g. Horton et al. 2015), similar studies have not been undertaken.

Classically, studies analysing the role of human influence on observed extreme temperature events are based on monthly/seasonal anomalies for large spatial domains (e.g. Stott et al. 2004). In Australia, the intensity of the 2012/2013 summer was five times more likely to occur in a climate under the influence of anthropogenic greenhouse gases, compared to a climate without these influences (Lewis and Karoly 2013). Moreover, Australia's hottest spring on record (2013) would not have occurred without anthropogenic influence (Lewis and Karoly 2014; Knutson et al. 2014). Although attribution studies are specific to the event and domain analysed, there is evidence that a relationship exists between larger-scale, longer-term extreme temperature anomalies, and those over smaller spatial and temporal scales (Angélil et al. 2014). Hence, the studies of Lewis and Karoly are indicative that a human signal exists in observed heatwaves over smaller domains and shorter temporal scales. Indeed, the intensity and frequency of heatwaves during the 2012/2013 Australian summer increased in occurrence

Fig. 2 Observed trends in Australian heatwave days over 1950–2013. A heatwave day must belong to a period of three or more consecutive days that have positive excess heat values (Nairn and Fawcett 2013). Hatching indicates statistical significance at the 5 % level. Updated from Perkins and Alexander (2013)



by respectively two- and three-fold respectively due to anthropogenic influence (Perkins et al. 2014a). While the aforementioned studies employed the same methodology (fraction of attributable risk, see Allen 2003), other methods also exist for determining anthropogenic influence (Allen and Tett 1999; Kokic et al. 2014). Such analyses have looked at long-term trends in daily extreme temperatures at global and continental scales (e.g. Kim et al. 2015), but have not yet been applied to Australian heatwaves.

3.2 Recent unprecedented heatwave events across Australia

Australia has experienced extreme heatwaves during the last decade. In late January and early February 2009, a severe heatwave occurred over Victoria that was followed by the most devastating bushfires in Australian history (the “Black Saturday” fires). Several records were set for high day- and night-time temperatures as well as for the duration of the event (National Climate Centre 2009). The heatwave occurred in association with a slow moving surface anticyclone and propagating Rossby waves. The land surface had also been particularly dry in the preceding weeks, which combined with the presence of a tropical low off northwest Western Australia and an active monsoon trough, provided ideal conditions for the advection of hot air towards southern Australia (Parker et al. 2013). Recent research also suggests that unprecedented Antarctic warming and a polar anticyclone over the Southern Ocean was at least partly responsible for the 2009 Victorian heatwave (Fiddes et al. 2015).

In January 2013, a record-breaking persistent heat event affected the majority of the continent, which was unprecedented spatially and temporally in observational records (Bureau of Meteorology 2013). Extremely hot air masses developed across north Australia that were driven southwards ahead of a series of cold fronts, creating a persistent hot air mass that sat over the continent (Bureau of Meteorology 2013). The event was associated with a delayed monsoon onset and slow moving weather systems over the continent, following a drier than average end to 2012. The heatwave affected set a new national daily maximum temperature record of 40.33 °C on 7th January 2013, consisting of seven consecutive days with maximum temperature above 39 °C (Bureau of Meteorology 2013).

4 Future changes

4.1 Projections of heatwave events

4.1.1 Heatwave projections from global climate models

Heatwaves are expected to continue in a world under anthropogenic influence, with recent studies suggesting an increase in their frequency and duration (Orlowsky and Seneviratne 2012; Coumou and Robinson 2013; Fischer et al. 2013). Large efforts have been devoted to understanding the impact of anthropogenic climate change on heatwaves in North America and Europe (e.g. Lau and Nath 2012, 2014; Andrade et al. 2014), but this is less so for Australian heatwaves. Relevant work for Australia are summarised below.

Tryhorn and Risbey (2006) and Alexander and Arblaster (2009), employing a single climate model, and the Coupled Model Intercomparison Project (CMIP) phase 3 climate models respectively, found a projected increase in heatwave duration and warm nights in the 21st century under greenhouse forcing. Recently, revised regional climate change projections

for Australia provide a regional assessment of plausible future projections of extreme temperatures (CSIRO 2015). Projections based on 24 CMIP phase 5 (CMIP5) climate models for the Representative Concentration Pathways (RCP) 4.5 (medium-low) and 8.5 (high) emission scenarios (Taylor et al. 2012) show that changes in extremes are similar to changes in annual means, consistent with observations (Alexander et al. 2007). Projected changes in the frequency of warm spells (including heatwaves) by 2100 show a significant increase among the CMIP5 ensemble for both RCP4.5 and RCP8.5 (CSIRO 2015).

The CMIP5 models project heatwaves to become more frequent, hotter, and longer across Australia by the end of the 21st century (Cowan et al. 2014). Patterns of change are similar under RCP4.5 (Fig. 3a, b) and RCP8.5 (Fig. 3c, d), but scale with anthropogenic influence. Projections for northern Australia show the largest increase in heatwave days, due to the narrow temperature distribution in the tropics (e.g. Diffenbaugh and Scherer 2011). Increases in intensity and frequency across the southern regions are substantial (Fig. 3a, b, c, d). Under a moving-threshold heatwave definition, which removes the effect of an increase in mean temperature, future changes in frequency are minimal, indicating a similar rate of increase to mean temperature (Cowan et al. 2014). However, the intensity across central-southern Australia still increases, implying that heatwaves are getting hotter at a faster rate than mean temperature in this region.

4.1.2 Regional and downscaled climate projections

Projected changes in temperature extremes have been quantified using dynamical downscaling techniques across Australia (Perkins et al. 2014b), resolution Tasmania (White et al. 2013b),

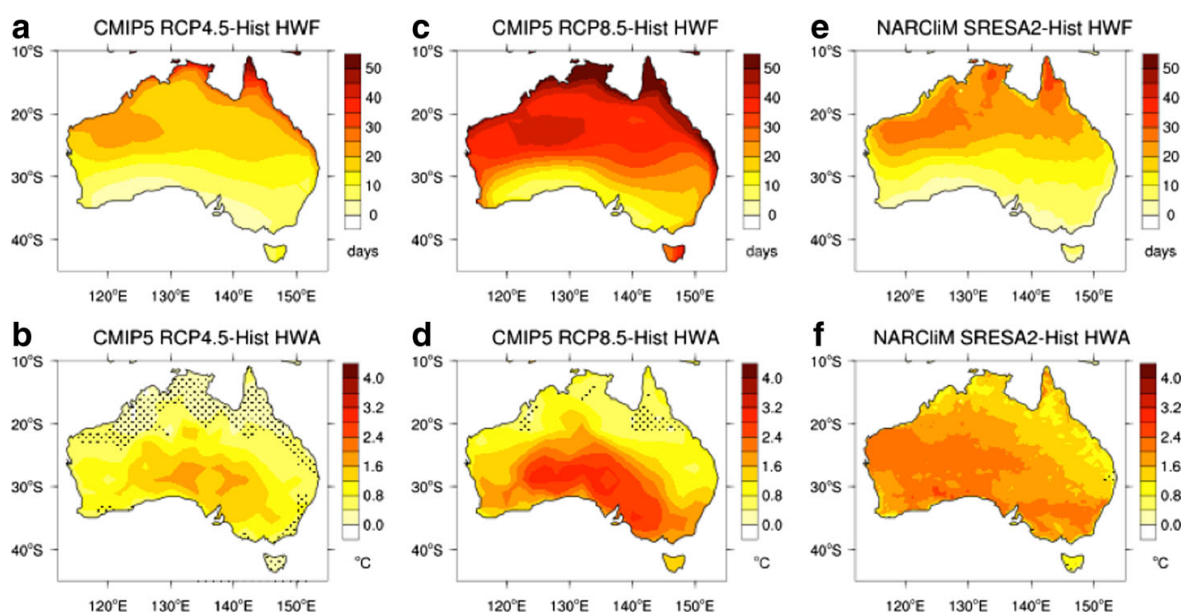


Fig. 3 Austral summer heatwave increases compared to historical climatology. (*top*) Ensemble average heatwave frequency (HWF; days per summer), and (*bottom*) heatwave amplitude (HWA; °C). (**a,b**) CMIP5 RCP4.5, (**c,d**) CMIP5 RCP8.5, and (**e,f**) 50 km downscaled NARCLiM SRES A2. CMIP5 increases are calculated over 2081–2100 compared to 1950–2005 climatology. NARCLiM increases are calculated over 2060–2079 compared to 1990–2009 climatology. Heatwaves are based on the definition described in Pezza et al. (2012), where a heatwave occurs when at least three consecutive days are above the monthly 90th percentile for maximum temperature. Stippling indicates where future and historical climatologies are *not* significantly different at the 95 % confidence level. (**a–d**) adapted from Fig. 3 in Cowan et al. (2014) and based on 15 CMIP5 models

and for NSW and the Australian Capital Territory (Evans et al. 2014). White et al. (2013b) show a significant average increase in warm spell duration including by 2100, relative to the current baseline for a high-emissions scenario across Tasmania.

While regional climate ensemble projections agree with large-scale trends from their host models, such studies add spatial detail in extreme temperature frequency and intensity projections (Perkins et al. 2014b). For example, Fig. 3e and f illustrate this using 50 km regional simulations for heatwave intensity and frequency respectively (Evans et al. 2014).

4.2 Projected changes in atmospheric circulation

Currently, understanding the dynamic/thermodynamic components behind future projections of Australian heatwaves is limited. Purich et al. (2014) found that under climate change, a poleward shift and intensification of the most severe heatwave-inducing anticyclones can be expected, consistent with projected subtropical ridge and SAM changes (e.g. Timbal et al. 2010; Kent et al. 2013). However, the significant rise in the number of heatwave events across southern and central Australia is currently predominantly attributed to thermodynamic changes (Purich et al. 2014).

There are suggestions that SSTs influence synoptic conditions associated with heatwaves globally (Della-Marta et al. 2007; Trenberth and Fasullo 2012), although whether local SST anomalies are caused by, or are responsible for, Australian heatwaves remains uncertain (e.g. Pezza et al. 2012; Boschat et al. 2015). Moreover, evidence provided by observations is limited, and the CMIP5 models fail to capture observed SST patterns prior to southern Australian heatwaves (Purich et al. 2014). Further research is required on this topic, as well as how future changes in the large-scale modes will impact Australian heatwaves (see Parker et al. 2014a), given that models project significant increases in extreme El Niño and La Niña events (Cai et al. 2014, 2015) and a continuation of positive SAM trends in the RCP8.5 scenario (Zheng et al. 2013).

4.3 Projections of marine heatwaves

As marine heatwaves is an emerging field, there are few studies exploring future changes. Southeastern and southwestern Australia are identified as hotspots of ocean warming (Foster et al. 2014), with the Tasman Sea in particular experiencing surface warming three-to-four times the global rate (Holbrook and Bindoff 1997; Ridgway 2007). The CMIP5 models project a net warming (relative to 1986–2005) of SST in the Australia region of 0.65–6.5 °C by 2050 under RCP2.6, rising to 0.99–9 °C and 1.22–2 °C under RCP4.5 and RCP8.5, respectively. The strongest signals are seen off the coasts of Tasmania and southwestern Australia, consistent with observed historical trends, and off the northwest shelf. This background warming is a significant driver of marine heatwaves, as the probability of large heat anomalies becomes much greater. In addition, changes in drivers such as ENSO can significantly impact marine heatwave occurrences off Western Australia (Feng et al. 2015). Changes in wind stress curl over the high-latitude South Pacific (e.g. through variations in the SAM) can impact eddy-driven marine heatwaves off southeastern Australia (Oliver et al. 2014a; Oliver and Holbrook 2014). However, there remains a large gap in understanding what future projections of marine heatwaves might entail.

5 Conclusions and remaining questions

As part of this Special Issue on Australian natural hazards, this paper summarizes scientific advances in the measurement and understanding of Australian atmospheric and marine heatwaves, and the state of our knowledge on future changes. While there is no single way to define heatwaves, it is clear that their intensity, frequency and duration has increased as anthropogenic influences on the climate has increased. Immediate research could focus on developing more impact-relevant projections on finer spatial scales. Moreover, investigating the human influence on observed trends in Australian heatwaves could be undertaken using internationally applied methods.

Considerable advance has been made in understanding the physical mechanisms driving Australian heatwaves, particularly relationships between ENSO and other modes of variability (Parker et al. 2014a; Perkins et al. 2015) and synoptic-scale dynamics (Pezza et al. 2012; Parker et al. 2014b; Boschhat et al. 2015). However, there is no comprehensive, Australia-wide study documenting the dynamics behind heatwaves. Consequently untangling causes and changes in Australian heatwaves should be prioritized, including land surface feedbacks and antecedent soil moisture, dynamic/thermodynamic components of heatwaves, and increases in the land-sea temperature gradient. The latter has not yet been studied in relation to Australian heatwaves, yet may be important, especially over coastal regions. Understanding the physical connections between heatwaves and drought would also be beneficial to stakeholders of both hazards. Such work is imperative towards a greater understanding of atmospheric heatwaves, as well as advancing Australia's international contribution towards this important field.

Much work remains to better understand marine heatwaves. Given local events in recent years (Pearce and Feng 2013) and the proposal of a measurement framework (Hobday et al. 2016), the Australian community is in a leading position. However, considerable work is required to generate future projections of marine heatwaves and understand interactions between driving mechanisms. Such work should be prioritized to bring our understanding of marine heatwaves in line with atmospheric events.

Lastly, there is a need for a more unified framework for identifying atmospheric events, following recent Australian efforts applied to marine events. The identification of events underpins subsequent research on dynamics, changes and impacts, thus a more unified framework allows for consistency across relevant studies and fields of research. This would require large collaboration across different research and industry sectors, and would need to be conducted at the global scale. This is an area that is likely to be active for many years to come, yet is imperative in addressing both regional and global grand challenges of heatwaves.

Acknowledgments S.E. Perkins-Kirkpatrick is supported by Australian Research Council grant number DE140100952. L.V. Alexander and E.C.J. Oliver are supported by Australian Research Council grant number CE110001028 and G. Boschhat by Australian Research Council grand number DP140102855. T. Cowan and A. Purich are supported by the Goyder Institute for Water Research, and the Australian Climate Change Science Program. J.P. Evans is supported by funding from the NSW Office of Environment and Heritage backed NSW/ACT Regional Climate Modelling (NARClIM) Project and the Australian Research Council as part of the Future Fellowship FT110100576. This paper was a result of collaboration through the 'Trends and Extremes' working group as part of the Australian Water and Energy Exchanges Initiative (OzEWEX).

References

- Alexander LV, Arblaster JM (2009) Assessing trends in observed and modelled climate extremes over Australia in relation to future projections. *Int J Climatol* 29:417–435. doi:[10.1002/joc.1730](https://doi.org/10.1002/joc.1730)
- Alexander LV, Tebaldi C (2012) Climate and weather extremes: observations, modelling and projections [in “the future of the World’s climate”]. Elsevier Science, ISBN 978-0-12-386917-3
- Alexander LV, Hope P, Collins D, Trewin B, Lynch A, Nicholls N (2007) Trends in Australia’s climate means and extremes: a global context. *Aust Meteorol Mag* 56:1–18
- Allen M (2003) Liability for climate change. *Nature* 421:891–892
- Allen MR, Tett SF (1999) Checking for model consistency in optimal fingerprinting. *Clim Dyn* 15:419–434
- Andrade C, Fraga H, Santos JA (2014) Climate change multi-model projections for temperature extremes in Portugal. *Atmos Sci Lett* 15:149–156
- Angélil O, Stone DA, Tadross M, Tummon F, Wehner M, Knutti R (2014) Attribution of extreme weather to anthropogenic greenhouse gas emissions: sensitivity to spatial and temporal scales. *Geophys Res Lett* 41: 2150–2155
- Arblaster JM, Alexander LV (2012) The impact of the El Niño-Southern Oscillation on maximum temperature extremes. *Geophys Res Lett* 39(20)
- Argüeso D, Evans JP, Fita L, Bormann KJ (2014) Temperature response to future urbanization and climate change. *Clim Dyn* 42:2183–2199. doi:[10.1007/s00382-013-1789-6](https://doi.org/10.1007/s00382-013-1789-6)
- Argüeso D, Evans JP, Pitman AJ, Di Luca A (2015) Effects of City expansion on heat stress under climate change conditions. *PLoS one* 10:e0117066. doi:[10.1371/journal.pone.0117066](https://doi.org/10.1371/journal.pone.0117066)
- Barlow KM, Christy BP, O’Leary GJ, Riffkin PA, Nuttall JG (2013) Simulating the impact of extreme heat and frost events on wheat production: the first steps. 20th International Congress on Modelling and Simulation, Adelaide, Australia, 1–6
- Benthuyssen J, Feng M, Zhong L (2014) Spatial patterns of warming off Western Australia during the 2011 Ningaloo Nino: quantifying impacts of remote and local forcing. *Cont Shelf Res* 91:232–246
- Boschat G, Pezza AB, Simmonds I, Perkins SE, Cowan T, Purich A (2015) Large scale and sub-regional connections in the lead up to summer heat wave and extreme rainfall events in eastern Australia. *Clim Dyn* 44:1823–1840. doi:[10.1007/s00382-014-2214-5](https://doi.org/10.1007/s00382-014-2214-5)
- Bureau of Meteorology (2012) Annual climate summary 2012. Bureau of Meteorology, Australia, Accessed at http://www.bom.gov.au/climate/annual_sum/2012/index.shtml
- Bureau of Meteorology (2013) Special climate statement 43 – extreme heat in January 2013. Bureau of Meteorology, Australia
- Cai W et al. (2014) Increasing frequency of extreme El Niño events due to greenhouse warming. *Nat Clim Chang* 4:111–116. doi:[10.1038/nclimate2100](https://doi.org/10.1038/nclimate2100)
- Cai W et al. (2015) Increased frequency of extreme La Nina events under greenhouse warming. *Nat Clim Chang* 5:132–137. doi:[10.1038/nclimate2492](https://doi.org/10.1038/nclimate2492)
- Coates L, Haynes K, O’Brien J, McAneney J, de Oliveira F (2014) Exploring 167 years of vulnerability: An examination of extreme heat events in Australia 1844–2010. *Environ Sci Pol* 42:33–44
- Coumou D, Robinson A (2013) Historic and future increase in the global land area affected by monthly heat extremes. *Environ Res Lett* 8:034018. doi:[10.1088/1748-9326/8/3/034018](https://doi.org/10.1088/1748-9326/8/3/034018)
- Cowan T, Purich A, Perkins S, Pezza A, Boschat G, Sadler K (2014) More frequent, longer, and hotter heat waves for Australia in the twenty-first century. *J. Climate* 27:5851–5871
- CSIRO and Bureau of Meteorology 2015. Climate change in Australia information for Australia’s Natural Resource Management regions: technical report. Australia
- Davin EL, Seneviratne SI, Ciais P, et al. (2014) Preferential cooling of hot extremes from cropland albedo management. *PNAS* 111:9757–9761. doi:[10.1073/pnas.1317323111](https://doi.org/10.1073/pnas.1317323111)
- Della-Marta P, Luterbacher J, von Weissenfluh H, Xoplaki E, Brunet M, Wanner H (2007) Summer heat waves over western Europe 1880–2003: their relationship to large-scale forcings and predictability. *Clim Dyn* 29: 251–275. doi:[10.1007/s00382-007-0233-1](https://doi.org/10.1007/s00382-007-0233-1)
- Diffenbaugh NS, Scherer M (2011) Observational and model evidence of global emergence of permanent, unprecedented heat in the 20th and 21st centuries. *Clim Chang* 107:615–624. doi:[10.1007/s10584-011-0112-y](https://doi.org/10.1007/s10584-011-0112-y)
- Donat MG, Alexander LV, Yang H, Durre I, Vose R, Caesar J (2013) Global land-based datasets for monitoring climatic extremes. *Bull Am Meteorol Soc* 96:997–1006. doi:[10.1175/BAMS-D-12-00109.1](https://doi.org/10.1175/BAMS-D-12-00109.1)
- Evans JP, Ji F, Lee C, Smith P, Argüeso D, Fita L (2014) Design of a regional climate modelling projection ensemble experiment – NARClIM. *Geosci Model Dev* 7:621–629
- Feng M, Hendon HH, Xie SP, Marshall AG, Schiller A, Kosaka Y, Pearce A (2015) Decadal increase in Ningaloo Niño since the late 1990s. *Geophys Res Lett* 42(1):104–112

- Fiddes SL, Pezza AB, Renwick J (2015) Significant extra-tropical anomalies in the lead up to the Black Saturday fires. *Int J Climatol*. doi:[10.1002/joc.4387](https://doi.org/10.1002/joc.4387)
- Fischer EM, Schär C (2010) Consistent geographical patterns of changes in high-impact European heatwaves. *Nat Geosci* 3:398–403
- Fischer EM, Seneviratne SI, Lüthi D, Schär C (2007) Contribution of land-atmosphere coupling to recent European summer heat waves. *Geophys Res Lett* 34(6). doi:[10.1029/2006GL029068](https://doi.org/10.1029/2006GL029068)
- Fischer EM, Rajczak J, Schär C (2012) Changes in European summer temperature variability revisited. *Geophys Res Lett* 39:L19702. doi:[10.1029/2012GL052730](https://doi.org/10.1029/2012GL052730)
- Fischer EM, Beyerle U, Knutti R (2013) Robust spatially aggregated projections of climate extremes. *Nat Clim Chang* 3:1033–1038
- Foster SD, Griffin DA, Dunstan PK (2014) Twenty years of high-Resolution Sea surface temperature imagery around Australia: inter-annual and annual variability. *PLoS one* 9(7):e100762
- Furrer EM, Katz RW, Walter MD, Furrer R (2010) Statistical modelling of hot spells and heat waves. *Clim Res* 43:191–205. doi:[10.3354/cr00924](https://doi.org/10.3354/cr00924)
- Gleeson MW, Strong AE (1995) Applying MCSST to coral reef bleaching. *Adv Space Res* 16:151–154
- Grotjahn R et al. (2015) North American extreme temperature events and related large scale meteorological patterns: a review of statistical methods, dynamics, modeling, and trends. *Clim Dyn*. doi:[10.1007/s00382-015-2638-6](https://doi.org/10.1007/s00382-015-2638-6)
- Hobday A, Alexander LV, Perkins SE, Smale DA, Straub SC, Oliver E, Bentuysen J, Burrows MT, Donat MG, Feng M, Holbrook NJ, Moore PJ, Scannell H, Sen Gupta A, Wernberg T (2016) A hierarchical approach to defining marine heatwaves. *Prog Oceanogr* 141:227–238. doi:[10.1016/j.pocean.2015.12.014](https://doi.org/10.1016/j.pocean.2015.12.014)
- Holbrook NJ, Bindoff NL (1997) Interannual and decadal temperature variability in the southwest Pacific Ocean between 1955 and 1988. *J Clim* 10:1035–1049
- Horton DE, Johnson NC, Singh D, Swain DL, Rajaratnam B, Diffenbaugh NS (2015) Contribution of changes in atmospheric circulation patterns to extreme temperature trends. *Nature* 522:465–469
- Hudson D, Marshall A, Alves O (2011) Intraseasonal forecasting of the 2009 summer and winter Australian heat waves using POAMA. *Weather Forecast* 26:257–279
- Indian Ocean Climate Initiative (2012) Western Australia's Weather and Climate: a Synthesis of Indian Ocean climate initiative stage 3 research. In: Bryson Bates, Carsten Frederiksen and Janice Wormworth (eds) CSIRO and Bureau of Meteorology, Australia
- Jones DA, Trewin BC (2000) On the relationships between the El Niño–Southern Oscillation and Australian land surface temperature. *Int J Climatol* 20(7):697–719
- Kala J, Evans JP, Pitman AJ (2015) Influence of antecedent soil moisture conditions on the synoptic meteorology of the black Saturday bushfire event in southeast Australia. *Quarterly Journal of the Royal Meteorological Society*, Accepted 29 May 2015
- Kämpf J, Doubell M, Griffin D, Matthews RL, Ward TM (2004) Evidence of a large seasonal coastal upwelling system along the southern shelf of Australia. *Geophys Res Lett* 31(9)
- Kataoka T, Tozuka T, Behera S, Yamagata T (2014) On the Ningaloo Niño/Niña. *Clim Dyn* 43:1463–1482
- Kent D, Kirono D, Timbal B, Chiew F (2013) Representation of the Australian sub-tropical ridge in the CMIP3 models. *Int J Climatol* 33:48–57. doi:[10.1002/joc.3406](https://doi.org/10.1002/joc.3406)
- Kim Y-H, Min S-K, Zhang X, Ziwers F, Alexander LV, Donat MG, Tung Y (2015) Attribution of extreme temperature changes during 1951–2010. *Clim Dyn*. doi:[10.1007/s00382-015-2674-2](https://doi.org/10.1007/s00382-015-2674-2)
- Knutson TR, Zeng F, Wittenberg AT (2014) Multimodel assessment of extreme annual-mean warm anomalies during 2013 over regions of Australia and the western Tropical Pacific. [in “Explaining Extremes of 2013 from a Climate Perspective”]. *Bull Amer Meteor Soc* 95(9):S26–S30
- Kokic P, Crimp S, Howden M (2014) A probabilistic analysis of human influence on recent record global mean temperature changes. *Clim Risk Manag* 3:1–12
- Krueger O, Hegerl GC, Tett SFB (2015) Evaluation of mechanisms of hot and cold days in climate models over central Europe. *Environ Res Lett* 10. doi:[10.1088/1748-9326/10/1/014002](https://doi.org/10.1088/1748-9326/10/1/014002)
- Lau N-C, Nath M (2012) A model study of heat waves over North America: meteorological aspects and projections for the twenty-first century. *J Clim* 25:4761–4784. doi:[10.1175/JCLI-D-11-00575.1](https://doi.org/10.1175/JCLI-D-11-00575.1)
- Lau N-C, Nath M (2014) Model simulation and projection of European heat waves in present-day and future climates. *J Clim* 27(10). doi:[10.1175/JCLI-D-13-00284.1](https://doi.org/10.1175/JCLI-D-13-00284.1)
- Lewis SC, Karoly DJ (2013) Anthropogenic contributions to Australia's record summer temperatures of 2013. *Geophys Res Lett* 40:705–709
- Lewis SC, Karoly DJ (2014) The role of anthropogenic forcing in the record 2013 Australia-wide annual and spring temperatures. [in “Explaining Extremes of 2013 from a Climate Perspective”]. *Bull Amer Meteor Soc* 95(9):S31–S34
- Lima FP, Wetthey DS (2012) Three decades of high-resolution coastal sea surface temperatures reveal more than warming. *Nat Commun* 3

- Loikith PC, Broccoli AJ (2012) Characteristics of observed atmospheric circulation patterns associated with temperature extremes over North America. *J Clim* 25:7266–7281
- Marshall AG, Hudson D, Wheeler MC, Alves O, Hendon HH, Pook MJ, Risbey JS (2013) Intra-seasonal drivers of extreme heat over Australia in observations and POAMA-2. *Clim Dyn* 43:1915–1937. doi:[10.1007/s00382-013-2016-1](https://doi.org/10.1007/s00382-013-2016-1)
- McBride JL, Mills GA, Wain AG (2009) The meteorology of Australian heatwaves. Understanding High Impact Weather, CAWCR Modelling Workshop, 30 Nov to 2 Dec 2009
- Mills KE, Pershing AJ, Brown CJ, Yong C, Fu-Sung C, Holland DS, Lehuta S, Nye JA, Sun JC, Thomas AC, Wahle RA (2013) Fisheries Management in a changing climate lessons from the 2012 ocean heat wave in the Northwest Atlantic. *Oceanography* 26:191–195
- Min SK, Cai W, Whetton P (2013) Influence of climate variability on seasonal extremes over Australia. *J Geophys Res Atmos* 118:643–654
- Miralles DG, Van Den Berg MJ, Teuling AJ, De Jeu RAM (2012) Soil moisture-temperature coupling: A multiscale observational analysis. *Geophys Res Lett*. doi:[10.1029/2012GL053703](https://doi.org/10.1029/2012GL053703)
- Miralles DG, Teulingb, AJ, van Heerwaarden, CC, de Arellano, JVG (2014) Mega-heatwave temperatures due to combined soil desiccation and atmospheric heat accumulation. *Nat Geosci*, 7:345–349.
- Munich Re (2009) Heavy losses due to severe weather in the first six months of 2009, press release, 27 July 2009, www.munichre.com/en/press/press_releases/2009/2009_07_27_press_release.aspx
- Nairn, J, Fawcett, R (2013) Defining heatwaves: Heatwave defined as a heat-impact event servicing all community and business sectors in Australia. CAWCR Tech. Rep. 60, 96 pp. [Available online at http://www.cawcr.gov.au/publications/technicalreports/CTR_060.pdf]
- National Climate Centre (2009). The exceptional January–February 2009 heatwave in southeastern Australia, Bureau of Meteorology, Special Climate Statement 17
- Nicholls N (2004) The changing nature of Australian droughts. *Clim Chang* 63:323–336
- Nicholls N, Lavery B, Frederiksen C, Drosowsky W, Torok S (1996) Recent apparent changes in relationships between the El Niño–Southern Oscillation and Australian rainfall and temperature. *Geophys Res Lett* 23: 3357–3360
- Olita A et al. (2007) Effects of the 2003 European heatwave on the Central Mediterranean Sea: surface fluxes and the dynamical response. *Ocean Sci* 3:273–289
- Oliver ECJ, Holbrook NJ (2014) Extending our understanding of South Pacific gyre ‘spin-up’: modeling the East Australian current in a future climate. *J Geophys Res* 119:2788–2805. doi:[10.1002/2013JC009591](https://doi.org/10.1002/2013JC009591)
- Oliver ECJ, Wotherspoon SJ, Chamberlain MA, Holbrook NJ (2014a) Projected Tasman Sea extremes in sea surface temperature through the 21st century. *J Clim* 27:1980–1998. doi:[10.1175/JCLI-D-13-00259.1](https://doi.org/10.1175/JCLI-D-13-00259.1)
- Oliver ECJ, Wotherspoon SJ, Holbrook NJ (2014b) Estimating extremes from global ocean and climate models: A Bayesian hierarchical model approach. *Prog Oceanogr* 122:77–91. doi:[10.1016/j.poccean.2013.12.004](https://doi.org/10.1016/j.poccean.2013.12.004)
- Orlowsky B, Seneviratne SI (2012) Global changes in extreme events: regional and seasonal dimension. *Clim Chang* 110:669–696. doi:[10.1007/s10584-011-0122-9](https://doi.org/10.1007/s10584-011-0122-9)
- Parker TJ, Berry GJ, Reeder MJ (2013) The influence of tropical cyclones on heat waves in southeastern Australia. *Geophys Res Lett* 40(23):6264–6270
- Parker TJ, Berry GJ, Reeder MJ, Nicholls N (2014a) Modes of climate variability and heat waves in Victoria, southeastern Australia. *Geophys Res Lett* 41:6926–6934
- Parker TJ, Berry GJ, Reeder MJ (2014b) The structure and evolution of heat waves in Southeastern Australia. *J Clim* 27:5768–5785. doi:[10.1175/JCLI-D-13-00740.1](https://doi.org/10.1175/JCLI-D-13-00740.1)
- Pearce A, Feng M (2013) The rise and fall of the “marine heat wave” off Western Australia during the summer of 2010/2011. *J Mar Syst* 111–112:139–156
- Perkins SE, Alexander LV (2013) On the measurement of heatwaves. *J Clim* 26:4500–4517. doi:[10.1175/JCLI-D-12-00383.1](https://doi.org/10.1175/JCLI-D-12-00383.1)
- Perkins SE, Lewis SL, King AD, Alexander LV (2014a). Increase simulated risk of the hot Australian summer of 2012/2013 due to anthropogenic activity as measured by heat wave frequency and intensity. [in “Explaining Extremes of 2013 from a Climate Perspective”]. *Bull Amer Meteor Soc* 95(9):S34–S36.
- Perkins SE, Moise A, Whetton P, Katzfey J (2014b) Regional changes of climate extremes over Australia – a comparison of regional dynamical downscaling and global climate model simulations. *Int J Climatol* 34: 3456–3478
- Perkins SE, Argüeso D, White CJ (2015) Relationships between climate variability, soil moisture, and Australian heatwaves. *J Geophys Res Atmos* 120(16):8144–8164
- Pezza AB, Van Rensch P, Cai W (2012) Severe heat waves in Southern Australia: synoptic climatology and large scale connections. *Clim Dyn* 38:209–224. doi:[10.1007/s00382-011-1016-2](https://doi.org/10.1007/s00382-011-1016-2)
- Purich A, Cowan T, Cai W, van Rensch P, Uotila P, Pezza A, Boschat G, Perkins S (2014) Atmospheric and oceanic conditions associated with Southern Australian heat waves: A CMIP5 analysis. *J Clim* 27:7807–7829. doi:[10.1175/JCLI-D-14-00098.1](https://doi.org/10.1175/JCLI-D-14-00098.1)

- Quesada B, Vautard R, Yiou P, Hirschi M, Seneviratne SI (2012) Asymmetric European summer heat predictability from wet and dry southern winters and springs. *Nat Clim Chang* 2:736–741
- Ridgway KR (2007) Long-term trend and decadal variability of the southward penetration of the East Australian current. *Geophys Res Lett* 34(13)
- Risbey JS, Pook MJ, McIntosh PC, Wheeler MC, Hendon HH (2009) On the remote drivers of rainfall variability in Australia. *Mon Weather Rev* 137:3233–3253
- Roughan M, Middleton JH (2004) On the east Australian current: variability, encroachment, and upwelling. *J Geophys Res: Oceans*(1978–2012) 109(C7)
- Russo S, Dosio A, Graversen RG, Sillmann J, Carrao H, Dunbar MB, Vogt JV (2014) Magnitude of extreme heat waves in present climate and their projection in a warming world. *J Geophys Res Atmos* 119:12–500
- Selig ER, Casey KS, Bruno JF (2010) New insights into global patterns of ocean temperature anomalies: implications for coral reef health and management. *Glob Ecol Biogeogr* 19:397–411
- Seneviratne SI, Lüthi D, Litschi M, Schär C (2006) Land-atmosphere coupling and climate change in Europe. *Nature* 443:205–209
- Sorte CJB, Fuller A, Bracken MES (2010) Impacts of a simulated heat wave on composition of a marine community. *Oikos* 119:1909–1918
- Steffen W, Hughes, L, Perkins S, (2014) Heatwaves: Hotter, Longer, More Often. Special Report by the Climate Council of Australia, Sydney, Australia. 62 pp. [Available online at <http://www.climatecouncil.org.au/heatwaves-report>]
- Stott PA, Stone DA, Allen MR (2004) Human contribution to the European heatwave of 2003. *Nature* 432(7017):610–614
- Taylor K, Stouffer R, Meehl G (2012) An overview of CMIP5 and the experiment design. *Bull Amer Meteor Soc* 93:485–498. doi:10.1175/BAMS-D-11-00094.1
- Timbal, B., et al., (2010) Understanding the anthropogenic nature of the observed rainfall decline across South Eastern Australia. CAWCR Tech. Rep. 026, Centre for Australian Weather and Climate Research, 202 pp. [Available online at http://www.cawcr.gov.au/publications/technicalreports/CTR_026.pdf.]
- Trenberth K, Fasullo J (2012) Climate extremes and climate change: the Russian heat wave and other climate extremes of 2010. *J Geophys Res* 117:D17103. doi:10.1029/2012JD018020
- Trewin BC (2009). A new index for monitoring changes in heatwaves and extended cold spells. In 9th International Conference on Southern Hemisphere Meteorology and Oceanography
- Trewin B, Vermont H (2010) Changes in the frequency of record temperatures in Australia, 1957–2009. *Aust Meteorol Oceanogr J* 60:113–119
- Tryhorn L, Risbey J (2006) On the distribution of heat waves over the Australian region. *Aus Meteorol Mag* 55: 169–182
- Wernberg T, Smale DA, Tuya F, Thomsen MS, Langlois TJ, De Bettignies T, Rousseaux CS (2013) An extreme climatic event alters marine ecosystem structure in a global biodiversity hotspot. *Nat Clim Chang* 3:78–82
- White CJ, Hudson D, Alves O (2013a) ENSO, the IOD and intraseasonal prediction of heat extremes across Australia using POAMA-2. *Clim Dyn* 43:1791–1810. doi:10.1007/s00382-013-2007-2
- White CJ, McInnes KL, Cechet RP, Corney SP, Grose MR, Holz G, Katzfey JJ, Bindoff NL (2013b) On regional dynamical downscaling for the assessment and projection of future temperature and precipitation extremes across Tasmania, Australia. *Clim Dyn* 41:3145–3165. doi:10.1007/s00382-013-1718-8
- Zander KK, Botzen WJW, Oppermann E, Kjellstrom T, Garnett ST (2015) Heat stress causes substantial labour productivity loss in Australia. *Nat Clim Chang* 5:647–651. doi:10.1038/nclimate2623
- Zheng F, Li J, Clark RT, Nnamchi HC (2013) Simulation and projection of the Southern Hemisphere annular mode in CMIP5 models. *J Clim* 26:9860–9879. doi:10.1175/JCLI-D-13-00204.1

Appendix G

Coauthored article

A copy of a published article coauthored during my PhD tenure and my contribution is included hereafter:

Cowan, T., G. C. Hegerl, I. Colfescu, M. Bollasina, **A. Purich**, and G. Boschat, 2017: Factors contributing to record-breaking heat waves over the Great Plains during the 1930s Dust Bowl. *Journal of Climate*, **30**, 2437–2461, doi:10.1175/JCLI-D-16-0436.1. ©American Meteorological Society. Used with permission.

A. P. developed the original heat wave identification code used by T. C. A. P. contributed to the development of ideas, writing and revising the manuscript.

Factors Contributing to Record-Breaking Heat Waves over the Great Plains during the 1930s Dust Bowl[✉]

TIM COWAN, GABRIELE C. HEGERL, IOANA COLFESCU, AND MASSIMO BOLLASINA

School of Geosciences, University of Edinburgh, Edinburgh, United Kingdom

ARIAAN PURICH

CSIRO Oceans and Atmosphere, Aspendale, Victoria, Australia

GHYSLAINE BOSCHAT

School of Earth Science, University of Melbourne, Melbourne, Victoria, Australia

(Manuscript received 7 June 2016, in final form 3 October 2016)

ABSTRACT

Record-breaking summer heat waves were experienced across the contiguous United States during the decade-long “Dust Bowl” drought in the 1930s. Using high-quality daily temperature observations, the Dust Bowl heat wave characteristics are assessed with metrics that describe variations in heat wave activity and intensity. Despite the sparser station coverage in the early record, there is robust evidence for the emergence of exceptional heat waves across the central Great Plains, the most extreme of which were preconditioned by anomalously dry springs. This is consistent with the entire twentieth-century record: summer heat waves over the Great Plains develop on average ~15–20 days earlier after anomalously dry springs, compared to summers following wet springs. Heat waves following dry springs are also significantly longer and hotter, indicative of the importance of land surface feedbacks in heat wave intensification. A distinctive anomalous continental-wide circulation pattern accompanied exceptional heat waves in the Great Plains, including those of the Dust Bowl decade. An anomalous broad surface pressure ridge straddling an upper-level blocking anticyclone over the western United States forced substantial subsidence and adiabatic warming over the Great Plains, and triggered anomalous southward warm advection over southern regions. This prolonged and amplified the heat waves over the central United States, which in turn gradually spread westward following heat wave emergence. The results imply that exceptional heat waves are preconditioned, triggered, and strengthened across the Great Plains through a combination of spring drought, upper-level continental-wide anticyclonic flow, and warm advection from the north.

1. Introduction

The aptly named “Dust Bowl” drought that plagued the contiguous United States during the 1930s caused widespread misfortune for many regional communities and severely dented the emerging economy. It covered almost one-third of the United States (Peterson et al. 2013), breaking all-time maximum temperature records across the Great Plains and the Mississippi basin

(Abatzoglou and Barbero 2014; Donat et al. 2016) that still hold at the time of analysis.¹ The record-breaking heat waves experienced during the Dust Bowl decade (1930–39) were not isolated incidences, but part of systematically hotter summers that emerged around 1930 across the Midwestern United States and peaked in 1936 (Cook et al. 2014; Donat et al. 2016). What triggered and subsequently amplified the Dust Bowl decade heat waves has been of great interest to the climate and hydrology communities, given the agricultural significance of the Great Plains, and the relatively smaller imposition

[✉] Supplemental information related to this paper is available at the Journals Online website: <http://dx.doi.org/10.1175/JCLI-D-16-0436.s1>.

Corresponding author e-mail: Tim Cowan, tim.cowan@ed.ac.uk

¹ As of the boreal summer of 2016, based on GHCNDEX (based on GHCN data; see Donat et al. 2013a), from <http://www.climdex.org/>.

by greenhouse gas–induced warming in the early twentieth century. Managing the risk that heat waves pose is underscored by the fact that state-of-the-art climate models project an intensification of heat extremes across the United States and Canada in the upcoming decades and beyond (Meehl and Tebaldi 2004; Diffenbaugh and Ashfaq 2010; Grotjahn et al. 2016; Jeong et al. 2016; Teng et al. 2016), potentially exposing a greater proportion of the population to these extreme events (Jones et al. 2015), as witnessed for example in Chicago in 1995 (Livezey and Tinker 1996).

The trigger of summer heat waves and their intensification during the Dust Bowl decade is still an open question some 80 years after their occurrence. Spring precipitation deficits across the central and western United States were observed prior to the Dust Bowl summers (Cook et al. 2011; Donat et al. 2016), which contributed to the drought severity over the Great Plains and the devastating dust storms (Mattice 1935; Cook et al. 2014). Aside from significantly low summer precipitation, anomalous deficits continued through the autumn (Schubert et al. 2004a). The spring precipitation deficit limited soil moisture availability over the Great Plains (and across the Midwest and Northwest; Donat et al. 2016), reducing evapotranspiration at the surface and increasing sensible heating throughout summer, as is common in water-limited regions (Yin et al. 2014). An increase in hot extremes following precipitation deficits has been observed across much of North America and Europe (e.g., Mueller and Seneviratne 2012). This combination of dry soils and midtropospheric anticyclonic blocking has also been implicated as the causal factor behind the European mega-heat waves of 2003 and 2010 (Fischer et al. 2007a,b; Miralles et al. 2014). The extent to which dry springs play a deterministic role in the increased Great Plains summer heat wave activity and intensity has yet to be examined and quantified in the context of the Dust Bowl decade; this is the first focus of this study.

No two individual heat waves are identical, so it is possible that multiple factors lead to single or seasonally clustered events (e.g., Grotjahn et al. 2016). Isolated heat waves across the United States often develop from propagating planetary waves (Teng et al. 2013, 2016; McKinnon et al. 2016) and can be amplified downstream by strong land–atmosphere coupling (Koster et al. 2004; Fischer et al. 2007a). The spring precipitation deficits during the Dust Bowl decade were associated with a weakening in the Great Plains low-level jet (a meridional jet in the lower troposphere), preventing advection of relatively moist warm tropical air from the Gulf of Mexico and Caribbean Sea (Brönnimann et al. 2009). Additionally, midtropospheric blocking in the United

States was a common feature during the late spring and early summer months of the Dust Bowl decade, possibly amplifying the drought conditions (Cook et al. 2011). For North American heat waves, an anomalous upper-level ridge essentially acts as a quasi-stationary blocking anticyclone that prevents synoptic-scale systems from disrupting the accumulation of heat (Lau and Nath 2012). An anomalous ridge persisted over the western United States in the spring and summer (March–July) of 1934, driving high temperature anomalies across the central Great Plains (Cook et al. 2014). Whether this ridging pattern was a systematic feature during the most extreme Great Plains heat waves is determined in the second part of this study using composite analysis.

This study differs from previous research by predominantly focusing on the Dust Bowl heat wave characteristics over the United States, in particular across the Great Plains, as opposed to only focusing on the link between summer heat and spring precipitation (Donat et al. 2016), or the relationship between decadal drought and tropical ocean conditions (e.g., Hoerling and Kumar 2003; Schubert et al. 2004b). We first provide an overview of the well-established metrics and the clustering technique used (section 2) and then quantify the Dust Bowl heat waves (sections 3a and 3b). We then focus on the roles of spring drought severity (sections 3c and 3d) and concurrent synoptic conditions during the earliest summer heat waves (section 3g). We also provide a cautionary note on the biases that emerge when calculating heat wave metrics using gridded reanalysis (sections 3e and 3f). A discussion of the implications of the results is provided in section 4. The expectation of this study is to establish the unique characteristics of heat waves over the Great Plains, and the conditions that distinguish the most exceptional events, like those witnessed during the Dust Bowl decade, to heat waves occurring amid later multiyear drought periods such as 1950s and 1980s.

2. Data and methods

a. Observational and reanalysis data

We utilize daily temperature data from stations networked across the United States and Canada that form part of the Global Historical Climate Network (GHCN)-Daily archive (Menne et al. 2012). The stations were either included in the United States Historical Climatology Network or nonmember stations that have passed the necessary quality assurance checks. Because so few high-quality stations exist in the early twentieth century, only stations that have daily maximum and minimum temperature (T_{\max} and T_{\min} , respectively) from 1920

onward, with less than 10% missing records, are used (e.g., Abatzoglou and Barbero 2014). We focus on the period 1920–2012 to encompass other decades with anomalous heat wave activity and to allow for a large sample size when constructing composites. Fourteen quality control flags, such as failed duplicate checks and failed lagged range checks, were taken into consideration and if any of these flags were raised the station was discarded. Station data homogeneity is also an issue, given inconsistencies in T_{\max} and T_{\min} that are noted in the 1980s due to an upgrade to electronic thermometers (Abatzoglou and Barbero 2014). Temporal inhomogeneities due to stations that are missing more than three consecutive months of measurements do not affect results (not shown). A total of 774 high-quality stations are selected from across North America, with 732 from the United States and 42 from southern Canada.

Daily precipitation observations from 796 GHCN stations are converted to monthly values to calculate the Standardized Precipitation Index (SPI) as a means of quantifying the historical meteorological drought conditions. The SPI, developed by McKee et al. (1993), describes how many standard deviations a particular precipitation value has deviated from the long-term mean, set over a given averaging period. The monthly precipitation time series is transformed into a normal distribution using a two-parameter gamma distribution fit. We consider an averaging period of three months for the SPI. As the SPI does not capture the effects of evapotranspiration, we approximate the contribution from soil moisture with a monthly Palmer Drought Severity Index (PDSI). The PDSI is a standardized drought index, combining precipitation and potential evapotranspiration information, and is significantly correlated with observed soil moisture over a number of United States regions (Dai et al. 2004). We use a self-calibrating PDSI taken from Dai (2011), which is based on the Penman–Monteith equation for calculating evapotranspiration.² The PDSI takes into account wind speed and humidity, and is calibrated for local

conditions making for a better comparison across North America (Dai 2011).

Gridded daily surface conditions and atmospheric circulation fields are taken from the Twentieth Century Reanalysis (20CR) version 2c [e.g., temperature (T_{\max} , T_{\min}), mean sea level pressure (MSLP), 10-m winds, 500-hPa geopotential height], with a T62 ($2^\circ \times 2^\circ$) resolution (Compo et al. 2011). Near-surface horizontal temperature advection (T_{adv}) is expressed as

$$T_{\text{adv}} = u \left(\frac{\partial T}{\partial x} \right) + v \left(\frac{\partial T}{\partial y} \right),$$

where u and v are the 10-m zonal and meridional winds, and $\partial T/\partial x$ and $\partial T/\partial y$ are the zonal and meridional 2-m air temperature gradients, respectively. Horizontal temperature advection is calculated daily and then averaged into months and seasons.

The ensemble average of the 20CR assimilation members is used, given that the spread between individual simulations in version 2 in capturing hot days averaged over the central United States is small during the 1930s (Donat et al. 2016). Soil moisture from 20CR is neglected given its unreliability over the central United States in the early twentieth century (Ferguson and Villarini 2012). Biases also exist in 20CR in representing the location and magnitude of heat maxima over the central United States during the summers of 1934 and 1936 (Donat et al. 2016). As a result, we first calculate heat wave metrics using station data, and then repeat the calculations for the 20CR daily temperatures to confirm the reliability of the gridded product for use in analyzing circulation patterns associated with selected heat waves.

b. Defining heat waves

A heat wave reflects an extended number of days when the daily T_{\max} and/or T_{\min} exceeds a given threshold, resulting in extremely hot days and a lack of nighttime relief (e.g., Nairn and Fawcett 2013). Here we define a heat wave event when the daily T_{\max} surpasses its 90th percentile threshold for more than three consecutive days, with T_{\min} exceeding its 90th percentile threshold for at least the second and third days (i.e., after the third day it can fall below the threshold; however, the heat wave is still considered to continue if T_{\max} continues to exceed its 90th percentile; Pezza et al. 2012). We use the daily 90th percentile threshold based on a centered 15-day window (each calendar day is referenced to the seven days before and after) that shifts each day, such that there is no monthly or seasonal dependency (Perkins and Alexander 2013). The percentile is calculated from a 1920–2012 baseline. The daily percentile approach has the effect of removing biases that

² Evapotranspiration (ET) is defined as

$$\text{ET} = \frac{\Delta(R_n - G) + \rho_a c_p (e_s - e_a)/r_a}{\left[\Delta + \gamma \left(1 + \frac{r_s}{r_a} \right) \right]},$$

where R_n is the surface net radiation flux, G is the soil heat flux, ρ_a is the mean air density at constant pressure, c_p is specific heat of air, Δ is the slope of the saturation vapor pressure temperature relationship, $(e_s - e_a)$ is the vapor pressure deficit of air, γ is the psychrometric constant, and r_s and r_a represent the bulk surface and aerodynamic resistances and so depend on roughness and wind speed.

may arise from heat waves that extend over consecutive months, although similar results are found using monthly percentiles (not shown; Cowan et al. 2014). For each station or 20CR grid point over North America (25.7°–73.3°N, 144.4°–56.3°W) heat wave days are detected, and then heat wave metrics are aggregated over each calendar season [i.e., winter: December–February (DJF), spring: March–May (MAM), summer: June–August (JJA), and autumn: September–November (SON)]. Here DJF refers to the winter prior to the heat wave summer (i.e., previous year's December).

We quantify five main heat wave metrics:

- 1) **HWN**: the total number of heat waves (events per season);
- 2) **HWF**: the frequency of heat wave days (total number of days per season);
- 3) **HWD**: the duration of the longest heat wave (days);
- 4) **HWA**: the amplitude of the hottest seasonal heat wave (anomaly of the hottest day of the hottest seasonal heat wave, °C); and
- 5) **HWT**: the timing of either the earliest, longest or hottest seasonal heat wave (summer is referenced to 1 June).

Unless specified otherwise, we refer to heat waves as summer events only. A further test was also carried out to determine if possible contamination between closely occurring heat waves [less than 15 days between events, as in Teng et al. (2016)] might lead to event count biases. The test showed that there is little difference between the decadal averages of heat wave metrics when events are separated by at least 15 days and those with no separation, aside from a broad-scale reduction in HWN and HWF (since fewer events are considered; not shown). Therefore, we consider all possible heat wave days, but we acknowledge the possibility of overestimating the total number of independent events and underestimating the longest summer event.

The heat wave metrics are calculated for the 774 GHCN stations and for North American grid points for 20CR, although we predominantly focus on three key Dust Bowl drought regions: the northern Great Plains (40°–50°N, 105°–85°W; temperate climate), the southern Great Plains (30°–40°N, 105°–85°W; subtropical climate) and the combined region (termed simply the Great Plains). The Great Plains here is identical to that area that has recorded a high number of hot days during the 1930s (Donat et al. 2016). When a station or grid point detects no seasonal heat wave activity then HWN and HWF are set to zero, whereas HWD, HWA, and HWT are set to missing values. For decadal averages of HWD, HWA, and HWT (as in Fig. 2), we require that the temporal coverage of heat wave data in question for a

given point must be greater than 50% (i.e., more than five years out of a decade must have heat waves detected). This prevents small sample sizes from skewing decadal averages. To address geographical biases when spatially averaging stations over a given region, stations are clustered into $2^\circ \times 2^\circ$ grids and areal averaged over that region [similar to Abatzoglou and Barbero (2014), who averaged over a 1° horizontal resolution]. The heat wave metrics are always calculated for each station prior to averaging over each region, as opposed to averaging temperatures first, given the areal extent of the regions.

Statistical significance of summer heat wave composites ranked by the anomalously dry or wet springs is assessed using a Wilcoxon sign-ranked test (Hollander and Wolfe 1999). This nonparametric test determines if two samples are distinguishable from each other at the 90% confidence level, based on the difference between the means of two sets of cases consisting of the 10 wettest and driest springs over a predefined region. The null hypothesis of this test is that the median difference between the composites is zero. Similar testing was carried out on the SPI-based composites using a Mann–Whitney U test and the results were very similar (not shown).³ The significance is indicated on the spatial maps comparing the heat wave metric composites. For composites that are averaged both spatially and temporally, we perform a Monte Carlo test where the significance between wet and dry spring cases is assessed by generating 1000 sets of 10 randomly sampled summers. Likewise, for circulation and surface condition composites associated with heat waves using 20CR (i.e., Fig. 11 onward), the significance is tested by generating 1000 null composites comprising randomly resampled summers, using identical sample sizes to that of each region's composite. A two-tailed t test is used to determine if a grid cell is significant at the 95% level based on whether that cell's value is greater or less than its equivalent cell in 975 out of the 1000 null composites.

c. Temporal aggregation of heat waves

By temporally aggregating heat waves (by date) we can assess the average circulation associated with heat waves on a week to week time frame. For this we only focus on the synoptic conditions of the earliest summer events. This avoids contamination of synoptic patterns associated with frequently recurring heat waves. We perform a temporal aggregation technique whereby the

³ The Mann–Whitney U test was not considered for the PDSI composite years given the partial dependence of PDSI and heat wave metrics (i.e., they both contain temperature in their definition), although we compare spring drying with summer heat waves.

earliest summer heat wave that occurs at each GHCN station is assigned a start date. All stations over the Great Plains are analyzed and the total number of GHCN stations for each summer day is counted and grouped together to form a unique station date index. We then calculate the cumulative sum of stations for each day that record a heat wave start until a threshold percentage of stations across the region of interest is exceeded. To capture the early summer atmospheric circulation conditions, the threshold of counted stations is arbitrarily set to 10%. For example, in 1934, 323 stations within the Great Plains registered at least one heat wave; we select the date when more than 32 stations (10%) have recorded a heat wave start, which, for 1934, is 5 June. This date differs in each summer depending on how many stations observe heat wave activity (see Fig. S9 in the online supplemental material) or the region of interest (i.e., northern, southern, or entire Great Plains). The 10% threshold captures the synoptic conditions both prior to and after the earliest summer heat wave, instead of secondary and tertiary heat waves that may emerge from the recurring circulation patterns (i.e., blocking anticyclones), as could happen by increasing the station count threshold to above 10% (see Fig. S12). We have performed sensitivity tests by lowering the threshold to 5% to capture very early heat wave conditions; however, this produces very similar results to the 10% threshold case (not shown).

Three distinct week-long phases are chosen over which the atmospheric and surface conditions are averaged around the earliest heat wave start date of the summer, based on the 10% GHCN station exceedance level:

- 1) **Week –1: 1–7 days prior** to the heat wave commencing (e.g., for 1934, this is 29 May–4 June);
- 2) **Week 1: 1–7 days after** the heat wave start (e.g., for 1934, this is 6–12 June); and
- 3) **Week 2: 8–14 days after** the heat wave start (e.g., for 1934, this is 13–19 June).

3. Results

a. Dust Bowl decade heat waves

Many of North America's highest daily T_{\max} and T_{\min} (TXx and TXn) records were set in the 1930s and 1940s, with extremes spanning the southeast United States through to northwest Canada (Figs. 1a,b). The 1930s decade holds the record for the hottest T_{\max} and T_{\min} decade averaged over the central United States (boxed region in Fig. 1a covering 30°–50°N, 105°–85°W, referred to as the Great Plains), exceeding the second and third warmest decades (1910–19 and 1940–49, respectively) by $\sim 1.5^{\circ}\text{C}$ (Fig. 1c). The summer of 1936 is the most

common record-breaking year for the hottest temperatures over the Great Plains, although records also fell in the early 1930s across the southwest and southeast United States (Figs. 1a,b). As many North American extreme temperature records were set prior to the 1950s, a decrease in extreme temperatures (i.e., TXx and TXn) has been observed since the 1930s (Fig. 1c). Despite a decline in the frequency of hot days since the 1950s (Morak et al. 2013), summer heat wave and winter warm spell frequency have increased across the western United States and central-western Canada since this decade (Perkins et al. 2012).

Along with record temperatures, the Great Plains experienced the highest number of summer heat wave days (HWF) in the 1930s of any decade post-1920 (up to and including 2012; Fig. 2a; the post-1960 decades are shown in Fig. S1). Many Great Plains stations exceeded 10 heat wave days per summer averaged over the Dust Bowl decade (~ 2 events per summer on average), with maximum heat wave durations (HWD) > 7 days and temperature anomalies (HWA) $> 10^{\circ}\text{C}$, particularly in the northern Great Plains (Figs. 2b and 2c, respectively). Even the average length of the heat waves (i.e., the ratio of HWF to HWN, as opposed to HWD) was greater in the 1930s, with a greater proportion of stations across North America (51.4%) with average event lengths > 5 days on average, compared to the 1940s and 1950s (28.2% and 37.9%, respectively; figure not shown). The prominent meridional gradient in HWA that increases with latitude is due to the smaller diurnal and seasonal variability in the subtropical climate of the southern United States (Perkins and Alexander 2013); the same feature is captured in the average heat wave temperature (not shown). In the 1940s, the northern Great Plains still experienced more than 7 heat wave days per summer, despite the anomalously wet conditions early in the decade (Brönnimann et al. 2009). The southern Great Plains experienced more than 10 heat wave days per summer on average in the 1950s with HWD exceeding 9 days, which coincided with a protracted drought over the southern United States (Cook et al. 2011). Heat wave activity rose again in the 1980s across the central eastern United States, dropped off in the 1990s, and then increased again in the 2000s, predominantly in the southern regions (Fig. S1). It is worth recalling that the decadal averages only include stations with at least 50% temporal coverage. When all stations with at least one heat wave per decade are included (with HWD and HWA set to zero for summers with no heat waves), the 1930s peak in heat wave activity is more prominent than for later decades (Fig. S2). Including stations with less than 50% coverage per decade tends to amplify the signal-to-noise ratio of the heat waves; however, for the remainder of the

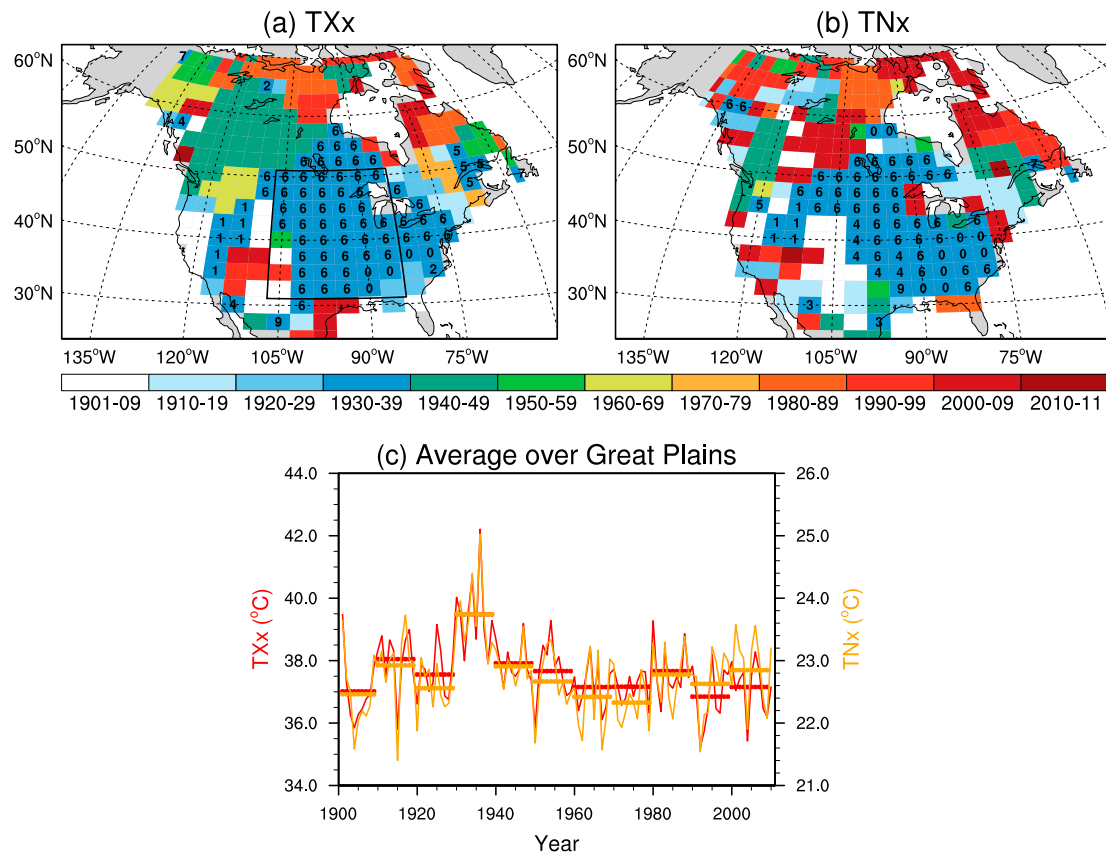


FIG. 1. Decades where the (a) highest daily maximum temperature (TXx) and (b) highest daily minimum temperature (TNx) occurred across North America over 1901–2010. (c) Average TXx (thin red) and TNx (thin orange) over the Great Plains region of North America [30°–50°N, 105°–85°W; box in (a)]. In (a) and (b), the single-digit numbers indicate the record years that occurred in the 1930s (i.e., 0 represents 1930, 4 represents 1934). In (c), the thick lines indicate decadal averages. Note that the vertical axis scales for TXx and TNx are different. Extreme temperature records are taken from the HadEX2 dataset calculated for the CLIMDEX (Datasets for Indices of Climate Extremes) project (Donat et al. 2013b).

paper we choose to only show decadal averages for stations with the 50% temporal coverage to prevent giving equal weight to decades with too few heat waves.

b. Interseasonal variations in Dust Bowl heat waves

Next we investigate the interannual and interseasonal variations of HWD during the most prominent heat wave years in the 1930s (1930–37). HWD is selected here, as the longest heat waves are often the hottest (HWA) and are a strong determinant in the total number of heat wave days (HWF; this is shown in Fig. S3). The correlation coefficient of HWD with HWA (HWF) for summer averaged over the Great Plains is 0.68 (0.89). Given that heat extremes are not just restricted to summer (Perkins and Alexander 2013), we also focus on spring and winter warm spells. Figure 3 (Fig. S3) highlights the interseasonal HWD (HWF) variations over 1930–37 from winter to summer. Large variations in HWD appear throughout the 1930s; for example, prior to the summer of 1934 protracted winter

warm spells and spring events impacted the western United States and northern Great Plains (Fig. 3, fifth row). Similarly, the Great Plains experienced extensive winter warm spells in 1930 and 1931 exceeding 8 days (Fig. 3a, first and second row), coinciding with the 1930/31 central Pacific El Niño event. Central Pacific El Niños are associated with winter precipitation deficits across the central eastern United States, through the equatorward displacement of the tropospheric jet and winter storms (Yu and Zou 2013). Although warm spell activity fell in the spring of 1931 (Fig. 3b and Fig. S3b, second row), drought conditions persisted over the Great Plains (Figs. 4d,e). Heat wave activity rebounded in the summer of 1931 (Fig. 3c, second row), extending into the autumn (not shown) and winter of 1931/32, particularly over the eastern United States, where HWF exceeded 20 days (Fig. S3a, third row). In general, aside from 1934 and 1936 we see a tendency for warm spell activity to drop in the spring (from winter), followed by a heat wave activity increase in summer.

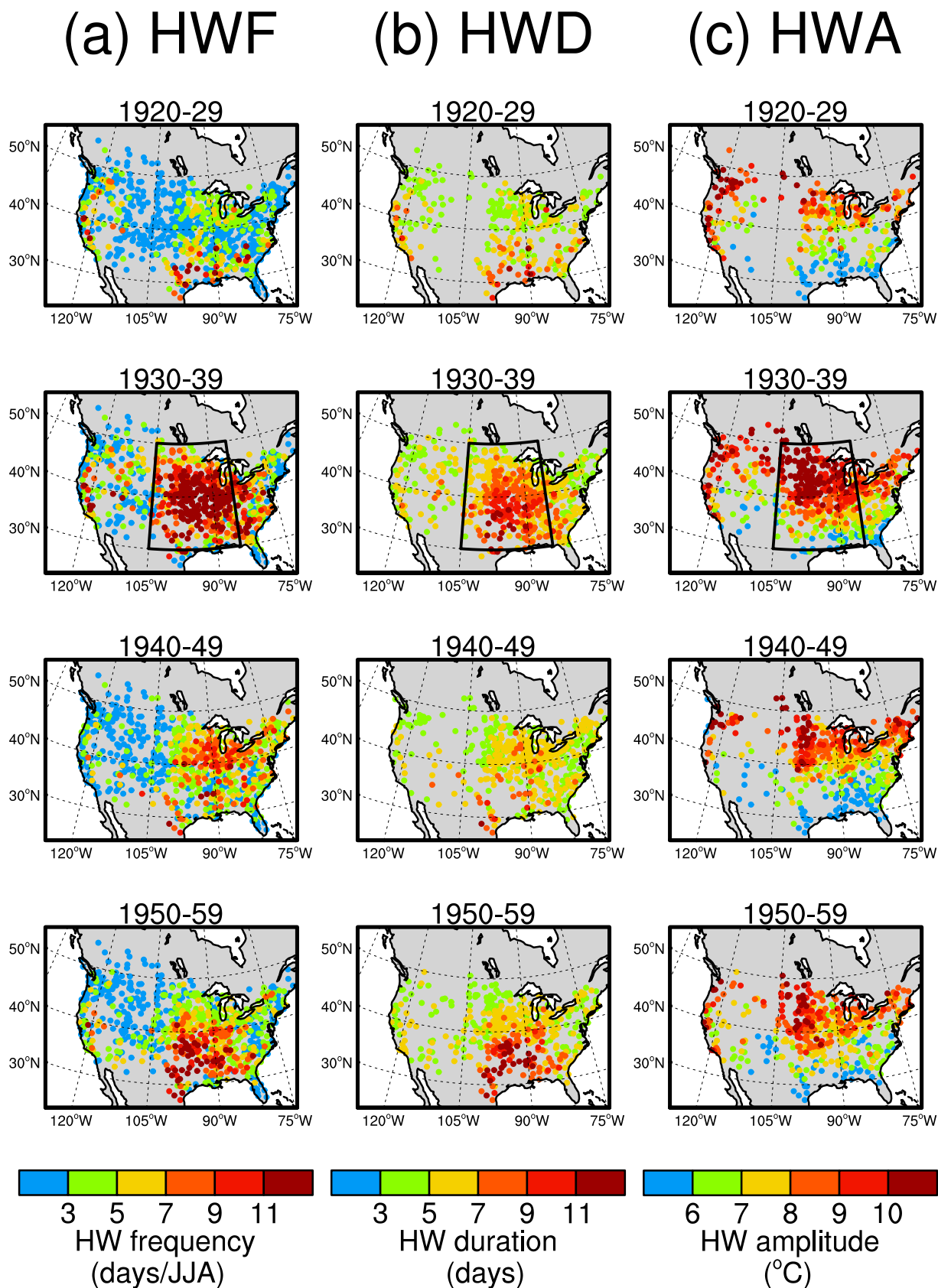


FIG. 2. Decadal averages of summer heat wave (a) frequency (HWF), (b) duration (HWD), and (c) amplitude (HWA) for GHCN-daily station observations over 1920–59. The decades over 1960–2012 are shown in Fig. S1. For HWD and HWA, only stations with more than 50% temporal coverage (i.e., summers with heat waves) for individual decades are shown. The box in the second row represents the Great Plains region, where the Dust Bowl heat wave activity was most severe.

(a) DJF (b) MAM (c) JJA

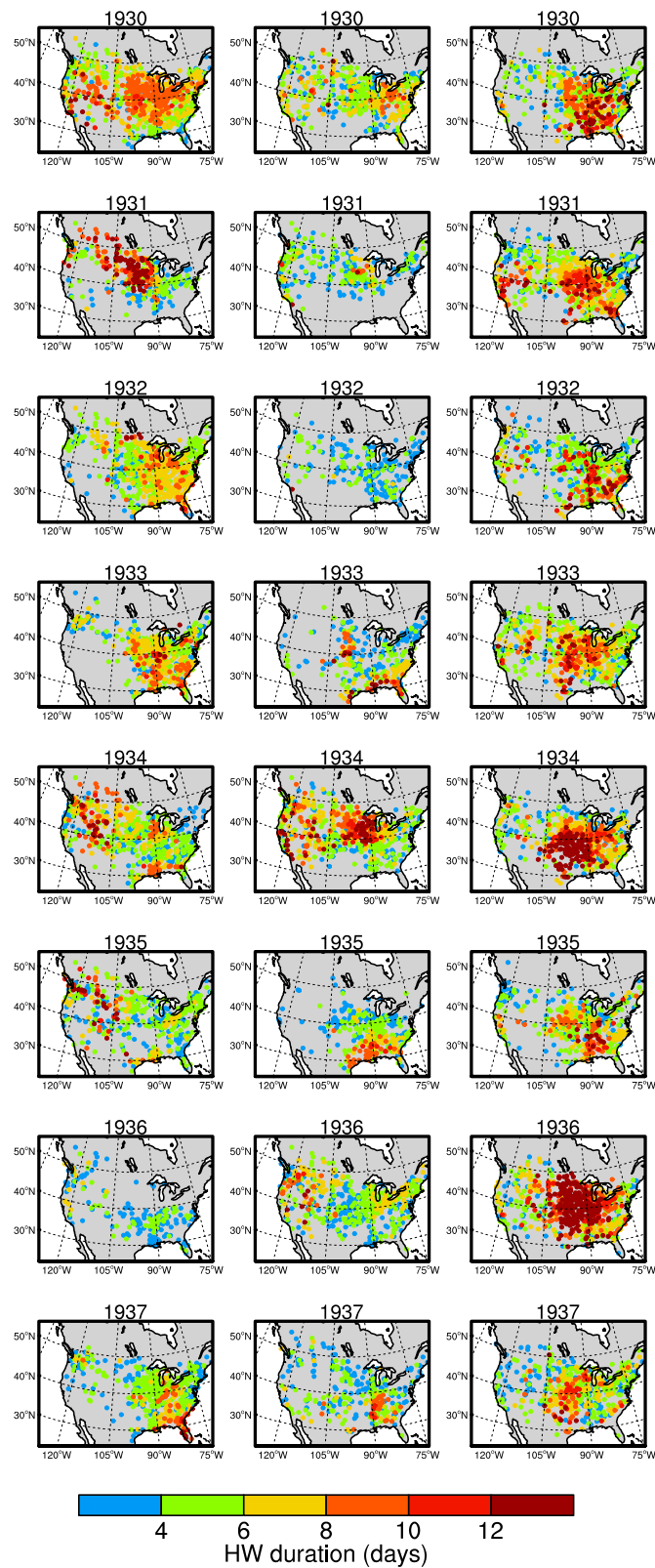


FIG. 3. Seasonal HWD over 1930–37 (i.e., most dominant heat wave seasons in the 1930s): (a) DJF, (b) MAM, and (c) JJA. The sparsity of colored dots reflects the lack of heat wave activity in individual seasons. The equivalent for HWF is shown in Fig. S3.

Great Plains

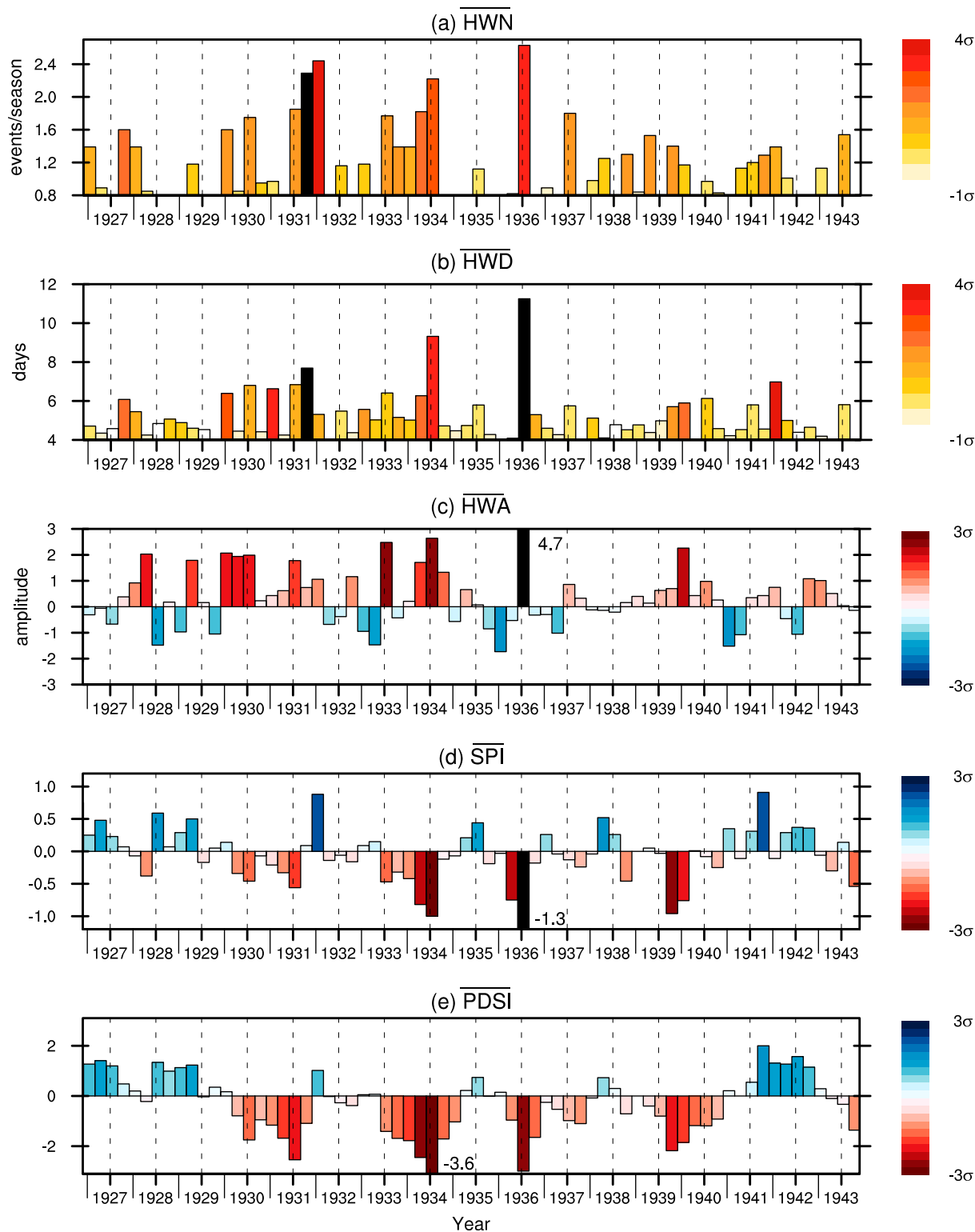


FIG. 4. Heat wave and drought metrics averaged across the Great Plains over 1927–43 for each season: (a) $\overline{\text{HWN}}$, (b) $\overline{\text{HWD}}$, (c) $\overline{\text{HWA}}$, (d) Standardized Precipitation Index (SPI), and (e) Palmer Drought Severity Index (PDSI). The overbar denotes the areal average. All heat wave metrics are calculated from station temperatures, with HWA standardized for each season to assist in comparisons. The SPI is calculated from station precipitation over three months and then aggregated into seasons and the PDSI is based on the self-calibrating index of Dai (2011). The right-hand side color bars represent the number of standard deviations (σ) each value reaches (from the mean for $\overline{\text{HWN}}$ and $\overline{\text{HWD}}$) based on seasonal aggregation. The darker colors represent more extreme values, while the values adjacent the vertical black bars indicate the most extreme summer index values that surpass the vertical axis limit. The vertical dashed lines indicate each summer.

The interseasonal variations in HWN, HWD, HWA and two drought indices (SPI and PDSI⁴), areal averaged over the Great Plains during the 1930s (indicated by the overbar), are shown in Fig. 4. Interseasonal variations averaged over the northern and southern Great Plains separately are shown in Fig. S4. We also highlight the interseasonal variations of the heat wave metrics and drought indices over the Great Plains from 1979 to 2012 as a way of placing the Dust Bowl conditions in the context of recent conditions (Fig. 5). Summer of 1936 emerged as the season with the most frequent and protracted heat waves, where HWN and HWD exceeded 2.5 events ($\sim 4\sigma$) and 11 days (above 4σ), respectively (Figs. 4a,b). HWA, standardized to facilitate seasonal comparison, exceeded 4σ in 1936, around twice the peak of 1934. Furthermore, five out of the six hottest Great Plains heat waves from 1920 to 2012 occurred in the 1930s (1930, 1931, 1933, 1934, 1936).⁵

Dry springs were a common feature shared between four (1930, 1931, 1934, 1936) of the hottest heat wave summers (Figs. 4d,e), although the springs of 1931 and 1934 were preceded by more than three anomalously dry seasons (i.e., carried through from the previous year). Average SPI values ≤ -1 and PDSI values ≤ -3 preceded the intense summers of 1934 and 1936 (Figs. 4d,e); for PDSI, this is classified as extreme drought (Dai 2011). Yet, despite 1936 being the third driest spring on record for the Great Plains (based on SPI, although 1936 was the driest spring on record if considering precipitation alone; Donat et al. 2016), and the driest on record over the southern Great Plains (Fig. S4i, Table 1), spring warm spell activity was relatively low (Figs. 4a–c). Across the northern Great Plains, from the summer of 1929 to 1941, only five seasons recorded above zero PDSI values (Fig. S4e), indicative of a decade of protracted drought. More widely, almost 75% of United States GHCN stations with the highest T_{\max} records during the 1930s recorded PDSI values ≤ -3 , and around 25% of these records were set in 1936 (Abatzoglou and Barbero 2014).

In the more recent period (1979–2012), the lack of decade-long droughts is immediately apparent, as measured by the SPI (Fig. 5d). The PDSI captures a protracted drought sequence in 1988/89, associated with a switch from El Niño to a strong La Niña event in the equatorial eastern Pacific. In the summer of 1988 HWN almost reaches two events, with a HWD of 6 days and

HWA of $\sim 2\sigma$. That summer aside, in general there is very little overlap between the severity and frequency of events in the later decades, with summers following dry periods like 1980, 2011, and 2012 showing relatively large HWN and HWD values (≥ 1.3 events, ≥ 6 days long) but modest HWA ($\leq 0.8\sigma$). Therefore, clearly the Dust Bowl decade heat waves were not only more frequent and longer, but substantially hotter than events at the turn of the twenty-first century. The Dust Bowl heat waves were also broader in their spatial extent of impact (Fig. 2), and emerged during extended periods (5+ yr) of drought.

c. Dry springs and heat wave activity

It has been well established that soil moisture, often represented by proxies such as the SPI, and heat wave intensity are strongly coupled in many water-limited regions (Mueller and Seneviratne 2012), including Australia (Perkins et al. 2015), Europe (Miralles et al. 2014; Fischer et al. 2007a,b), and the United States (Donat et al. 2016). To quantify the impact of preceding dry spring conditions on heat wave activity we utilize the SPI and PDSI. Two composites are formed each consisting of summers that follow the 10 driest and 10 wettest springs (MAM) over 1920–2012. These are termed the *dry-spring* and *wet-spring* composites, respectively, with springs ranked separately by the SPI and PDSI averaged over the entire Great Plains, and over the northern and southern regions separately (see Table 1). By selecting the far tails of the distribution we test whether antecedent soil moisture leading up to summer, as represented by the lowest ranked SPI and PDSI values, is crucial in determining longer and more severe heat waves, or possibly earlier event emergence.

A spatial comparison of HWN, HWD, and HWA (variations in HWN and HWD are similar to HWT and thus it is excluded here) between the dry- and wet-spring composites is shown in Fig. 6 for the SPI rankings, given the possible temperature dependency between the summer heat wave metrics and the spring PDSI (results based on the PDSI are shown in Figs. S5 and S6). The heat wave differences following dry and wet springs averaged over the Great Plains is shown in Fig. 7, with a regional separation into the northern Great Plains and southern Great Plains shown in Fig. S7. A comparison for HWT with events separated into three classes—the earliest, longest, and hottest heat waves—is shown in Fig. 8.

On average, following an exceptionally dry spring, the majority of Great Plains stations exhibit substantially more heat waves (≥ 1.5 events), as well as longer (≥ 7 days) and hotter events ($\geq 8^\circ\text{C}$), compared to those after wet springs (Figs. 6a–c). Many stations across the southern Great Plains show significant differences (according to a

⁴ These indices are indicators of soil moisture conditions (e.g., Dai et al. 2004), used to assess how drought severity influences heat waves, instead of soil moisture from gridded reanalysis (Ferguson and Villarini 2012).

⁵ The other summer is 1988, which is the fifth hottest following 1936, 1934, 1933, and 1930.

Great Plains (1979–2012)

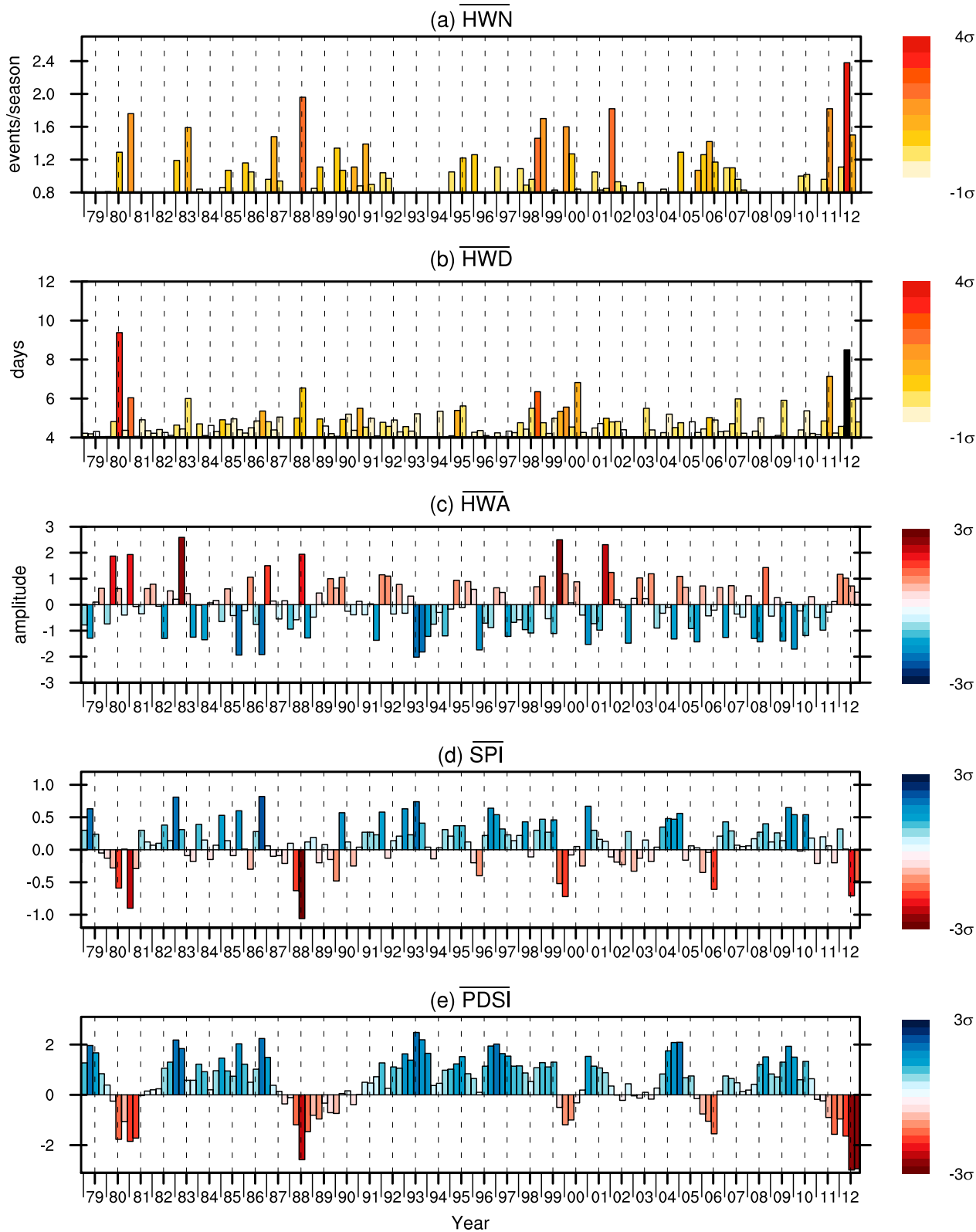


FIG. 5. As in Fig. 4, but for 1979–2012.

TABLE 1. The top 10 driest and wettest boreal springs (MAM), based on the SPI and PDSI averaged over the entire Great Plains, northern Great Plains, and southern Great Plains. Springs during the 1930s are in bold. The springs are ranked from top (driest on record) to middle (10th driest), followed by middle (10th wettest) to bottom (wettest on record).

	Great Plains		Northern Great Plains		Southern Great Plains	
	SPI	PDSI	SPI	PDSI	SPI	PDSI
Driest	1925	1934	1934	1934	1936	1925
	1934	1925	1958	1931	1925	1954
↓	1936	1981	1980	2012	1972	1963
	1956	1963	1926	1977	1954	1956
↓	1988	1931	1988	1988	1963	1967
	1972	2012	1956	1989	1967	1934
↓	1963	1956	1925	1926	1986	1981
	1967	1954	1928	1981	1971	2006
	1954	1977	1931	1925	1956	2000
10th driest	1996	1988	1994	1990	1930	1936
10th wettest	1975	1995	1953	1996	1923	1922
	1927	1942	1975	1975	1929	1993
↑	1929	1920	1922	1973	1997	1920
	1938	1993	1995	1995	1979	1997
↑	1990	1927	1998	1997	1945	1983
	1945	1997	1979	2001	1957	1958
↑	1944	1983	1927	1983	1944	1979
	1979	1975	1938	1986	1990	1949
	1922	1979	2007	1927	1922	1975
Wettest	1973	1973	2011	1979	1973	1973

Wilcoxon signed-rank test) for HWN and HWD, due to the lack of heat wave activity after wet springs. Hotter heat waves are more obvious in the northern Great Plains (Fig. 6c; Fig. S7c), where event anomalies are $\sim 2^\circ\text{C}$ warmer than those in the southern Great Plains, despite their shorter durations and fewer recurrences. In terms of HWN, there are ~ 0.6 – 0.8 more events, on average, after a dry spring than after a wet spring, and these tend to be $\sim 1.4^\circ$ – 1.8°C warmer and ~ 2 – 3 days longer (Figs. 7a–c). The significance in the difference between regionally averaged composites is tested by randomly resampling 1000 sets of 10-yr composites, made up of any summer between 1920 and 2012; this tests whether each heat wave composite could happen by chance after anomalously wet, dry, or average spring preconditioning. The error bars of the resampled 1000 composites signify the 5th and 95th percentiles; thus, for the dry-spring composites, HWN, HWD (based on SPI only) and HWA are unlikely to have occurred by pure chance alone (i.e., are statistically significant). The significant differences in heat wave activity over the Great Plains between the wet and dry spring composites suggests that initial summertime surface conditions are an important factor in determining variations in summer heat wave activity.

d. Dry springs and heat wave timing

For the HWT composites (from SPI-ranked springs), all three heat wave classes (i.e., earliest, longest, hottest) emerge significantly earlier following a dry spring than a

wet spring over the Great Plains and far eastern United States (Fig. 8). The earliest heat waves commence around mid-late June in the dry-spring composite on average, whereas the wet-spring composite events occur well into July/early August (Figs. 8a,b). It is worth noting that more stations are excluded from the wet-spring composite due to a lack of heat wave activity (less than 50% of years in each decade; see the methods section), particularly across the southern Great Plains. This may be due to seasonal atmospheric conditions that persist well beyond spring that dampen any heat wave development, or the anomalously wet surface conditions suppressing heat accumulation through evaporative cooling. Around 25% of stations across the United States show a statistically significant difference in the HWT of their earliest heat wave between the dry and wet composites at the 90% level (stations with a yellow outline in Fig. 8). A possible argument is that the earlier HWT is not necessarily indicative of warmer conditions, but arises from the greater frequency of events (e.g., summers where $\text{HWN} > 2$) after warm dry springs compared to cooler and wetter springs. This assumption is tested for summers where only one event emerges (i.e., $\text{HWN} = 1$; discarding multiple event summers). The results (not shown) indicate that even in the case of single event summers, heat waves occur earlier following dry springs compared to wet springs. Therefore the difference in HWT between the wet- and dry-spring composites is not necessarily due to event frequency; however, this may partially explain some disparity in warm summers where

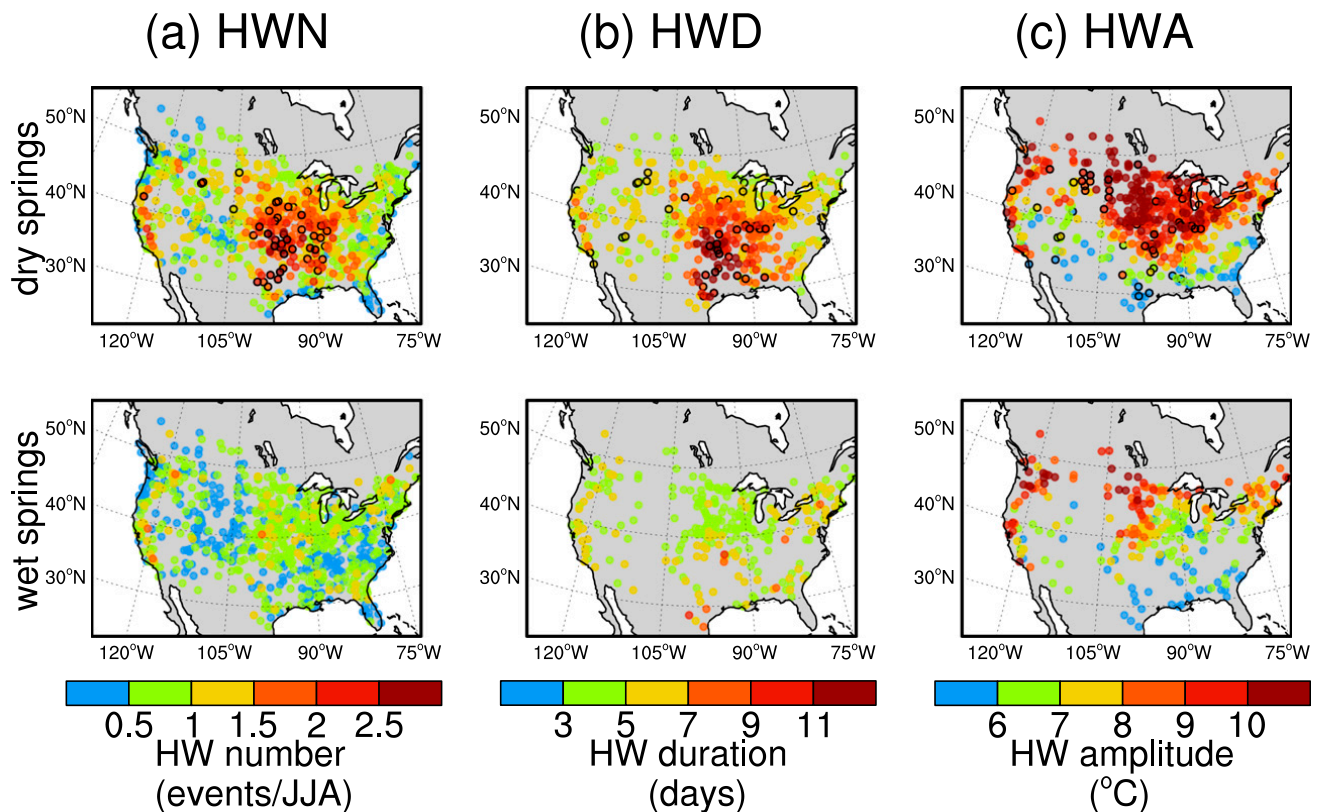


FIG. 6. Composite of summer heat wave metrics following the (top) 10 driest and (bottom) 10 wettest springs over 1920–2012, based on the SPI averaged across the Great Plains; (a) HWN, (b) HWD, and (c) HWA. The sparsity of points in the bottom panels for HWD and HWA reflects the lack of heat wave activity in more than 50% of the summers for the 10-yr samples (as described in the methods section). Black outlined circles indicate stations that show a statistically significant difference at the 90% level between composites, based on a two-sample Wilcoxon signed-rank test (Hollander and Wolfe 1999). Significant differences are only marked on the dry-spring composite maps.

$\text{HWN} > 3$ events or when wet summers follow wet springs (i.e., persistence of atmospheric conditions).

The HWT values of the longest and hottest events are virtually identical for each of the composites (Figs. 8c–f), as protracted heat waves develop when conditions allow for heat accumulation in the lower troposphere, amplifying heat wave intensity (Miralles et al. 2014). Across the Great Plains, these events tend to emerge in late June/early July following dry springs, with events developing earlier (later) in the northern (southern) region (Fig. S7d). On average, the earliest heat waves in the dry-spring composite commence around 27 June, while the longest and hottest events develop ~ 8 –10 days later (Fig. 7d, red dots). Events following wet springs tend to emerge between 17–19 days (earliest) and 16–17 days (longest, hottest) after the dry-spring events. Averaged over the Dust Bowl decade, the earliest heat waves emerged around 3–4 July, closer to the dry-spring composite as expected (not shown). As such, the drought severity in the 1930s may have partly contributed to earlier heat emergence, despite only three springs featuring in the top 10 driest (1931, 1934, 1936; see Table 1).

All three classes of HWT following dry springs are statistically significant (i.e., dry-spring HWTs lie below the 5th percentile of the resampled decades). Following a wet spring, the HWT of all heat wave classes lie toward the far end of the resampled distribution, however they are only statistically significant for the SPI-ranked springs. Averaged over the northern Great Plains, the dry-spring HWT lies farther toward the tail (i.e., occurs much earlier) of the resampled distribution, more so than the wet-spring HWT (i.e., occurs near the center of the resampled distribution; Fig. S7d), as for HWN and HWA. The evidence implies that dry northern soils help determine the emergence date of a heat wave, as well as their recurrence and severity. For the southern Great Plains, where the variance of precipitation is greater (Seager and Hoerling 2014), wetter springs appear to dampen heat wave activity (HWN, HWD, HWA) and delay emergence (HWT) more so than northern Great Plains heat waves that form following wet springs (Fig. S7, bottom panels). Another notable difference between the regions is that heat waves commence ~ 10 days earlier in the north compared to the south.

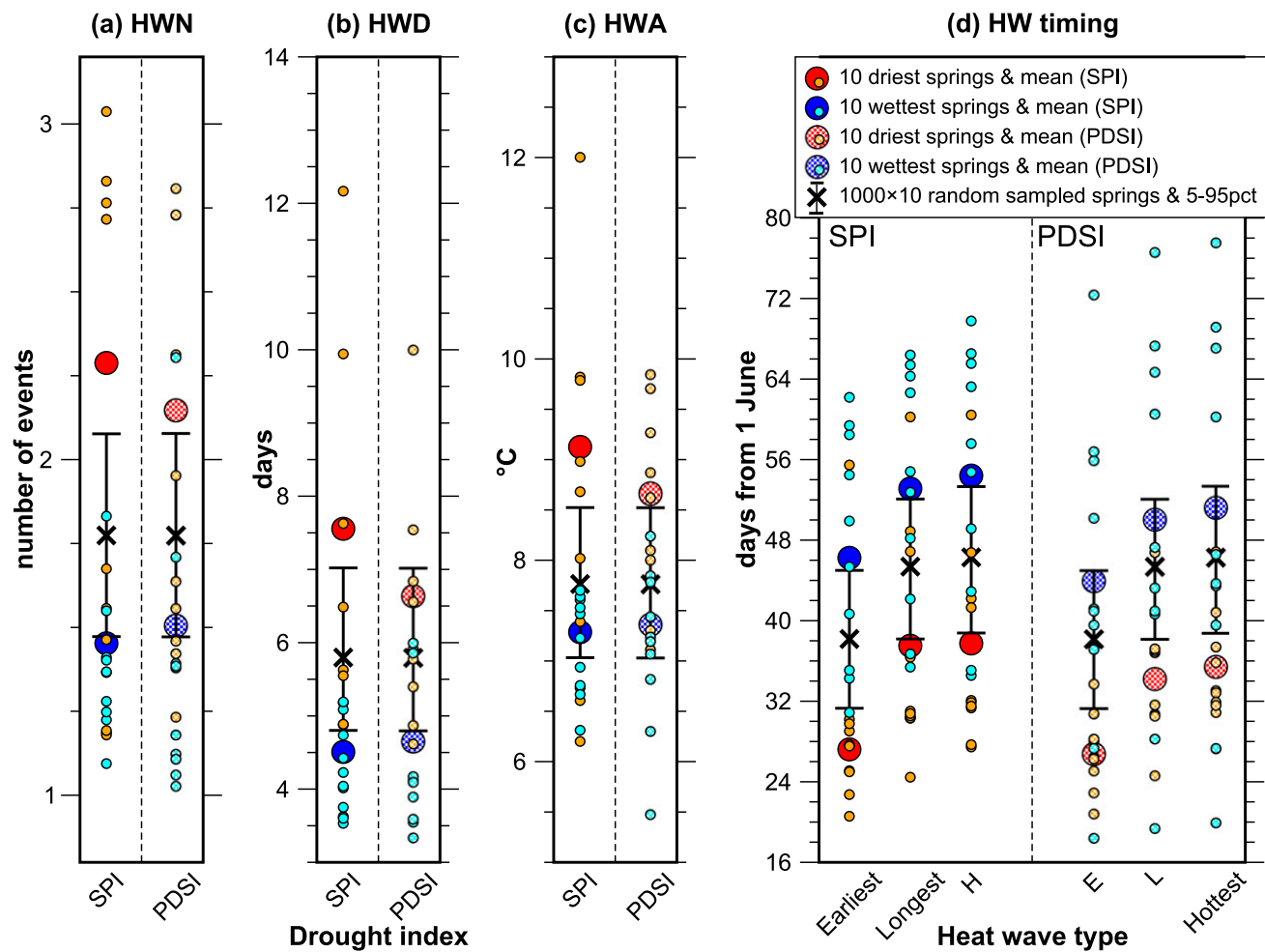


FIG. 7. Summer heat wave metrics from the 10 driest and 10 wettest springs over 1920–2012, averaged across the Great Plains: (a) HWN, (b) HWD, (c) HWA, and (d) heat wave timing (HWT). HWT is shown for the earliest, longest, and hottest heat waves. HWN encompasses all summer heat waves, while HWD and HWA are applicable to the longest and hottest heat waves, respectively. Small filled/shaded orange (light blue) circles represent individual summers following the 10 driest (wettest) springs based on the drought indices, while the large filled red and blue circles represent the summer composite averages. Solid (shaded) circles represent the metrics ranked using the SPI (PDSI). As a test of significance, 1000 sets of 10 randomly sampled years are averaged over all stations in the Great Plains (crosses), with the error bars showing the 5th and 95th percentiles. As such, the composite averages (large circles) lying outside the error bars are unlikely to have occurred by chance alone. The ranking of wet/dry springs for each region is taken from the years in Table 1.

e. Biases in the 20CR

Following on from quantifying the link between anomalous spring conditions and heat wave activity, we now investigate the typical circulation patterns associated with heat waves that occurred over the northern or southern Great Plains (or both); for this we utilize the 20CR gridded ensemble.⁶ Before analyzing the circulation we assess the suitability of the 20CR in capturing heat wave metrics for the three dry-spring summers from the

1930s (1931, 1934, and 1936; see Table 1). A comparison between the GHCN stations and the 20CR ensemble shows that the gridded product broadly captures the location of the HWD and HWN centers over the Great Plains, but it greatly overestimates the HWD by more than 15 days (Fig. 9a). The gridded ensemble also simulates a strong northwest bias, particularly evident in 1934, which is difficult to verify given the sparsity of available Canadian stations in the 1930s with long homogeneous records.

Given the biases in HWD, it follows that HWF biases exist in 20CR (Fig. S8a) as HWD and HWF are proportional, although HWA shows slightly better agreement with the stations over the Great Plains and into southern Canada (Fig. S8b). For other exceptional

⁶ Note that 20CR does not assimilate temperature observations but is constrained by surface pressure; see Compo et al. (2011) for details.

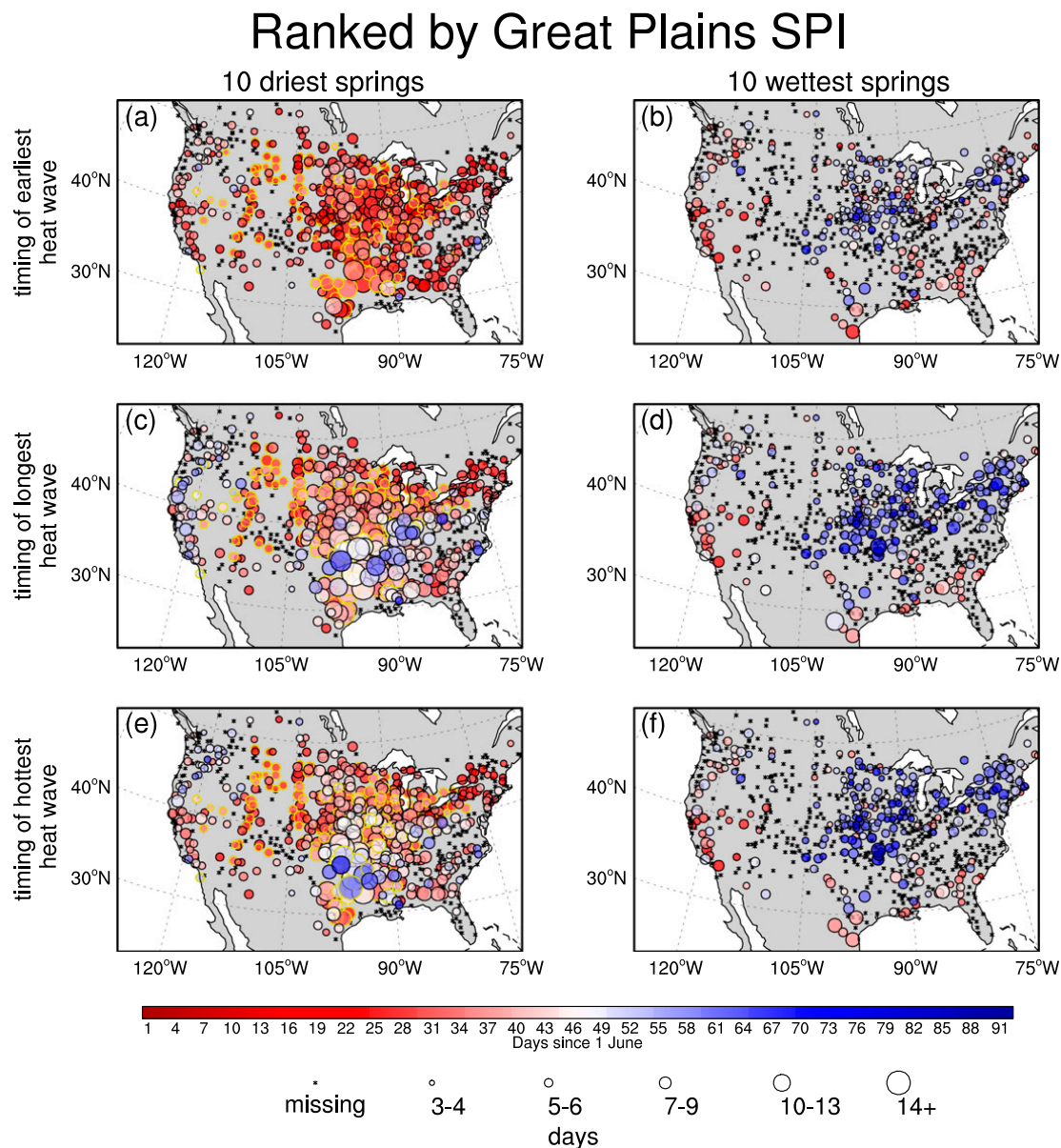


FIG. 8. Composite of summer heat wave timing (HWT; shaded) following the (left) 10 driest and (right) 10 wettest springs over 1920–2012, based on the SPI averaged across the Great Plains. (a),(b) HWT of the earliest event, (c),(d) HWT of the longest event, and (e),(f) HWT of the hottest event. HWT is measured as days since 1 June, where dark red (blue) indicates the start (end) of summer. The circle size indicates the average HWD (in days) of the summer heat waves for each composite for a particular station, while the black asterisks indicates stations that have less than 50% of summers for the 10-yr samples. Yellow circles indicate stations that show a statistically significant difference at the 90% level between composites for the HWT only, based on a two-sample Wilcoxon signed-rank test. The proportion of stations across the United States and Canada that show statistically significant timings based on the SPI ranking is ~25%.

heat wave summers in the northern and southern Great Plains, such as 1954 and 1988, the biases in HWF are smaller in magnitude (not shown). The comparison between 20CR and GHCN stations is marginally better for HWN for the three prominent Dust Bowl summers (Fig. 9b) although specific regional biases are apparent over California and the southeast United

States. Taking these biases into account, we utilize 20CR for identifying the types of synoptic conditions experienced just prior, during, and in the follow-on week after the earliest heat waves. Recent work by Donat et al. (2016) highlighted the magnitude and spatial biases for temperature in 20CR over the Great Plains, and yet considered it applicable in investigating

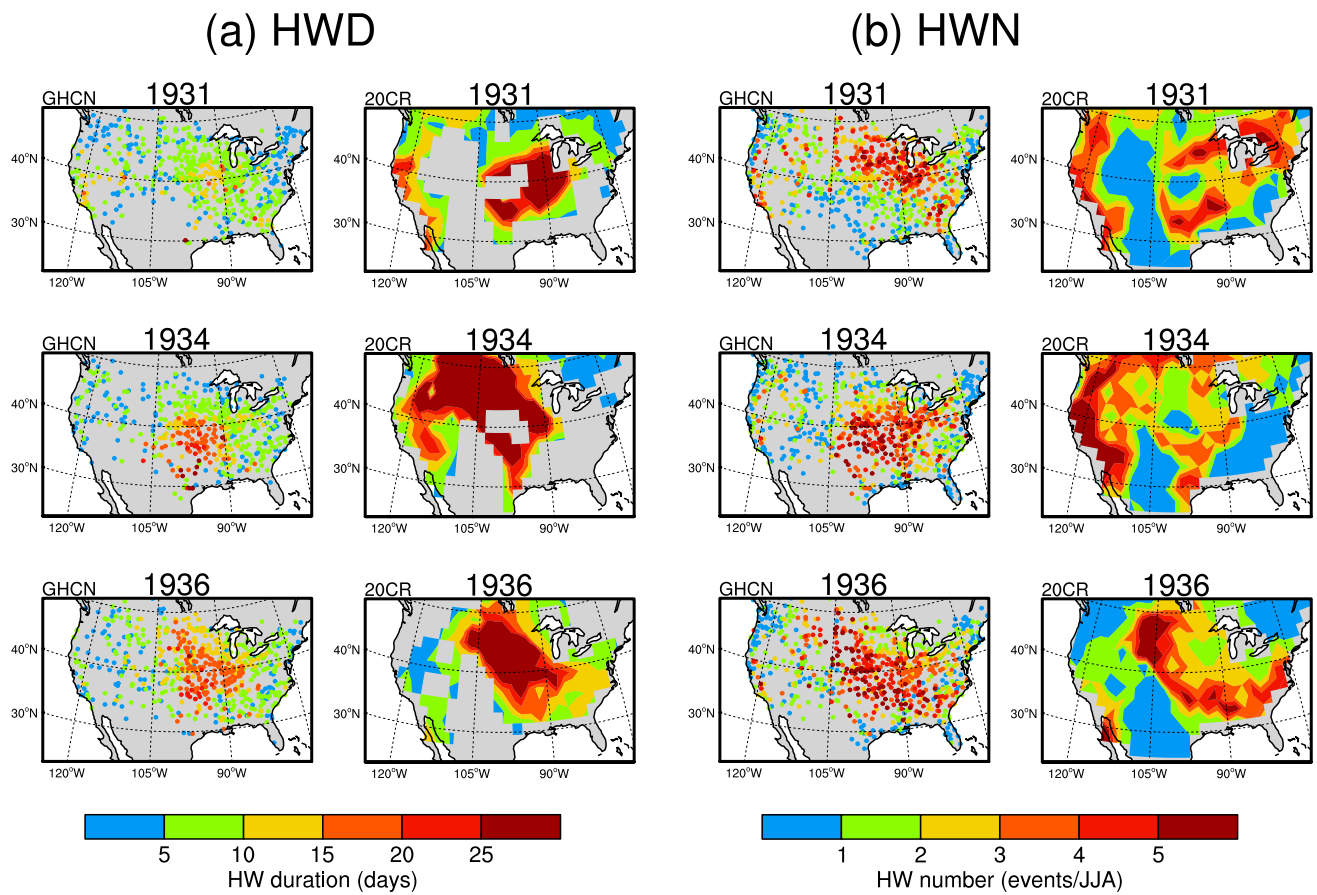


FIG. 9. Comparison of (a) HWD and (b) HWN between (left) GHCN-daily station observations and (right) 20CR for the summers of (top) 1931, (middle) 1934, and (bottom) 1936. The equivalent for HWF and HWA is shown in Fig. S8.

the continental-wide atmospheric circulation during extreme summers in isolation.

f. Aggregating exceptional heat waves

To reiterate, we only investigate the synoptic conditions of the earliest summer events. This conservative approach of evaluating the earliest heat waves instead of all heat waves prevents potential contamination from the same stationary synoptic pattern that could persist for multiple weeks throughout summer, spawning numerous heat waves. Events are aggregated based on timing only when heat wave summers are classified as *exceptional* in terms of HWF. This is determined by ranking the spatially averaged HWF values separately over the northern and southern Great Plains, for every summer from 1920 to 2012. HWF is chosen as it combines information from HWD and HWN. High HWF values are generally associated with summers that feature the longest and hottest heat waves; these have the greatest impact on communities and infrastructure in water-limited regions (e.g., Steffen et al. 2014). We define *exceptional* heat wave summers as those in the top

third of all summers ranked separately for both the northern and southern Great Plains (i.e., 31 out of a possible 93 summers). Summers with exceptional HWF values in both the northern and southern Great Plains are then placed in a separate group that represents the entire Great Plains; these are determined to be the most severe heat waves covering a wider area. The ranked summers and the resultant HWF values averaged over each region are listed in Table 2. The combined northern and southern Great Plains composite consists of 13 summers (and larger average HWF), while the northern and southern Great Plains composites feature 18 summers each (lower HWF). A sufficiently high percentage of stations (>70%) display at least one heat wave event during these exceptional summers making the comparison between the regional composites fair (Fig. S9). Temporal aggregation of the circulation over the week-long phases around the earliest heat wave start date (10% of stations; see methods section) is applied only for the exceptional heat wave summers for each region.

An example of the anomalous MSLP in week 1 (1–7 days) of the heat wave start date for the exceptional

TABLE 2. Summers with *exceptional* heat wave activity, defined as the top third of HWF across the distribution over 1920–2012 ($N = 31$). The top third HWF values are taken from the northern and southern Great Plains separately ($N = 18$), whereas the HWF values in the Great Plains column indicate summers when both the regions exhibit exceptional heat wave activity ($N = 13$). The years are listed in descending order (i.e., highest to lowest) and those in bold (bold with an asterisk) are boreal summers following weak-moderate (strong) El Niño events, based on MSLP and SST-based El Niño–Southern Oscillation metrics. Years listed in italics (italics with an asterisk) are boreal summers following weak-moderate (strong) La Niña episodes. Note that **HWF** represents the average for the composites for each region.

Northern Great Plains		Southern Great Plains		Combined regions (North South)	
Year	HWF	Year	HWF	Year	HWF _N HWF _S
1988	15.04	1954	17.99	1936	19.59 19.97
<i>1955</i>	<i>9.39</i>	<i>2011</i>	<i>17.57</i>	1934	10.07 23.35
1941	8.42	1980	16.43	1953	7.02 13.83
1921	7.56	1952	16.22	1931	13.11 6.80
1995	7.29	<i>1943</i>	<i>11.37</i>	<i>1930</i>	<i>7.35</i> 11.65
<i>1976</i>	<i>6.76</i>	1998*	8.99*	1933	10.03 8.75
1959	6.59	1925	8.75	1947	10.43 7.87
1940	6.49	<i>2000</i>	<i>8.61</i>	1937	10.06 7.41
1991	5.91	2010	8.43	1983*	8.37* 7.82*
1987	5.86	<i>1951</i>	<i>7.63</i>	<i>2012*</i>	<i>6.15*</i> 9.05*
1948	5.84	1924	7.20	1935	4.78 6.50
1968	5.09	2007	7.10	1932	4.81 6.25
1949	5.07	2006	6.54	<i>1956</i>	<i>4.57</i> 6.33
1973	4.58	1978	6.21		
2002	4.25	1990	6.05		
<i>2001</i>	<i>4.13</i>	1969	5.97		
1964	4.13	1944	5.74		
1961	4.08	1922	5.72		
HWF	6.47	HWF	9.58	HWF	8.95 10.43

summers from 1930 to 1937 is shown in Fig. 10. The cluster of stations varies every summer, ranging from tighter grouping in the northern United States in 1931 to a much wider and more scattered coverage in 1935 and 1936, including stations outside the Great Plains (in magenta). From 1933 to 1935 a strong positive MSLP anomaly is observed over the western United States coupled with a negative anomaly over the eastern regions. Weak positive MSLP anomalies over the Midwest are also a feature in 1930, 1931 and 1936. The positive MSLP anomalies over the Midwest show a tendency to strengthen during the week after the heat wave emerges (not shown). The positive MSLP anomaly represents an extension of the subtropical Pacific high, similar to the patterns present across the Midwest in the springs of 1934 and 1936, along with a weaker negative anomaly pattern over the eastern United States (Donat et al. 2016). The presence of a well-formed negative anomaly associated with southern United States heat waves leads to warm southerly anomalies from the Gulf of Mexico (Lau and Nath 2012).

g. Circulation during exceptional heat waves

We first assess how well 20CR captures the heat, in terms of T_{\max} and T_{\min} anomalies, in the weeks (week -1 , week 1, week 2) encompassing the earliest heat wave

(Fig. 11), determined from the station heat wave dates. Circulation composites in the form of MSLP and 500-hPa geopotential height anomalies (Fig. 12) and horizontal temperature advection and 10-m winds (Fig. 13) provide an assessment of the weekly synoptic pattern evolution and flow of heat associated with regionally specific heat waves. Absolute MSLP patterns (rather than anomalies) that highlight the extension of the subtropical highs and weakening of the Midwest United States pressure trough are shown in Fig. S11. For temperature, despite the existence of regional biases between 20CR and GHCN observations (Fig. 11 for T_{\max} , Fig. S10 for T_{\min}), particularly along coastal and mountainous regions (i.e., Rocky Mountains at $\sim 110^\circ\text{W}$), the broad-scale patterns of anomalous warming and cooling compare well. The disparity between 20CR and observations actually improves after the event emergence in weeks 1 and 2, most prominently in regions that experience the most severe heat (Figs. 11b,e,h and Figs. S10b,e,h).

For northern Great Plains exceptional heat waves, warm anomalies $> 1^\circ\text{C}$ appear in a small number (~ 15) of north-central stations ($\sim 50^\circ\text{N}$) in the week prior to the heat wave start (Fig. 11a). The heat progressively shifts southward and intensifies across the northeast ($T_{\max} > 1.5^\circ\text{C}$) in week 1, although temperatures moderate as the event fades in week 2

Earliest heatwave (days 1-7 after event start)

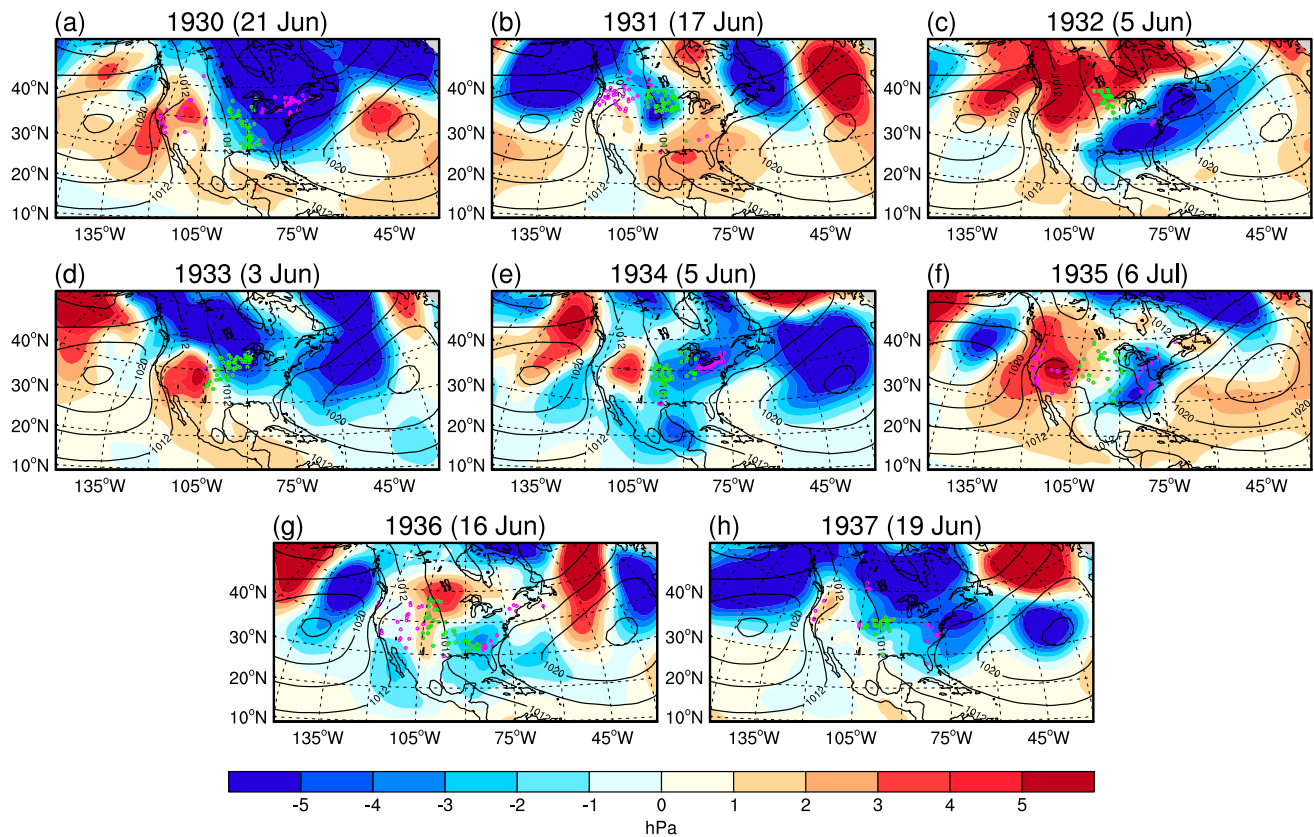


FIG. 10. Mean sea level pressure (MSLP) anomalies (color) and monthly climatologies (contours, from -2.5 to 2.5 hPa with intervals of 1 hPa) averaged over select days (1–7 days) after the commencement of the earliest summer heat wave over 1930–37. The earliest summer heat wave is defined as the date when 10% of GHCN daily stations over each region, respectively, have registered a heat wave start (i.e., cumulative count of stations from 1 June). The locations of the 10% of stations that have registered a heat wave start are shown as green dots, while stations outside of the Great Plains that also exhibit a heat wave start are shown as magenta dots.

(Figs. 11b,c). The associative circulation pattern is one dominated by a prominent Rossby wave train propagating from the northeast Pacific in week 1, with an anomalous upper-level cyclonic pattern east of the Aleutian low region and a downstream anticyclone anomaly extending eastward encompassing the northern Great Plains (Fig. 12b). A strengthening surface trough over the west and a small westward extension of the Atlantic subtropical high are features during week 1 of the heat wave start (Fig. S11b). This results in anomalous easterlies over the southeast United States and southerlies extending north into the northern Great Plains (Fig. 13b). Despite a lack of temperature advection and a weakening of the anomalous upper-level anticyclone in week 2 after heat wave commencement (Fig. 12c), most of the northern Great Plains area remains warmer than average (Fig. 11c); however, the moderation in temperatures reflect the smaller HWF values over the northern Great Plains. The 500-hPa wave pattern is similar to that associated with heat waves over

southeastern Canada, as simulated by a high-resolution atmospheric model forced with historical SST anomalies (Lau and Nath 2012), leading to strong subsidence and adiabatic warming. Thus, adiabatic heating from subsidence induced by an anomalous upper-level anticyclone, not surface temperature advection, appears to be more important in the emergence of northern Great Plains heat waves.

Heat originates in the Southeast prior to southern Great Plains heat waves, and then intensifies and extends northeastward, while T_{\max} anomalies in the West and far Northwest remain anomalously cool ($< -1^{\circ}\text{C}$; Fig. 11d; T_{\min} shown in Fig. S10d). An anomalous upper-level trough extends to the surface over the central North America and farther west, while to the south an anomalous ridge spans the Gulf of Mexico to the northeastern United States (Fig. 12d). A Rossby wave train is apparent during week 1 of the heat wave, with an equivalent barotropic structure over the northern latitudes (Fig. 12e). As such, anomalous southerlies at the

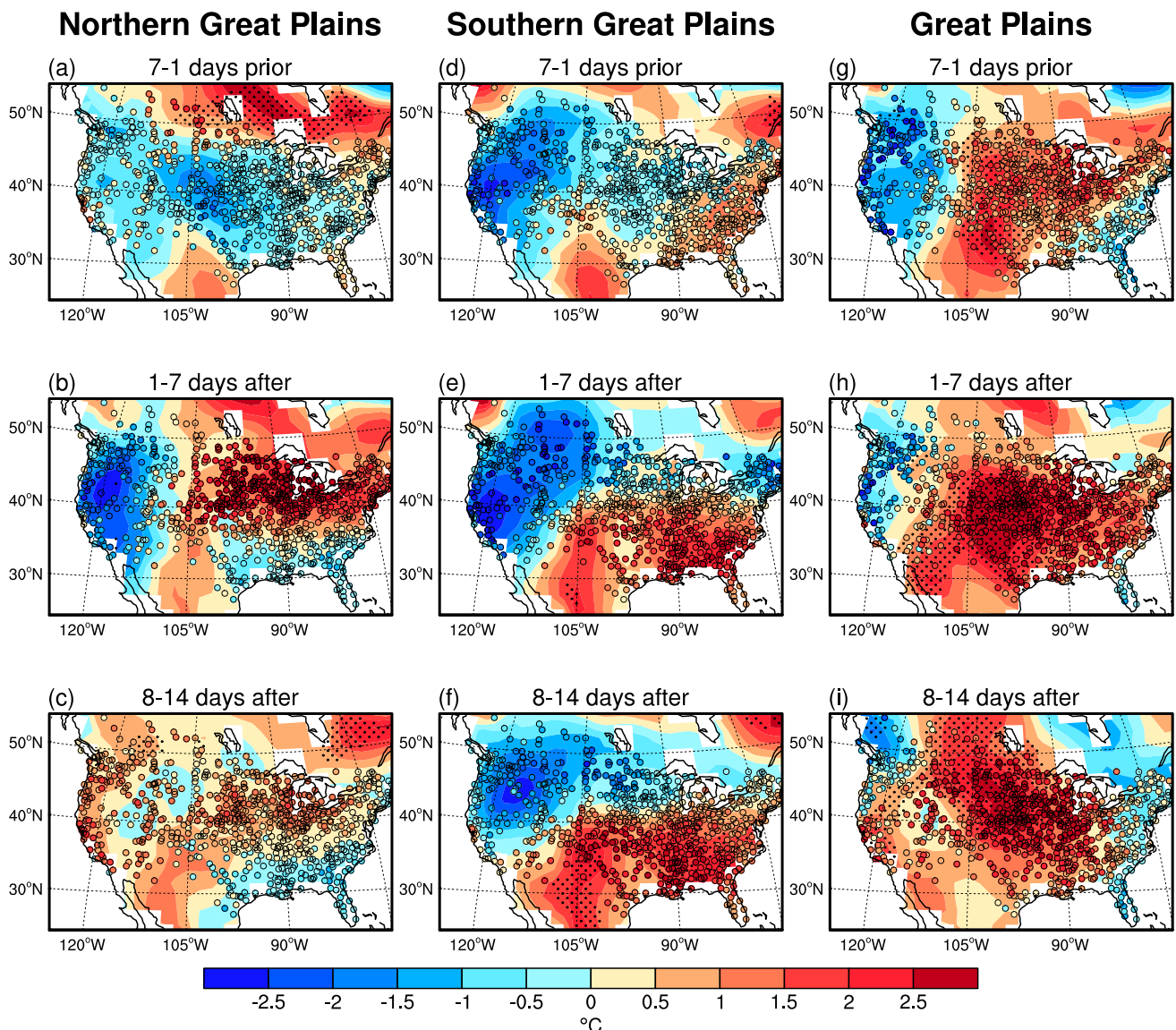


FIG. 11. Composite of T_{\max} anomalies from 20CR (contours) and GHCN-daily stations (dots) averaged over select days (top) prior to (7–1 days prior), (middle) during (1–7 days after), and (bottom) after (8–14 days after) the earliest summer heat wave, for summers when there was exceptional heat wave activity over the (left) northern Great Plains, (middle) southern Great Plains, and (right) entire Great Plains. The earliest summer heat wave is defined as per Fig. 10. The years used in each composite, based on exceptional heat wave activity, are shown in Table 2. Significant T_{\max} anomalies for 20CR are shown with stippling and represent anomalies that are considered significant at the 95% level based on a two-tailed test compared to 1000 randomly resampled composites.

surface advect relatively warm moist air from the Gulf of Mexico across the southern Great Plains (Figs. 13e,f). The small westward extension of the Atlantic subtropical high into the South is also apparent (Fig. S11e), weakening the Midwest trough. In week 2 after the heat wave start the upper-level ridge extending across southern United States appears slightly broader with the continued presence of the anomalous anticyclone over the southern Great Plains, with surface conditions continuing to force advection from the south. This allows T_{\max} and T_{\min} anomalies to remain anomalously warm (Fig. 11f and Fig. S10f), indicating the strength of subsidence and

adiabatic warming associated with the anomalous anticyclone that dominates the anomalous advection.

Anomalous temperatures already exceeding 0.5°C are observed at numerous central stations prior to the Great Plains heat waves, with heat extending from the Deep South to the Great Lakes (Fig. 11g). The heat intensifies rapidly over the central and eastern regions as an upper-level anticyclonic anomaly and surface ridge anomaly strengthen (equivalent barotropic), sitting adjacent to a deepening surface trough to the east (Fig. 12h). Warm, dry air is advected toward the central Great Plains ($\sim 40^{\circ}\text{N}$), circulated from an already warm southern

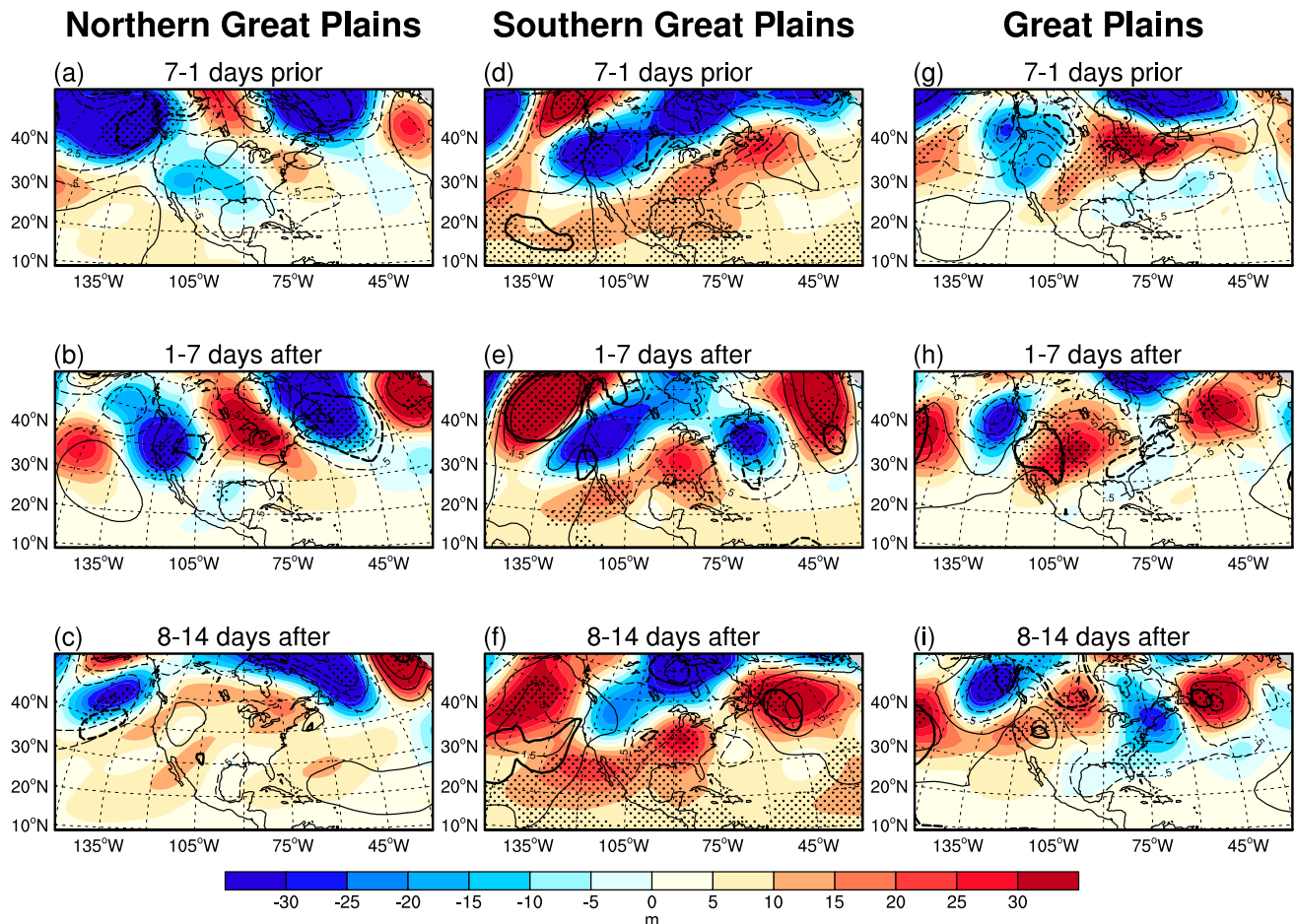


FIG. 12. Composite of 500-hPa geopotential height (color) and mean sea level pressure (MSLP; contours) anomalies averaged over select days (top) prior to (7–1 days before), (middle) during (1–7 days after), and (bottom) after (8–14 days after) the earliest summer heat wave where there was exceptional heat wave activity over the (a) northern, (b) southern, and (c) entire Great Plains. The earliest summer heat wave is defined as in Fig. 10. Significant heights and MSLP are within the stippling and thick contours, respectively, and represent anomalies that are considered significant at the 95% level based on a two-tailed test compared to 1000 randomly resampled composites. MSLP contours cover -2.5 to 2.5 hPa with intervals of 1 hPa.

United States and Mexico (Fig. 13h). As the heat wave develops, heat spreads rapidly westward across the Midwest, with temperature anomalies exceeding 2.5°C , reducing the zonal temperature gradient to the west (Fig. 11i and Fig. S10i). The MSLP pattern in week 1 resembles the pressure dipole pattern associated with the dry springs of 1934 and 1936 (Donat et al. 2016) and early summer conditions from 1933 to 1936 (Fig. 10), and also represents the partial breakdown of the Midwest trough (Fig. S11i). The strong southward warm advection from the subsidence region in the Northwest leads to heat wave intensification and a protracted continental-wide heat wave. The anomalous circulation persists through week 2 (Fig. 12i), and despite a weakening of the anomalous surface ridge, warm advection persists in the South and Midwest (Fig. 13i). Choosing a later heat wave start date (e.g., greater station cumulative count threshold at 33% instead of 10%) results in similar synoptic patterns; for

the Great Plains events, an anomalous surface ridge develops over the Midwest alongside a continental-wide upper level anticyclone anomaly that persists into the second week after the heat wave start (Fig. S12). This suggests that the circulation features are robust with respect to the heat wave start date selection.

4. Discussion and conclusions

This study quantified the record-breaking heat waves over the Great Plains in the 1930s Dust Bowl decade, assessing their spatial extent, duration, frequency, amplitude, and emergence timings. Record-breaking heat wave events are diagnosed using in situ observations and the Twentieth Century Reanalysis, although the latter tends to show stronger and more extensive anomalies. Of the 13 summers that were classified as having *exceptional* heat waves (Table 2)

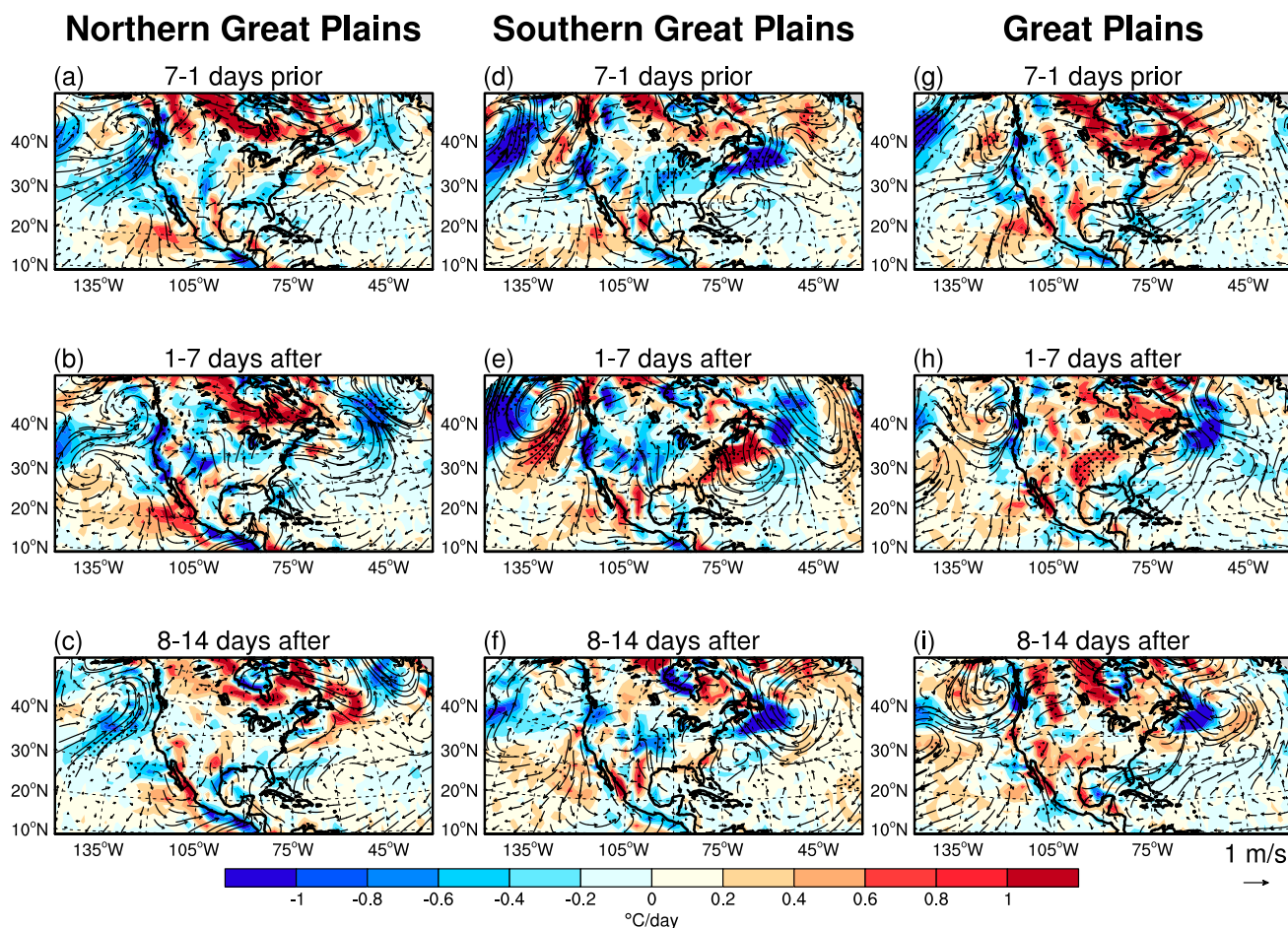


FIG. 13. Composite of anomalous horizontal temperature advection (color) and 10-m winds (vectors) averaged over select days (top) prior to (7–1 days before), (middle) during (1–7 days after), and (bottom) after (8–14 days after) the earliest summer heat wave where there was exceptional heat wave activity over the (left) northern, (middle) southern, and (right) entire Great Plains. The earliest summer heat wave is defined as in Fig. 10. Significant temperature advection anomalies are shown with stippling and significant wind anomalies are thicker; both represent anomalies that are considered significant at the 95% level based on a two-tailed test compared against 1000 sets of randomly resampled composites.

across the Great Plains, eight occurred in the 1930s. Important contributing factors to heat wave activity across the Great Plains, namely anomalously dry spring conditions and early-summer synoptic conditions, were then examined. It was shown that spring precipitation deficits alone (SPI) or a combination of decreased precipitation and anomalously hot conditions (PDSI) not only coincide with earlier summer heat wave emergence, but are also associated with significantly more frequent, longer, and hotter events, even in the case of summers where only one heat wave is observed. In general, dry springs over the northern Great Plains tend to result in earlier and hotter heat waves than for the southern Great Plains, despite longer and more frequent recurrence of events in the south. The risk of heat waves emerging early and redeveloping later in summer increases after a dry spring for the following reasons:

- 1) The surface is anomalously dry (e.g., early 1930s), such that evaporative cooling is essentially negligible, leading to heating of the lower boundary layer through increased sensible heat fluxes during the heat wave, amplifying the heat (Miralles et al. 2014; Yin et al. 2014).
- 2) The tendency exists for quasi-stationary upper-level ridging and blocking, coinciding with a near-surface anticyclone to persist from late spring to summer, that suppresses convection and disrupts advection of relatively moist air from the Gulf of Mexico (prolonging the dry conditions) as observed in 1934⁷ and 1936 (Cook et al. 2014; Donat et al. 2016).

⁷ A similar upper-level blocking pattern occurred in the winter of 1934 as shown in Cook et al. (2014).

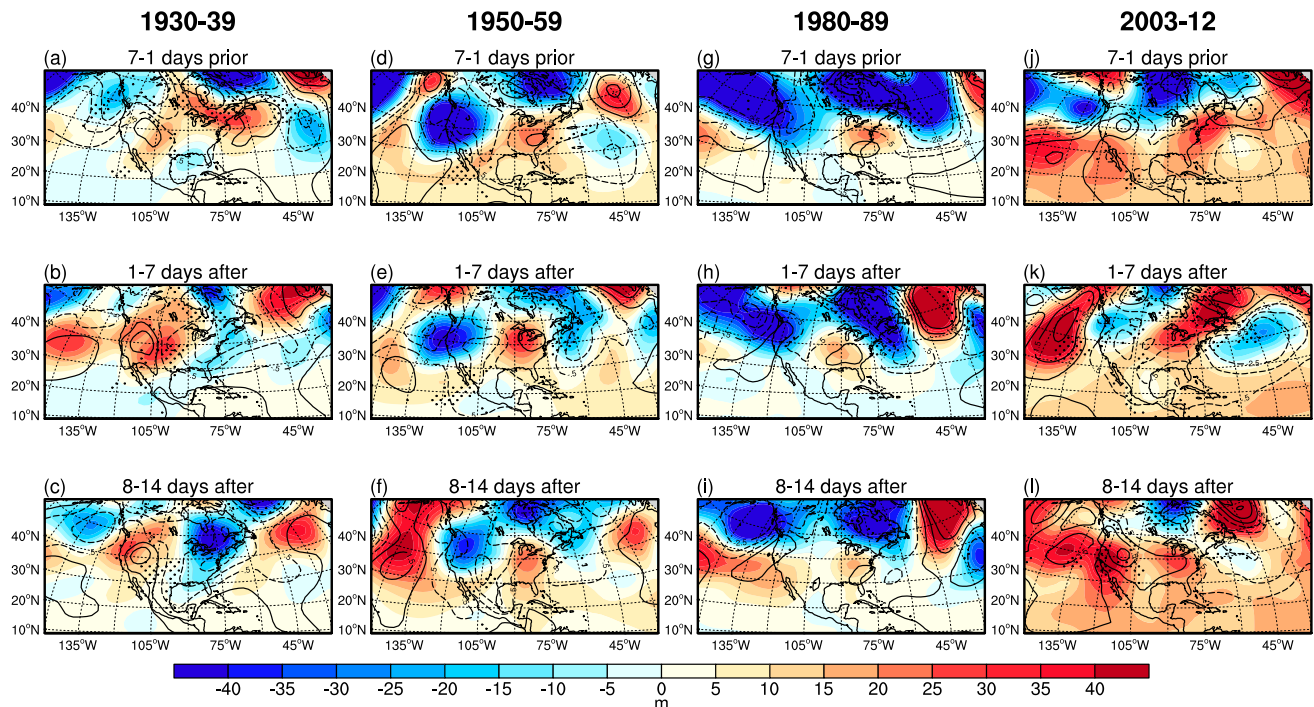


FIG. 14. Composite of 500-hPa geopotential height (color), mean sea level pressure (MSLP; contours) and horizontal temperature advection (stippling) anomalies averaged over select days (top) prior to (7–1 days before), (middle) during (1–7 days after), and (bottom) after (8–14 days after) the earliest summer heat wave when there was exceptional heat wave activity over the Great Plains, for (a)–(c) 1930–39, (d)–(f) 1950–59, (g)–(i) 1980–89, and (j)–(l) 2003–12. Only horizontal temperature advection anomalies $\geq 0.6^{\circ}\text{C day}^{-1}$ are shown, while MSLP contours cover -2.5 to 2.5 hPa with intervals of 1 hPa. The earliest summer heat wave is defined as in Fig. 10.

To quantify the extent to which anomalously dry soil contributed to maintaining an upper-level ridge during the Dust Bowl heat waves would require running sensitivity experiments utilizing a coupled atmosphere–land surface model, including the role of SSTs (Cook et al. 2009). Such models have already been used to determine of the role of precipitation and temperature anomalies on soil moisture variations during drought over the Great Plains (Livneh and Hoerling 2016), and whether initial soil moisture conditions increase summer drought severity through feedbacks on precipitation (Saini et al. 2016). As for heat waves in general, sensitivity experiments based on the 2003 European heat waves have shown that a 25% reduction in soil moisture forces a positive height response in the midtroposphere sitting aloft a surface low (Fischer et al. 2007b). Similarly, Oglesby and Erickson (1989) also related soil moisture deficits to low surface pressures and upper-level ridging in the North American summer using a global atmospheric general circulation model. A possible next step would be to utilize a large enough ensemble of model experiments to test heat wave sensitivity to anomalous soil moisture perturbations and the impact on the overlying circulation (e.g., Fischer et al. 2007a,b).

A further question is why the heat waves in later decades were not as severe as those during the Dust Bowl. Figure 14 displays a comparison of the surface and upper-level circulation between the 1930s and the anomalously dry decades of the 1950s, 1980s, and late 2000s (2003–12), calculated for the weeks before, during, and after heat wave onset. The characteristic anomalous synoptic pattern with a blocking surface anticyclone and upper-level ridge that developed over the Midwest and northeast United States is apparent in the 1930s, along with the advection of anomalously warm air from the northwest to the Great Plains (Figs. 14a–c). Strong adiabatic warming induced by subsidence, along with warm advection, is typical of Midwestern heat waves (Lau and Nath 2012; Grotjahn et al. 2016, and references therein). In contrast, for the heat waves of the 1950s and 1980s we see an upper-level quasi-stationary anticyclone anomaly coupled to a weak surface high anomaly over the eastern United States (Fig. 14, middle columns); this synoptic pattern is conducive to warm moist air from the Gulf of Mexico. The composite circulation pattern over the 2003–12 decade shows a broad upper-level ridge anomaly stretching from the west Pacific to northeast United States and

anomalous surface anticyclone over the west advecting warm air from the northwest in week 2 (Fig. 14l). As such, temperature advection from the north was comparatively weaker, given the lack of an anomalously deep surface low over the southeast (i.e., weaker pressure gradient). This implies that the 1930s heat waves were more severe due to anomalous circulation patterns arising over the continent, leading to strong subsidence-induced warming during heat wave onset, followed by warm advection from the north increasing the event severity.

The link of heat wave to SSTs, both interannual and decadal, has not been covered in this study, although the role of SSTs in forcing historical North American heat waves is an active research area (e.g., Wang et al. 2014; Donat et al. 2016; McKinnon et al. 2016, and references therein). The broad consensus is that SSTs in the Pacific and Atlantic Oceans both acted as potential triggers and amplifiers to the Dust Bowl drought and heat waves (Donat et al. 2016), with idealized SST experiments supporting this argument (e.g., Schubert et al. 2004a,b), although dust forcing and land degradation may have extended the spatial extent of the drought (Cook et al. 2009, 2013). Anomalously warm Atlantic SSTs in the summer months effectively weakened the Great Plains low-level jet, amplifying drought triggered in the spring by Pacific SSTs (Brönnimann et al. 2009). However, for individual summers, such as 1934 and 1936, SST forcing from the tropical Pacific is thought to have played a minor role, as opposed to the bigger role played by the cool Pacific/warm Atlantic in the 1950s drought (Cook et al. 2011). In general, La Niña events tend to increase the frequency of heat wave events across the United States (Jia et al. 2016), although this depends on how heat waves and summer seasons are defined, and the fact that the link is not very strong statistically (Kenyon and Hegerl 2008). Our exceptional heat wave summers occur more often following an El Niño (15 events) than a La Niña (10 events; see Table 2); however, La Niña episodes were associated with sporadic dry seasons in 1988/89, 1999/2000, and 2010–12 (Figs. 5d,e).

Instead of tropical SSTs, it has been suggested that anomalously warm SSTs along the west coast of North America may contribute to drier than average springs, as indicated by a correlation patterns between central United States precipitation and northeast Pacific SSTs (Donat et al. 2016). The SST pattern of the 1930s warm spring and summers is somewhat opposite to that suggested to play a role in eastern United States heat waves in recent decades (i.e., cold North Pacific anomalies; McKinnon et al. 2016). It appears that protracted dry conditions over multiple seasons prior to the severest Dust Bowl summers, along with

characteristic synoptic patterns that initially warmed the Great Plains through subsidence and then through advection, culminated in the record-breaking heat waves of the 1930s. In the decades since, vast improvements in land practices through irrigation and greater drought awareness (Cook et al. 2013) have likely reduced both the severity of drought-induced soil erosion and the risk of springtime dust storms, thus alleviating the threat of the Great Plains temperatures surpassing the Dust Bowl records. It is likely that warmer heat waves will arise in the future over central North America due to enhanced land–atmosphere feedbacks, given large-scale warming. Recent modeling evidence also suggests that the aforementioned heat wave synoptic patterns (i.e., characteristic of the Dust Bowl circulation with an upstream anticyclone over the North Pacific and blocking anticyclone over the central regions) is unlikely to change in the future (Teng et al. 2016). Critically, future work will be aimed at better understanding the role of SSTs in triggering Dust Bowl-type heat waves, the importance of spring precipitation deficits carrying through to summer, and whether an early-twentieth-century greenhouse gas forcing played any role in the Dust Bowl heat severity. The ultimate aim is to provide better predictive capability of the most severe heat waves across the Great Plains based on a set of key indicators.

Acknowledgments. This study forms part of the Transition into the Anthropocene (TITAN) project, funded by a European Research Council (ERC) Advanced Grant (EC-320691), and was further supported by the EUCLEIA project funded by the European Union's Seventh Framework Programme (FP7/2007–13) under Grant Agreement 607085. G. Hegerl is also supported by National Centre for Atmospheric Science (NCAS) and the Wolfson Foundation and the Royal Society as a Royal Society Wolfson Research Merit Award (WM130060) holder. We thank the National Oceanic and Atmospheric Administration/National Climatic Data Center (NOAA/NCDC) for the use of the GHCN daily data. Support for the 20CR Project version 2c dataset is provided by the United States Department of Energy, Office of Science Biological and Environmental Research, and by the National Oceanic and Atmospheric Administration Climate Program Office.

REFERENCES

- Abatzoglou, J. T., and R. Barbero, 2014: Observed and projected changes in absolute temperature records across the contiguous United States. *Geophys. Res. Lett.*, **41**, 6501–6508, doi:10.1002/2014GL061441.

- Brönnimann, S., and Coauthors, 2009: Exceptional atmospheric circulation during the “Dust Bowl.” *Geophys. Res. Lett.*, **36**, L08802, doi:10.1029/2009GL037612.
- Compo, G. P., and Coauthors, 2011: The Twentieth Century Reanalysis Project. *Quart. J. Roy. Meteor. Soc.*, **137**, 1–28, doi:10.1002/qj.776.
- Cook, B. I., R. L. Miller, and R. Seager, 2009: Amplification of the North American “Dust Bowl” drought through human-induced land degradation. *Proc. Natl. Acad. Sci. USA*, **106**, 4997–5001, doi:10.1073/pnas.0810200106.
- , R. Seager, and R. L. Miller, 2011: Atmospheric circulation anomalies during two persistent North American droughts: 1932–1939 and 1948–1957. *Climate Dyn.*, **36**, 2339–2355, doi:10.1007/s00382-010-0807-1.
- , —, —, and J. A. Mason, 2013: Intensification of North American megadroughts through surface and dust aerosol forcing. *J. Climate*, **26**, 4414–4430, doi:10.1175/JCLI-D-12-00022.1.
- , —, and J. E. Smerdon, 2014: The worst North American drought year of the last millennium: 1934. *Geophys. Res. Lett.*, **41**, 7298–7305, doi:10.1002/2014GL061661.
- Cowan, T., A. Purich, S. Perkins, A. Pezza, G. Bosch, and K. Sadler, 2014: More frequent, longer, and hotter heat waves for Australia in the twenty-first century. *J. Climate*, **27**, 5851–5871, doi:10.1175/JCLI-D-14-00092.1.
- Dai, A., 2011: Characteristics and trends in various forms of the Palmer Drought Severity Index during 1900–2008. *J. Geophys. Res.*, **116**, D12115, doi:10.1029/2010JD015541.
- , K. E. Trenberth, and T. Qian, 2004: A global dataset of Palmer Drought Severity Index for 1870–2002: Relationship with soil moisture and effects of surface warming. *J. Hydrometeorol.*, **5**, 1117–1130, doi:10.1175/JHM-386.1.
- Diffenbaugh, N. S., and M. Ashfaq, 2010: Intensification of hot extremes in the United States. *Geophys. Res. Lett.*, **37**, L15701, doi:10.1029/2010GL043888.
- Donat, M. G., L. V. Alexander, H. Yang, I. Durre, R. Vose, and J. Caesar, 2013a: Global land-based datasets for monitoring climatic extremes. *Bull. Amer. Meteor. Soc.*, **94**, 997–1006, doi:10.1175/BAMS-D-12-00109.1.
- , and Coauthors, 2013b: Updated analyses of temperature and precipitation extreme indices since the beginning of the twentieth century: The HadEX2 dataset. *J. Geophys. Res. Atmos.*, **118**, 2098–2118, doi:10.1002/jgrd.50150.
- , A. D. King, J. T. Overpeck, L. V. Alexander, I. Durre, and D. J. Karoly, 2016: Extraordinary heat during the 1930s US Dust Bowl and associated large-scale conditions. *Climate Dyn.*, **46**, 413–426, doi:10.1007/s00382-015-2590-5.
- Ferguson, C. R., and G. Villarini, 2012: Detecting inhomogeneities in the Twentieth Century Reanalysis over the central United States. *J. Geophys. Res.*, **117**, D05123, doi:10.1029/2011JD016988.
- Fischer, E. M., S. I. Seneviratne, D. Lüthi, and C. Schär, 2007a: Contribution of land–atmosphere coupling to recent European summer heat waves. *Geophys. Res. Lett.*, **34**, L06707, doi:10.1029/2006GL029068.
- , —, P. L. Vidale, D. Lüthi, and C. Schär, 2007b: Soil moisture–atmosphere interactions during the 2003 European summer heat wave. *J. Climate*, **20**, 5081–5099, doi:10.1175/JCLI4288.1.
- Grotjahn, R., and Coauthors, 2016: North American extreme temperature events and related large-scale meteorological patterns: A review of statistical methods, dynamics, modeling, and trends. *Climate Dyn.*, **46**, 1151–1184, doi:10.1007/s00382-015-2638-6.
- Hoerling, M., and A. Kumar, 2003: The perfect ocean for drought. *Science*, **299**, 691–694, doi:10.1126/science.1079053.
- Hollander, M., and D. A. Wolfe, 1999: *Nonparametric Statistical Methods*. John Wiley and Sons, 787 pp.
- Jeong, D. I., L. Sushama, G. T. Diro, M. N. Khaliq, H. Beltrami, and D. Caya, 2016: Projected changes to high temperature events for Canada based on a regional climate model ensemble. *Climate Dyn.*, **46**, 3163–3180, doi:10.1007/s00382-015-2759-y.
- Jia, L., and Coauthors, 2016: The roles of radiative forcing, sea surface temperatures, and atmospheric and land initial conditions in U.S. summer warming episodes. *J. Climate*, **29**, 4121–4135, doi:10.1175/JCLI-D-15-0471.1.
- Jones, B., B. C. O'Neill, L. McDaniel, S. McGinnis, L. O. Mearns, and C. Tebaldi, 2015: Future population exposure to US heat extremes. *Nat. Climate Change*, **5**, 652–655, doi:10.1038/nclimate2631.
- Kenyon, J., and G. C. Hegerl, 2008: Influence of modes of climate variability on global temperature extremes. *J. Climate*, **21**, 3872–3889, doi:10.1175/2008JCLI2125.1.
- Koster, R. D., and Coauthors, 2004: Regions of strong coupling between soil moisture and precipitation. *Science*, **305**, 1138–1140, doi:10.1126/science.1100217.
- Lau, N.-C., and M. J. Nath, 2012: A model study of heat waves over North America: Meteorological aspects and projections for the twenty-first century. *J. Climate*, **25**, 4761–4764, doi:10.1175/JCLI-D-11-00575.1.
- Livezey, R. E., and R. Tinker, 1996: Some meteorological, climatological, and microclimatological considerations of the severe U.S. heat wave of mid-July 1995. *Bull. Amer. Meteor. Soc.*, **77**, 2043–2054, doi:10.1175/1520-0477(1996)077<2043:SMCAMC>2.0.CO;2.
- Livneh, B., and M. P. Hoerling, 2016: The physics of drought in the U.S. central Great Plains. *J. Climate*, **29**, 6783–6804, doi:10.1175/JCLI-D-15-0697.1.
- Mattice, W. A., 1935: Dust storms. *Mon. Wea. Rev.*, **63**, 113–115, doi:10.1175/1520-0493(1935)63<113b:DS>2.0.CO;2.
- McKee, T. B., N. J. Doesken, and J. Kleist, 1993: The relationship of drought frequency and duration to time scales. *Proc. Eighth Conf. on Applied Climatology*, Anaheim, CA, Amer. Meteor. Soc., 179–183.
- McKinnon, K. A., A. Rhines, M. P. Tingley, and P. Huybers, 2016: Long-lead predictions of eastern United States hot days from Pacific sea surface temperatures. *Nat. Geosci.*, **9**, 389–394, doi:10.1038/ngeo2687.
- Meehl, G. A., and C. Tebaldi, 2004: More intense, more frequent, and longer lasting heat waves in the 21st century. *Science*, **305**, 994–997, doi:10.1126/science.1098704.
- Menne, M. J., I. Durre, R. S. Vose, B. E. Gleason, and T. G. Houston, 2012: An overview of the global historical climatology network-daily database. *J. Atmos. Oceanic Technol.*, **29**, 897–910, doi:10.1175/JTECH-D-11-00103.1.
- Miralles, D. G., A. J. Teuling, C. C. van Heerwaarden, and J. Vilà-Guerau de Arellano, 2014: Mega-heatwave temperatures due to combined soil desiccation and atmospheric heat accumulation. *Nat. Geosci.*, **7**, 345–349, doi:10.1038/ngeo2141.
- Morak, S., G. C. Hegerl, and N. Christidis, 2013: Detectable changes in the frequency of temperature extremes. *J. Climate*, **26**, 1561–1574, doi:10.1175/JCLI-D-11-00678.1.
- Mueller, B., and S. I. Seneviratne, 2012: Hot days induced by precipitation deficits at the global scale. *Proc. Natl. Acad. Sci. USA*, **109**, 12 398–12 403, doi:10.1073/pnas.1204330109.
- Nairn, J., and R. Fawcett, 2013: Defining heatwaves: Heatwave defined as a heat-impact event servicing all community and business sectors in Australia. CAWCR Tech. Rep. 060, 84 pp.

- Oglesby, R. J., and D. J. Erickson, 1989: Soil moisture and the persistence of North American drought. *J. Climate*, **2**, 1362–1380, doi:[10.1175/1520-0442\(1989\)002<1362:SMATPO>2.0.CO;2](https://doi.org/10.1175/1520-0442(1989)002<1362:SMATPO>2.0.CO;2).
- Perkins, S. E., and L. V. Alexander, 2013: On the measurement of heat waves. *J. Climate*, **26**, 4500–4517, doi:[10.1175/JCLI-D-12-00383.1](https://doi.org/10.1175/JCLI-D-12-00383.1).
- , —, and J. R. Nairn, 2012: Increasing frequency, intensity and duration of observed global heatwaves and warm spells. *Geophys. Res. Lett.*, **39**, L20714, doi:[10.1029/2012GL053361](https://doi.org/10.1029/2012GL053361).
- , D. Argüeso, and C. J. White, 2015: Relationships between climate variability, soil moisture, and Australian heatwaves. *J. Geophys. Res.*, **120**, 8144–8164, doi:[10.1002/2015JD023592](https://doi.org/10.1002/2015JD023592).
- Peterson, T. C., and Coauthors, 2013: Monitoring and understanding changes in heat waves, cold waves, floods, and droughts in the United States: State of knowledge. *Bull. Amer. Meteor. Soc.*, **94**, 821–834, doi:[10.1175/BAMS-D-12-00066.1](https://doi.org/10.1175/BAMS-D-12-00066.1).
- Pezza, A. B., P. van Rensch, and W. Cai, 2012: Severe heat waves in southern Australia: Synoptic climatology and large scale connections. *Climate Dyn.*, **38**, 209–224, doi:[10.1007/s00382-011-1016-2](https://doi.org/10.1007/s00382-011-1016-2).
- Saini, R., G. Wang, and J. S. Pal, 2016: Role of soil moisture feedback in the development of extreme summer drought and flood in the United States. *J. Hydrometeor.*, **17**, 2191–2207, doi:[10.1175/JHM-D-15-0168.1](https://doi.org/10.1175/JHM-D-15-0168.1).
- Schubert, S. D., M. J. Suarez, P. J. Pegion, R. D. Koster, and J. T. Bacmeister, 2004a: On the cause of the 1930s Dust Bowl. *Science*, **303**, 1855–1859, doi:[10.1126/science.1095048](https://doi.org/10.1126/science.1095048).
- , —, —, —, and —, 2004b: Causes of long-term drought in the U.S. Great Plains. *J. Climate*, **17**, 485–503, doi:[10.1175/1520-0442\(2004\)017<0485:COLDIT>2.0.CO;2](https://doi.org/10.1175/1520-0442(2004)017<0485:COLDIT>2.0.CO;2).
- Seager, R., and M. Hoerling, 2014: Atmosphere and ocean origins of North American droughts. *J. Climate*, **27**, 4581–4606, doi:[10.1175/JCLI-D-13-00329.1](https://doi.org/10.1175/JCLI-D-13-00329.1).
- Steffen, W., L. Hughes, and S. Perkins, 2014: Heatwaves: Hotter, longer, more often. Climate Council of Australia, 63 pp. [Available online at <https://www.climatecouncil.org.au/heatwaves-report/>.]
- Teng, H., G. Branstator, H. Wang, G. A. Meehl, and W. M. Washington, 2013: Probability of US heat waves affected by a subseasonal planetary wave pattern. *Nat. Geosci.*, **6**, 1056–1061, doi:[10.1038/ngeo1988](https://doi.org/10.1038/ngeo1988).
- , —, G. A. Meehl, and W. M. Washington, 2016: Projected intensification of subseasonal temperature variability and heat waves in the Great Plains. *Geophys. Res. Lett.*, **43**, 2165–2173, doi:[10.1002/2015GL067574](https://doi.org/10.1002/2015GL067574).
- Wang, H., S. Schubert, R. Koster, Y.-G. Ham, and M. Suarez, 2014: On the role of SST forcing in the 2011 and 2012 extreme U.S. heat and drought: A study in contrasts. *J. Hydrometeor.*, **15**, 1255–1273, doi:[10.1175/JHM-D-13-069.1](https://doi.org/10.1175/JHM-D-13-069.1).
- Yin, D., M. L. Roderick, G. Leech, F. Sun, and Y. Huang, 2014: The contribution of reduction in evaporative cooling to higher surface air temperatures during drought. *Geophys. Res. Lett.*, **41**, 7891–7897, doi:[10.1002/2014GL062039](https://doi.org/10.1002/2014GL062039).
- Yu, J.-Y., and Y. Zou, 2013: The enhanced drying effect of Central-Pacific El Niño on US winter. *Environ. Res. Lett.*, **8**, 014019, doi:[10.1088/1748-9326/8/1/014019](https://doi.org/10.1088/1748-9326/8/1/014019).